

BIROn - Birkbeck Institutional Research Online

Enabling Open Access to Birkbeck's Research Degree output

Rhyolite Generation at a Migrating Volcanic Centre: Atitlán, Guatemala

<https://eprints.bbk.ac.uk/id/eprint/55877/>

Version: Full Version

Citation: Gilchrist, Finley Jack (2025) Rhyolite Generation at a Migrating Volcanic Centre: Atitlán, Guatemala. [Thesis] (Unpublished)

© 2020 The Author(s)

All material available through BIROn is protected by intellectual property law, including copyright law.

Any use made of the contents should comply with the relevant law.

[Deposit Guide](#)
Contact: [email](#)

Rhyolite Generation at a Migrating Volcanic Centre: Atitlán, Guatemala

Finley Jack Gilchrist

Thesis submitted for the degree of Doctor of Philosophy

2023



Department of Earth and Planetary
Sciences, Birkbeck College,
University of London

Volcano Petrology Group, Natural
History Museum, London

Abstract

Volcanic super-eruptions are some of the most devastating natural events on Earth. Each eruption is unique, so it is vital to study the deposits of as many eruptions as possible to understand the processes that can lead to their formation. Several factors are tied to the formation of massive volumes of eruptible silicic magma that feed these eruptions, and one factor is migration of the position of the associated volcanic arcs in which they occur.

To examine the potential link between the migration of volcanic arcs and large-scale explosive eruptions, I have studied the Atitlán Volcanic centre (AVC), which lies in the central Guatemalan segment of the Central American volcanic arc (CAVA). Here volcanism is strongly controlled by trenchwards arc migration and large explosive eruptions are relatively commonplace. The AVC has produced several super-eruptions in the last 14 Ma, the most recent being the 75 ka Los Chocoyos (LCY) eruption, in which 510 km³ (dense rock equivalent) of volcanic material was erupted. The eruption's vents (and likely the feeding magma body) lay between the old and new positions of the arc, in an area now occupied by the Atitlán caldera. Several pre- and post-caldera stratovolcanoes associated with the Atitlán caldera mark the migration of arc. The shift in the nature of the activity from stratovolcano construction to explosive activity occurred shortly after the trenchward migration of the stratovolcanoes' locations. Explosive activity appears to have ceased after volcanism migrated out of the caldera margins.

This investigation involved the use of multiple different methods involving sample collection fieldwork, whole rock major, minor, trace element and radiogenic isotope geochemistry, mineral chemistry and the use geothermobarometric and computational petrogenetic models. These showed that stratovolcano lavas are K₂O and LILE enriched andesites, caused by hybridisation of mafic magmas with highly potassic rhyolite melts generated in the upper crust.

Products of the LCY eruption contained at least four different magma types, including three rhyolites that are classified according to their mineralogy and K₂O content into amphibole-bearing "low-K", biotite-bearing "high-K" rhyolites, and the newly identified amphibole- and biotite-bearing "medium-K" rhyolite. The fourth magma type is represented by a mafic recharge magma. Petrogenetic modelling showed that the high-K LCY rhyolite is the result of fractional crystallisation of the K₂O and LILE enriched stratovolcano magmas. However, the low-K LCY rhyolite cannot be generated from the same source, and it is likely generated from a LILE-poor magma. The medium-K rhyolite is geochemically similar to the low-K rhyolite and is classified as a sub-group of this magma.

Isotopic values of the stratovolcanoes become more radiogenic away from the trench and the LCY magmas have intermediate isotope values between the stratovolcano endmembers. Extraction of magma from the width of the AVC (marked by initial and final positions of the stratovolcanoes) and subsequent homogenisation can explain the intermediate isotopic signature of the LCY magmas compared to the stratovolcano endmembers. Arc migration therefore had a strong control on both the position of the large-volume rhyolite magma bodies, and on their compositions. With the formation of the most recent stratovolcano (Volcán Atitlán) outside of the caldera margins, closer to the trench, and the cessation of explosive activity, it appears that the longevity of these explosive rhyolitic volcanic systems can therefore also be controlled by arc migration.

Table of Contents

| | |
|---|-----------|
| Chapter 1: Introduction and Background | 20 |
| 1.1 Research aims and objectives, and thesis structure..... | 20 |
| 1.2 Current understanding of the generation of silicic magmas and caldera-forming events..... | 24 |
| 1.2.1 Generating and storing evolved magmas | 25 |
| 1.2.2 Triggering mechanisms for large volume silicic eruptions..... | 29 |
| 1.2.3 Where (and when) do silicic super-eruptions occur? | 32 |
| 1.3 The Central American volcanic arc..... | 35 |
| 1.3.1 Structure of the Central American volcanic arc..... | 35 |
| 1.3.2 History of volcanic activity along the CAVA | 40 |
| 1.3.3 Along-arc geochemical variations | 41 |
| 1.3.4 Across-arc geochemical variations..... | 44 |
| 1.4 The Atitlán Volcanic Centre | 47 |
| 1.4.1 Stratigraphy of the Atitlán volcanic centre and description of the units..... | 47 |
| 1.4.2 The AVC stratovolcanoes | 50 |
| 1.4.3 The AVC rhyolites | 51 |
| Chapter 2: Sampling and Analytical Methods..... | 55 |
| 2.1 Fieldwork..... | 55 |
| 2.2 Sample preparation | 62 |
| 2.2.1 Whole rock powders | 62 |
| 2.2.2 Thin sections | 62 |
| 2.3 Instrumental analyses | 63 |
| 2.3.1 Major elements..... | 63 |
| 2.3.2 Trace elements..... | 63 |
| 2.3.3 Radiogenic isotopes | 65 |
| 2.4 Petrography and petrology | 68 |
| 2.4.1 Petrographic imaging | 68 |
| 2.4.2 EPMA analyses | 69 |
| 2.4.3 LA-ICP-MS..... | 71 |
| Chapter 3. Petrography, Mineralogy and Mineral Chemistry | 73 |
| 3.1 Terminology | 73 |
| 3.1.1 Los Chocoyos (LCY) pumices | 73 |
| 3.1.2 Rock groupings..... | 73 |
| 3.1.3 Open system terminology:..... | 73 |
| 3.2 Petrography and mineral chemistry | 74 |

| | |
|---|------------|
| 3.2.1 Stratovolcano lavas | 74 |
| 3.2.1.1 Stratovolcano petrography | 75 |
| 3.2.1.2 Stratovolcanoes mineral chemistry | 89 |
| 3.2.2 Intermediate composition clasts | 96 |
| 3.2.2.1 Petrography of the intermediate composition clasts | 96 |
| 3.2.2.2 Mineral chemistry of the intermediate composition clasts..... | 99 |
| 3.2.3 LCY pumices | 101 |
| 3.2.3.1 LCY pumice petrography | 101 |
| 3.2.3.2 LCY pumice mineral chemistry | 105 |
| 3.2.4 Post-LCY pumices | 107 |
| 3.2.4.1 Post-LCY pumice petrography..... | 107 |
| 3.2.4.2 Mineral chemistry of the post-LCY pumices | 112 |
| 3.2.5 Enclaves and mingled pumices | 114 |
| 3.2.5.1 Mineral and rock textures of the enclaves and mingled pumices | 114 |
| 3.2.5.2 Mineral chemistries of the enclaves and mingled pumices..... | 121 |
| 3.2.6 Intrusive rocks | 124 |
| 3.3 Summary | 125 |
| 3.3.1 Plagioclase composition comparison:..... | 125 |
| 3.3.2 Pyroxene composition comparisons | 127 |
| 3.3.3 Olivine composition comparisons | 127 |
| Chapter 4. Geochemistry of the AVC samples | 130 |
| 4.1 Whole rock major element results | 130 |
| 4.1.1 Stratovolcano lavas | 131 |
| 4.1.2 Recharge magma | 133 |
| 4.1.3 Los Chocoyos (LCY) pumices | 133 |
| 4.1.4 Post-LCY pumices | 134 |
| 4.1.5 Intrusive rocks..... | 135 |
| 4.2 Whole rock trace element results..... | 135 |
| 4.2.1 Stratovolcano lavas | 135 |
| 4.2.2 Recharge magma | 138 |
| 4.2.3 LCY pumices | 140 |
| 4.2.4 Post-LCY pumices | 141 |
| 4.2.5 Intrusive rocks | 142 |
| 4.3 Whole rock radiogenic isotope results | 143 |
| 4.3.1 Stratovolcano lavas | 143 |
| 4.3.2 Recharge magma | 149 |
| 4.3.3 The LCY pumices | 149 |

| | |
|---|------------|
| 4.3.4 Post-LCY pumices | 149 |
| 4.3.5 Intrusive suite..... | 150 |
| 4.4 Glass compositions | 150 |
| 4.4.1 Major elements..... | 150 |
| 4.4.1.1 Rhyolite pumice matrix glasses..... | 150 |
| 4.4.1.2 Post-LCY intermediate tephra matrix glasses | 152 |
| 4.4.1.3 Stratovolcano hosted glass | 153 |
| 4.4.2 Trace elements..... | 156 |
| Chapter 5: Origin and evolution of the AVC magmas | 159 |
| 5.1 Origin of the AVC stratovolcano suite..... | 159 |
| 5.1.1 The basaltic andesites | 159 |
| 5.1.1.1 North-western CAVA basaltic andesite chemistry..... | 159 |
| 5.1.1.2 The AVC basaltic andesites | 162 |
| 5.1.2 The stratovolcano andesites | 163 |
| 5.1.2.1 Nature of the stratovolcano series | 163 |
| 5.1.2.2 EME-AFC modelling of the formation of the AVC stratovolcano suite | 166 |
| 5.1.2.3 Constraining storage conditions of the stratovolcano lavas..... | 167 |
| 5.1.3 The anteliths and VHkMs..... | 174 |
| 5.1.3.1 Nature of the anteliths..... | 175 |
| 5.1.3.2 Origin of the VHkMs | 175 |
| 5.1.3.3 Antelith petrology | 178 |
| 5.1.3.4 Overview of antelith formation and evolution | 180 |
| 5.2 Origin of the recharge magmas | 181 |
| 5.2.1 Nature of the recharge magmas | 181 |
| 5.2.2 Thermobarometry..... | 183 |
| 5.2.3 EME-AFC modelling of the enclave | 184 |
| 5.2.4 Comparison of the recharge magma and the stratovolcano lavas and implications for the evolution of the magma system | 188 |
| 5.2.5 Amphibole chemometry | 192 |
| 5.3 Origin of the LCY pumices | 194 |
| 5.3.1 Identification of the LCY pumices | 194 |
| 5.3.2 Nature of the LCY rhyolites | 196 |
| 5.3.3 Modelling the formation of LCY rhyolites | 197 |
| 5.3.3.1 The low-K LCY rhyolite | 198 |
| 5.3.3.2 The high-K LCY rhyolite | 201 |
| 5.3.4 Storage conditions of the LCY rhyolites | 202 |
| 5.3.4.1 The low-K LCY rhyolite | 205 |

| | |
|---|------------|
| 5.3.4.2 The medium-K LCY rhyolite..... | 206 |
| 5.3.4.3 The high-K LCY rhyolite | 206 |
| 5.3.5 Comparing the high- and lower-K LCY rhyolites | 207 |
| 5.3.6 The LCY crystal mush..... | 212 |
| 5.4 The post-LCY pumices | 212 |
| 5.4.1 Origin of the intermediate tephras..... | 213 |
| 5.4.1.1 The D1 andesite | 213 |
| 5.4.1.2 The I1 basaltic andesite..... | 215 |
| 5.4.1.3 Origin of the intermediate tephras..... | 217 |
| 5.4.2 The post-LCY rhyolites..... | 218 |
| 5.4.2.1 Characteristics of the post-LCY rhyolites | 218 |
| 5.4.2.2 Storage conditions of the post-LCY magmas | 220 |
| 5.4.2.3 Formation and history of the post-LCY rhyolites | 223 |
| Chapter 6: Spatial and temporal evolution of the AVC..... | 226 |
| 6.1 Estimating the Quaternary arc migration rate..... | 227 |
| 6.2 Evolution of the AVC..... | 229 |
| 6.2.1 Phases of the AVC | 229 |
| 6.2.2 Timing of formation of the magma bodies | 230 |
| 6.2.3 Variations in radiogenic isotope ratios within the AVC | 235 |
| 6.2.4 Rhyolite petrogenesis at the AVC | 237 |
| 6.3 Arc migration and the formation of large-volume magma bodies..... | 240 |
| 6.3.1 Formation of the silicic mush..... | 240 |
| 6.3.2 Magmatic fluxing of a wide area by stratovolcano systems..... | 241 |
| 6.3.3 Timing of the storage and accumulation of the rhyolites..... | 242 |
| 6.3.4 A possible regional trend? | 243 |
| 6.4 A perfect storm? | 245 |
| 6.5 Global comparisons..... | 247 |
| 6.5.1 Arc comparisons..... | 247 |
| 6.5.2 Comparison with other large caldera-forming eruptions..... | 249 |
| Chapter 7: Conclusions and future work | 251 |
| 7.1 Introduction | 251 |
| 7.2 Evolution of the AVC's magmatism..... | 251 |
| 7.3 The effects of arc migration..... | 255 |
| 7.4 Broader implications of this study | 256 |
| 7.4.1 Regional activity | 256 |
| 7.4.2 Global considerations | 257 |

| | |
|--|------------|
| 7.5 Future work..... | 258 |
| 7.5.1 Petrogenetic studies and/or tephra identification of nearby centres..... | 258 |
| 7.5.2 Constraining the arc migration rate of the northern CAVA..... | 260 |
| 7.5.3 Further work into the AVC..... | 261 |
| 7.5.3.1 Further geochemical and petrological investigations..... | 261 |
| 7.5.3.2 In situ isotope studies | 263 |
| 7.5.3.3 Thermal modelling..... | 264 |
| References..... | 266 |
| Appendix A: Whole rock data | 296 |
| A.1 Major and minor elements..... | 297 |
| A.2 Trace elements | 301 |
| A.3 Radiogenic isotopes..... | 305 |
| Appendix B: Microanalysis data..... | 308 |
| B.1 EPMA data | 309 |
| B.2 LA-ICP-MS data | 314 |
| Appendix C: GEOROC K₂O discrimination plots..... | 321 |
| Appendix D: EME-AFC | 335 |
| D.1 Introduction to EME-AFC..... | 335 |
| D.2 Model variables and partition coefficients..... | 337 |
| D.2.1 Modelled stratovolcano series | 337 |
| D.2.2 Modelling of the enclave magma | 339 |
| D.2.3 Modelling the enclave with apatite..... | 341 |
| D.2.4 Modelling of the low-K LCY rhyolite | 343 |
| D.2.5 Modelling of the high-K LCY rhyolite | 345 |
| Electronic Appendices | 347 |

Table of Figures

Chapter 1

| | |
|--|----|
| 1.1 Hillshade map of the Central Guatemalan volcanic segment..... | 21 |
| 1.2 Caldera sizes of the CAVA | 23 |
| 1.3 Transcrustal magma system | 27 |
| 1.4 Eruption triggers..... | 31 |
| 1.5 Global distribution of large silicic centres | 33 |
| 1.6 Tephra inventory for the CAVA..... | 35 |
| 1.7 Structural map of Central America | 36 |
| 1.8 Map of the positions of the CAVA | 37 |
| 1.9 Conceptual model for magma generation variations in segments of the CAVA | 39 |
| 1.10 Subduction variations along the CAVA..... | 40 |
| 1.11 3D aerial view of the Central Guatemalan volcanic segment..... | 41 |
| 1.12 Geochemical variations along the CAVA | 43 |
| 1.13 Conceptual model for changes in melt regimes along the CAVA | 44 |
| 1.14 Across-arc geochemical variations in eastern Guatemala | 46 |
| 1.15 U-Th ages for the AVC rhyolites..... | 53 |

Chapter 2

| | |
|---|----|
| 2.1 Hillshade map of the AVC and distal field locations | 55 |
| 2.2 Hillshade map of the AVC and proximal field locations | 56 |
| 2.3 Field photographs of lava-hosted xenoliths..... | 58 |
| 2.4 Field photograph of LCY pyroclastic flow deposit..... | 58 |
| 2.5 Field photographs of the post-LCY eruption deposits | 59 |
| 2.6 Field photographs of the I eruption deposits..... | 59 |
| 2.7 Field photographs of the W eruption deposits | 60 |
| 2.8 Photograph of granitoid xenolith hand specimen | 61 |

Chapter 3

| | |
|--|----|
| 3.1 Total alkali silica diagram for the andesitic materials of the AVC..... | 75 |
| 3.2 Mineral phase proportions of the stratovolcano basaltic andesites | 76 |
| 3.3 BSE photomicrographs of the basaltic andesites | 77 |
| 3.4 BSE photomicrographs of orthopyroxene and olivine from the basaltic andesites | 77 |
| 3.5 BSE photomicrographs of glomerocrysts from the basaltic andesites..... | 78 |
| 3.6 Mineral phase proportions of the stratovolcano andesites | 79 |
| 3.7 BSE photomicrograph of xenoliths/glomerocrysts from Volcán San Pedro | 80 |
| 3.8 BSE photomicrographs of biotite and amphibole from the andesite lavas | 81 |
| 3.9 Mineral phase proportions of the stratovolcano high-silica andesites..... | 83 |
| 3.10 BSE photomicrographs of typical mineral textures from the high-silica lavas | 84 |
| 3.11 BSE photomicrographs of a glomerocryst from a high-K lava | 85 |
| 3.12 Mineral phase proportions of the stratovolcano-hosted anteliths..... | 86 |
| 3.13 BSE photomicrographs of the anteliths..... | 87 |

| | |
|--|-----|
| 3.14 PPL photomicrograph of biotite and amphibole cluster in the Volcán Tolimán antelith | 88 |
| 3.15 Plagioclase compositions from the basaltic andesites | 90 |
| 3.16 Pyroxene compositions from the basaltic andesites | 90 |
| 3.17 Plagioclase compositions from the andesite lavas | 92 |
| 3.18 Pyroxene compositions from the andesite lavas and the I1 pumice | 92 |
| 3.19 Amphibole compositions from the stratovolcano and the D1 pumice | 93 |
| 3.20 Plagioclase compositions from the high-K lavas | 94 |
| 3.21 Pyroxene compositions from the high-K lavas | 95 |
| 3.22 Plagioclase compositions from the anteliths | 95 |
| 3.23 Pyroxene compositions from the anteliths | 96 |
| 3.24 Mineral phase proportions of the post-LCY mafic pumices | 97 |
| 3.25 BSE photomicrograph of variable groundmass textures from the D1 pumice | 98 |
| 3.26 BSE photomicrographs of the mineral textures of the D1 pumice | 99 |
| 3.27 BSE photomicrographs of the mineral textures of the I1 pumice | 100 |
| 3.28 Plagioclase compositions from the andesite pumices | 101 |
| 3.29 Pyroxene compositions from the andesite pumices and the D2 rhyolite pumice .. | 101 |
| 3.30 Mineral phase proportions of the LCY pumices | 102 |
| 3.31 BSE photomicrographs of plagioclase from the rhyolite pumices | 103 |
| 3.32 BSE photomicrograph of the ferromagnesian phases of the lower-K LCY rhyolites | 104 |
| 3.33 BSE photomicrograph of resorbed quartz typical of the LCY pumices | 105 |
| 3.34 Plagioclase compositions from the rhyolite pumices | 106 |
| 3.35 An vs. Or content of the plagioclase from the rhyolites | 106 |
| 3.36 Amphibole compositions from the rhyolite pumices | 107 |
| 3.37 Mineral phase proportions of the post-LCY pumices | 108 |
| 3.38 BSE photomicrograph of mineral phases from the post-LCY rhyolites | 109 |
| 3.39 BSE photomicrograph of glomerocrysts from the post-LCY rhyolites | 111 |
| 3.40 BSE photomicrograph of ferromagnesian phases from the crystal-rich I pumice ... | 112 |
| 3.41 Plagioclase compositions of the post-LCY rhyolites | 113 |
| 3.42 BSE thin section scan of an LCY mingled pumice | 115 |
| 3.43 BSE photomicrographs of plagioclase from the mingled LCY pumice | 116 |
| 3.44 BSE photomicrographs of ferromagnesian phases from the mingled LCY pumice.. | 117 |
| 3.45 BSE photomicrographs of clinopyroxene from the mingled D2 pumice | 118 |
| 3.46 Mineral phase proportions of the I eruptions' enclaves | 119 |
| 3.47 BSE photomicrograph of the diktytaxitic groundmass of an enclave | 120 |
| 3.48 BSE photomicrographs of mineral textures from the enclaves of the I pumice | 121 |
| 3.49 BSE photomicrographs of apatite hosted in the I eruptions' enclaves | 122 |
| 3.50 Plagioclase compositions from the mingled pumices and enclaves | 123 |
| 3.51 Amphibole compositions from the mingled pumices and enclaves | 124 |
| 3.52 Pyroxene compositions from the mingled pumices and enclaves | 125 |
| 3.53 Violin plot of plagioclase compositions from the AVC | 126 |
| 3.54 Violin plots of pyroxene compositions from the AVC | 128 |
| 3.55 Violin plots of olivine compositions from the AVC | 129 |

Chapter 4

| | |
|--|-----|
| 4.1 Total alkali silicic and K ₂ O discrimination diagrams for the rocks of the AVC | 131 |
| 4.2 Major element Harker diagram for the rocks of the AVC..... | 132 |
| 4.3 Incompatible trace element Harker diagram for the rocks of the AVC..... | 136 |
| 4.4 Spider diagram of the andesites and basaltic andesites of the AVC..... | 137 |
| 4.5 Eu/Eu* vs. Sr/Sr* variations diagrams..... | 138 |
| 4.6 Compatible trace element Harker diagram..... | 139 |
| 4.7 Spider diagrams of the rhyolite pumices..... | 141 |
| 4.8 Spider diagram of the plutonic rocks..... | 143 |
| 4.9 Radiogenic isotope vs. SiO ₂ bivariate diagrams | 144 |
| 4.10 Strip plots of the radiogenic isotopes divided by volcano | 145 |
| 4.11 ⁸⁷ Sr/ ⁸⁶ Sr vs. ¹⁴³ Nd/ ¹⁴⁴ Nd bivariate diagram..... | 146 |
| 4.12 ⁸⁷ Sr/ ⁸⁶ Sr and ¹⁴³ Nd/ ¹⁴⁴ Nd vs. ¹⁷⁶ Hf/ ¹⁷⁷ Hf bivariate diagrams | 147 |
| 4.13 Uranogenic vs. thorogenic Pb isotope correlation diagram | 148 |
| 4.14 Matrix glass Harker diagram for the rhyolite pumices | 151 |
| 4.15 Matrix glass compositions for the intermediate composition post-LCY pumices ... | 153 |
| 4.16 Major element Harker diagram for the stratovolcano lava hosted rhyolite melts .. | 154 |
| 4.17 Trace element Harker diagram for the stratovolcano lava hosted rhyolite melts .. | 157 |
| 4.18 Spider diagram for the rhyolite melts hosted in the Volcán Tecolote antelith | 158 |

Chapter 5

| | |
|---|-----|
| 5.1 ⁸⁷ Sr/ ⁸⁶ Sr vs. ¹⁴³ Nd/ ¹⁴⁴ Nd variations of CAVA lavas..... | 160 |
| 5.2 Geochemical variations along-arc | 161 |
| 5.3 Select bivariate diagrams showing inflection points and mixing lines | 164 |
| 5.4 Major element results for modeling the formation of the stratovolcano lavas | 167 |
| 5.5 Trace element results for modelling the formation of the stratovolcano lavas | 168 |
| 5.6 Pyroxene thermobarometry results | 169 |
| 5.7 Plagioclase hygrometry results..... | 170 |
| 5.8 Amphibole thermobarometry and hygrometry results..... | 171 |
| 5.9 Ba vs. Sr content of the VHkMs in the Volcán Tecolote antelith | 177 |
| 5.10 Amphibole chemometry of the Volcán Tecolote antelith | 179 |
| 5.11 Major element results for modelling the formation of the recharge magma | 185 |
| 5.12 Trace element results for modelling the formation of the recharge magma | 186 |
| 5.13 logfO ₂ vs. temperature estimates from amphiboles | 187 |
| 5.14 ASI vs. SiO ₂ for the stratovolcano lavas and the recharge magma..... | 189 |
| 5.15 SrO vs. An content of stratovolcano lava and recharge magma plagioclase | 191 |
| 5.16 Sr/Y and Zr/Hf vs. SiO ₂ of stratovolcano lavas and VHkMs | 192 |
| 5.17 Amphibole chemometry comparing the amphiboles hosted in the different recharge magmas..... | 193 |
| 5.18 Major element bulk rock compositions of the AVC rhyolite pumices..... | 195 |
| 5.19 Bivariate plots of matrix glass trace elements for the LCY rhyolites..... | 196 |
| 5.20 Major element results for the modelling for formation of the low-K LCY rhyolite .. | 199 |
| 5.21 Trace element results for the modelling for formation of the low-K LCY rhyolite .. | 200 |
| 5.22 Major element results for the modelling for formation of the high-K LCY rhyolite .. | 202 |
| 5.23 Trace element results for the modelling for formation of the high-K LCY rhyolite .. | 203 |

| | |
|---|-----|
| 5.24 Plagioclase ‘bump’ textures in the lower-K LCY rhyolites | 208 |
| 5.25 Matrix glass La vs. Th/U for the LCY pumices..... | 211 |
| 5.26 Amphibole chemometry and thermobarometry for the D1 pumice..... | 214 |
| 5.27 BSE photomicrograph showing pyroxene textures in the I1 pumice | 216 |
| 5.28 BSE photomicrograph showing groundmass textures in the I1 pumices..... | 217 |
| 5.29 BSE photomicrographs of the post-LCY amphiboles..... | 220 |
| 5.30 Amphibole chemometry for the crystal-rich I pumice..... | 222 |
| 5.32 Amphibole compositions of the crystal rich I pumice and the I recharge magmas. | 224 |

Chapter 6

| | |
|---|-----|
| 6.1 Maps showing migration paths for the different volcanoes of Guatemala | 228 |
| 6.2 Cartoon of the conceptual model of the AVC approximately 400 ka..... | 231 |
| 6.3 Cartoon of the conceptual model of the AVC approximately 100 ka..... | 232 |
| 6.4 Cartoon of the conceptual model of the AVC following the LCY eruption | 233 |
| 6.5 Cartoon of the conceptual model of the AVC (present day) | 234 |
| 6.6 Map showing the known outcroppings and hypothetical positioning of the pre-LCY AVC stratovolcano lineaments..... | 236 |

List of Tables

| | |
|---|-----|
| Table 1.1 Stratigraphy of the major stratovolcanoes and tephras of the AVC | 48 |
| Table 2.1 List of samples used in this study | 57 |
| Table 2.2 Preferred values for Pb isotope ratios for reference standard NBS981 | 68 |
| Table 4.1 Correlation coefficients for the alkali elements vs. SiO ₂ | 133 |
| Table 5.1 Temperature estimates for the LCY rhyolites | 210 |
| Table 6.1 Global arc migration rates | 226 |

Acknowledgements

This project would not have been possible without the help of so many people and I'm so happy to be able to thank everyone who has made this thesis possible. First and foremost I want to thank my supervisors Dr Chiara Maria Petrone and Professor Hilary Downes, for taking me on and believing in my project, for all their knowledge support and guidance, and for getting me to the finish line!

Next, I want to thank all the people that have helped me with all the collection and analyses. Thanks to Chris Newhall for his advice on field locations, Matt Purvis for all his knowledge and driving skill, to Spike for his company, and to the Bestia Roja for ferrying us around Guatemala. I'm deeply grateful to the staff of the NHM for guiding me through all the hoops required for studying here and for performing sample preparation and analyses at the museum, in particular Dr Eileen Cox, Dr Emma Humphreys-Williams, Callum Hatch, Innes Clatworthy, Dr Alex Ball, Dr Tobias Salge, John Spratt, and Dr Yannick Buret. I'm especially grateful for their efforts to ensure the labs were running with as little disruption as possible for all of us users in the face of the pandemic.

I'm also indebted to many other people who have performed chemistry and analyses for me. These include Dr Katharina Kreissig and Dr Julie Prytulak for their work on our Sr isotope pilot project, Dr Ian Millar, Dr Doris Wagner, Dr Nicola Atkinson and Vanessa Pashley for preparing and running the analyses for the main isotope project, and Dr Sam Hammond and Dr Katrina Nilsson-Kerr for guiding me through the chemistry and for running the trace element analyses.

Finally, finishing this thesis would not have been possible without all of my friends and family. Huge thanks and love to Mum, Rosie and Zoe for never stopping believing in me, to all my friends who would nod kindly when I explained what I had been doing, my fellow rock PhDs Eoin Reddin, Gerallt Hughes, Mihaela Swift, Clara Matthews Torres and Catherine Harris for all the great discussions (about volcanoes or not), and to DTP cohort 5 who went through it all with me. Lastly, I want to thank Angela, without whose love and support I don't know if I would've finished. I'm massively grateful to everyone and send much love to you all!

*“In the overthrow of the mighty pillars lands were broken and seas arose in tumult;
and when the lamps were spilled destroying flame was poured out over the Earth”*

- J. R. R. Tolkien

Chapter 1: Introduction and Background

1.1 Research aims and objectives, and thesis structure

Large volume caldera-forming eruptions (defined as erupting 100 to >1,000 km³ of dacite to rhyolite tephra with volcanic explosivity indexes (VEI, an estimate of eruption magnitude; Newhall & Self (1982) of 7-8) are beginning to be recognised as relatively common events in the geological record. Occurrence frequencies are estimated as 625-1200 years for VEI 7 events, and 14,300-17,000 years for VEI 8 events (Rougier et al., 2018; Lin et al., 2022). Understanding where and why these eruptions occur is key for future long-term hazard assessments of the world's most powerful eruptions, which are commonly associated with evolved magmas in subduction-related volcanic arcs.

The distribution of these calderas and the nature of their eruptions are inconsistent within or between volcanic arcs. Variables such as caldera and eruption deposit size, SiO₂ content of the erupted magma, density of calderas in the arc and eruption frequency can all vary greatly (Hughes & Mahood, 2008, 2011; Sheldrake et al., 2020). Thus, multiple factors (such as convergence rate and the subsequent magma flux rate, convergence obliquity, crustal thickness and age, arc migration, and slab age) appear to control the formation, volume and frequency of caldera-forming eruption at convergent margins (Hughes & Mahood, 2008, 2011; Sheldrake et al., 2020).

The question of why some regions of the world are more susceptible to large-volume silicic eruptions is still an open one. One of the key variables that is correlated to increased susceptibility to such an eruption is arc migration, suggested to be because fresh magmatism can exploit previously unfused material and/or volatiles from the melt column (Hughes & Mahood, 2011), although this has not been tested. In this study, I investigate the causal links between arc migration and caldera-forming eruptions to answer the question of whether arc migration is directly linked to an increased frequency of caldera-forming eruptions and/or increases in eruption size and SiO₂ contents of the magma, using the case study of Volcan Atitlan in the Central American volcanic arc (CAVA) in Guatemala.

The CAVA has produced numerous large-volume volcanic eruptions (Kutterolf et al., 2016; Schindlbeck et al., 2016a, 2016b, 2018), and shows a heterogeneous distribution of eruption sizes (among other related variables) along the strike of the arc. In general, the larger and more silicic eruptions are located towards the northern end of the CAVA. The

Atitlán Volcanic Centre (AVC) in central southern Guatemala was host to the largest Quaternary eruption of the CAVA, the VEI 8 Los Chocoyos event (referred to as LCY; Cisneros de León et al., 2021a). Several other nearby centres have either produced known large caldera-forming eruptions such as the L-tephra of the Amatitlán caldera (Kutterolf et al., 2016) and the Tierra Blanca Joven from the Ilopango caldera (Smith et al., 2020), or contain proposed caldera structures (e.g., the Xela centre; Duffield et al., 1993; Fig. 1.1).. The reason why this section of the CAVA produces such voluminous eruptions compared to the rest of the arc is not fully known – in fact, the northern portion of the CAVA has one of the highest caldera densities in the world (Hughes & Mahood, 2011). This thesis explores the potential causes of the ‘supersizing’ of activity in this region.

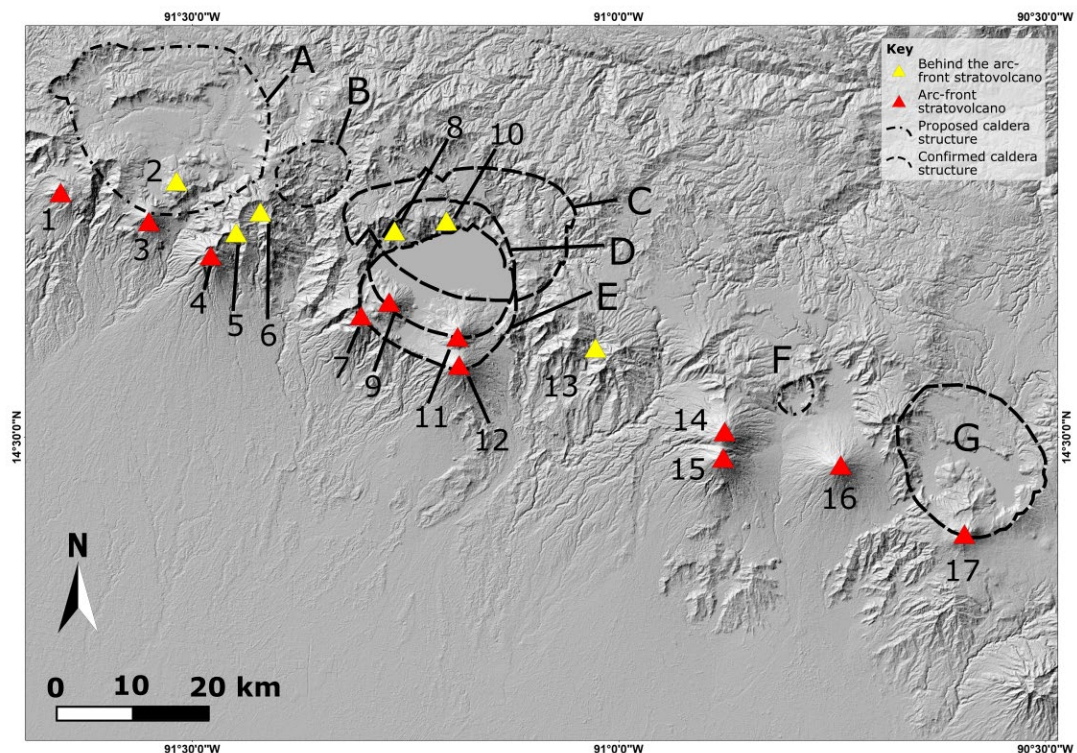


Figure 1.1. Hillshade map of the Central Guatemalan segment of the CAVA, caldera structures denoted by letters, stratovolcanoes by numbers: A – Xela, B – Ixtahuacan, C – Atitlán I, D – Atitlán II, E – Atitlán III, F – Barahona, G – Amatitlán; 1 – Chicabaj, 2 – Almologna/Cerro Quemado, 3 – Santa María/Santiagouito, 4 – Pecul, 5 – Zunil, 6 – Tzanjuyub, 7 – Paquisis, 8 – San Marcos, 9 – San Pedro, 10 – Tecolote, 11 – Tolimán, 12 – Atitlán, 13 – Xejolón, 14 – Acatenango, 15 – Fuego, 16 – Agua, 17 – Pacaya. The three Atitlán calderas young progressively south. Caldera locations from: Xela-Duffield et al. (1993); Atitlán and Ixtahuacan-Newhall (1980); Barahona-Bornhorst et al. (1982); Amatitlán-Wunderman & Rose, (1984)

One distinct physical difference between this arc segment and the rest of the CAVA is the occurrence of regional migration, which dominates the structure and historical activity of volcanic centres. The direction of this migration is south-westwards towards the trench (Alvarado et al., 2007). Stratovolcanoes in each centre are typically formed of pairs or chains, with the younger cones erupting on the southern edges of older stratovolcanoes or

calderas (Halsor & Rose, 1988; Fig. 1.1). Based on the positions of the calderas in older parts of the migration trend (i.e., north of the arc front; Fig. 1.1), there is a temporal and spatial relationship between trenchwards arc migration and formation of the magma bodies that fed these caldera-forming eruptions. This migration has progressed for a long duration, shown by the progressive shift of the locations of the three Atitlán calderas (Fig. 1.1).

There are differences in the nature of the calderas in the CAVA that may also be at least partially tied to this relationship. Across El Salvador and Nicaragua, caldera and eruption sizes are typically much smaller than those in Guatemala and tend to have less silicic compositions (Fig. 1.2). These calderas are also typically missing the migration-related structure compared to those in Guatemala, the exception being the Malpaisillo caldera in Nicaragua (the largest caldera in Nicaragua; medium-sized gray circle in in Fig. 1.2), which lies between the older and newer locations of the arc (Stoppa et al., 2018). While several physical variables which could impact the size and composition of the caldera-forming events vary along the arc (e.g. crustal thickness, slab dip; sections 1.2.3; 1.3.1), trenchwards arc migration has never been considered a factor. Arc migration might have a key relationship with large-volume silicic magmatism and, in order to fully understand the nature of silicic magmatism at the CAVA, this will be examined. The study may have implications for large-scale caldera-forming eruptions at convergence margins globally.

The AVC is a good location to study this relationship, due to the preservation of volcanic materials from all stages of its activity. In order to determine whether there is a link between arc migration and large-volume silicic magmatism, an updated petrogenetic model for the magmatism at the AVC must be first produced. This will address several gaps in our understanding of this system. Significant advances have been made in our knowledge of the nature of magmatic systems, and in our ability to computationally model these. In the context of these recent advances, this thesis will investigate the petrology and geochemistry of the magmas in the AVC. Using new models, it will attempt to explain the interactions between the different magmas that occur in the AVC, and what links the magma types may have to arc migration.

This project therefore aims to provide a holistic model for the evolution of the AVC. This will include studying the formation of the magma bodies that were erupted during the Los Chocoyos event, their relationships with other magmas that have been erupted at the AVC,

and what influence regional arc migration has had on their evolution. Several research questions will be addressed to answer this problem:

1. How were the different magmas of the AVC formed and stored?
2. What effect did arc migration have on the formation of the LCY magma bodies?
3. How applicable are the findings of this study to other caldera-forming systems at convergent margins globally?

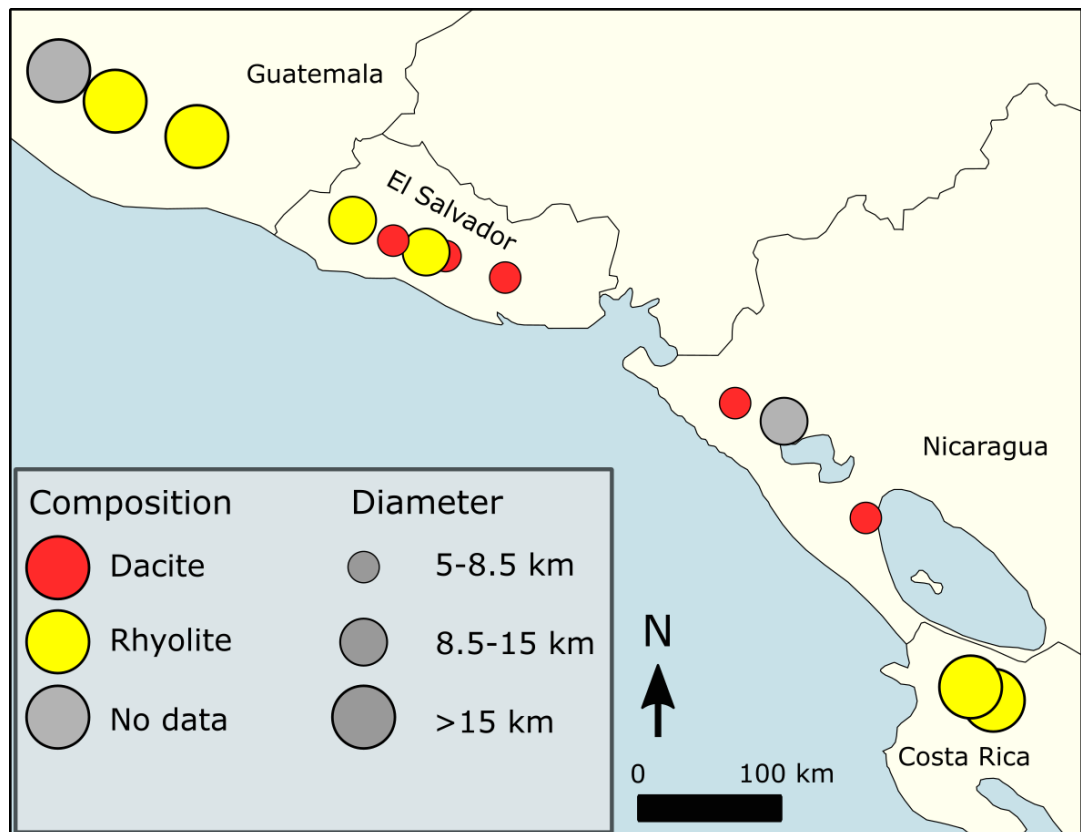


Figure. 1.2. Caldera sizes and most silicic whole rock erupted compositions for large calderas (>5 km diameter) found within the CAVA. Adapted from Hughes & Mahood (2011) with additional data from Duffield et al. (1993) and Stoppa et al. (2018).

This thesis has the following objectives to answer the research questions:

1. I will address research question 1 by characterising the petrology and geochemistry of representative samples from all rock-types from the AVC using a variety of bulk rock analyses including XRF and radiogenic isotopes, and microanalytical methods. Using these results, I will produce models for the formation of the magmatic units using various published geothermobarometric methods and a computer model for the compositional evolution of the magmas.

2. I will address research question 2 by using radiogenic isotope data to compare the AVC stratovolcanoes and the LCY pumices, as well as using inferences from previously published data.
3. I will address research question 3 by comparing the physical characteristics (including calculating estimates of migration rates) of northern CAVA with other volcanic arcs, as well as comparing the AVC specifically with other volcanic centres that have produced similarly sized caldera-forming eruptions.

These steps are outlined in seven chapters. The first chapter provides an overview of the current knowledge of how large volume silicic magma bodies are formed, stored and erupted, to place the AVC in a global context. It will then review the regional geochemical picture to discuss the processes that control magma evolution in the CAVA, which will constrain the processes which may be active at the AVC.

The second chapter will provide a background to the volcanic units erupted from the AVC and show where there are gaps in our understanding of the generation of magmas of all compositions there. It then details the methods for the field campaign and the analytical data collection. Chapters three and four will describe the results of the petrological and geochemical analyses respectively. Chapter five provides petrogenetic models for the AVC magmas, using the petrological and geochemical data. Chapter six builds on the models from chapter five to provide a holistic model for the Quaternary history of the AVC, also considering the potential impacts of regional arc migration as well as several other physical factors. Finally, chapter seven outlines the conclusions of this thesis and considers several potential ways that future projects could further investigate the local, regional, and global impact of arc migration on magmatism.

1.2 Current understanding of the generation of silicic magmas and caldera-forming events

A recent study (Cassidy & Mani, 2022) has shown that the likelihood of a large, potentially globally impacting caldera-forming eruption during this century is 1 in 6. It is therefore crucial to develop an understanding of the processes that result in the formation and eruption of these huge reservoirs of silicic magmas and thus to forecast where and when these eruptions may occur. A significant part of this research should include studies of past examples of these events, in order to build up a reliable picture of the processes that produce these devastating eruptions. To mitigate future hazards, it is critical to identify volcanic systems that have the potential to generate these magmas and then install long-

term monitoring systems on these volcanoes in order to understand their background state of unrest and what the lead-up to an eruption may look like (Newhall et al., 2018; Wilson et al., 2021).

Despite the lack of coordinated international action (Cassidy & Mani, 2022), this research is well underway. There have been major developments in our understanding of what the magma systems that feed these eruptions may look like and how they develop (section 1.2.1), what events may lead to the triggering of an eruption (section 1.2.2), and the physical factors of convergent margins that are correlated with increased caldera densities and eruption sizes (section 1.2.3). Within the context of these new understandings, I will develop a conceptual model for the evolution of the AVC.

1.2.1 Generating and storing evolved magmas

The origin and storage of large-volume bodies of evolved magmas that feed these eruptions has been one of the fundamental questions of igneous petrology for generations of scientists. This section outlines the current state of understanding of the nature of large-volume silicic magmatism and will provide a new framework to investigate the petrogenesis of the magmas of the AVC and the impact that arc migration may have had on the process.

Super-eruptions have shown enormous variability in their erupted products, eruption durations, timescales of magma assembly, the nature of their magma systems, the tectonic environment in which they are formed, etc. This means that application of a single unifying model for their formation is difficult and may be impossible (Gregg et al., 2012; Wilson et al., 2021; and references therein). This further highlights our need to form a global understanding of the variations in super-eruption.

Several general mechanisms have been proposed to explain the formation of silicic magmas. The present consensus is that all eruptions are fuelled by primitive magmatism sourced from the mantle (Smith, 1979; Hildreth, 1981; Annen et al., 2006; Cashman et al., 2017), however the mechanism that links these magmas with the silicic output is still debated. Fractional crystallisation of primitive melts can reproduce the observed geochemistry of many eruptions (Vogel et al., 2006; Deering et al., 2008; Dufek & Bachmann, 2010; Bindeman et al., 2019; Lubbers et al., 2020). Nevertheless, there are several difficulties in explaining the generation of a large-volume of silicic melts only by fractional crystallisation (e.g., Bowen, 1928) although it is thought to be one of the primary

processes by which smaller volumes of intermediate to evolved magmas are generated (Gill, 1981; Grove & Kinzler, 1986; Rogers & Hawkesworth, 1989; Turner et al., 1992; Grove et al., 2002, Grove et al., 2003). Other studies have suggested that partial melting of crustal material also contributes to the formation of silicic magmas (Smith & Leeman, 1987; Huppert & Sparks, 1988; Atherton & Petford, 1993; Tepper et al., 1993; Rapp & Watson, 1995; Sisson et al., 2005; Annen et al., 2006). This is especially important in regions where there may be fertile crust which have not been previously been depleted of more easily fusible phases (Annen & Sparks, 2002) which, in the context of large-volume silicic systems, could be tied to regions of young crust and/or regions where magmatism has recently migrated to (Hughes & Mahood, 2011)..

The reality most likely lies somewhere between these two end-members, and the relative contribution of fractional crystallisation and crustal assimilation will likely vary significantly between centres (Fowler & Spera, 2010). Numerous computational models testing one or both of these processes have since been developed (e.g., DePaolo, 1981; Spera & Bohrsen, 2001; Gualda et al., 2012).

Further processes add complications to the two-end-member model. Single-crystal studies have highlighted the diversity in isotopic signatures of crystal phases (e.g., zircon and quartz) in deposits of a single eruption of silicic magma that may not be revealed when whole rock samples are analysed (Bindeman, 2008). Several different magmas of varying ages and compositions can therefore be present in a system (Fig. 1.3) and may be mixed or recycled before/during an eruption (Bindeman & Simakin, 2014). The presence of antecrysts (crystals that were not grown from the host magma but are sourced from a different magma system) within volcanic material highlights the potential for recycling of material in long-lived magma systems (Nakada et al., 1994; Harford & Sparks, 2001; Cooper & Reid, 2003; Charlier et al., 2005; Davidson et al., 2007, Allan et al., 2017). Other processes such liquid immiscibility, magma mixing/recharge and melt rejuvenation (Sisson et al., 2005; Bindeman & Simakin, 2014) can also have significant effects on the final magmatic product that is frozen as a snapshot by eruption. Sorting out the various signals to determine the pre-eruptive evolution of the magma system is therefore highly complex.

A key aspect of magma plumbing systems that is recognised is the obsolescence of traditional 'magma chamber' models. Instead, geophysical and petrological evidence point towards large regions of the crust with melt in low proportions (from a few percent up to 50% melt by volume; Farrell et al., 2014; Cashman et al., 2017) contained in a crystal

‘mush’ (Bachmann & Bergantz, 2004, 2008; Hildreth & Wilson, 2007; Bachmann & Huber, 2016; Fig. 1.3). Repeated injection and crystallisation of magmas leads to the formation of these large ‘mush’ zones, regions of very high crystallinity that contain low melt-fractions, which can be sustained for long periods of time by the continuous input of new material and heat in the form of recharge mafic magmas (Bachmann & Bergantz, 2004; Bachmann et al., 2007; Miller & Wark, 2008). The presence of these crystalline mush frameworks enables the intermittent assemblage of super-eruption-feeding magma bodies by crystal fractionation (Dufek & Bachmann, 2010), melt formation (from surrounding country rock and/or remelting/remobilisation of previous intrusions) and extraction (Bachmann & Bergantz, 2004; Hildreth, 2004) and homogenisation (Huber et al., 2009, 2012), as well as further recharge from mafic magmas. A consequence of the fractionation process, as well as reactive flow as the extracted melts ascend (Jackson et al., 2018), is that shallower magmas tend to be more silicic (Fig. 1.3). While a crystalline mush is thought to be present beneath most volcanic systems, under specific circumstances this can lead to the assembly of supersized magma bodies. Thermally mature systems with high melt fluxes are more likely to be able to maintain a magma system from which large magma bodies can be assembled and potentially erupted (Sparks et al., 2022).

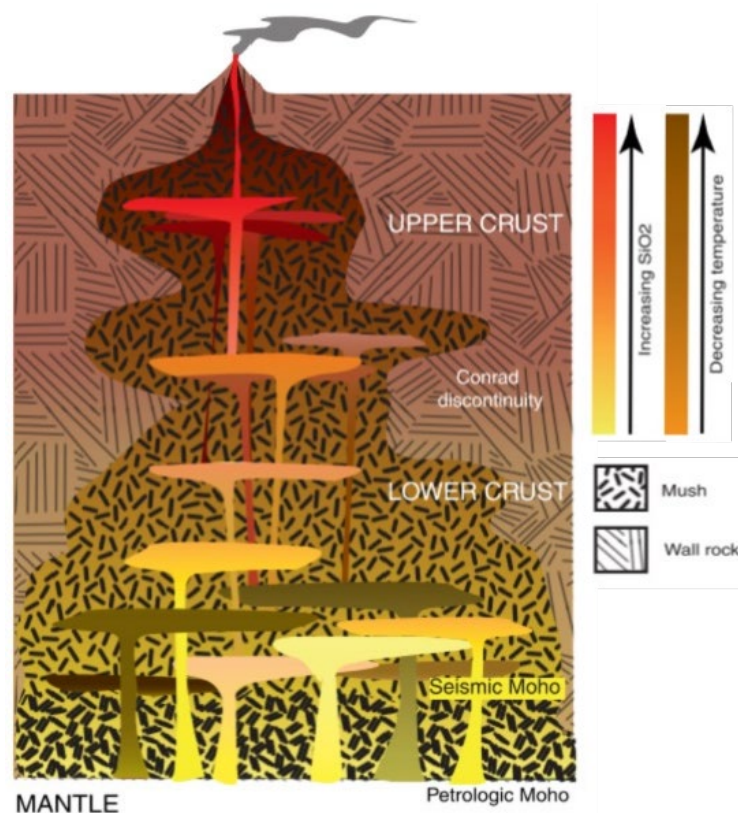


Figure 1.3. Conceptual model for a transcrustal magma system. Differentiation occurs to progressively greater extents at decreasing depths. Melts of variable compositions are stored in transient melt lenses within a crystal rich mush, and these lenses can exist concurrently (from Cashman et al., 2017).

This mush model also answers questions about the longevity of silicic magma systems. Large magma bodies that feed ignimbrite eruptions would cool rapidly when emplaced in cold country rock and, if not sustained by a high magma flux, would solidify on timescales on the order of hundreds of thousands of years (Gelman et al., 2013). The longevity of the system also depends on the maturity of the system. Many studies have suggested that repeated injections of primitive magmas into the crust 'primes' it to maintain the existence of these silicic magma systems in a potentially extractable state over long timescales (Lipman et al., 1978; de Silva & Gosnold, 2007; Grunder et al., 2008). Buffering of the system from cooling too rapidly is achieved by preventing convection by 'locking up' of the crystal matrix and by latent heat released by crystallisation (Annen, 2009; Huber et al., 2009; Bachmann & Huber, 2016b).

Thermal modelling of magmatic systems in the mid- to shallow crust shows that regions containing large amounts of magma ($\geq 10^3 \text{ km}^3$) can be maintained at these crystallinities by high magma fluxes ($5\text{-}8 \times 10^{-3} \text{ km}^3/\text{yr}$) on long timescales ($10^5\text{-}10^6$ years) (Costa, 2008; Gelman et al., 2013). Mature systems that have experienced magmatism over these timescales where mush systems can develop are more likely to produce large volumes of silicic magma. Estimates suggest that long-lived systems can sustain melt in an eruptible/extractable state at lower magma fluxes on the order of $10^{-3}\text{-}10^{-2} \text{ km}^3/\text{yr}$ (Karakas et al., 2017). The presence of recycled zircon crystals of ages on the same order of magnitude as the estimated lifetimes of these systems supports this estimate (Brown & Fletcher, 1999; Vasquez & Reid, 2002; Deering et al., 2016; Cisneros de León et al., 2021a). Magma recharges from the lower crust therefore supply the heat and material required to sustain large volume silicic magma systems.

The crystal mush model can also explain compositional gaps (Daly gaps) that have been observed at volcanic centres of various types, including large silicic centres (Bachmann & Huber, 2016). Primitive and crystal-poor melts may easily be erupted due to their low viscosity, but at higher crystallinities extraction of both melt and crystals is much more difficult. Instead, stalled melts with crystal mushes undergo the processes of hindered settling and/or compaction fractionates a compositionally evolved magma from the mush (Dufek & Bachmann, 2010). These composition gaps may be obscured by open system processes, particularly in regions with thicker crust.

While the existence of homogeneous crystal-rich dacitic ignimbrites (the "monotonous intermediates" of Hildreth, 1981) clearly supports the idea of the mush model (Bachmann

& Huber, 2016a), crystal-poor rhyolites (such as the Los Chocoyos magma examined in this study) are more difficult to reconcile, as movement of viscous melts through the highly crystalline matrix is a slow process that can easily stall (McKenzie, 1985; Wickham, 1987). These deposits typically grade upwards from a crystal-poor base to a more crystal-rich and generally less silicic material at the top (Lipman, 1967; Hildreth, 1981). The crystal-poor bodies of melt represent portions of the mush system which have been extracted by processes such as settling, compaction, filter pressing (Brophy, 1991; Sisson & Bacon, 1999; Thompson et al., 2001; Bachmann & Bergantz, 2004; Solano et al., 2012; Ellis et al., 2014) or through deformation related to regional tectonic-related or local stresses (Holtzman et al., 2003; Etheridge et al., 2021) to form a cap on the system (Bacon & Druitt, 1988; Hildreth & Fierstein, 2000; Bacon & Lanphere, 2006).

The crystal mush model also helps explain the highly complex nature of some ignimbrite deposits, where several petrologically and geochemically distinct magmas can be identified in the same eruption sequence (Rose et al., 1979; Bégué et al., 2014). Several individual melt bodies may be tapped in one eruption (Cashman & Giordano, 2014, and references therein). These systems are likely highly complex and ‘trans-crustal’ (Fig. 1.3), with differentiation of magmas occurring throughout the melt column in several different melt lenses (Cashman et al., 2017; Liu & Lee, 2020; Sparks et al., 2022).

For exceptionally large silicic eruptions (super-eruptions with magma volumes of $>300 \text{ km}^3$; Sparks et al., 2005), specific conditions relating to the host rock and the state of the magma system must be met. In order to keep growing the magma body without triggering an eruption, the pressure from magma injection is buffered by several processes: the viscous relaxation time of the crust (related to the thermal history, i.e., older, hotter crust is more ductile), recharge rate, the size of the magma chamber, and crucially the presence of an exsolved volatile layer (Edmonds & Woods, 2018; Townsend et al., 2019; Caricchi et al., 2021). An exsolved volatile layer dramatically increases the compressibility of a magma body, allowing for growth without over-pressuring the overlying crust. This prevents brittle fracture of the crust, which could create magma pathways to the surface and result in eruption.

1.2.2 Triggering mechanisms for large volume silicic eruptions

The mush model provides explanations for several problems with large volume silicic magmatism that have been identified in the past twenty years. For crystal-poor magmas, melts must be extracted from the crystal mush and briefly stored in an eruptible state.

These must be rapid processes as thermomechanical modelling shows that low-crystallinity magmas cannot be maintained in the upper crust for any extended length of time (Fialko & Simons, 2001; Annen, 2009; Gelman et al., 2013). Using diffusion chronometry, this assembly process for large silicic eruptions has been shown to occur on timescales of decades to centuries (Sparks et al., 2022). Once these magmas have been accumulated, a final event is required to take them from storage to eruption. These ‘trigger’ events have been widely debated in the literature (e.g., Caricchi et al., 2021), and several possibilities are outlined here (Fig. 1.4). Early suggestions used the presence of mafic enclaves or mingled pumices as evidence that recharge events could trigger an explosive eruption (Sparks et al., 1977; Fig. 1.4A). Estimates for timescales between recharge and eruption for large silicic events vary widely, between months to 1,000s of years (Snyder, 2000; Martin et al., 2008; Costa et al., 2020), where the lag is likely related to the time required to start convection in the silicic magmas (Snyder, 2000). An influx of mafic magmas can pressurise the host magma body through increases in pressure due to replenishment and through induced volatile exsolution. Undercooling of the recharge magmas causes rapid crystallisation (Sparks & Marshall, 1986), resulting in volatile exsolution and pressurisation of the system (Tait et al., 1989; Huppert & Woods, 2002). The resulting decrease in density resulting from bubble formation in the mafic magmas could cause mixing (Eichelberger, 1980). Supply of the exsolved gas (gas sparging) to the overlying silicic magma has also been suggested as an efficient method of heat transfer and remobilisation (Bachmann & Bergantz, 2006).

Other triggering events that do not rely on mafic recharge have also been proposed. These include other ‘local’ mechanism such as magma buoyancy (Malfait et al., 2014; Fig. 1.4B), downward-propagating faults in the magma chamber roof (Gregg et al., 2012; de Silva & Gregg, 2014; Cashman & Giordano, 2014; Fig. 1.4C) or volatile oversaturation (Blake, 1984; Stock et al., 2016; Edmonds & Woods, 2018; Arzilli et al., 2019; Cassidy et al., 2019; Annen et al., 2023; Fig. 1.4D). In the first case, sufficient overpressure to induce ‘magma-up’ faulting and dyke propagation can be provided simply because the silicic magma having a significantly lower density than the surrounding country rock. The inverse has also been proposed, arguing that in the case of the largest magma bodies (those with caldera areas $\geq 100 \text{ km}^2$), elevated temperatures and low roof aspect ratios reduce the likelihood of a reservoir-triggered eruption by buffering overpressures from the chamber (Gregg et al., 2012; de Silva & Gregg, 2014). Instead, uplift results in downward-propagating faults that trigger the eruption from above. This mechanism is also possibly tied to the maximum

possible size these extracted melt bodies can reach, as chamber roofs in shallowly emplaced magmas cannot exceed a certain amount of uplift without triggering eventual failure and eruption (Gregg et al., 2012; de Silva & Gregg, 2014). The final case of ‘local’ eruption triggering involves volatile oversaturation, whereby crystallisation of anhydrous mineral phases increases the volatile contents of the host magma (known as second boiling; Edmonds & Woods, 2018), the dissolved volatiles causing overpressure in the magma body and producing a buoyancy force that drives fault propagation upward (Blake, 1984).

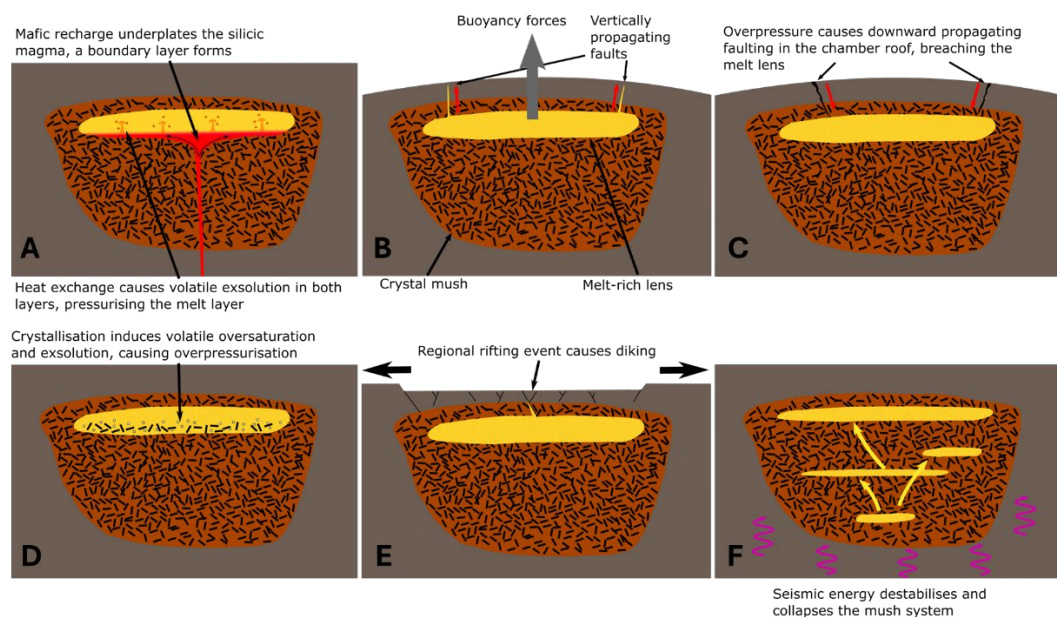


Figure 1.4: Different models of triggering of large silicic eruptions: A) Mafic recharge into the system underplates the silicic lens – cooling of the mafic magma results in exsolution of volatiles and subsequent lowering of the mafic magma’s density. Volatile exsolution may also occur in the heated silicic magma, and this separate volatile phase pressurises the magma chamber; B) Buoyancy forces from the melt-rich lens cause the formation of vertically propagating faults and dykes, resulting in eruption when these reach the surface; C) Surface deformation caused by growth of the magma body in the upper crust causes downward propagating faults, resulting in eruption when these reach the magma body; D) Exsolution of a volatile phase by crystallisation within the system (so-called ‘second boiling’) causes pressurisation of the system; E) Regional rifting (e.g. in the Taupo volcanic zone) has been proposed to have interacted with shallow magma bodies, resulting in their eruption; F) Seismic activity may destabilise perched magmatic systems. Author’s own figure.

On top of these ‘local’ triggering mechanisms, other external triggers have been suggested which are tied to regional tectonic processes or synchronous global events. Having a silicic system in a semi-stable eruptible state could mean that it is exceptionally sensitive to outside influences such as rifting or tectonic destabilisation. In the Taupo volcanic zone in New Zealand, large volumes of magma are stored and erupted in a small region. This is due in part to the extensive rifting in the area, which creates a large amount of space for ascending magmas to fill (Spinks et al., 2005). This rifting may result in the propagation of

dykes between magma bodies and the surface, resulting in eruption (Allan et al., 2012, 2017; Cabaniss et al., 2018; Fig. 1.4E).

Regional seismic events may also have an influence. Tectonic seismicity has long been debated as a potential trigger for increased magmatism (Michell, 1759; Yokoyama, 1971; Nakamura, 1975; Linde & Sacks, 1998). Magma bodies in a critical state may respond to seismicity, and there are numerous proposed mechanisms in which seismicity can influence magmatism including dike unclamping, bubble nucleation and mush collapse (Seropian et al., 2021; Fig. 1.4F).

1.2.3 Where (and when) do silicic super-eruptions occur?

Large volume silicic eruptions are restricted to the continental crust in specific regions of the world and are typically the result of complex interactions of different variables including crustal thickness, mantle productivity, the nature of the thermomechanical modification of the local crust, tectonic regime, and many others (Bryan, 2007; Hughes & Mahood, 2008, 2011; Bryan & Ferrari, 2013; Best et al., 2016; Sheldrake et al., 2020; Wilson et al., 2021). In order to discuss the potential causes of large-volume explosive volcanism at and around the AVC, the details of regions that have experienced similar activity must be investigated for comparison. Fig. 1.5 shows the locations of such regions, most of which are located at convergent margins, although there are several exceptions. There is a large variation in the caldera density of different arcs, and convergent margins are host to greater number of calderas where:

- They over-lie slabs that are experiencing rollback such as the Great Basin Igneous province and Sierra Madre Occidental province spanning southwest USA and north-western Mexico (Ferrari et al., 2007; Bryan et al., 2008; Best et al., 2016; Andrews et al., 2022) or the provinces of the Central Andean plateau including the Altiplano-Puna volcanic complex (De Silva et al., 2006; Kay et al., 2010; Salisbury et al., 2011; Brandmeier, 2014; Freymuth et al., 2015; Best et al., 2016)
- The physical conditions of the margin fulfil specific requirements, such as elevated convergence rates and/or convergence obliquity, thickened and/or older overlying crust, maturity of the magmatic system, migration of magmatism, and extensional stress regimes in the crust (Hughes & Mahood, 2008, 2011; Sheldrake et al., 2020; Wilson et al., 2021).

Non-convergent margin related calderas are present in two tectonic settings:

- At mature hotspots, e.g., Yellowstone caldera, USA (Pierce & Morgan, 2009);
- Where continental rifting is occurring (e.g., the silicic large igneous provinces or SLIPs; Bryan, 2007; Bryan & Ferrari, 2013)

Crustal thickness is one of the key variables that has been correlated with increased occurrence of silicic calderas (Hughes & Mahood, 2008, 2011). The effects of thicker crust are twofold. The region of the crust in which the ascending mafic magma reaches neutral buoyancy is deeper, and there is also increased heat loss due to increased contact with surrounding rock, which will have further negative effects on its buoyancy (Chaussard & Amelung, 2014). These factors act to increase the lifetimes of magmas in thickened continental crust over other types. These longer residence times result in greater amounts of magma stored over the lifetime of a system, which means that significant mush systems can be developed like the type that are required for the production and eventual extraction of magma bodies that feed these super-eruptions (Cashman et al., 2017; Karakas et al., 2017). These factors also tend towards increasing the silica content of the magmas, as an increased duration of storage promotes further fractionation of the magmas as well as increases the likelihood of the formation and addition of partial melts from the crust (Hughes & Mahood, 2008, 2011).

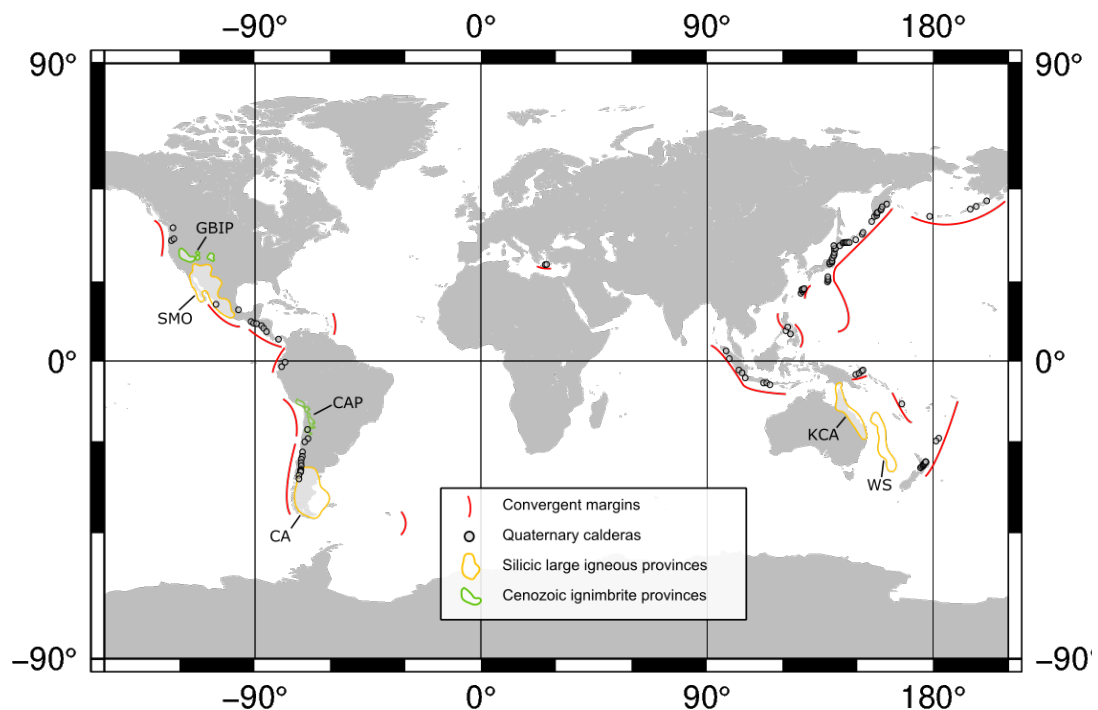


Figure 1.5. Map showing the distribution of some of the largest silicic centres. Quaternary calderas are calderas >5 km in diameter, locations are from Hughes & Mahood (2011); silicic large igneous provinces are from the Phanerozoic, KCA-Kennedy Connors-Auburn 320-280 Ma, CA-Chon Aike 188-153 Ma, WS-Whitsunday 132-95 Ma, SMO-Sierra Madre Occidental 38-20 Ma, locations and ages from Bryan (2007); Cenozoic ignimbrite provinces, GBIP-Great Basin Igneous Province 36-18 Ma, CAP-Central Andean Plateau 11-1 Ma, locations and ages from Best et al. (2016).

There is a large global variability in the caldera density in convergent margins. Studies have shown that there are several variables which control the likelihood of a region producing one or more super-eruptions. These include having trench-normal convergence rates of 70-95 mm/yr, the presence of old and thick continental crust, proximity to previous structures or to regions of extensional stress (Hughes & Mahood, 2008, 2011), and in regions where the magma column is in a new position, either due to the relative youth of the system or because of arc migration (Hughes & Mahood, 2011).

In several regions including the CAVA, there also appears to be a timed component to the silicic volcanism where the arc experiences periods of elevated explosive activity (Fig. 1.6). Pulses of elevated explosive silicic activity within regions are commonly observed in the rock record across various timescales (de Silva et al., 2015; Paterson & Ducea, 2015) and can have one of several explanations. These can be related to the breakup and formation of continents (silicic large igneous provinces; Bryan, 2007; Bryan & Ferrari, 2013), regional 'flare-ups' (de Silva et al., 2015; Paterson & Ducea, 2015), or smaller scale pulsed activity as is observed at the CAVA (Schindlbeck et al., 2018; Fig. 1.6).

Ignimbrite 'flare-ups' are periods of activity at convergent margins where caldera-forming eruptions occur much more frequently than the typical rate for the region (Coney, 1978). These events produce magmas called the 'monotonous intermediates' of Hildreth (1981). They are also tied to changes in the regions' tectonic configuration, being caused by processes including slab-rollback and/or related crustal delamination, landward arc migration, and asthenosphere flow (Ferrari et al., 2002; Farmer et al., 2008; Kay & Coira, 2009; Best et al., 2016; Chapman et al., 2021). Because of the landward arc migration, volcanoes related to flare-up events are commonly situated behind the volcanic arc front. Key examples of these are the southern Great Basin ignimbrite province (Best et al., 2016), the Sierra Madre Occidental province (Ferrari et al., 2002), and the Altiplano-Puna volcanic complex (Kay & Coira, 2009).

These flare-ups are similar to the style of magmatism at the northern end of the CAVA. The tephra record from this region shows that there is a cyclicity of increased explosivity along the arc (Schindlbeck et al., 2018; Fig. 1.6), and the calderas here (at least in the north) are located behind the arc. However, there are crucial differences: the arc migration is trenchward, the opposite of that typically found during flare-up events; the magma compositions differ from those typically found at flare-up sites (i.e., the monotinous intermediates); and the volumes of erupted material are much smaller than those produced during flare-ups. It

is unlikely that the elevated pulses of explosive activity in this region of the CAVA have been caused by flare-up events, but the similarities between the eruptive history of the CAVA (Fig. 1.6) and these events invite comparison. Examination of large-volume silicic magmatism at migrating centres with a comparison to flare-ups could be useful to answer questions about their petrogenesis, even if only to rule out certain processes.

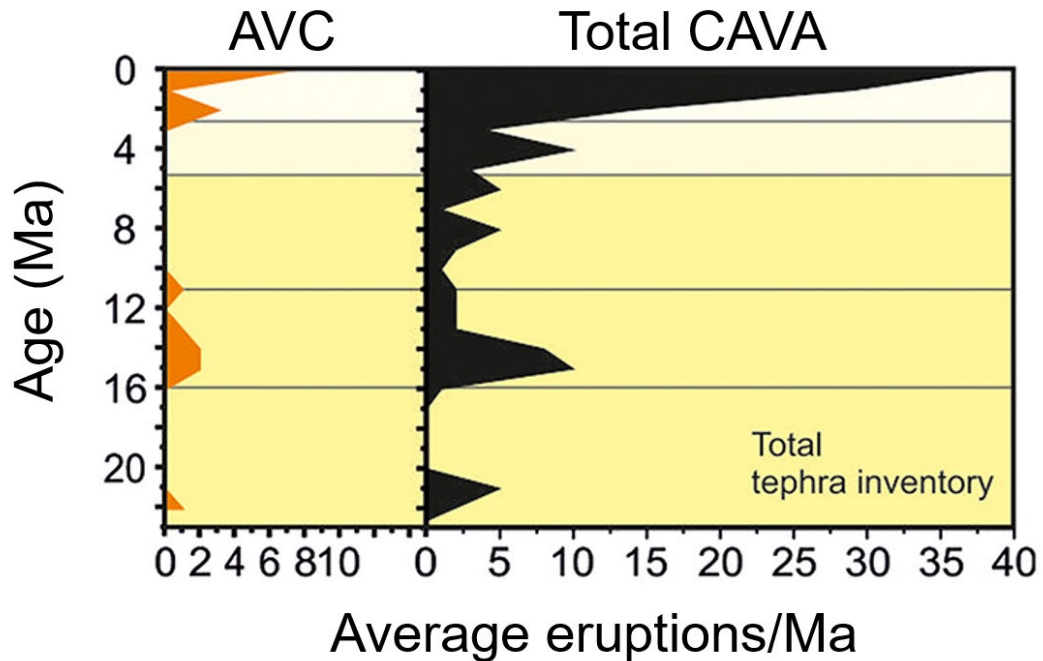


Figure 1.6. Tephra inventory for the Atilán Volcanic Centre compared with the total tephra inventory for the CAVA. From Schindlbeck et al. (2018)

1.3 The Central American volcanic arc

1.3.1 Structure of the Central American volcanic arc

The CAVA results from subduction of the Cocos plate underneath the Caribbean plate at a convergence rate of 73-85 mm/yr (DeMets, 2001). This region is influenced by the complex structural arrangement of several different crustal blocks, and the interactions between these different bodies has further impacts on magmatism. Figure 1.7 shows the positions of these blocks, as well as the interaction of the main tectonic units. These are the North American plate (NA), the Cocos oceanic plate (COCOS), the Caribbean plate (CA), as well as a forearc sliver (FAS) that is detached from the Caribbean plate. The key crustal blocks in this region are the Chortis, Maya and Patuca blocks. The Chortis block underlies southern Guatemala, El Salvador and NW Honduras and underlies much of the CAVA in this region and is therefore the main focus when discussing the AVC. It is bounded by the Polochic and Montagua fault zones in the Guatemala suture zone to the north (with the Maya block on

the far side) and the forearc sliver to the south-west (Case et al., 1984; Malfait & Dinkleman, 1972; Gazel et al., 2021). The south-eastern edge borders the Patuca block (Gazel et al., 2021). This section will give a brief overview of the nature of these different blocks and their interactions with one-another to give context to the geochemical nature of volcanism at this convergent margin.

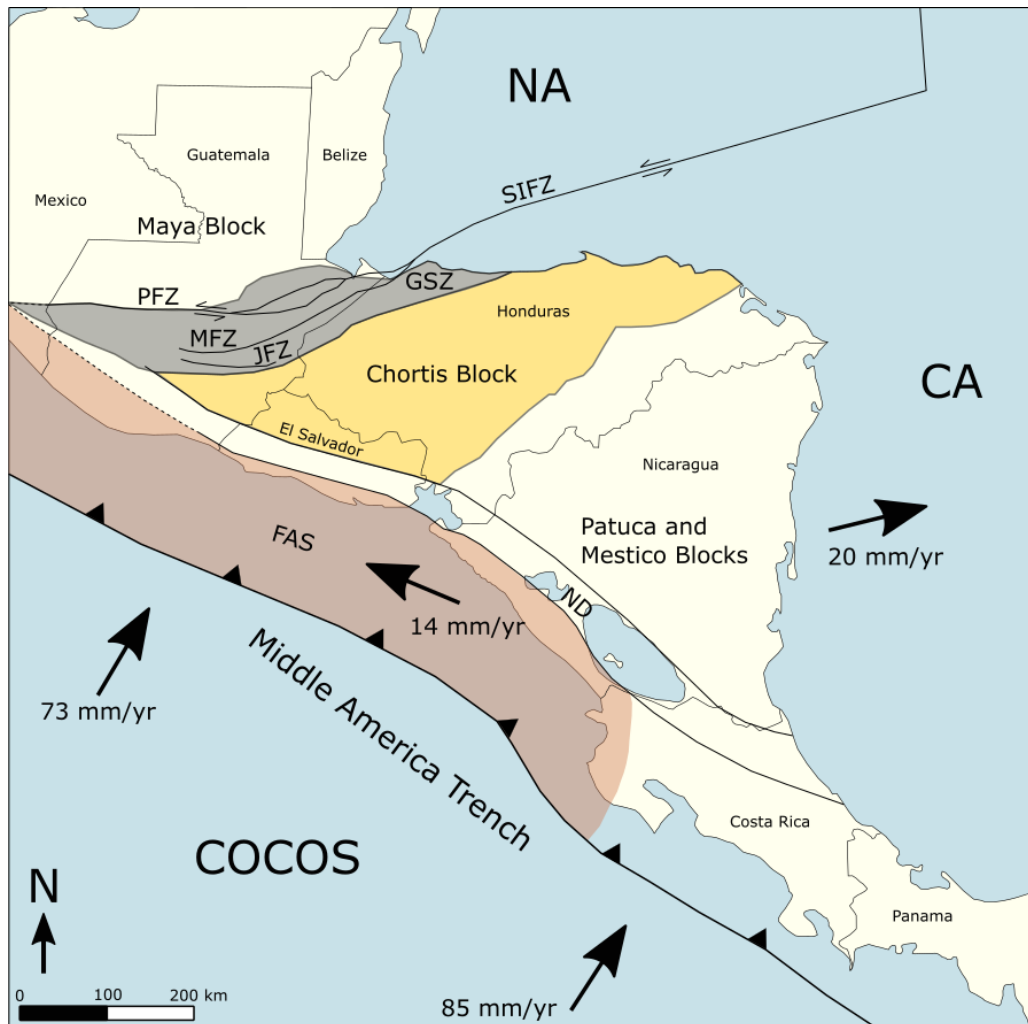


Figure 1.7. Structural map showing the major tectonic features of the CAVA. PFZ – Polochic fault zone, MFZ – Montagua fault zone, JFZ – Jocotan fault zone, SIFZ – Swan Island fault zone, ND – Nicaraguan depression, NA – North American plate, CA – Caribbean plate. The coloured regions are the most relevant crustal blocks to this project: brown highlighted area labelled FAS – Forearc sliver, grey highlighted zone GSZ – Guatemalan Suture zone, yellow highlighted zone-Chortis block. Plate motions from DeMets (2001), Guzman-Speziale (2001) and Phipps Morgan et al. (2008). Location of major faults from Dengo et al. (1970), Pflaker (1976), Burkart & Self, (1985), Rogers & Mann (2007) and Funk et al. (2009).

Several authors (Dollfus & Montserrat, 1868; Sapper, 1897; Stoiber & Carr, 1973 and Carr, 1974) recognised the segmented nature of the CAVA, whereby different segments are identified either by changes in the strike of the volcanic front, right lateral offsets between segments, or both. These breaks are highlighted by black arrows in Fig. 1.8. Seismic imaging of the subducting Cocos plate shows that there are no significant changes in the nature of

the slab underlying these offsets, indicating that the volcanic segmentation must therefore be controlled by deformation of the overlying crust (Gazel et al., 2021). The segmentation of the arc results in obliquity between the strikes of the segments and the subducting slab, causing the depth from the volcano to the top of the slab to increase to the southeast of each segment (Fig 1.9).



Figure 1.8. Map showing the location of the present (line of black triangles) and past (orange and brown highlighted areas) locations of the CAVA front, as well as the locations of behind-the-front volcanoes and associated structural features. Black box shows location of study area shown in Fig. 1.1, AVC – Atitlán volcanic centre, GG –Guatemala graben, IP – Ipala graben, HD – Honduran depression. Position of past arcs from Alvarado et al. (2007), location of the behind-the-arc fields from Walker et al. (1995) and Patino et al. (1997). Black arrows mark the segment breaks of the volcanic front, from Stoiber & Carr (1973) while red arrows mark the direction of arc migration. The most north-westerly volcano on this map is Volcán Tacaná, which represents the start of the CAVA

The larger-scale tectonic setting also exerts strong controls on the volcanism of Central America. The margin between the North American and Caribbean plates used to be the (now inactive) Jocotan fault zone (JFZ). The currently active plate boundary is now the sinistral Polochic and Montagua faults zones (PMFZs). Further structural complications

were presented by Malfait and Dinkleman (1972), who suggested that the western end of the Caribbean plate is pinched between the Cocos and the North American plates as they converge obliquely (Fig. 1.7, large black arrows denote plate motions relative to the North American plate). As the Caribbean plate moves eastward, the western end is pinned, resulting in extension of the western end of the Caribbean plate that may be accommodated by rotation of crustal blocks along the PMFZ (Burkart & Self, 1985). This could also explain the segmented nature of the arc (Burkart & Self, 1985). Extension is also tied to the formation of N-S trending grabens (Fig. 1.8) throughout south-eastern Guatemala, northern Honduras, and western El Salvador (Álvarez-Gómez et al., 2019). This rotation has a further structural implication that the strike of each segment of the arc is oblique to that of the subducting slab (Fig. 1.9). Motion of the Caribbean plate relative to the surrounding plates, calculated from GPS signals, shows a decrease through southern Guatemala from east to west (Lyon-Caen et al., 2006). A large part of the difference is made up for by N-S striking normal faults within the plate which produce 0.9 cm/yr of horizontal deformation, with a significant proportion of that extension (0.5 cm/yr) occurring at the Guatemala City and Ipala grabens (Guzmán-Speziale, 2010; Franco et al., 2012). Recent studies have shown that there is no current extension in western Guatemala (Ellis et al., 2019; Garnier et al., 2022). During the Pliocene, extensional faulting occurred in this region, but gradually ceased eastward during the Pleistocene, such that there would have been little to no tectonic activity around the AVC in this time (Garnier et al., 2022). It should be noted that the time resolution of this study was restricted by the available outcrops, and as such the exact timing of fault cessation at the AVC is not well constrained.

Extensional tectonic regimes at convergent margins are strongly associated with an increased likelihood of the occurrence of large-volume silicic eruptions, and so the absence of such a regime in the western portion of Guatemala's volcanic arc requires further explanation for its explosivity.

Several threads of evidence also suggest the existence of a forearc sliver bounded by a right-lateral transtensional fault parallel to and potentially situated beneath the active volcanic front and the Middle America trench (DeMets, 2001; Álvarez-Gómez et al., 2008, 2019; Franco et al., 2012; Staller et al., 2016; Alonso-Henar et al., 2017; Ellis et al., 2019; see Fig. 1.7), which presents a zone of weakness underneath the volcanic systems. It is uncertain whether this fault underlies the AVC (Ellis et al., 2019). Various models have attributed the segmentation of the arc to the relative motion between the forearc sliver and the Caribbean plate.

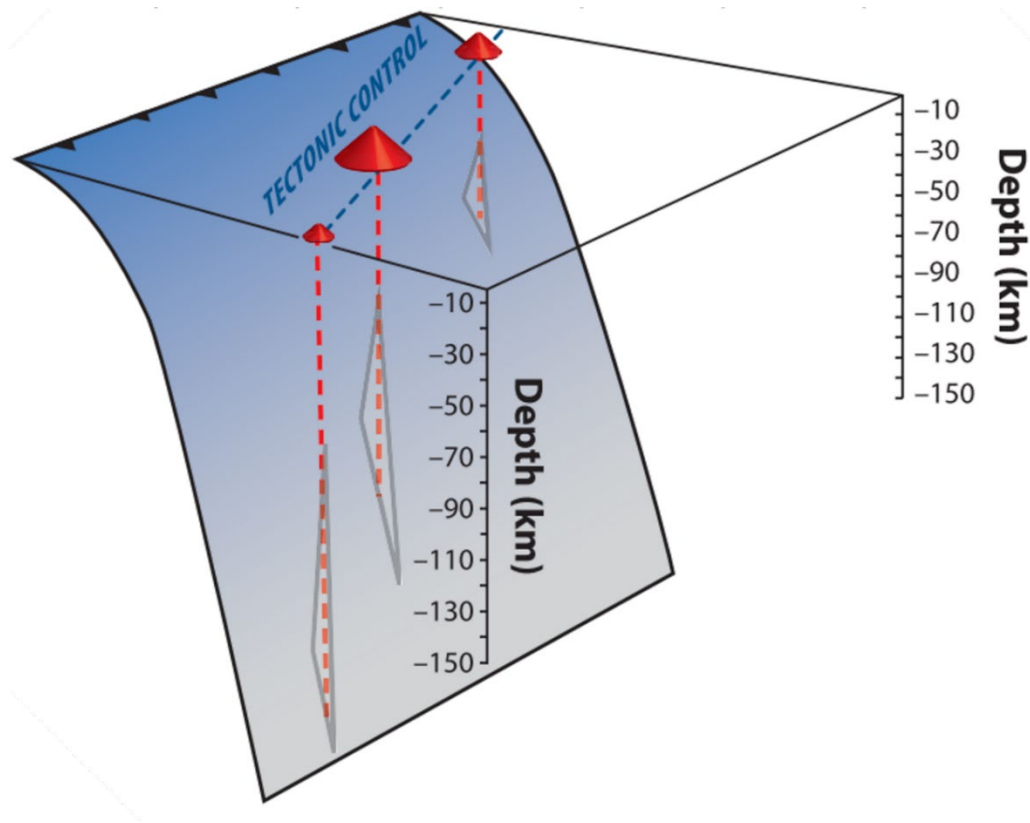


Figure 1.9. Cartoon showing the relationship between the subducting slab and the oblique segments of the CAVA, and the resulting differences in depths to the volcanoes. From Gazel et al. (2021).

Two key structural elements vary systemically along the strike of the CAVA. These are the angle of subduction and the thickness of the crust underlying the volcanic arc. Both peak around Nicaragua, where the maximum dip and minimum thickness are recorded (Fig. 1.10). The north-western and south-eastern ends of the arc have moderate slab-dips (48° and 44° , respectively), while the maximum subduction angle is $>60^\circ$ in the centre of the arc around Nicaragua (Syracuse & Abers, 2006; MacKenzie et al., 2008). Crustal thickness is between 30-35 km for most of the arc with a broad minimum through Nicaragua but increases in western Guatemala and central Costa Rica to 35-45 km (MacKenzie et al., 2008; Lücke, 2014).

Significant differences exist in the structure and makeup of the crust underlying the volcanic arc beneath these regions. The Guatemalan segments mainly rest on the thickened continental crust of the Chortís block (Heydolph et al., 2012; Fig. 1.7). The base of this block is composed of orthogneisses, metagranites and schists (Manton, 1996; Ratschbacher et al., 2009). These are overlain by low-grade metasediments that have been thrust by slivers of high-grade metamorphic rocks, sequences of metavolcanics and metasediments, and portions of ophiolite sequences (Harlow & Davies, 2004; Chiari et al., 2006; Tsujimori et al., 2006; Geldmacher et al., 2008; Brueckner et al., 2009; Ratschbacher et al., 2009; Torres-

de Leon et al., 2012; Flores et al., 2013). Local outcrops of Cretaceous granites and granodiorites are present at the volcanic arc front (Williams & McBirney, 1969; Newhall, 1987; Heydolph et al., 2012). A more detailed review of the structure of the crustal blocks of the CAVA is presented by Gazel et al. (2021).

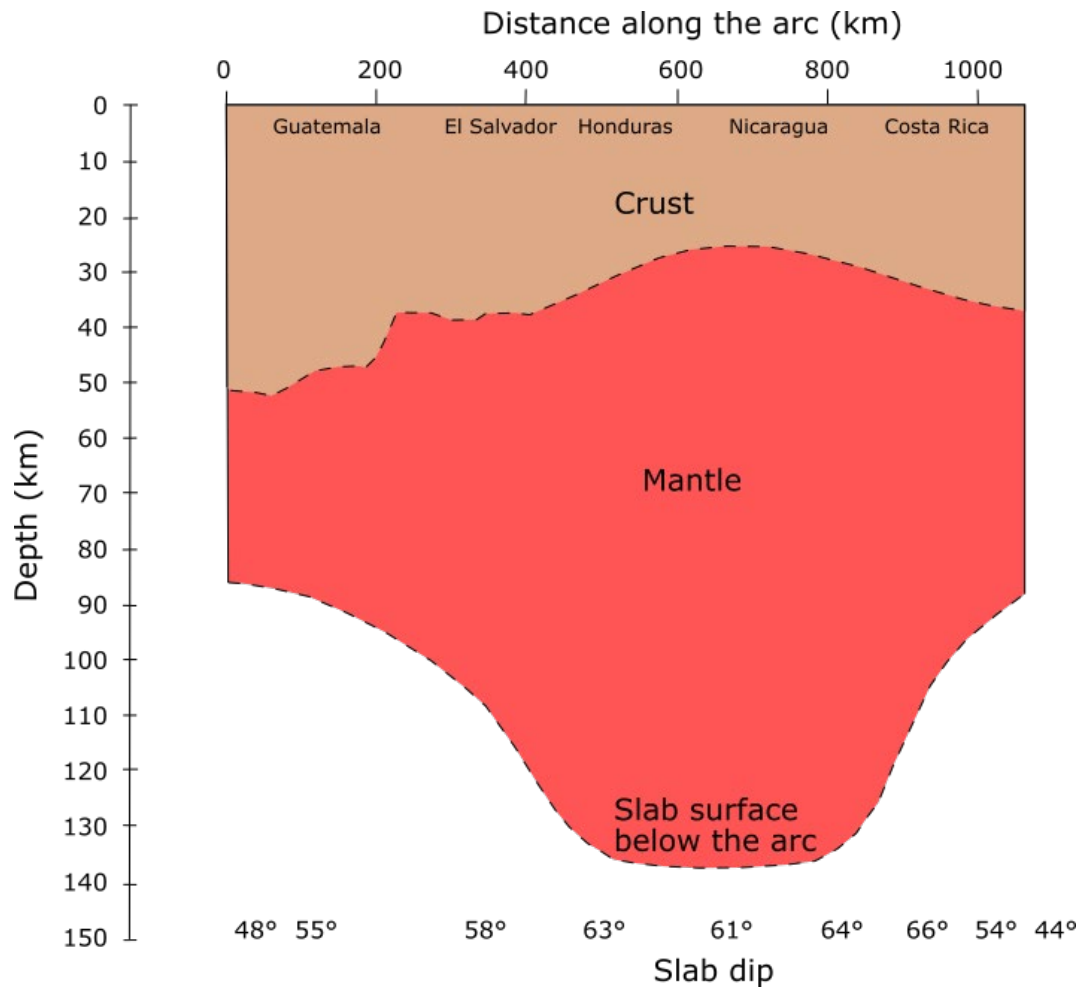


Figure 1.10. Estimated depth to the crust-mantle boundary and to the slab surface from the arc-front, as well as along-arc variations in slab dip. Adapted from Wehrmann et al. (2014), with data from Syracuse & Abers (2006) and MacKenzie et al. (2008). The starting location (0 km) is measured from Volcán Tacaná.

1.3.2 History of volcanic activity along the CAVA

Geochemical and geochronological evidence suggests that magmatic activity at the CAVA began at 75 Ma (Malfait & Dinkleman, 1972; Buchs et al., 2010; Whattam & Stern, 2015, 2016; Hauff et al. (2000) suggested that late-Cretaceous subduction of the Cocos plate caused the onset of CAVA volcanism. Variations in the position of the arc since then (roughly defined as activity since the Oligocene) are shown in Fig. 1.8. Arc migration has been ongoing since then in a general trench-wards direction, likely caused by slab rollback (Alvarado et al., 2007; Saginor et al., 2011). This trenchward younging trend is most consistent in the northwest portion of the arc (Guatemala and El Salvador), while in the

south-eastern regions older volcanic deposits occasionally lie further of the present arc front.

Arc migration is ongoing and, in the north-western segments of the arc, is manifested in the structures of the volcanoes. Stratovolcanoes are commonly paired in a north-south alignment, with the trenchward volcanoes being younger (Fig. 1.1 and 1.11). Calderas that predate the stratovolcanoes on their southern margins are also occasionally present to the north of the active arc (Rose et al., 1999; Fig. 1.1).

Alongside apparently regular phases of stratovolcano construction, the CAVA also shows periods of time where silicic eruptions are more frequent. Tephrostratigraphy of the arc (Fig. 1.6) shows five pulses of elevated tephra productivity (inferring greater explosive eruptions of various compositions) since the Miocene at >21, 17-11, 10-7, 6-3 and <2 Ma (Schindlbeck et al., 2018).

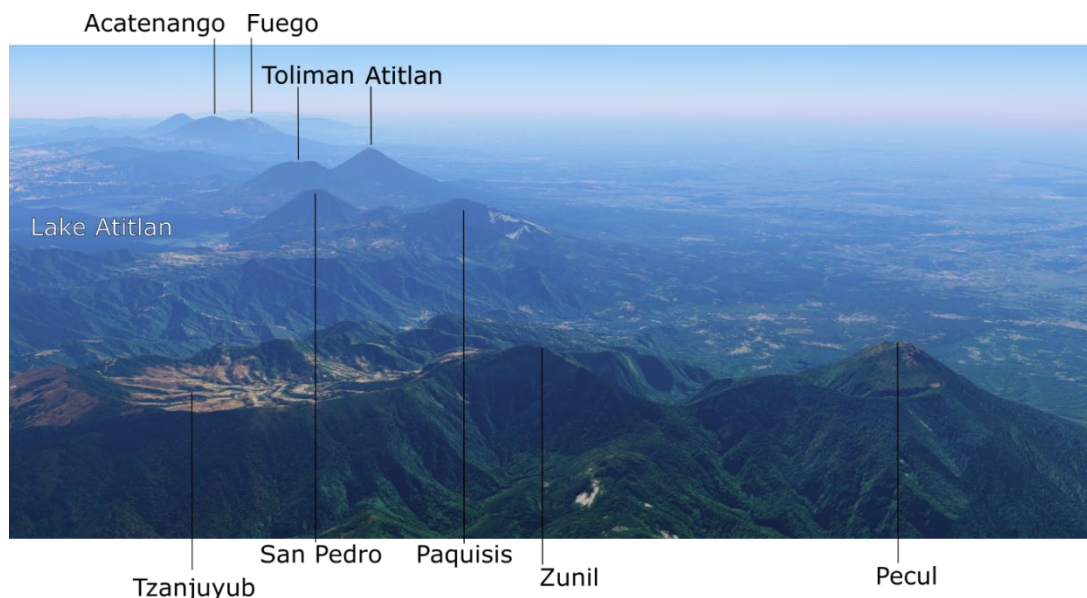


Figure 1.11. 3D view looking south-east along the Guatemalan segment of the CAVA from above Volcán Santa María showing several of the paired (Acatenango-Fuego; Tolimán-Atitlán) and linear (Tzanjuyub-Zunil-Pecul) volcanic structures, and the positioning of Lake Atitlán with respect to the current arc front. Volcanoes young to the right (south) of the image, except for Volcáns San Pedro and Paquisis, where the younger Volcán San Pedro is instead to the north of Volcán Paquisis, in the caldera margin. Taken using Google Earth

1.3.3 Along-arc geochemical variations

Many studies have been made of the temporal and spatial variation of the chemistry of the CAVA magmas. As this thesis will partly examine the most recent evolution of the arc, I will briefly describe the different influences on the chemistry of the magmas. This section summarises the past studies of the volcanic arc and the various melt inputs that have been suggested. Studies of the CAVA are broadly divided into along- and across-arc variations,

the combination of which is vital to understand the geochemical variations at individual volcanoes.

The CAVA shows systematic variations in several geochemical variables along-strike (Fig. 1.12; McBirney, 1969; Carr, 1984; Feigenson & Carr, 1986, 1993; Carr et al., 1990, 2003, 2007, 2014; Leeman et al., 1994; Chan et al., 1999; Patino et al., 2000; Rüpke et al., 2002; Feigenson et al., 2004; Vogel et al., 2004, 2006; Eiler et al., 2005; Walker et al., 2007; Sadofsky et al., 2008; Heydolph et al., 2012; Saginor et al., 2013; Wehrmann et al., 2014; Turner & Langmuir, 2015; Gazel et al., 2021). For most of these variables, the patterns are broadly symmetric, reaching a maximum or minimum value towards the middle of the arc in Nicaragua (the exception being $^{87}\text{Sr}/^{86}\text{Sr}$, which has a cosine-shaped trend along strike). The above-mentioned studies have described a series of processes and inputs at the CAVA in order to explain these variations. These can be divided into four categories: A: inputs from continental crustal contamination (high influence reflected by high Sr but low Nd isotope ratios, Fig. 1.12A and B respectively); B: inputs from the subducting slab (e.g., increasing input leading to increasing $^{87}\text{Sr}/^{86}\text{Sr}$ ratios, Fig. 1.12A; and Ba/La Fig. 1.12C); C: degree of partial melting of the overlying mantle wedge (increased degree of mantle melting shown by lower La/Yb ratios, Fig. 1.12D); and D; inputs related to the presence of enriched mantle beneath the Galapagos hot spot, such as highly elevated La/Yb (as shown by the four-fold increase in La/Yb in volcanic rocks from Costa Rica compared to those from Guatemala; Fig. 1.12D; (Gazel et al., 2011, 2015).

Most of the along-strike geochemical variations can be attributed to slab dip, although the mechanisms by which they affect the geochemistry of the melts vary. The increased slab dip beneath Nicaragua (Fig. 1.10) also increases the degree of fracturing of the slab around the hinge, increasing the amount of water that flows through the slab (Fig. 1.13). This in turn increases the amount of hydrous alteration of the slab (Patino et al., 2000; Abers et al., 2003; Ranero et al., 2003; Grevemeyer et al., 2007; Ivandic et al., 2008; Van Avendonk et al., 2011).

The increased slab dip also affects the distance from the slab surface to the crust and the width of the mantle available to be fluxed by fluids released from the slab (Fig. 1.13). This affects the degree of melting that may occur in the mantle wedge (Carr et al., 1990, 2007; Feigenson & Carr, 1993; Rüpke et al., 2002).

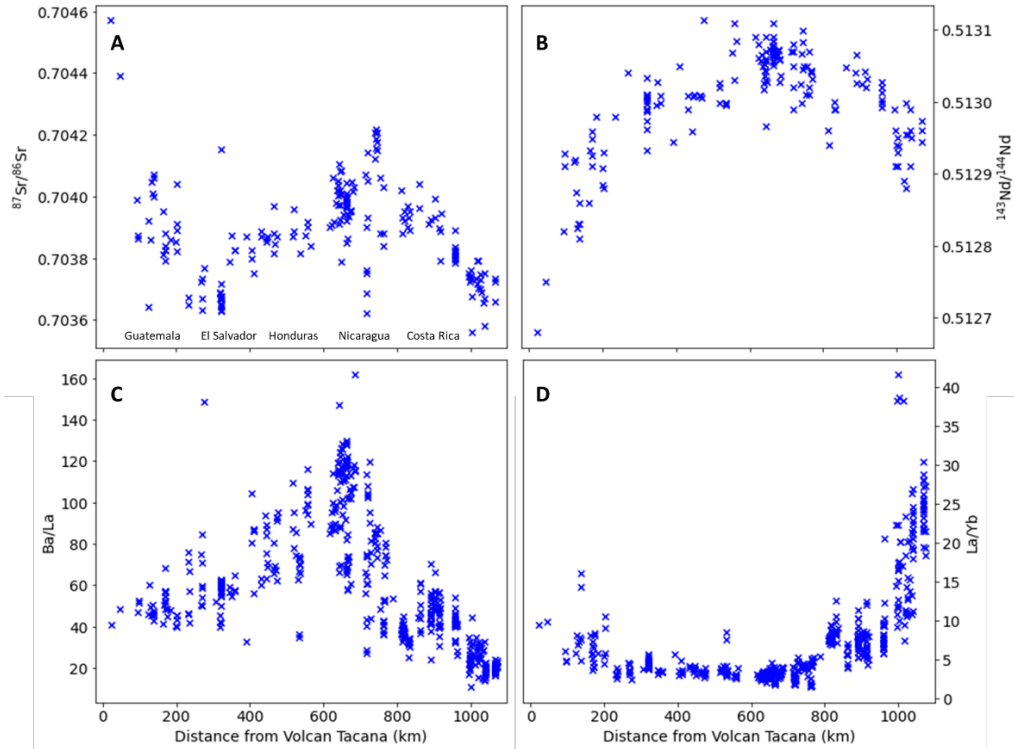


Figure 1.12. Geochemical variations with distance along-arc starting at Tacana volcano on the Mexican-Guatemalan border. Note the divergence in trends between Sr-isotope and Nd-isotope and Ba/La ratios in Guatemala (see text). Published data from RU_CAGeochem (Carr et al., 2014).

Two further complications affect the geochemical variations, which makes it difficult to parse the geochemical signals on which the two model groups rely. Firstly, Guatemala shows a reversal of the Sr-isotope trend resulting in the cosine-shaped trend (Fig. 1.12A), the values here instead increasing with decreasing slab dip (c.f., Fig. 1.10). This is explained by the presence of more radiogenic continental crust of the Chortis block (Feigenson et al., 2004; Walker et al., 2007; Heydolph et al., 2012). Secondly, the geochemistry of the south-eastern end of the CAVA shows a much more enriched nature (Fig. 1.12D). The presence of nearby Galapagos hot spot may explain this trend, as its ocean island basalt melt signatures are preserved in the downgoing slab and transmitted to the melts generated in the region of the overlying mantle wedge (Feigenson et al., 2004; Gazel et al., 2011; Hoernle et al., 2008). Lateral flow within the mantle wedge towards the north-west has influenced the geochemistry of the arc-front lavas up to north-western Nicaragua, as these melts are swept north-west parallel to the arc front. No evidence of this signal is found in El Salvador or Guatemala (Gazel et al., 2009).

A final influence on the geochemical variation is the variable depths to the slab below the volcanoes within segments (Fig. 1.9). A correlation is seen between the size of a volcanic centre and its position along a segment, where the largest volume centres are usually near

the centre of the segment with intermediate depths to the slab (between 90 and 110 km), while volcanoes with shorter or greater depths are typically smaller (Gazel et al., 2021). Crucially, the AVC is such a centre that lies in the middle of a segment (Fig. 1.8), although the Xela centre that lies on the end of the same segment could be a similar sized volcano based on the size of the proposed caldera by Duffield et al. (1993).

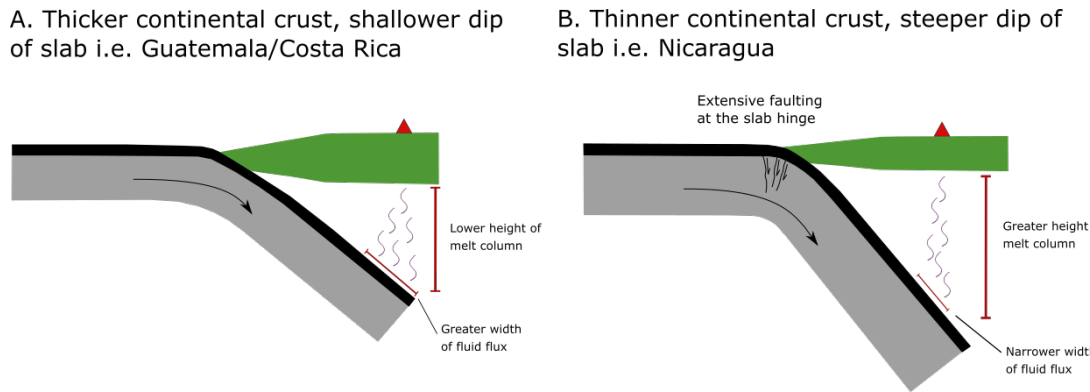


Figure 1.13. Illustration of the variations in the nature of the convergence and magma generation at the CAVA. A) Melting regime beneath Guatemala/Costa Rica where the slab is subducted at a low angle and has subsequently has a broader region of the mantle wedge which is fluxed by slab fluids. B) Melting regime under Nicaragua where the steeper dip has resulted in extensive faulting at the slab hinge resulting in greater fluid flow into the slab interior, and in a narrower region of the mantle wedge that is fluxed by slab fluids.

Geochemical variations between volcanoes along segments are tied to this physical variation. In general, smaller centres have much greater composition variability in elements and element ratios that are related to the slab fluids (e.g., Ba/La), in contrast to the largest centres which have much less heterogeneity in the slab signals in their magmas (Gazel et al., 2021). This could be explained in two ways: (1) the largest centres are in a ‘sweet-spot’ where their underlying mantle wedge receives the greatest flux from the slab, resulting in higher degrees of partial melting and causing geochemical homogenisation of the melts; (2) the larger magma systems at these larger volcanoes simply homogenise the geochemical signatures (Gazel et al., 2021). As the AVC is one of the larger centres, it is important to consider this when examining the geochemistry of its magmas.

These along-arc geochemical variations are also present in the silicic magmas of the CAVA (Vogel et al., 2006). As they mimic the variations seen in the more primitive lavas of the arc, it has been suggested that the silicic tephtras have a genetic relationship with the mantle-derived melts.

1.3.4 Across-arc geochemical variations

Understanding the cause of the geochemical variations along the volcanic arc and within long-lived volcanic centres requires an understanding of how and why the magma

geochemistry changes across the arc. There are two different types of volcanism located behind the currently active volcanic front of the CAVA: 1) fields of cinder cones, older polygenetic volcanic cones, and rare calderas (hereafter referred to as behind-the-volcanic-front (BVF) volcanoes, and outlined in Fig. 1.8); and 2) north-south aligned stratovolcano chains or pairs, where younger cones are found on the southern end of these lineaments (several key examples shown in Figs. 1.1 and 1.11).

The BVF volcanoes have been investigated by numerous authors. They are most evident in south-eastern Guatemala and Honduras (Walker et al., 1995, 2000, 2011; Patino et al., 1997) and are related to decompression melting caused by extension of the Caribbean plate related to the large-scale tectonic interactions (Carr et al., 1990). Hence, they are commonly associated with rifting structures (e.g., Guatemala and Ipala grabens and Honduran depression in Fig. 1.8).

Geochemical variations in these cinder cone fields correlate with distance from the arc-front (Fig. 1.14). $^{87}\text{Sr}/^{86}\text{Sr}$, $^{207}\text{Pb}/^{204}\text{Pb}$ and $^{206}\text{Pb}/^{204}\text{Pb}$ all show positive correlations, while $^{143}\text{Nd}/^{144}\text{Nd}$ shows a negative correlation (Walker et al., 1995). This is attributed to an increase in the radiogenic nature of the crust towards the centre of the Chortís block, from which the magmas feeding the cinder cone fields acquired the geochemical signature during their ascent. If this geochemical trend in the crust is consistent along the Guatemalan section of the CAVA, then one could expect to see similar geographic variations in the radiogenic isotope values of the lavas of the AVC. The geographic variations then could allow us to trace the relative inputs that magmas from the width of the AVC have had into the silicic magmas, allowing us to test the influence of migration and the extraction of magmas from the width of the AVC.

The second group of across-arc variations are related to the commonly north-south aligned groups of volcanoes seen in the northwestern segments of the CAVA. These occur either as chains or pairs, where younger cones are usually found on the southern ends of these lineaments, or as calderas with stratovolcanoes built on their southern margins (Sapper, 1925; Dengo et al., 1970; Halsor & Rose, 1988, 1991). In the central Guatemalan segment of the arc, there are at least six Quaternary chains. These are (from west to east): Almolonga/Cerro Quemado-Santa María-Santiaguito, Ixtahuacan-Tzanjuyub-Zunil-Pecul, San Marcos-Paquisis-San Pedro, Tecolote-Tolimán-Atitlán, Acatenango-Fuego and Amatitlán-Pacaya (Figs. 1.1 and 1.11). These chains are related to the short-term (on the scale of 10^3 - 10^5 years) migration of the mantle magma source feeding individual centres

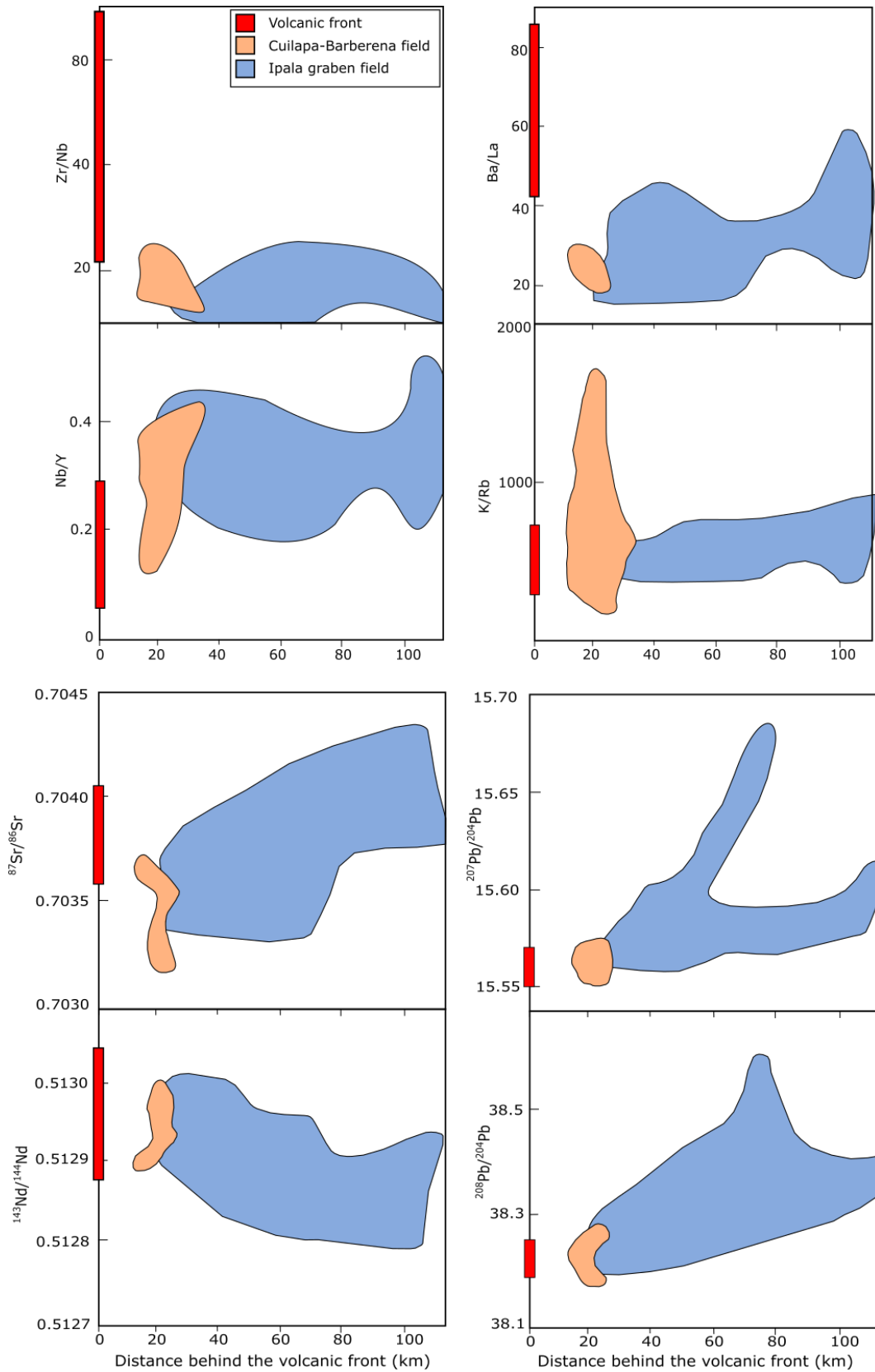


Figure 1.14. Geochemical variations with distance from the volcanic front for volcanic samples from south-eastern Guatemala. Trace element ratios do not vary significantly behind the front, whereas the isotopic ratios tend to increase (or decrease in the case of $^{143}\text{Nd}/^{144}\text{Nd}$) with further distance from the volcanic front. This is likely due to increases in the radiogenic nature of the crust further away from the arc front. Redrawn from Walker et al. (1995).

(Halsor & Rose, 1988). Studies of geochemical variations of aligned cones in Guatemala and El Salvador show that the older northern-most volcanoes have higher TiO_2 and HFSE contents, comparable to the BVF lavas (Halsor & Rose, 1988, 1991). Similar north-south chains of volcanic structures occur in Nicaragua, but these are not tied to the regional migration trend (Dengo et al., 1970).

While the presence of pre-existing stratovolcano lineaments at the AVC is impossible to know due to the presence of the Atitlán III caldera, the overwhelming tendency of stratovolcanoes to form these chains (especially evident in the case of the immediately neighbouring Ixtahuacan chain) makes it likely that the stratovolcano activity preceding the formation of the caldera took this form. Magmatism prior to the LCY-event was likely strongly controlled by migration.

1.4 The Atitlán Volcanic Centre

1.4.1 Stratigraphy of the Atitlán volcanic centre and description of the units

Koch & McLean (1975) produced a stratigraphy of the pyroclastic units of the Guatemalan highlands, recognising 26 separate airfall units in the region. They did not assign them to individual centres, although they did classify the Los Chocoyos (their H) and W tephras as likely to be from Lake Atitlán. Later studies (Newhall, 1980, 1987; Newhall et al., 1987; Rose et al., 1979, 1987) revealed much more about the volcanic history of the Atitlán caldera, described its volcanic products and related their stratigraphic positions to the Guatemalan volcanic record. Studies of the tephrostratigraphy of the region have further recognised tephras that may be related to the AVC (Kutterolf et al., 2008a, 2008b, 2016; Schindlbeck et al., 2018). Broadly, the AVC activity has been divided into four phases, based on repetitions of stratovolcano growth followed by voluminous silicic eruptions before southward migration of the locus of activity. Examination of drill cores from the Cocos plate off the coast of Central America shows that this activity correlates well with regional pulses of activity in the CAVA (Fig. 1.6; Schindlbeck et al., 2018). Activity at the AVC is described as follows and is presented in Table 1.1:

Phase I (14-11 Ma) consists of five crystal-rich ignimbrite eruptions, known as the María Tecún tuffs, which occurred over several hundred thousand years. They were preceded by stratovolcanoes that are only preserved as lithic fragments in these tuffs. The cumulative thickness of the eruption deposits is over 1,000 m and the phase culminated in the formation of the Atitlán I caldera (Fig. 1.1; Newhall, 1987).

Phase II (10-8 Ma) followed phase I immediately but was distinct spatially. Numerous tuff units are associated with the Atitlán II caldera, including the Panajachel tuff breccia, the large volume San Jorge tuff (which resulted in the formation of the Atitlán II caldera, Fig. 1.1), the Catarata tuffs, and the Los Idolos dacites (Newhall, 1987). This phase was followed by a long period of quiescence.

| Phase | Name/Unit | Age (ka) | Description | Ref |
|--------------------------|---------------------------------|------------------------|--|--------------------|
| Phase IV | Volcán Atitlán | 10-AD 1856 | Stratovolcano consisting of small basaltic andesite lava flows and deposits from pyroclastic density currents. Paired on the southern edge of Volcán Tolimán | a, b, c, d, e |
| | Volcán Tolimán | 56-10 | Stratovolcano consisting of predominantly andesitic lavas, including the parasitic cone Cerro del Oro | a, b, c, d, e, f |
| Transition Period | I eruptions | 56 | Series of at least five small phreatomagmatic tephra (total volume approximately 7 km ³) with a bimodal composition variation (basaltic andesite and rhyolite). Rhyolites contain andesitic enclaves | a, g, h |
| | F eruptions Volcán San Pedro | Between 60-56 60-43 | Series of several small tephra deposits Stratovolcano consisting of basaltic andesite to andesite lavas. Several mafic tephra layers are found between the D2 and F tephra and are tentatively correlated with this volcano | a, h a, b, c, d |
| | D2 eruption | Between 75-60 | A small (unknown volume) rhyolite pumice fall deposit overlying the D1 deposit; includes a minor mafic component | a, h |
| | D1 eruption | Between 75-60 | A small (unknown volume) andesite pumice fall deposit with great thickness on the northwestern lake edge but minor presence elsewhere | a, h |
| Phase III | Los Chocoyos (LCY) eruption | 75/98 | VEI 8 (510 km ³ DRE) eruption with fall, flow, and surge phases, of rhyolite composition with a minor mafic component | a, g, i |
| | W eruption | 130 | Large (83 km ³ DRE) rhyolite eruption with a basal andesite component | a, g, j |
| | Atitlán Older Tephra (AOT) | 310 | Large (65 km ³ DRE) rhyolite eruption tentatively correlated to the AVC | j |
| | Volcán Paquisis | 440 | Stratovolcano consisting of basaltic andesite to andesite (with rare dacite) lavas. | a |
| | R-tephra | Unknown (>1,400) | Small deposit with a fall and flow phase. May not be from the AVC but included for completeness | a, k |
| | Volcán San Marcos | 1,800-1,400 | Stratovolcano consisting predominantly of basaltic andesite to andesite (with rare dacite) lava flows | a |
| Phase II | Volcán Tecolote | 1,800-830 | Stratovolcano consisting predominantly of basaltic andesite to dacite lavas | a |
| | Phase II tuffs | 9,000-7,000 | Eruption of the small to moderate sized San Pablo, Finca Natividad, Panajachel, San Jorge, and Catarata tephra. | a |
| Phase I | Phase II stratovolcanoes | 10,000 | Series of stratovolcanoes of unknown compositions that preceded the phase II tuffs | a |
| | Maria Tecun tuffs | 12,000-11,000 | Series of five large volume () ignimbrites, distinctive in their highly crystalline nature and advanced degree of welding | a |
| Phase I | Phase I stratovolcanoes | 14,000-12,000 | Series of stratovolcanoes of unknown compositions that preceded the Maria Tecun tuffs, only preserved as xenoliths within the deposits | a |

Table 1.1. Major volcanoes and tephra of the AVC in stratigraphic order. Citations are a-C. G. Newhall (1980); b-Rose et al. (1980); c-C. G. Newhall et al. (1987); d-Halsor & Rose (1988); e-Halsor & Rose (1991); f-Halsor (1989); g-Cisneros de León et al. (2021a); h-Rose et al. (1987); i- Baudry et al., 2024; j-Kutterolf et al. (2016); k-Koch & McLean (1975)

Phase III (1.0-0.06 Ma) and phase IV (0.06 Ma-present) are better preserved and their stratigraphy is presented in Table 1.1 following the work of Newhall (1980,1987), Rose et al. (1987) and Kutterolf (2008a, 2008b). The relative positions of the features are shown in Fig. 1.1. Formation of two stratovolcano lineaments began at approximately 1 Ma (Newhall, 1980, 1987), the remnants of Volcáns San Marcos (on the northwestern edge) and Paquisis (on the southwestern edge) mark the presence of a western lineament, while Volcán Tecolote is the only pre-LCY stratovolcano that indicates the presence of the east/central lineament (Fig. 1.1). Volcáns Tolimán and Atitlán are the likely post-LCY continuation of this lineament. Despite caldera formation removing most of the material that would confirm the presence of these lineaments, the dominant trend for lineament formation at stratovolcanoes in this segment of the CAVA and the relative positioning of the different AVC stratovolcanoes suggests that chains of stratovolcanoes were present in the now-excavated region of the caldera.

Several large pumice eruptions, including the Los Chocoyos (LCY) caldera-forming eruption, make up the suite of Quaternary explosive activity. These mark the boundary between the initial stratovolcano construction period and an extended period dominated by rhyolitic eruptions. The W pumice (130 ka) is the oldest of the confirmed AVC tephras (Rose et al., 1987). Two other silicic eruptions may also have been sourced from this centre. These are the R tephra of Koch & McLean (1975) which has an age estimate of >1.4 Ma, and the Atitlán Older tephra (AOT, 306 ka) of Kutterolf et al. (2016). The latter deposit has a substantial volume (approximately 65 km³ DRE). The W and AOT eruptions are both rhyolites and have highly potassic compositions (AOT – 3.5-4.3 wt.% K₂O; W – 4.5-5.2), overlapping with the composition of one of the rhyolites erupted during the LCY event (the high-K LCY rhyolite with 4.2-4.6 wt.% K₂O; (Rose et al., 1979; 1987; Kutterolf et al., 2008a, 2016, Cisneros de León et al., 2021a).

The AOT is correlated to the AVC through proximal tephra deposits, although only 5-10 locations form this correlation (Kutterolf et al., 2016). This places the source of the AOT in the vicinity of the AVC but, unlike the W pumice, the evidence to confidently correlate it with a specific centre is weaker. Neither eruption has left evidence of a caldera existing before the LCY eruption, although such evidence would most likely have been destroyed by the much larger LCY event. Another nearby centre could also provide an alternative source for the AOT. A caldera named Xela has been proposed in the Quetzaltenango valley (Fig. 1.1), but no tephras have yet been correlated with it (Duffield et al., 1993).

The LCY eruption is by far the largest pumice eruption from Phase III activity and is also the largest known eruption from the CAVA (Cisneros de León et al., 2021a). It had a VEI of 8 based on a tephra volume estimate of $1220 \pm 150 \text{ km}^3$ (Cisneros de León et al., 2021a) and an estimated column height of 40 km (Brocard & Moran-Ical, 2014). Most of the tephra erupted (approximately 90%) was of high-K composition, based on the estimated 60% proportion of this composition in the pyroclastic flow deposits and the fact that it made up the entirety of the fall deposit (Rose et al., 1979). During the ignimbrite phase of the eruption, the other 40% of the volume erupted was of a low-K rhyolite (2.7 wt.% K_2O ; note that the term “low-K” is in reference to the high-K composition and it actually falls within the medium-K calc alkaline trend. This naming convention has been kept to be in keeping with the published literature).

After the LCY eruption, a period of mixed activity marked a transitional period from the end of pumice eruptions and phase III to phase IV. Several pumice eruptions (the D, F and I eruptions in Table 1.1) occurred during a period in which stratovolcano-forming activity recommenced. Volcán San Pedro was the first of the new phase IV stratovolcanoes and was built inside the caldera margin in the shadow of Volcán Paquisis. Its position relative to the older stratovolcano means that it was the continuation of the western AVC lineament. After the formation of Volcán San Pedro, Volcáns Tolimán and Atitlán formed on the southern edge of the caldera and lie on the same trend as Volcán Tecolote, marking the continuation of the east/central lineament (Fig. 1.1).

The overlap between the cessation of pumice eruptions and renewal of stratovolcano activity causes some ambiguity with the dating of the boundary between phases III and IV. The final eruption of rhyolite at the AVC (I pumice in Table 1.1) occurred around 56 ka (Cisneros de León et al., 2021a) and overlapped with formation of Volcán San Pedro. There is therefore some overlap between Phases III and IV depending on whether they are divided by stratovolcano migration, their place in the stratigraphy or by the cessation of eruption of the rhyolite pumice suite. For simplicity, in this thesis, the start of phase IV will be marked as occurring after the eruption of the I pumice (56 ka).

1.4.2 The AVC stratovolcanoes

Apart from descriptions in Newhall (1980, 1987), little is known about the petrogenesis of the pre-LCY stratovolcanoes (Volcáns Tecolote, San Marcos and Paquisis). The possibility that the silicic tephras of the CAVA are petrogenetically related to preceding, more primitive volcanoes, requires a thorough understanding of their magma systems. Many

similar lavas were erupted from these volcanoes, with compositions predominantly ranging from basaltic andesites to andesites, but including minor amounts of dacites, as well as 'disequilibrium andesites' (Newhall, 1980; 1987). These host a disequilibrium assemblage of mineral phases (olivine, ortho- and clinopyroxenes, amphiboles, biotites, plagioclase and quartz), but quantitative data for these volcanoes have not been published (Newhall, 1980; 1987). These studies also identified the presence of amphibole-bearing xenoliths and suggested that these were cumulates and could indicate long residence times for the magmas. These xenoliths were used as evidence that the "disequilibrium andesites" were the result of mixing of silicic melts with more mafic magmas.

The post-LCY stratovolcanoes (Volcáns San Pedro, Tolimán and Atitlán) have been investigated more thoroughly. They predominantly have basaltic andesite to andesite compositions with rarer dacites and lack the disequilibrium andesites. Volcáns San Pedro and Tolimán are generally more silicic and dominantly built of lava flows, while Volcán Atitlán is composed of both lava flows and pyroclastic density current deposits (Newhall, 1980; Rose et al., 1980). The products of these three volcanoes have higher K₂O, Rb, Ba and REE contents than other lavas from this segment of the CAVA (Rose et al., 1980). They have medium-K calc-alkaline compositions, apart from some rare dacites which have high-K calc alkaline compositions.

There are further differences between Volcán Atitlán and the preceding two volcanoes. Volcán Atitlán (similar to other trenchward volcanoes of volcano pairs in the CAVA) has a subtly different geochemistry. These younger, more trenchward volcanoes have typically lower abundances of the LILEs than their landward counterpart, as well as higher Na₂O/K₂O ratios (Halsor & Rose, 1988). These differences are unlikely to be due to mixing of remnant rhyolite magma from the AVC because this model is not supported by the REE contents (Halsor & Rose, 1988), although mixing of mafic magmas with a more silicic component has been proposed (Halsor & Rose, 1991). Rhyolitic melt inclusions have been found in Volcán Tolimán lavas (Halsor, 1989) as well as disequilibrium mineral assemblages in both Volcán Tolimán and San Pedro lavas (Halsor & Rose, 1991). These rhyolitic melt inclusions are highly potassic (>5 wt.% K₂O), much greater than in the high-K LCY pumices, potentially making them a suitable mixing endmember.

1.4.3 The AVC rhyolites

Vogel et al. (2006) presented a model for the generation of silicic ignimbrite magmas at the CAVA based on extraction of melts (either by melting or from extraction of melt from

nearly completely crystallised magma bodies) from the magmatic systems feeding the pre-existing stratovolcanoes. The along-arc geochemical variations observed in these stratovolcanoes (section 1.3.3) are also observed in the CAVA rhyolites (Vogel et al., 2004,2006; Kutterolf, et al., 2008a), strongly suggesting that the ignimbrites are linked to the subduction zone. However, in the specific case of the AVC, previous studies have expressed doubt about the link between the phase III volcanoes and the Quaternary rhyolites (Rose et al., 1987).

Rose et al. (1979, 1987) suggested that, after the LCY magma was formed, it underwent further chemical processing. They divided the eruption into two geochemical phases: an initial fall phase of homogeneous high-K (4.2-4.6 wt.% K₂O) biotite-bearing low crystallinity rhyolite, followed by an ignimbrite phase with both high-K rhyolite and a low-K (2.7 wt.% K₂O) amphibole-bearing lower-silica rhyolite. Their petrological work put the formation temperatures at 740-780°C and 810-890°C, respectively, at locations in the mid- to deep crust, although the depth estimates were not confirmed quantitatively. Rose et al. (1979) suggested that these two magmas may have been genetically related, with the high-K LCY magma being the product of fractionation of the low-K LCY magma. Rose et al. (1987) also suggested that different degrees of partial melting of an unidentified crustal source could produce different composition magmas. The low-K LCY magmas geochemically resemble the post-LCY Quaternary rhyolites of Atitlán, i.e., the D2, F and I tephras in Table 1.1, which may suggest they are from the same magma system or formed through similar petrogenetic processes (Rose et al., 1987). In contrast, the older W and AOT pumices are more potassic, similar to the high-K LCY rhyolite (Cisneros de León et al., 2021a; Rose et al., 1987). All these pumices contain both biotite and amphibole, which may be the result of variable storage conditions (Rose et al., 1987).

A basic sequence of events for the AVC rhyolites is presented based on the above review of the literature:

- Initial development of high-K silicic magmas, a portion of which was erupted as the AOT and/or W tephra.
- Subsequent development of a large (hundreds of km³) body of high-K rhyolite.
- Evolution and separation of the high-K rhyolite from this magma body.
- Sequential eruption of the two different rhyolites during the LCY caldera-forming event.

- Repeated smaller eruptions of lower-K magma remnants as the D2, F and I tephra sequence, or formation of new aliquots of a similar magma from the same source region.

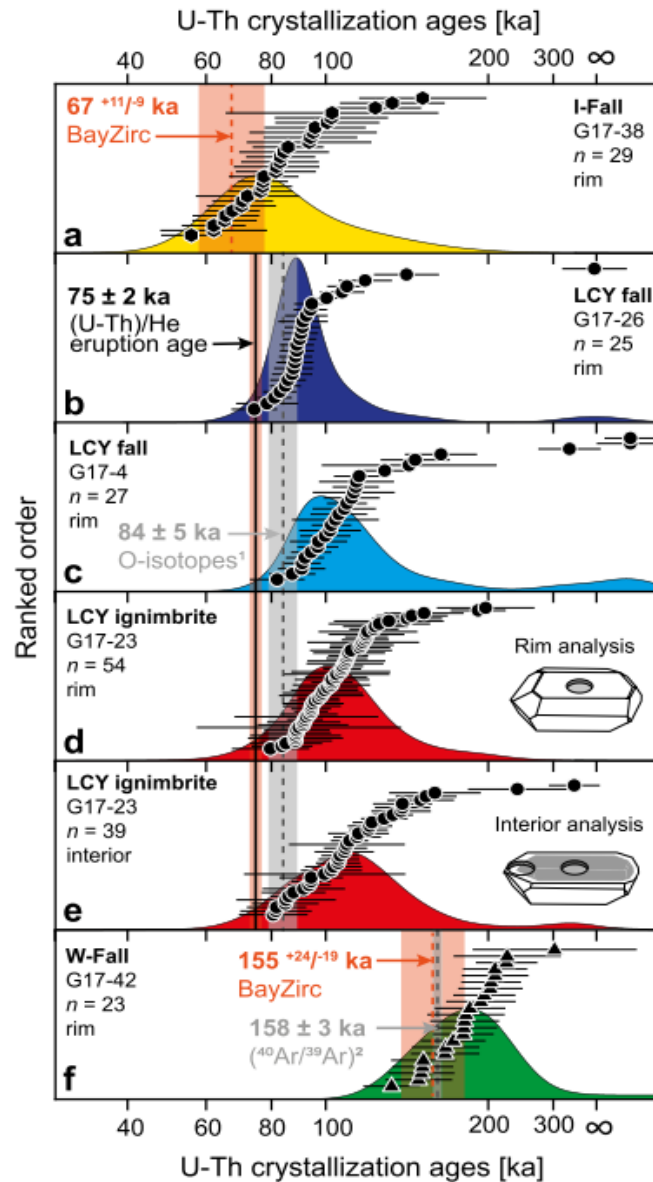


Figure 1.15. Published ranked order and relative probability plots for U-Th zircon crystallisation ages for the deposits from the W, LCY, and I eruptions. Solid black line represents mean LCY eruption age, orange dashed lines represent Bayesian eruption estimates, and dashed grey lines are previously published eruption ages. Note the wide range of ages in each deposit leading up to the eruption. All error bars are 1σ . Taken from Cisneros de León et al. (2021a)

Recent studies (Kutterolf et al., 2016; Cisneros de León et al., 2021a; Baudry et al., 2024) have yielded more accurate estimates for volumes and eruption ages of the W, LCY and I eruptions of the AVC (Table 1.1; Fig. 1.15). As well as increasing the volume estimates of these eruptions (increasing the classification of the LCY eruption from VEI 7 to 8), Cisneros de León et al. (2021a) used new techniques to examine the magmatic histories. Zircon U-Th/He and U/Th disequilibrium dating methods can accurately estimate maximum and

minimum ages for crystal populations in magmas (Schmitt, 2011; Danišík et al., 2017). The results from Cisneros de León et al. (2021a) revised the eruption age and suggested that magma accumulation started at least 80 kyr before the climactic eruption, and that accumulation rates peaked at <35 ka before the eruption, although their eruption age estimate has been challenged recently by Baudry et al., (2024), who have produced an estimate of 98 ± 6 ka. Estimates for the timing of magma accumulation for the W and I eruptions were of similar periods of time (Cisneros de León et al., 2021a; Fig. 1.15).

These more accurate timescales can be compared to the timings of stratovolcano activity. Age estimates for arc migration (i.e., the presence of Volcán Paquisis at the location of the modern arc front (Newhall, 1980; Fig. 1.1)) are similar to the maximum ages of zircons in the W pumice (Cisneros de León et al., 2021a; Fig. 1.15) and to the age estimates of the AOT (Kutterolf et al., 2016). The silicic magmas were likely stored in the same region of the present caldera. Even though there is no evidence for any caldera associated with these eruptions, the large sizes of the W eruption (83 km^3) would have likely formed one, so the absence of any remaining caldera structure would be explained because it was destroyed in the LCY event.

Chapter 2: Sampling and Analytical Methods

2.1 Fieldwork

Fieldwork was undertaken within and around the AVC over two weeks in April 2019 to collect samples of the major volcanic groups that record the activity of the past 15 Ma. Sample locations were identified from the sample map of Newhall (1980) as well as information from a local guide. However, several locations identified from the Newhall (1980) map were inaccessible or destroyed due to development of the area. Figs. 2.1 and 2.2 show the field locations of the samples used in this study, and a full sample map is shown Electronic Appendix I. The analysed samples are shown in Table 2.1, and these samples are held in the NHM petrology collection.

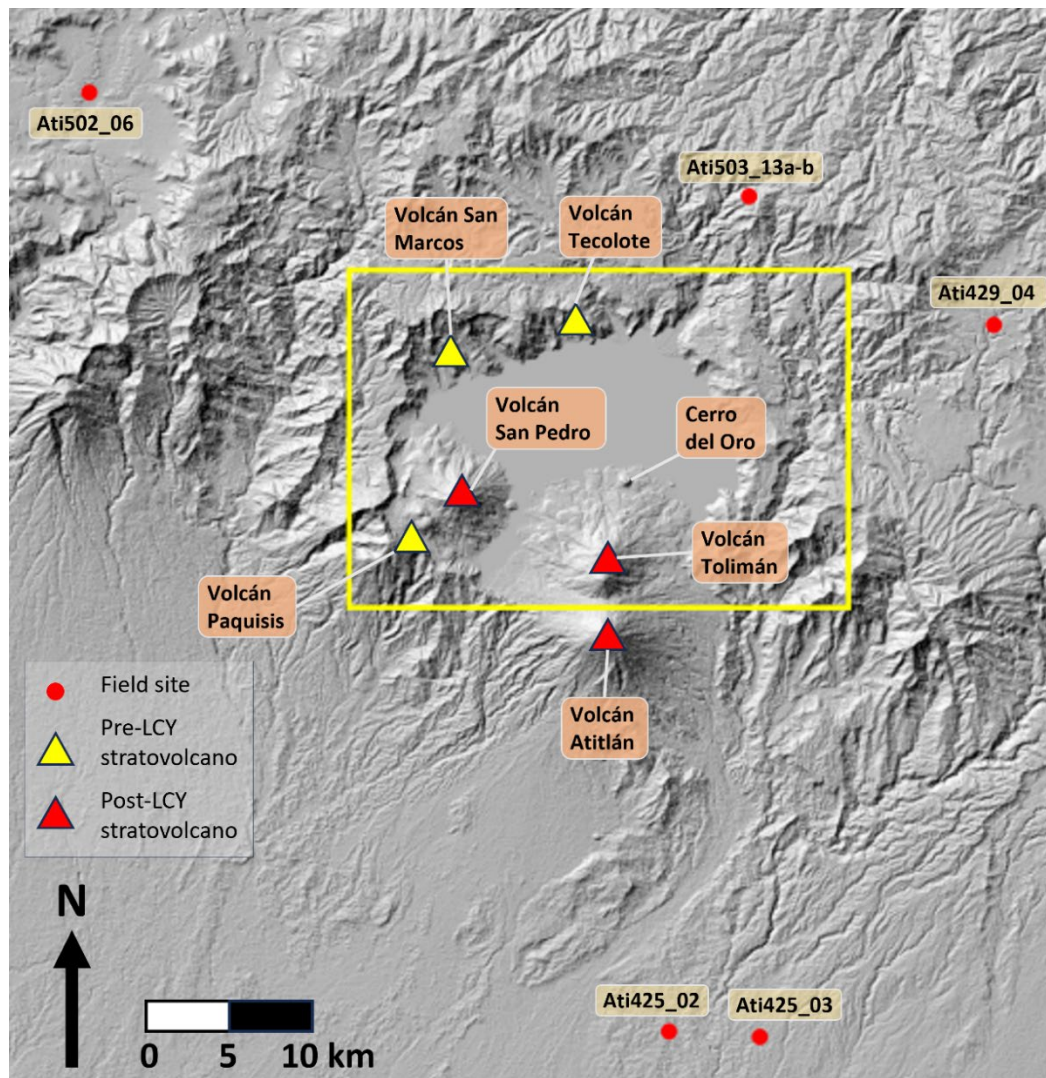


Figure. 2.1. Map showing the location of the pre- and post-LCY stratovolcanoes, as well as the distal field sites (red dots). The yellow rectangle marks the field of Fig. 2.2, the proximal field site map

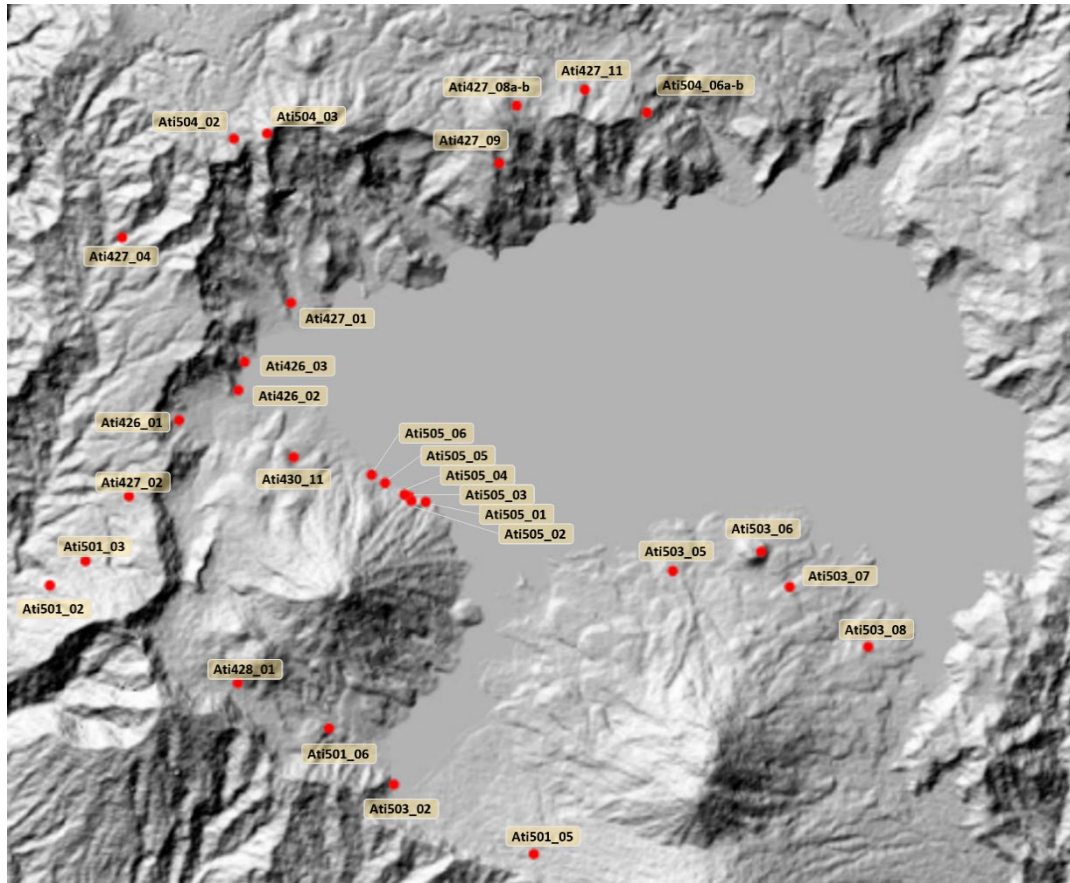


Figure. 2.2. Field site map of the proximal sites to Lake Atitlán of the samples used in this thesis. Corresponding museum collections BM numbers are shown in Table 2.1.

Sampling was intended to obtain representative material from the main phases of volcanic activity of the AVC rather than a more detailed coverage which (especially in the case of the stratovolcano sequences) would have been much more expensive and time consuming. A second period of fieldwork would have widened the range of samples available for the study but was impossible due to travel restrictions related to the Covid-19 pandemic. Because of the typically tropical climate of much of the sampling area, and the age of most of the samples, care was taken to sample parts of outcrops and to take pieces of individual clasts from pyroclastic deposits that showed as little alteration as possible. The six proximal stratovolcanoes were targeted for sampling from lava flows, pyroclastic density currents' deposits, and pumice/scoria airfall deposits. In the case of Volcán San Marcos, all samples showed signs of hydrothermal alteration. In addition to the stratovolcanoes, the Cerro del Oro parasitic dome on the flank of Volcán Tolimán was also sampled. Crustal xenoliths were also occasionally seen in lava flows. The most significant were found in sample Ati427_08 from Volcán Tecolote and Ati503_06 from Cerro del Oro (Fig. 2.3) where they were found on the scale of centimetres to metres, while a smaller granodiorite xenolith was found in sample Ati501_05d from Volcán Atitlán.

| BM number | Field number | Latitude | Longitude | Whole Rock | Thin Section | Description |
|-----------------|---------------|-----------|------------|---------------|-----------------|---------------------------|
| BM.2019,P3(1) | Ati425_02 | 14.371172 | -91.103996 | N | Y | LCY PDC pumice |
| BM.2019,P3(1) | Ati425_02 (t) | 14.371172 | -91.103996 | Y | Y | LCY PDC pumice |
| BM.2019,P3(2) | Ati425_03 (b) | 14.374034 | -91.153399 | Y | Y | LCY PDC pumice |
| BM.2019,P3(3) | Ati426_01 | 14.694605 | -91.301351 | Y | Y | Granitoid |
| BM.2019,P3(4) | Ati426_02 | 14.701173 | -91.288312 | Y | Y | Granitoid |
| BM.2019,P3(5) | Ati426_03a | 14.701173 | -91.288312 | N | Y | D1 airfall pumice |
| BM.2019,P3(8) | Ati426_03h | 14.706865 | -91.286914 | Y | Y | D2 airfall pumice |
| BM.2019,P3(16) | Ati427_01a | 14.718811 | -91.277656 | Y | N | D1 airfall pumice |
| BM.2019,P3(21) | Ati427_02a | 14.678032 | -91.312036 | Y | N | D2 airfall pumice |
| BM.2019,P3(23) | Ati427_02e | 14.678032 | -91.312036 | Y | N | F airfall pumice |
| BM.2019,P3(24) | Ati427_04a | 14.733915 | -91.313619 | Y | Y | D2 airfall pumice |
| BM.2019,P3(26) | Ati427_04f/g | 14.733915 | -91.313619 | Y | Y | F airfall pumice |
| BM.2019,P3(30) | Ati427_08a | 14.762103 | -91.228106 | Y | Y | V. Tecolote lava |
| BM.2019,P3(31) | Ati427_08b | 14.762103 | -91.228106 | Y | Y | V. Tecolote lava |
| BM.2019,P3(32) | Ati427_09 | 14.750022 | -91.231844 | Y | Y | V. Tecolote lava |
| BM.2019,P3(33) | Ati427_11 | 14.765610 | -91.213083 | Y | Y | V. Tecolote scoria |
| BM.2019,P3(34) | Ati428_01 | 14.638060 | -91.288340 | N | Y | I airfall pumice |
| BM.2019,P3(39) | Ati429_04 | 14.748433 | -90.976733 | Y | N | LCY PDC pumice |
| BM.2019,P3(55) | Ati430_11a | 14.686533 | -91.276383 | Y | N | I airfall pumice |
| BM.2019,P3(55) | Ati430_11a(e) | 14.686533 | -91.276383 | N | Y | I enclave |
| BM.2019,P3(56) | Ati430_11b | 14.686533 | -91.276383 | Y | N | I airfall pumice |
| BM.2019,P3(58) | Ati501_02 | 14.658767 | -91.329283 | Y | Y | V. Paquisis lava |
| BM.2019,P3(59) | Ati501_03 | 14.663983 | -91.321617 | Y | Y | V. Paquisis lava |
| BM.2019,P3(61) | Ati501_05a | 14.600968 | -91.224049 | Y | Y | V. Atitlán PDC bomb |
| BM.2019,P3(62) | Ati501_05b | 14.600968 | -91.224049 | N | Y | V. Atitlán airfall scoria |
| BM.2019,P3(63) | Ati501_05c | 14.600968 | -91.224049 | N | Y | V. Atitlán PDC bomb |
| BM.2019,P3(64) | Ati501_06d | 14.600968 | -91.224049 | N | N | V. Atitlán xenolith |
| BM.2019,P3(65) | Ati501_06a | 14.628300 | -91.268533 | Y | N | D2 airfall pumice |
| BM.2019,P3(66) | Ati501_06b | 14.628300 | -91.268533 | N | Y | D2 airfall pumice |
| BM.2019,P3(67) | Ati501_06c | 14.628300 | -91.268533 | Y | N | Andesite scoria |
| BM.2019,P3(75) | Ati502_06a-b | 14.871067 | -91.469333 | Y | Y | LCY PDC pumice |
| BM.2019,P3(76) | Ati503_02 | 14.616017 | -91.254633 | Y | Y | Granitoid |
| BM.2019,P3(79) | Ati503_05 | 14.661917 | -91.193833 | Y | Y | V. Tolimán lava |
| BM.2019,P3(80) | Ati503_06 | 14.665916 | -91.174795 | N | Y | Cerro del Oro lava |
| BM.2019,P3(81) | Ati503_07 | 14.658483 | -91.168500 | Y | N | V. Tolimán lava |
| BM.2019,P3(82) | Ati503_08 | 14.645733 | -91.151333 | Y | Y | V. Tolimán lava |
| BM.2019,P3(87) | Ati503_13a-b | 14.815750 | -91.109383 | N | N | W ashfall |
| BM.2019,P3(88) | Ati504_02 | 14.755200 | -91.289317 | Y | N | V. San Marcos lava |
| BM.2019,P3(89) | Ati504_03 | 14.756167 | -91.282167 | Y | N | V. San Marcos lava |
| BM.2019,P3(92) | Ati504_06a-b | 14.760817 | -91.199517 | Y | Y | V. Tecolote lava |
| BM.2019,P3(95) | Ati505_01 | 14.676950 | -91.247733 | Y | Y | V. San Pedro lava |
| BM.2019,P3(96) | Ati505_02 | 14.677467 | -91.251317 | N | Y | V. San Pedro lava |
| BM.2019,P3(97) | Ati505_03 | 14.677933 | -91.251267 | Y | N | V. San Pedro lava |
| BM.2019,P3(98) | Ati505_04 | 14.678283 | -91.252350 | Y | N | V. San Pedro lava |
| BM.2019,P3(99) | Ati505_05 | 14.680800 | -91.256233 | Y | N | V. San Pedro lava |
| BM.2019,P3(100) | Ati505_06a | 14.682733 | -91.259233 | Y | Y | Basal I PDC scoria |
| BM.2019,P3(107) | Ati505_06h | 14.682733 | -91.259233 | Y | Y | I PDC pumice |
| BM.2019,P3(107) | Ati505_06h(e) | 14.682733 | -91.259233 | Y | Y | I enclave |

Table 2.1: Natural History Museum (NHM) collections number (BM), field number, location, use, and description of all used samples in this study

The voluminous deposits from the LCY eruption were particularly targeted and were sampled six times. Fig 2.4 shows an example of one of these outcrops. Care was taken to sample all mineralogically distinct clasts in these deposits. The entire stratigraphy of the LCY eruption deposits was not sampled, as the pyroclastic flow units are known to contain both previously reported pumice types (high- and low-K rhyolites), so, only the pyroclastic

flow deposits were sampled. Care was taken to also sample pumices that showed evidence of mingling (e.g., banded pumices), although no enclaves were found.

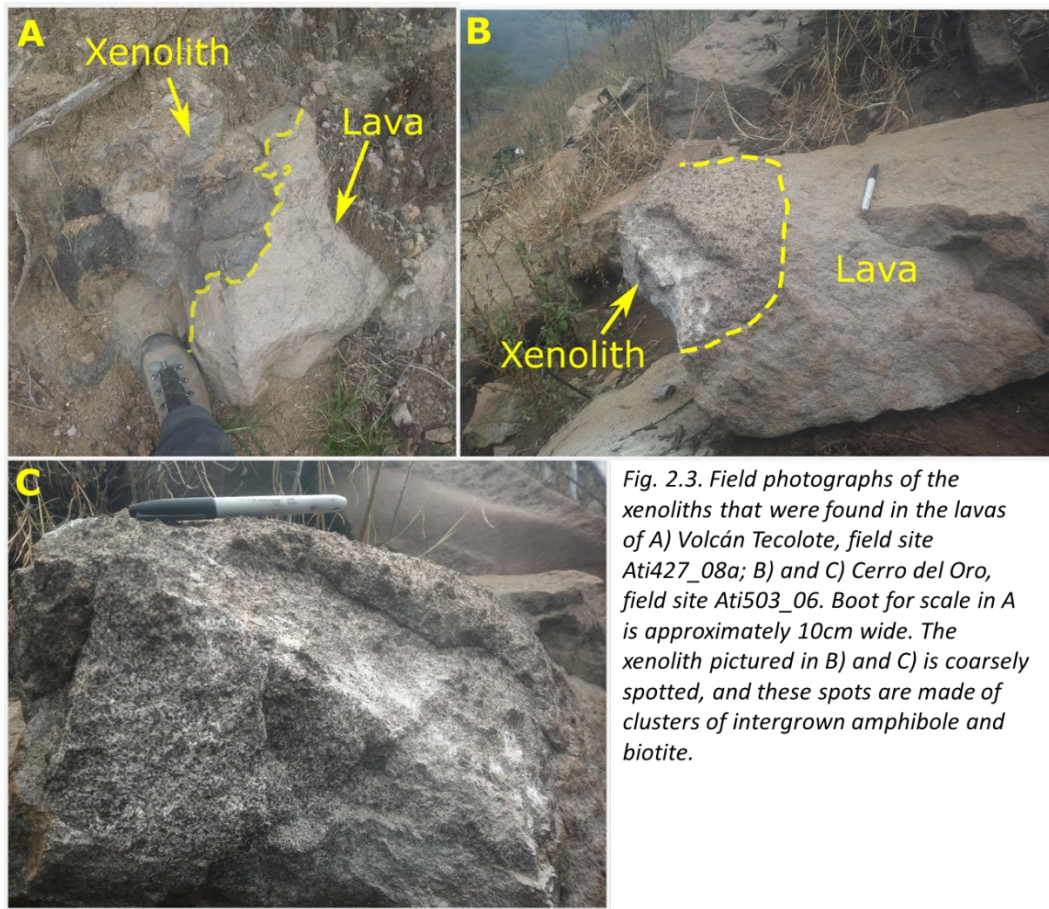


Fig. 2.3. Field photographs of the xenoliths that were found in the lavas of A) Volcán Tecolote, field site Ati427_08a; B) and C) Cerro del Oro, field site Ati503_06. Boot for scale in A is approximately 10cm wide. The xenolith pictured in B) and C) is coarsely spotted, and these spots are made of clusters of intergrown amphibole and biotite.



Fig. 2.4. Example of a pyroclastic flow deposit from the LCY eruption (location Ati425_03; vehicle for scale).

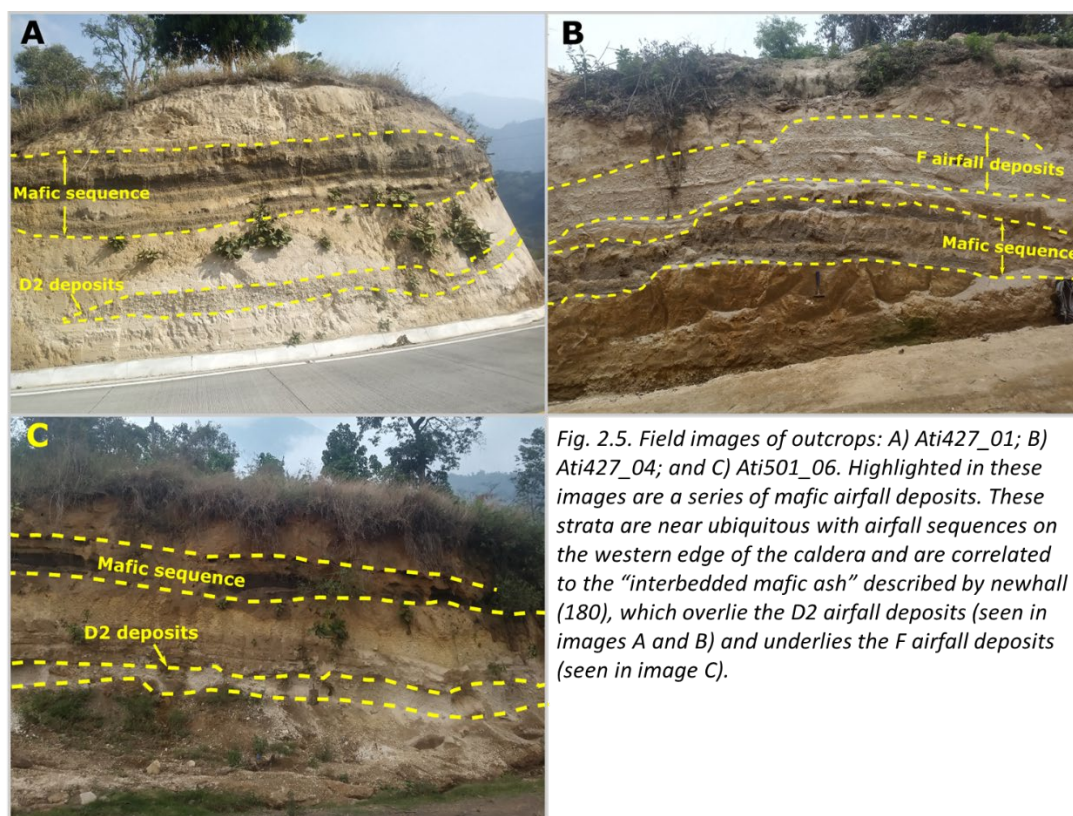


Fig. 2.5. Field images of outcrops: A) Ati427_01; B) Ati427_04; and C) Ati501_06. Highlighted in these images are a series of mafic airfall deposits. These strata are near ubiquitous with airfall sequences on the western edge of the caldera and are correlated to the “interbedded mafic ash” described by Newhall (180), which overlie the D2 airfall deposits (seen in images A and B) and underlies the F airfall deposits (seen in image C).



Fig. 2.6. Images of the deposits from the I eruption sequence from field site Ati505_06. A) shows the lower sequence of the eruption, which have a more mafic characteristic. Inset shows surge deposits interbedded between andesitic pumices. Within the inset, the underlying unit is sampled as Ati505_06a. Image B) is located around the corner indicated by the arrow in A and stratigraphically overlies the sequence in A. It shows the upper rhyolite pumices of the I eruptions (sampled as Ati505_06h)

Deposits from the post-LCY pumice eruptions described by Newhall (1980) were sampled, taking pumice, enclaves, mingled pumices, and ash portions. Apart from at location Ati505_06, only airfall deposits were taken from these eruptions. Location Ati505_06 contained basal pyroclastic surge deposits, from which sample Ati505_06a was taken, while airfall pumices were sampled as Ati505_06h. Several different outcrops were sampled in

deposits from the same eruption, although no single site contained deposits from all eruptions. Some pumice deposits did not contain pumices of sufficiently large size for compositional analyses. Fig 2.5 shows examples of deposits of the post-LCY eruption sequence. These deposits were identified by the presence of the distinctive band of mafic airfall layers described by Newhall (1980). Fig. 2.6 shows deposits from the I eruptions. In all locations, sampling of the uppermost unit of the I eruption sequence was prioritised, due to its easily identifiable nature and typically large deposit volume.

An ash deposit from the pre-LCY W eruption (Table 2.1; Fig. 2.7) was sampled, although no pumices were obtained, and the AOT (Kutterolf et al., 2016) was not found. Bulk rock samples were also obtained from most of the Atitlán phases I and II ignimbrites (Table 2.1), although later examination at the NHM revealed that most showed signs of advanced weathering. At this stage, it was decided to revise the direction of the study to focus on the most recent period of activity (phases III and IV), and samples from phases I and II were not studied further.

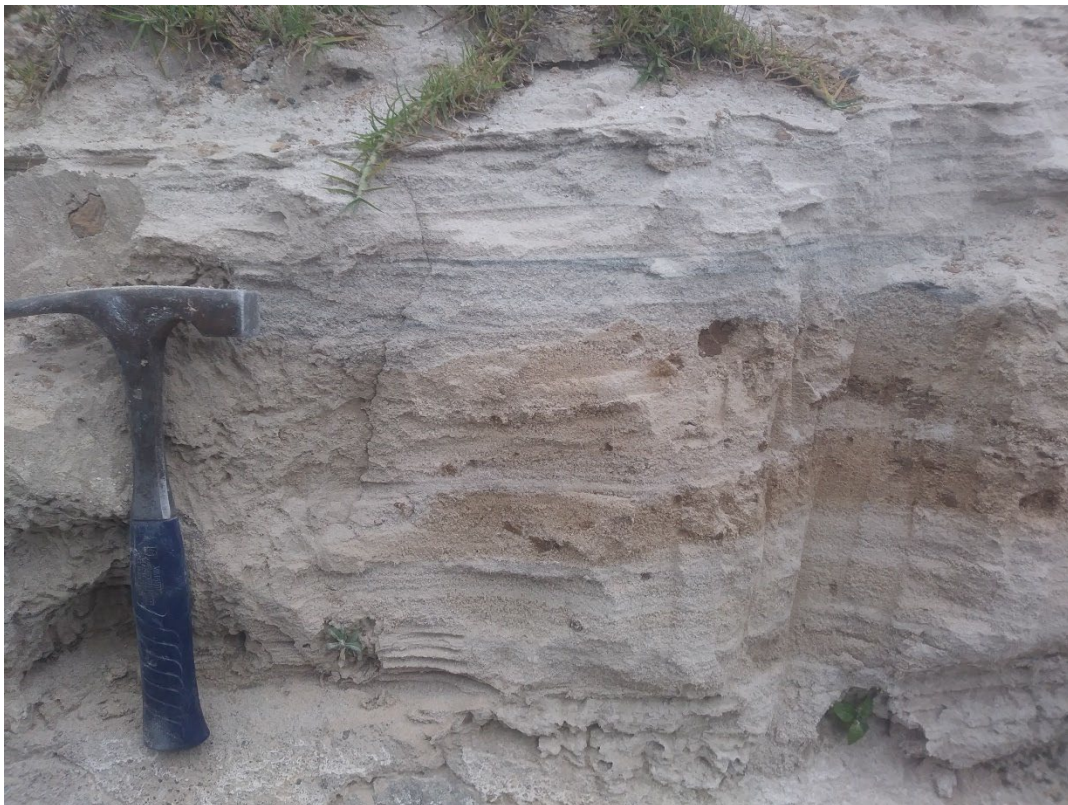


Fig. 2.7. Image of sample Ati503_013a-b, ash deposits of the W eruption, showing coarse grainsize and the varying colouration

The D eruption deposits were most commonly found towards the northwest of the caldera, and the D1 deposit was thickest in this region. Mingled pumices were observed in the D2 deposits. Outcrops containing the overlying F pumice and mafic scoria layers were more

commonly found towards the west of the caldera. Finally, the I pumice deposits were restricted to the area around Volcán San Pedro. Typically, only the final white pumice units were found but, in location Ati505_06 (Table 2.1), a full sequence of the eruption deposits was sampled including basal mafic surge deposits (Fig. 2.6). Enclaves were common in all deposits of the I pumice.

Three granitoid specimens were also sampled. Two of them of similar appearance were sampled from outcrops near the town of San Juan la Laguna (samples Ati426_01 and Ati426_02). Crystal grainsizes were <1 cm, and the rocks contained quartz, plagioclase and orthoclase feldspars and biotite. Small mafic xenoliths were present in both. A third granitoid was collected approximately 3 km southwest of Santiago Atitlán at the lake shoreline (sample Ati503_02). This sample had a distinct and highly variable appearance. It is a medium-grained leucogranite, commonly containing finer-grained bands, with large crystals of pyrite dispersed throughout. Elsewhere in this outcrop, a much coarser grained rock with up to 5 cm sized crystals of feldspar, quartz and muscovite mica was found. Both portions of this outcrop were sampled. A granitoid xenolith hosted within a lava bomb from Volcán Atitlán (Fig. 2.8) was also sampled, although the material was highly fragile and weathered, and subsequently deemed unsuitable for further analysis.



Figure 2.8. Photograph of sample Ati501_05d, a granitoid xenolith hosted within a Volcán Atitlán bomb. £1 coin for scale

2.2 Sample preparation

After selection, samples were usually prepared as whole rock powders for whole rock composition) and made into thin sections. For the pumice deposits, large individual pumices were chosen for analysis. However, several pumice samples contained only enough material for either bulk rock analysis or for thin sections. Samples from other deposits of the same eruption which were mineralogically similar were used to investigate both aspects in these cases. To ensure that these analogue samples were identical to the pumice type, their respective stratigraphic positions, hand specimen appearances and mineral assemblages were compared. In the case of mingled pumices, no whole rock compositions were obtained.

2.2.1 Whole rock powders

All sample preparation was undertaken at the Natural History Museum, London. Forty-two samples from Atitlán eruptive phases III and IV were selected for whole rock analysis based on the freshness of their appearance. Any sample that was revealed to contain abundant xenoliths or enclaves that would be impossible to remove were rejected from these analyses, as they would not provide accurate compositions for the hosting lavas. Pumice and scoria samples were washed thoroughly using an ultrasonic bath to ensure no glass shards, crystals or soil were present that may affect the analysis and were then dried overnight in an oven. Single pumice clasts were used to produce powders. The surfaces of lava samples were cut off to ensure any exterior alteration was not included. Samples were crushed in a steel jaw-crusher until finer than 4 mm. Chips of material that were larger than 4 mm after repeated passes through the jaw-crusher were first crushed to <4 mm sizes in a brass gravity mortar and remixed with the rest of the sample before powdering to ensure homogeneity. During this stage, any obvious enclaves or xenocrysts/antecrysts/megacrysts within the samples were removed. The crushed material was then ground to a powder in an agate planetary mill to ensure minimal contamination to major elements in the milling process. Between samples, the mill cleaned by running with 100 ml of clean sand and deionised water and then rinsed further with deionised water.

2.2.2 Thin sections

Thirty-three polished thin sections were prepared from the different volcanic units of phase III and IV, with duplicates for the pumice eruptions where low crystallinity might affect petrological examination. Additionally, three granitoid samples and eight phase I-II samples

were prepared. The rocks were initially cut into billets with a water-cooled diamond-tipped rock-saw. During the cutting process, areas with enclaves or megacrysts/antecrysts were specifically targeted for inclusion. The billets were mounted onto thin sections and were thinned to approximately 30 μm thickness and polished for SEM and EMPA.

2.3 Instrumental analyses

2.3.1 Major elements

Whole rock powders were sent to Activation Laboratories in Canada in two batches for major element analyses by X-ray fluorescence using a Panalytical Axios Advanced wavelength dispersive XRF analyser. The samples were prepared as fusion disks. 0.75 g of the sample was combined with 9.75 g of a mixture of lithium metaborate, lithium tetraborate and lithium bromide. This mixture was fused in platinum crucibles and poured into moulds. The resulting disks were analysed following the lithium borate flux-fusion technique (Norrish & Hutton, 1969).

In the first run of 30 samples, reference standards FK-N, IF-G, BE-N, DR-N, NIST 696, BIR-1a, SCH-1, KH3, NCS DC73304 (GBW 07106), NCS DC19003a, NCS DC11016 and NIST 88b, a duplicate of sample Ati502_06 and two method blanks were included in the analysis to assess quality control. For the second run of 14 samples, reference standards BE-N, DR-N, GS-N, PM-S, WS-E, NCS DC86316, NCS DC73304 (GBW 07106), AMIS 0129, SARM 3, OREAS 22f and AMIS 0454 were used as quality control.

Loss-on-ignition (LOI) was determined by weight difference after heating the sample powders to 1000°C. Volatile-free weight-percents of major element oxides were recalculated to 100 wt.% after removal of the LOI component. After this stage, one pumice sample (Ati427.02e) was removed from further consideration, because its LOI was too high (>9 wt.%). Detection limits were 0.01 wt.%, except for MnO which was 0.001 wt.%. The data, relative errors, LOI and accuracy are presented in Appendix A.1.

2.3.2 Trace elements

Trace elements were determined by solution inductively coupled plasma mass spectrometry (ICP-MS) at the Earth Sciences Department at the Open University in Milton Keynes, UK. Two sample batches were run. For the preparation of the sample solutions, 0.1 g of the sample powders were measured out and prepared in Teflon containers. A method blank was prepared simultaneously. The samples were then dissolved in a mixture of 0.5 ml 15M HNO₃ and 2 ml concentrated HF. The containers were sealed and boiled at 120°C for

24 hours on a hot plate. Twice during the dissolution the containers were placed in a sonic bath for 20 minutes. The dissolved samples were evaporated to near dryness before being redissolved in 2 ml of concentrated HCl and boiled for 24 hours again. They were evaporated to near dryness a second time and then were redissolved in a mixture of 2 ml 15 HNO₃ and 2 ml Milli-Q grade deionised water. These solutions were boiled for four hours and subsequently Milli-Q grade deionised water was further added to them to make up to a volume for a 1000-fold dilution.

An Agilent 8800 ICP-QQQ-MS instrument was used for the analyses. In the first run, reference standards BIR-1, W2, DNC-1, BHVO-2, AGV-1, BCR-2 and RGM-1 were used as reference materials. A procedural blank, BHVO-2, and a duplicate of sample Ati501_06c were used as monitor samples to assess drift during the run. In the second run, reference standards BIR-1, W2, DNC-1, BHVO-2, AGV-1, RGM-1 and BE-N were used as reference materials. A procedural blank, BHVO-2, and a duplicate of sample Ati429_03 were used as monitor samples. In both runs, the three monitor samples (procedural blank, BHVO-2 and the duplicate) were analysed between approximately every five rock samples. Monitoring solutions of Zr at 25, 50, 100 and 150 ppb, and 2% HNO₃ were included at the start of the runs.

Analyses were undertaken in both “no gas” and “He collisional gas” mode for all elements besides the rare earth elements (REEs), which were also analysed in O₂ reactive gas mode. The use of gases in the collision cell can reduce molecular interference during the run but may also reduce the precision of the analysis. Subsequently, the choice of which analysis mode to use (either no gas mode or He collisional mode) was based on comparisons of the accuracy and precision of the analysed monitor standards. The REEs were the exception, where O₂ reactive gas mode was used in all cases. Elements measured in the “no gas” mode were Li, Sc, Ti, Ga, Sb, Ba, Hf, Ta, Th and U, while elements measured in He collisional gas mode were V, Cr, Mn, Co, Cu, Zn, Rb, Sr, Y, Zr, Nb, Sn, Cs, Tl and Pb. Be, Rh, In, Tm and Bi were used as internal reference standards.

Drift was monitored using both the natural duplicated samples and BHVO-2. Drift corrections were applied if the drift was statistically significant (R^2 value of 0.8 or better for deviation) and calculated against BHVO-2. Drift correction magnitudes were calculated using a linear regression of BHVO-2 values. Two samples in the first run (Ati427_11 and Ati503_08) showed anomalously high Ta values compared to Nb, which for arc volcanic rocks should have a relationship. These were re-run and returned values that appeared

more appropriate considering the measured Nb values. The data, detection limits, errors and relative deviation are presented in Appendix A.2.

For most of the elements run in both batches, the accuracy of the analyses was better than 5% relative error (in comparison to certified BHVO-2 values). Exceptions in batch 1 are Sc (6.23%), compatible elements (V, Cr, Mn, Co, Ni all between 5.02-10.25%), Zn (5.42%), Ba (6.67%), Pr (6.72%), Hf (6.93%), Yb (6.45%), and Pb (14.02%). Exceptions in batch 2 are Y (5.79%), Nb (5.91%), Sn (12.11%), Ta (5.37%), Pb (7.86%). Elements with low concentrations (<0.5ppm) also were more likely to have higher uncertainties. The analysed procedural blanks measured values below detection limits for all elements.

2.3.3 Radiogenic isotopes

A full suite of radiogenic isotope analyses was run using an awarded grant from the National Environmental Isotope Facility (NEIF number 2248.0320). Preparation and analyses were performed by Finley Gilchrist, Doris Wagner, Nicola Atkinson and Vanessa Pashley at the NERC Isotope Geosciences Laboratories (NIGL) in Keyworth, United Kingdom.

150-200 mg of sample was weighed into 15ml Savillex Teflon beakers and leached in 5 mls of 6M HCl at 60°C for 2 hours. After discarding the leachate, the samples were washed and centrifuged twice in mQ water, dried and reweighed. 1-2mls of 2x Teflon-distilled 16M HNO₃ and 5-6 mls of 29M HF were added, and the sample beakers were left closed on a hotplate at 110°C overnight. After evaporating to dryness, a further 1-2 mls of HNO₃ were added, and the samples were left on the hotplate closed overnight. The samples were then converted to chloride form using 10 mls of 2x quartz-distilled HCl. The samples were then dissolved in c. 2 ml of 1M HCl + 0.1M HF in preparation for column chemistry, and centrifuged.

A second aliquot of sample was weighed into 15ml Savillex beakers, leached and dissolved as above prior to Pb separation and analysis.

Primary columns consisting of 2 mls of Eichrom AG50x8 cation exchange resin in 10ml Biorad Poly-Prep columns were used to separate bulk high field strength elements (HFSE: Ti, Hf, Zr), a fraction containing Sr, Ca and Rb, and a bulk rare-earth element (REE) fraction.

Samples were loaded onto the columns in c. 1.5 mls of 1M HCl + 0.1M HF, and the HFSE were immediately eluted in 10 ml of 1M HCl + 0.1M HF. This fraction was evaporated to dryness in preparation for separation of Hf. Sr, Ca and Rb were eluted in 30 mls of 1.5M

HCl, and evaporated to dryness in preparation for separation of Sr. Finally, the REE were eluted in 10 mls of 6M HCl and evaporated to dryness in preparation for separation of Nd.

Hafnium separation followed a procedure adapted from Münker et al. (2001). HFSE concentrates from the primary columns were dissolved in c. 2 mls of 6M HCl and loaded onto columns packed with 1 ml of EICHROM LN-SPEC ion exchange resin packed into 10ml Biorad Poly-Prep columns. Matrix elements were eluted in 10-20 mls of 6M HCl, and 2 portions of 2 mls of milliQ water was then passed through the column to remove HCl from the columns prior to subsequent elution steps involving peroxide (mixing of HCl and peroxide would result in immediate elution of HFSE from the columns). The columns were then washed with several 10 ml column volumes of a solution containing citric acid, nitric acid and peroxide. In this medium, titanium citrate complexes show a distinctive bright orange colour, allowing Ti to be quantitatively removed from the column by repeated washing. Once all traces of Ti were removed from the columns, 5mls of peroxide-free citric acid + nitric acid solution were eluted, again to avoid mixing of peroxide with HCl solutions. Zr was then washed from the columns using 50-80 ml of 6M HCl + 0.06M HF. Finally, HF was collected in 10 mls of 6M HCl + 0.2M HCl.

For Sr separation, samples from the primary column separation were dried down and taken up in c. 2 mls of 2.5M HCl and pipetted onto quartz-glass columns containing 4 mls of AG50x8 cation exchange resin. Matrix elements were washed off the column using 48 mls of calibrated 2.5M HCl and discarded. Sr was collected in 12 mls of 2.5M HCl and evaporated to dryness.

Sm and Nd were separated using 2mls of EICHROM LN-SPEC ion exchange resin packed into 10ml Biorad Poly-Prep columns. The bulk REE fraction was dissolved in 200 microlitres of 0.2M HCl and loaded onto the columns. La, Ce and Pr were eluted using a total of 14 mls of 0.2M HCl. Nd was collected in 3 mls of 0.3M HCl.

Dissolved samples for Pb were converted to bromide form using 2 mls of concentrated HBr. Pb was separated using columns containing 100 µls of Dowex AG1x8 anion exchange resin using standard bromide separation methods.

Hf fractions were dissolved in 1 ml of 2% HNO₃ + 0.1M HF, prior to analysis on a Thermo Scientific Neptune Plus mass spectrometer operated in static multicollection mode.

Correction for ¹⁷⁶Yb on the ¹⁷⁶Hf peak was made using reverse-mass-bias correction of the ¹⁷⁶Yb/¹⁷³Yb ratio empirically derived using Hf mass-bias corrected Yb-doped JMC475

solutions (Nowell & Parrish, 2001). ^{176}Lu interference on the ^{176}Hf peak was corrected by using the measured ^{175}Lu and assuming $^{176}\text{Lu}/^{175}\text{Lu} = 0.02653$. The column procedure used to separate Hf effectively removes most of the Yb and Lu, so these corrections are minimal.

The Hf standard solution JMC475 was analysed during each analytical session and sample $^{176}\text{Hf}/^{177}\text{Hf}$ ratios are reported relative to a value of 0.282160 for this standard (Nowell & Parrish, 2001). Multiple analyses of JMC475 across the time of analysis gave a mean $^{176}\text{Hf}/^{177}\text{Hf}$ value of 0.282145 ± 0.000005 (1-sigma), and two analyses of BCR-2 rock standard run with the samples gave a value of 0.282997 ± 0.000002 (1-sigma). Data are reported relative to $^{179}\text{Hf}/^{177}\text{Hf} = 0.7325$.

Nd fractions were dissolved in 1ml of 2% HNO_3 prior to analysis on a Thermo Scientific Neptune Plus mass spectrometer operated in static multicollection mode. Data were normalised to $^{146}\text{Nd}/^{144}\text{Nd} = 0.7219$. Multiple analyses of JNd-I across the time of analysis gave a mean value of 0.512068 ± 0.000014 (1-sigma). Results are quoted relative to a value of 0.512115 for this standard. Eight analyses of the BCR-2 rock standard run with the samples gave a value of 0.512643 ± 0.000003 (1-sigma).

Sr fractions were loaded onto outgassed single Re filaments using a TaO activator solution and analysed in a Thermo Scientific Triton mass spectrometer in multi-dynamic mode. Data are normalised to $^{86}\text{Sr}/^{88}\text{Sr} = 0.1194$. Multiple analyses of the NBS987 standard across the time of analysis gave a value of 0.710259 ± 0.000006 (1-sigma). Sample data is normalised using a preferred value of 0.710250 for this standard. Two analyses of the BCR-2 rock standard run with the samples gave a value of 0.705009 ± 0.000015 (1-sigma).

Prior to Pb isotope analysis, each sample was spiked with a thallium solution, which was added to allow for the correction of instrument-induced mass bias. Samples were then introduced into a Thermo Scientific Neptune Plus multicollector ICP-MS. For each sample, five ratios were simultaneously measured ($^{206}\text{Pb}/^{204}\text{Pb}$, $^{207}\text{Pb}/^{204}\text{Pb}$, $^{208}\text{Pb}/^{204}\text{Pb}$, $^{207}\text{Pb}/^{206}\text{Pb}$ and $^{208}\text{Pb}/^{206}\text{Pb}$). Each individual acquisition consisted of 75 sets of ratios, collected at 5-second integrations, following a 60 second de-focused baseline.

The precision and accuracy of the method was assessed through repeat analysis of an NBS 981 Pb reference solution (also spiked with thallium), as well as two analyses of the BCR-2 rock standard (shown in Appendix A.3). The average values obtained for each of the measured NBS 981 ratios were then compared to the known values for this reference material. Preferred values are shown in Table 2.2. Pb isotope drift was monitored through

comparison against reference standard NBS981. No drift was observed through each run, and as such no drift corrections were applied. Internal uncertainties (the reproducibility of the measured ratio) were propagated relative to the external uncertainty.

| $^{206}\text{Pb}/^{204}\text{Pb}$ | $^{207}\text{Pb}/^{204}\text{Pb}$ | $^{208}\text{Pb}/^{204}\text{Pb}$ | $^{207}\text{Pb}/^{206}\text{Pb}$ | $^{208}\text{Pb}/^{206}\text{Pb}$ |
|-----------------------------------|-----------------------------------|-----------------------------------|-----------------------------------|-----------------------------------|
| 16.9417 | 15.4996 | 36.724 | 0.91488 | 2.1677 |

Table 2.2. Preferred values for Pb isotope ratios for reference standard NBS 981

Samples from the phase III stratovolcanoes were age-corrected based on published ages from Newhall (1980). Standard errors and data are shown in Appendix A.3.

2.4 Petrography and petrology

2.4.1 Petrographic imaging

All petrographic imaging was undertaken at the Imaging and Analysis Centre (IAC) at the Natural History Museum (NHM), London. Thin sections were initially investigated for major phases with polarised light microscopy using a Zeiss Axioscope. Once crucial spots were identified for quantitative analysis, the samples were carbon coated to 10 nm thickness to increase sample surface conductivity in preparation for use in the scanning electron microscope (SEM) and electron probe microanalyser (EPMA). SEM images were taken in backscatter electron (BSE) mode on the FEI Quanta 650 FEG SEM, using a voltage of 20 kV and a working distance of approximately 10 mm. Crystals were analysed for textures (zoning, melt inclusions) and suitability for later targeted quantitative analysis.

SEM imaging is produced by the interaction of an electron beam with the sample surface. The electron beam is produced by a field-emission gun in the used SEM. In backscattered mode, the number of electrons reaching the detector (and the subsequent intensity of the grey-scale image) is proportional to average atomic number of analysed spots. Adjustments to the brightness/contrast ratios within the SEM software can be used to highlight compositional variations (e.g. zoning and/or resorption bands) within crystals. Decisions on where to conduct further compositional analyses were made based on these observed variations within crystals. BSE image maps of the samples were compiled using a mosaic of images acquired at lower magnifications and stitched using the FEI MAPS SEM-mosaic software. Examinations of these maps were instrumental in estimating phase proportions (using point counting) and describing qualitative populations of the different mineral phases. Point counting was performed using a minimum of 300 points using ImageJ software.

2.4.2 EPMA analyses

Compositions of mineral and groundmass phases were analysed on the Cameca SX100 and JEOL JXA-8530F electron probe microanalysers (EPMA). EPMA is a non-destructive analytical technique that is used to obtain in-situ compositional information of material on the micro-scale, both taking point analyses as well as compositional profiles and maps. The compositional information obtained for this project was focused on point analyses, to characterise composition variations within individual crystals as well as to classify variations in samples' crystal populations.

EPMA estimates compositions by targeting points with an accelerated beam of electrons. The interaction of this beam with atoms in the targeted spot area produces X-rays with wavelengths that are characteristic of the atoms, producing specific peaks on a spectrograph. The size of these peaks is directly proportional to the concentration of each element in the spot, and the composition of the spot can therefore be estimated with calibration of standards of known compositions.

Due to the Covid-19 pandemic, the time available on the EPMA was limited, so two different EPMA were used. The Cameca SX100 produces an electron beam using a tungsten filament and uses five wavelength dispersive X-ray spectrometers (WDX) and one energy dispersive X-ray detector (EDX). The JEOL JXA-8530F produces an electron beam using a field emission gun. It measures spectra using 5 wavelength dispersive spectrometers (WDS) and one energy dispersive spectrometer (EDS).

Both instruments are hosted in the IAC in the NHM. Again due to time constraints caused by the Covid-19 pandemic, the same machine specifications were used for all mineral phases: a beam current of 20 nA, an electron gun voltage of 20 kV, and a defocussed spot size of 5 μm . Na was analysed first to reduce the impact of alkali mobility. Elements analysed during mineral analyses were Al, Ba, Ca, Cl, Cr, F, Fe, K, Mg, Mn, Na, Ni, Si, Sr and Ti. For glass analyses, elements Al, Ca, Cl, F, Fe, K, Mg, Mn, Na, P, Si and Ti were measured. All element peaks were analysed for 30 s, apart from K, Cl and Na which were analysed for 10 s. Peak overlap corrections were applied to F and Fe (F and Fe both produce peaks at similar wavelengths and so require correcting where both elements are desired), and matrix effects were accounted for using the built-in programs for each machine: the Cameca PAP procedure (Pouchou & Pichoir, 1984) in the Cameca SX100, and the ZAF (Z-stopping power, backscattering factor and X-ray production power; A-absorption; F-fluorescence) correction program in the JEOL.

Standard deviations of the analyses were typically <1.0 wt.% for the major elements of each mineral in analyses from both instruments, however in the JEOL analyses Na was higher than in the Cameca's, being typically <2.0 wt.%. Glass analyses were an exception, having typically higher uncertainties (typically <3.0% in most elements but higher in elements closer to detection limits). Data from glasses have been presented and consequently should be viewed with greater uncertainty in their measured values. Calibration checks were performed on standards BCR2G, Isle of Rhum plagioclase and Eagle station olivine. Detection limits are <200 ppm for elements F, Si, Sr, Ba and Na, and <100 ppm for elements Ti, K, Cl, Ca, Cr, Mn, Fe, Mg and Al in the JEOL analyses, but were higher in analyses performed on the Cameca. Most elements showed detection limits <300 ppm, although K was on average slightly higher than other elements (typically 250-300 ppm) and Na was significantly higher (<700 ppm). Uncertainties, precisions and variance for the secondary standards used, and the calibration data are shown in Appendix B.1.

The use of two EPMA's, and a single universal calibration scheme for analysing all phases is justified when comparing the sets of data. Electronic Appendix II shows all spot analyses and the machine they were analysed on for comparison. The vast majority of analyses yielded values that were expected for their phases, however the JEOL gave values that had a greater spread of totals for phases such as plagioclase and pyroxenes, and so a greater number of these had to be discarded. To counteract this, a large number of spots were analysed in each sample to add redundancies. The JEOL software also had an issue extracting F contents: the JEOL overlap correction did not consistently extract the F peak and returned null analyses.

Mineral compositions were recalculated by oxygen stoichiometry (olivine on a 4 O basis, plagioclase on a 8 O basis and pyroxenes on a 6 O basis). Ferric and ferrous iron values were estimated based on charge balancing for all minerals. Amphiboles were recalculated following Hawthorne et al. (2012) on the basis of 24 anions (O, OH, F and Cl). Biotites have been recalculated following the machine learning method of Li et al. (2020) on the basis of 13 anions (11 O + 2(O, OH, F and Cl)). Minerals which did not have acceptable stoichiometric recalculations (shown by warnings on site totals by the above authors of the recalculation spreadsheets) were rejected. Additionally, for plagioclase, pyroxene and olivine, spots with wt.% oxide totals $98.5 < \text{Total} < 101.5$ were excluded, with the majority in the range $99.5 < \text{Total} < 100.5$. For the glass analyses, stoichiometric recalculations are not applicable, and accepted values varied and were chosen compared to totals in high quality

literature databases (e.g., GEOROC). Amphiboles with totals <96 wt.% oxide were excluded, while for glasses the value was <93 wt.%, and biotites were rejected with <91 wt.%.

2.4.3 LA-ICP-MS

Laser ablation inductively coupled plasma mass spectrometry (LA-ICP-MS) was performed on volcanic glasses and melt inclusions. This method is used to obtain in-situ trace element data and in this project is very useful for the quantification of trace element budgets in volcanic glasses. A high energy laser aerosolises a region of the sample surface, and the vaporised material is carried into the attached ICP-MS by an inert carrier gas. Ar plasma converts this material into ions, which are accelerated and deflected using a magnetic field and are then collected by a detector. The mass of the ions, their charge, and the strength of the magnetic field control the amount of deflection the ions undergo, and so the concentration of each ion in the targeted region can be estimated.

The analyses were conducted on an Agilent 7700x quadrupole ICP-MS coupled with an ESI New Wave Research NWR193 excimer laser at the LODE laboratory in the IAC at the NHM. Due to the difference in the nature of the desired analyses (matrix glass vs. melt inclusions), two runs with different set-ups were used. For the first run targeting matrix glasses, the laser was operated using a spot size of 25 μm , a 7 Hz repetition rate and a fluence of 3.5 Jcm^{-2} , while the laser setup for the second run had spot sizes of 10-15 μm , a repetition rate of 6 Hz and a fluence of 2.8 Jcm^{-2} .

To maintain consistency, spot locations were chosen based on EPMA spot locations. Sites which had returned unusual or poor quality EPMA analyses (e.g. unexpected totals likely reflecting an analysis of either the melt inclusion wall or the presence of microlites/low analytical totals) were not analysed.

For the larger spot sizes in the first run, the isotopes ^{27}Al , ^{29}Si , ^{43}Ca , ^{51}V , ^{53}Cr , ^{59}Co , ^{60}Ni , ^{66}Zr , ^{85}Rb , ^{88}Sr , ^{89}Y , ^{93}Nb , ^{133}Cs , ^{137}Ba , ^{139}La , ^{140}Ce , ^{141}Pr , ^{145}Nd , ^{147}Sm , ^{151}Eu , ^{157}Gd , ^{159}Tb , ^{163}Dy , ^{165}Ho , ^{167}Er , ^{169}Tm , ^{173}Yb , ^{175}Lu , ^{177}Hf , ^{181}Ta , ^{204}Pb , ^{206}Pb , ^{207}Pb , ^{208}Pb , ^{232}Th and ^{238}U were analysed, while for the smaller spot sizes in the second run, a reduced list of isotopes was used: ^{28}Si , ^{85}Rb , ^{88}Sr , ^{133}Cs , ^{137}Ba , ^{139}La , ^{140}Ce , ^{141}Pr , ^{145}Nd , ^{147}Sm , ^{151}Eu , ^{157}Gd , ^{159}Tb , ^{163}Dy , ^{165}Ho , ^{167}Er , ^{169}Tm , ^{173}Yb , ^{175}Lu , ^{204}Pb , ^{206}Pb , ^{207}Pb , ^{208}Pb , ^{232}Th and ^{238}U . A dwell time of 10 ms was used for most isotopes, while a dwell time of 5 ms was used for ^{27}Al , ^{43}Ca and ^{66}Zr , 20 ms was used for ^{139}La , ^{141}Pr , ^{235}U , and 30 ms for ^{206}Pb , ^{207}Pb , and ^{238}U .

Silicon was used as the internal standard and was also used to monitor any contamination by microlites (in the case of the matrix glasses) and the host phase (in the case of the melt inclusions). Analyses showing abnormally low silicon values indicating the inclusion of these phases were discarded. NIST612 was the primary reference material, while BCR2g, GSD-1g and NIST610 were the standards used to track accuracy and precision. Data reduction was performed using in-house developed software to track heterogeneity of the spectra with respect to time. Portions of the spectra that showed evidence of an unwanted mineral inclusion during ablation were removed. Representative data, limits of detection, standard errors, analyses' metadata, and standard data are provided in Appendix B.2. Full results are presented in Electronic Appendix II.

Chapter 3. Petrography, Mineralogy and Mineral Chemistry

3.1 Terminology

Many terms, both in the study of Atitlan and in general petrology and petrography, have ambiguous meanings. I will therefore briefly define terms used in this thesis.

3.1.1 *Los Chocoyos (LCY) pumices*

Previous studies (Rose et al., 1979,1987; Newhall, 1980) identified two dominant juvenile clast types in the deposits of the Los Chocoyos eruption. These are a 'high-K' biotite-bearing pumice and a 'low-K' amphibole-bearing pumice. The low-K pumice was named with reference to the high-K pumice (Rose et al., 1979,1987) and actually falls within the medium-K field of the K_2O discrimination diagram of Peccerillo & Taylor (1976); however the original name will be retained to be consistent with the literature.

3.1.2 *Rock groupings*

There are five groupings of the AVC samples based on various factors including the SiO_2 content, the rock-type, and the phase of activity it was erupted in. These groupings are:

- The stratovolcano basaltic andesites to dacites, subdivided into the phase III (pre-LCY) and phase IV (post-LCY) stratovolcanoes as described in section 1.4.1.
- The LCY rhyolite pumices.
- The post-LCY intermediate and rhyolite pumices from the D, F and I eruption sequences following the LCY event (section 1.4.1).
- The recharge magmas found in the various pumice eruptions. The descriptions provided in this section include the mingled pumices as well as discrete enclaves within this definition.
- The intrusives, plutonic rocks sampled from within the caldera.

3.1.3 *Open system terminology:*

Magma mixing is a well-known phenomenon in volcanic rocks and evidence of it is common in those sampled from the AVC. Different terms for magma mixing and crustal contamination have been used throughout the literature. I will use the following terms for the different mixing textures and processes that may have occurred in this centre:

- Mixed – where two or more mixing magmas have reached chemical homogeneity and are indistinguishable (Sparks & Marshall, 1986)
- Mingled – where two or more mixing magmas have not reached textural homogeneity, and the textural evidence for this process is preserved either as banding or the presence of enclaves of the less voluminous magma (Sparks & Marshall, 1986)
- Xenoliths – hand-specimen sized pieces of non-juvenile material that are not obviously petrogenetically related to the host lava
- Anteliths (following Bach et al., 2012) – non-juvenile lithic material petrogenetically related to the host lava but distinct from glomerocrysts by their larger size. They have sizes between tens of centimetres and metres.
- Glomerocrysts – micro-scale crystal clots that are likely fragments of a crystal mush, related to the host juvenile clast. Typically formed of several intergrown crystals of one or more phases but may also contain variable amounts of interstitial glass.
- Recharge magmas – magmas intruded into more evolved magma bodies. When not mixed, these are preserved as either discrete enclaves or mingled pumices.

3.2 Petrography and mineral chemistry

3.2.1 Stratovolcano lavas

Basaltic andesites have been investigated from the Cerro las Minas cinder cone on Volcán Tecolote as well as from Volcáns Atitlán and Paquisis. As the most mafic samples of the AVC, they are key to understanding the differences in the petrology of the stratovolcano lavas, as they each may have been the fuel that drove volcanism at this centre. Fig. 3.1 shows their compositions on a TAS diagram, on which Volcáns Tecolote (sample Ati427_11) and Atitlán (sample Ati501_05a) are very similar, while the Volcán Paquisis sample (Ati501_03) is more evolved. The basal scoria from the I1 eruption (sample Ati505_06a) also falls in this compositional range. Samples of andesite/low-silica dacite were investigated from Volcáns Tolimán (samples Ati503_05, Ati503_06, and Ati503_08), San Pedro (samples Ati505_01 and Ati505_02), Tecolote (samples Ati427_08a, Ati427_08b, Ati427_09, and Ati504_06a) and Paquisis (Ati501_02), as well as andesitic materials from the D1 pumice eruption (sample Ati426_03a) and mafic enclaves from the I pumice eruptions (Ati430_11a(e) and Ati505_06h(e)). In the presentation of the geochemical results below, the andesites and dacite have been split into two categories: the ‘andesites’ are stratovolcano lavas with SiO₂ contents

<60 wt%, while the ‘high-K andesites’ are those andesites with > 60 wt% SiO₂ and also include the dacitic lava (sample Ati427_08a) from Volcán Tecolote (Fig. 3.1).

3.2.1.1 Stratovolcano petrography

Basaltic andesites

The three basaltic andesites samples show several key similarities despite their different eruption styles (Volcán Tecolote sample Ati427_11 – scoria; Volcán Atitlán sample Ati501_05a – bomb from pyroclastic flow; Volcán Paquisis sample Ati501_03 – lava flow). They are moderately to strongly vesiculated (45% - Tecolote, 10% - Paquisis, 25% - Atitlán) with spherical to elongated vesicles. The samples are all porphyritic, with Volcáns Tecolote and Atitlán having approximately 20-30% phenocrysts, while the Volcán Paquisis sample has around 45%. All samples have highly crystalline groundmasses with microlites that reflect the phenocryst populations.

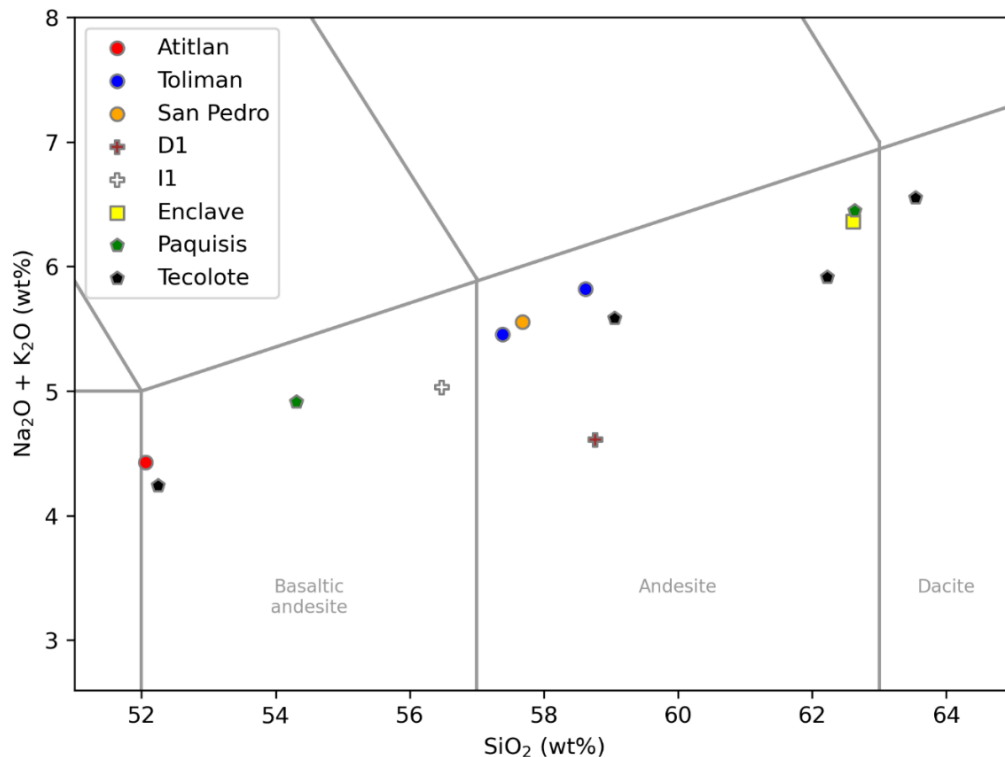


Figure 3.1. Total alkali silica (TAS: after Peccerillo & Taylor, 1976) diagram for the investigated samples of stratovolcano lavas and andesitic pumices of the AVC

These lavas are also similar in their mineral assemblages, all containing phenocrysts of plagioclase, clinopyroxene and olivine, with accessory Fe-Ti oxides. Orthopyroxenes are also

present in the samples from Volcáns Paquisis and Atitlán. Phase proportions are also similar (Fig. 3.2), with plagioclase always being the most abundant phase (55-75% of the phenocrysts, with the lower value being from the Volcán Paquisis sample). Olivines are more abundant in the more mafic samples (20-25% vs. 6%), and clinopyroxenes show the reverse (6-14% vs. 20%). Fig. 3.3 shows some of the textures of the different mineral phases.

Plagioclase appearances vary between these samples. Most phenocrysts in the basaltic andesites are lath-shaped with oscillatory zoning and commonly show synneusis textures. However, crystals from the Volcán Atitlán bomb have very thin normally-zoned rims and, together with those from Volcán Paquisis, also commonly show sieve textures (Fig. 3.3A). Plagioclase phenocrysts from Volcán Tecolote are smaller, being <1.0 mm compared to up to 2-3 mm in the other samples.

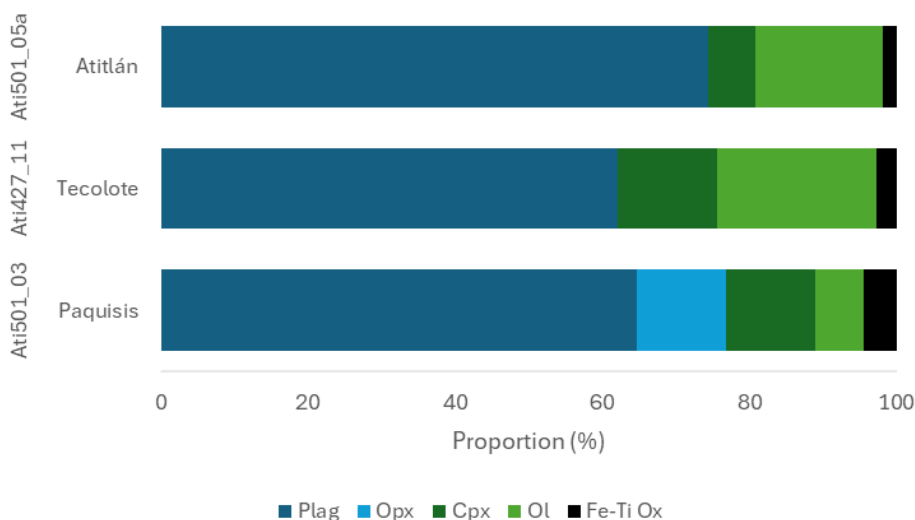


Figure 3.2. Mineral phase proportions of the stratovolcano basaltic andesites sampled from the AVC. Plag- plagioclase, Opx – orthopyroxene, Cpx – clinopyroxene, Ol – olivine, Fe-Ti Ox – Fe-Ti oxides.

Olivines vary in their appearance. Skeletal forms occur in all samples but are dominant in the Volcán Tecolote scoria (Fig. 3.3B) and rare in the Volcán Atitlán lava, where they have more tabular forms (Fig. 3.3A). Resorption via embayment is observed in the Volcán Atitlán olivines. Zoning in the olivines is very similar, with normal and diffuse zoning in nearly all crystals. Crystals are relatively large (up to 1 mm in length), but in the Volcán Paquisis lava they are mostly much smaller (<0.1 mm). Volcan Paquisis olivines also show a texture where their rims are covered in microlites of orthopyroxenes (Fig. 3.4). Rare crystals from Volcán Atitlán also show this texture.

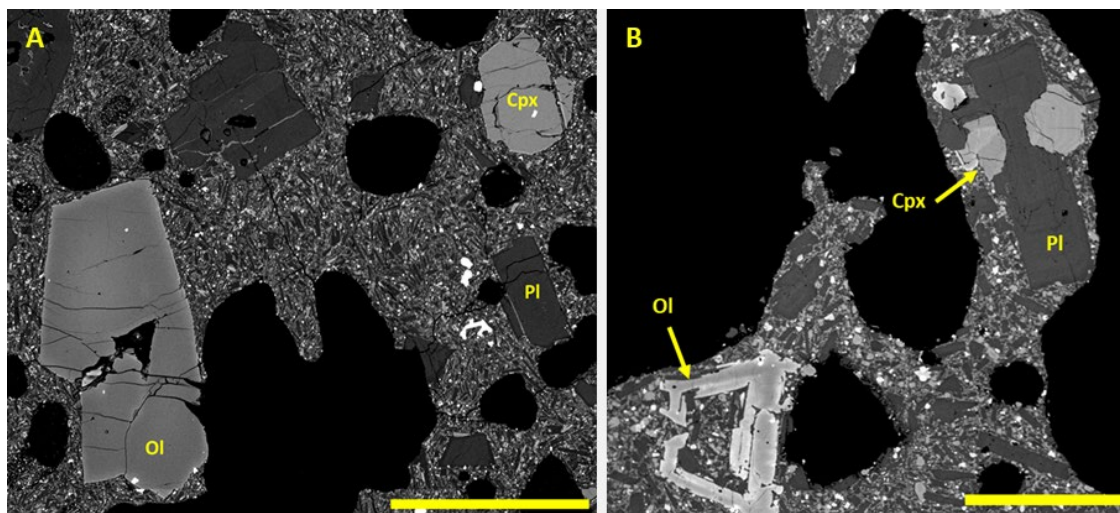


Figure 3.3. BSE (back-scattered electron) photomicrographs of the three major phases of the most primitive basaltic andesites of A) Volcán Atitlán – sample Ati501_05a; and B) Volcán Tecolote – sample Ati427_11. Ol-olivine, Pl-plagioclase, Cpx-clinopyroxene. Scale bars = 0.5 mm

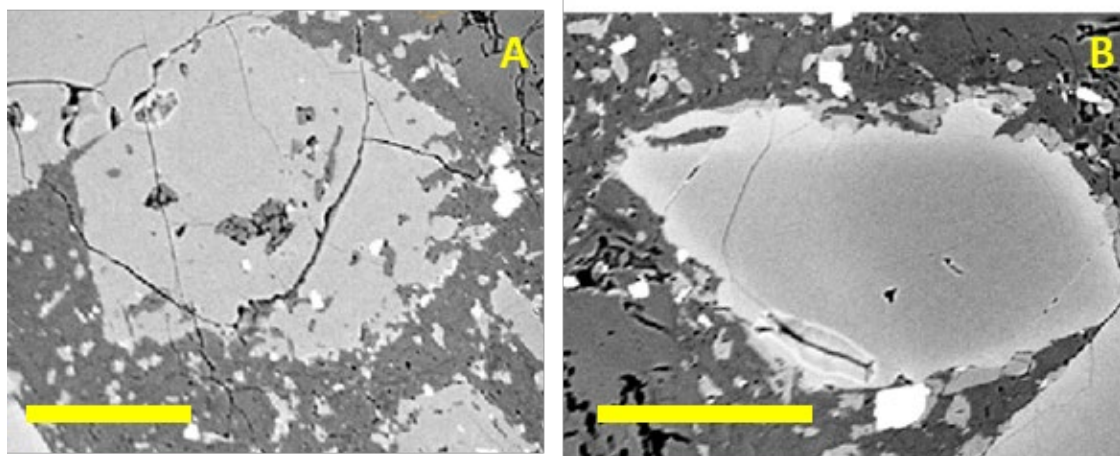


Figure 3.4. BSE photomicrograph of: A) orthopyroxene; and B) olivine phenocrysts from sample Ati501_03 showing the irregular rim texture caused by the attachment of orthopyroxene microlites to the crystal margins. Scale bar = 0.1 mm.

Clinopyroxene phenocrysts are subhedral to euhedral with prismatic forms in all samples. They are smaller in the Volcán Tecolote sample (<0.2 mm) and are most frequently intergrown with plagioclase and olivine crystals (Fig. 3.3B). In the other two samples, they are larger, but rarely larger than 1-2 mm. Zoning is ubiquitous and typically oscillatory. Sieve textures in the samples from Volcáns Tecolote and Atitlán are similar and occasionally occur in the clinopyroxene cores, while those in the Volcán Paquisis sample are typically coarser and more commonly occur in the mantles and rims. Like the olivines in the Volcan Paquisis sample, clinopyroxenes are frequently rimmed by microlites of orthopyroxene. Occasionally orthopyroxenes also occur as inclusions in or intergrown with clinopyroxenes. Rare phenocrysts of orthopyroxene are only present in the Volcán Paquisis sample and have similar forms to the clinopyroxenes.

Glomerocrysts are present in the samples from Volc  ns Paqu  sis and Atitl  n, where they take very different forms (Fig. 3.5). In the Volc  n Atitl  n sample, they are present as two types. One is as highly elongate (up to 3 mm long but <0.5 mm wide) mixtures of microphenocrysts (<0.1 mm sized) of the same phases as the phenocrysts but held together by large amounts of interstitial melt that is variably glassy to fully crystallised (Fig. 3.5A). The other is large intergrowths of mostly clinopyroxene and olivine phenocrysts (Fig 3.5C). In the Volc  n Paqu  sis lava, they are typically larger clusters of two or more mineral phases that are intergrown. These are rarely more than 1-2 mm in size (Fig. 3.5C).

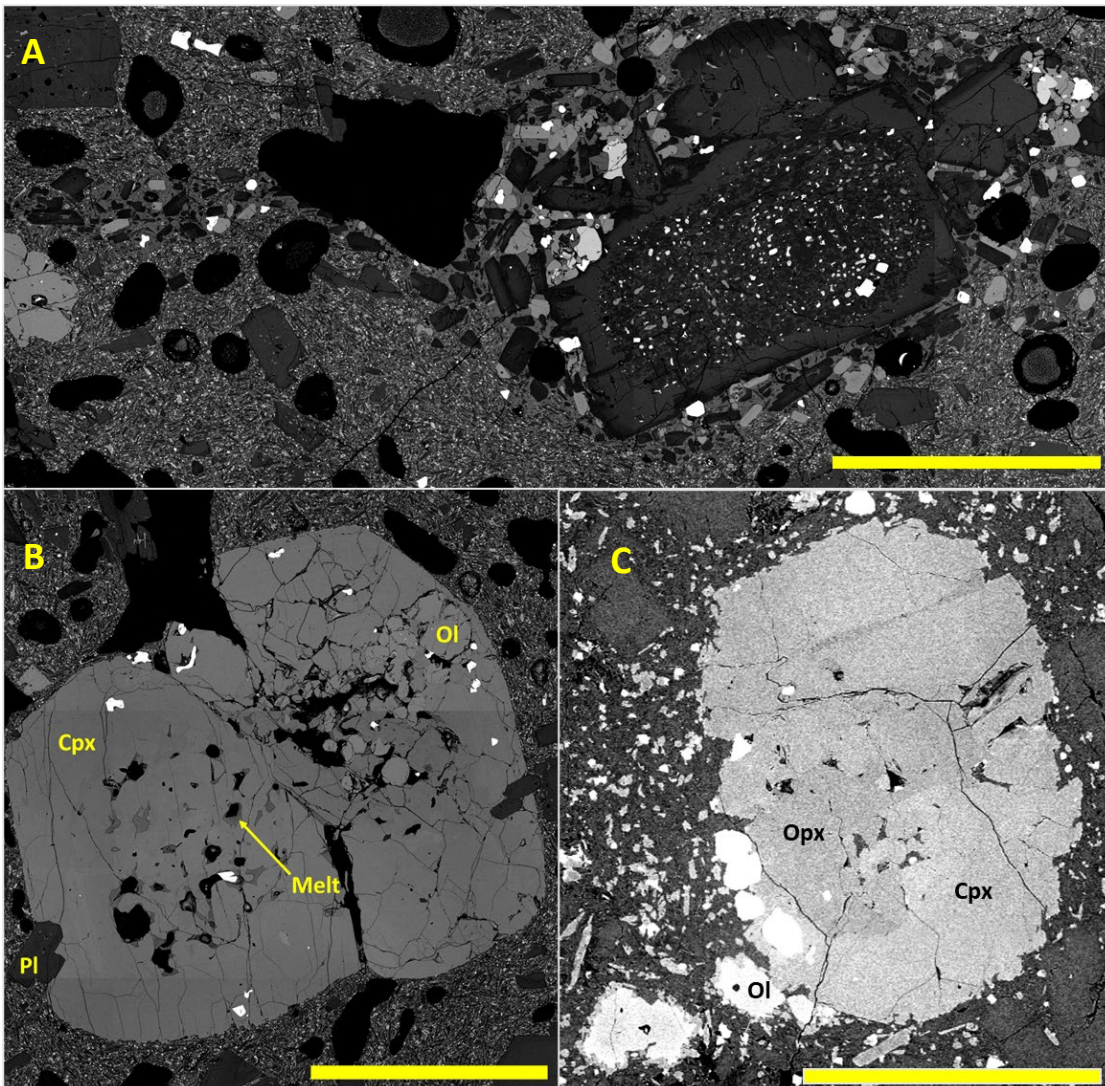


Figure 3.5. BSE photomicrographs of different glomerocrysts from A) and B) Volc  n Atitl  n sample Ati501_05a; and C) Volc  n Paqu  sis sample Ati501_03. A) Highly elongate glomerocryst containing clumped microphenocrysts and interstitial glass, scale bar = 1.0 mm; B) Glomerocryst consisting of intergrown olivine (Ol) and clinopyroxene (Cpx) with minor plagioclase (Pl) and melt inclusions, scale bar = 1.0 mm; C) Glomerocryst from Volc  n Paqu  sis consisting of intergrown clinopyroxene and orthopyroxene (Opx) crystals with minor olivine. The irregular margins on these crystals are pyroxene microlites. Scale bar = 0.3 mm.

Andesite lavas

Mafic andesite lavas (<60 wt.% SiO₂) were examined from Volcáns Tecolote (sample Ati504_06a), San Pedro (samples Ati505_01 and Ati505_02) and Tolimán (samples Ati503_05, Ati503_06, and Ati503_08). These samples are porphyritic with 40-50% phenocrysts and always contain phenocrysts of plagioclase (70-75% of crystal volume), ortho- and clinopyroxenes (15-22% of crystal volume), and accessory microphenocrysts of Fe-Ti oxides (<1%). Phase proportions are compared in Fig. 3.6. Amphibole is present in minor amounts (<5%) in several samples as large phenocrysts (up to 5.0 mm). Some samples from Volcán Tolimán additionally contain very minor amounts of olivine (<5% of crystal volume; samples Ati503_05 and Ati503_08) and very rarely biotite (sample Ati503_08). Accessory mineral phases also include apatite.

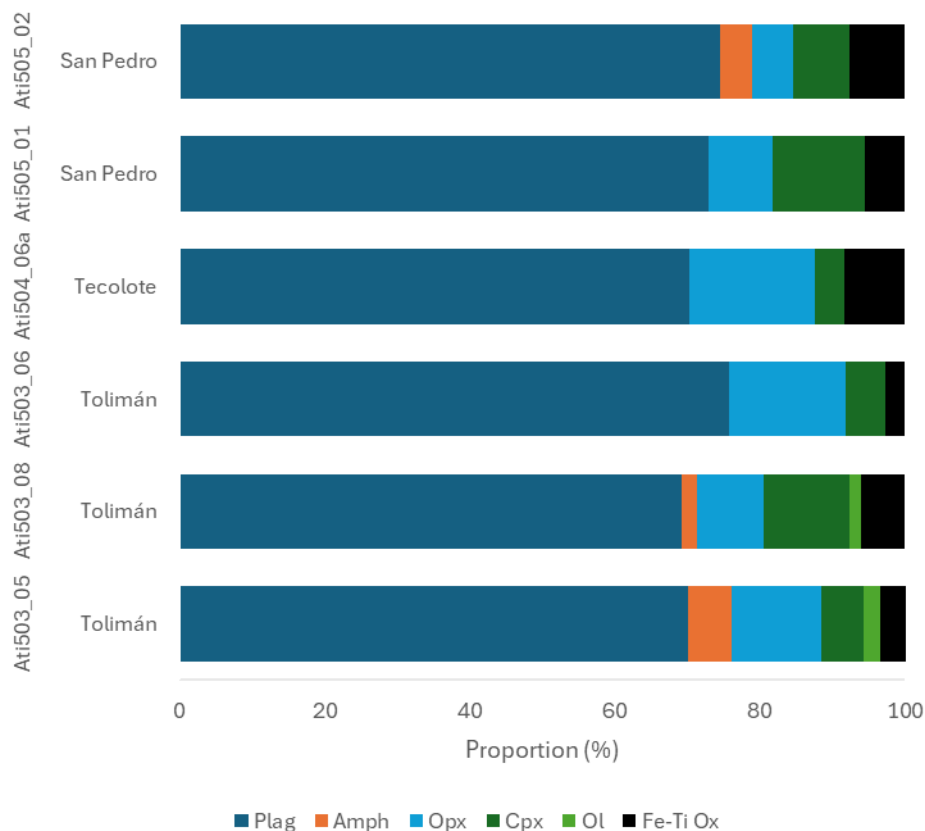


Figure 3.6. Mineral phase proportions for the stratovolcanoes' andesite lavas. Key as in Fig. 3.2, with the addition of Amph – amphibole

All of these samples have partially crystallised groundmasses with abundant microlites. They have vesicularities of 7-15%, with irregularly-shaped vesicles typically 0.1-1.0 mm in size. Glomerocrysts are common in these lavas, and one Volcán San Pedro sample (Ati505_01) contains a xenolith composed mostly of small clinopyroxene grains with minor plagioclase (Fig.

3.7A). The lava sample from the Cerro del Oro cone on Volcán Tolimán (Ati503_06) also contains a large antelith composed of predominantly orthopyroxene and plagioclase with very minor amounts of amphibole and biotite.

Plagioclase crystals in these lavas are subhedral to euhedral with lengths up to 2 mm. They are predominantly lath-shaped, but the largest crystals have lower aspect ratios with more tabular forms. Synneusis textures are also relatively common. Oscillatory and patchy zoning and resorption surfaces are very common. Sieve textures are also occasionally present, mostly in the cores and mantles of the larger crystals.

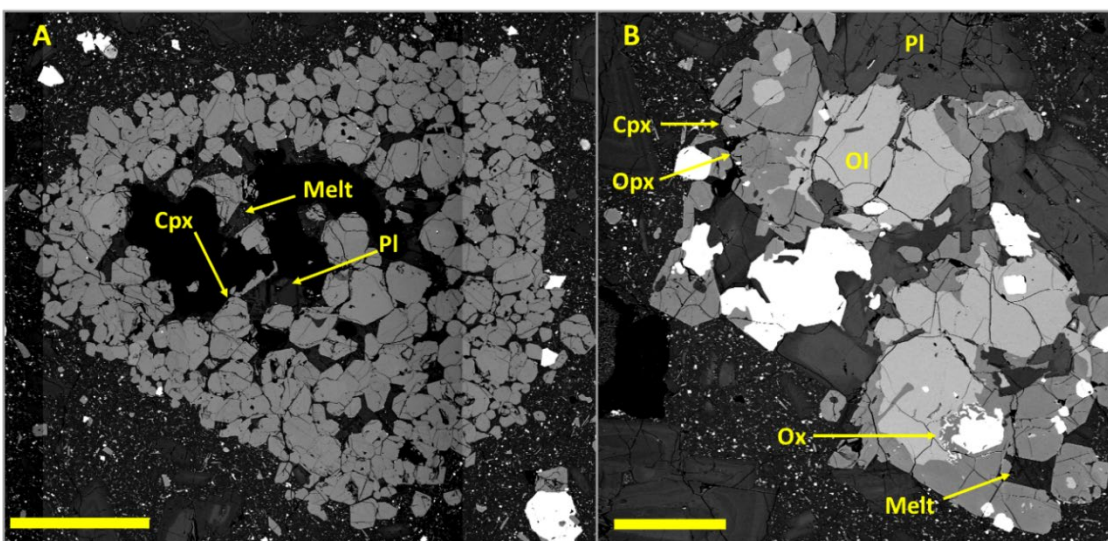


Figure 3.7. BSE photomicrographs of A) a crystalline xenolith from a lava flow from Volcán San Pedro sample Ati505_01. It shows a relatively fine-grained nature and the possible coarsening towards the centre, as well as the increasing amounts of plagioclase and interstitial recrystallising glass. Greyscale variations are artifacts of the image montaging process. Scale bar is 0.5 mm; and B) Example of a glomerocryst from Volcán San Pedro sample Ati505_01. Note the texture of the olivine with pyroxene (and in the lower right crystal myrmekitic Fe-Ti oxide) grown around the margin, as well as the small pockets of interstitial glass. Similar glomerocrysts are observed in all intermediate andesite lavas, although more commonly without the Fe-Ti oxide texture. Scale bar = 0.25 mm. Pl-plagioclase, Ol-olivine, Cpx-clinopyroxene, Opx-orthopyroxene, Ox-Fe-Ti oxides.

Both ortho- and clinopyroxenes are present in all these samples as euhedral to subhedral phenocrysts or glomerocrysts with lengths <1.0 mm. They are commonly associated with plagioclase and/or accessory inclusions of Fe-Ti oxides and/or apatite. Minor reverse and normal zones are the most common textures, and less commonly crystals also display patchy/sector zoning and resorption surfaces. Rarer crystals contain strong single reverse zones.

Olivines typically occur as smaller crystals (up to 0.2 mm) with subhedral forms, although are also rarely present as much larger (up to 1 mm long) phenocrysts. These crystals always have

rimms of orthopyroxene of varying thicknesses around them, similar to those in some basaltic andesites.

When present, amphibole phenocrysts invariably contain areas of either fine- to coarse breakdown material consisting of plagioclase, pyroxene and Fe-Ti oxides (Fig. 3.8A). This texture becomes coarser towards the crystal rims, although sometimes the breakdown material is pervasive throughout the crystal. In some samples, no actual amphibole remains, instead only amphibole pseudomorphs composed of clusters of the same minerals as found in the reaction rims are observed. When the crystal shape can be made out, these crystals are typically large (up to 5 mm) and have tabular to prismatic forms. The one biotite-bearing sample (sample Ati503_08) also has similar textures on these crystals (Fig. 3.8B).

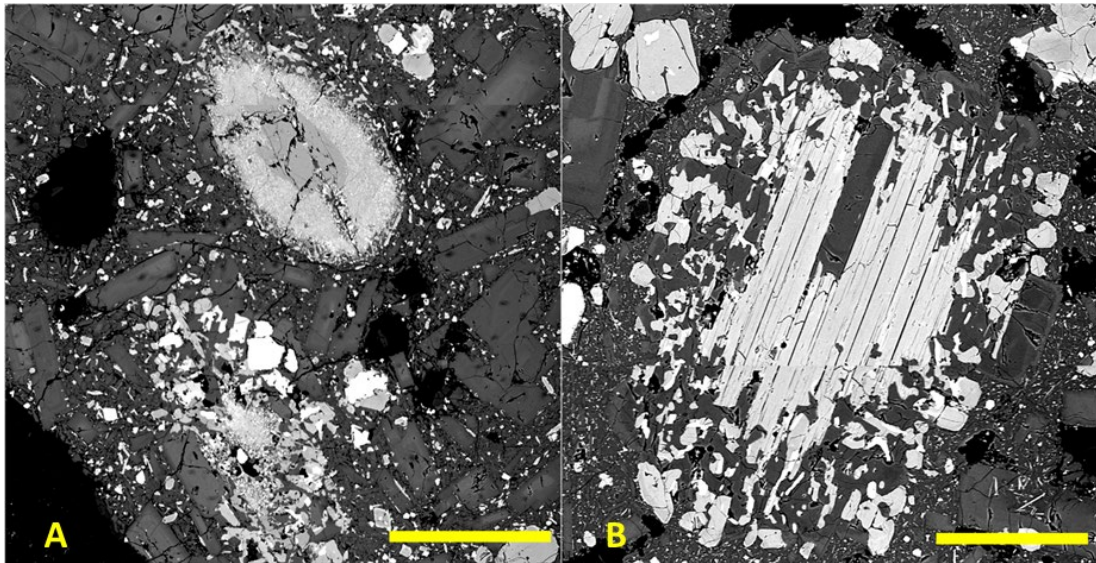


Figure 3.8. BSE photomicrographs of A) amphiboles from Volcán San Pedro sample Ati505_02; and B) biotite from Volcán Tolimán sample Ati503_08, both showing extensive breakdown textures on their margins. Also note the variation in coarse and fine-grained textures between the two amphiboles in A). Scale bars 0.4 and 0.2 mm respectively

Glomerocrysts in the andesite lavas have a wide range of forms and mineral assemblages. Most commonly they are clusters of several intergrown crystals, typically pyroxenes and larger Fe-Ti oxide grains (Fig. 3.7). The Volcán San Pedro lava (sample Ati505_01) contains abundant glomerocrysts with several unique textures. They contain rounded olivine crystals with much coarser rims of many larger pyroxene grains, as well as numerous plagioclase crystals with strong normal zoning (Fig. 3.7B). They also contain moderate to large amounts of partially recrystallised interstitial glass.

The xenolith from the Volcán San Pedro lava is dominantly (>90% by volume) composed of small (approximately 0.1 mm wide) grains of clinopyroxene, with 10% partially recrystallised interstitial melts and small plagioclase crystals. There is also a large void space in the centre of the xenolith, and the glass and plagioclase crystals are concentrated on the edges of this empty portion of the xenolith (see Fig. 3.7A). The plagioclase crystals are strongly normally zoned.

High-K, high-silica andesites

High-K, high-silica andesite lavas ($\text{SiO}_2 > 61$ wt.%) were examined from Volcáns Tecolote (samples Ati427_08a, Ati427_08b, and Ati427_09) and Paquisis (sample Ati501_02). These lavas are broadly similar to the lower-silica andesites, being porphyritic (crystallinities of 32-45%) with similar vesicularities (5-15%) and vesicle forms (irregular and typically <0.5 mm), set in a partially microcrystalline groundmass with abundant microlites and glass. Mineral textures are also very similar. However, there are several differences between these and the lower silica andesites, for example the high-silica andesites do not contain olivines. They otherwise have mostly the same mineral assemblages with ubiquitous plagioclase and ortho- and clinopyroxene phenocrysts, and Fe-Ti oxides and apatite as accessory phases. Plagioclase proportions are slightly lower (56-70%), while amphiboles and biotite are present in varying amounts (Fig. 3.9). There is a general inverse correlation between pyroxenes and amphiboles in terms of abundances; increasing proportions of one are reflected in a decreasing proportion of the other (amphibole varies between 0 and 20% of the mineral proportion, while pyroxenes are between 2 and 20%). Biotite is present in samples Ati427_08a and Ati427_08b in small amounts (<1 vol.%), both as larger crystals (<1.0mm) and inclusions in the amphiboles (Fig. 3.10).

While the mineral assemblages are similar to the more mafic andesites described above, their textures are slightly different (Fig. 3.10). Amphibole crystals show a wider range of textures and in general were better preserved. Those in samples Ati427_08a, Ati427_08b, and Ati427_09 showed very minor or absent reaction rims, and those in other samples had rims of varying thicknesses. They commonly have minor reverse or normal zones, and occasionally patchy zoned cores (Fig. 3.10). Pyroxene textures are also subtly different, as zoning is more common and tends to be more complex, showing multiple/oscillatory and sector zones in individual crystals. Clinopyroxenes are also very commonly heavily fractured and smaller (<0.2 mm) and sometimes occur as rims on orthopyroxene crystals (Fig. 3.10). In the Volcán Paquisis

high-K andesite, orthopyroxenes are present in at least two populations. One has a thick rim of more Mg- and Ca-rich pyroxene and in crystals with abundant fracturing or inclusions, patchy zonation of similar compositions occurs in the interiors. The other population is comparatively un-zoned.

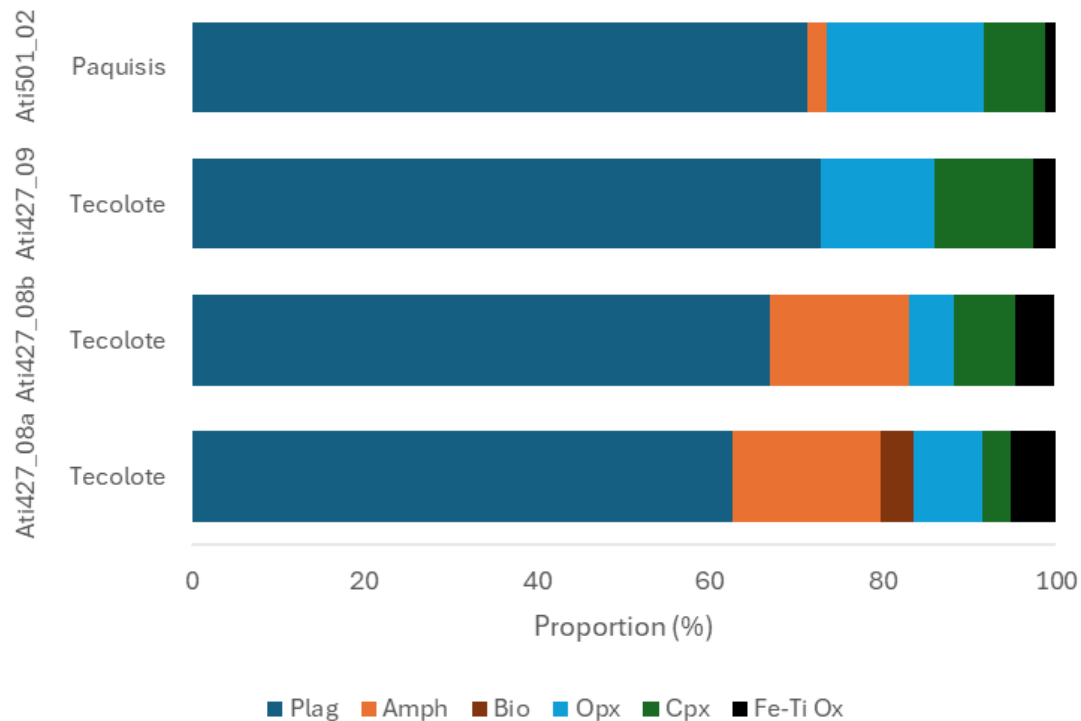


Figure 3.9. Mineral phase proportions for the stratovolcanoes' high-silica andesite lavas. Key the same as Fig. 3.2 with the addition of Bio – biotite.

Potentially related to older age of the volcanoes from which these more evolved samples were taken, these samples also show greater evidence of alteration/secondary mineralisation. Amorphous silica is commonly observed in the groundmasses of most of these lavas, and plagioclase, Fe-Ti oxides and pyroxene crystals are commonly altered. Care was taken to avoid obviously altered crystals but more caution is advised when examining the EPMA data.

One sample (sample Ati501_02 from Volcán Paquisis) also shows a significant difference in grainsize. While most samples have maximum grainsizes for the different mineral phases of 1-2 mm, a much greater proportion of crystals in this lava are of this size, and the largest crystals are 3-4 mm.

One final difference comes from the glomerocrysts and anteliths. While most of these in the intermediate andesites contain mainly pyroxenes with plagioclase and occasional olivine, glomerocrysts in the higher-silica lavas contain greater proportions of amphiboles and lack

olivine. Plagioclase crystals (predominantly in these glomerocrysts but also occasionally in the phenocryst populations) commonly are missing their cores (Fig. 3.11). The glomerocrysts also frequently show alteration and commonly contain larger volumes of glass both as interstitial glass and as melt inclusions (Fig. 3.11).

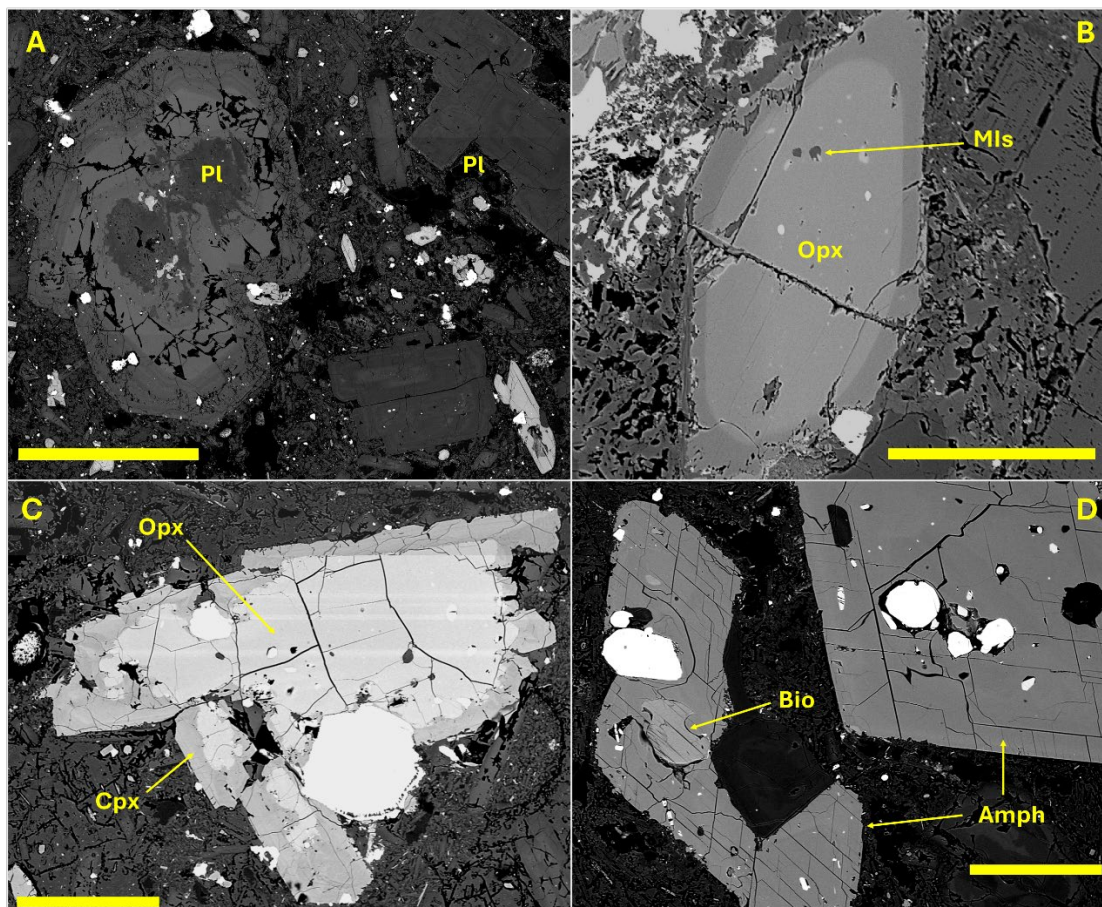


Figure 3.10. BSE photomicrographs of typical mineral textures for the high-K andesites/dacites of Volc  ns Paquisis and Tecolote, Pl-plagioclase, Cpx-clinopyroxene, Opx-orthopyroxene, MIs-melt inclusions, Bio-biotite, Amph-amphibole. A) Several plagioclase crystals of varying forms and interior textures from samples Ati427_08b. Scale bar = 1 mm; B) Normally zoned orthopyroxene crystals from sample Ati501_02, scale bar = 0.2 mm; C) Large orthopyroxene crystal rimmed by complexly zoned clinopyroxene from sample Ati427_08a, scale bar = 0.25 mm; D) Patchy and reverse zoned amphibole crystals containing an inclusion of biotite, from sample Ati427_08a. Note the very minor breakdown rims, scale bar = 0.25 mm

Anteliths

Two large (1-2 m) anteliths have been examined from lavas from Volc  ns Tolim  n and Tecolote. They show similar textures (Fig. 2.3), being largely biminerally with mineral proportions of approximately 45% plagioclase and 45% of either amphibole (Ati427_08a from Volc  n Tecolote) or orthopyroxene (sample Ati503_06 from Volc  n Tolim  n; Fig. 3.12). They have heteradcumulate textures where the ferromagnesian phase partially envelops the plagioclase (Fig. 3.13). Grainsizes for both samples are similar, with crystals of the two

dominant phases typically having maximum lengths of 1-3 mm. Biotite, Fe-Ti oxides and apatites also occur as minor phases, although there are differences to where and how biotite occurs in each sample. Plagioclase grains are also very similar in texture, being strongly normally zoned with patchy zoned cores (Fig. 3.13).

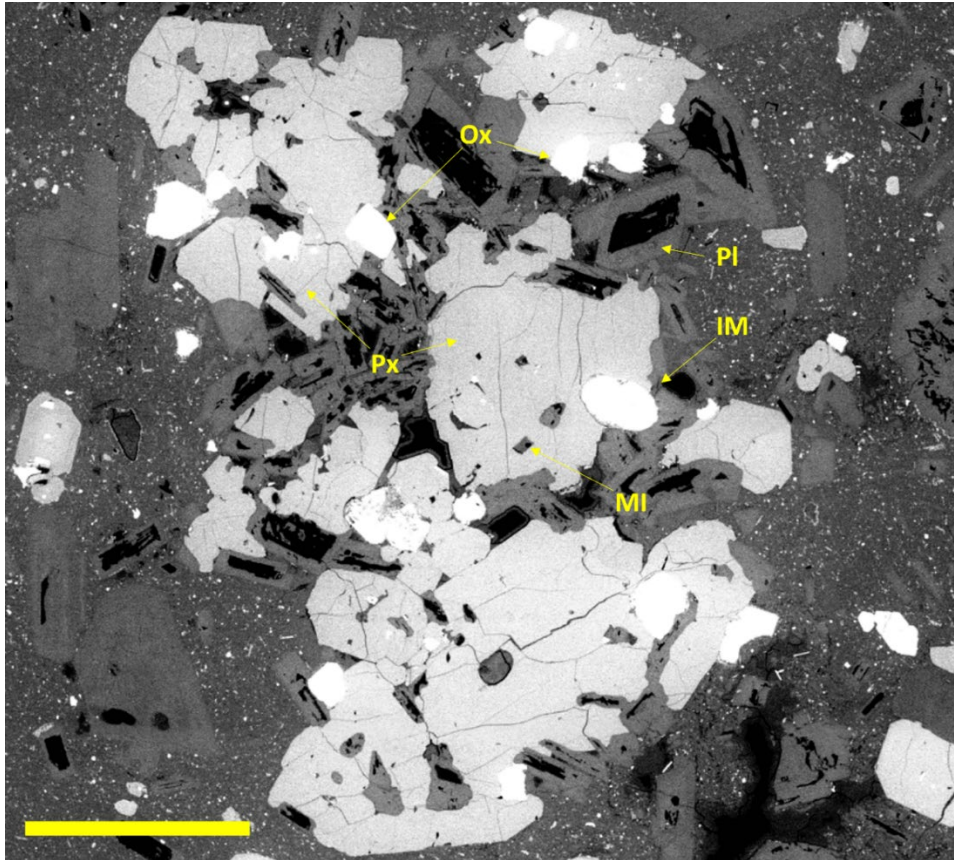


Figure 3.11. Typical glomerocryst texture containing intergrown clino- and orthopyroxenes, small lath-shaped plagioclase, Fe-Ti oxides, and both melt inclusions and interstitial glass. Note the missing cores from the plagioclase crystals, which is a common texture in these glomerocrysts, as are alteration textures like sericitic plagioclase. From samples Ati427_09. Scale bar = 0.5 mm

As well as the minor differences in mineralogy, there are several other textures unique to each antelith. The Volcán Tecolote antelith is hypocrystalline, containing about 30% by volume aphyric glass and vesicles. The vesicles have three main appearances: (a) small highly elongate curvilinear bubbles typically associated with a crack on a crystal surface; (b) moderately sized rounded bubbles up to 0.2 mm wide that lose their shape when they touch the groundmass crystals; and (c) large diktytaxitic voids formed in the interstices between plagioclase microphenocrysts that grade into type b (see Fig. 3.13A for examples). Type (a) vesicles may or may not feed into a type (b) or (c) vesicles.

Amphiboles are typically large (up to 2.5 mm long) and usually elongate with high aspect ratios. They have a poikilitic texture as they are intergrown with plagioclase, both with enveloping microphenocrysts and intergrowth with the phenocrysts. However the intergrowth is unusual in that the amphibole crystals are only intergrown with the plagioclase mantles and are very rarely in contact with the plagioclase cores (Fig. 3.13A). Patchy zonation is ubiquitous in the amphiboles (Fig. 3.13A). Breakdown reaction textures on the amphibole rims are small if present at all.

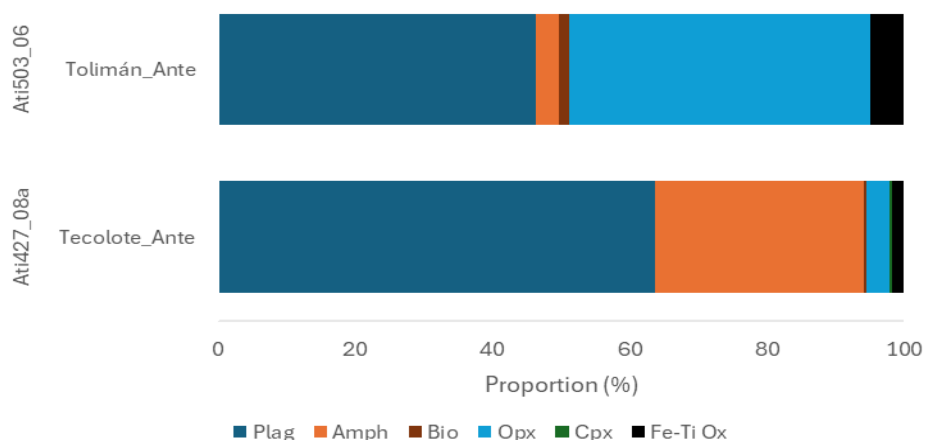


Fig. 3.12. Mineral phase proportions of the anteliths of Volcáns Tecolote and Tolimán. Key as in Fig. 3.2

Plagioclase crystals in the Volcán Tecolote antelith share the above-mentioned texture with those from Volcán Tolimán antelith (strong single normal zones), however they have some unique textures. The antelith from Volcán Tecolote has an inequigranular texture with a range of sizes down to microphenocrysts clustered in the glass (see lower left of Fig. 3.13A), however the zoning textures are the same regardless of crystal size. Additionally, some of the larger plagioclase show sieve textures, which are absent in the other antelith.

Finally, the Volcán Tecolote antelith has a crucial difference in the remaining 10% of its crystal population. It has a much greater abundance of Fe-Ti oxides, as well as clusters of pyroxene (mostly ortho- but with minor amounts of clinopyroxene) with minor biotite (Fig. 3.13A). These clusters make up approximately 6% of the antelith volume. The pyroxenes in these clusters are typically highly fractured and rimmed by amphibole (Fig. 3.13A).

The Volcán Tolimán antelith also has several specific textures. It is 90% equigranular plagioclase and orthopyroxene, with large (5-7 mm wide) clusters of intergrown biotite and amphibole making up the remaining 10% (Fig. 3.14). Biotite occurs in small amounts attached to or included in the orthopyroxenes (Fig. 3.13B).

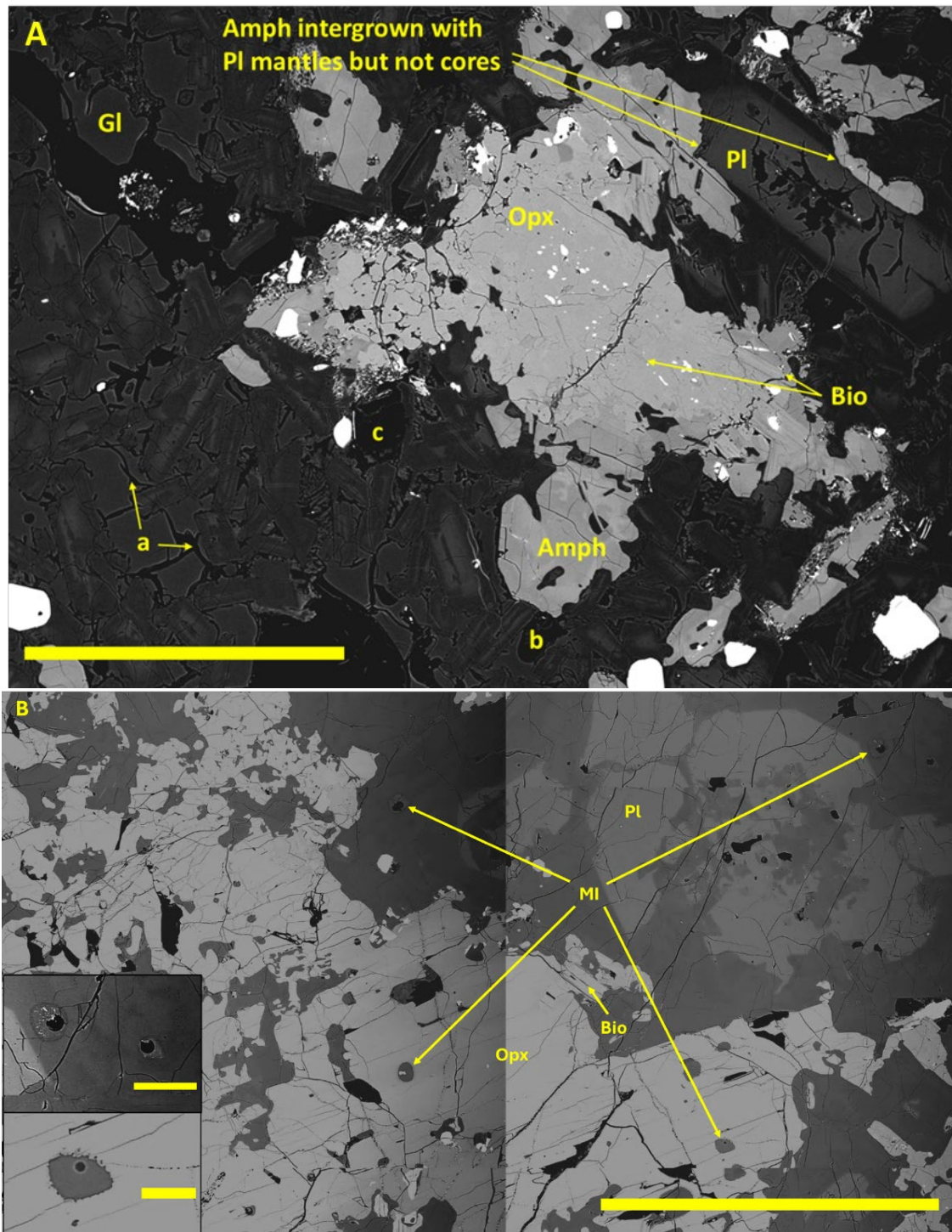


Figure 3.13. Textures in the anteliths of Volcán Tecolote sample Ati427_08a and Volcán Tolimán sample Ati503_06 (from the Cerro del Oro parasitic cone). Gl-glass, Pl-plagioclase, Amph-amphibole, Opx-orthopyroxene, MI-melt inclusion, Bio-biotite. A) BSE image of the antelith in the Volcán Tecolote dacite. Examples of the three vesicles styles are labelled a, b and c, as well as the intergrowth textures of the four main mineral phases. Note the patchy zoning of the amphibole and the cores of the plagioclase, as well as the abrupt nature of the normal zoning in the plagioclase. The lower left of the image also shows clusters of small phenocrysts and microphenocrysts of plagioclase. Scale bar is 0.5 mm. B) BSE image of the Cerro del Oro andesite antelith, with insets of the melt inclusions in plagioclase (above) and orthopyroxene (below). Note the similar patchy texture to the plagioclase crystal as in image A, the intergrowth textures between the plagioclase and the orthopyroxene in the upper left, as well as the differences in recrystallisation styles between melt inclusions in opx vs. pl. Scale bar in main image is 1 mm.

Both major mineral phases commonly contain inclusions of high-K rhyolite glass (Fig. 3.13). These inclusions are commonly partially devitrified, however the recrystallisation texture is different depending on the host phase. It is much more extensive in the plagioclase crystals to the point that none were available for EPMA analysis, and the crystallising phase is most commonly microscopic (<0.005 mm) Fe-Ti oxides. In the orthopyroxene-hosted melt inclusions, their edges have crenulate forms that may suggest ingrowth of the host crystal into the inclusions, while nucleation of new crystals in the interiors of the inclusions is rarer (see inset of Fig. 3.13B).

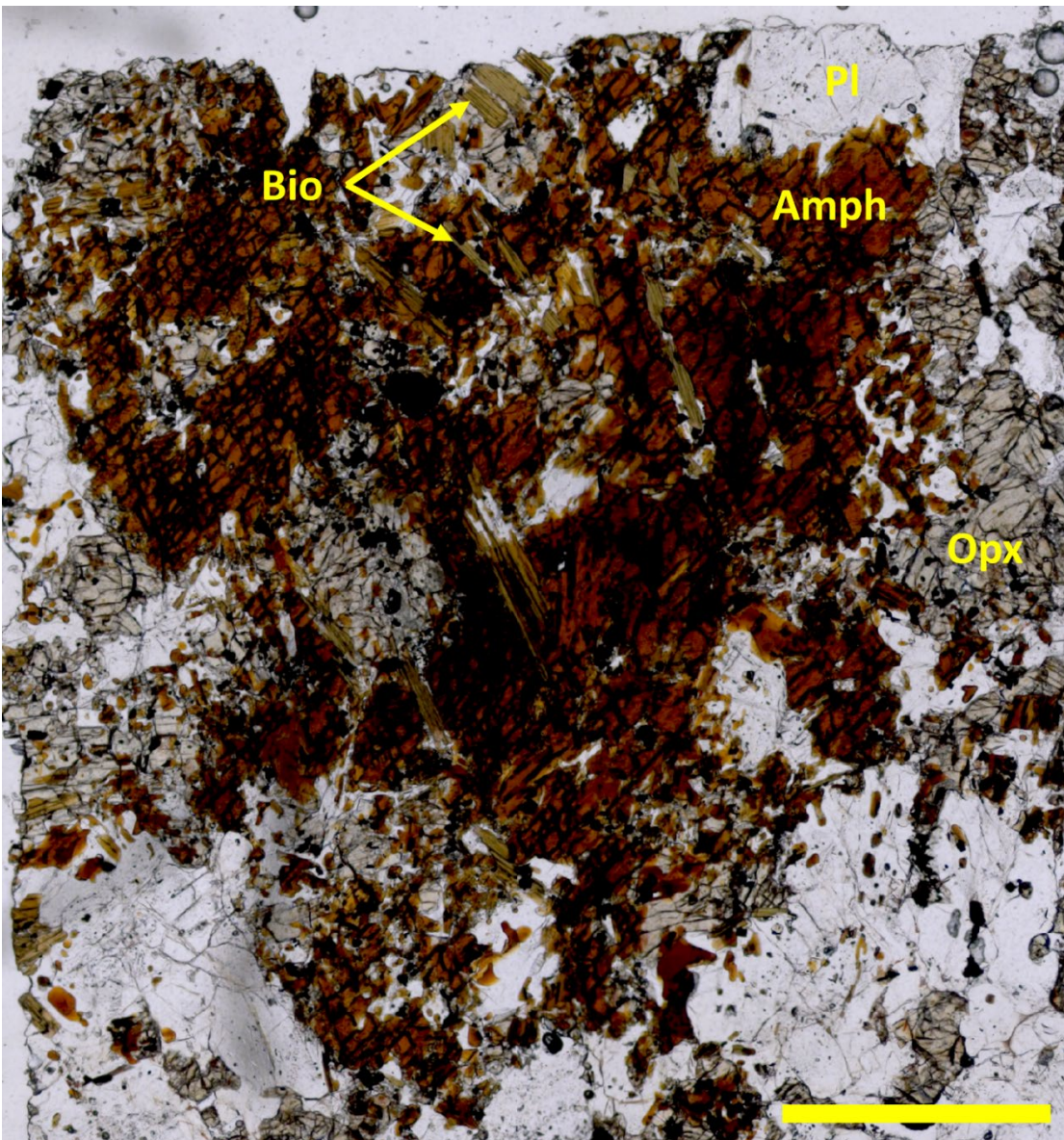


Fig. 3.14. Plane polarised light photomicrograph of a biotite (Bio) and amphibole (Amph) cluster found within the antelith of Volcán Tolimán sample Ati503_06. Bio-biotite, Amph-amphibole, Pl-plagioclase, Opx-orthopyroxene. Scale bar is 1 mm.

Melt inclusions

Glass inclusions are common in both groups of andesites described above, as well as in the pyroxenes of the antelith from Volcán Tolimán. They are most abundant in pyroxenes however, they are also occasionally observed in crystals of plagioclase, olivine and Fe-Ti oxides (their relative scarcity in the last two phases may reflect the relatively lower proportion of these phases). These inclusions are typically small (<0.2 mm wide) and contain vapour bubbles. Crystalline phases are commonly present in these inclusions, most frequently Fe-Ti oxides and/or apatite. Despite this, the glass in these inclusions is mostly pristine, allowing for EPMA analysis. Glass compositions are presented in section 4.4.

3.2.1.2 Stratovolcanoes mineral chemistry

Basaltic andesites

Despite the similar bulk rock compositions for the basaltic andesite samples from Volcans Tecolote and Atitlán (Fig. 3.1), they have contrasting plagioclase compositions (Fig. 3.15). Volcán Tecolote crystals have lower anorthite ($An\% = (Ca/(Ca+Na+K)) \times 100$, cores An_{68-80} and rims An_{48-78}) compared to those from Volcán Atitlán (cores An_{79-93} , mantles An_{73-88} , rims An_{70-80}). The distribution of An compositions is fairly narrow for both lavas, with one exception of a low-An antecryst in the Volcán Atitlán sample. Compositions are shown in Electronic Appendix II. In comparison, the slightly more silicic Volcán Paquisis basaltic andesite has correspondingly lower An% in its plagioclase with mantle and rim compositions almost entirely in the labradorite field (An_{50-68}). The cores are, however, bytownites (An_{70-76}).

For pyroxenes, both of the more mafic samples contain minor amounts of diopside, with most crystals being augites. In comparison, clinopyroxenes in the more silicic Volcán Paquisis samples are less calcic and plot almost entirely in the augite field, with some minor pigeonites. The orthopyroxenes in Volcán Paquisis (and orthopyroxene rims from the Volcán Atitlán samples) are all enstatites with similar compositions (Fig. 3.16).

Olivines are present in all basaltic andesites and commonly show similar normal zoning, although there is a spectrum of how these normal zones occur. Olivines from the Volcán Atitlán samples show zoning less commonly. All core-rim boundaries are diffuse, but the diffuse zones are wider in the Volcán Tecolote and widest in the Paquisis samples. Compositions from all the

studied volcanoes show similar ranges (Fo_{58-78}) although the Volcán Tecolote olivines reach Fo_{81} . The distribution of compositions however is quite different, with over 45% of all analyses being in tight composition groupings of Fo_{70-74} and Fo_{78-81} for Volcáns Atitlán and Tecolote, respectively. The cores from these samples have a narrow range of high-Fo compositions, with a large spread of lower-Fo compositions in the diffused mantles and rims. Those from Volcán Paquisis have a much more even distribution, likely tied to the much more diffuse style of zoning.

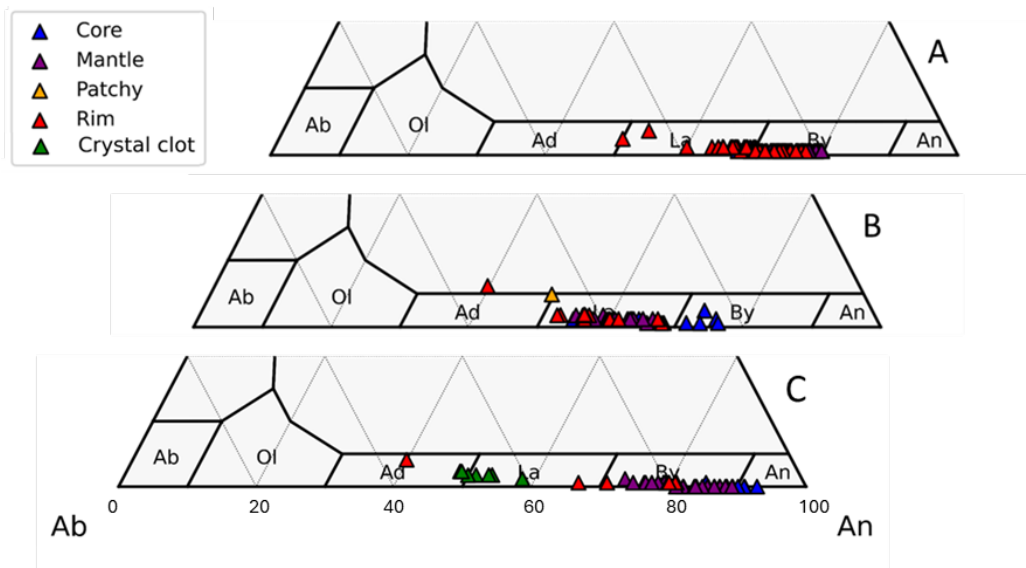


Figure 3.15. Plagioclase compositions divided by type from basaltic andesites of A) Volcán Tecolote, sample Ati427_11; B) Volcán Paquisis sample Ati501_03; and C) Volcán Atitlán sample Ati501_05a. Ab-Albite, Ol-Oligoclase, Ad-andesine, La-labradorite, By-bytownite, An-anorthite. All plagioclase and pyroxene diagrams plotted using python-ternary (Harper et al., 2015) and Thermobar (Wieser et al., 2022). Feldspar ternary diagram after Deer et al. (1992). Crystal clots in C) are shown in Fig. 3.5A

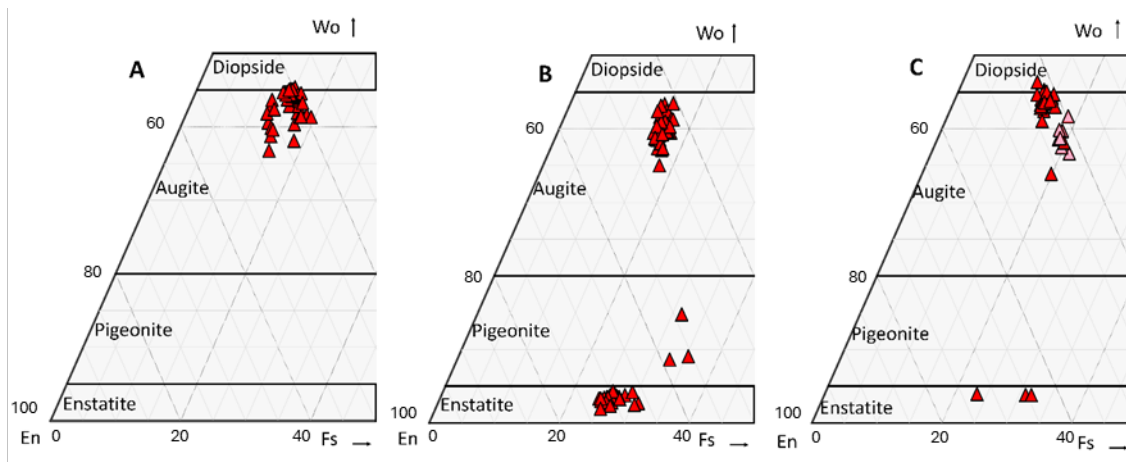


Figure 3.16. Pyroxene compositions for basaltic andesite lavas from Volcáns A) Tecolote; B) Paquisis; and C) Atitlán. Also included in C are pyroxene compositions taken from the elongate glomerocrysts (pink), showing their different composition from the rest of the clinopyroxenes. Plotted using python-Ternary (Harper et al., 2015) and Thermobar (Wieser et al., 2022). Fields after Morimoto et al. (1988).

There are several unusual glomerocrysts in the Volcán Atitlán sample which have very different mineral compositions compared to the host lava. They have two populations of plagioclase microphenocryst compositions (An_{49-60} and An_{79-81}). The first of these is much more Ab-rich than almost all of the phenocrysts from the lava (Fig. 3.15). The clinopyroxene compositions are also subtly different than the average in the lava, with higher Fs and lower Wo components (Fig. 3.16). Olivine compositions (Fo_{64-72}) are also slightly lower than the average phenocrysts. Interstitial glass in these glomerocrysts have trachyandesite compositions (3.9-4.1 wt.% K_2O).

Andesite lavas

Plagioclase compositions for the andesites of Volcáns San Pedro (samples Ati505_01 and Ati505_02), Tolimán (samples Ati503_05, Ati503_06 and Ati503_08) and Tecolote (Ati504_06a) have a similar and wide range of compositions. Samples from Volcán San Pedro and Volcán Tolimán have cores An_{50-92} , mantles An_{36-85} , and rims An_{37-81} , while the compositions from the Volcán Tecolote sample have a lower minimum value (An_{89} ; Fig. 3.17), as expected for a more silicic lava (Fig. 3.1). These have similar maximum An for core compositions to those of the basaltic andesites, but a much greater range for overall compositions (c.f. fig. 3.15). There are also rare alkali feldspar compositions in patchy zones in some phenocrysts in the Volcán San Pedro lavas (Fig. 3.17).

Both clino- and orthopyroxene phenocryst compositions from these andesites are fairly similar. Clinopyroxenes are mostly augites with rare diopsides and pigeonites, although Volcán Tolimán clinopyroxenes have a greater spread of compositions to higher En components (Fig. 3.18). Orthopyroxenes are all enstatites, typically with a narrow range of compositions with En_{66-74} . In one of the Volcán San Pedro lavas, a clinopyroxene-dominated xenolith has a narrow range of compositions ($Wo_{43-45}En_{43-44}Fs_{12-13}$) in the range of the phenocryst compositions in the lava.

Olivine phenocrysts from the andesite samples all show the same diffuse normal zoning patterns, but the composition ranges vary between the different volcanoes. Olivines from the Volcán San Pedro lavas have cores Fo_{72-76} and rims Fo_{62-71} , while the Volcán Tolimán olivines have cores Fo_{75-82} and rims Fo_{66-78} . Olivines were not found in the Volcán Tecolote andesite sample. These compositions are very similar to those of the olivines phenocrysts in the basaltic andesites (comparisons in section 3.3).

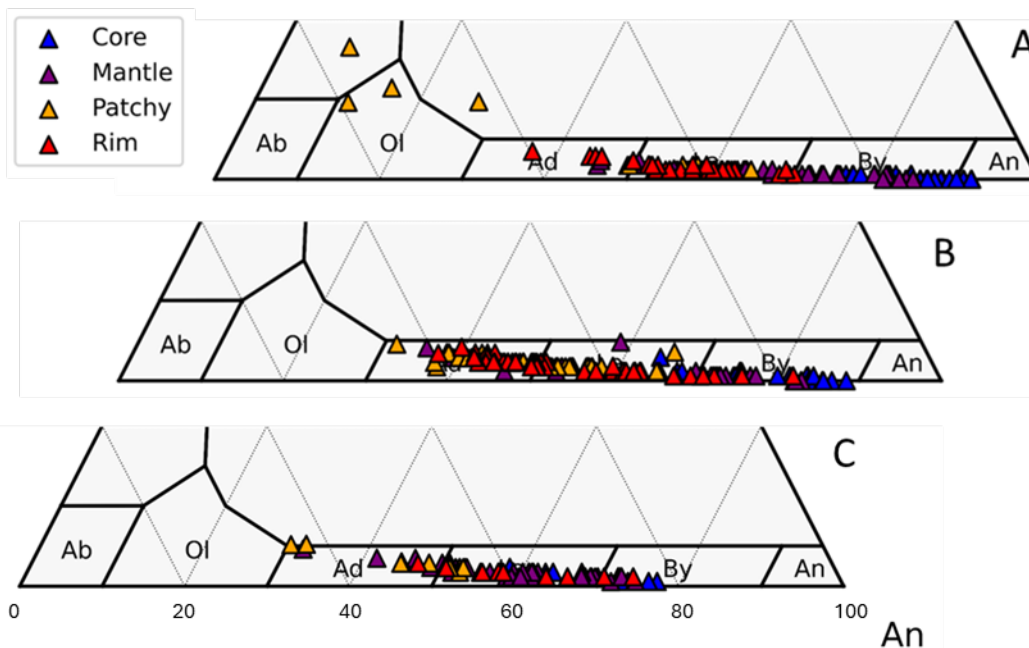


Figure 3.17. Plagioclase compositions divided by type from the andesites of A) Volcán San Pedro; B) Volcán Tolimán; and C) Volcán Tecolote

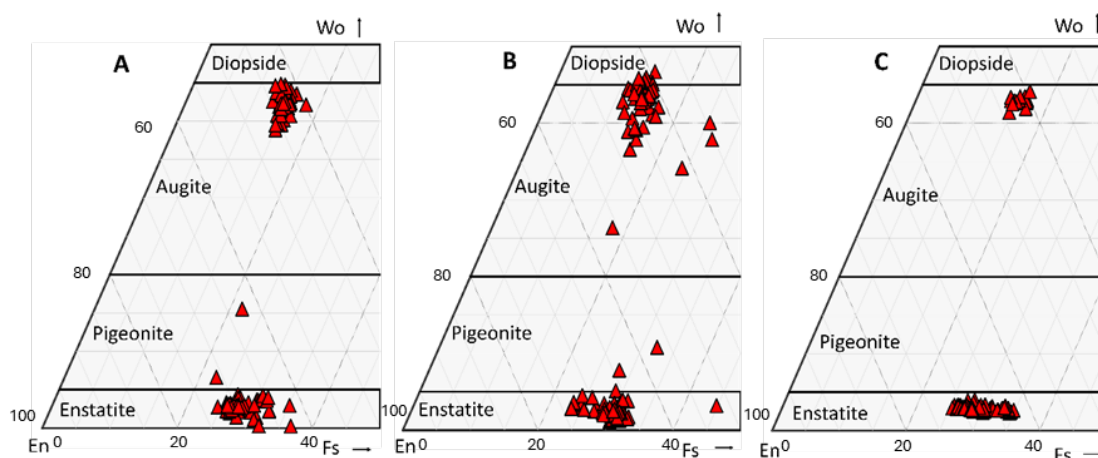


Figure 3.18. Pyroxene compositions from the andesitic lavas from: A) Volcán San Pedro; B) Volcán Tolimán; C) Volcán Tecolote

Amphiboles were only present in samples Ati503_05, Ati503_08 from Volcán Tolimán and in both Volcán San Pedro samples. No amphiboles were observed in the Volcán Tecolote andesite sample. Amphiboles are all magnesiohastingsites in composition and they overlap each other (Fig. 3.19). Zoning in crystals is difficult to make out due to the pervasive breakdown textures.

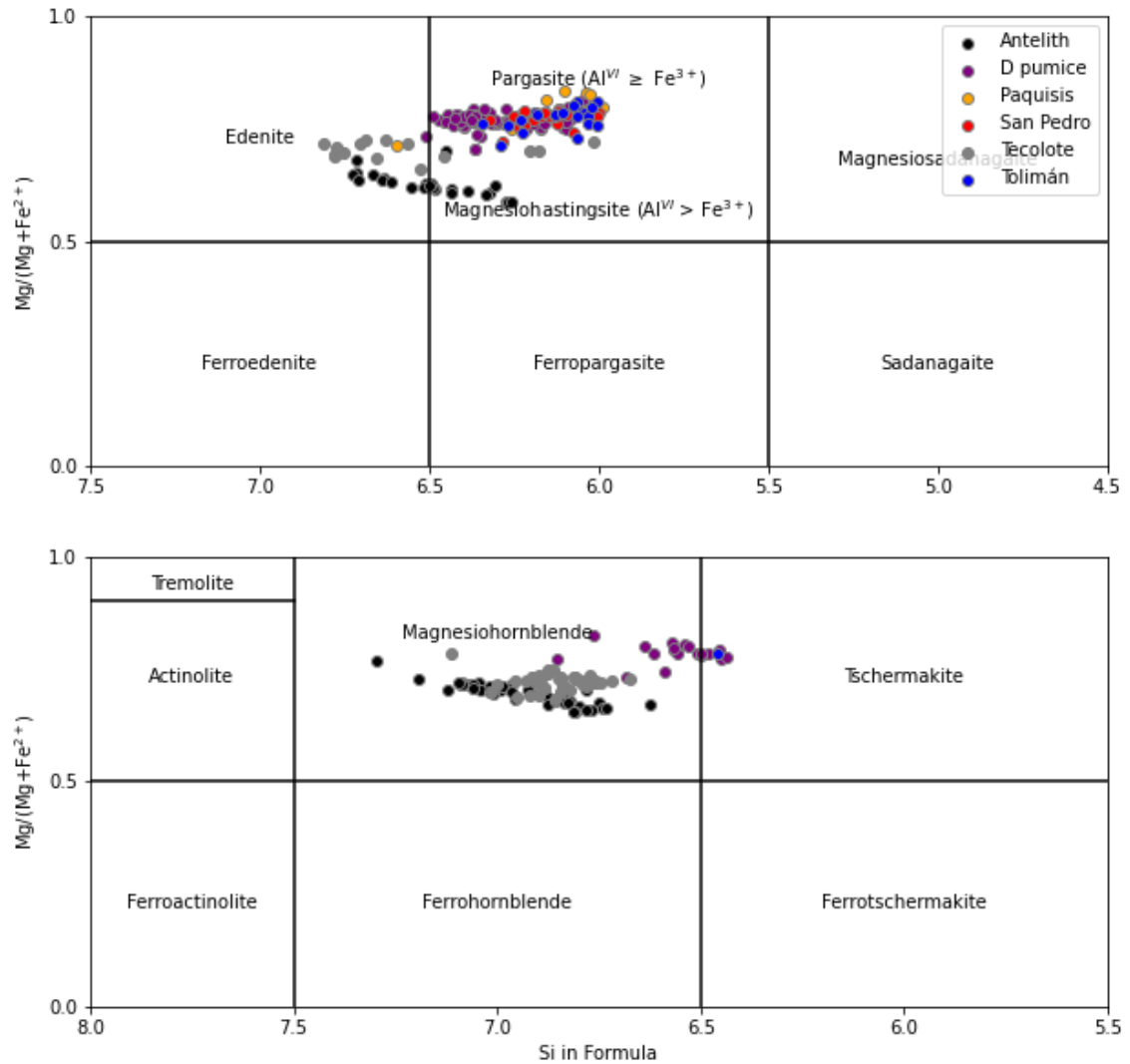


Figure 3.19. Amphibole compositions from the andesite lavas of Volcáns San Pedro and Tolimán, the high-K andesite lavas of Volcáns Paquisis and Tecolote, the D1 andesitic pumice and the Volcán Tecolote antelith. Plotted using Thermobar (Wieser et al., 2022). Fields after Leake et al. (1997), top panel $Ca_B \geq 1.50$; $(Na + K)_A \geq 0.50$; bottom panel $Ca_B \geq 1.50$; $(Na + K)_A < 0.50$.

High-K, high-silica andesites

High-K lavas from Volcán Tecolote (samples Ati427_08a and Ati427_09) have a wide range of disequilibrium textures, with an accompanying large range in plagioclase compositions (cores An_{52-89} , mantles An_{27-74} and rims An_{14-74}). In contrast, disequilibrium textures are rarer in the high-K Volcán Paquisis lava (sample Ati501_02), and the resulting variation in plagioclase compositions is fairly tight, with An_{39-65} (Fig. 3.20). Comparison of the plagioclase of all the stratovolcano lavas shows that, in general, lavas with greater SiO_2 contents contain plagioclase with lower An content (section 3.3.1).

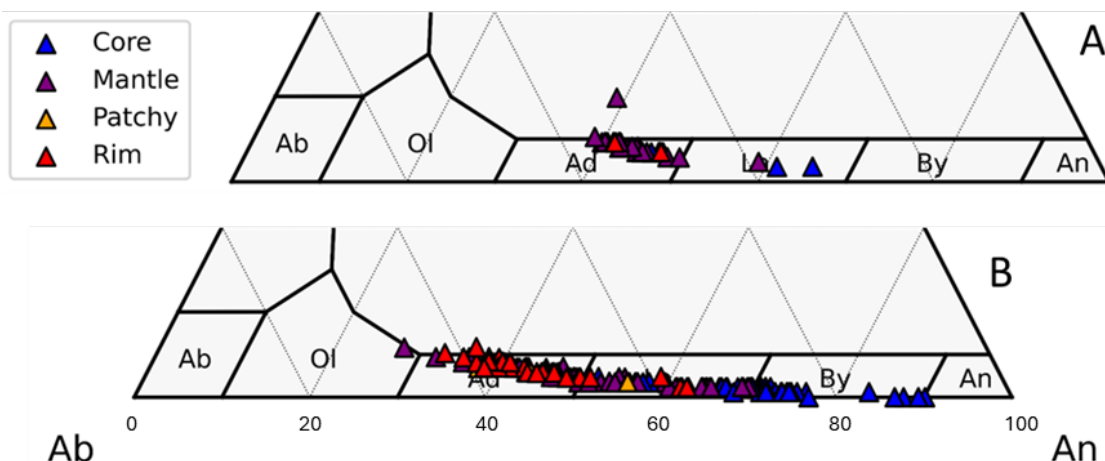


Figure 3.20. Plagioclase compositions divided by type for the high-K andesites of A) Volcán Paquisis; and B) Volcán Tecolote.

All the high-K lavas contain both ortho- and clinopyroxenes. The orthopyroxene compositions from lavas of both volcanoes are very similar, being enstatites of $Wo_{1.6-4.2}En_{57-73}Fs_{24-40}$. There is a greater difference in the clinopyroxene compositions. Crystals in the Volcán Paquisis samples have a much smaller spread of compositions ($Wo_{43-44}En_{38-42}Fs_{13-17}$), while those in the Volcán Tecolote sample show more variation ($Wo_{29-45}En_{39-50}Fs_{12-23}$, Fig. 3.21). Compositionally, pyroxenes in the high-K andesites have generally lower magnesium numbers ($Mg\# = Mg/(Mg+Fe^{2+})$) than those in the andesites.

Amphiboles from these two volcanoes have very different compositions. Those in Volcán Tecolote range from magnesiohornblendes through edenites to magnesiohastingsites, while the Volcán Paquisis amphiboles are almost entirely magnesiohastingsites and have a more magnesian composition (Fig. 3.19). The Volcán Paquisis amphiboles have similar but slightly more magnesian compositions to the lower-silica andesites, while the Volcán Tecolote amphiboles are distinctly different with more silicic and iron-rich compositions.

Anteliths

The two anteliths have slightly different plagioclase compositions but are similar in their clear bimodal distribution (Fig. 3.22). Plagioclase crystals from the Volcán Tecolote antelith have high An cores (An_{65-89}) with intermediate mantles (An_{34-71}) and low-An patchy zoning and rims (An_{34-44} ; Fig. 3.22A). Those from the Volcán Tolimán antelith have similar compositions but the rims and patchy zones have lower An% (An_{46-55}). These compositions are very similar to the range of the plagioclase phenocrysts in the andesite and high-K andesite lavas (Fig. 3.22).

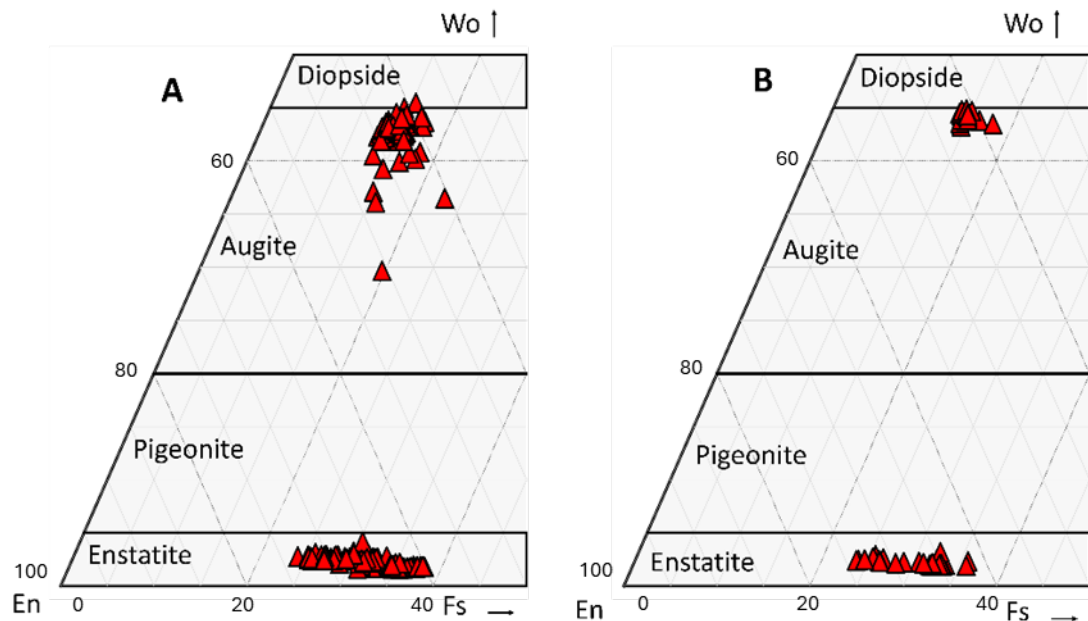


Figure 3.21. Pyroxene compositions for high-K lavas from A) Volcán Tecolote; and B) Volcán Paquís.

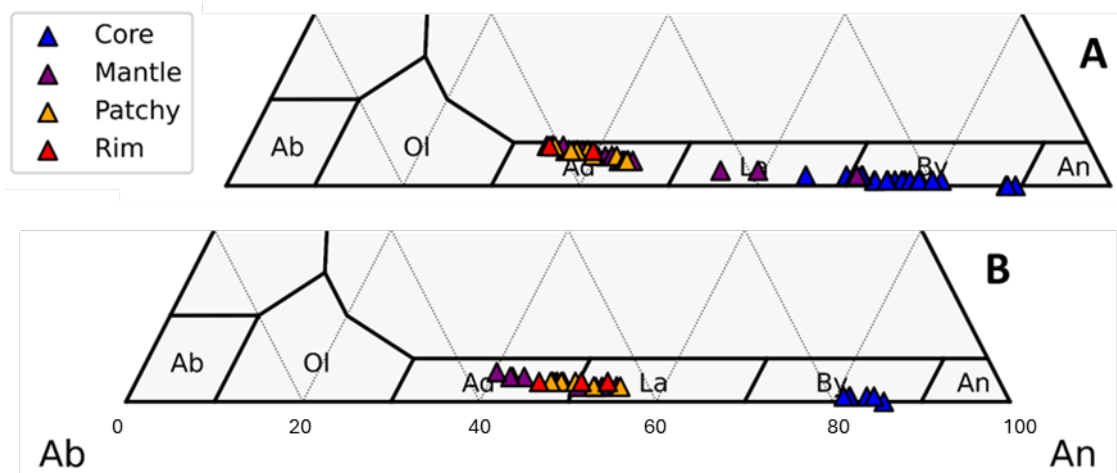


Figure 3.22. Plagioclase compositions for the anteliths from A) Volcán Tecolote; and B) Volcán Tolimán. Note the similar bimodal groupings of the core vs. the rim and patchy zone compositions.

Their orthopyroxene compositions are also similar, as both populations are tightly grouped in a restricted range of enstatite content, although the Volcán Tecolote compositions have a slightly higher ferrosilite component. Orthopyroxenes inside the amphibole and biotite crystal clots (Fig. 3.14) had much more magnesian compositions (section 3.3). The Volcán Tecolote antelith also contains rare diopside to higher-Ca augite clinopyroxenes (Fig. 3.23), and these are on average slightly more magnesian than those clinopyroxenes from the andesite and high-K andesites lavas.

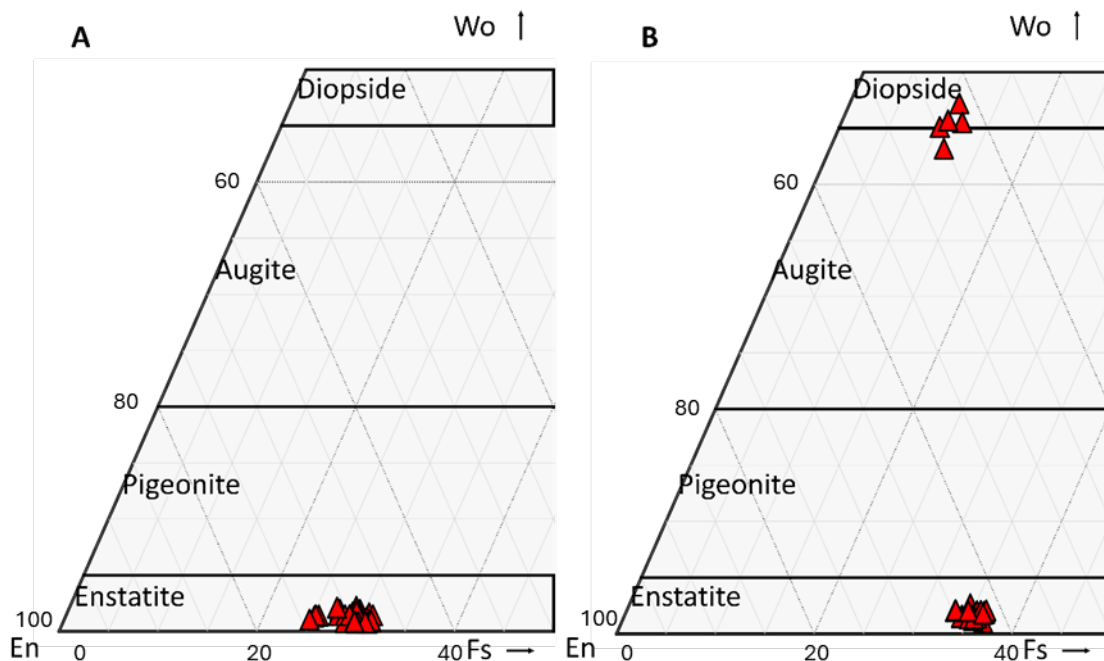


Figure 3.23. Pyroxene compositions for the anteliths of A) Volcán Tolimán; and B) Volcán Tecolote.

Amphiboles in the Volcán Tecolote antelith have similar compositions to phenocrysts in the lavas (magnesiostengite through edenite to magnesiohornblende, Fig. 3.19). However they are all richer in FeO and, in contrast to most of the other amphibole populations in AVC andesites which have mostly constant $Mg/(Mg + Fe^{2+})$ values against Si in formula, they have a positive correlation for this (Fig. 3.19).

3.2.2 Intermediate composition clasts

3.2.2.1 Petrography of the intermediate composition clasts

Intermediate to mafic composition clasts from the initial phases of the D (sample Ati426_03a) and I eruptions (Ati505_06a) are labelled “D1” and “I1” samples, respectively. They have slightly different compositions, with the D1 clast being slightly more silicic but having lower alkali contents (Fig. 3.1). They are both porphyritic with groundmasses of mostly aphyric and vesiculated glass and have similar crystallinities (approximately 25% by volume calculated via point counting, as outlined in section 2.4.1). The more significant differences between these rocks are discussed below.

D1 pumice

This pumice contains plagioclase (58%), amphibole (21%), orthopyroxene (14%) and Fe-Ti oxides (7%; Fig. 3.24). Maximum crystal sizes are ≤ 1.0 mm, however there are two crystal size

populations; the thin section contains a small region populated almost entirely by microphenocryst-sized (up to 0.1 mm) crystals of amphibole, plagioclase and Fe-Ti oxides (Fig 3.25).

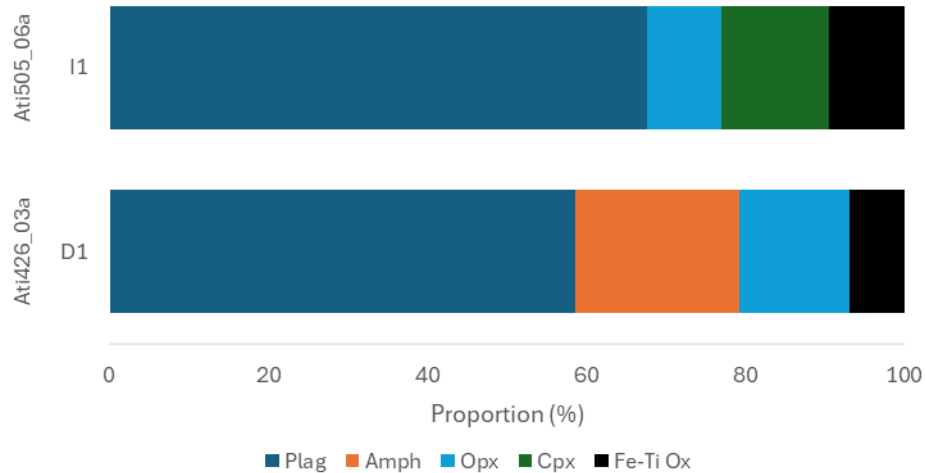


Fig. 3.24. Mineral phase proportions of the post-LCY intermediate and mafic clasts. Key as in Fig. 3.2

Examples of the mineral textures are shown in Fig. 3.26. Plagioclase phenocrysts are euhedral to subhedral lath-shaped crystals dominantly ≤ 1.0 mm long, with rare larger tabular but subhedral crystals. Disequilibrium textures are very common, with sieve textures and patchy zoning present in almost every crystal. Oscillatory, normal and reverse zoning are also present in many crystals, and resorption surfaces are occasionally observed (Fig. 3.26).

Amphibole phenocrysts are euhedral to subhedral tabular or prismatic crystals ≤ 0.6 mm wide. Most show patchy and/or reverse zoning, most commonly restricted to crystal cores (Fig. 3.26A). Larger phenocrysts may have several concentric zones and, unlike the crystals from the lavas, none of these amphiboles show breakdown rim textures. Orthopyroxenes are present as subhedral tabular crystals up to 0.5 mm wide and, unlike the amphiboles and plagioclase, do not show significant textures, which if present are typically simple zoning (Fig. 3.26B). Inclusions of plagioclase, Fe-Ti oxides and apatites are common. Fe-Ti oxides have a large range of sizes in this sample. Most are included in glomerocrysts or as inclusions in the other phenocryst phases, but there are numerous larger phenocryst-sized (up to 1.5 mm wide) crystals. These are rounded and the larger phenocrysts are globular.

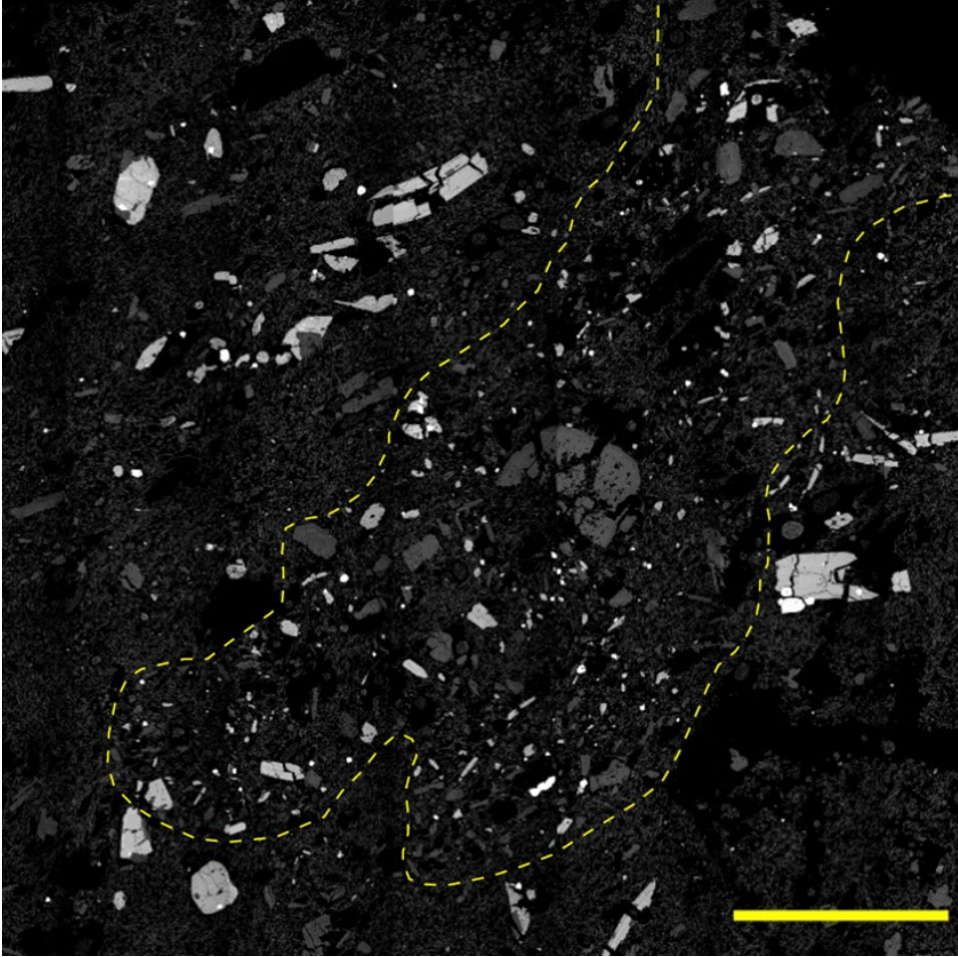


Figure 3.25. BSE image of the area of the D1 pumice (sample Ati426_03a) with a markedly different crystal size distribution. Region is outlined by the yellow dashed line. Scale bar = 2.0 mm.

I1 scoria

The I1 scoria include plagioclase (68%), ortho- and clinopyroxenes (22%), Fe-Ti oxides (10%) and minor olivine (<1%). The groundmass is mostly composed of vesiculated glass, although some microphenocrysts and microlites of plagioclase, pyroxenes and Fe-Ti oxides are present (Fig. 3.27). Glomerocrysts containing one or more crystals of each phase are present.

Most of the plagioclase are present as micro to moderate sized (from microlites to ≤ 0.8 mm long) lath-shaped euhedral to subhedral crystals, with some rarer large (>1.0 mm) crystals with more tabular forms. Crystals in both populations show varied textures. Synneusis textures are common, and oscillatory and patchy zoning and resorption surfaces are ubiquitous. Occasionally the crystals contain large melt inclusions. Sieve textures are almost entirely absent (Fig. 3.27).

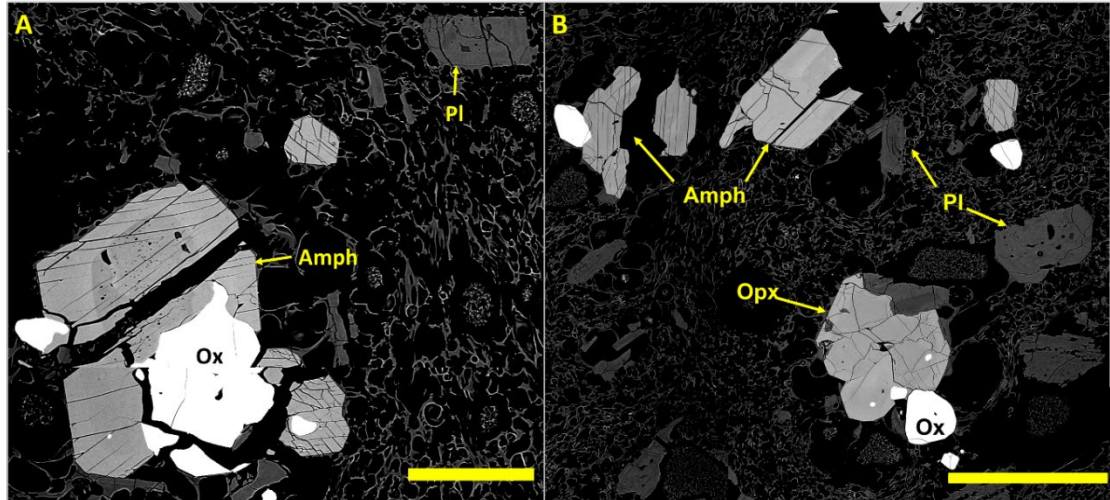


Fig 3.26. BSE photomicrographs of mineral textures present in the D1 andesite pumice (sample Ati426_03a). A) An amphibole (Amph) grain showing clear zonation, with a highly resorbed core (including both patchy zones and sieve textures) and several zones in the crystal mantle. It is also intergrown with a large Fe-Ti oxide (Ox) grain. In the upper right of the image, a plagioclase (Pl) grain is present also showing patchy, normal, and reverse zones as well as sieve textures. Scale bar is 0.2 mm. B). Amphibole grains in the upper left of the image showing clear zonation, with an orthopyroxene grain showing minor normal zonation and several plagioclase grains again showing several disequilibrium textures. Scale bar is 0.5 mm.

Clinopyroxenes are moderately sized (≤ 1.0 mm) subhedral tabular to prismatic crystals. They are very commonly normal, patchy and sector zoned (Fig. 3.27B, D). Rims and patchy zones may be sieve textured. Orthopyroxenes form glomerocrysts or small euhedral grains (< 0.5 mm), as well as rims on olivine crystals (Fig. 3.27B, C). Zonation is rare. Olivines have a low abundance ($< 1\%$ by volume), are anhedral, always show rims of orthopyroxene and rarely clinopyroxene (Fig. 3.27C, D), and have myrmekitic Fe-Ti oxides which extend into the orthopyroxene rims (Fig. 3.27B, C).

3.2.2.2 Mineral chemistry of the intermediate composition clasts

Plagioclase phenocrysts from the D1 pumice have a similarly narrow range (An_{56-85}) and there is little grouping of compositions based on location of the analytical points in the crystal (Fig. 3.28A). Their compositions are most similar to those from the basaltic andesites (c.f. Fig. 3.15). The plagioclase microphenocrysts compositions fall in the range of the phenocrysts, but with slightly lower average An content. Plagioclase in the I1 scoria has a slightly wider composition range which includes lower-An (An_{45-89}) compositions (Fig. 3.28), despite the host pumice having a lower whole rock SiO_2 content (Fig. 3.1).

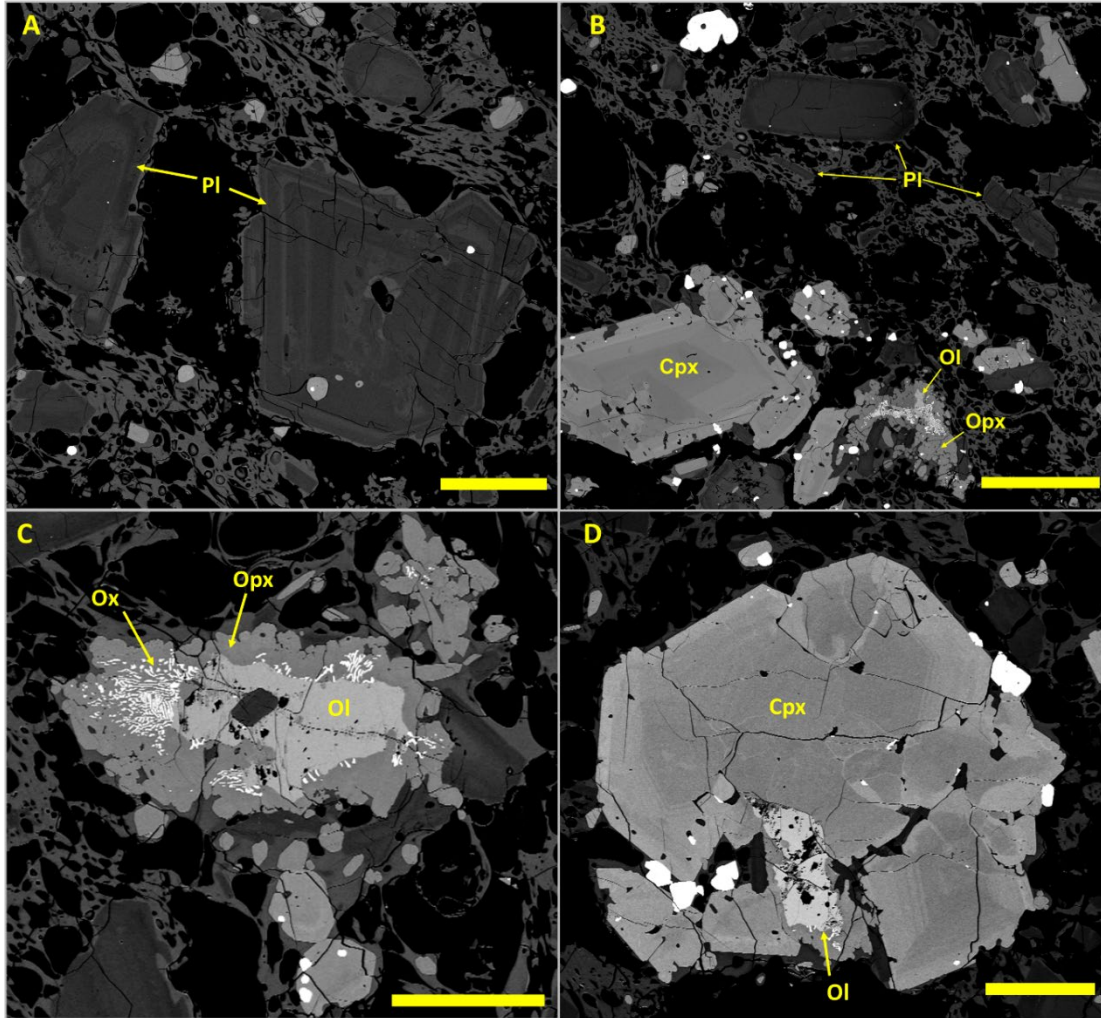


Fig. 3.27. BSE photomicrographs of mineral textures present in the I1 basaltic andesite scoria (sample Ati505_06a). A) Plagioclase phenocrysts showing the abundance of mineral textures common in plagioclase in this rock, including patchy, normal, reverse, and oscillatory zones as well as melt inclusions. Scale bar is 0.25 mm. B) Clinopyroxene (Cpx) grain showing clear zonation with a patchy zoned core and sieve textured rim, as well as an olivine grain with myrmekitic Fe-Ti oxide (Ox) and an orthopyroxene (opx) rim. Scale bar is 0.5 mm. C) Olivine grain with a myrmekitic Fe-Ti oxide and orthopyroxene rim. Scale bar is 0.2 mm. D) Clinopyroxene grain with several zonation types including patchy, sector and oscillatory, surrounding an olivine grain. Scale bar is 0.2 mm.

Amphibole phenocrysts are present in the more silicic D1 pumice and absent in the I1 scoria. These mostly have magnesiohastingsite compositions, although some have magnesiohornblende and rare tschermakite cores (Fig. 3.19). On average the amphibole microphenocryst compositions are slightly more primitive (higher Al_2O_3 , lower SiO_2) than those of the phenocrysts. Compared to the amphiboles in similar composition lavas from Volc  ns San Pedro and Tolim  n, they have a much greater range of Si values in the mineral formulas, although with similar $\text{Mg}/(\text{Mg} + \text{Fe}^{2+})$ values (Fig. 3.19).

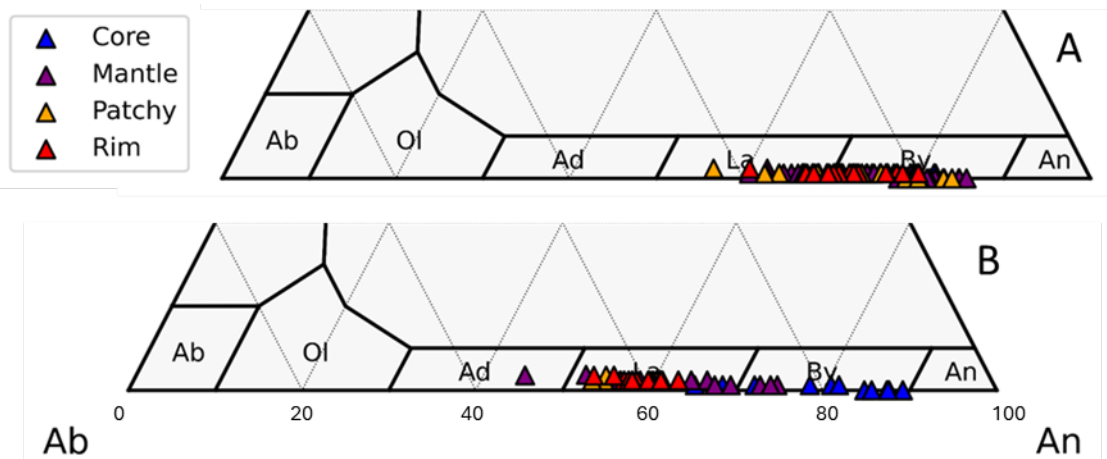


Figure 3.28. Plagioclase compositions separated into type for the A) D1; and B) I1 basaltic andesite scoria

Orthopyroxene compositions are similar in the two intermediate clasts (Fig. 3.29), enstatites with En_{67-75} , although the I1 basaltic andesite scoria has on average a slightly higher Wo component. These are slightly more Mg-rich than those in the lavas of all but the Volcán Paquisis basaltic andesite, as well as those found in the D2 rhyolite pumice (compared in section 3.3 and Fig. 3.29). Clinopyroxenes of the I1 scoria are also different to those elsewhere in this centre as they tend to be more calcic (Fig. 3.29), while those in the lavas tend to be more augitic. The cores tend to be more diopsidic, while the rims and patchy/sector zones are less so.

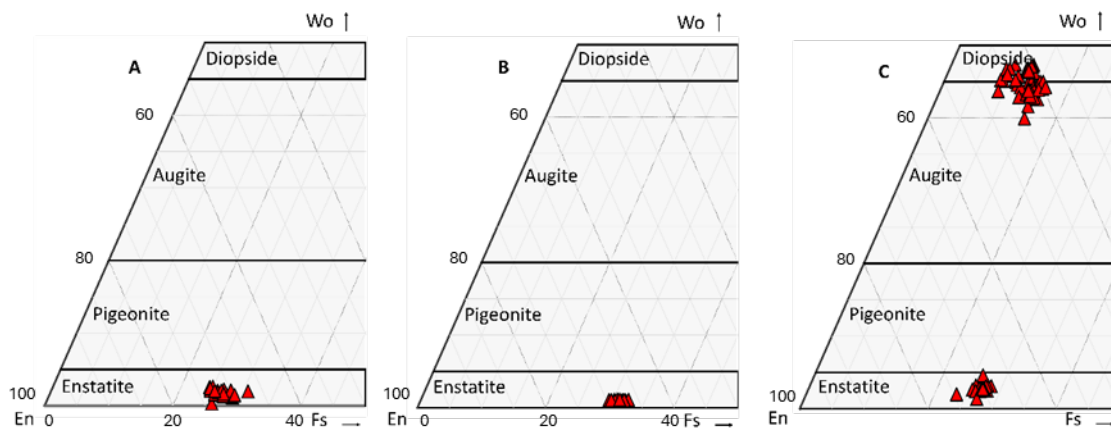


Figure 3.29. Pyroxene compositions for the A) D1; B) D2; and C) I1 scoria. The D2 pumice is included in this comparison as there are no other pyroxenes in the post-LCY pumice group to compare with.

3.2.3 LCY pumices

3.2.3.1 LCY pumice petrography

Two rhyolite compositions have previously been identified from the deposits of the LCY eruption. These are a biotite-bearing rhyolite with elevated K_2O contents (>4 wt.% K_2O in

whole rock), and an amphibole-bearing (both high-Ca and cummingtonite varieties) rhyolite with lower K₂O contents (approximately 2.7 wt.% K₂O). These were named the high-K and low-K rhyolites respectively (Rose et al., 1979,1987; Newhall, 1980). A pumice bearing both biotite and cummingtonite was sampled from the LCY eruption deposit during fieldwork for this project (sample Ati425_03). Pumices containing both these phases have not previously been reported in the LCY deposit, however published glass shard analyses of this eruption show compositions that overlap the bulk rock composition of this sample with an intermediate-K₂O content to the other two rhyolite groups (Cisneros de León et al., 2021a). Subsequently we have named this type the “medium-K rhyolite” in reference to the two previously identified rhyolite types.

Pumices from all three types were investigated, as well as a banded pumice containing mafic material (high-K pumice: Ati425_02(t); medium-K pumice: Ati425_03; low-K pumice: Ati425_02; mingled pumice: Ati502_06; the mingled pumice will be further described in section 3.2.5). The non-mingled pumice types share similar textures. They are all crystal-poor, with the low-K pumice having <10% crystals and the medium- and high-K pumices <5% crystals by volume (estimated from point counting of thin sections). Plagioclase and quartz are present as phenocrysts in all pumices, and Fe-Ti oxides, apatite and zircons are accessory phases (Fig. 3.30). The high-K LCY pumice is unique in being the only AVC rhyolite where the pumices may have either spherical or tube-shaped vesicles.

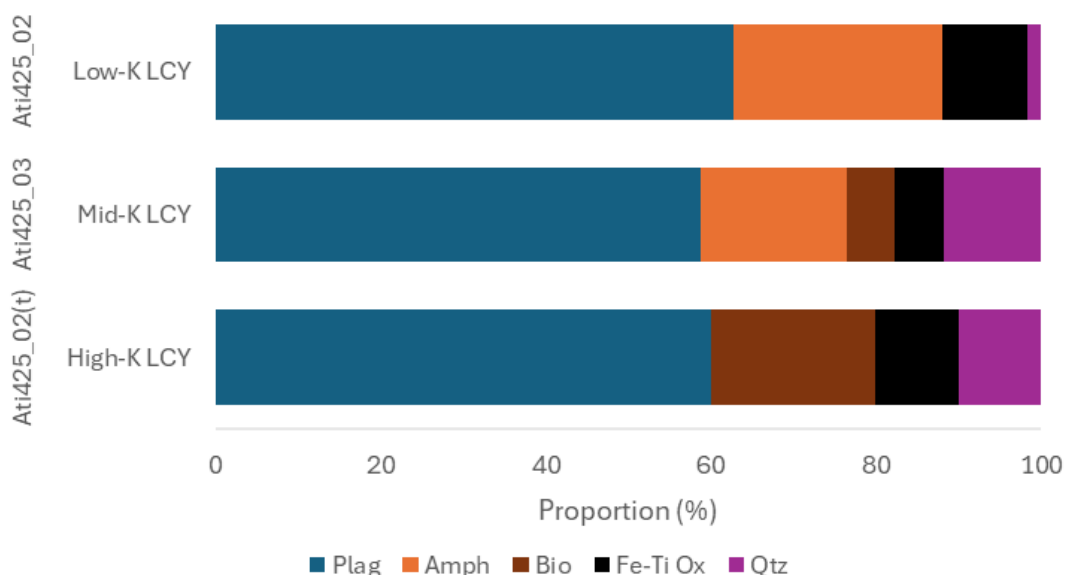


Figure 3.30. Mineral phase proportions for the different LCY pumices. Key as in Fig. 3.2, with the addition of Qtz – quartz

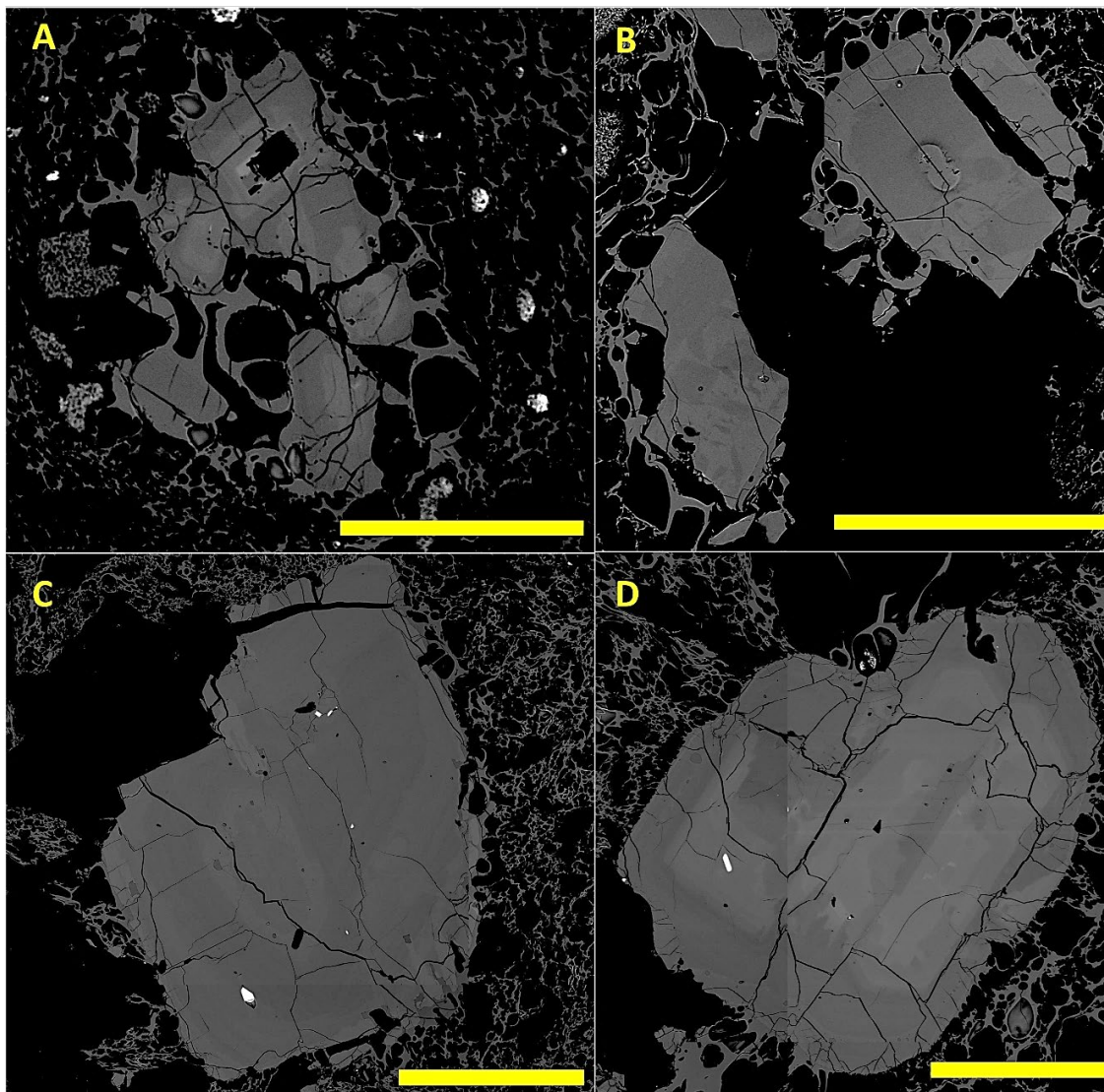


Figure 3.31. BSE photomicrographs of plagioclase crystals from the A) high-K LCY (sample Ati425_02(t)); B) medium-K LCY (sample Ati425_03(b)); C) D2 (sample Ati426_03h); and D) F rhyolite (sample Ati427_04f/g) pumices. Scale bars are all 0.5 mm. Note the large variety of textures and compositions (shown by variations in greyscale value, lighter=higher An) that can be present in each group.

Plagioclase are the most abundant phase in all LCY pumices (58-65% of crystals, although the lower crystallinity may mean these and other mineral phase proportion estimates are imprecise; Fig. 3.30) and their textures are similar (Fig. 3.31). They occur as euhedral to subhedral or fragmented tabular phenocrysts. Crystal sizes are up to 3 mm in length, although they are smaller in the medium-K pumice (typically <1.5 mm long). Synneusis textures are also present in some crystals, and resorption and zoning are common. Zoning is most commonly present as patchy, normal and oscillatory zones, with sieved zones in some crystal cores and resorption surfaces in the mantles. Reverse zones are observed in some crystals of the medium- and low-K pumices, as are 'bumps', roughly circular or oval raised regions on the

polished surface of the crystal (Fig. 3.31B). These bumps do not have any compositional difference compared to the surrounding region of the crystal. They may be artifacts from the polishing process, but the fact that they only occur in two LCY pumices argues against this. These features are also visible in polarised light.

Cummingtonites in the medium-K pumice and high-Ca amphiboles in the low-K pumice have similar prismatic, euhedral to subhedral forms, with crystals sizes <1.0 mm long. They lack reaction rims, but some rare crystals show rounding. Intergrown cummingtonite and high-Ca amphibole is also occasionally observed in the low-K pumice, where cummingtonite is overgrown by high-Ca composition amphibole (Fig. 3.32A). This is also a texture seen in the mingled LCY pumice (see section 3.2.5). Minor zoning is present in some high-Ca amphiboles of the low-K pumice.

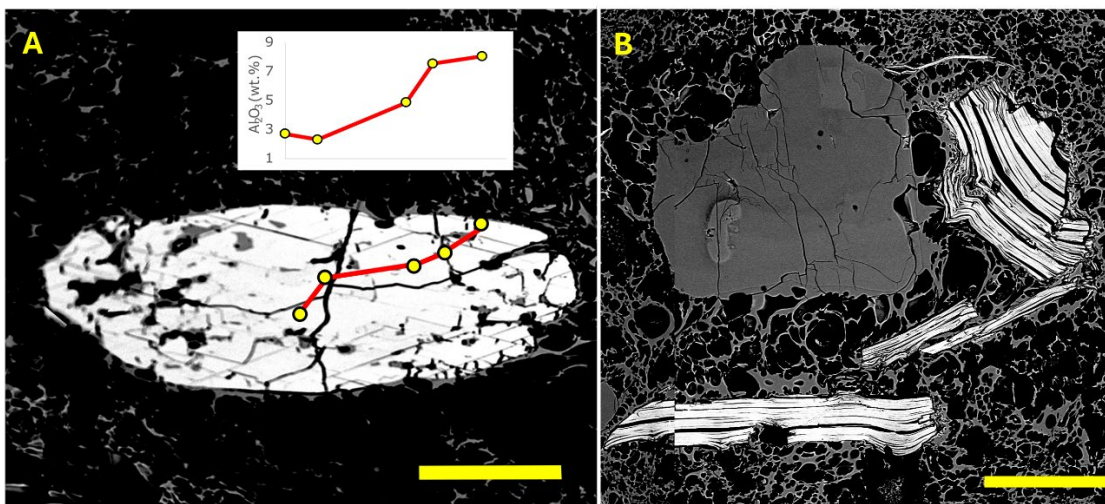


Fig. 3.32. Photomicrographs of ferromagnesian phases of A) cummingtonite overgrown by high-Ca amphibole in the low-K LCY rhyolite (sample Ati425_02); and B) biotite in the medium-K LCY rhyolite (sample Ati425_03(b)). Inset in A) is a core to rim compositional transect of Al_2O_3 . Scale bars are 0.2 mm

Biotite is present in the medium- and high-K pumices, with phase proportions of approximately 6% and 20%, respectively. Crystals have subhedral tabular forms and are commonly fractured along the cleavage planes (Fig. 3.32B). Biotite crystals in the low-K pumice are <0.4 mm wide, while those in the medium-K pumices are slightly larger (up to 0.5 mm wide).

Quartz is present in small amounts in all three samples (approximately 10-12% mineral proportion in the high- and medium-K pumices, <5% in the low-K pumice). It is present as <1 mm wide crystals that are highly rounded and embayed, and occasionally also contains melt inclusions (Fig. 3.33).

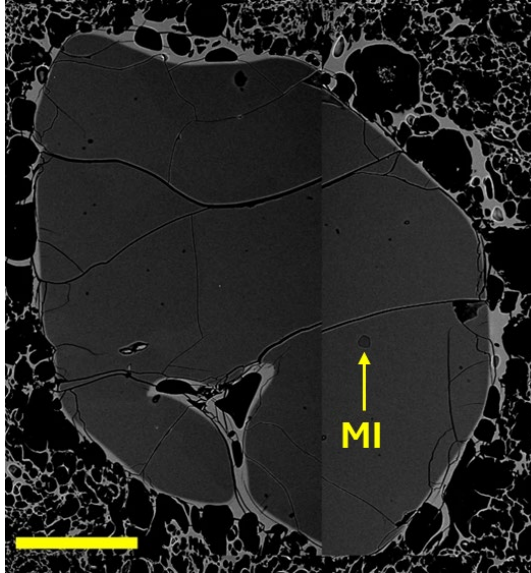


Figure 3.33. BSE photomicrograph of a typical quartz crystal from the LCY pumice (sample Ati425_03(b)). These crystals all have similar forms, with rounded edges, embayments, and melt inclusions (MI). Scale bar = 0.25 mm

3.2.3.2 LCY pumice mineral chemistry

Plagioclase compositions for the different LCY pumice groups have subtle but significant differences. Plagioclase in the high-K biotite-bearing pumice's have cores An_{24-69} , mantles An_{21-40} , rims An_{23-31} , and patchy zones An_{30-34} . The medium-K biotite- and cummingtonite-bearing pumices have cores An_{30-68} , mantles An_{28-50} , patchy zones An_{27-41} and rims An_{29-37} , and the low-K amphibole-bearing pumices have cores An_{37-64} , mantles An_{33-48} , rims An_{33-44} and patchy zones An_{26-42} (Fig. 3.34). All these pumices share similar composition ranges, but the medium- and low-K pumices have similar minimum An values that are lower than those of the high-K pumices.

Further differences emerge when comparing the Or values for these pumices. Fig. 3.35 compares the An vs. Or proportions for plagioclase in the six different rhyolites and shows that generally An and Or values have a negative correlation. Of the LCY pumices, the higher K_2O in the pumice is related to the host plagioclase having higher Or. There is one small variation to this, as at values $<An_{35}$, the medium-K pumice has a differing trend where Or values increase at roughly constant An (Fig. 3.35).

High-Ca amphiboles are only present in the low-K LCY pumice samples. Their compositions span a wide range from magnesiohornblende to edenite and pargasite (Fig. 3.36). This is a very similar composition range to that in the amphiboles in the mingled pumice from this eruption,

although most of the high-Ca amphiboles in the unmingled pumice have $Al^{VI} > Fe^{3+}$ and so are pargasites, while the mingled amphiboles have $Al^{VI} < Fe^{3+}$ and so are magnesiohastingsites (Fig. 3.36). This is also a similar range to that observed in the amphiboles of the post-LCY pumices, with some variations.

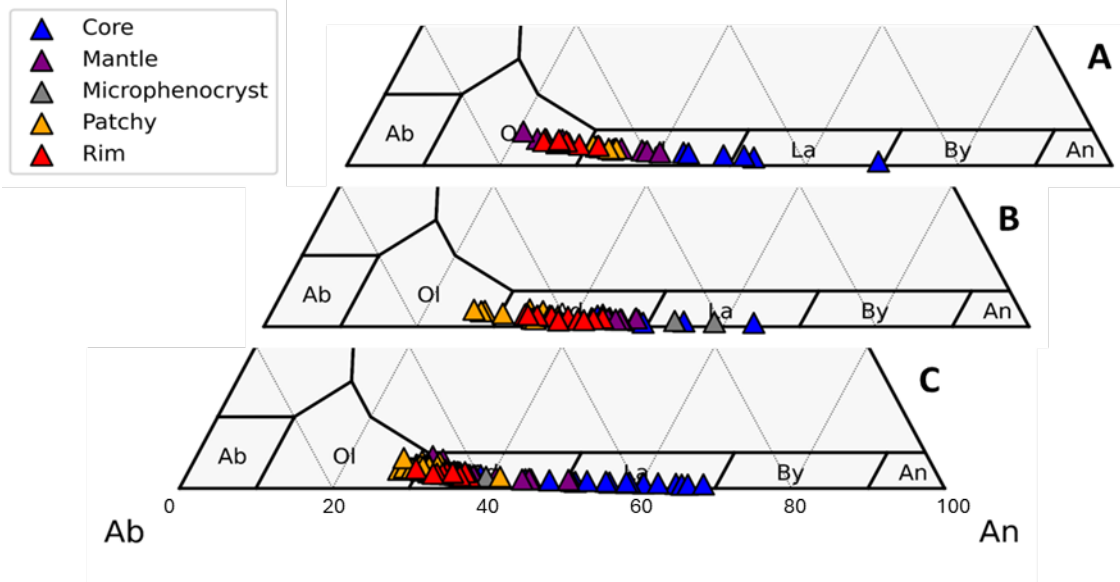


Figure 3.34. Feldspar discrimination diagram showing the variations in plagioclase compositions from the LCY rhyolite pumices; A) high-K LCY; B) medium-K LCY; and C) low-K pumices.

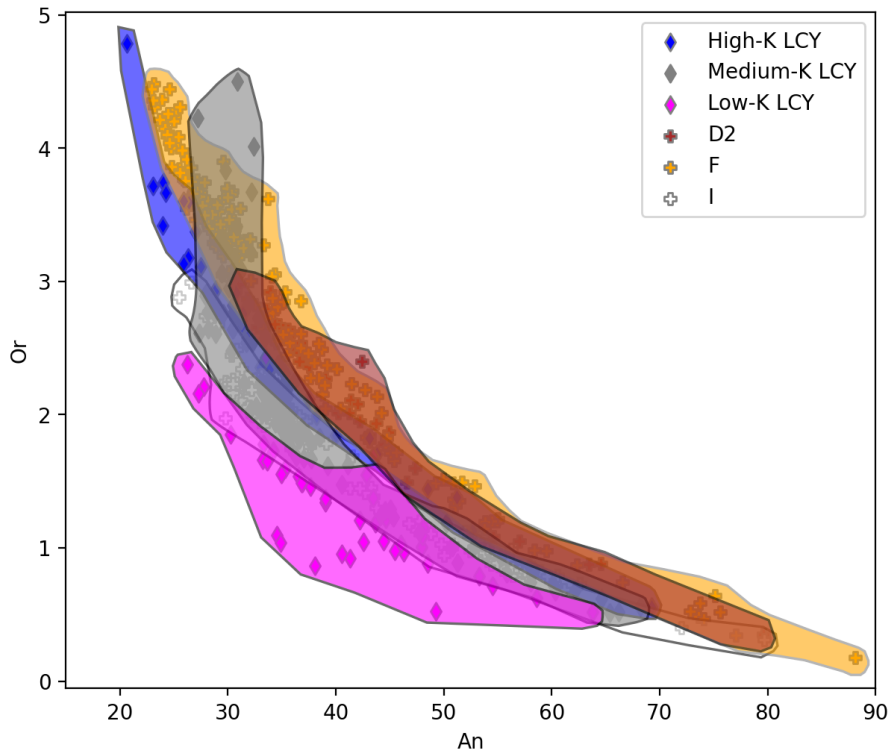


Figure 3.35. An vs. Or content for all plagioclase compositions from the different AVC rhyolite pumices, showing that they have distinctly different potassium contents depending on their host.

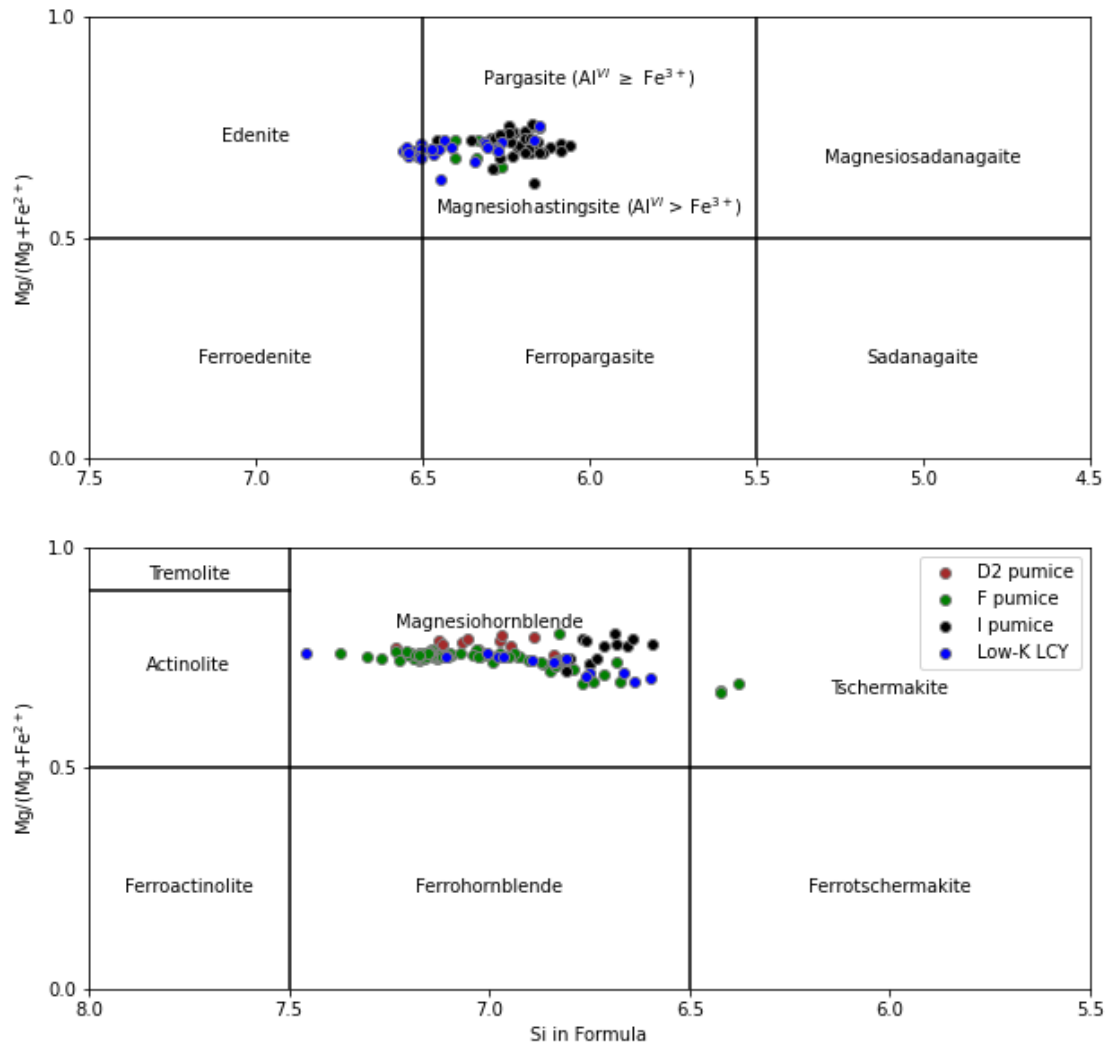


Figure 3.36. High- Ca amphibole compositions from the rhyolites of the AVC (low-K LCY, D2, F and I pumices). Fields after Leake et al. (1997), top panel $Ca_B \geq 1.50$; $(Na + K)_A \geq 0.50$; bottom panel $Ca_B \geq 1.50$; $(Na + K)_A < 0.50$.

Biotite is present in the two pumices with higher K_2O contents. Analyses for these frequently had low totals (<94%) and, due to their relative low phase proportions on top of the already low crystallinities for these samples, comparisons may not be representative. However, biotites from the medium-K pumice in general have lower $FeO(t)/MgO$ values (0.8-1.25 vs. 1.05-1.25), and those in medium-K magmas typically have a much wider range of cation contents. Analysed compositions are presented in Electronic Appendix II.

3.2.4 Post-LCY pumices

3.2.4.1 Post-LCY pumice petrography

Post-LCY eruptions formed three rhyolite pumice deposits: the D2 (samples Ati426_03h, Ati427_04a), F (sample Ati427_04f/g) and I (samples Ati428_01, Ati505_06h). The I rhyolites have been described as a series of five geochemically similar magmas (Rose et al., 1987), and a

full study of the petrological variations between these deposits is beyond the scope of this project. I will therefore focus on the rhyolites in the deposits of the uppermost units and present them as an example of the sequence.

The post-LCY pumice samples are all porphyritic with aphyric glassy groundmasses. All have phenocrysts of plagioclase, high-Ca amphibole and biotite, while the D2 pumice also contains orthopyroxene. The F pumice additionally contains quartz. Accessory phases in all the pumice samples include Fe-Ti oxides, apatite and zircon, with apatite and zircon generally found as inclusions in phenocrysts while the Fe-Ti oxides occur both as inclusions and as slightly larger phenocrysts/microphenocrysts. The different pumices have varying textures and slightly varying crystallinities. These are approximately: D2: 6%; F: 10%; and I: 10-20%, with the I pumices having large variations in crystallinity between the two samples. Phase proportions are compared in Fig. 3.37.

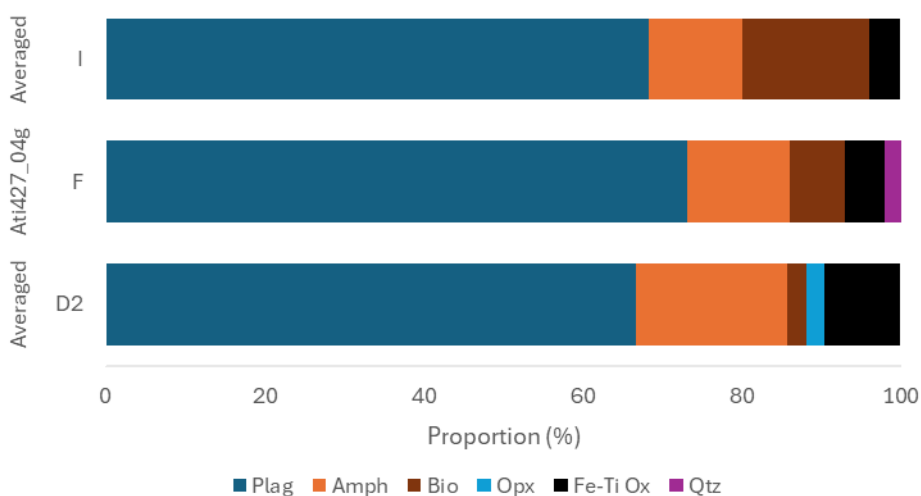


Figure 3.37. Mineral phase proportions of the post-LCY pumices. Key as in Fig. 3.2

D2 pumice

Plagioclase makes up 67% of the mineral assemblage as up to 1.2 mm long subhedral crystals. The irregular crystal shapes derive both from fracturing and extensive resorption of the crystal exteriors. Resorption surfaces are also common throughout the crystal interiors and other textures such as patchy, normal, reverse and oscillatory zoning, sieve and synneusis textures and melt inclusions are also common (see Fig. 3.31C). While the other post-LCY pumices have patchy zones only in the crystal cores, the D2 pumice is unique in having patchy zones in the crystal cores with low-An content material as well as in the crystal mantles where high-An

material is infilling. These high-An patchy zones are also typically associated with melt inclusions.

Amphiboles form 20% of the mineral assemblage and are small to moderately sized (up to 0.5 mm long) euhedral to subhedral prismatic crystals. Rare crystals have more elongate forms (up to 3 mm long) with higher aspect ratios (Fig. 3.38). Crystals occasionally have patchy, normal and reverse zones. Sieve textures and resorption surfaces are rarer.

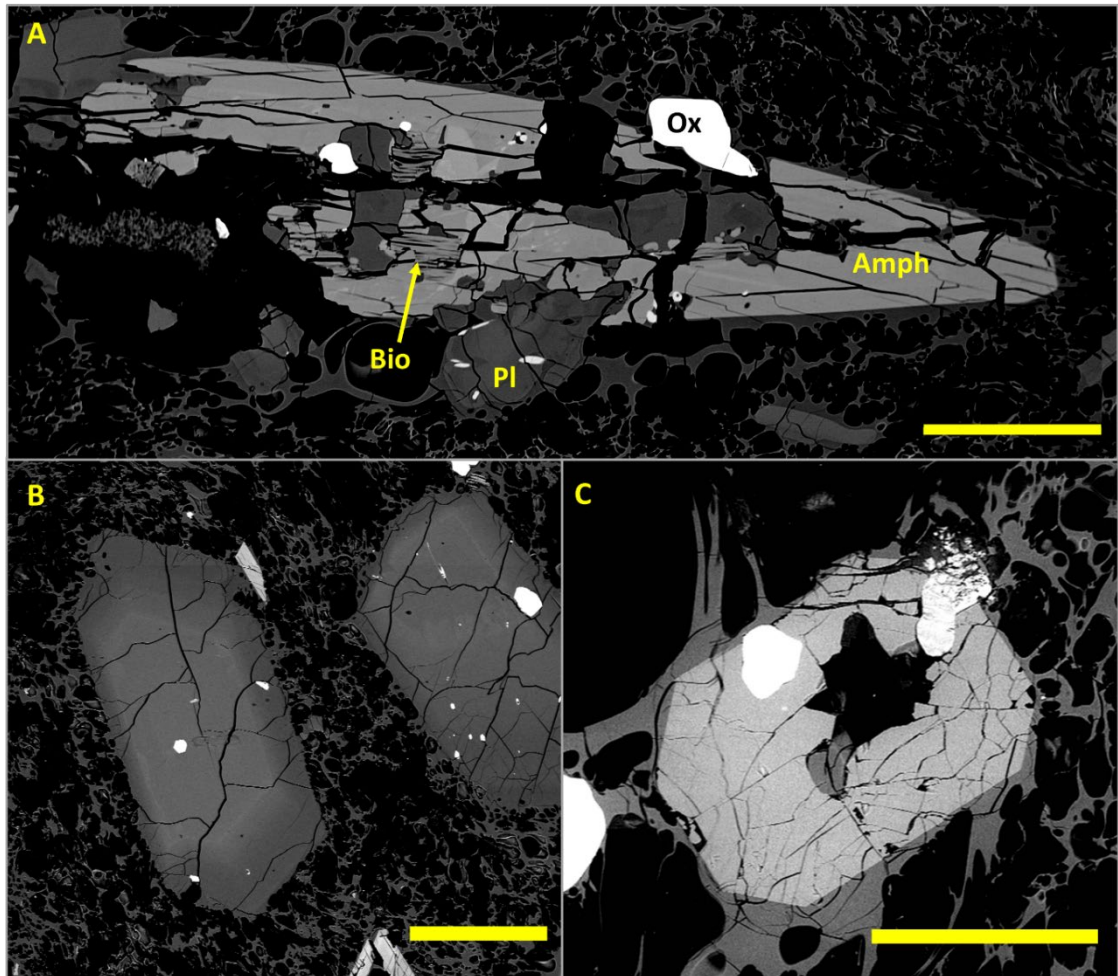


Fig. 3.38. BSE photomicrograph of mineral phases from the post-LCY pumices: A) An amphibole crystal from the D2 pumice sample Ati426_03h, showing patchy zonation in its core as well as inclusions of plagioclase, biotite and Fe-Ti oxides. Scale bar is 0.25 mm; B) Typical plagioclase phenocrysts from I pumice sample Ati505_06h. Both crystals show typical normal zonation, while the crystal on the right also shows resorption in the core. Scale bar is 0.25 mm; and C) Orthopyroxene crystal from the D2 pumice sample Ati426_03h. Scale bar is 0.2 mm;

Orthopyroxenes and biotites are both minor phases (<5% each). Orthopyroxenes are small to moderate sized (up to 0.5 mm long) subhedral crystals (Fig. 3.38C). Most are untextured, with some minor sieve textures present. The biotite crystals are smaller (<0.2 mm) and are commonly present as inclusions or small grains in amphibole or plagioclase phenocrysts (Fig.

3.38A). Accessory phases including Fe-Ti oxides, apatite, and zircon make up the mineral phases.

F pumice

Plagioclase makes up 72% of the mineral assemblage and crystals have subhedral tabular forms with lengths up to 1.5 mm. They show a diverse range of textures including patchy, reverse and oscillatory zoning, sieve textures and melt inclusions, and occasionally resorption surfaces (Fig. 3.31D).

Amphiboles form 14% of the mineral assemblage and are moderate to large sized (0.6-1.6 mm long) euhedral to subhedral crystals. Small crystals are rare. Individual crystals usually show patchy zoning in their cores, and oscillatory zoning in the mantles and rims is common. The cores also have coarse sieve textures that are commonly infilled with plagioclase, Fe-Ti oxides and apatites. The latter two phases are also common as inclusions in the mantles and rims. Biotite makes up approximately 7% of the mineral assemblage, Fe-Ti oxides 5% and quartz <2%. Quartz crystals are >1 mm in size and are rounded and embayed, similar to those in the LCY pumices.

The F pumice contains unique glomerocrysts, which are large (>2.0 mm wide) rounded and fine-grained (crystals <0.1 mm long) clumps of plagioclase, amphibole, biotite and minor Fe-Ti oxides (Fig. 3.39). Mineral proportions are approximately equal for the phases other than the Fe-Ti oxides. Plagioclase crystals show patchy and normal zoning, and amphiboles also display some patchy zoning.

I rhyolite

The I rhyolites have different types of pumice clasts, divided by varying crystallinities (10 vs. 20%). The higher crystallinity sample (Ati505_06h) is the most crystal-rich of the post-LCY pumices. It is also the sample with the greatest size distribution for crystals, with minor amounts of microlites/microphenocrysts of all present mineral phases in the groundmass.

Plagioclase makes up 70% of the mineral assemblage of this rhyolite, and form predominantly <1.0 mm long subhedral to euhedral lath-shaped crystals (Fig. 3.38B). Rare crystals are larger (up to 2.0 mm long) and have more tabular forms. Plagioclase crystals are usually not intergrown with other crystal phases (except the accessory phases). This pumice is unusual

among the rhyolites in that most of the crystals have simple textures, with minor normal chemical zoning being the most common. Patchy, reverse and oscillatory zoning, resorption surfaces, and synneusis and sieve textures are typically found in the larger crystals. Melt inclusions are occasionally present in both populations.

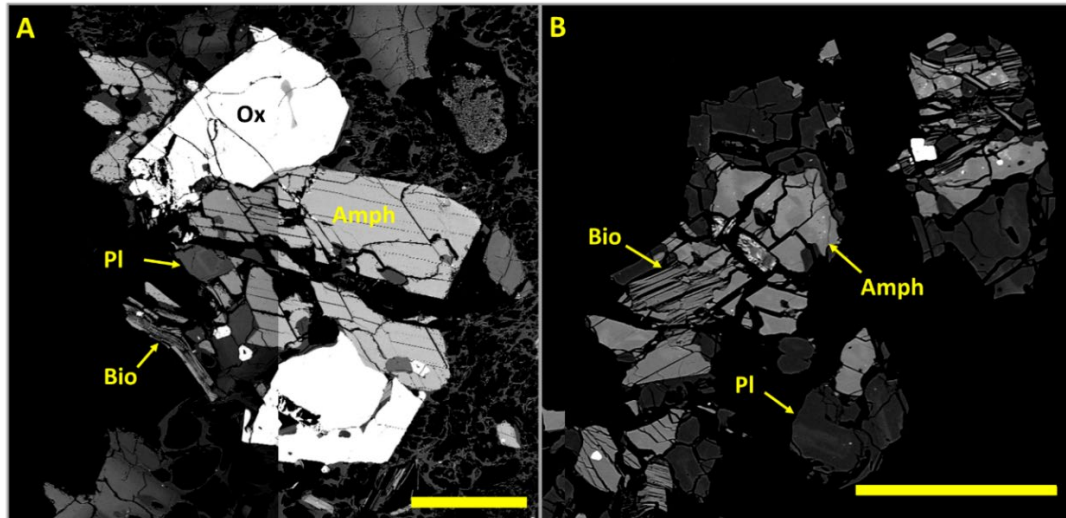


Figure 3.39. BSE photomicrographs of glomerocrysts from the I and F pumices: A) Glomerocryst containing amphibole (Amph), plagioclase (Pl), biotite (Bio), and Fe-Ti oxides (Ox) from I pumice sample Ati505_06h; and B) glomerocryst with the same mineral assemblages but with finer grain sizes from F pumice sample Ati427_04g/f. Scale bars are 0.25 mm

Biotite is more abundant than amphibole in sample Ati505_06h (15%), which is unique to the post-LCY rhyolites. Crystals are up to 0.4 mm long euhedral to subhedral crystals. They typically have tabular forms but are occasionally present with more platy forms and are usually at least partially fractured along their cleavage planes. They are commonly associated with amphibole (Fig. 3.40).

Amphiboles make up 10% of the crystal assemblage and occur as subhedral and commonly fractured crystals up to 1.0 mm long. Crystals are prismatic to tabular. Almost all crystals are intergrown with other mineral phases. Plagioclase occurs in either crystal cores or rims, while biotite is present on the edges of amphiboles (Fig. 3.40A). Most crystals show one simple normal zone, with a rounded contact surface (Fig. 3.40B). Occasionally melt inclusions are found in crystal cores.

Glomerocrysts are common and are like those in the F pumice in their mineral assemblages (Fig. 3.39). They have larger grainsizes (up to 0.5 mm), and Fe-Ti oxides are of the same size and abundance as the other phases. This contrasts with the F pumice glomerocrysts where oxides only occur as minor accessory phases.

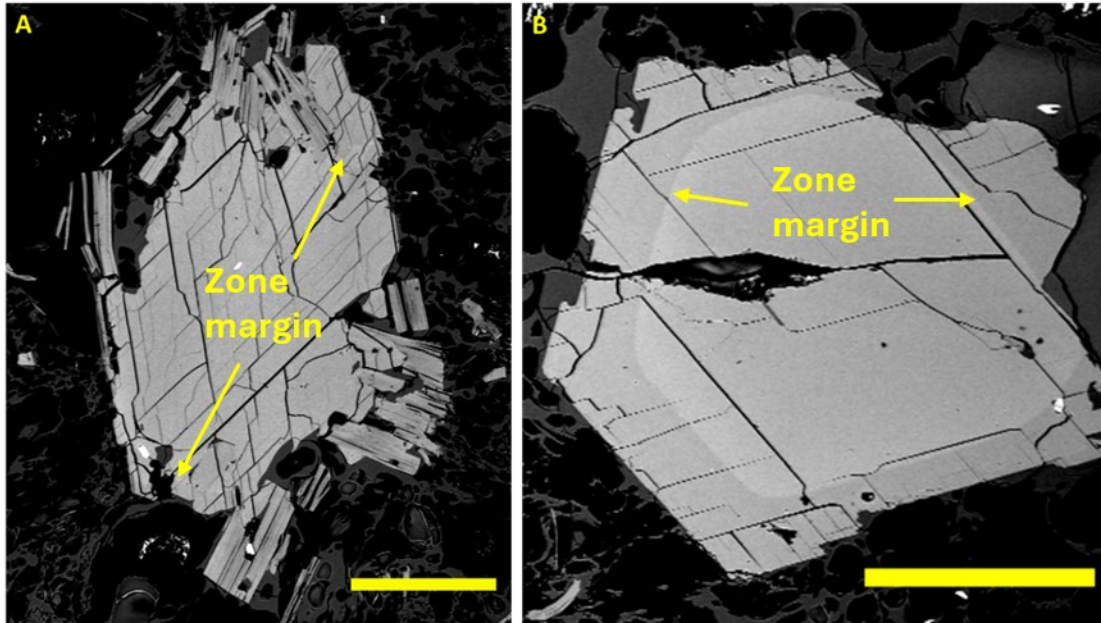


Figure 3.40. BSE photomicrograph of the ferromagnesian phases of the crystal-rich I pumice sample Ati505_06h: A) Amphibole grain with minor zoning and biotite overgrowths; B) Amphibole crystal clearly showing the rounded zoning profile common in this rock. Scale bars are 0.2 mm

3.2.4.2 Mineral chemistry of the post-LCY pumices

Rhyolites from the three post-LCY eruptions (the D2, F and I) contain plagioclase, high-Ca amphiboles and biotite. These phases show some notable differences in the different samples, as well as differences from the LCY pumices.

Plagioclases in pumices from these eruptions have similar compositions. Cores have wide variations of labradorite and bytownite compositions, whereas mantles are more sodic (predominantly andesine and rarer labradorite). Patchy zones and rims are even more sodic, with compositions of plagioclases from the F and I rhyolites extending into the oligoclase field. In comparison, the D2-hosted plagioclases are more calcic, with compositions like those in the LCY pumices (Figs. 3.35 and 3.41; section 3.3.1).

The post-LCY pumices show similar trends in their compositions to the LCY plagioclase (Fig. 3.35). The F and D2 pumices have overlapping plagioclase compositions and have similar and even slightly higher Or values than those in the high-K LCY pumice. The F pumice crystals extend to more potassic compositions than the D2. Plagioclase in the I pumice samples have lower Or, more like those from the medium-K LCY pumice (Fig. 3.35). Compared to the LCY pumices, the post-LCY pumice plagioclases all extend to higher maximum An content. They also

follow the general trend that pumices with higher bulk-rock K₂O contents contain plagioclase with higher Or.

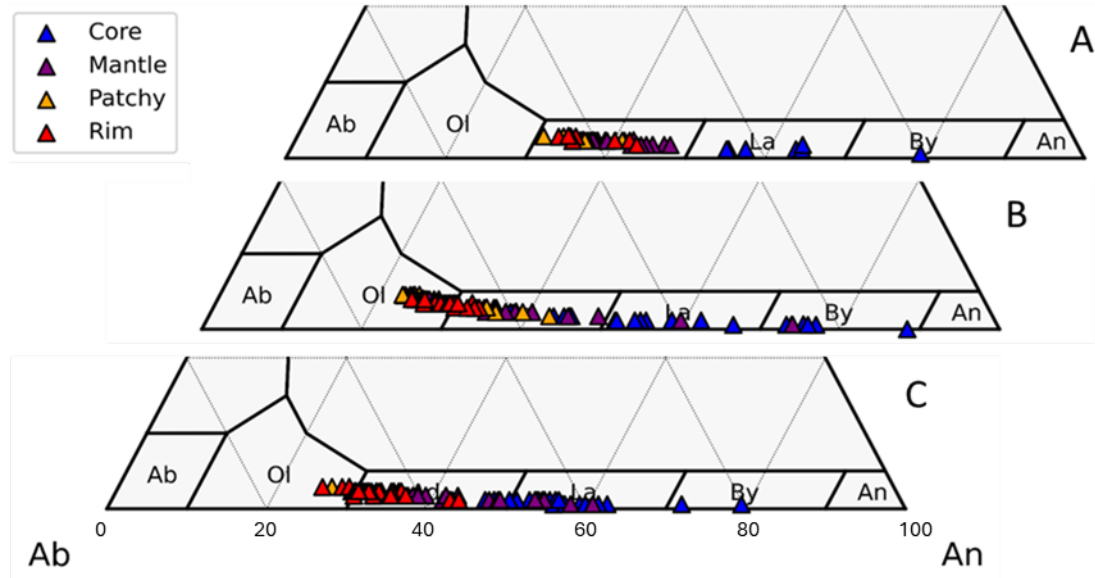


Fig. 3.41. Plagioclase compositions from the post-LCY eruptions; A) D2; B) F; and C) I pumices.

Amphibole phenocrysts in post-LCY pumices range from magnesiohastingsites to magnesiohornblendes, although there are some variations between the different groups (Fig. 3.36). The D2 amphiboles are entirely magnesiohornblendes and have higher $Mg/(Mg+Fe^{2+})$ than the other amphiboles. The F pumices have the widest range of compositions, although they are mostly magnesiohornblendes. Crystal cores are magnesiohastingsites, similar in composition to the low-K LCY amphiboles. Finally, amphiboles from the crystal-rich I pumice are the least silicic and are predominantly magnesiohornblendes. They are strongly normally zoned with magnesiohastingsite cores and magnesiohornblende rims.

Biotite compositions of the F and I rhyolites differ significantly, with those in the F pumice having higher $FeO(t)/MgO$ ratios, which are slightly lower than those of the high-K LCY pumice. Biotites in the I rhyolite sample have overlapping $FeO(t)/MgO$ ratios with the lowest values in biotites of the medium-K LCY rhyolite. Analysed values are shown in Electronic Appendix II.

Orthopyroxenes are only present in the D2 pumice and have a narrow range of enstatite compositions. They have a slightly greater ferrosilite component to the D1 andesitic pumices (Fig. 3.29).

The F pumice additionally contains glomerocrysts with microphenocryst-sized grains. The plagioclases are predominantly andesine (An₂₆₋₅₂), like those of the phenocryst mantles. Amphiboles and biotites share the same compositions as the phenocrysts. Compositions are shown in Electronic Appendix II.

3.2.5 Enclaves and mingled pumices

Evidence for magma mingling is present in three of the four investigated eruption deposits from the AVC and has also been reported from the W eruption (Newhall, 1980) which was not investigated as part of this study. Only clasts from two of these eruptions show cognate enclaves, where the mingling magma has not been fully disaggregated and thus preserves some of the original textures and mineral assemblages. These are clasts from the D2 and the uppermost I pumice deposits, while mingled pumices were also analysed from the LCY and I eruptions. The mineral and whole rock textures of these clasts, and their mineral compositions, are described below.

3.2.5.1 Mineral and rock textures of the enclaves and mingled pumices

LCY mingled pumice

The LCY mingled pumice sample (Ati502_06) has a distinct texture compared with the other investigated mingled pumices from this centre. It is distinctly banded, and the bands are not just caused by the presence of variable amounts of disaggregated recharge magma (Fig. 3.42). Several of these bands are also unmingled (i.e., they have no discolouration, microlites or microphenocrysts, no change in vesicle size or shape from other unmingled pumices).

These unmingled bands have their own unique textures. Mineralogy, crystallinity and glass chemistry vary between the bands, with crystal-rich bands and crystal-poor bands. The bands have variable thicknesses on the order of millimetres (Fig. 3.42). Different bands contain different ferromagnesian minerals, with some containing amphibole and others biotite. EPMA analyses of the groundmass glass in the different unmingled bands reveals significant variations between them, most strikingly in K₂O with contents between 2.5 and 3.6 wt.%. These may correlate to the medium-K and low-K LCY rhyolites (sections 1.4.3, 4.1.3).

Mineral textures are highly variable. Plagioclase crystals occur as a typically larger and more tabular type, typically found in the unmingled rhyolite bands, and a smaller and more lath-shaped crystal type is more commonly found in the mingled bands. The tabular crystals share

the same textures as those in the unmingled lower-K LCY pumices, while crystals hosted by the recharge magma or with diktytaxitic texture matrix on their exteriors often have extensive sieve textures and commonly occur as interlinked clots of microphenocrysts and phenocrysts attached to larger crystals of ferromagnesian phases (Fig. 3.43).

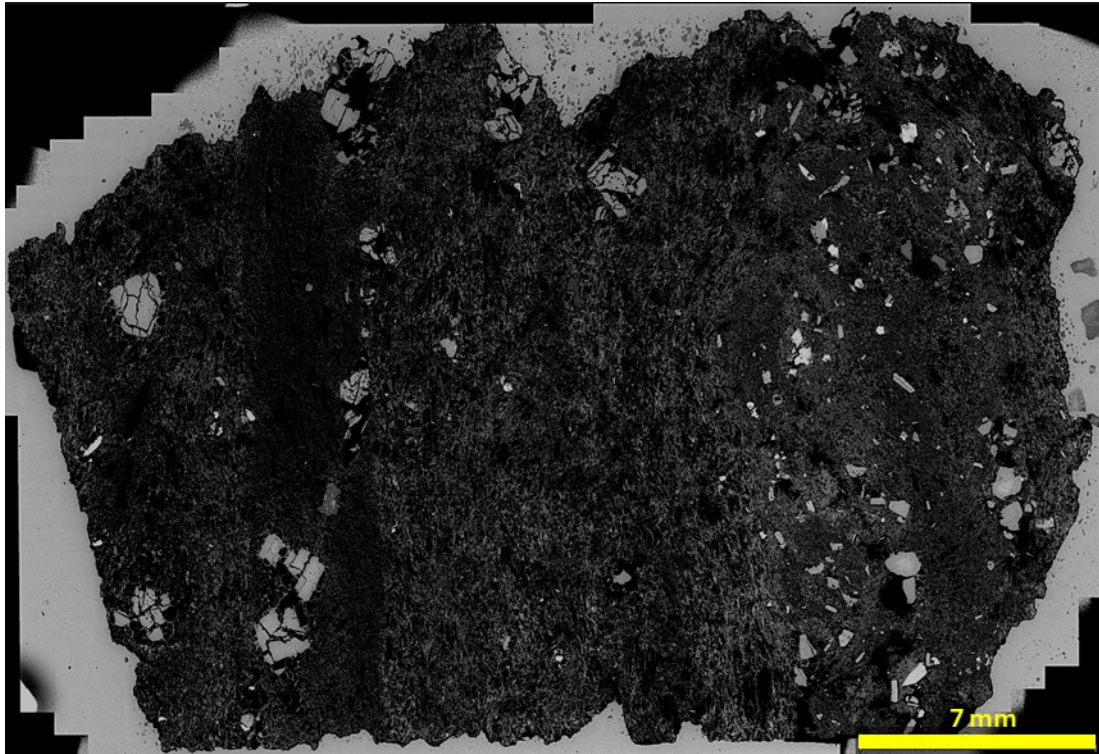


Figure 3.42. BSE thin section scan of a mingled pumice from the LCY eruption, sample Ati502_06. Note the several sub-vertical bands running through the slide, distinguished by changes in their groundmass texture and crystallinity. The right-most region of the sample is much more crystal-rich and the groundmass here is much more microlite rich, giving it a brighter colour.

Both cummingtonites and high-Ca amphiboles occur in the mingled pumice. Some patchy zoned crystals are found in which the patchy zones are composed of these different amphiboles. Amphiboles also display a wide range of textures, from euhedral to anhedral, with prismatic to acicular forms and a large range of sizes from microlites to moderate-sized phenocrysts (<1.0 mm). Highly rounded crystals are occasionally present, as are large melt inclusions in crystal interiors. Rare amphibole crystals have grown around small clinopyroxene grains (Fig. 3.44A) or have intergrown cummingtonite and high-Ca amphibole regions (Fig. 3.44B).

Olivine, ortho- and clinopyroxenes and biotite are present in this sample in low amounts. Olivine and clinopyroxene are similar and have moderate-sized (typically 0.2-0.5 mm) subhedral prismatic forms (Fig. 3.44C and D). They are commonly intergrown with clusters of

plagioclase microphenocrysts like those shown with amphiboles and commonly have remnant enclave groundmass adhering to their margins (Fig. 3.44). Olivines also commonly show large embayments in their rims. Orthopyroxenes are unique to the mingled pumice of the LCY eruption and have not been found in the mingled clasts of the other AVC eruptions AVC. However, none of the orthopyroxene crystals have any remnant groundmass on their margins, nor do they lie in bands that contain greater amounts of disaggregated recharge material. The fact that no unmingled LCY pumices also contain this mineral means that the orthopyroxene is unique to the mingled pumice. These crystals are typically subhedral to anhedral and can be highly fractured. Biotite is present only in bands of the pumice which have higher K_2O in their groundmass glass compositions.

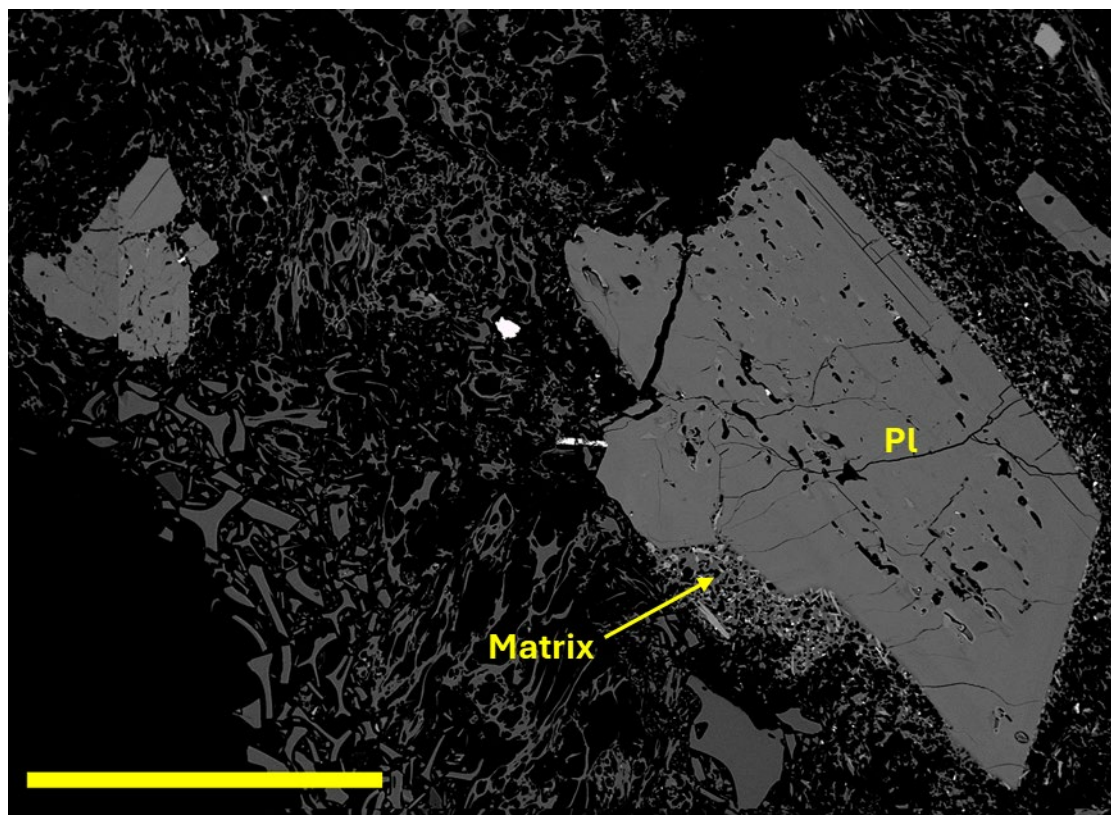


Figure 3.43. BSE image of plagioclase crystals from a mingled LCY pumice, sample Ati502_06. Note the sieve textures and adhered microlite-rich groundmass on both crystals. Note also the intergrown microphenocryst textures in the plagioclase crystals on the left. Scale bar = 0.5 mm

D2 enclaves and mingled pumice

The mingled pumice sample from the D2 eruption (Ati501_06b) contains two distinct regions. There are several small (approx. 5.0 mm wide) un-disaggregated mafic enclaves, which are surrounded by disaggregated diktytaxitic matrix that has been well-mingled with the host magma. This mingled region contains a mixed mineralogy of plagioclase, amphibole, biotite -

and clinopyroxene and has a vesiculated and microlite-rich groundmass. Because of the advanced mingling, extraction of enough material for whole-rock geochemical analyses was impossible.

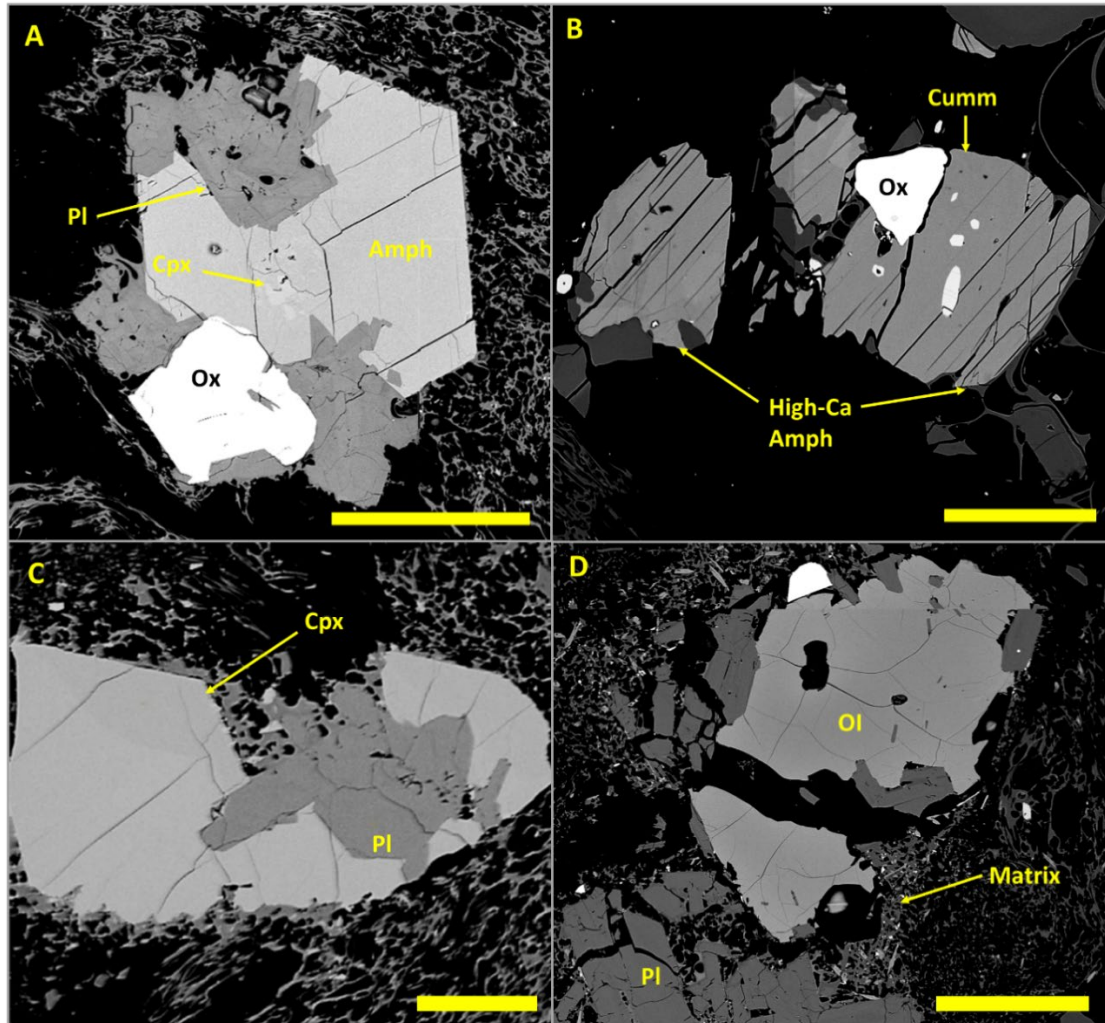


Figure 3.44. BSE photomicrographs of ferromagnesian crystals from the mingled LCY pumice, sample Ati502_06. A) Amphibole (Amph) crystal with a clinopyroxene (cpx) core and intergrown plagioclase (Pl) and Fe-Ti oxide (Ox) microphenocrysts; B) amphibole crystal with a cummingtonite (Cumm) core and high-Ca amphibole (High-Ca Amph) rims; C) Clinopyroxene (Cpx) crystal intergrown with plagioclase microphenocrysts; and D) Olivine (Ol) crystal intergrown with plagioclase microphenocrysts. Matrix is adhered to the margins of the crystal cluster. All scale bars are 0.25 mm apart from C, which is 0.1 mm.

The intact enclaves have textures similar to those of the enclaves in the LCY and I eruptions, with a diktytaxitic groundmass with microlites and microphenocrysts of plagioclase, clinopyroxene, amphibole and Fe-Ti oxides. However, they are slightly more vesiculated than the others. These enclaves also have a different phenocryst assemblage, containing plagioclase, clinopyroxene and olivine. Enclaves from the other pumice eruptions have significant amounts of amphibole, while for this sample amphibole is restricted to the

groundmass. Thin normal zones on the rims of the phenocrysts are common, and sector zoning in the clinopyroxenes is also present (Fig. 3.45). Both plagioclase and olivine also occasionally show angular void spaces in their interiors. Crystals sizes are also similar, with most phenocrysts being <0.5 mm long. Plagioclase and olivine have elongated tabular and prismatic forms respectively, with olivine occasionally showing skeletal forms. Clinopyroxenes are more tabular.

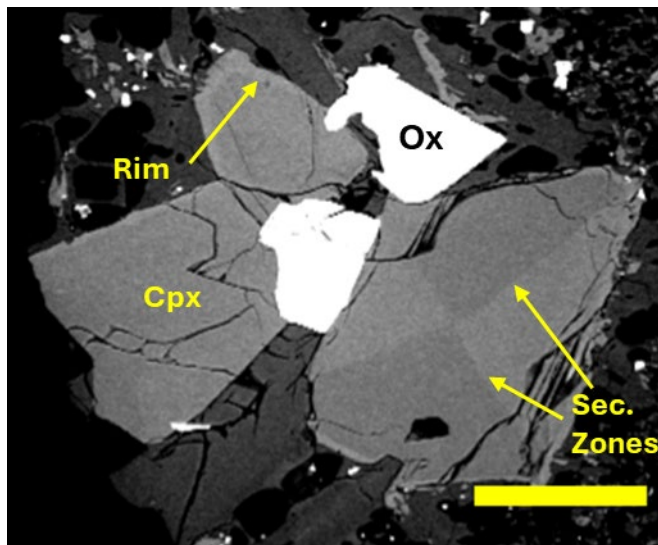


Figure 3.45. BSE photomicrograph of clinopyroxene (Cpx) and Fe-Ti oxide (Ox) textures in the mingled D2 pumice (sample Ati501_06b), highlighting the zone types present. Sec. zones – sector zones. Scale bar is 0.1 mm.

I enclaves and mingled pumice

Three samples from the I eruption deposits that show evidence of magma mixing (either mafic enclaves sampled from the pumice deposit or mingled pumices) have been analysed (samples Ati428_01, Ati430_11a(e), and Ati505_06h(e)). One sample (Ati428_01) consists of a mingled pumice that also contains several discrete mafic enclaves as well as bands containing disaggregated mafic material and unmingled rhyolite, similar to the texture of the lower-K LCY mingled pumice. These enclaves are sparsely porphyritic (approximately 5% phenocrysts by volume) with phenocrysts of plagioclase, amphibole, clinopyroxene and minor olivine. Mineral proportions are plagioclase (43-59%), amphibole (25-32%), subordinate clinopyroxene (2-16%) and olivine (0-7%), and smaller microlites of Fe-Ti oxides (2-8%; Fig. 3.46). However, most of the enclaves is composed of diktytaxitic matrix textures (interlinked typically skeletal and/or acicular microphenocrysts and microlites with interstitial vesiculated glass; Fig. 3.47) with microphenocrysts and microlites of predominantly plagioclase amphiboles well as smaller microlites of Fe-Ti oxides. Vesicularity varies greatly even on the microscopic scale as the

enclaves were disaggregating, but overall crystallinities of undisaggregated enclaves are 40-60%.

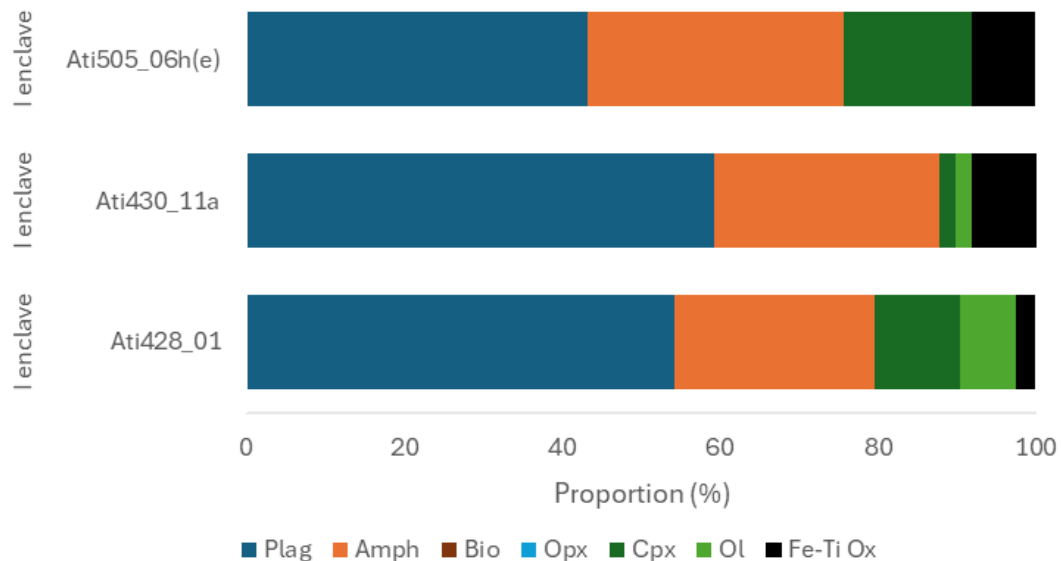


Figure 3.46. Mineral phase proportions of the enclaves found in the I eruptions' deposits. Key as in Fig. 3.2

The two discrete enclaves prepared from these eruption deposits (samples Ati430_11a(e) and Ati505_06h(e)) have slightly different textures. They have slightly lower vesicularity (approximately 35-40%) and slight differences in mineralogy, as one also contains biotite and some plagioclase crystals with higher An contents. Some regions are present in the discrete enclaves with a subtly different diktytaxitic groundmass texture. These are moderate to large regions (around 0.4 mm in length) with increased vesicularity (Fig. 3.47). They are circular to elongate in shape (some interconnecting to form long fractures) and are commonly associated with voids. These fractures and voids are also regions where the mineralogy of the groundmass changes. Amphibole microlites are almost entirely absent in these regions, and instead plagioclase makes up almost the entire mineral proportion (Fig. 3.47).

Plagioclase in the enclaves of the I eruption deposits are moderate sized (typically <0.6 mm long, but some longer) euhedral to subhedral lath-shaped crystals. Zoning is typically simple and normal; however, it can be more complex in the larger crystals. Some reversely zoned crystals are also present. Sieve textures are present in a few crystals.

Amphibole crystals have two main populations defined by their forms, with a group with more prismatic forms compared to one with acicular forms. Both show similar textures, with coarse sieve textures common. These groups show a difference in zoning, with the more prismatic

forms commonly showing a single normal zone. Patchy zoning is present but rare in this population. There is no evidence of any formation of breakdown rims in any amphibole crystals.

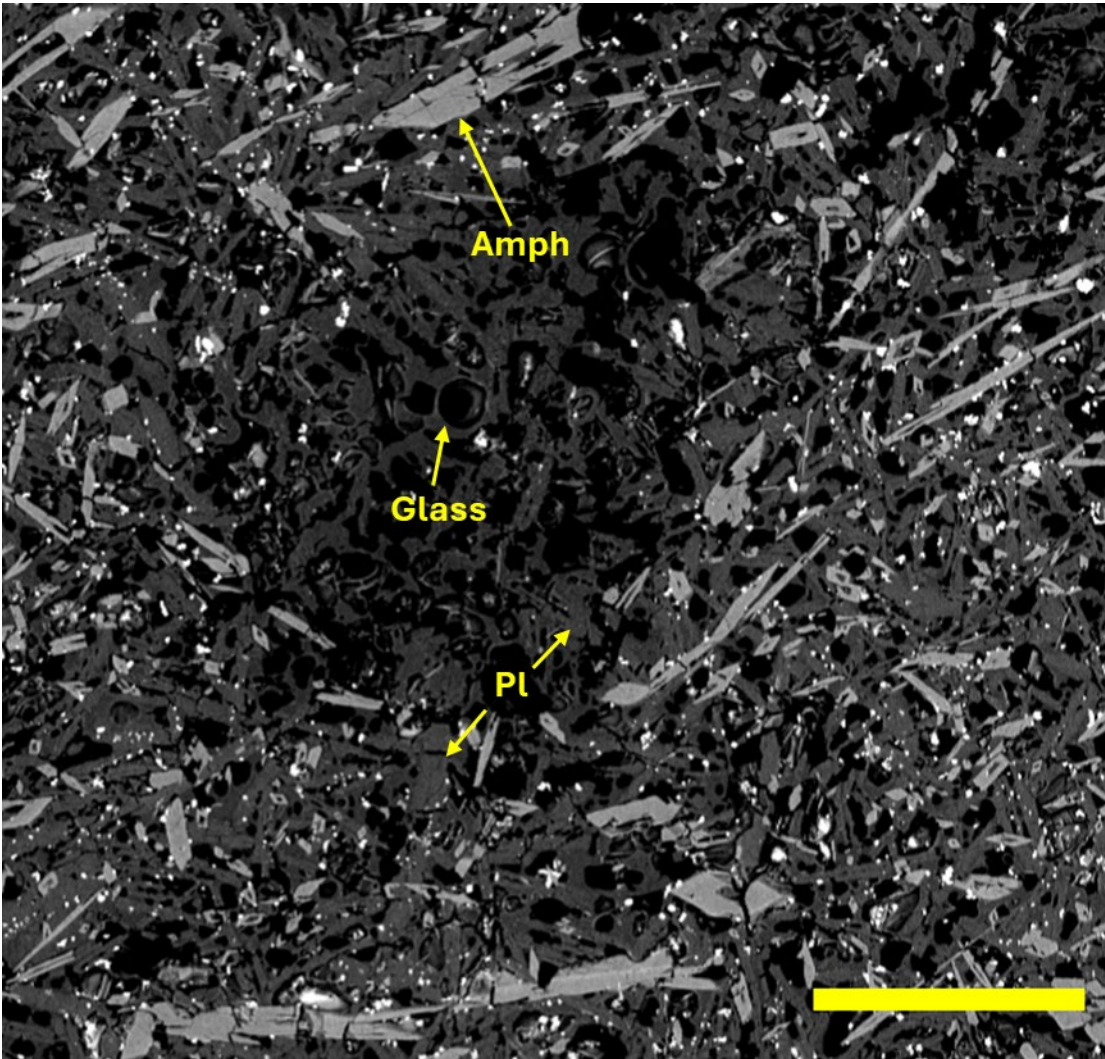


Figure 3.47. BSE photomicrograph of the groundmass texture of an enclave from the I pumice eruption (sample Ati430_11a(e)). Note the diktytaxitic texture and the roughly circular region in the centre of the image where amphibole and Fe-Ti oxide crystals are almost entirely absent. Amph – amphibole, Pl – plagioclase. Scale bar = 0.2 mm

Most of the pyroxenes in these enclaves are clinopyroxenes. There are rare orthopyroxenes, which contrasts with the mingled pumice in which none were found. Pyroxene crystals are small to moderate sized (up to 0.3 mm) subhedral prismatic forms. Normal zoning is common (Fig. 3.48A). Orthopyroxenes are small (<0.1 mm) and have rims of clinopyroxene. On clinopyroxene phenocrysts, thin rims of amphibole (sometimes skeletally formed) are also present.

Minor mineral phases include olivines, biotites and Fe-Ti oxides. Olivines are rare, small to moderate sized (up to 0.4 mm wide) subhedral crystals (Fig. 3.48B). Biotite is only present when in contact with plagioclase and/or amphibole crystals. One biotite crystal shows a rim of amphibole. Fe-Ti oxides occur as skeletal microphenocrysts, inclusions in other mineral phases and as microlites in the groundmass.

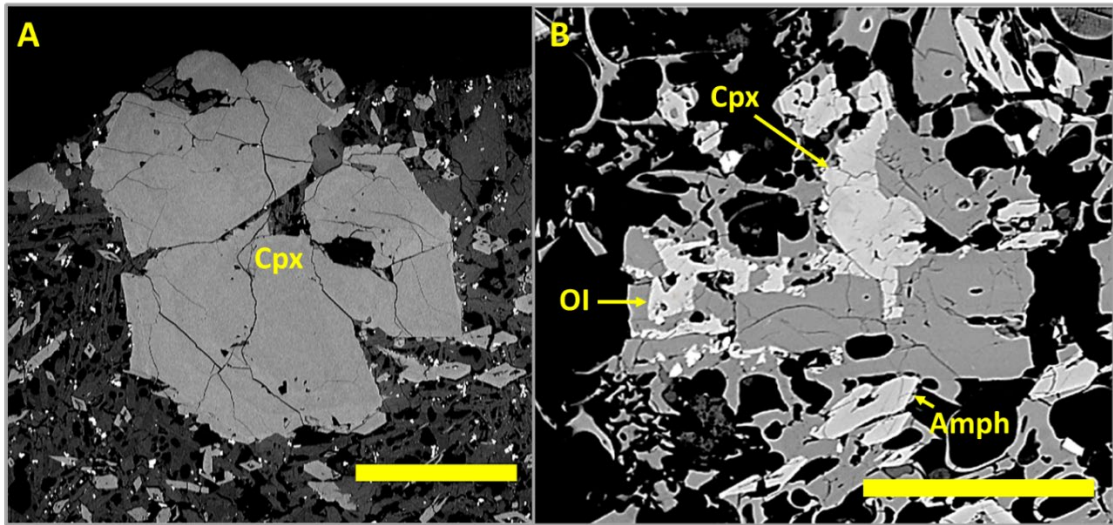


Figure 3.48. BSE photomicrographs of mineral textures from the enclaves of the I pumices. A) Normally zoned clinopyroxene from sample Ati430_11a(e); B) Olivine, clinopyroxene, and amphibole microphenocrysts from sample Ati428_01. Scale bars are 0.2 mm.

Apatite is an accessory phase commonly seen in the enclaves from the I eruption deposits. It is predominantly present in the outer portion of phenocrysts (Fig. 3.49A) or as discrete needles in the groundmass (Fig. 3.49B). They can be quite large for an accessory mineral, up to 0.2 mm long in some cases.

3.2.5.2 Mineral chemistries of the enclaves and mingled pumices

The mineralogies of all of the different examined mingled pumices and enclaves are similar and are therefore simpler to compare. As the mingled pumices are likely to have experienced more extensive chemical and thermal homogenisation (which may impact the subsequent chemistry of the mineral phases) than the enclaves, there are several differences in mineral composition ranges between the two (Fig. 3.50).

Plagioclase compositions in the mingled pumices of the lower-K LCY and I eruptions both have bimodal compositional distributions with low-An peaks around An₂₅₋₄₀, and high-An peaks around An₅₅₋₇₀ and An₇₀₋₉₀ for the I and LCY pumices, respectively (Fig. 3.50). Each have minor amounts of intermediate composition feldspars. Both clasts have feldspars (either analyses

from the rims of phenocrysts or from microphenocrysts) that plot on a roughly linear trend within the miscibility gap (Fig. 3.50).

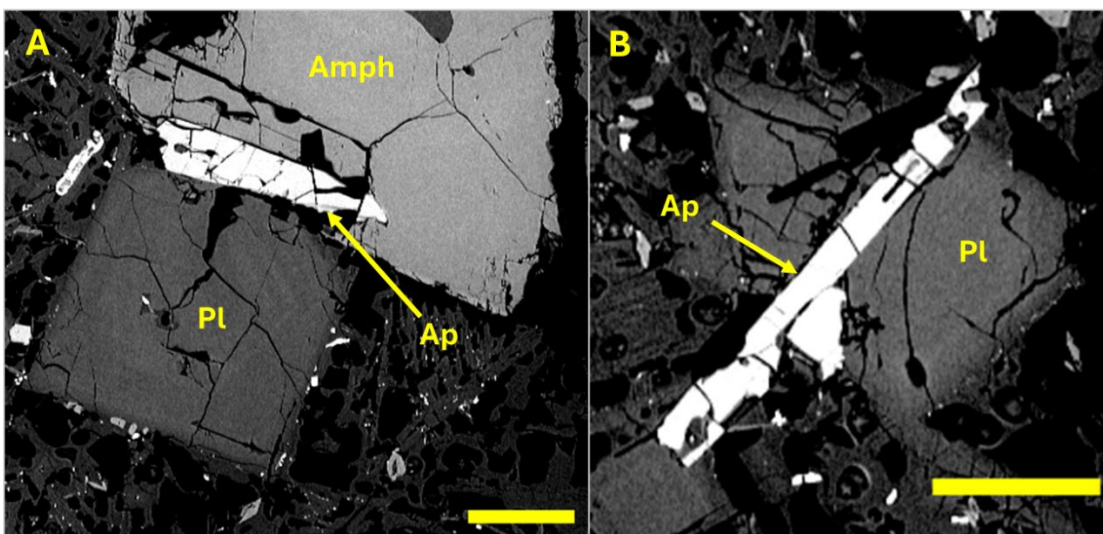


Figure 3.49. BSE photomicrograph of apatite mineral textures within the I hosted enclaves. A) Apatite grown in the outer portion of an amphibole crystal towards the rim; B) Apatite needle grown with a plagioclase microphenocryst in the groundmass. Both images from samples Ati505_06h(e). Scale bars are 0.1 mm.

One enclave from the I eruption shows a very similar bimodality to its plagioclase composition distribution as the mingled I pumice, with peaks in the same An ranges. The other enclaves show unimodal distributions around the similar An ranges (approximately An₅₀₋₉₀, Fig. 3.50); however, the range in the D2 pumice is skewed by several high-An core analyses. Like the plagioclase described above, there are also several microlite and rim compositions that plot in the miscibility gap (Deer et al., 1993; Fig. 3.50).

Fig. 3.51 shows the amphibole compositions from the mingled I and LCY pumices, as well as from the I enclaves. The mingled pumices have very similar compositions, with amphiboles dominantly being magnesiohastingsite with rare pargasites. They also extend into the magnesiohornblende and even tschermakite fields. These are very similar ranges to amphiboles from apparently unmingled pumices from the same eruption deposits (c.f. Fig. 3.36). In contrast, enclave-hosted amphiboles are restricted to magnesiohastingsite and rare edenite compositions.

Clinopyroxenes from these clasts also share significant differences (Fig. 3.52). They are very rare in the mingled pumices and tend to be augites with high Wo components. In comparison, enclaves of the D2 and I eruptions show similar wide distributions with curved groupings on pyroxene discrimination plots. Crystals from both eruptions are predominantly augites with

less common diopsides, although those from the I eruption have higher average Wo-contents. The groupings both appear to have two trends of compositions, one extending to lower-Wo compositions, and one going to greater Fs compositions at constant Wo values. Orthopyroxenes are much rarer and are only observed in the I and LCY clasts. They are enstatites, and the LCY analyses have a greater Fs component.

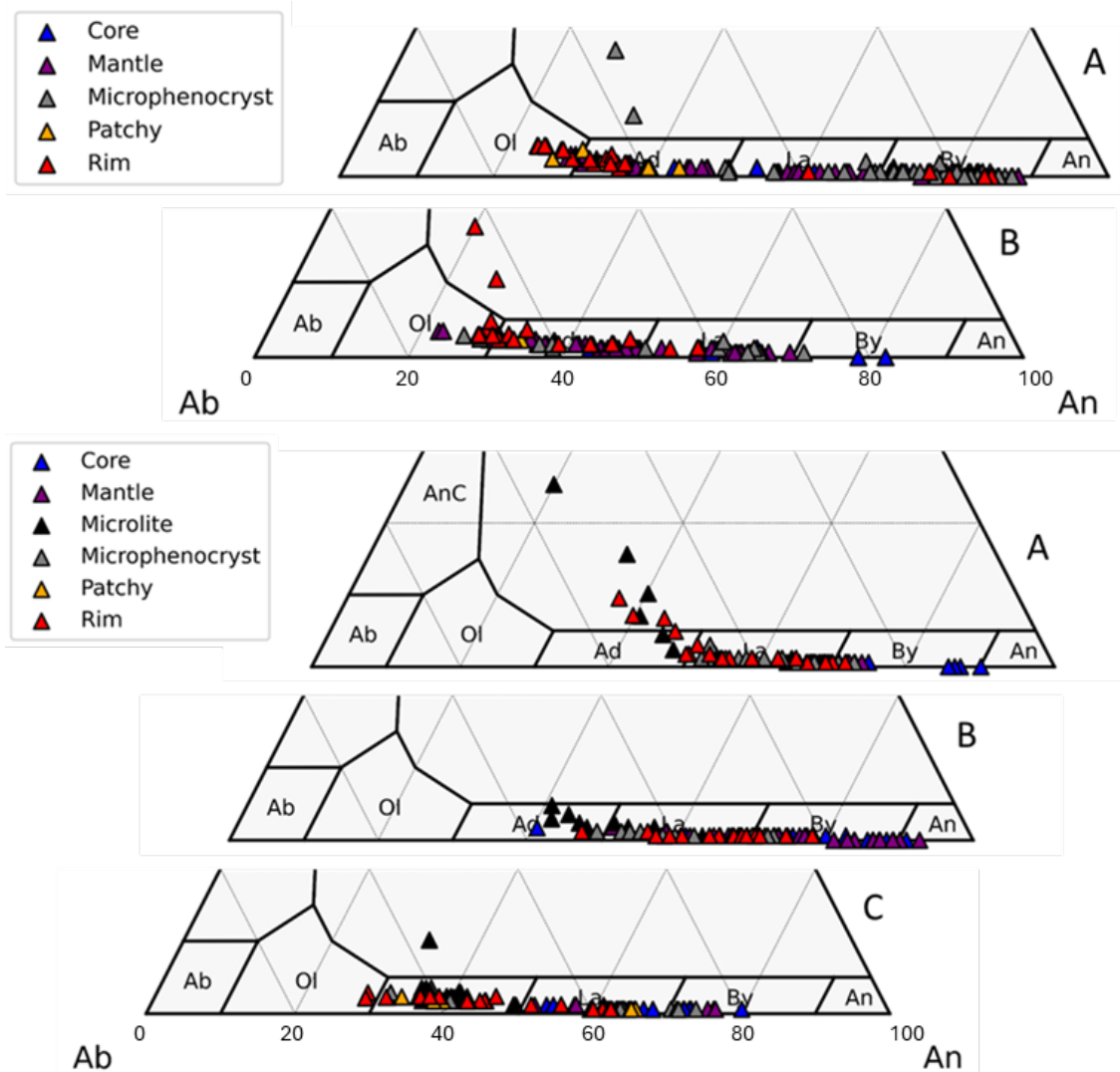


Figure 3.50. Plagioclase compositions. Upper image: the mingled pumices of the A) lower-K LCY; and B) I eruption deposits. Lower image: the enclaves of the A) D2; and B and C) I eruption deposits, samples Ati430_11a(e) and Ati505_06h(e) respectively. B and C presented on different charts due to differences in enclave textures (see results description).

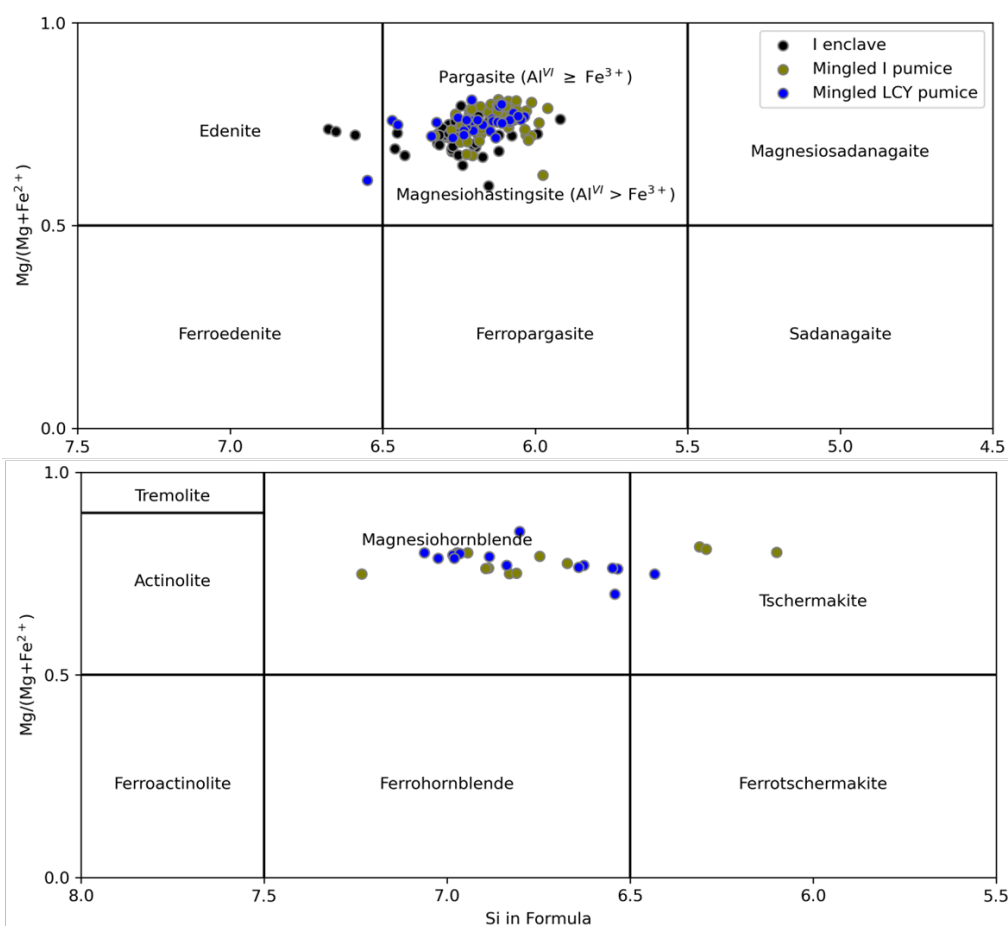


Figure 3.51. Amphibole compositions from the mingled pumices of the lower-K LCY and I eruptions and from the enclaves of the I eruption. Fields after Leake et al. (1997), top panel $Ca_B \geq 1.50$; $(Na + K)_A \geq 0.50$; bottom panel $Ca_B \geq 1.50$; $(Na + K)_A < 0.50$.

3.2.6 Intrusive rocks

Three plutonic rocks were sampled from the AVC, as well as a granitoid xenolith from Volcán Atitlán (sample Ati501_05d). They are all granitoids with 70-78 wt.% SiO_2 , containing plagioclase, orthoclase, mica and quartz, with common perthite textures. They show some differences in their accessory phases and phase abundances. The least felsic sample (Ati426_01) contains only apatite, Fe-Ti oxides and zircon as accessory phases, while the intermediate composition rock (Ati426_02) also contains titanite, and the most felsic one contains large (up to 2.0 mm wide) pyrite crystals and muscovite rather than biotite. The most felsic sample (Ati503_02) is also almost entirely leucocratic and, while the others have mostly equigranular textures with crystals sizes < 1.0 cm, this sample has highly heterogeneous grain size, from fine-grained bands to regions of very coarse-grained (up to 5.0 cm) rock.

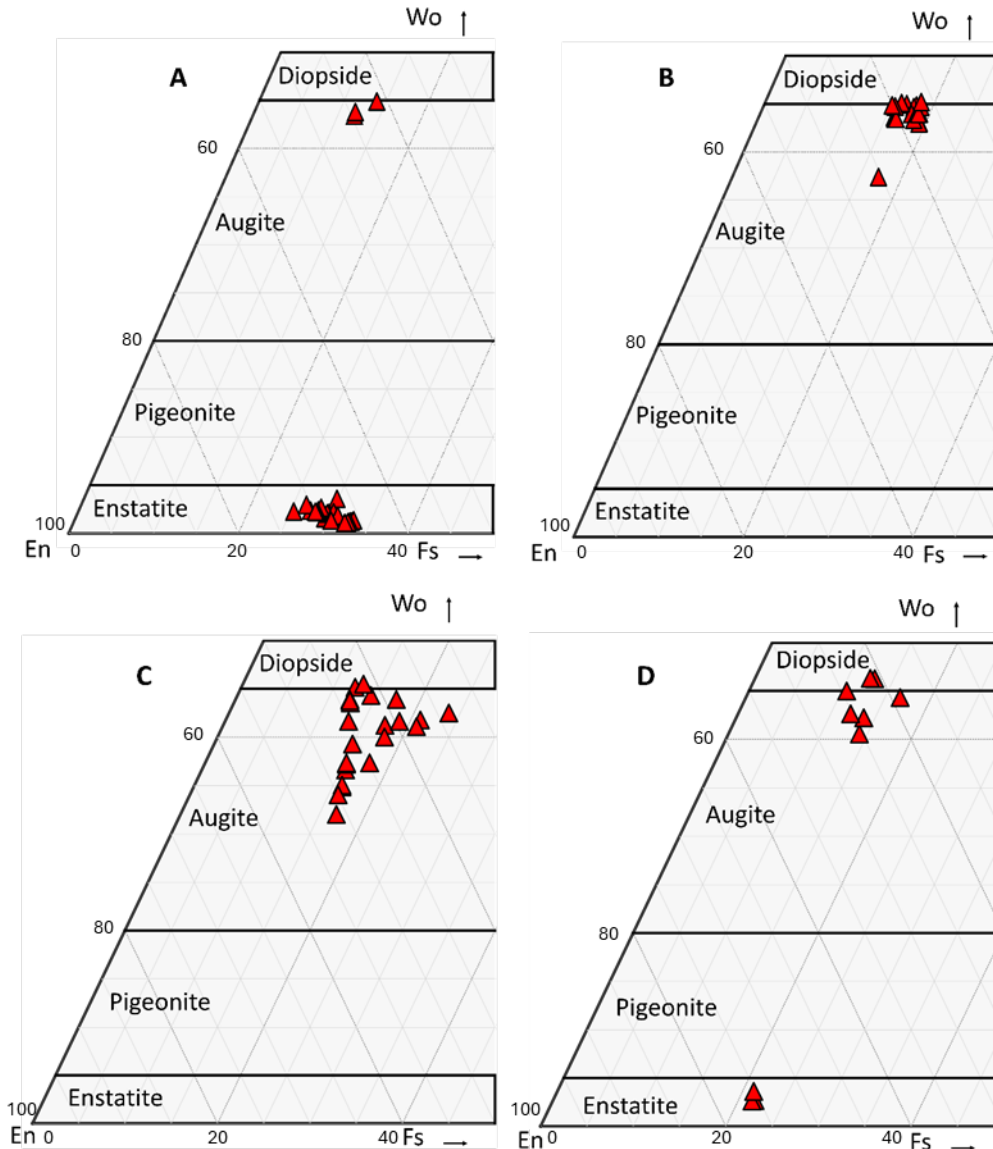


Figure 3.52. Pyroxene compositions from the mingled pumices of the A) lower-K LCY; and B) I eruptions; and from the enclaves from the C) D2; and D) I eruptions.

3.3 Summary

3.3.1 Plagioclase composition comparison:

Fig. 3.53 compares the plagioclase compositions and composition groupings for the different sub-groups of volcanic materials of the AVC. For the stratovolcano lavas, the compositional ranges are very broad, between approximately An₃₀₋₉₀, and the An contents of the crystals decrease from cores to mantles to the rims. Patchy zones have similar compositions to rim compositions. The basaltic andesites are expectedly grouped at higher average An contents, and the average An content increases as the silica content of the rock increases. The anteliths

in the stratovolcano lavas follow a unique trend, with both showing bimodal composition groupings around similar compositions. These cores form one group, with compositions between approximately An_{70-90} , while the mantles, patchy zones and rims all fall between An_{55} .

30.

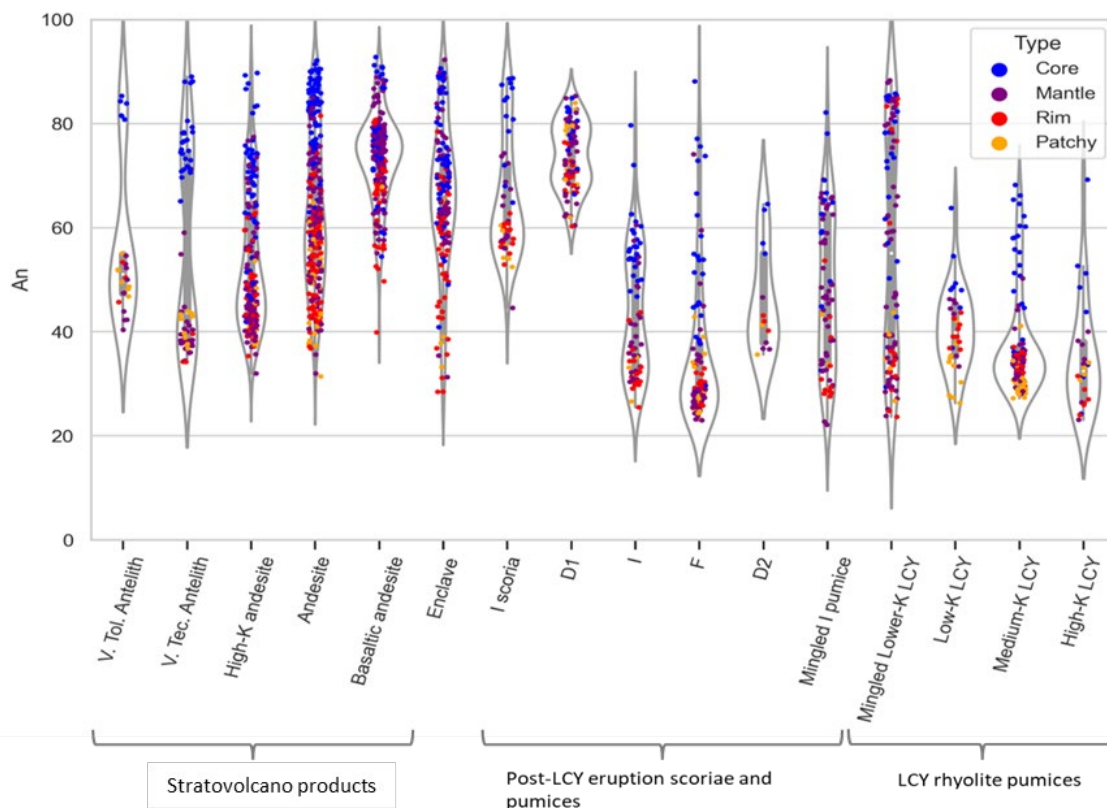


Fig. 3.53. Violin plots comparing An compositions of plagioclase found in the main groups of volcanic materials from the AVC. Enclave refers to plagioclase in mafic enclaves found in the I pumice eruptions deposits. The scatter points are coloured based on their position in the crystal, where 'Patchy' refers to patchy zonation caused by resorption.

Compositions show similar wide ranges in the recharge magmas, but with distinct structures depending on whether the recharge magma was present as an enclave or as a mingled pumice. A unimodal distribution was present in the enclaves, while the mingled pumices have bimodal distribution. In both the mingled pumices, the low-An group was centred around An_{20-50} , while the higher An compositions were higher in the mingled LCY pumice (An_{70-90}) compared to the mingled I pumice (An_{55-70}). In contrast to the bimodal distribution in the anteliths, the groupings were not controlled entirely by location within the crystal, as cores, mantles and rims were present in both peaks. The exceptions were patchy zones, which were only present in the lower-An region.

The andesite pumices showed unique compositional groupings. The basaltic andesite I scoria had a similar range of plagioclase compositions to the basaltic andesites from the stratovolcanoes; however, the distribution of compositions was weighted more heavily towards lower An values. The D1 pumice was stranger; despite having a more silicic composition than the I scoria, it had a tight composition grouping between An₆₀₋₉₀, and was the only sample from the entire AVC that did not have any compositions lower than An₆₀.

Finally, the plagioclase from the rhyolite pumices all shared similar compositions. They have fairly wide composition distributions, typically An₂₅₋₈₀. These are split between core compositions which have a wide An range (An₄₀₋₈₀), with a narrower spread of rim and patchy zone compositions between An₂₀₋₄₀.

3.3.2 Pyroxene composition comparisons

Figure 3.54 show violin plots of Mg# for clinopyroxene and orthopyroxene compositions. The clinopyroxenes have similar values for all analysed samples and there is no large distinction between zones. Crystal clots in sample Ati501_05a from Volcán Atitlán (Fig. 3.5) have the lowest Mg#s of all the AVC crystals.

In contrast, orthopyroxenes show more variation between units. Stratovolcano lavas have decreasing orthopyroxene Mg#s with increasing evolution. The anteliths from the different volcanoes have distinct compositions, as the Volcán Tecolote antelith (sample Ati427_08a) has lower Mg#s than those from the Volcán Tolimán antelith (sample Ati503_06).

From the pumice units, the D1 and I scoria have similar compositions to the basaltic andesites, while those in the mingled LCY pumice and the D2 rhyolite are more like crystals from the intermediate composition lavas. Unexpectedly, the orthopyroxenes from the I enclave have the highest Mg#s of all, although few crystals were found and analysed.

3.3.3 Olivine composition comparisons

For the most part, olivines in volcanic material of the AVC share very similar compositions of Fo₇₀₋₈₀ (Fig. 3.55). However, the stratovolcanoes lavas have a much greater range of olivine compositions (Fo₅₅₋₈₅.) These are similar for olivines in both the basaltic andesites and the andesites, although the olivines in basaltic andesites have a lower range of Fo compositions than in the andesitic lavas. This may simply be related to the higher proportion of olivine in the basaltic andesites.

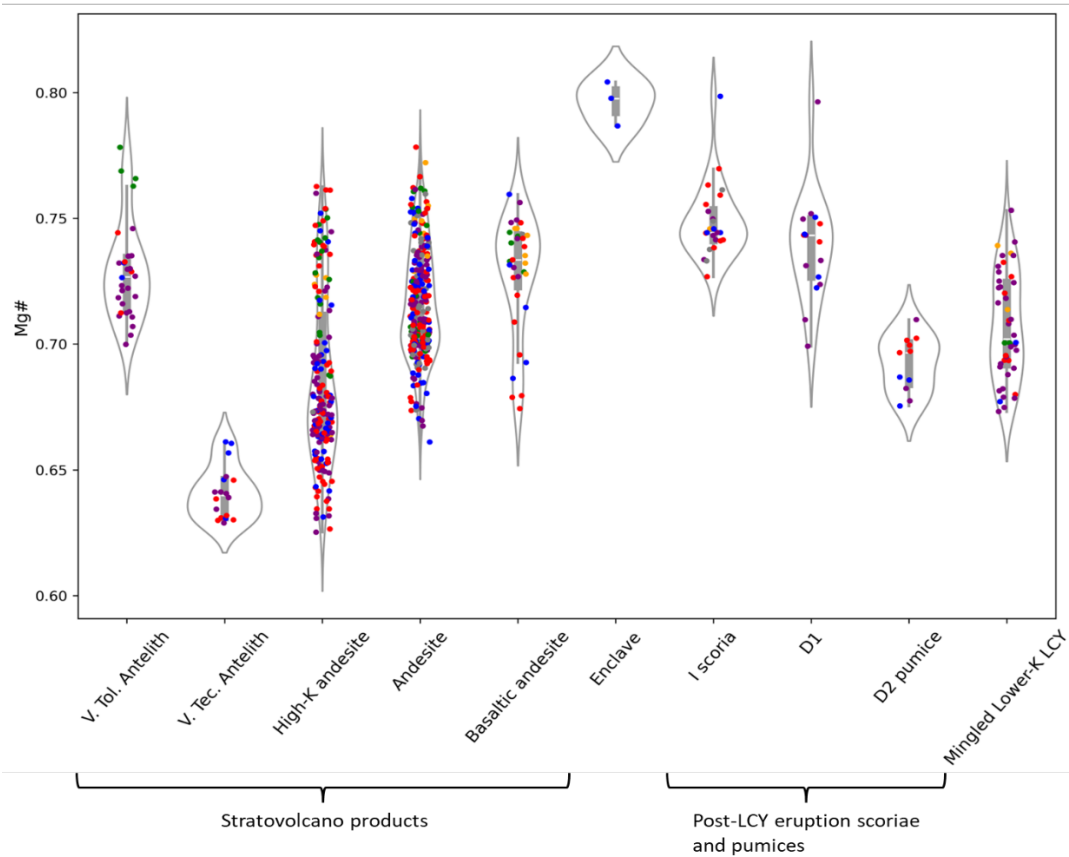
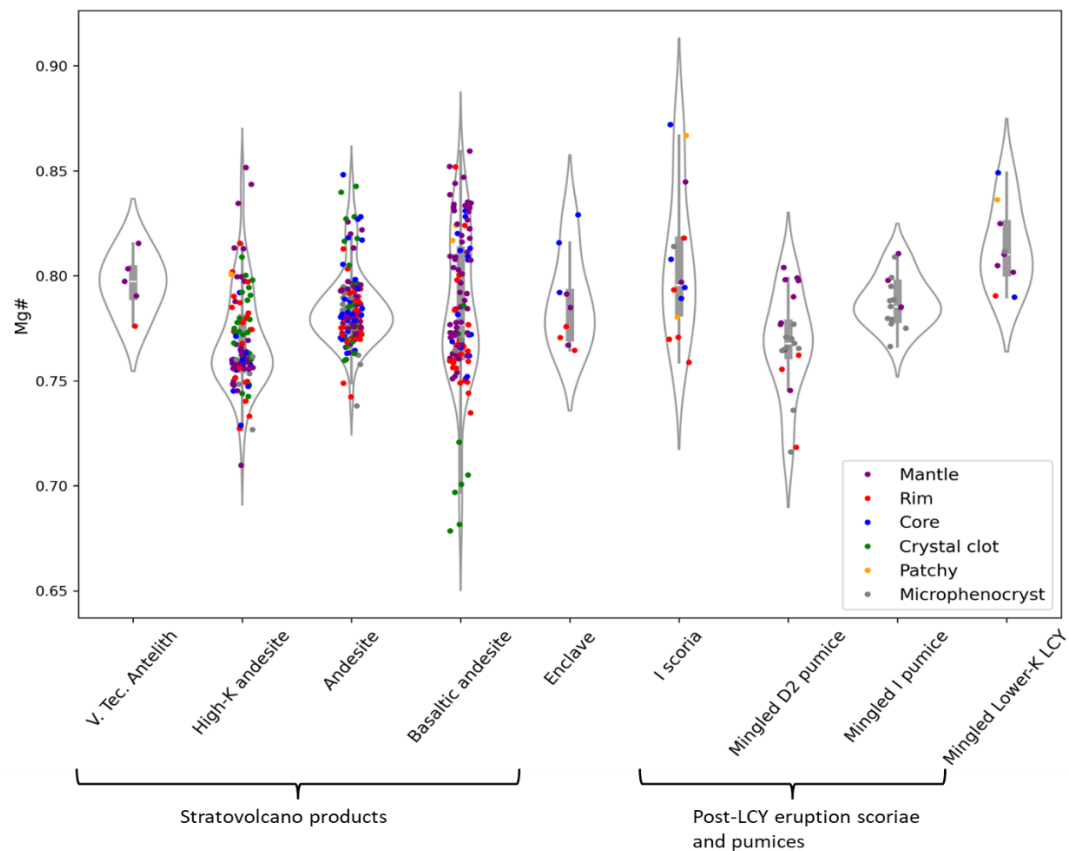


Fig. 3.54 Violin plots of upper: orthopyroxene; and lower; clinopyroxene Mg# for units of the AVC

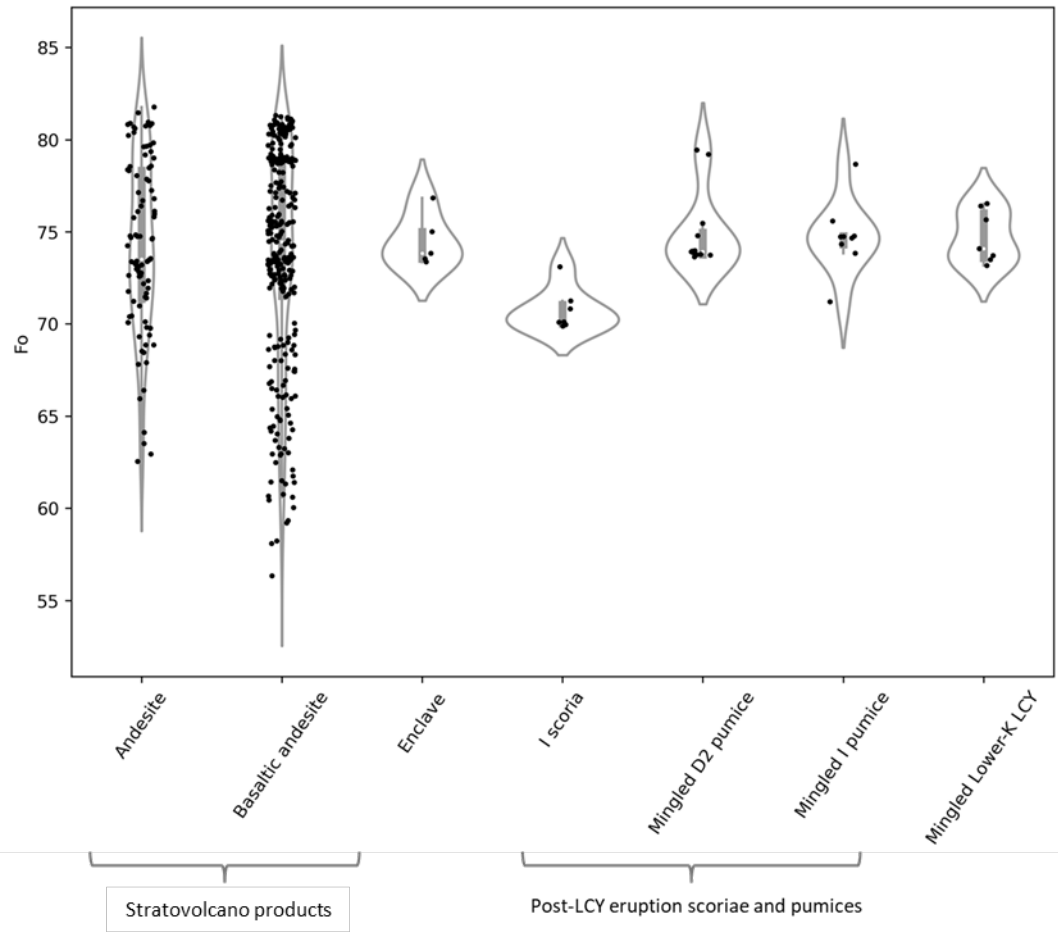


Fig. 3.55. Violin plot of Fo values for olivines from the various AVC units. These are not divided by location in the crystal as there was no clear distinction between zones.

Chapter 4. Geochemistry of the AVC samples

In this chapter I outline the whole rock major element, trace element, and radiogenic isotope results. Within these three divisions I separately describe the geochemical characteristics of the different groups outlined in section 3.1.2. These are the stratovolcano basaltic andesites to dacites (52.0-65.0 wt.% SiO₂; phase III - green pentagons and phase IV - red circles), the recharge magmas (only one sample analysed for whole rock composition – sample Ati505_06h(e), 62.6 wt.% SiO₂; yellow square), the LCY pumices (76.2-77.6 wt.% SiO₂; diamonds), the post-LCY pumices (the D, F and I eruptions; 56.5-73.4 wt.% SiO₂; crosses), and finally the intrusives (70.0-76.0 wt.% SiO₂; stars).

Also included in this chapter is presentation of the major and trace element compositions of the volcanic glasses that were present either in the groundmasses of the pumices, or as melt inclusions or interstitial glass in lavas or anteliths.

4.1 Whole rock major element results

All whole rock major element oxide data as well as uncertainties and detection limits are presented in Appendix A.1. All data have LOI <6 wt.%; any analyses with higher values have been removed. Results are within <5% relative error for most oxides and are only greater in oxides present in low concentrations (concentrations of <0.2 wt.%; see Appendix A). Detection limits are <0.01 wt.% for all oxides apart from MnO, which has a limit of <0.001 wt.%. Two lava samples (Ati427_09 and Ati504_02) also contained significantly anomalous trace element compositions and so have also not been plotted but are also shown in the appendices.

The whole rock XRF analyses (normalised to 100 wt.% on water-free basis) are shown on the total alkali-silica (TAS) diagram (Fig. 4.1). Analysed materials from the AVC span a wide range of compositions from basaltic andesites to high-silica rhyolites (Fig. 4.1). All AVC rocks are calc-alkaline with some subdivisions based on K₂O contents from medium-K calc-alkaline to high-K alkaline (Fig. 4.1). Figure 4.2 shows the Harker variation diagrams for the AVC. Data from previously published studies of igneous rocks from the CAVA are also shown on Figures 4.1 and 4.2. Figures also include two unpublished whole rock data points from the pre-LCY W eruption provided by Steffan Kutterolf (GEOMAR) for comparison.

In the Harker diagrams (Fig. 4.2) the samples all fall on simple linear trends for most of the elements between the different analysed groups. The major exceptions are the alkali elements and P₂O₅. For the alkalis, there is a large range of compositions, especially for K₂O

where samples fall in both the medium- and high-K calc-alkaline fields. For P_2O_5 , all samples except the enclave lie on a linear trend.

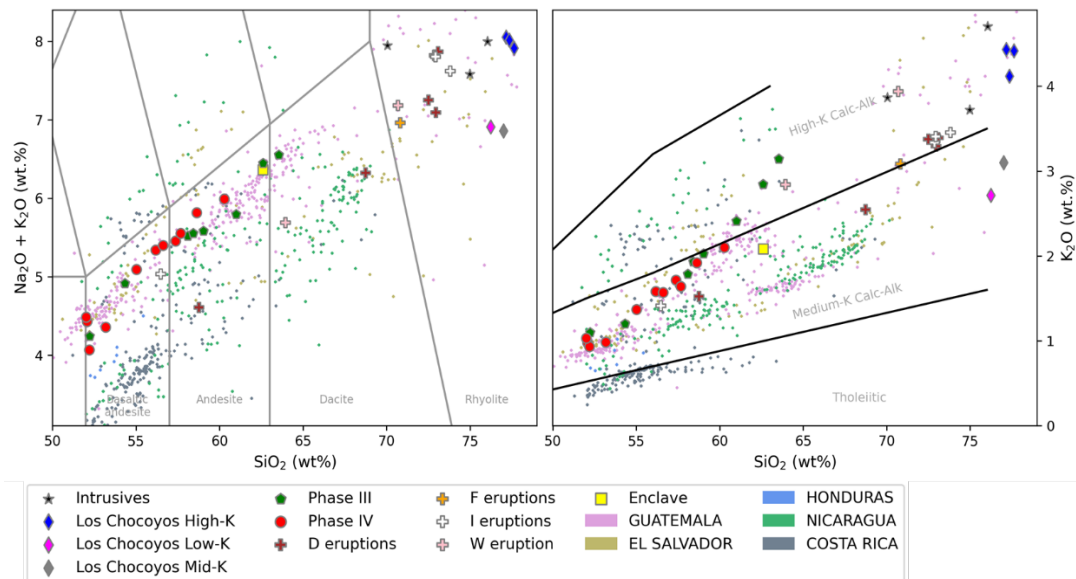


Figure 4.1. Total alkali-silica diagram and K_2O discrimination diagram (after Peccerillo & Taylor, 1976) for whole rock analyses of AVC materials. Also shown are other CAVA volcanic materials from the GEOROC database. The AVC suite falls along a similar trend to previously analysed rocks from Guatemala for total alkalis but differs significantly for K_2O . Analytical uncertainties (1 s.d.) are smaller than the size of the symbols.

4.1.1 Stratovolcano lavas

AVC stratovolcano (phase III and IV, pre- and post-LCY respectively) lavas have between 52.0 and 64.9 wt.% SiO_2 . On Figure 4.1, they form a linear trend and have calc-alkaline compositions, however the pre-LCY lavas extend to higher SiO_2 contents. All the stratovolcano rocks fall along a similar trend to other CAVA lavas from Guatemala and El Salvador (Fig. 4.1), but they have higher total alkalis compared to lavas from Nicaragua and Costa Rica.

Compatible major element oxides (MgO , Fe_2O_3 , CaO , Al_2O_3 and TiO_2) show negative linear trends with increasing SiO_2 . In contrast, Na_2O and K_2O show positive trends (Fig. 4.2) and have inflection points around 57 wt.% SiO_2 , where the slope of the trend changes. In general, lavas with > 57 wt.% SiO_2 have decreasing Na_2O and more rapidly increasing K_2O contents with increasing SiO_2 . Correlation coefficients for the whole stratovolcano series (Table 4.1) are lower than those for the two parts of the series divided at 57 wt.% SiO_2 , particularly those for Na_2O .

Lavas with <60 wt.% SiO_2 plot exclusively in the medium-K calc-alkaline field of the K_2O diagram, while those with the highest SiO_2 contents cross into plot in the high-K calc-alkaline field (as defined by Peccerillo & Taylor (1976)). These alkali trends differ from those

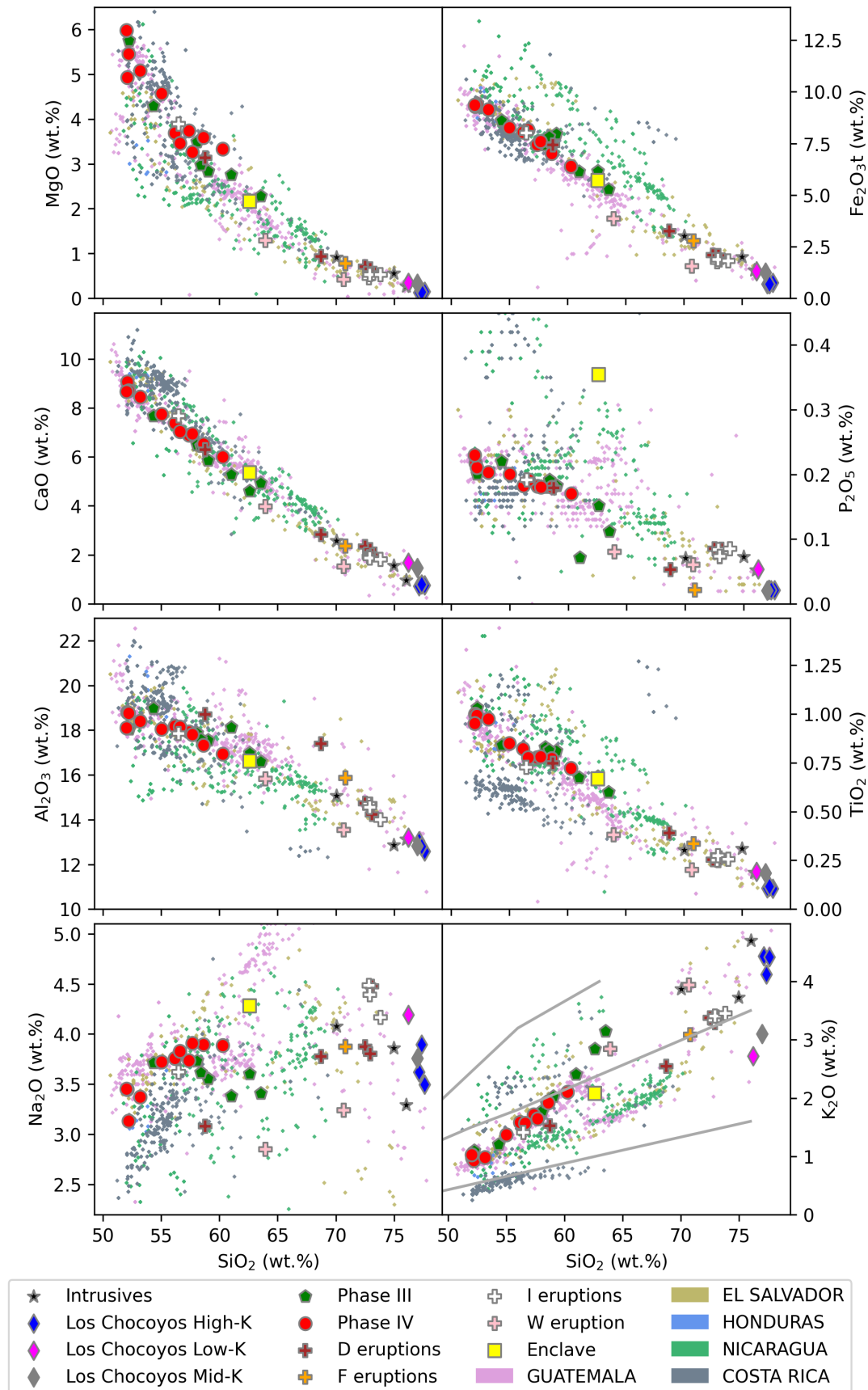


Figure 4.2. Major element Harker diagrams for the whole rock materials of the AVC, samples the same as Fig. 4.1. Analytical uncertainties (1 s.d.) are smaller than the symbol sizes.

seen in other CAVA volcanoes (Fig. 4.2). Only Volcán Tacana has a similar trend for both alkalis, with a flat trend for Na₂O and a steep positive trend for K₂O.

| | Na ₂ O (whole series) | Na ₂ O (<57 wt.% SiO ₂) | Na ₂ O (>57 wt.% SiO ₂) |
|------------|----------------------------------|--|--|
| Cor. Coef. | 0.21 | 0.86 | -0.68 |
| | K ₂ O (whole series) | K ₂ O (<57 wt.% SiO ₂) | K ₂ O (>57 wt.% SiO ₂) |
| Cor. Coef. | 0.98 | 0.95 | 0.99 |

Table 4.1. Correlation coefficients for the alkali elements comparing values when taken as a whole series versus the correlations of two separate series divided by an inflection point at 57 wt.% SiO₂.

4.1.2 Recharge magma

The enclave from the I rhyolite is among the most evolved analysed andesitic material of the AVC (62.6 wt.% SiO₂). It falls on most of the same major oxide trends as the other andesites but diverges in the alkalis. While the enclave has similar total alkali contents to the AVC andesite lavas (Fig. 4.1), it has significantly higher Na₂O concentrations and drops off the trend line for K₂O (Fig. 4.2). This enclave is also unique in having the greatest enrichment of P₂O₅ in any AVC andesitic sample (0.35 vs. 0.07-0.23 wt.% P₂O₅). Comparison of P₂O₅ contents of other CAVA andesites shows that it is also high compared to most other lavas (Fig. 4.2). These differences in the alkali contents and P₂O₅ are greater than the analytical uncertainty and so are significant.

4.1.3 Los Chocoyos (LCY) pumices

As mentioned in section 1.4, two types of rhyolite pumices have previously been described from the Los Chocoyos deposit (Rose et al., 1979, 1987; Cisneros de León et al., 2021a). In section 3.2.3.1, an additional pumice was described with a distinct mineralogy from the previously identified LCY pumice types. All three pumices have compositions of 76.2-77.7 wt.% SiO₂, and they can be easily differentiated by their K₂O contents. As the two previously identified LCY pumice types were named the “low-K” (2.7 wt.% K₂O and high-Ca amphibole-bearing) and “high-K” (4.1-4.4 wt.% K₂O and biotite-bearing) LCY pumices (Rose et al., 1979, 1987; Cisneros de León et al., 2021a), this nomenclature has been retained and the new pumice type has therefore been termed the “medium-K” (3.1 wt.% K₂O and cummingtonite-amphibole and biotite-bearing) LCY pumice. Its composition is similar to published data (Rose et al., 1979, 1987; Cisneros de León et al., 2021a). In fact, within the compositional data of Cisneros de León et al. (2021a), two sub-groupings in K₂O can be seen in their low-K LCY pumice group which match well with the division between the low- and medium-K pumices identified here. Differences in the alkalis between the low- and

medium-K rhyolites are greater than the analytical uncertainty and so are significant enough to warrant this distinction.

Variations between these different pumice units are shown in Figs. 4.1 and 4.2. The low-K LCY pumice has the lowest SiO₂ content (76.2 wt.%), followed by the medium-K pumice (77.0 wt.% SiO₂) and the high-K pumices (77.2-77.7 wt.% SiO₂). The low and medium-K pumices have similar MgO, Fe₂O₃(T), CaO and TiO₂ concentrations, while the medium-K pumice has P₂O₅ contents that are more like the high-K pumices. Variations in Al₂O₃ (and to some extent Na₂O) between the analysed LCY pumices are gradual and correlate with differences in SiO₂.

These LCY pumice units follow similar variations in alkali contents as those of the andesites, i.e., higher K₂O contents are mirrored by lower Na₂O contents. The different pumice units also plot in different fields on the K₂O discriminatory diagram (Fig. 4.2), with the low- and medium-K pumice units falling in the calc-alkaline series field while the high-K pumices are high-K calc-alkaline. This somewhat mirrors the trends observed in the andesites, where the lavas tend to be high-K calc-alkaline and the enclave is medium-K calc-alkaline (Fig. 4.2).

4.1.4 Post-LCY pumices

The two intermediate composition clasts have similar compositions in terms of differentiation (D1 = 58.8 wt.% SiO₂; I1 = 56.5 wt.% SiO₂), however there are several differences in their other major oxide compositions. The I1 scoria falls on the same trend as the rest of the AVC lavas, while the D1 pumice shows some major differences from other andesites in Al₂O₃ and the alkalis (Fig. 4.2). These differences are greater than the analytical uncertainty of these measurements. Al₂O₃ shows a slight elevation compared to lavas with similar SiO₂ contents and there are significant depletions in the alkalis. In particular, the D1 pumice has the lowest value for Na₂O of all the analysed AVC rocks from this study, including the pumices. The depletion in both major alkali oxides is unique to this rock, as the typical patterns showing enrichments in one oxide are usually matched with depletions in the other.

Three post-LCY rhyolite/rhyodacite pumice units (D2, F and I pumices) show quite wide variations in whole rock compositions, especially for the D2 pumices which range from 68.6 to 73.1 wt.% SiO₂. The F pumice also has a lower SiO₂ content (70.8 wt.%). Most of the compositions for the D2 and I rhyolite pumices, however, lie in a narrower range between 72.5 and 73.1 wt.% SiO₂. This wide range of compositions may be related to the wide range

of crystallinities in these rocks, which range from 5.0 to 20% by volume (section 3.2.4.1). Apart from their alkali contents, the other major element abundances are higher than those in the LCY pumices (Fig. 4.2). In the K₂O discrimination diagram, these pumices fall along the dividing line between high- and medium-K calc-alkaline fields (Fig. 4.1).

4.1.5 Intrusive rocks

Three intrusive rocks were analysed from the AVC (section 2.1). These were all high-K calc-alkaline granites (Fig. 4.2). They fall on similar trend lines to the rhyolites for most major oxides but have higher K₂O content. The leucocratic pyrite-bearing granite has a composition like the high-K LCY pumices.

4.2 Whole rock trace element results

4.2.1 Stratovolcano lavas

Full trace element results and uncertainties are shown in Appendix A.2. Figure 4.3 shows a selection of trace element Harker diagrams and Figure 4.4 shows the rare earth element (REE) and incompatible trace element spider diagrams for the basaltic andesite to dacite samples, also comparing the enclave and the intermediate composition post-LCY pumices. Two samples (sample Ati427_09 from Volcán Tecolote and sample Ati504_02 from Volcán San Marcos) have abnormally high REE contents and show petrographic evidence of alteration, so they have not been plotted and not included in the discussion. These increases may be due to alteration which can cause elevated REE contents (Patino et al., 2003), especially shown by the abnormal negative Ce anomaly in sample Ati504_02.

REE variations for the stratovolcano lavas are fairly consistent. In general, the abundance of each element increases with increasing differentiation (using SiO₂ as a proxy), although this increase is less pronounced in the MREEs. These lavas also have a strong negative trend for Eu anomaly ($Eu/Eu^* = E_N / ((Sm_N * Gd_N)^{0.5})$, where N = chondrite-normalised using the values of Sun & McDonough, 1989) when plotted against SiO₂ (Fig. 4.5). This measurement tracks the deviation of Eu from the REE slope due to its more variable valence state and subsequent changes in its compatibility (most significantly in plagioclase). Similarly, Sr anomaly ($Sr/Sr^* = Sr_N / ((Ce_N * Nd_N)^{0.5})$, N as above; after Vukadinovic, 1993) track changes in expected Sr concentrations due to plagioclase fractionation because of Sr's high compatibility in this phase and Ce and Nd's typically similar behaviour. There is a good positive correlation between Eu anomaly and Sr anomaly (Fig. 4.5).

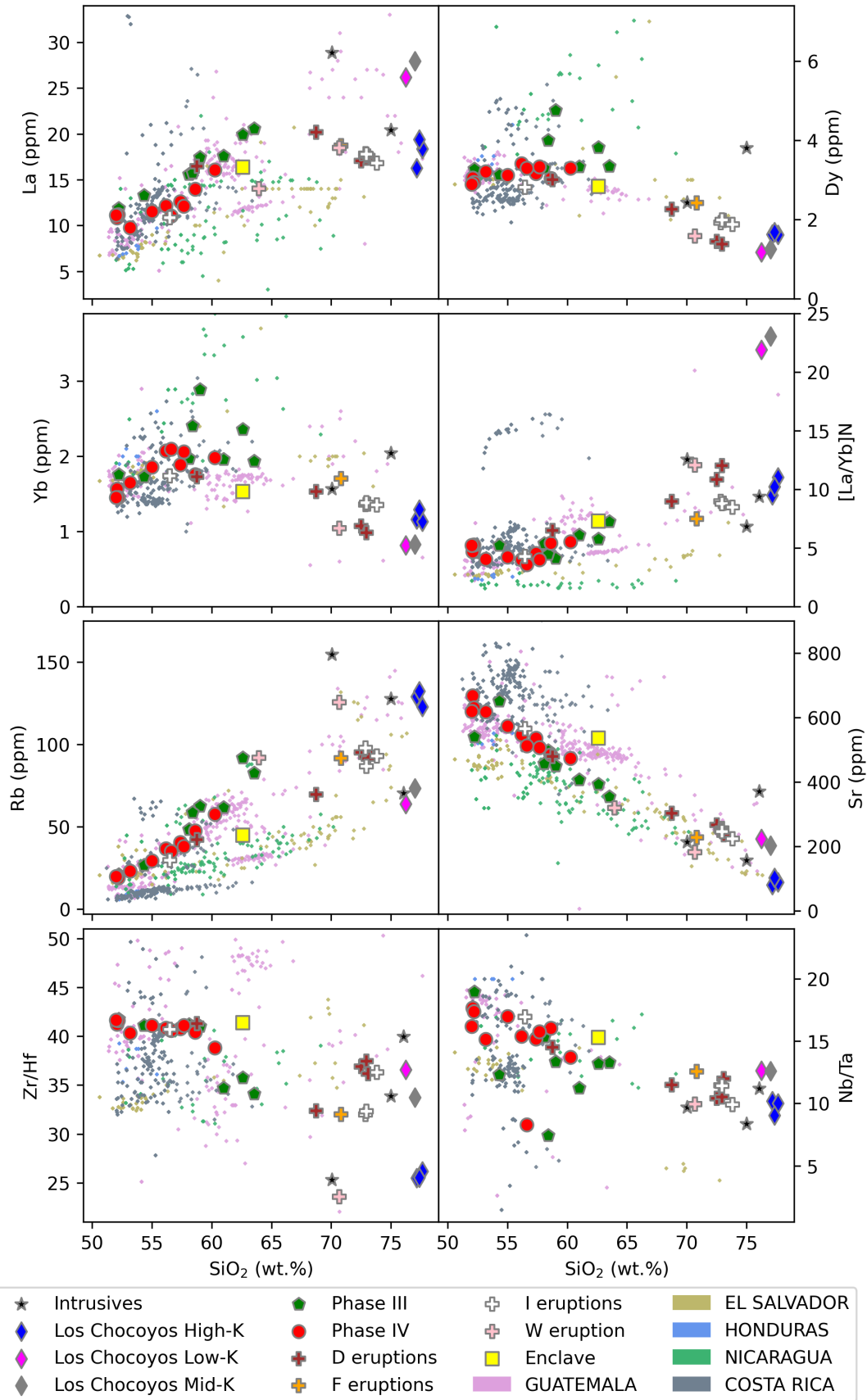


Figure 4.3. Selected incompatible trace element Harker diagrams and trace element ratios for AVC materials. Symbols as in Fig. 4.1. Analytical uncertainties (1 s.d.) are smaller than the symbol sizes. $[La/Yb]_N = La/Yb$ normalised to chondrite values.

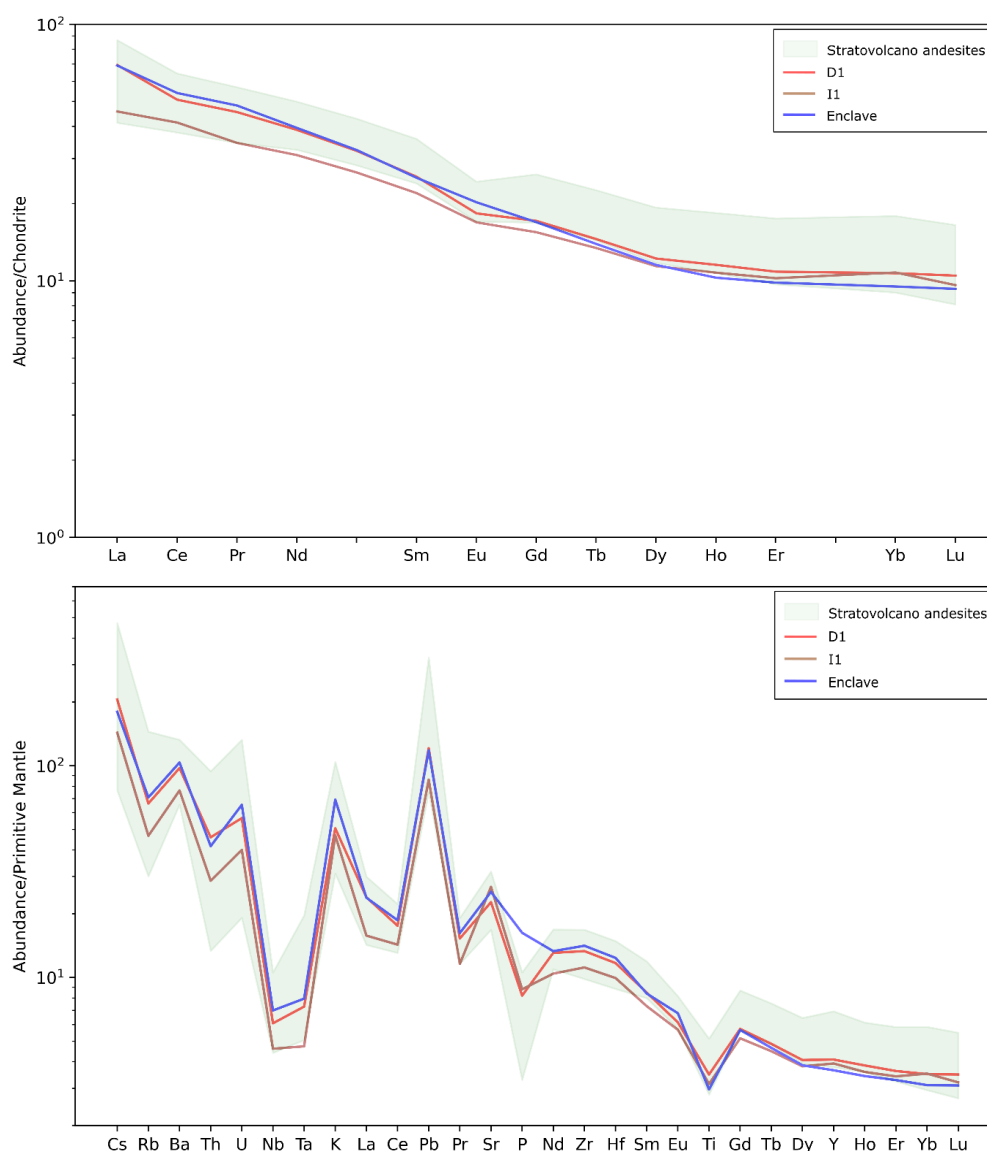


Figure 4.4. Spider diagrams of A) REE variations; and B) trace element variations, for the andesites of the AVC. Shaded region contains all variations of the stratovolcano lavas/scoriae and the lines are for the andesitic pumices and the enclave from the I pumice. Normalising values from Sun & McDonough (1989).

For the large ion lithophile elements (LILEs, Cs-U and K, Sr and Pb) of the stratovolcano materials, there is a similar trend for abundances to increase with increasing differentiation (with the main exception of Sr). The saw-toothed pattern shown by these elements also smooths out, caused by decreasing Ba contents (Fig. 4.4). Sr is the only LILE that shows a negative correlation with SiO_2 for these samples.

For the high field strength elements (HFSEs; Nb, Ta, Nd, Zr, Hf, Ti and Y), there are greater variations between the different elements. Some are likely related to the varying influences of different mineral phases as the evolving melts enter or leave their respective stability fields (e.g., Zr and Hf in zircon, and Ti in titanomagnetite and ilmenite). In general, abundances of these elements increase with increasing differentiation. Ti is the main

exception to this with a consistent negative correlation with SiO_2 , and the most evolved of the pre-LCY stratovolcano lavas have negative correlations for Zr and Hf. For Ta, Nd and Y, significant amounts of scatter start to emerge in the more silicic stratovolcano materials. All these samples show significant Nb-Ta depletions that are typical for volcanoes on convergent margins. Nb/Ta ratios decrease with increasing evolution (Fig. 4.4), although there are several samples which have much lower values for this tracer.

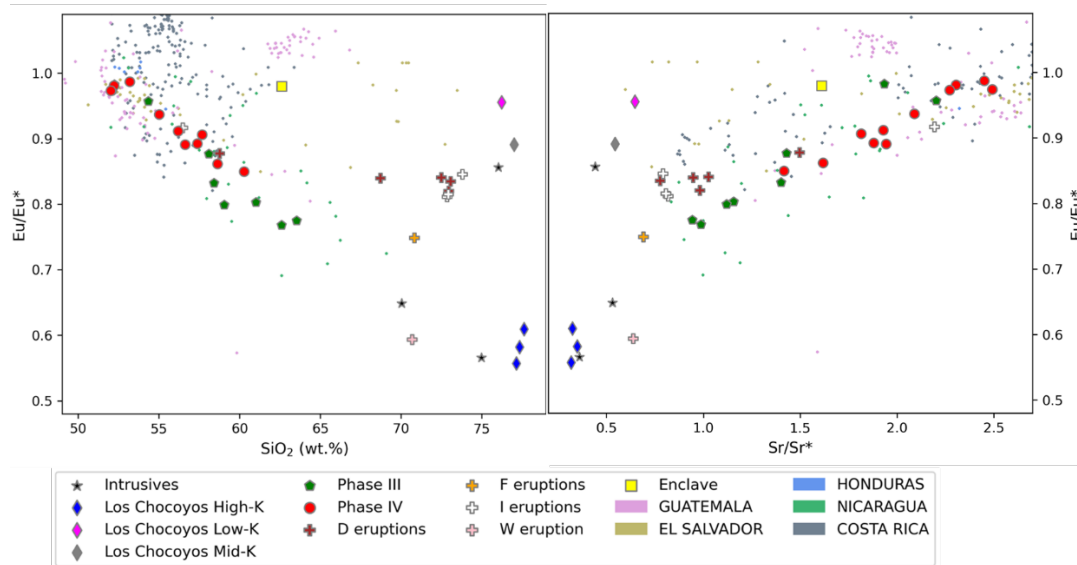


Figure 4.5. Eu/Eu^* vs. SiO_2 and vs. Sr/Sr^* for AVC materials. Note the poorly developed Eu and Sr anomalies for the enclave relative to the other andesitic materials, as well as the similarly small anomalies in the low- and medium-K LCY pumices. Analytical uncertainties (1 s.d.) are smaller than the symbol sizes.

The compatible elements (Sc, V, Cr, Co, Ni and Cu) all show strong negative correlations with SiO_2 for the stratovolcano materials (Fig. 4.6). This trend is not linear and, while it varies from element to element, it is steep between 52 and 58 wt.% SiO_2 and shallows at higher SiO_2 contents, forming an L- or spoon-shaped curve. This resembles the pattern for MgO (Fig. 4.2). The andesite trends are near detection limits for Ni, Cu and Cr.

4.2.2 Recharge magma

The recharge magma falls significantly off of the compositional trends for the stratovolcano lavas. It has relatively lower REE concentrations when compared to similar composition lavas (Figs. 4.3, 4.4). The enclave also has slightly steeper slopes REE than those of other intermediate composition materials (Fig. 4.4). The enclave also completely lacks a Eu anomaly ($\text{Eu}/\text{Eu}^* = 0.98$; Fig. 4.5), despite having a similar SiO_2 content to the most silicic andesites. It similarly has a somewhat higher Sr anomaly in comparison to these more silicic andesites (Fig. 4.5). These differences are greater than the analytical uncertainties of the measurements, suggesting that they are statistically significant.

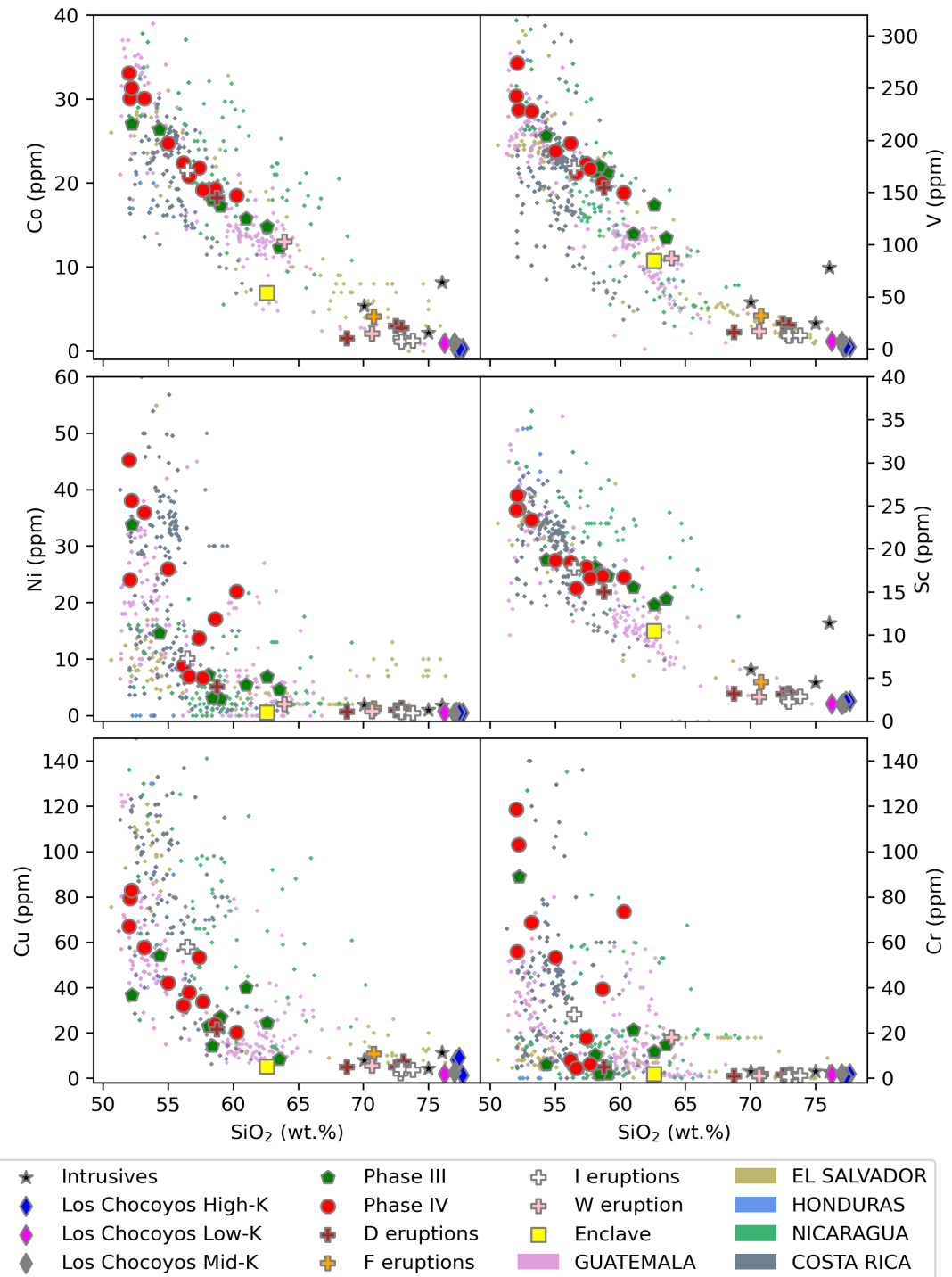


Figure 4.6. Compatible trace element Harker diagram, showing the variations of these elements with SiO_2 . The primitive and intermediate materials have much greater reductions in Ni, Cu and Cr with increasing SiO_2 . The enclave typically has lower values (especially in the case of Co, V and Sc) than the lavas with similar SiO_2 contents. Symbols as in Fig. 4.1. Analytical uncertainties (1 s.d.) are smaller than symbol sizes.

The enclave magma has lower values for several of the LILEs than comparable stratovolcano lavas (the main exception being Sr, for which it lies above the stratovolcano trend; Figs. 4.3, 4.4). These differences again are greater than the analytical uncertainties, suggesting statistical significance.

For the HFSEs, the enclave is somewhat similar to the stratovolcano trends, although for the ratios of Nb/Ta and significantly Zr/Hf, the enclave lies above them. For the compatible elements, the inverse is true. The enclave always has lower values than the any stratovolcano lava (Fig. 4.6), and this difference is greater than the analytical uncertainty for the measurement and therefore is statistically significant.

4.2.3 LCY pumices

Fig. 4.7 shows the REE patterns and spider diagrams for the various Los Chocoyos pumice samples. Both plots show that the medium-K and low-K LCY have very similar trace element patterns, with element variations typically within analytical uncertainty. To simplify presentation of the trace element results for these pumices, these two groups will be discussed together under the term 'lower-K' LCY pumices. In general, however, the medium-K pumice has slightly higher abundances for each element. Several differences in REE can be seen between the lower-K and high-K LCY pumices. These are the relative enrichment in the LREEs and the greater steepness of the slopes of the lower-K LCY group with $[La/Yb]_N$ between 22-23 for the lower-K rhyolites, and 9.5-11 for the high-K rhyolites (Fig. 4.3), and the absence/near absence of Eu anomalies for the lower-K group (0.96-0.89) in comparison to the relatively large anomalies present in the high-K pumices (0.61-0.56, Figs. 4.5, 4.7). Both groups have spoon-shaped REE patterns with their greatest relative depletions in Dy-Er (Fig. 4.7).

There are several statistically significant differences in trace element values between the LCY pumices. The high-K pumices have greater enrichments in almost all LILEs (the exceptions being Sr, and Pb in one sample), and present a concave pattern between Cs-U with a large depletion in Ba. They also have a large relative depletion in Sr (Figs. 4.5 and 4.7). The lower-K group, in contrast, is comparatively depleted in the LILEs. These magmas present a different pattern for the elements Cs-U, lacking a significant depletion in Ba, and showing relative enrichment in Th.

For the HFSEs, the LCY pumices generally follow the lower-K and high-K LCY groupings outlined above. For Hf and Zr, the high-K LCY pumices have lower concentrations, while they are relatively enriched in Nb, Ta and Y. Nb/Ta ratios are the opposite, with the high-K LCY pumices having the lowest values and the lower-K LCY pumices having elevated values. For almost all the analysed trace elements and trace element ratios, the high-K LCY pumices have concentrations resembling those of the W pumice (Figs. 4.3, 4.5 and 4.7).

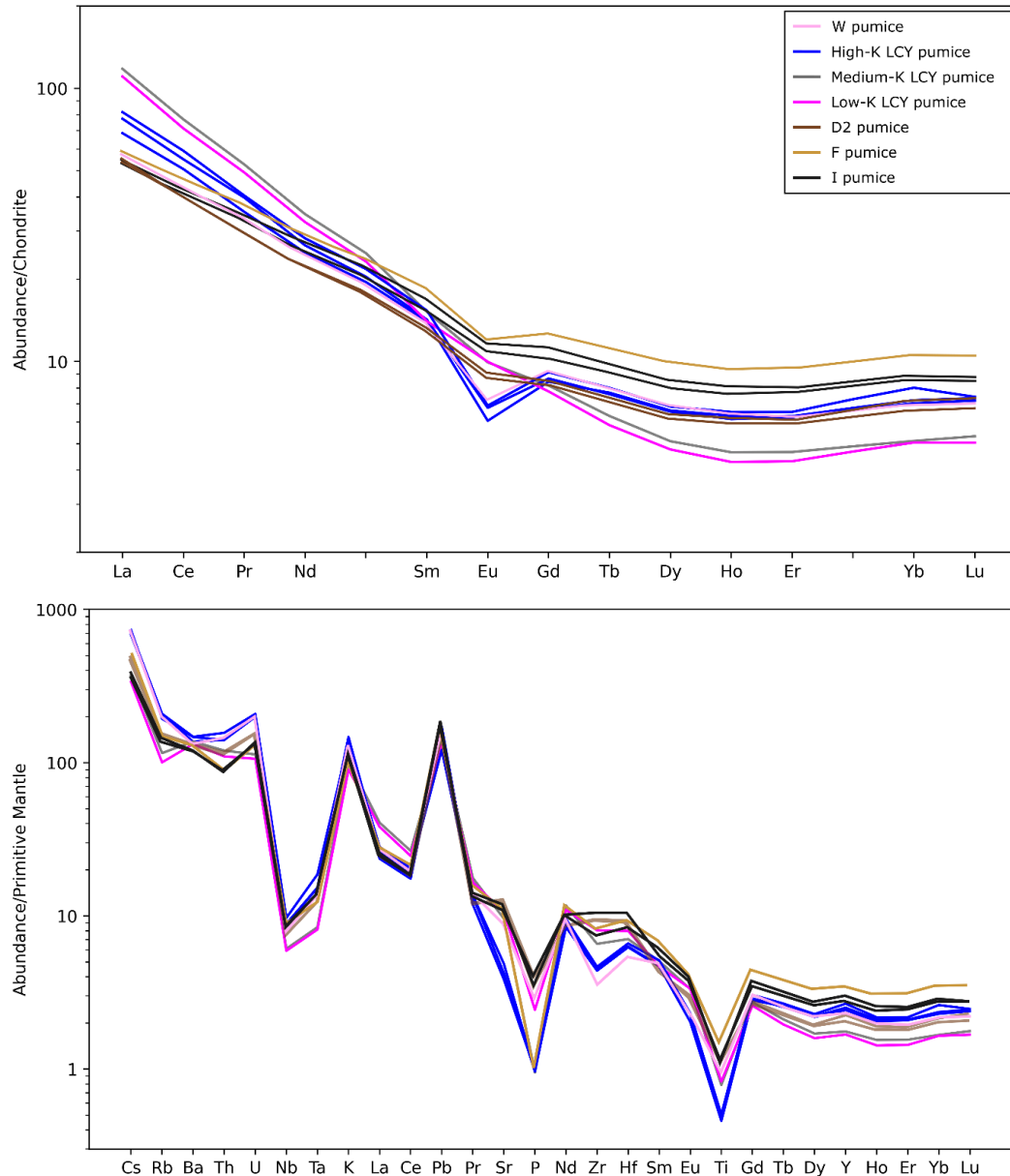


Figure 4.7. Spider diagrams of A) REE variations; and B) trace element variations for the different AVC pumice types. Normalising values from Sun & McDonough (1989).

Finally, the LCY pumices show the lowest values of the compatible elements in any of the analysed AVC materials (Figs. 4.6 and 4.7). The two groups have typically very similar values for these elements, however for V and Co they are lower in the high-K LCY pumice. However, these are within the analytical uncertainties, so may not be statistically significant.

4.2.4 Post-LCY pumices

The two intermediate post-LCY pumices in general lie in the stratovolcano trends for all trace elements, and as such their variations are not described further here. Fig. 4.7 shows spider diagrams for the trace element variations of the post-LCY rhyolites, the D2, F and I

rhyolites (in order of oldest to youngest). REE contents are in general intermediate between the values for the most evolved andesites and the LCY pumices (Fig. 4.3). There are subtle but statistically significant variations for REE abundances between these different pumices, with them all having very similar values for the LREEs. The trends diverge from each other with greater atomic number. The D2 pumices have the lowest abundances for the M- and HREEs for this group, and the F pumice the highest. The I rhyolite pumices have intermediate values. Eu anomalies values for the post-LCY pumices (Figs. 4.5, 4.7) are typically small (0.85-0.75), with values between those of the lower-K and high-K LCY pumices, with the F pumice having the closest to the large anomalies observed in the high-K LCY pumice (0.75 compared to 0.56-0.61).

The LILEs in the post-LCY rhyolites have most similar abundances and patterns on the spider diagrams to the lower-K LCY pumices (Fig. 4.7). They have moderate enrichments in the elements Cs-U, and the pattern on the spider diagram (Fig. 4.7) shows a weak saw-toothed pattern, with a minor relative enrichment in Ba. Compared to the lower-K LCY rhyolite, they have a slightly greater enrichments in Rb, Sr and Pb, and a greater depletion in Th. Between the different post-LCY rhyolites, for most elements the three pumices are alike. However, the D2 and F rhyolites have similar and slightly higher values for Cs and Ba than the I rhyolite, while the F and I rhyolites are more similar for Th and U.

The HFSEs abundances for the post-LCY rhyolites are typically intermediate between the lower-K and high-K LCY rhyolites. The main exceptions to this are Zr, Hf and Ti, which have comparatively elevated values. However, values for Zr/Hf are like those of the lower-K LCY rhyolites (Fig. 4.3). In the post-LCY rhyolite group, most HFSEs have similar abundances in each rhyolite.

4.2.5 Intrusive rocks

The sampled intrusive rocks have highly variable compositions and do not typically follow similar trends, although they often resemble those of the high-K LCY. LILE enrichments are highly variable between the three analysed intrusive rocks, with enrichment in Rb and Cs like the high-K LCY rhyolite. Ba shows the greatest depletions of the high-SiO₂ rocks. U and Th are most like those of the lower-K LCY and post-LCY rhyolites, which are depleted relative to the high-K LCY rhyolite. The exception is the leucogranite, which is highly enriched in both these elements (Fig. 4.8).

These rocks show the typical depletions in Nb and Ta (Fig. 4.8) that are expected of igneous rocks formed at convergent margins. For most of the other HFSEs, their abundances resemble those of the rhyolites. The major exceptions are Zr and Hf, which both show much more significant depletions than those in the rhyolites.

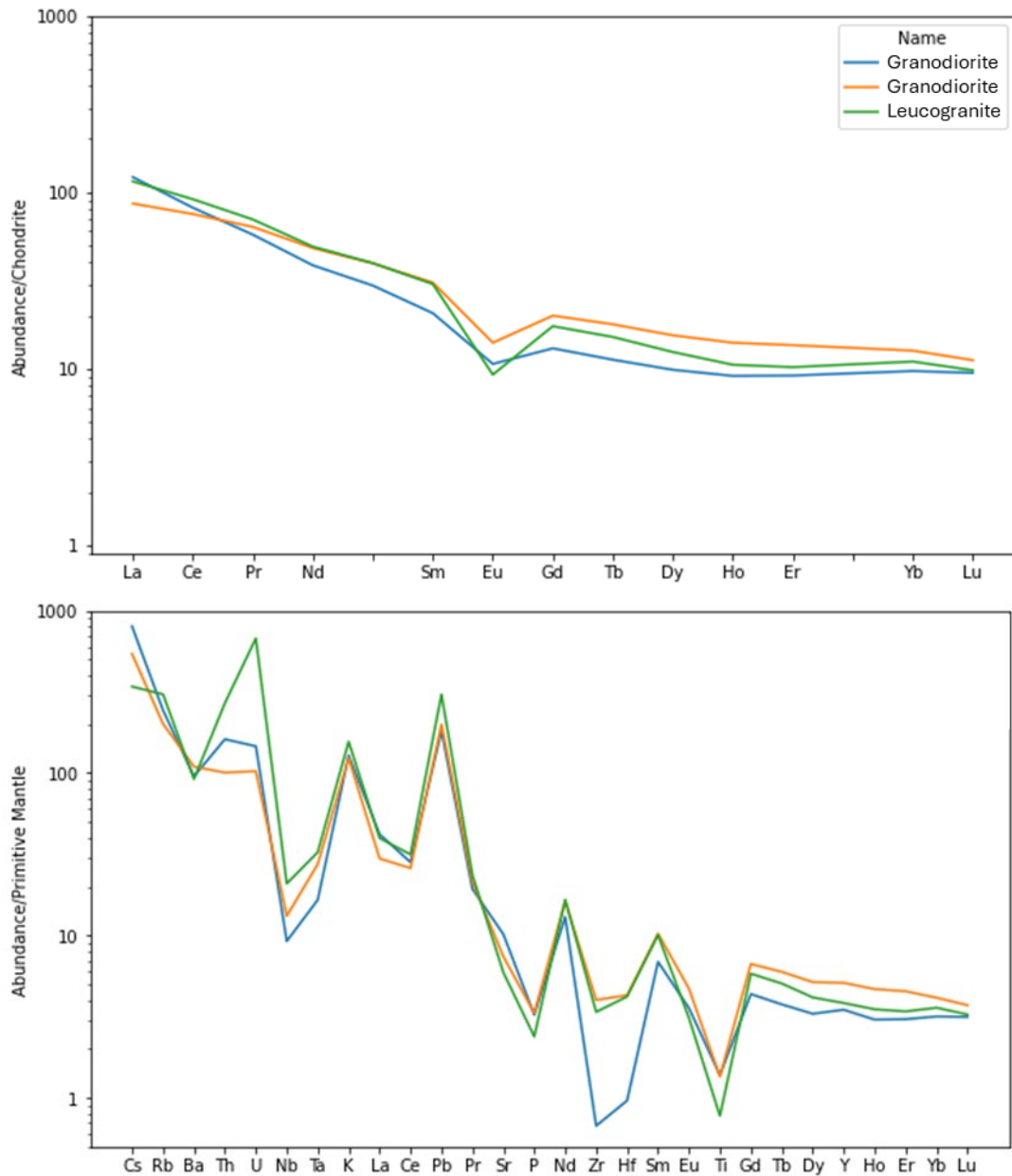


Figure 4.8. Spider diagrams of A) REE variations; and B) trace element variations for the intrusive rocks of the AVC. Normalising values from Sun & McDonough (1989).

4.3 Whole rock radiogenic isotope results

4.3.1 Stratovolcano lavas

Radiogenic isotope data and uncertainties are presented in Appendix A.3. For all analysed isotope ratios, the stratovolcano lavas can be broadly grouped into pre- and post-LCY

distributions. The pre-LCY lavas generally have higher values for $^{87}\text{Sr}/^{86}\text{Sr}$ and all analysed Pb isotope ratios and lower values for $^{143}\text{Nd}/^{144}\text{Nd}$ and $^{176}\text{Hf}/^{177}\text{Hf}$ (Fig. 4.9) compared to the post-LCY lavas. There is no correlation for any isotope ratio with SiO_2 (Fig. 4.9).

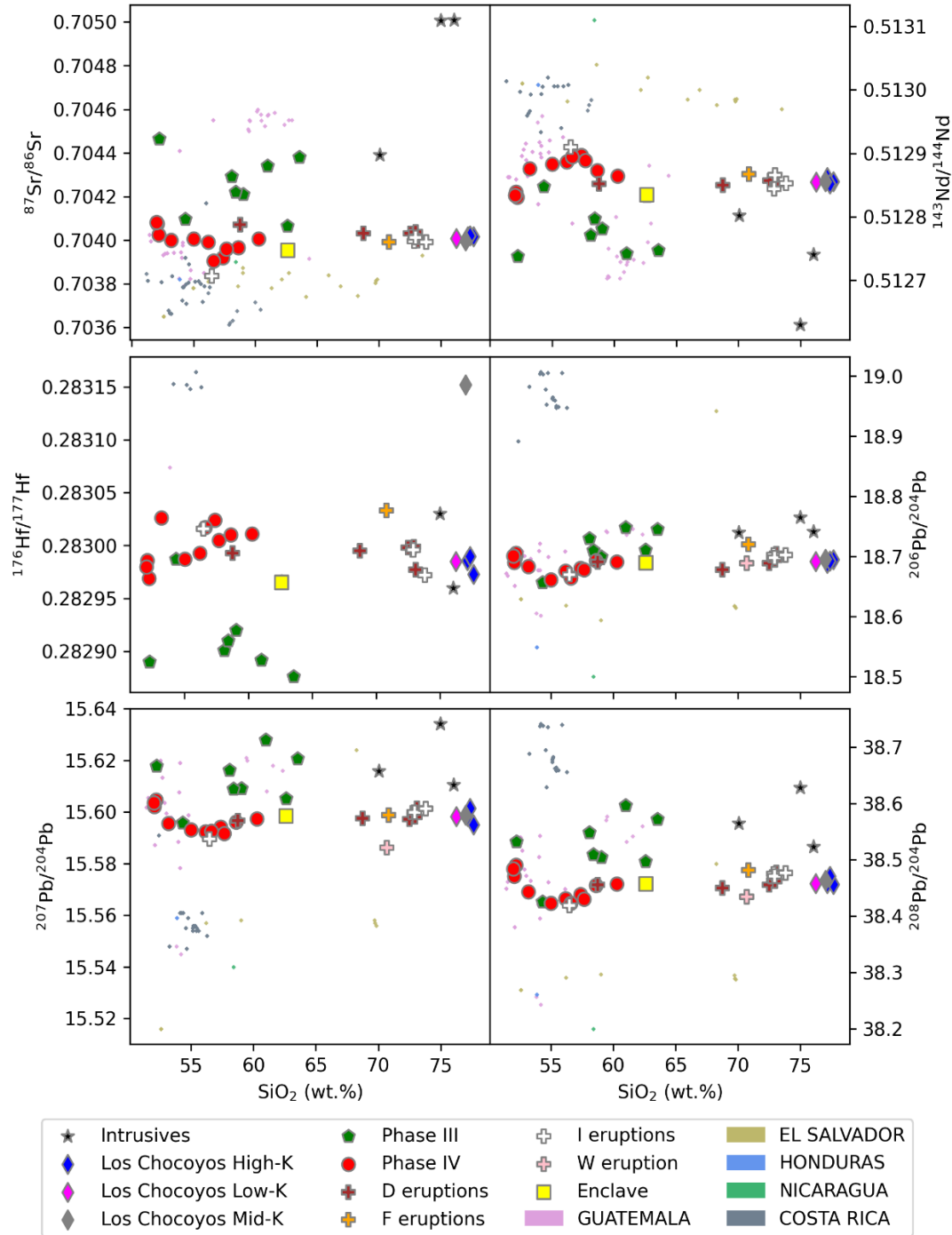


Figure 4.9. Plots of radiogenic isotopes against SiO_2 . Note in Hf isotope space, the medium-K LCY pumice has anomalously high values. Analytical uncertainties (2 s.e.) are smaller than the symbol sizes.

The isotope values appear to be geographically controlled, with variations linked to the position of the samples relative to the trench. The stratovolcanoes furthest from the trench

(Volcáns Tecolote and San Marcos) are distinctly grouped in isotope space compared to samples from Volcáns Paquisis, San Pedro, Tolimán and Atitlán, well outside the analytical uncertainties (Fig. 4.9; 4.10). The exceptions are the most mafic samples from Volcán Atitlán, which do not follow the geographical trend. Despite being the closest stratovolcano to the trench, these lavas have isotopic signatures roughly intermediate between the lavas erupted from the pre-LCY stratovolcanoes and those from the other post-LCY stratovolcanoes.

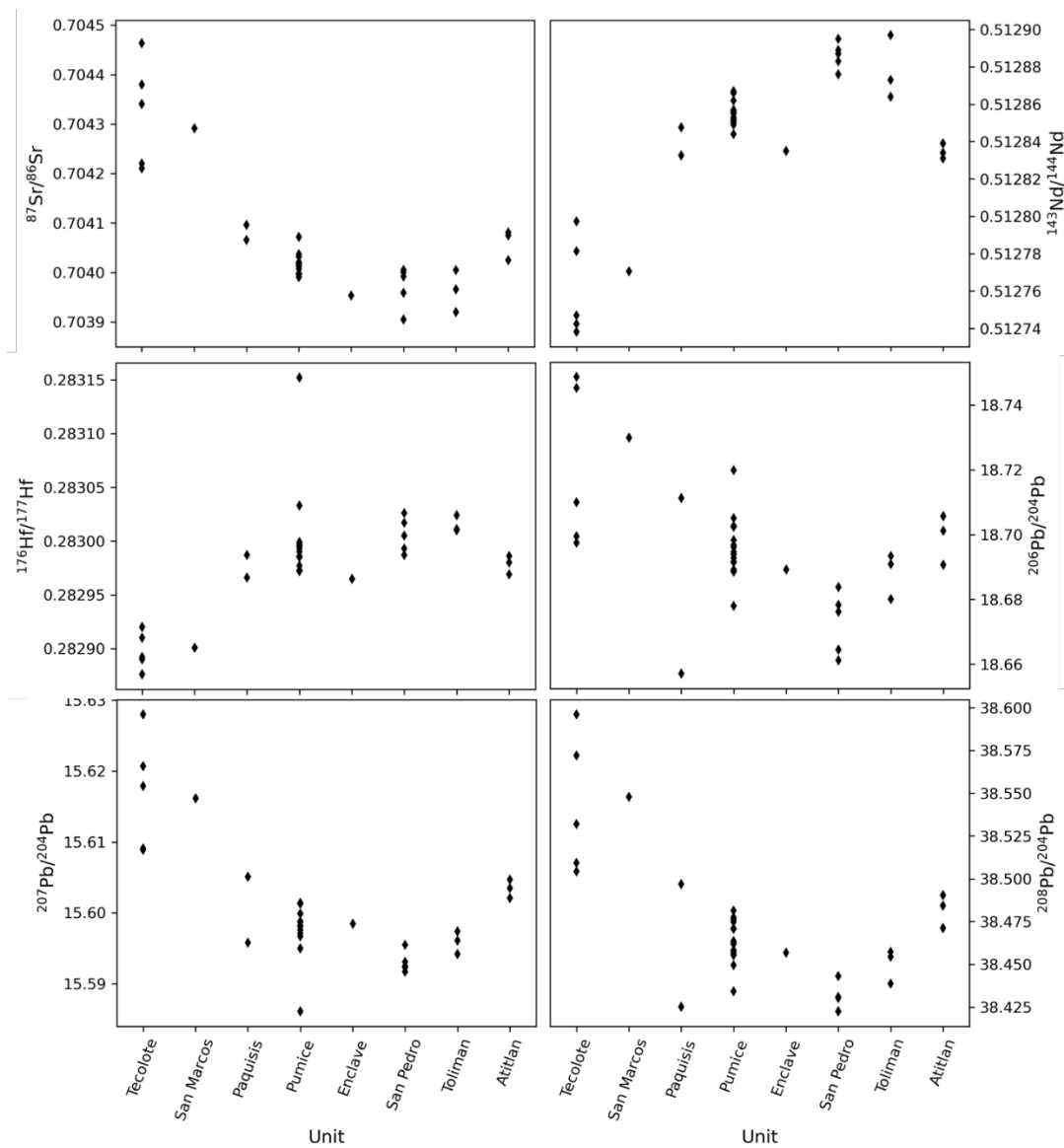


Figure 4.10. Strip plots for the radiogenic isotopes of the different volcanoes of the AVC, as well as the pumice samples and the enclave. The stratovolcano strips are organised in age order with decreasing age from left to right. In general, the position of the strips also records increasing closeness to the trench from left to right, with the two northernmost stratovolcanoes (Volcáns Tecolote and San Marcos) furthest left.

This trend is most significantly apparent when comparing the most mafic materials of the AVC, the basaltic andesites of Volcán Atitlán (sample Ati501_05a-c) and the Cerro las Minas cinder cone from Volcán Tecolote (sample Ati427_11). They both have the same SiO₂ content (52.0-52.2 wt.%) and very similar trace element values (section 4.2.1), however very different values for all radiogenic isotopes (Fig. 4.9). In this figure, the Cerro las Minas sample is the green pentagon while the samples from Volcán Atitlán are red circles.

Bivariate diagrams of the different isotope ratio (e.g. $^{87}\text{Sr}/^{86}\text{Sr}$ vs. $^{143}\text{Nd}/^{144}\text{Nd}$, $^{176}\text{Hf}/^{177}\text{Hf}$ vs. $^{143}\text{Nd}/^{144}\text{Nd}$; Figs. 4.11-4.12) show that most of the lavas lie on linear trends, although two lavas from the pre-LCY lavas fall off these trends in Pb isotope space (Fig. 4.13).

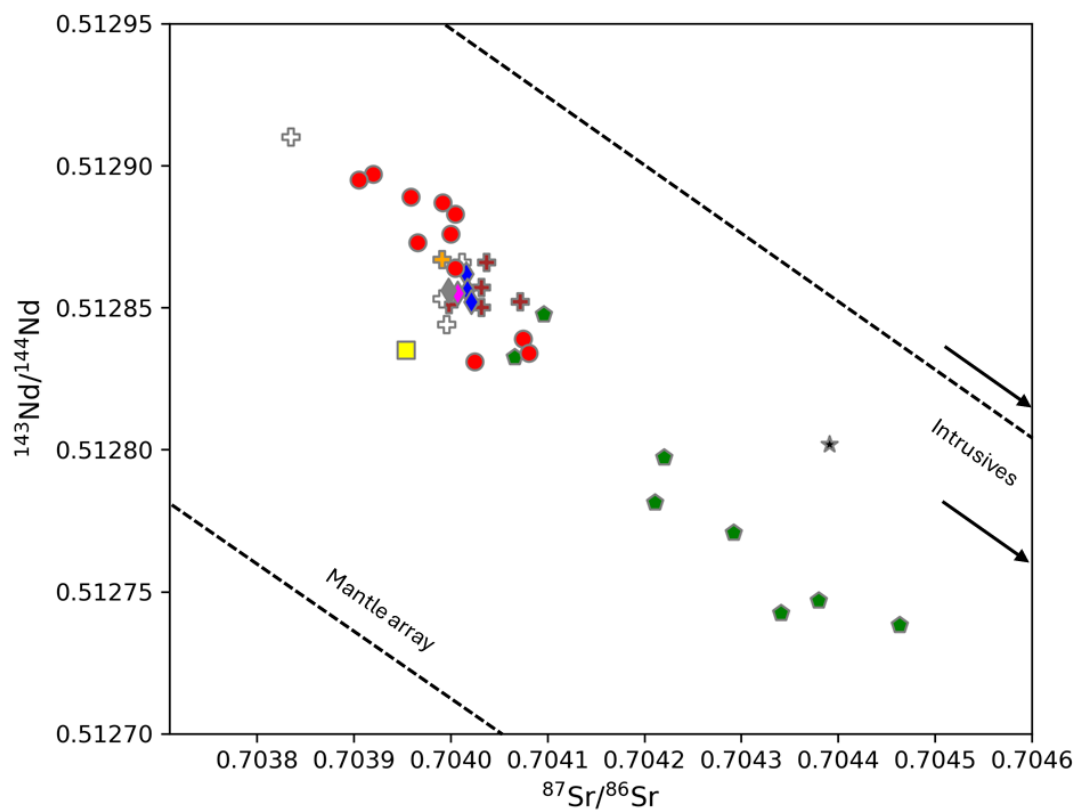


Figure 4.11. $^{87}\text{Sr}/^{86}\text{Sr}$ vs. $^{143}\text{Nd}/^{144}\text{Nd}$ for AVC rocks. AVC volcanic materials all fall on a linear trend parallel to and within the mantle array (dashed lines). Arrows on the right of the image point towards two intrusive samples. The enclave (yellow square) falls slightly off the trend formed by the other volcanic materials. Analytical uncertainties are smaller than the symbol sizes. Mantle array after DePaolo & Wasserburg (1979)

While radiogenic isotope data for the rest of the CAVA is relatively sparse (predominantly being rocks with SiO₂ <65 wt.% and most rocks having been analysed only for $^{87}\text{Sr}/^{86}\text{Sr}$ and $^{143}\text{Nd}/^{144}\text{Nd}$), some basic comparisons can be made. The northern pre-LCY lavas are the most radiogenic of all CAVA samples except those from Volcán Tacana. Otherwise, the post-LCY lavas resemble the rest of the published Guatemalan lavas (Fig. 4.9).

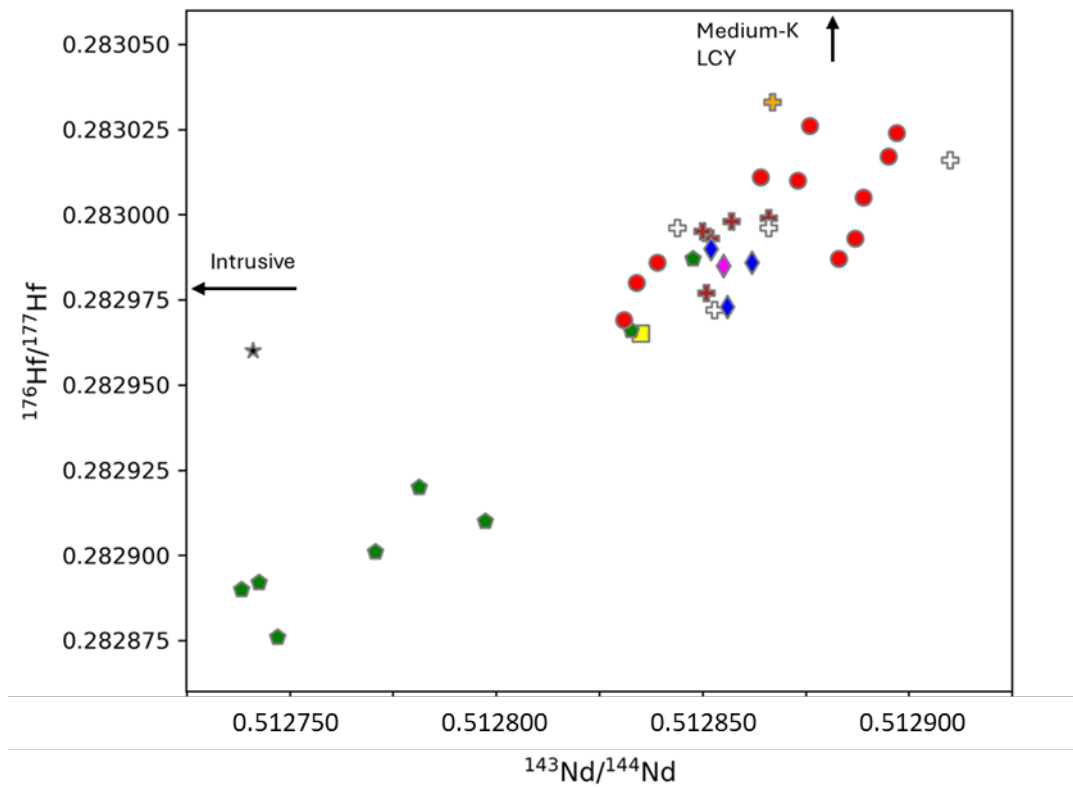
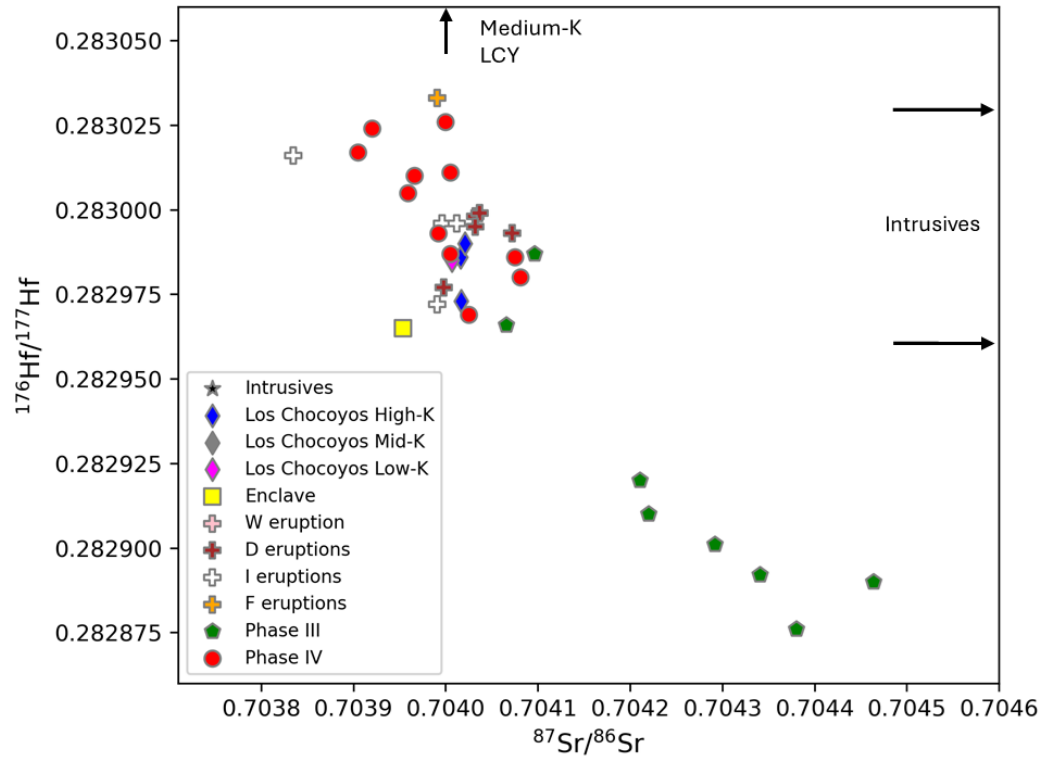


Figure 4.12. Plots of $^{87}\text{Sr}/^{86}\text{Sr}$ and $^{143}\text{Nd}/^{144}\text{Nd}$ against $^{176}\text{Hf}/^{177}\text{Hf}$. The volcanic material of the AVC forms a roughly linear trend in both plots, while the granitoid intrusives plot outside of this trend, indicated by the black arrows. The medium-K LCY rhyolite has anomalously high values for $^{176}\text{Hf}/^{177}\text{Hf}$ and has been cut off, its position again indicated by a black arrow. Analytical uncertainties are smaller than the symbol sizes.

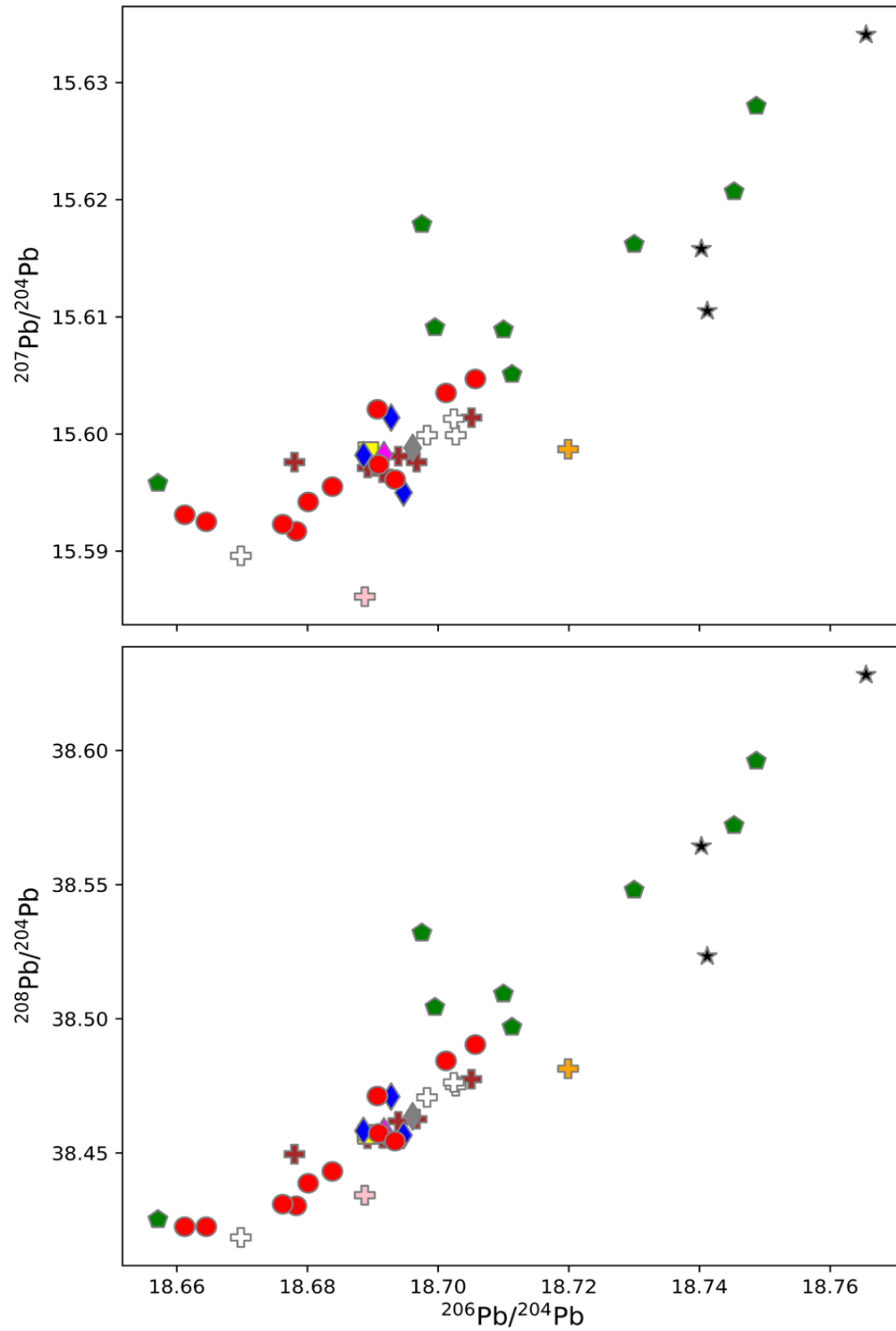


Fig. 4.13. Upper panel uranogenic lower panel thorogenic Pb isotope correlation diagrams. These samples all fall on linear trends for both ratios. One pre-LCY sample has the lowest value for each ratio and lies on the bottom left of both plots, (Figs. 4.9, 4.11 and 4.12). In Pb isotope space, the F pumice sample (orange plus) also lies off the main trend line. Analytical uncertainties (2 s.e.) are smaller than the symbol sizes.

4.3.2 Recharge magma

The enclave also has intermediate isotope ratio values that are like those of the rhyolite pumices. However, it plots just outside the linear trends for $^{87}\text{Sr}/^{86}\text{Sr}$ vs. $^{143}\text{Nd}/^{144}\text{Nd}$ and $^{176}\text{Hf}/^{177}\text{Hf}$ vs. $^{87}\text{Sr}/^{86}\text{Sr}$ (Figs. 4.11 and 4.12), and therefore its correlation between $^{87}\text{Sr}/^{86}\text{Sr}$ and the other isotope ratios is weaker. Compared to the rhyolite pumices, the enclave lies outside of the pumice range for Sr, Nd and Hf isotope ratios but lies within the range for the Pb isotopes ($^{87}\text{Sr}/^{86}\text{Sr} = 0.70395$ vs. $0.70398\text{--}0.70404$, $^{143}\text{Nd}/^{144}\text{Nd} = 0.51284$ vs. $0.51285\text{--}0.51287$, $^{176}\text{Hf}/^{177}\text{Hf} = 0.28297$ vs. $0.28297\text{--}0.28299$; Fig. 4.9).

4.3.3 The LCY pumices

For all isotope ratios, the LCY pumices lie between the pre- and post-LCY lavas, although typically having values closer to the post-LCY lavas (Figs. 4.9-4.13). Despite the large variations in major and trace element composition between the high- and lower-K LCY rhyolites (sections 4.1.3 and 4.2.3), they have very similar radiogenic isotope ratios. The only exception is for $^{176}\text{Hf}/^{177}\text{Hf}$, where the medium-K sample has an anomalously high value (0.28315 compared to $0.28303\text{--}0.28288$ for the rest of the volcanic samples).

4.3.4 Post-LCY pumices

For almost all analysed isotope ratios, the more mafic clasts (D1 and I1) fall within the range of values shown by the post-LCY stratovolcanoes (Fig. 4.9). The D1 pumice has an intermediate composition for all ratios, like those analysed from the D2 pumices and generally having intermediate values closer to the AVC's averages. The I1 scoria, on the other hand, is more of an outlier and plots more towards the limits of the range of the post-LCY stratovolcano lava compositions. It has the lowest measured values of $^{87}\text{Sr}/^{86}\text{Sr}$, $^{207}\text{Pb}/^{204}\text{Pb}$ and $^{208}\text{Pb}/^{204}\text{Pb}$, and the highest $^{143}\text{Nd}/^{144}\text{Nd}$ value, of all AVC material.

The post-LCY rhyolite pumices have similar isotope ratios to the LCY pumices (intermediate between the two groups of stratovolcano lavas), although they have a wider range of values and the spread is greater than the analytical uncertainty (Figs. 4.9-4.13). There is one exception: the analysed F pumices have values that lie well outside the range for the other rhyolite pumices for all isotope ratios except $^{87}\text{Sr}/^{86}\text{Sr}$ and $^{207}\text{Pb}/^{204}\text{Pb}$. It does not show systematic variation; for $^{143}\text{Nd}/^{144}\text{Nd}$ and $^{176}\text{Hf}/^{177}\text{Hf}$ it has more similar values to the post-LCY stratovolcano lavas, while for the two other Pb ratios it is more similar to the pre-LCY stratovolcano lavas.

4.3.5 Intrusive suite

The granitoid intrusive rocks do not fall on the same trend of the volcanic rocks, and do not cluster systematically together (Figs. 4.9-4.13). They tend to have higher values of the Pb isotope ratios and $^{87}\text{Sr}/^{86}\text{Sr}$ and lower values for $^{143}\text{Nd}/^{144}\text{Nd}$ (Fig. 4.9). These samples behave different for $^{176}\text{Hf}/^{177}\text{Hf}$ (although one sample, Ati426_01, returned a null result for Hf isotopes). For this ratio they lie close to the range of the rhyolite pumices (excluding the anomalously high medium-K LCY pumice) and have scattered values, with different samples having values higher, lower, or within the range of these samples (Fig. 4.9).

4.4 Glass compositions

Glass compositions were analysed by EPMA from pumice matrices, melt inclusions hosted by minerals in the stratovolcano lavas (described in section 3.2.1), stratovolcano anteliths (Fig. 3.13), and stratovolcano lava groundmass. Analytical uncertainties are presented in Appendix B.1, and the compositions are presented in Electronic Appendix II.

4.4.1 Major elements

4.4.1.1 Rhyolite pumice matrix glasses

To account for the influence of crystal content on the whole rock chemistry of the pumices, the matrix glass compositions for the different pumices (compositions normalised to 100 wt.%) are compared in Fig. 4.14. This is most important for the post-LCY pumices due to their large range of crystallinities compared to the LCY pumices that have a more modest range from 3.0 to 10 vol.%. The results for each oxide have a relatively narrow distribution for most eruption units, with a typical variation of ~ 1.0 wt.% in SiO_2 (most likely accounted for by analytical variability) and mostly show horizontal trends for the major oxides (except for weak negative correlations for CaO and Na_2O and a stronger negative correlation for Al_2O_3 . These negative correlations are most likely accounted for by the normalisation of the analyses to 100%)

There are broad overlaps between different degrees of evolution for pumices glass compositions (using SiO_2 as a proxy). The D2 and I pumices are the least evolved (75.0-76.0, average 75.6 ± 0.20 and 75.0-76.6, average 75.6 ± 0.5 wt.% SiO_2 , respectively). The low-K and high-K LCY pumices have the next highest ranges (76.3-77.6, average 76.7 ± 0.9 and 76.6-77.6, average 77.2 ± 0.2 wt.% SiO_2 , respectively), followed by the medium-K LCY and F pumices (77.0-77.8, average 77.6 ± 0.2 and 76.9-77.7, average 77.5 ± 0.2 wt.% SiO_2 ,

respectively). Averages are shown with one standard deviation from the mean. However, the published glass compositions for the W pumices (Cisneros de León et al., 2021a) extend to the highest SiO₂ compositions (77.2–78.0, average 77.6 ± 0.2 wt.% SiO₂).

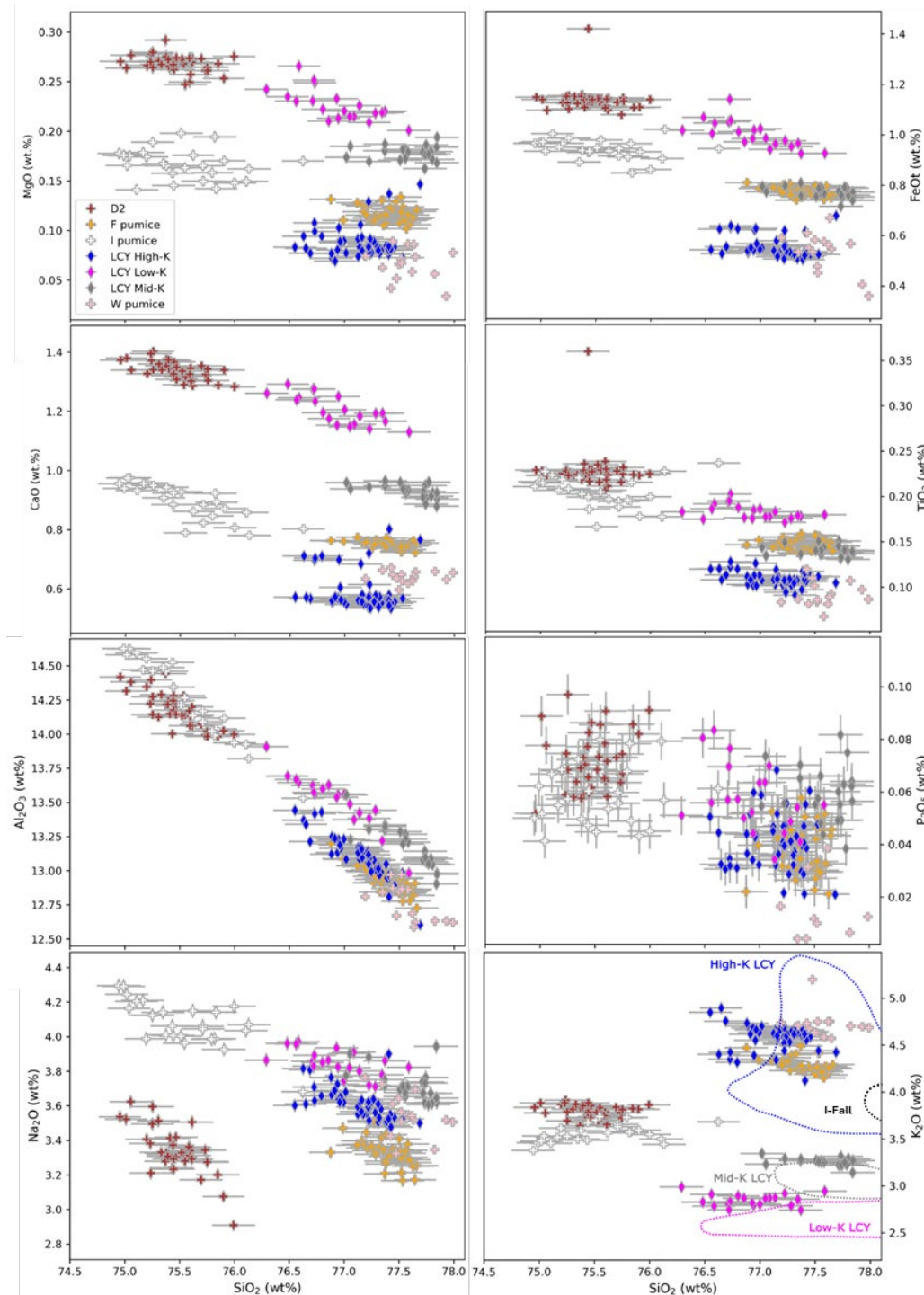


Figure 4.14. Matrix glass Harker diagrams for the rhyolite pumices of the AVC. Included for comparison are the W pumice glass composition from Cisneros de León et al. (2021a). Overlain on the K₂O vs. SiO₂ plot are also the LCY and I glass shard composition fields from the same publication – they did not differentiate the medium- and low-K LCY pumices but their distinct groupings have been outlined. Error bars are 1 s.d.

The glass compositions from the various rhyolites units have similar MgO, FeOt, CaO and TiO₂ concentrations (Fig. 4.14). For these oxides, the D2 pumice typically has the highest

concentration, followed by the low-K LCY pumice. The I and medium-K LCY pumices typically have intermediate values for these elements, while the F pumice has similar or lower concentrations to these two units. Finally the low-K LCY and W pumices have the lowest values for these oxides.

Al_2O_3 shows a strong negative correlation with SiO_2 for all rhyolite glasses, however this correlation is most likely due to SiO_2 variability in the analyses. The D2 and I pumices have similar Al_2O_3 contents. For the higher SiO_2 pumices, there are two separate trends, one formed of the low-K and medium-K LCY pumices with higher Al_2O_3 values, and the other formed of the high-K LCY, F and W pumices with lower Al_2O_3 . Na_2O and K_2O contents of the LCY pumices show the same trends that are evident in the whole rock analyses (Fig. 4.2), i.e., samples with higher K_2O typically have lower Na_2O and *vice versa*, although for Na_2O these differences are close to the analytical uncertainties of the measurements. The non-LCY AVC pumices do not strictly follow this trend. For K_2O , the post-LCY pumices plot between the medium- and high-K LCY pumices with values $\text{I} < \text{D2} < \text{F}$. The pre-LCY W pumice instead has greater or equal K_2O contents than the high-K LCY pumice.

Na_2O shows a weak negative correlation with SiO_2 for all the rhyolite glasses. Variations between the LCY pumices are closer than the differences for K_2O . The F and D2 pumices have similar concentrations for Na_2O , while the I pumice has the highest values. The W pumice resembles the high-K LCY pumice but with more scatter. Variations in P_2O_5 are more difficult to determine due to the significant amount of scatter in the analyses, and these variations are close to the analytical uncertainties of the measurements so may not be statistically significant. In general, pumice units with higher SiO_2 have lower P_2O_5 .

4.4.1.2 Post-LCY intermediate tephra matrix glasses

The I1 basaltic andesite scoria and the D1 andesitic pumice have somewhat comparable matrix glass compositions. Matrix glasses in both samples are dacites with intermediate K_2O and high Na_2O contents (Fig. 4.15). This is especially unusual for the D1 pumice, as it has very low whole rock Na_2O (3.1 wt.%, the lowest of any rock analysed; Fig. 4.2). The D1 pumice also has elevated Al_2O_3 contents in both its whole rock composition and in the analysed glasses. Curiously, these glasses have very high P_2O_5 compared to the stratovolcano lavas (stratovolcano P_2O_5 is 0.07-0.23 wt.%), and in the I1 scoria they are similar to the analysed enclave (enclave P_2O_5 = 0.35 wt.%).

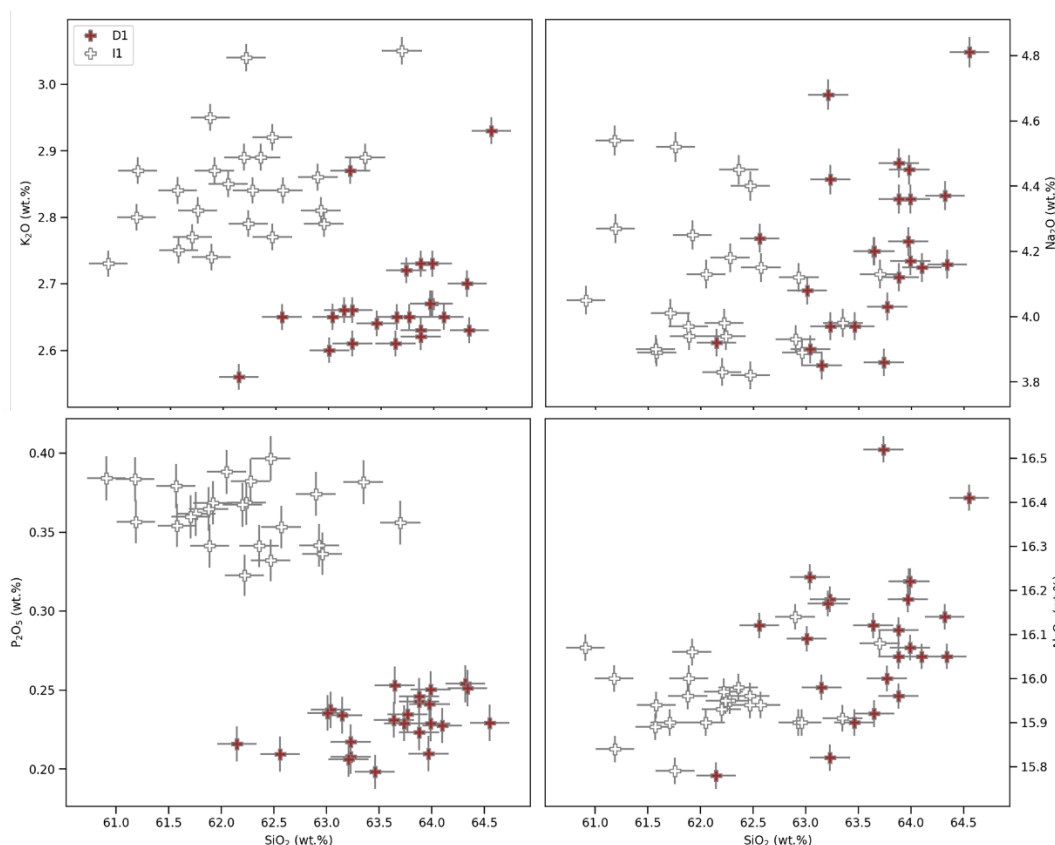


Figure 4.15. Matrix glass compositions for the two intermediate composition clasts of the D and I eruption sequences. Error bars are 1 s.d.

4.4.1.3 Stratovolcano hosted glass

Rhyolite melt inclusions are common in clinopyroxene and orthopyroxene phenocrysts in the stratovolcano rocks. Figure 4.16 compares the major element composition variations of melt inclusions in pyroxenes, as well as glass found in the groundmass, in interstitial spaces in glomerocrysts and in larger anteliths.

The pyroxene-hosted melt inclusions are broadly similar with compositions between 68 and 79 wt.% SiO_2 . Most of the clinopyroxene melts cluster around 73-78 wt.% and tend to have smaller distributions, while the orthopyroxene-hosted melts are more broadly distributed. Aside from the differences in SiO_2 , the melt inclusions have similar ranges for most other major oxides, with orthopyroxene-hosted melts having slightly higher P_2O_5 and FeO(T) . TiO_2 in orthopyroxene-hosted melt inclusions shows two potential groupings, with some similar compositions to the clinopyroxene-hosted melts and the others extending to higher TiO_2 concentrations than that found in clinopyroxene-hosted inclusions.

For inclusions in both pyroxene types, CaO , Al_2O_3 and Na_2O all have moderate negative correlations with SiO_2 (likely due to the normalisation process) whereas K_2O has a positive

correlation. The other major oxides do not show a significant correlation with SiO_2 , although this may be due to low concentrations of these oxides (MgO , P_2O_5 and TiO_2 all <1.0 wt.% and <2.0 wt.% FeO(T)).

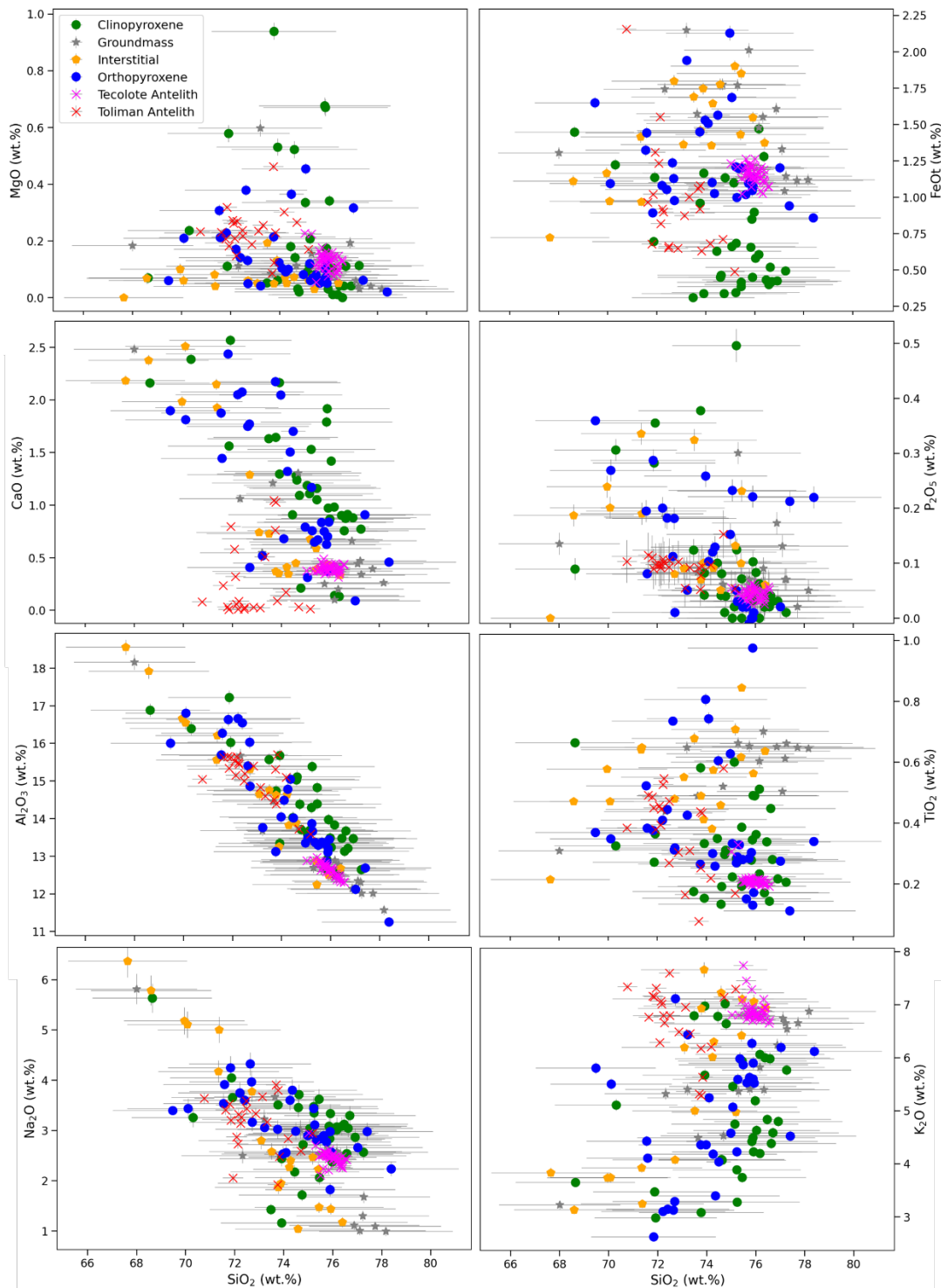


Figure. 4.16. Major element oxide results for rhyolite glass found in the stratovolcano lavas, divided by host phase/location. Note the tight clustering of the Volcán Tecolote antelith-hosted glass. Error bars are 1 s.d.

Antelith-hosted melts were analysed from two different hosts, one from melt inclusions in orthopyroxenes in a Volcán Tolimán antelith (sample Ati503_06), and the other from the

interstitial glass in a Volcán Tecolote antelith (sample Ati427_08a). Significant differences exist between these two groups of analyses. The Volcán Tolimán analyses show a much greater amount of scatter compared to the Volcán Tecolote glass. This may be due to a variety of post-entrapment processes that could impact the original composition of the melts. Care was taken to ensure that all the analysis spots did not impact the host crystal or any interior secondary minerals, and that any that showed signs of having done so were removed. Nonetheless it may still be possible that some of the scatter could also result from misaligned analyses. The tight composition grouping of the Volcán Tecolote glass is likely due to the high melt volume in the antelith, resulting in interconnection of melt pockets and homogenisation of compositions.

The Volcán Tolimán glasses are slightly less evolved than the Volcán Tecolote melts (70.7-75.2 compared to 75.4-76.6 wt.% SiO_2). The Volcán Tecolote glasses are also some of the most evolved of any lava-hosted rhyolite glass observed in this study. In general, the Volcán Tolimán analyses have higher MgO, P_2O_5 , TiO_2 and Na_2O contents. Al_2O_3 also shows higher values, and this may result from the lower degree of evolution of the Volcán Tolimán melts rather than a different petrogenetic process (Fig. 4.16). The strong negative correlation between SiO_2 and Al_2O_3 shown by all melts is again likely the result of analytical uncertainties. FeO(T) and CaO contents are lower in the Volcán Tolimán glasses, while K_2O contents are broadly similar and much higher than the other rhyolite glasses (>6.0 wt.%). CaO compositions for Volcán Tolimán are also unusually low compared to the general trend (Fig. 4.16). Due to their highly potassic nature, these glasses are termed very-high potassium melts (VHKMs). Numerous melt inclusions within the stratovolcano lavas have similarly elevated K_2O contents.

Glass in the groundmasses of lavas from Volcáns Tolimán and Tecolote has a similar range of compositions compared to glass found in interstitial spaces in glomerocrysts in the stratovolcano lavas (Fig. 4.16). These have the widest range of compositions (67.6-78.2 wt.% SiO_2) of all the stratovolcano-hosted glass. They have no obvious correlations with SiO_2 for MgO, FeO(T) and P_2O_5 , have a negative correlation for CaO, Al_2O_3 and Na_2O (again most likely a result of the normalisation to 100%), and have positive correlations for TiO_2 and K_2O . There is a slight divergence in K_2O contents at higher SiO_2 contents, with some interstitial glass having relative enrichments compared to the groundmass glasses.

Note on the quality of stratovolcano-hosted rhyolite glass analyses:

A large amount of scatter is present in the major element analyses of melt inclusions and in the interstitial glasses. This is especially obvious in CaO, Na₂O and K₂O, where the ranges of concentrations are relatively large. The cause of these variations is not obvious but could be due to accidental inclusion of the host mineral phase in the spot and/or post entrapment crystallisation of the glass. Thus, these large variations in composition should be considered when discussing their origins.

4.4.2 Trace elements

Trace elements were acquired only on melt inclusions and antelith-hosted rhyolite glasses using LA-ICP-MS (section 2.4.3). Analytical procedures and uncertainties are presented in Appendix B.2, while the full data are presented in Electronic Appendix II.

Melt inclusion's trace element concentrations are similarly highly variable to the major elements. They show wide spreads for their compositions, and do not appear to follow any trends based on melt host phase (Fig. 4.17), with a minor exception in the M- and HREEs, where the clinopyroxene hosted melt inclusions have slightly greater concentrations than those in glasses hosted in other phases. This large variation and the relatively smaller number of points that passed the checks (i.e., did not have elevated values for elements like MgO/CaO that would imply analysis of the host crystal) means that assigning any trends or relationships to this data set is difficult.

In contrast to the melt inclusions, the trace element data collected from the anteliths do show more consistent trends, again similar to those observed in the major elements. These data points are more tightly grouped, and the groups of the two different anteliths are fairly similar to one another, with the caveat that the data points from Volcán Tolimán (sample Ati503_06) show a higher amount of scatter in their distribution (Fig. 4.17).

This scatter varies by element (Fig. 4.17). The scatter is quantified by the relative standard deviation (RSD) of the analysed points. For most elements, this scatter is either within the analytical uncertainties and so can simply be attributed to this or may simply be heterogeneities in the melt compositions. In the Volcán Tecolote antelith glass, scatter in most elements is typically low and the melt compositions were therefore fairly homogeneous (Figs. 4.16 and 4.17). Two notable exceptions are Ba and Sr. These elements have a large compositional ranges and high RSDs (Ba: 500-1100 ppm, 20.0; Sr: 12-35 ppm, 28.9, respectively). These ranges are much greater than their analytical uncertainties (Fig.

4.17) and therefore these variations are statistically significant. In comparison, the M- and HREEs have high RSDs, but their high analytical uncertainties likely mean that this scatter is not significant. This is further shown in Figure 4.18.

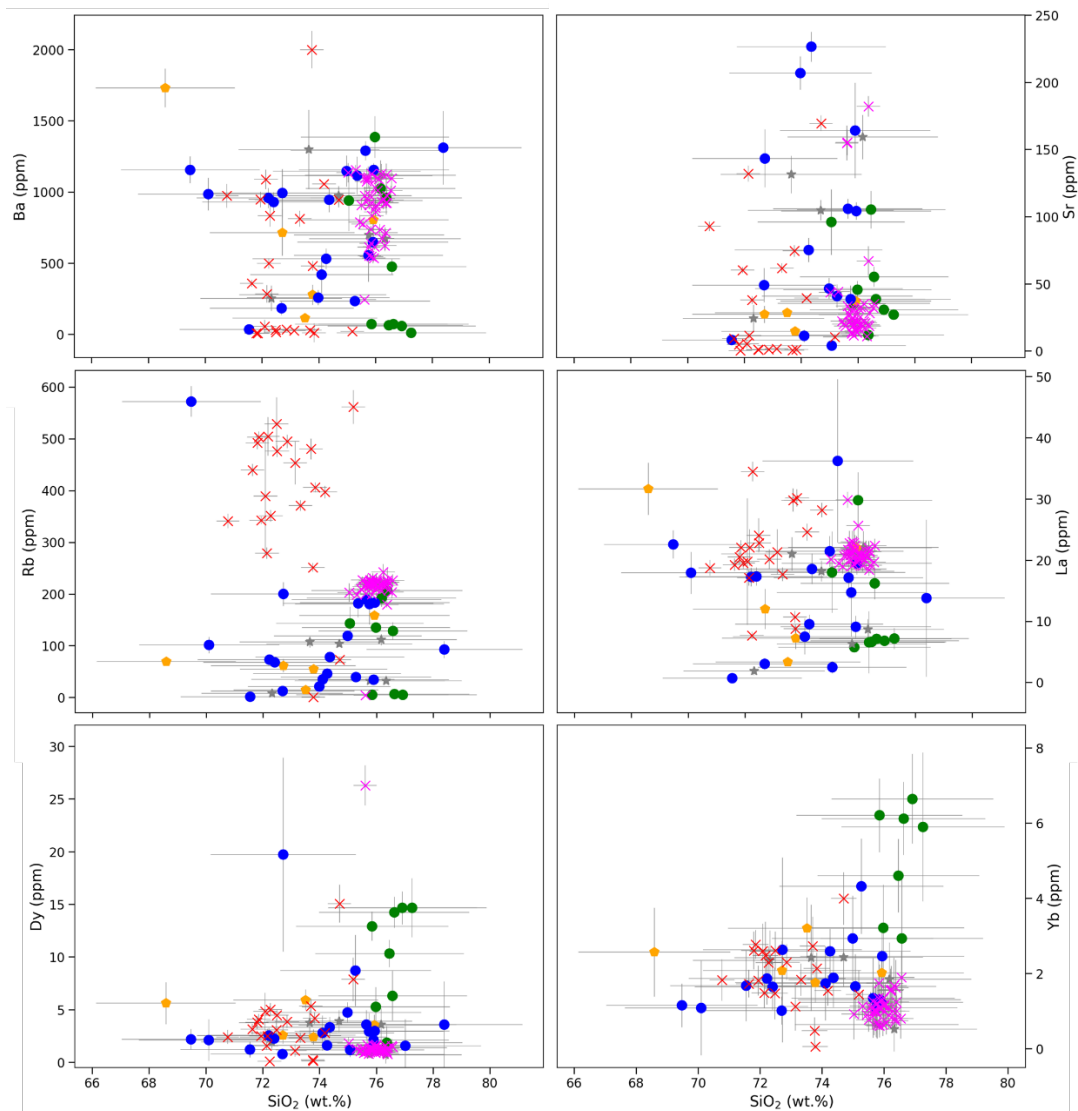


Figure 4.17. Trace element Harker diagrams for selected elements for the rhyolite glasses hosted by the AVC stratovolcano lavas. Vertical error bars are 2 s.e., while horizontal error bars are 1 s.d. Symbols as in Fig. 4.16.

The scatter in the M- to HREEs makes it difficult to determine precisely the shape of the REE slope. Calculated $[La/Yb]_N$ values are 8.0-20. Using the average values, the slope has a concave pattern with the greatest depletions in the MREEs (Fig. 4.18). Most of the analyses show a large negative Eu anomaly (0.5-0.13), with a few anomalously higher points.

These VHKM are highly enriched in the LILEs (e.g. Cs, Rb and Ba) and have a U-shaped pattern for the elements Cs-U on the spider diagram, resembling the high-K LCY rhyolite (Fig. 4.18). For the HFSEs, the analysed glasses mostly have ranges of abundances like those of the AVC rhyolite pumices, however the glasses are relatively enriched in Zr and Hf. The

REEs commonly have fairly flat slopes, with little or no depletion in the MREEs (Fig. 4.18), although the relatively large analytical uncertainties for these elements makes determining this to a high degree of accuracy impossible.

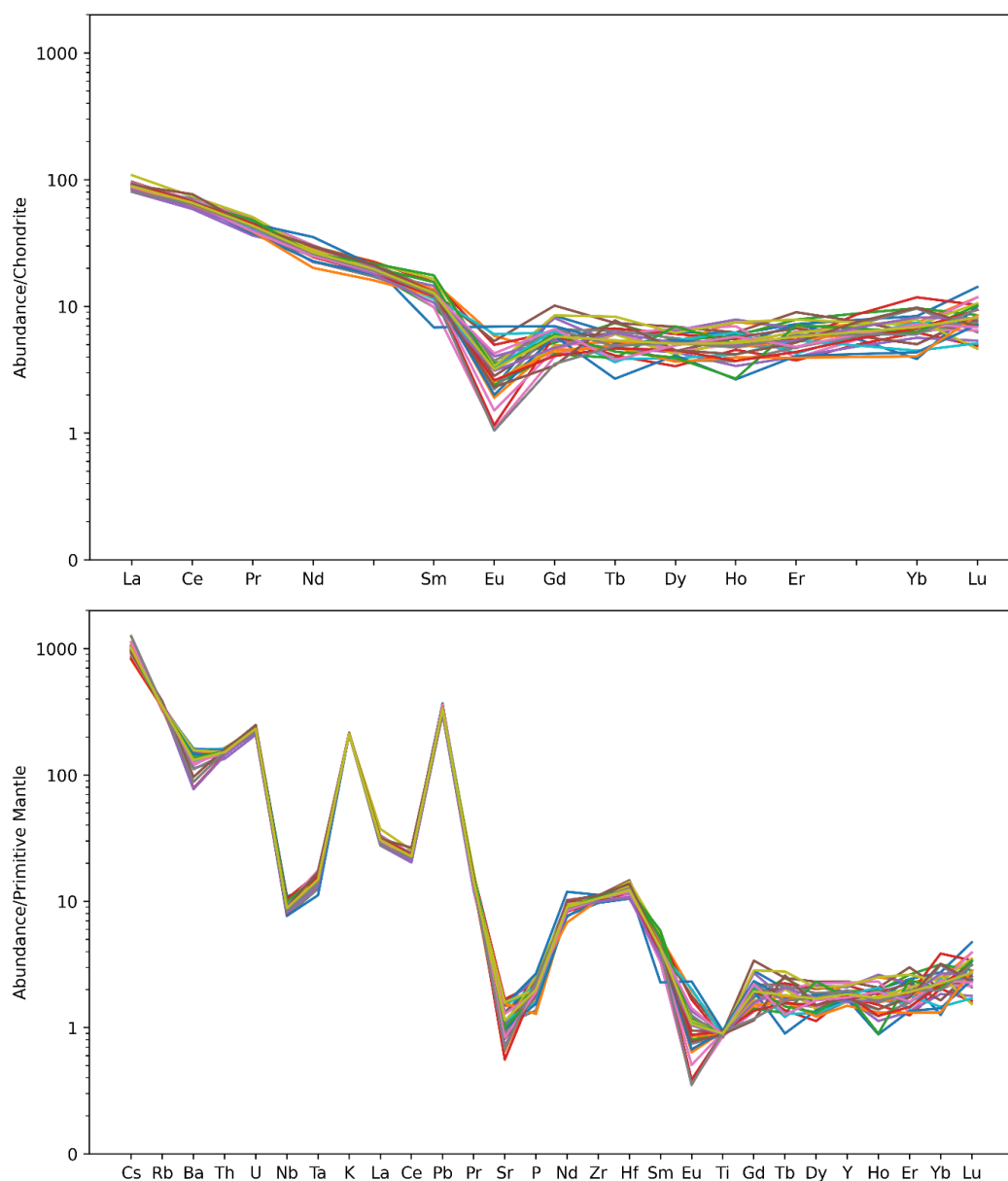


Figure 4.18. Spider diagrams of A) REE variations; and B) trace element variations for the VHKM of the Volcán Tecolote antelith. Because of spot-size restrictions, this is the only sample where it is possible to display all analysed trace elements. Significant variation is present in the analyses for some elements (Ba, Sr and the M- and HREEs in particular). Normalising values from Sun & McDonough (1989).

Chapter 5: Origin and evolution of the AVC magmas

The AVC contains a wide variety of compositionally distinct volcanic materials, from basaltic andesites to high-silica rhyolites, with significant chemical differences within these divisions. The occurrence of each rock-type is controlled both by the location of the volcano and the underlying magmatic system, as well as the different phases of activity. This chapter considers the petrology and geochemistry of these different magmas to propose mechanism(s) of formation and explains the causes of differences between the magmatic groups.

This chapter is split into sections which will discuss the different igneous materials described in Chapter 4: (1) the AVC stratovolcano lavas and their anteliths; (2) the recharge magmas; (3) the LCY pumices; and (4) the post-LCY pumices. Each section uses a combination of several datasets, including estimates for the intensive magmatic variables using various geothermometers, geobarometers and geohygrometers, together with analysis of groundmass and mineral textures, and numerical petrogenetic modelling.

5.1 Origin of the AVC stratovolcano suite

5.1.1 *The basaltic andesites*

5.1.1.1 *North-western CAVA basaltic andesite chemistry*

Along the Guatemalan segment of the CAVA arc-front (Fig. 1.1), the most common (and typically the most primitive) stratovolcano lavas are high-silica basalts to basaltic andesites (Heydolph et al., 2012; GEOROC, 2021). These have similar compositions to the most primitive samples analysed in this study (basaltic andesites from Cerro las Minas, sample Ati427_11, and samples Ati501_05a, Ati501_05b and Ati501_05c from Volcán Atitlán; Figs. 4.1-4.3). These magmas drive volcanism in this section of the arc, so it is important to understand their origin. Comparison between the AVC basaltic andesites and those from elsewhere in the arc reveals some important details.

The primitive AVC basaltic andesites have very similar major and trace element geochemistries (sections 4.1.1 and 4.2.1) that imply they have similar origins (i.e. from mantle-derived melts), but they have significantly different radiogenic isotope values (section 4.3.1) that require explanation. The northernmost basaltic andesite sample (Ati427_11 from the Cerro las Minas cinder cone on Volcán Tecolote) has the most radiogenic signature. Possible controls on the isotope values are numerous, and in this section, the best explanation for the observations will be explored.

Previously identified controls on the isotopic composition of the CAVA basaltic andesites are tied to variations in the following inputs from the various compositional endmembers of Carr et al. (1990): enriched mantle, modified mantle (created from depleted mantle by the addition of a small volume of sediment-derived fluid), and a crustal component. For the most part, the CAVA magmas are derived from mixtures of enriched and modified mantle which leads to an unusual positive correlation between $^{87}\text{Sr}/^{86}\text{Sr}$ and $^{143}\text{Nd}/^{144}\text{Nd}$ (Fig. 5.1), and variations in their inputs (tied to variations in subduction angle; section 1.3.1) leads to the striking along-strike geochemical variations that have been observed (section 1.3.3). Carr et al. (1990), however, identified that the Guatemalan volcanic front followed an isotopic trend that was independent of the rest of the arc which had a more typical negative correlation (Fig. 5.1). This trend leads towards a crustal component (CR in Fig. 5.1), suggesting that interaction with this component is the dominant control on the isotopic composition of Guatemalan arc magmas.

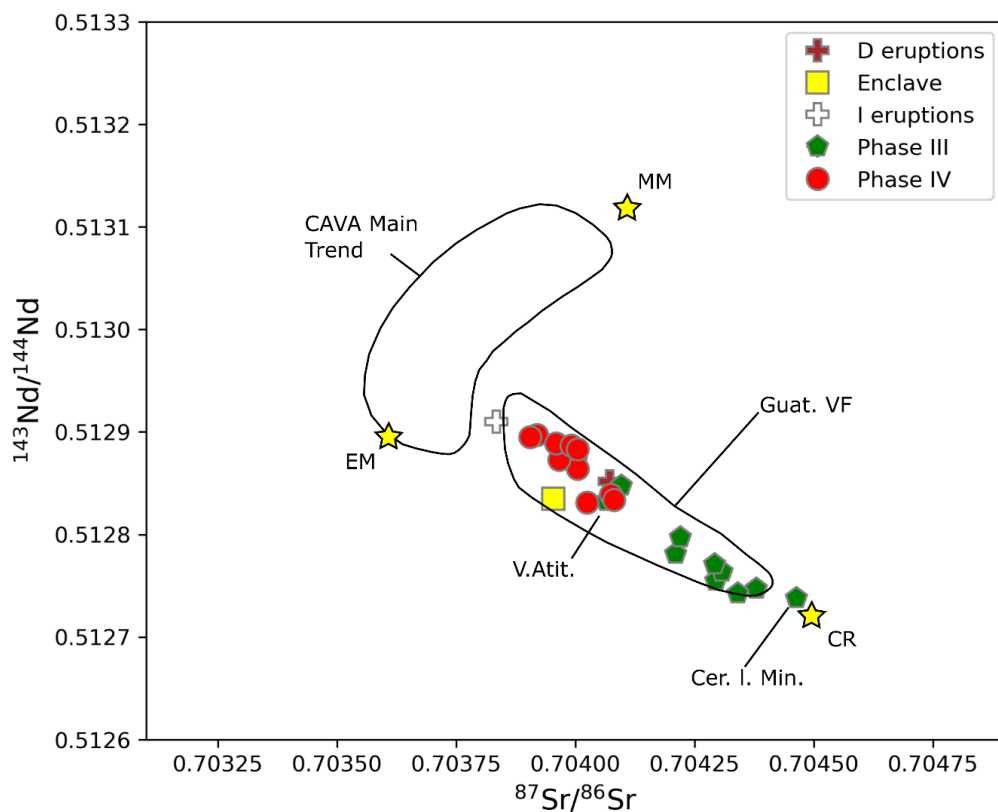


Figure 5.1. Plot of $^{87}\text{Sr}/^{86}\text{Sr}$ vs. $^{143}\text{Nd}/^{144}\text{Nd}$ for the AVC materials <66 wt.% SiO_2 . As there is no correlation with SiO_2 for these materials (Fig. 4.14), all of them have been included in the plot as it is assumed that they have not undergone significant changes to their isotopic signatures during their evolution. For comparison, the Cerro las Minas (Cer. I. Min.) and Volcán Atitlán (V. Atit.) samples are indicated. Also included in the plot are the published trend for the Guatemalan volcanic front (Guat. VF), the trend for the rest of the CAVA (CAVA Main Trend), and various mantle endmembers (yellow stars) as described by Carr et al. (1990): the enriched mantle (EM), modified mantle (MM), and the crust (CR). Uncertainties (2 s.e.) are smaller than the symbol sizes.

This is also shown by the S-shaped $^{87}\text{Sr}/^{86}\text{Sr}$ and n-shaped $^{143}\text{Nd}/^{144}\text{Nd}$ curves when plotted against distance along the arc (Fig. 5.2), showing that a different mechanism controls isotope compositions in the northwestern part of the arc. The AVC samples in this study lie within the field shown in Fig. 5.1, suggesting that their isotopic variation was similarly controlled by variable inputs from a crustal component. The Guatemala lavas likely obtained these signatures in the lower crust (Jicha et al., 2010; Singer et al., 2011, 2013; Heydolph et al., 2012). This crustal component has been proposed to be either obducted MORB (Jicha et al., 2010; Singer et al., 2011, 2013) or pyroxenite cumulates (Heydolph et al., 2012). The mantle wedge therefore appears to have little influence over the Guatemalan arc magmas in comparison to those of the rest of the CAVA. If there were variations in the influence of the mantle acting in the AVC, then trace element ratios that have been used to track these (e.g., Ba/La and U/Th (Rüpke et al., 2002; Carr et al., 2003, 2014)) would show differences between the pre- and post-LCY stratovolcano lavas. This is not the case (Fig. 5.2).

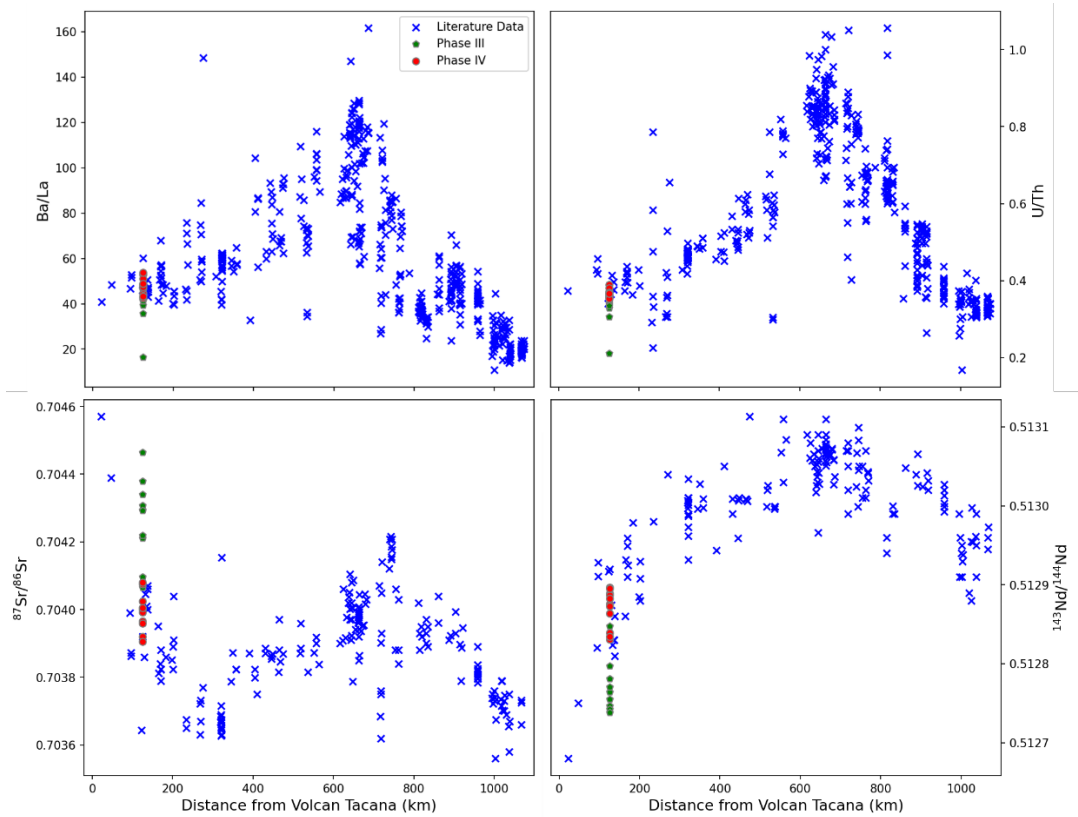


Fig. 5.2. Variations of different geochemical parameters against distance along the CAVA, compared with data from the AVC stratovolcanoes (green and red symbols). Literature data from RU_CAGeochem database (Carr et al., 2014). Note the difference for the AVC samples when comparing trace element (top row) with radiogenic isotope (bottom row) – the AVC samples from phases III and IV (i.e. pre- and post-LCY) have very similar trace element compositions but very different radiogenic isotope signatures.

Unlike the trace element ratios, significant isotope variations are observed in the AVC samples (Fig. 5.2). Section 4.3.1 showed that the northern pre-LCY phase III stratovolcano lavas had a more radiogenic signature than those of the southern post-LCY phase IV lavas. While it could be argued based on the trend in Fig. 5.2 that the pre-LCY phase III stratovolcano magmas have had a greater interaction with the crustal component, there is an alternative explanation. Walker et al. (1995) used the behind-the-front volcanic fields of eastern Guatemala to show that the isotopic composition of the underlying crust becomes increasingly radiogenic with increasing distance from the trench (section 1.3.4; Fig. 1.14). Donnelly et al. (1990) also showed that the crustal blocks underlying this region contain isotopically more enriched material further away from the trench. With the likely assumption that this is the case for the crust in central Guatemala, the observed geographical control on isotopic trends in the AVC is highly likely to be due to systematic variations in the isotopic composition of the lower crust which are inherited by the ascending mantle-derived melts.

5.1.1.2 The AVC basaltic andesites

The most mafic of the basaltic andesite lavas sampled at the AVC was sample Ati427_11 from a scoria cone (Cerro las Minas) on Volcán Tecolote, while three samples were taken from Volcán Atitlán (samples Ati501_05a, Ati501_05b, and Ati505_05c), with only sample Ati501_05a analysed in thin section. The contrasting physical nature of the samples from the different volcanoes (both in hand specimen and micro-scale textures) indicates different histories and eruptive processes. Olivines show more skeletal forms in the Cerro las Minas sample (Fig. 3.3). Skeletal phenocrysts indicate high degrees of undercooling, caused by sudden quenching (Lofgren, 1974; Bacon, 1986) or by rapid ascent (Armienti et al., 1994). In this case, ascent-driven undercooling is the most likely cause as this sample was not quenched in cooler magmas prior to eruption.

In comparison to the Cerro las Minas scoria, the Volcán Atitlán sample likely interacted with a more complex magmatic plumbing system. They contain several melt-rich glomerocrysts (section 3.2.1.1; Fig. 3.5) which strongly resemble those from Volcán de Fuego (Berlo et al., 2012; Liu et al., 2020). These have been interpreted as being 'semi-liquid' parts of the crystal mush that were introduced into the ascending magma (Berlo et al., 2012) and are strong evidence for previous episodes of magmatism. Further evidence of magma mixing is seen in clinopyroxene overgrowths on olivine crystals (section 3.2.1.1), a texture associated with magma mixing and olivine reaction with melt (Coombs & Gardner, 2004; Zellmer et al.,

2016). The presence of these glomerocrysts and evidence of mixing and crystal exchange suggest there is an established magma plumbing system beneath Volcán Atitlán, where previous episodes of magmatism had stalled and equilibrated at various depths. This is consistent with persistent magmatism at a stratovolcano such as Volcán Atitlán, in contrast to the ephemeral nature of scoria cones such as Cerro las Minas.

5.1.2 The stratovolcano andesites

5.1.2.1 Nature of the stratovolcano series

On a TAS diagram (Fig. 4.1), the primitive to intermediate andesites show a simple linear trend similar to those of other arc volcanoes (e.g., Ducea et al., 2015); however more complex trends are shown in the separate alkali oxides (Figs. 4.1 and 4.2). Above 57 wt.% SiO_2 , the stratovolcano lavas follow a steeper trend for K_2O which crosses into the high-K calc alkaline field and also follow a reversed slope of the trend for Na_2O (section 4.1.1). A trend of SiO_2 vs K_2O which crosses into the high-K calc-alkaline field is highly unusual as magmas tend to evolve within their particular fields when undergoing fractional crystallisation (Nandedkar et al., 2014, and references therein), and only spread into adjacent fields through mechanisms other than fractional crystallisation (e.g., mixing; Roberts & Clemens, 1993). Comparisons with other CAVA volcanoes show that only Volcán Tacana has a similar trend (Fig. 4.1), while published lava compositions from the AVC do not cover this composition range (GEOROC, 2024). Globally, this type of higher angle slope for the K_2O trend into the high-K calc alkaline field is typically only observed at volcanic arcs grown on thicker continental crust such as the central or southern Andes (Dickinson, 1975; GEOROC, 2021). Plots comparing K_2O trends in the AVC with GEOROC data of other global subduction zones are shown in Appendix C.

Comparison of the stratovolcano alkali trends with the VHKM compositions commonly found in these lavas (compositions shown in section 4.4.1.3), shows that after the inflection points, the stratovolcano trends point strongly towards the VHKM compositions (Fig. 5.3), especially for Na_2O . These inflection points are seen in numerous trace element and ratio trends, particularly the LILEs, the compatible elements, and variables like La/Yb and Dy/Yb (Fig. 5.3). This could imply that, after these inflection points, the stratovolcano series lie on a mixing line with the VHKM compositions.

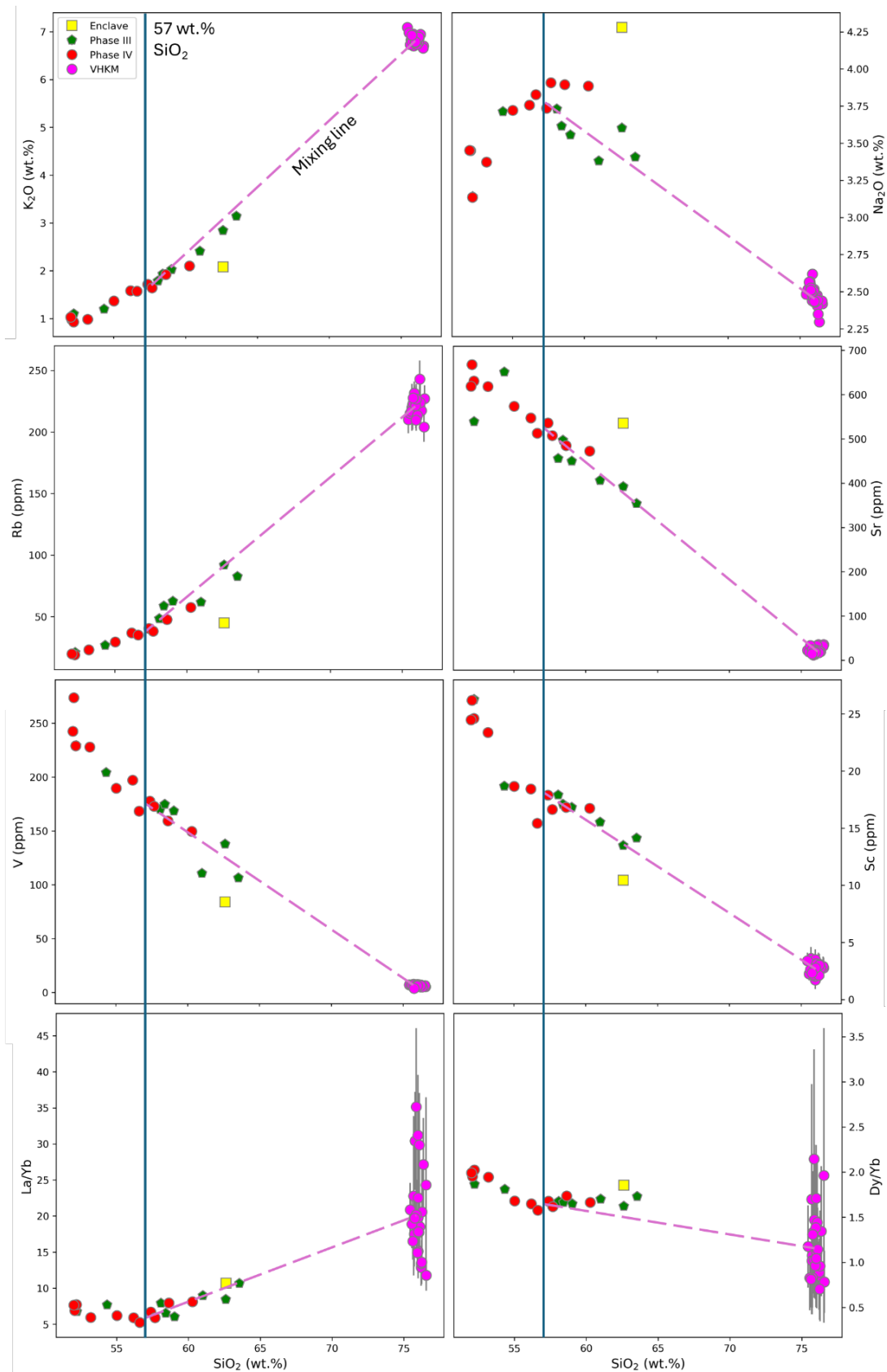


Fig. 5.3. Select bivariate diagrams comparing the geochemistry of the AVC stratovolcano lavas, the enclave, and the VHKM compositions from sample Ati427_08a. A line at 57 wt.% SiO_2 marks the identified potential inflection points and mixing lines have been drawn from the average composition of the VHKMs to these points. Analytical uncertainties are 1 s.d. for the major elements and 2 s.e. for the trace elements.

The relatively shallow compatible element trends may also indicate imperfect fractional crystallisation. Concentrations of these elements are expected to rapidly decrease during fractional crystallisation due to their strong compatibility with the fractionating phases (e.g. O'Hara & Fry, 1996). This is not evident in the AVC stratovolcano lava trends (Fig. 4.6), suggesting that other processes have occurred. These trends are strong evidence that mixing with VHKM had a strong control on the compositional variation of the AVC stratovolcano magmas, in agreement with previous suggestions by Newhall (1980, 1987) and Halsor (1989).

Halsor (1989) identified melt inclusions with similar composition to the VHKM seen in this study and suggested that they were responsible for compositional evolution at Volcán Tolimán but could not provide an explanation for the origin of the melt inclusions. With VHKM melt inclusions present in all analysed AVC lavas with whole rock compositions >57.5 wt.% SiO_2 , mixing of these melts can satisfactorily explain the geochemical trends of the stratovolcano lavas.

Olivine crystals in the stratovolcano andesites often display overgrowths of orthopyroxene and occasionally Fe-Ti oxides (section 3.2.1.1; Figs. 3.4B and 3.7B), a texture commonly linked to magma mixing (Coombs & Gardner, 2004; Reubi & Blundy, 2009; Zellmer et al., 2016). This further supports the suggestion that mixing had a strong control on the magmatic evolution of the AVC andesites.

Although transitions from the calc-alkaline to high-K calc-alkaline series in individual stratovolcanoes due to fractional crystallisation are rare (Roberts & Clemens, 1993; Nandedkar et al., 2014), formation of melts similar to the VHKM that influence the compositions of andesite magmas through mixing are present elsewhere. Reubi & Blundy (2008) described lavas from Volcán de Colima (Mexico) that contain high-K melt inclusions, thought to be derived from partial melting of biotite-bearing crustal rocks. Although the andesites do not have elevated K_2O contents, they show enrichments in the other LILEs, and the high-K melts is the likely source.

Humphreys et al. (2010) identified similar melts in lavas from Soufrière Hills volcano that were attributed to diffusion of K_2O from high-K mafic melts that were mixing. Similar exotic melts occur in eruptive products from Mt. St. Helens (Heliker, 1995; Blundy et al., 2008), Kurile-Kamchatka (Tolstykh et al., 2007; Kovalenko et al., 2017), Slovakia (Rottier et al., 2020), the Andes (Stechern et al., 2017) and Italy (Di Martino et al., 2011).

No AVC stratovolcano high-silica andesites or dacites plot in the medium-K calc-alkaline region (Fig. 4.1). This shows that mixing with the VHKM and additional fractional crystallisation are the dominant processes through which evolution of the magma systems feeding the stratovolcanoes occurred. The nature of this process will be tested by geochemical modelling in the following section (section 5.1.2.2).

5.1.2.2 EME-AFC modelling of the formation of the AVC stratovolcano suite

To show that the geochemical evolution of the AVC stratovolcano magmas was strongly influenced by the VHKM, the compositional evolution of the stratovolcano magmas was numerically modelled, using the “Equilibrated Major Element – Assimilation with Fractional Crystallisation” (EME-AFC; Burton-Johnson et al., 2019) model. This is an empirical model that uses partition coefficients to simulate major and trace element variations. It was chosen because it was designed for use in hydrous systems evolving towards felsic compositions (i.e., dacites and rhyolites) that include amphibole and biotite in their fractionating assemblage. The model was developed to target the gap in the MELTS family of models (Ghiorso & Sack, 1995; Gualda et al., 2012) due to the inability of MELTS to model such systems.

The starting magma composition used in the modelling was a Volcán Atitlán basaltic andesite (sample Ati501_05a) and the “assimilant” was an averaged VHKM composition from the melts in the Volcán Tecolote antelith. The high-K lava from Volcán Tecolote that contains the antelith (sample Ati427_08a) was used as the target composition, as it has the highest SiO₂ content and is assumed to represent the most evolved AVC stratovolcano magma composition.

Final model results are shown in Fig. 5.4 (model run conditions are shown in Appendix D.2.1, and the full model spreadsheet is presented in Electronic Appendix III). The total model error for the major oxides was $\sum D^2 = 1.75$. It yielded good fits for all elements except Na₂O, which was partially overestimated and had the greatest contribution to the model error (0.79). Figure 5.5 shows that the trace element results for the same model accurately reproduced the trace element spider diagrams. Values for the LILEs were accurately modelled, while there was a slight overestimation for the HFSEs and REEs. The shape of the primitive mantle-normalised Nb-Ta slope was also inverted compared to the measured values. With these caveats in mind, these are good fits to the observed stratovolcano lava compositions.

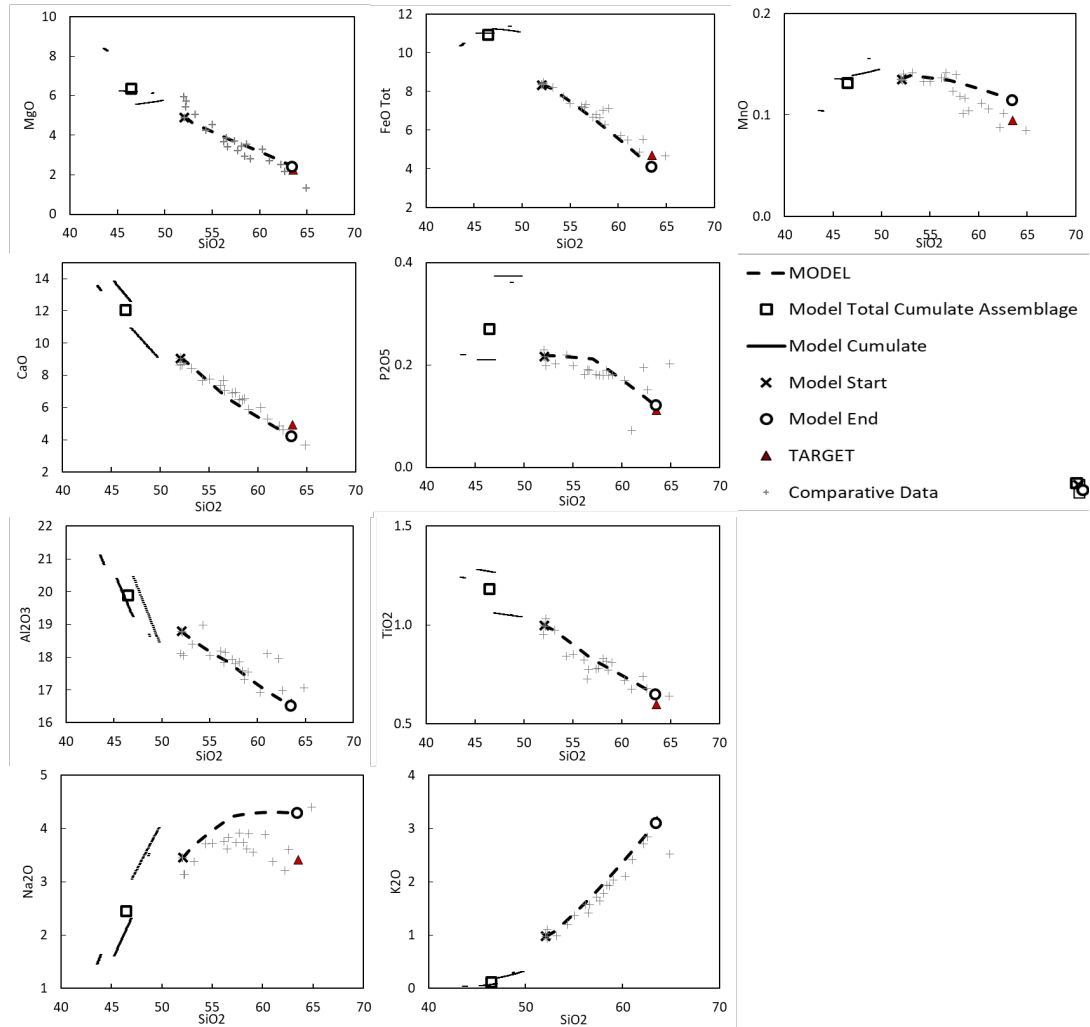


Figure 5.4. Major element oxide results for the modelling of the evolution of the AVC stratovolcano lavas. Comparative data is from this study. Note the strong fits for the majority of the oxides apart from Na_2O , which does not follow the trend inversion that the samples show. Separate mineral compositions are shown by the thin black lines, whose average composition makes up the model cumulate.

5.1.2.3 Constraining storage conditions of the stratovolcano lavas

Storage conditions of the basaltic andesites

Thermobarometry and hygrometry were performed on primitive basaltic andesite lava samples Ati427_11 from Volcán Tecolote and Ati501_05a from Volcán Atitlán using the Thermobar package (Wieser et al., 2022; Figs. 5.6 and 5.7) and the methods outlined below. Clinopyroxene and plagioclase were used as they are abundant in both samples. Olivine crystals typically showed skeletal forms (Fig. 3.3), suggesting they were not in equilibrium with the melt. The iterative plagioclase-liquid hygrometry method from Thermobar using 30 iterations was used initially to estimate temperatures and water contents using equation 23 of Putirka (2008) and the Waters & Lange (2015) hygrometer, respectively. In all cases, presented uncertainties are the published model errors.

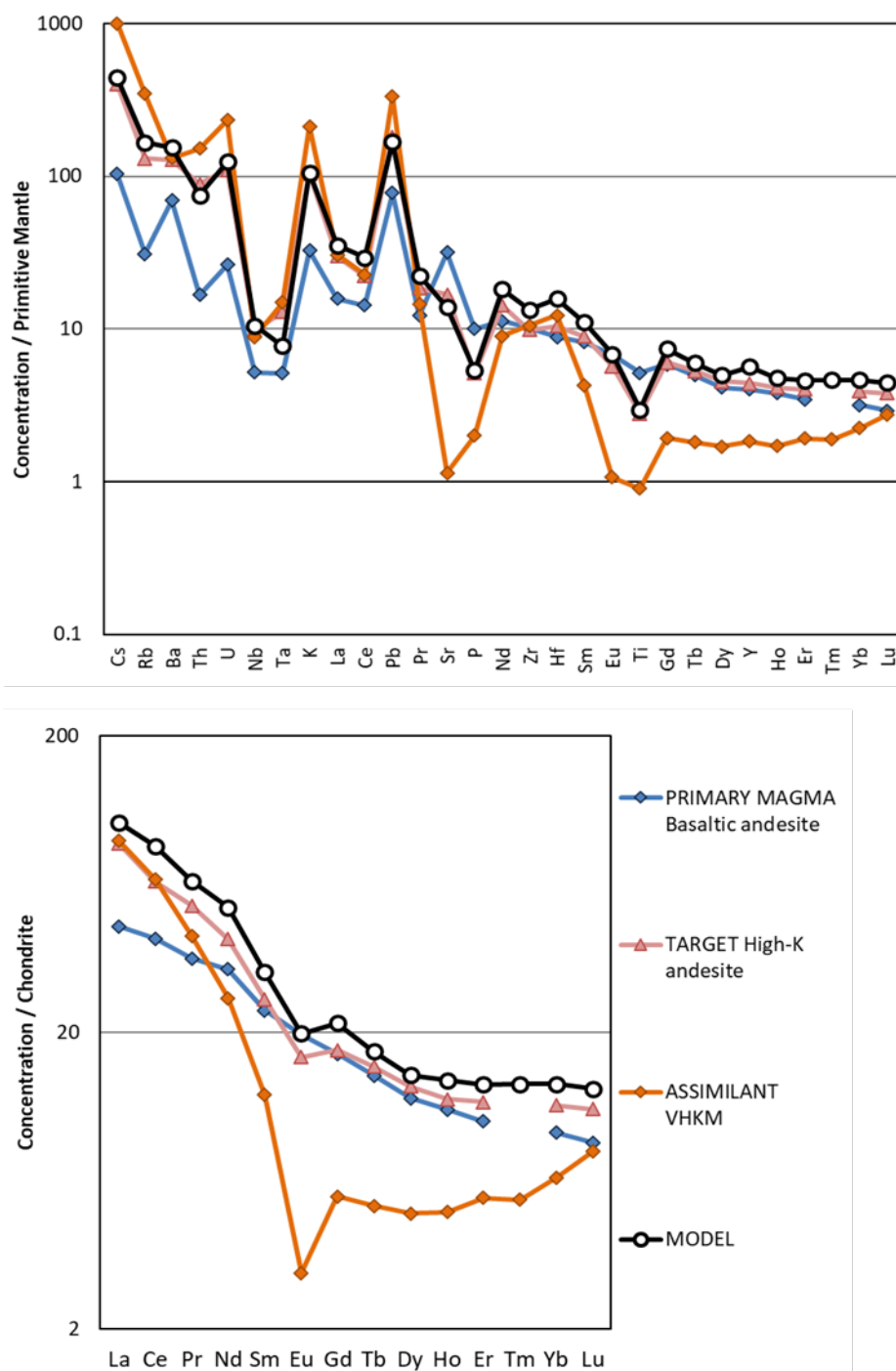


Fig. 5.5. Trace element results for the modelling of the AVC stratovolcano magmas. In general, the model overestimates the concentrations of most elements (particularly the REEs) but reproduces the shapes of the spider diagrams. The assimilant (VHKM) is an averaged composition of EPMA and LA-ICP-MS analyses of melts in the Volcán Tecolote antelith. Fig. 4.18 shows the range of trace element concentrations analysed. Values for Primitive Mantle and Chondrite are from Sun & McDonough (1989).

Whole rock compositions were used as 'liquid', and the An-Ab/liquid partition coefficient equilibrium test of Putirka (2008) was applied (i.e., samples with $0.11 < K_D < 0.45$ were not used). Pressures between 200 and 400 MPa were used for the calculations as pressures do not significantly affect estimates of H₂O content (Waters & Lange, 2015).

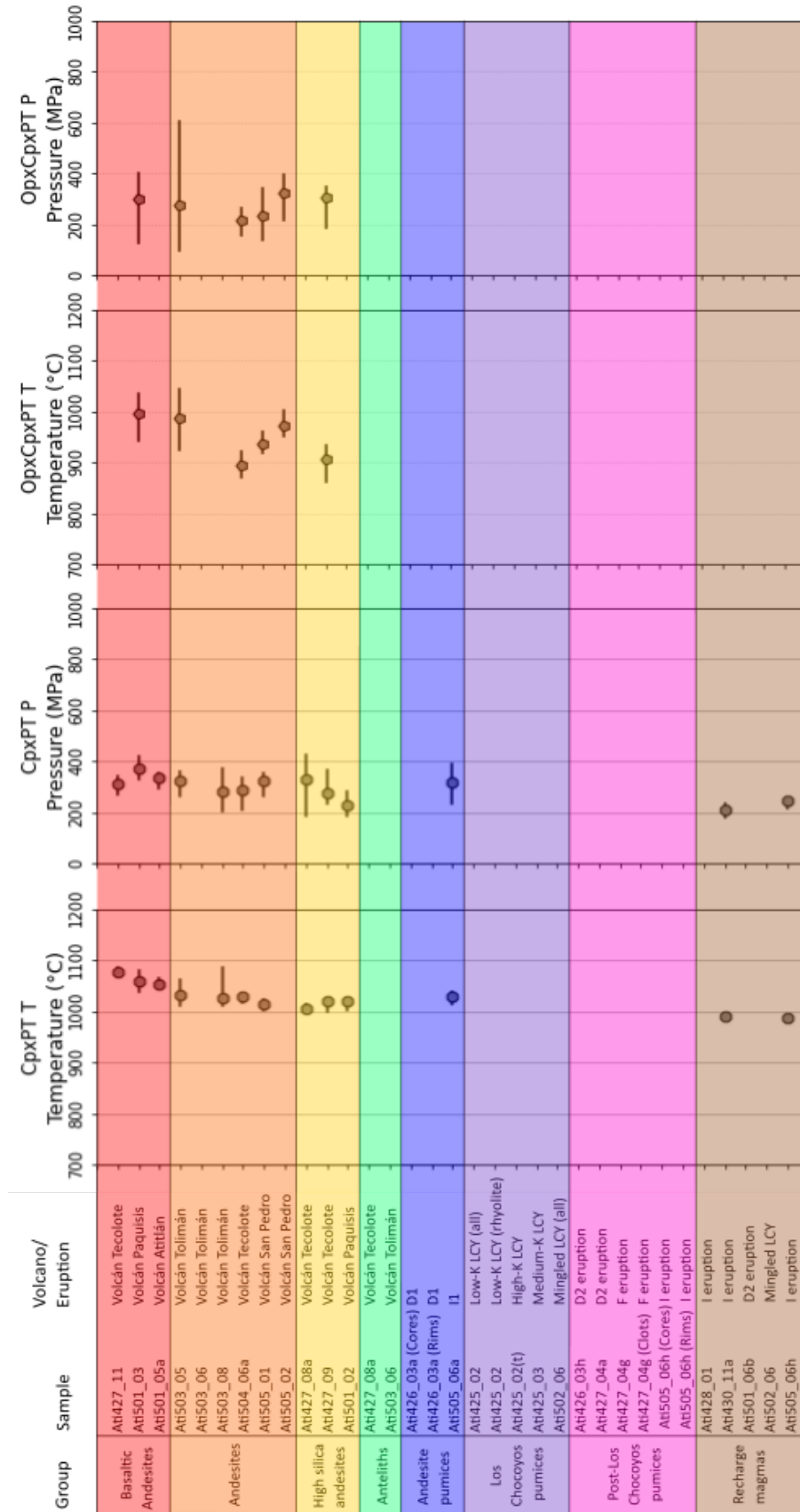


Figure 5.6. Pyroxene thermobarometry results for the different groups of AVC samples . Symbols are the average of the thermobarometry estimates, while the line represents the total range. CpxPT T and P estimated using Jorgenson et al. (2022); Opx and Cpx T and P estimated using equations 36, 37 and 39 of Putirka (2008) respectively. Model errors are reported in text.

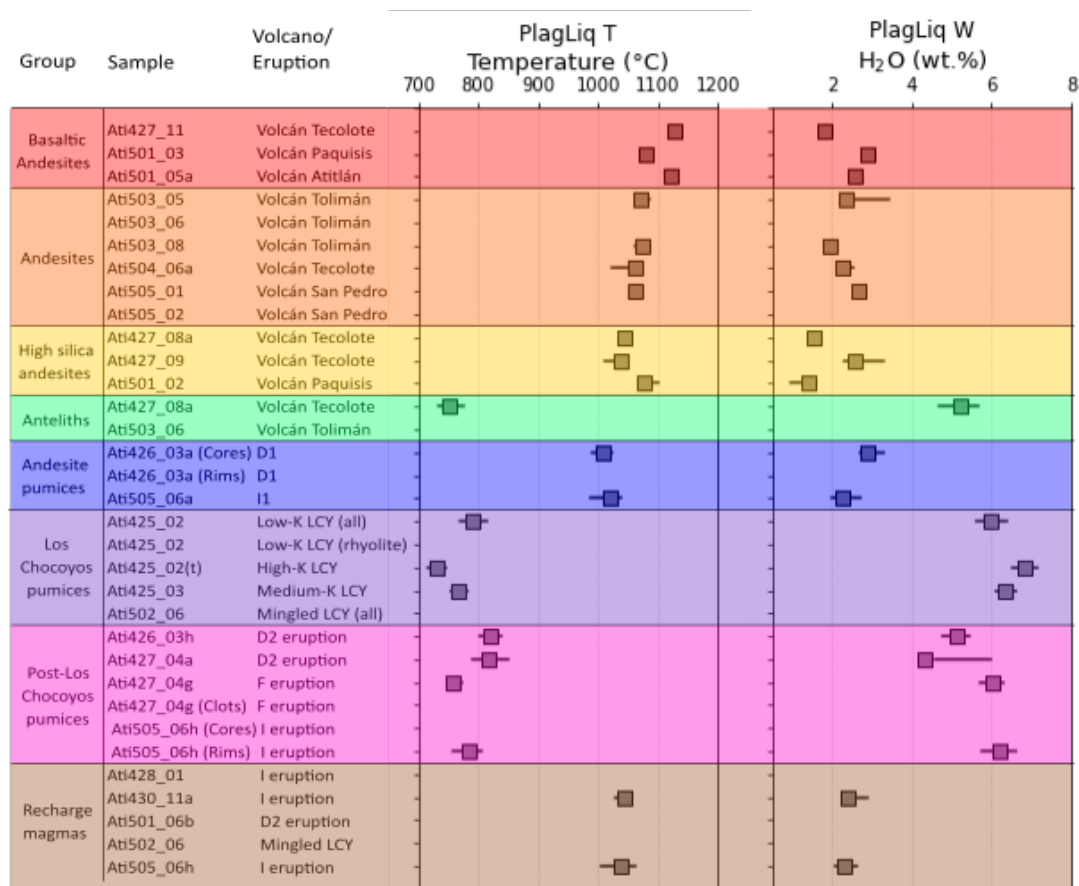


Figure 5.7. Plagioclase hygrothermometry of the different groups of AVC samples. Equation 23 of Putirka (2008) and the hygrometer of Waters & Lange (2015) were used.

Pressure and temperature estimates were obtained using the machine-learning based clinopyroxene thermobarometer of Jorgenson et al. (2022), using the water estimates obtained above. Whole rock compositions were again used for liquids, and the Fe-Mg partition coefficient test was used to identify analyses in equilibrium with this composition. The compositions used fall within the calibration dataset of the model. The barometry results are presented with caution because recent studies have questioned the reliability of clinopyroxene as a thermobarometer (Tommasini et al., 2022; Wieser et al., 2023a; 2023b), which show that these barometers are highly imprecise and can only reasonably distinguish a general region of the crust in which the crystal equilibrated. While clinopyroxene thermobarometers are used here (and precise values and model errors are quoted), this information provides only a broad estimate, rather than precise and accurate depth measurements.

The two samples showed slight differences in the estimates of their intensive variables. They have similar temperature estimates from plagioclase hygrothermometry (in all comparisons Cerro las Minas scoria vs. Volcán Atitlán: 1124-1129 vs. 1118-1125 \pm 43°C), but the Cerro las Minas scoria was less hydrous (1.70-1.93 vs. 2.46-2.67 \pm 0.35 wt.% H₂O). Cpx-

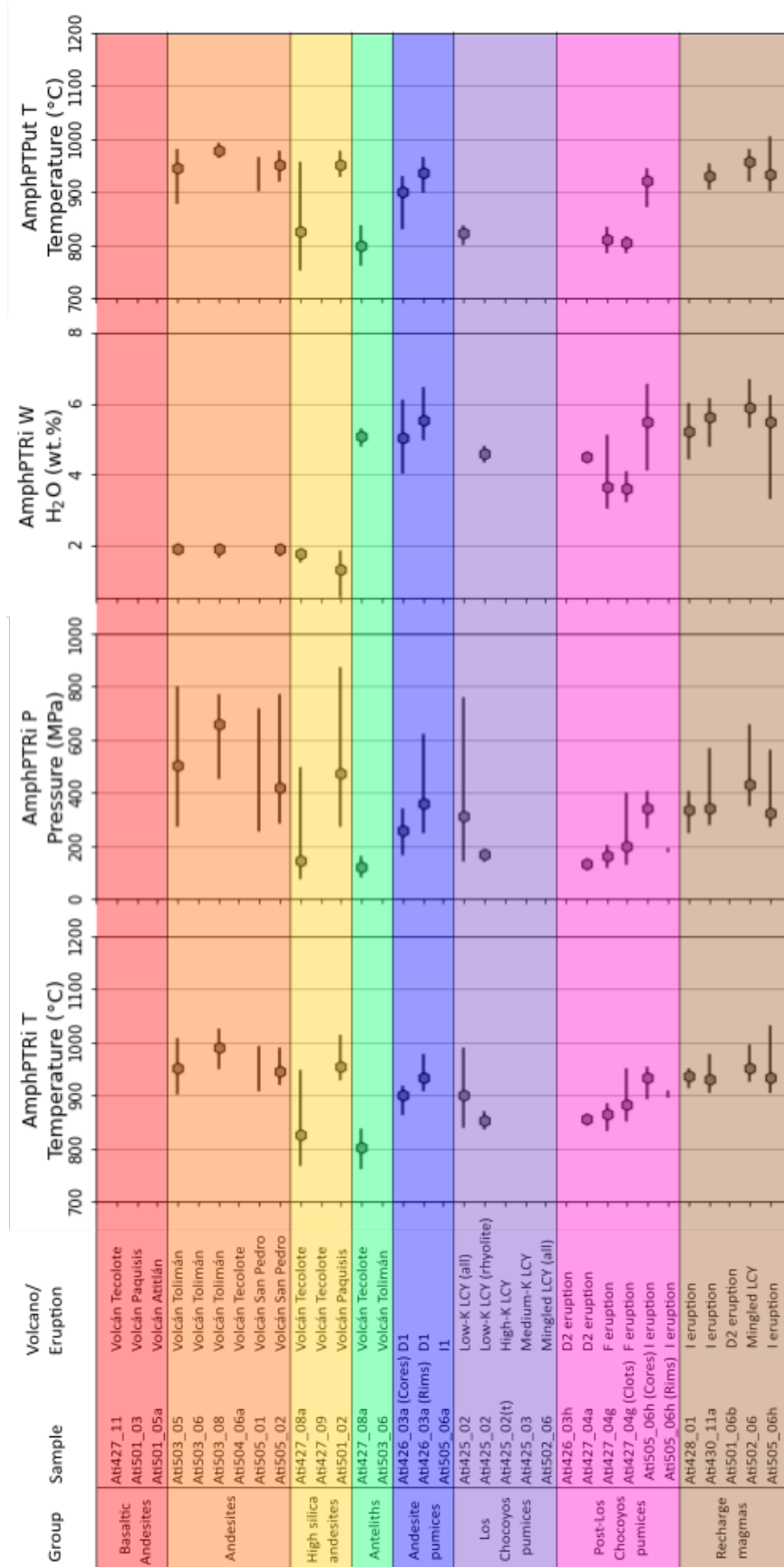


Figure 5.8. Amphibole thermobarometry and hygrometry of the different groups of AVC samples. The methods of Ridolfi (2021) were used to estimate temperature, pressure and H₂O content (AmphPTRi T, AmphPTRi P, and AmphPTRi W respectively), and equation 5 of Putirka (2016) was also used to estimate temperature (AmphPTPut T).

liquid results show the Cerro las Minas scoria equilibrated at similar depths (275-349 vs. 303-363 \pm 270 MPa) at marginally hotter average temperatures (1070-1088 vs. 1046-1069 \pm 45 °C). The lower water content may account for the slightly smaller positive Sr and Eu anomalies in the scoria compared with the Volcán Atitlán lavas (Sr/Sr* = 2.09 vs. 2.48-2.80, Eu/Eu* = 0.98 vs. 0.97-0.98; Fig. 4.5) because the magmas will enter the plagioclase stability field sooner in a drier magma (Müntener et al., 2001).

Storage conditions of the AVC andesite magmas

Formation of the stratovolcano magmas was influenced by mixing with the VHkMs, with the influence generally increasing with magma evolution. This has a detrimental effect on the usefulness of thermobarometers, as fewer crystals are in equilibrium with the potential melt compositions (either whole rock or melt inclusions). Estimates of intensive variables are therefore problematic and are considered on a case-by-case basis. Although the presence of amphibole and orthopyroxene means that additional barometric equations can be used, all amphiboles have partial or full breakdown rims, indicating that they were out of their stability field and had undergone slow decompression and/or subsequent reheating that is typical of stratovolcano amphiboles (Garcia & Jacobson, 1979; Conte, 1993; Rutherford & Hill, 1993; Schmidt & Sigmarsson, 1998; Browne & Gardner, 2006; Buckley et al., 2006; Ridolfi et al., 2008; Rutherford & Devine, 2008; Ridolfi et al., 2010). Unaltered regions of these amphiboles are still useful for estimating storage conditions in a previous reservoir at greater depths (Ridolfi et al., 2008), but are not useful for constraining the location and conditions of upper crustal reservoirs. Amphibole-based geobarometry also must be taken with caution due to concerns about their reliability (e.g., Ridolfi, 2021).

Temperature and pressure estimates were obtained using the same clinopyroxene thermobarometry method used on the basaltic andesite samples described above, as well as through the two-pyroxene thermobarometer using equations 36 and 37 (based on whether the clinopyroxene Mg# was $>$ or $<$ 0.75) and equation 39 of Putirka (2008), and through several amphibole thermobarometers (equation 5 of Putirka, 2016; Ridolfi et al., 2010; Ridolfi, 2021). In all cases, the amphibole compositions were within the range of compositions used to calibrate the models. Temperatures were also estimated using the plagioclase-liquid hygrometer, both using whole rock as a representative liquid and using the plagioclase-liquid matching method of Wieser et al. (2022) using analysed pyroxene-hosted melt inclusions where available. The same assumptions and equilibrium checks as described for the basaltic andesites were used here.

The stratovolcano andesites all show similar ranges for intensive variables (Figs. 5.6-5.8). Pressure estimates are typically 200-400 MPa (± 270 for clinopyroxene-liquid and ± 320 for two-pyroxene), while those from amphiboles with reaction rims typically have a much greater range and higher values (300-800 MPa $\pm 12\%$). This is evidence of deep amphibole fractionation that is common beneath arc volcanoes (e.g., Cawthorn & O'Hara, 1976; Foden & Green, 1992; Romick et al., 1992; Macpherson et al., 2006; Davidson et al., 2007; Peters et al., 2017). However, the large published model uncertainties mean that these values only indicate the general region of the crust.

Storage temperatures of the magmas recorded by plagioclase and clinopyroxene shortly before eruption all show similar values. The intermediate composition magmas were stored at 800-1000°C (recorded by the two-pyroxene thermobarometer; equation 36, error $\pm 45^\circ\text{C}$, equation 37, error $\pm 60^\circ\text{C}$), 1075-1170°C (clinopyroxene-liquid thermobarometer, error $\pm 45^\circ\text{C}$) or 1000-1100°C (plagioclase-liquid thermohygrometry, error $\pm 43^\circ\text{C}$). Their estimated water contents are more variable ($1.7\text{-}2.5 \pm 0.35$ wt.% H_2O). Amphibole temperature estimates from both the Ridolfi (2021) and Putirka (2016) equations were similar (900-1000°C, ± 22 or $\pm 30^\circ\text{C}$, respectively).

Results from the plagioclase thermohygrometer showed consistency of temperature estimates both within and between different lava samples, although they (and the clinopyroxene-liquid thermobarometer) are systematically higher than those obtained from the two-pyroxene or amphibole methods. This may be caused by using the whole rock composition as the liquid composition, as later crystallising materials that would be in equilibrium with matrix liquids would be more evolved and therefore yield lower temperature estimates. The intermediate composition lavas sampled did not contain enough melt inclusions or analysable regions of matrix glass to attempt clinopyroxene-/plagioclase-liquid calculations using glass compositions.

Many different factors increase the difficulty in estimating intensive variables in the higher-silica stratovolcano lavas. The changing mineral assemblage reduces the number of usable models as clinopyroxene becomes increasingly scarce, although amphibole is more stable (shown by the reduced presence of breakdown rims) and therefore could be used for these more evolved lavas. Temperature and pressure estimates for the high-K andesites have generally lower minimum values than the intermediate andesites but show a wider range (Figs. 5.6-5.8). Water content estimates are highly variable, which may be a consequence of the increased activity of volatiles in these more evolved magmas.

Tests were conducted on the equilibrium between clinopyroxenes and plagioclase with their melt inclusions for the high-K andesites, however none passed these tests. This is unsurprising given the high-silica rhyolite compositions of these glasses, compared to the intermediate composition hosts.

5.1.3 The anteliths and VHKM

Plutonic xenoliths (and the melts within them) have long been considered to be important clues for investigating the evolution of volcanic systems (e.g., Hermes & Cornell, 1981; Tollan et al., 2012; Cooper et al., 2016, 2019). Investigations of such rocks from the AVC should provide details about the evolution of the stratovolcano magmas. Newhall (1980, 1987) identified the presence of ‘disequilibrium andesites’ that frequently contain “hornblende-pyroxene gabbros”. These were suggested to be cumulates formed on the margins of magma plumbing systems, resulting from prolonged storage, and were thought to be important clues to the evolution of the stratovolcano magmas. These are certainly the same as the two anteliths described in this study. While two samples cannot be fully representative of the range of anteliths likely present in the AVC, they are sufficient to make some inferences about the magmatic systems beneath the AVC stratovolcanoes.

These anteliths exclusively host VHKM (Figs. 4.16 and 4.17), suggesting that there is a strong relationship between the two. In this section, the origin of the anteliths and the relationship between the anteliths and their melts will be discussed. As the VHKM likely had a control on the evolution of the stratovolcano magmas, and the anteliths contain abundant volumes of VHKM (sections 3.2.1.1 and 4.4.1.3), understanding these anteliths is crucial for understanding these systems.

While being predominantly present in the anteliths, VHKM have been identified as melt inclusions in all AVC lavas with >57.5 wt.% SiO₂. However, the lava-hosted melts have highly heterogeneous compositions that could suggest that they have undergone variable amounts of post-formation evolution. This makes identifying chemical trends difficult (sections 4.4.1.3). Alternatively, the homogeneity of melt compositions in the anteliths implies that they are close to their initial compositions, and so this study focuses on them. Mixing and/or fractionation would variably affect the melt compositions, leading to a range of compositions (Kent, 2008). A narrow compositional range for the population could be explained by entrapment or quenching before these processes could significantly affect their composition.

5.1.3.1 Nature of the anteliths

Both investigated anteliths have cumulate textures (section 3.2.1.1), and it is likely that the original rocks formed as such. However, they both show abundant secondary textures that suggest that further processing occurred in the crust, and so identification of the original cumulate composition is difficult. In particular, sample Ati427_08a appears to have been caught in the middle of a melt reaction, as it contains approximately 30% by volume melt. A large volume of the crystals in this rock were involved in this reaction, and there are very few regions which appear to retain the original structure. Fig. 3.10A shows an orthopyroxene crystal with intergrown biotite, surrounded by an overgrowth of amphibole and plagioclase crystals; similar crystal clusters also include rare clinopyroxene. Based on this texture, the pyroxenes and biotite (together with plagioclase) are likely to have been part of the original pre-melt reaction mineral assemblage. These are the same phases that make up the bulk of the other antelith (sample Ati503_06; Fig. 3.10B). Based on these observations, it is likely that orthopyroxene (\pm clinopyroxene) and plagioclase were the original cumulus phases in these two samples. The presence of hydrous phases with non-cumulate appearances is evidence of additional post-formation processes. Within sample Ati503_06, amphibole and biotite occur as roughly spherical clusters (Figs. 2.3, 3.14), which are highly unlikely to have been formed by cumulate crystallisation processes. Instead, post-formation reactions could have been responsible.

One such reaction is hydration crystallisation; Beard et al. (2004, 2005a) showed that gabbroic cumulates with high-An plagioclase, two pyroxenes and Fe-Ti oxides can react with hydrous melts to form amphibole, biotite and minor quartz, and would crystallise low-An plagioclase rims. These phases and textures are observed in both anteliths (section 3.2.1.1). According to these authors, this reaction and the resultant textures may be very common in hydrous magmatic systems.

*5.1.3.2 Origin of the VHKM*s

The common presence of VHKM in both anteliths suggests a close relationship. The most significant examples of these melts are those in sample Ati427_08a. The antelith is hypocrySTALLINE with ~30% of glass by volume (section 3.2.1.1). The glass contains vesicles and shows no sign of recrystallisation (Fig. 3.10A), suggesting that it was molten prior to eruption and quenched rapidly. The glasses are compositionally very homogeneous compared to other VHKM (section 4.4.1.3), and the combination of these factors suggests

that they are likely very close to their initial melt compositions. If this was a primary melt, then this antelith represents a frozen melt reaction.

The mineral textures and melt compositions give clues to the nature of this reaction. Clusters of biotite and pyroxene frequently have overgrowths of amphiboles and/or plagioclase, and the pyroxenes (predominantly orthopyroxene with rare clinopyroxene) typically have fragmented, rounded and partially resorbed textures (Fig. 3.10A), similar to those observed in breakdown reactions (Beard et al., 2004). The highly corroded nature of the orthopyroxene crystals indicates that they may have been primary minerals in the protolith and they were being reacted out. The melt reaction therefore likely included orthopyroxene and biotite as reactants, while the presence of amphibole and plagioclase on the rims of the clusters suggests that they grew during or after the reaction.

Further clues to the nature of the melt reaction are found in the melt compositions, which are strongly enriched in K_2O , LILEs, Nb and Hf (Fig. 4.17), features that are commonly indicative of melts involving biotite (Beard et al., 2005b; Reubi & Blundy, 2008). The glasses also have significant Eu anomalies and Sr and Ba depletions (Fig. 4.17), which are tied to the influence of plagioclase in the melt (Blundy & Wood, 1991). There is a moderately strong positive correlation between Ba and Sr (Fig. 5.9; $r = 0.83$) and significantly larger variation in their concentrations than in any of the other elements (section 4.4.1.3). Neither element shows any correlations with any other major or trace elements. These observations, as well as the presence of an Eu anomaly in the glass (Fig. 4.18), imply that plagioclase influenced the melt compositions. There are two possible explanations for these variations: A) heterogeneously nucleated plagioclase micro/nanolites could have affected these element concentrations on a spot-by-spot basis; or B) crystallisation of low-An plagioclase locally depleted the concentration of these elements in parts of the melt.

BSE images of the glass show no evidence of plagioclase microlites (Fig. 3.10A), so the second explanation is more probable. Ba and Sr (and potentially Eu, although studies of the effect of An content on Eu compatibility are rarer; e.g. Trail et al., 2012) are both more compatible in low-An plagioclase (Blundy & Wood, 1991). Late-crystallising low-An mantles/rims and patchy cores could have partially controlled the concentrations of Ba and potentially Sr and Eu in the melt.

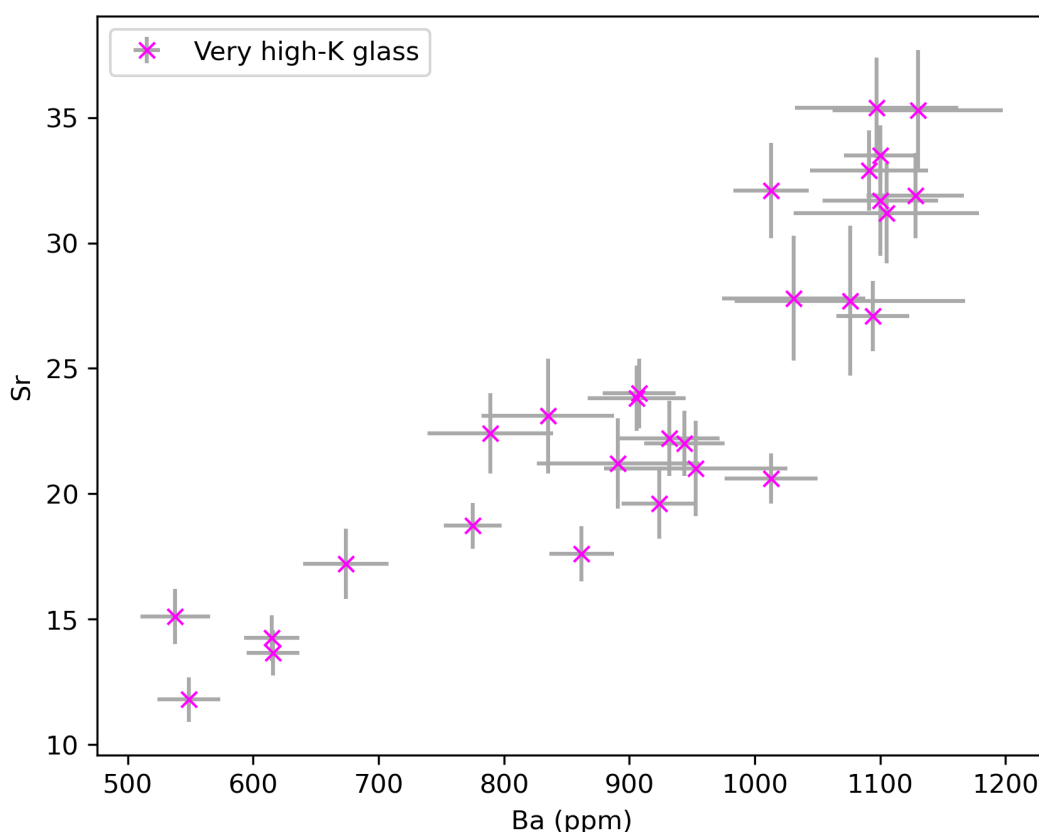


Figure 5.9. Ba vs. Sr content of the VHKBs present in the Volcán Tecolote antelith (sample Ati427_08a), showing a good positive correlation. Correlations between other elements are very rare for these melts. Analytical uncertainties are 2 s.e.

While textural evidence strongly suggests that biotite and pyroxenes were reactants in the melt reaction that formed the VHKBs (Fig. 3.10A), further details of the reaction are unclear. Many studies have examined either dehydration or water-present melting, which can form residual pyroxene or amphibole and exhaust biotite (c.f. Table 1 and 2 of Weinberg & Hasalová, 2015). The precise melting reaction is hard to confirm due to uncertainty regarding the nature of the protolith. However using the mineral phases observed in the assumed protolith and the remnant antelith, some possible reactions can be suggested. Dehydration melting reactions of biotite do not produce the observed phase assemblages, since they all form garnet/cordierite, K-feldspar or orthopyroxene (orthopyroxene is present but its form and presence in the supposed protolith means that it is not a reaction product; Thompson, 1982; Le Breton & Thompson, 1988; Vielzeuf & Holloway, 1988; Spear, 1993; Vielzeuf & Montel, 1994; Patiño Douce & Beard, 1995, 1996). Instead, water-present melt reactions may be more appropriate. With the assumptions that K-feldspar was absent, there was minor quartz in the protolith, and the orthopyroxenes were not reaction products, then melt reactions also involving peritectic amphibole are the most likely solutions (reactions 16, 17a, 19 and 21a in Table 2 of

Weinberg & Hasalová, 2015). As amphibole and plagioclase are residual phases, the requirement for peritectic amphibole makes sense. Zoning in the amphibole may reflect very different crystallisation processes, i.e., an initial peritectic amphibole that gave lower melt K₂O estimates from chemometry, and subsequent amphiboles grown from the VHKM that yield melt estimates with much higher K₂O (section 5.1.3.3).

While the anteliths have a clear relationship with the VHKMs, other rocks in the vicinity of the AVC have appropriate mineral assemblages that could act as sources. Intrusive rocks are present along wide sections of the western margin of the caldera and in the southeast (Newhall, 1987), and are thought to be related to phase I and II activity of the AVC (Williams & McBirney, 1969). All the plutonic rocks investigated in this study, and several of those previously described, contain biotite and similar mineral assemblages that are required for the melt reactions described above. The dominant trend for AVC stratovolcano lavas is towards high-K contents, in contrast to other CAVA lavas (Fig. 4.1). The abundant presence of biotite-bearing intrusive rocks around the AVC and the observed K₂O enrichments may not be coincidental.

5.1.3.3 Antelith petrology

In antelith sample Ati4278_08a, amphiboles commonly show a pseudo-poikilitic texture, having grown around small plagioclase crystals (Fig. 3.10A). They are also commonly intergrown with the plagioclase rims, suggesting that amphiboles and the plagioclase rims grew simultaneously. The bimodal normal and patchy zoning (Fig. 3.53) likely indicates a two-stage evolution. The high-An cores are left over from the protolith, and then resorption and subsequent growth of low-An patchy zones and rims/mantles occurred. Abundant euhedral plagioclase microphenocrysts with equilibrium compositions commonly occur in clusters or freely floating in the interstitial glass, suggesting that they grew directly from the melt. These microphenocrysts share a similar normal zoning pattern with the phenocrysts and have the same compositions. The amphibole textures also suggest variable conditions. Assuming that they formed late (which is likely given their common occurrence as overgrowths on other phases), then their strong zonation was derived from (at least) two-stage crystallisation after formation of the melt and during ascent.

This is further supported by amphibole chemometry and thermobarometry. Estimated equilibrium melt compositions using the Ridolfi & Renzulli (2012) chemometer show large variations with a positive correlation in K₂O and SiO₂ content (2.0-6.5 and 65-78 wt.%, respectively; Fig. 5.10), with an *r* value of 0.74. Amphiboles which gave the higher

estimates likely grew from the VHkMs due to the similarity between analysed and modelled melt compositions. Amphiboles which yielded equilibrium melt estimates with <74 wt.% SiO₂ show much greater scatter in their K₂O estimates and may not have been in equilibrium with the melt from which they were generated and/or may not be purely magmatic amphiboles. There is a strong possibility that the amphiboles in the anteliths were formed through melting or crystallisation reactions involving hydrous fluids, which would render them invalid for use in thermobarometry calculations (Ridolfi et al., 2010; Ridolfi & Renzulli, 2012). The reliability of the K₂O chemometers is also problematic; the equations of Zhang et al. (2017) do not accurately reproduce the measured melt compositions, despite showing a better accuracy in their calibrations (Fig. 6f in Zhang et al., 2017). Their figure also shows that, at intermediate K₂O contents in the melt (approximately 2-4 wt.%), the Ridolfi & Renzulli (2012) chemometer overestimates melt K₂O contents significantly. Furthermore, neither calibration is well represented by amphiboles in equilibrium with melts with >5 wt.% K₂O. Therefore it may be a coincidence that the Ridolfi & Renzulli (2012) chemometer accurately reproduced the analysed melt compositions.

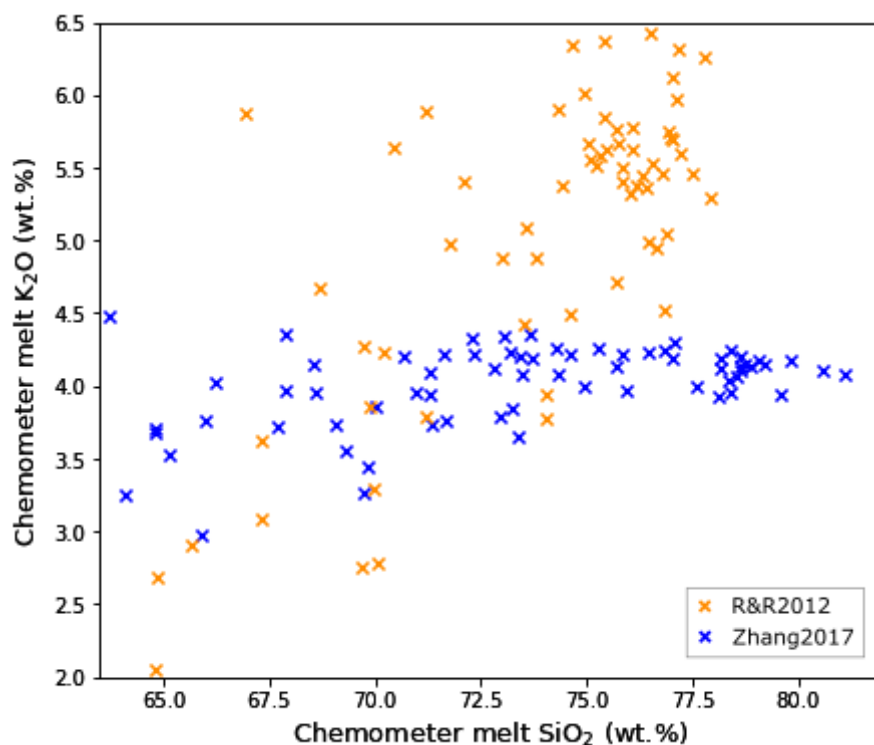


Figure 5.10. Amphibole chemometry of the crystals in the Ati427_08a antelith, contrasting the two different calibrations. R&R2012 – Ridolfi & Renzulli (2012); Zhang et al. (2017) using equations 1 (SiO₂) and 12 (K₂O). Note the overestimation of SiO₂ for a group of analyses >77.5 wt.% SiO₂ by the Zhang et al. (2017) equation, as well as the difference in slopes, where the Ridolfi and Renzulli (2012) results predict a positive correlation, while the Zhang et al. (2017) equations show no correlation

Assuming that those amphibole chemometry that reproduced the VHKM compositions were accurate, and they crystallised from this melt, then they can be used for thermobarometry. Figure 5.8 shows estimates for the Ati427_08a antelith using the Ridolfi (2021) thermobarometer for amphiboles which have predicted equilibrium melts with >74 wt.% SiO₂ and >5 wt.% K₂O. This predicts that these amphiboles crystallised at 89-166 MPa ($\pm 12\%$) and 766-837°C (± 22). The Ridolfi (2021) hygrometer yielded estimates of 4.88-5.30 (± 0.78) wt.% H₂O. Uncertainties quoted are the published model errors.

Plagioclase-melt hygrometry using the rim and patchy zoned plagioclase and the VHKM as the melt from Ati427_08a was performed using the plagioclase-liquid matching method of Wieser et al. (2022), the temperature equation 24a of Putirka (2008) and the hygrometer equation of Waters & Lange (2015). A pressure estimate of 150 MPa was used. Temperatures given by this method were 734-774°C (± 36), slightly lower than the amphibole thermometer, and water contents were 4.7-5.7 wt.% H₂O (± 0.35), showing better agreement with the amphibole hygrometer than the thermometer.

Thermobarometry results broadly suggest that at least the last phase of crystallisation or melt reaction occurred in the upper crust. However, the large uncertainties associated with these estimates means that these values should not be assumed as precise depths but only as indicators of the general region of the crust where equilibrium occurred. The occurrence of the Volcán Tecolote antelith in a lava erupted near the top of the stratovolcano stratigraphic sequence, and the observation that this is typical of later lavas of the AVC stratovolcanoes (Newhall, 1980, 1987), suggests that the hydration process is restricted to times where the magmatic system had reached thermal and/or geochemical maturity.

5.1.3.4 Overview of antelith formation and evolution

Both anteliths show textures that suggest that they have experienced changes from their protoliths. Arc magmas of intermediate compositions stored in the mid- and lower crust commonly exsolve a volatile phase (Edmonds & Woods, 2018). Another source of H₂O could be dehydration of deep amphibole cumulates; long-lived magmatism at arc volcanoes is proposed to both 1) form large amounts of amphibole-rich cumulates in the deep crust, and 2) subsequently elevate the geotherm above the amphibole stability field, promoting release of stored H₂O (Davidson et al., 2007). In whatever way an aqueous phase was formed, it would have profound impacts on the mush systems. Interaction of this phase with shallow pyroxene-rich cumulates could result in hydration crystallisation reactions, crucially forming biotite. As the system thermally matured and/or because of

local heating during intrusion events, water-present partial melting of cumulates (particularly pyroxene and biotite) would result in residual amphibole and VHKM formation. This process is observed in the frozen melt reaction in sample Ati427_08a. Assuming that sufficient water was being moved into the system, then large regions of the crystal mush could be prepared for subsequent melt reactions.

Based on the chemical and textural variation in the anteliths, the following summarises the sequence of events that plausibly formed the VHKM:

- Formation of pyroxene and plagioclase cumulates in the upper portion of the mush system during the long lifetimes of the overlying stratovolcanoes.
- Hydration of these cumulates to form biotite (\pm amphibole).
- Melt reaction to form Al-rich amphibole + melt. High-An plagioclase microphenocryst cores likely formed.
- Interaction of melt with residual plagioclase and amphibole resulting in resorption and recrystallisation, forming patchy zoned textures, as well as normal zoning in plagioclase and secondary Al-poor amphiboles.
- Entrainment of antelith in ascending lava, and minor breakdown rim textures develop on the amphiboles.

One crucial aspect of this theory is that it requires a long amount of time: sufficient to develop a mush system and large deposits of cumulates and to thermally mature the system, and to allow the saturation and exsolution of a volatile phase. The timescales of these processes are thought to be in the range of 10^4 to 10^5 yr (Lipman et al., 1978; de Silva & Gosnold, 2007; Grunder et al., 2008; Gelman et al. 2013; Edmonds & Woods, 2018; Petrelli et al., 2018; 2020).

5.2 Origin of the recharge magmas

5.2.1 Nature of the recharge magmas

Recharge magmas were identified in three AVC rhyolite pumice eruptions (LCY, D2 and I). These are hotter (estimated ~ 900 - 1050°C , depending on the method and sample; section 5.2.2; Figs. 5.6 and 5.7), more mafic magmas than their hosts, also confirmed by their darker colour in hand specimens, diktytaxitic quench textures in their matrices, and crenulated margins (section 3.2.5.1). The recharge magmas from this centre have an unusual range of compositions; one analysed from the I eruptions in this study was a high-silica andesite (sample Ati505_06h(e) with 62.6 wt.% SiO_2), while previously published

recharge magmas from the W and LCY eruptions were both basaltic andesites (52.8 and 54.5 wt.% SiO₂ respectively; Rose et al., 1987). These recharge magmas were not therefore necessarily primary magmas and in the case of the analysed high-silica andesite recharge magma in this study, have undergone their own compositional evolution. Recharge magmas of intermediate compositions are unusual but have been observed at other centres (Schmitt et al., 2001, Andersen et al., 2019, Boro et al., 2020). During this discussion, the term “enclave” will refer exclusively to the sample from the I eruption deposits which was analysed for whole rock geochemistry – several other enclaves and mingled pumices from the various eruptions were studied in thin section (section 3.2.5), and discussion of their microscopic textures and mineral compositions will refer to these collectively as the “recharge magmas”. It is unknown what their compositions were, although in the case of the petrologically analysed enclaves from the I pumice, it is assumed that they are of the same composition as the one that was powdered for whole rock composition, due to their similar appearances and identical mineral assemblages in hand specimens.

The availability of only one recharge magma clast for whole rock analyses hampers the ability to provide robust arguments for evolution of these magmas. However the clast shows unique textures and compositional variations compared to the stratovolcano magma series that should be investigated. Further field sampling and analysis of recharge magmas would provide support for these arguments.

The mineral phases provide good evidence for the origin of the recharge magmas. Most recharge magmas contained abundant amphibole, the exception being sample Ati501_06b from the D2 eruption. They are only slightly zoned, never have breakdown rims and show only minor internal resorption, suggesting they were in equilibrium with their host magmas and were rapidly quenched. Other minerals (plagioclase, clinopyroxene, olivine and rare orthopyroxene) show few disequilibrium textures, and those present indicate fast growth related to high degrees of undercooling (i.e. skeletal or acicular forms, sector zoning in clinopyroxenes; Bacon, 1986; section 3.2.5.1). Apart from the mingling textures in the mingled pumices, there is little textural evidence of geochemical mixing; orthopyroxene overgrowths on olivines are entirely absent, and other indicators of mixing (e.g. zoning in the cores and/or mantles of crystals, resorption surfaces) are also rare. This suggests that the evolution of these magmas was not significantly controlled by mixing (in contrast to the stratovolcano magmas which were heavily influenced by mixing).

Rocks in which amphibole and olivine coexist are rare, and since their presence together could not be ascribed to magma mixing, it is possible that they represent an equilibrium assemblage. Experimental phase diagrams show that this combination of minerals is typically restricted to a small range of temperatures and pressures, approximately 970-1000°C and 150-300 MPa in basaltic andesites (Moore & Carmichael, 1998), and 975-1025°C and 550 to >800 MPa in andesites with high H₂O contents (Krawczynski et al., 2012). These are similar to those estimated using thermobarometry (Fig. 5.8, section 5.2.2), further corroborating the equilibrium assemblage hypothesis.

The analysed enclave also has distinct major and trace element geochemistry compared to the stratovolcano lavas (Figs. 4.1, 4.2, and 4.3). Most significantly, it has comparatively high P₂O₅, Na₂O, and Sr and lower K₂O and Rb. The enclave therefore represents a unique high-silica andesite composition. It shows no sign of enrichment in the LILEs, unlike the stratovolcano lavas, suggesting that it was separate from the VHKM source. Its composition is interpreted to suggest a second evolutionary mechanism to generate andesites from the feeding basaltic andesites, which is investigated in the following sections.

5.2.2 Thermobarometry

The conditions recorded by the different thermobarometric methods vary depending on the mineralogy being used (Figs. 5.6-5.8). The crystals in the D2-hosted recharge magma (sample Ati501_06b) frequently show disequilibrium textures (section 3.2.5.1) and were highly likely not to have been in equilibrium with their host melt. Thus, no thermobarometric methods were applied to them. Similarly, use of clinopyroxene-liquid and plagioclase-liquid methods in the mingled LCY pumice (sample Ati502_06) was not possible as an estimate for the composition of the more mafic magma is lacking. Amphibole thermobarometers (equation 5 thermometer of Putirka, 2016 and thermobarometer of Ridolfi, 2021) were used on phenocrysts from the mingled LCY pumice (sample Ati502_06) and I-hosted recharge magmas (samples Ati430_11a(e) and Ati505_06h(e)). To ensure that only amphibole that was in equilibrium with the mafic portion of the sample was used, chemometric tests were applied (section 5.2.5) and only crystals that passed these were used. These amphiboles were also within the calibration ranges of the thermobarometers. The hosted amphiboles show lower pressure estimates but similar temperature estimates compared to the stratovolcano lavas (250-600 MPa \pm 12% and 900-1000 \pm 23.5°C).

Only clinopyroxenes from the two I eruption recharge magma samples were analysed for thermobarometry, and they reveal a different story (Fig. 5.6). As only the enclave from

sample Ati505_06h(e) was analysed for whole rock composition, it was assumed that sample Ati430_11a(e) had a similar enough composition for use as the “liquid” in the clinopyroxene-liquid thermobarometer. They have a much lower and narrower range of pressure estimates (200-250 \pm 270 MPa), as well as higher average temperatures (985-995 \pm 44.9°C) in comparison to the estimates obtained from the amphiboles. Note that these pressure estimates are similar to the model uncertainties so should be regarded with caution, again likely showing only the approximate region of the crust in which they equilibrated. The recharge magmas yielded lower pressure and temperature estimates on average (Fig. 5.6-5.8) than the stratovolcano lavas.

The results of plagioclase-liquid hygrometry suggest a similarity between the storage temperatures of the recharge magmas and the stratovolcano lavas. Again, this method was only performed on the I-hosted enclaves using the same liquid composition as for the above clinopyroxene method. Temperature and water content estimates are similar using the plagioclase-liquid method (1000-1060°C and 2-3 \pm 0.35 wt.% H₂O), although there is a large discrepancy for hygrometer results between the plagioclase-liquid and amphibole (Ridolfi, 2021) methods. The amphibole hygrometer produces estimates of approximately 4-6 \pm 0.84 wt.% H₂O, much higher than those obtained using the plagioclase-liquid method, and also much larger than the model errors.

5.2.3 EME-AFC modelling of the enclave

Modelling the formation of the enclave was undertaken using the same starting material and methods as above. Final model parameters are shown in Appendix D.2.2, which resulted in a good final model error of $\sum D^2 = 1.00$. The modelled evolution trends of the major elements are shown in Fig. 5.11, and the full model spreadsheet is provided in Electronic Appendix III. The modelled trace element values have a worse fit than those of the stratovolcano series, apart from the LILEs (Cs, Rb, Ba, Th, U, Sr) which almost exactly re-create the observed values (Fig. 5.12).

Despite the good fit for the major elements, there are several issues that arise when comparing the model results with the analysed material. The largest difference is caused by MnO, which is modelled significantly higher than observed. This might be due to the particular sensitivity of this element to orthopyroxene in the model, which can result in large variations in MnO with even minor changes in the amount of fractionating orthopyroxene.

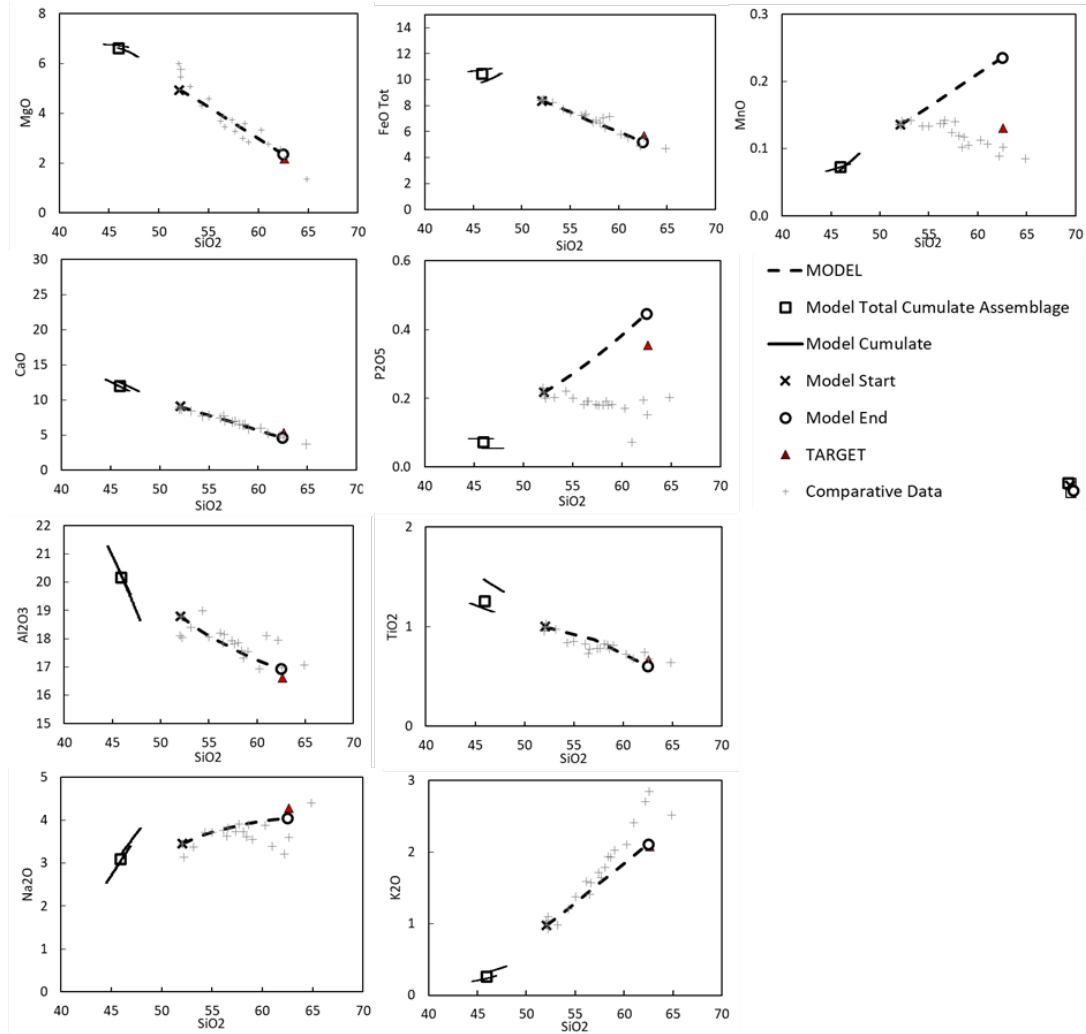


Figure 5.11. Major element oxide results for the modelling of the formation of the enclave (sample Ati505_06h(e)). Comparative data is the same as Fig. 5.4. Note the strong fits for most of the oxides apart from MnO.

There are several additional differences in the trace elements between the model and the analysed compositions. The modelled REE and Y values have a similar pattern to the analysed material, with enriched LREEs and similar MREEs and HREEs (Fig 5.12). However, the modelled values are significantly higher and show a Eu anomaly (Fig. 5.12, bottom left). Eu partition coefficients were the same as those used in the stratovolcano model because the stratovolcano lavas and the enclave have similar estimated fO_2 values (therefore likely to have similar Eu valence states and compatibilities; Fig. 5.13). As plagioclase is still required in the fractionating assemblage (shown by the moderate depletion in Sr relative to the starting material), this results in a small modelled negative Eu anomaly.

For the REEs, the elevated modelled values might result from both a lack of apatite in the model and poorly constrained partition coefficients for amphibole in basaltic andesites. Apatite was omitted from the model fractionating assemblage due to the enrichment in

P₂O₅ in the analysed rock (Fig. 4.2). Additionally, the default REE partition coefficients for amphibole may be too low. Values on the GERM database show that K_ds for REEs in amphiboles in similar composition melts are between 1 and 3, while the model default values are all <1.

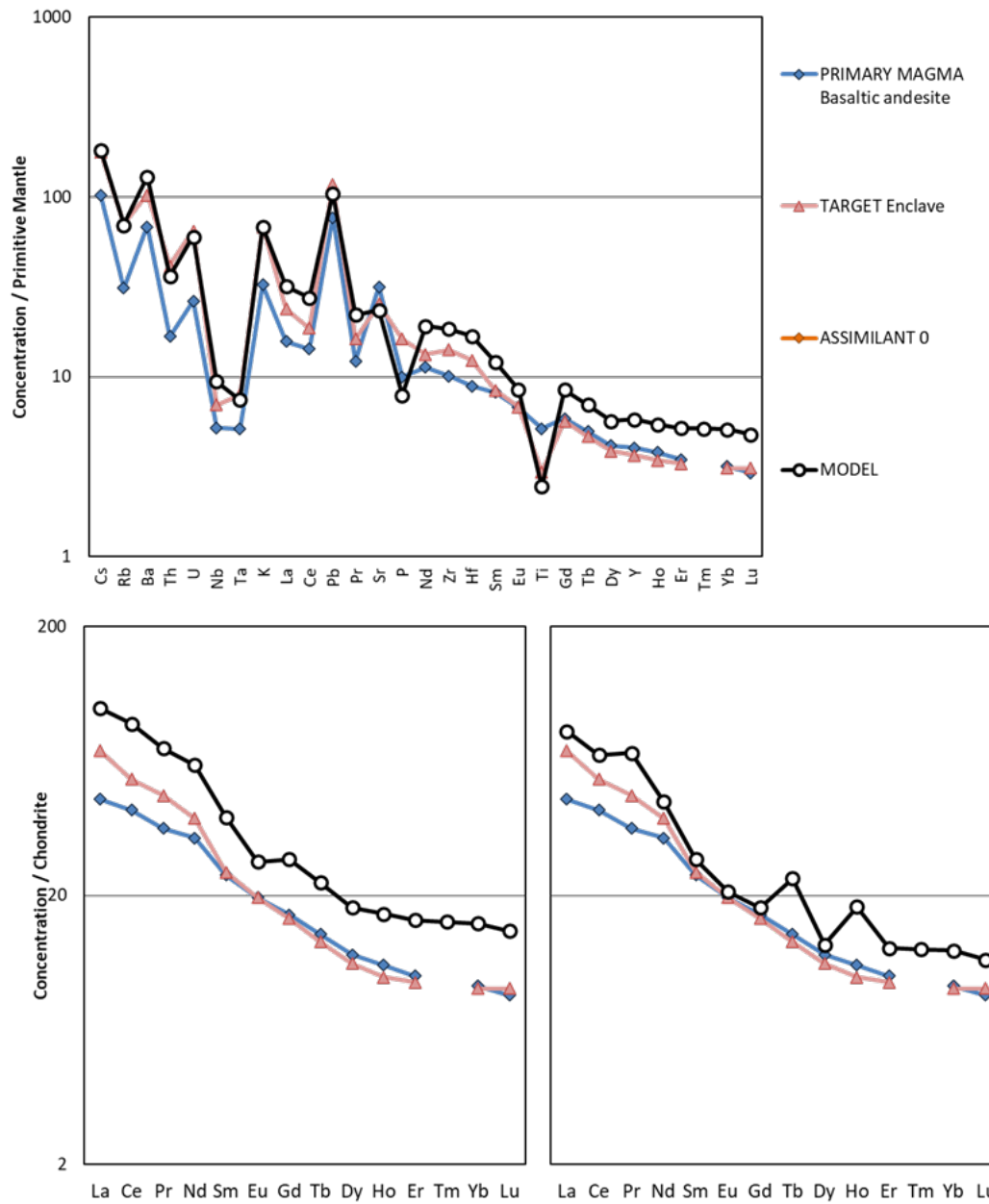


Figure 5.12. Trace element results for the modelling of the recharge magma. Top: Trace element variations including the original REE partition coefficients. Note the very good replication of the LILE (elements Cs-U) in this plot. Two REE plots are included here. Left: original partition coefficients; right: adjusted partition coefficients; details in text. The 'jagged' slope of the right REE plot is the result of missing partition coefficients. Note the absence of an Eu anomaly in the right plot and the subsequent better fit for the MREEs. Values for Primitive Mantle and Chondrite are from Sun & McDonough (1989).

To address the concerns with under-fractionation of the REEs, a second model was run with greater amounts of apatite in the fractionating assemblage and higher amphibole-REE partition coefficients from Fujimaki et al. (1984). This shows a closer fit to the observed

trace element values (Fig. 5.12, bottom right), particularly for the MREEs, although with a slightly worse model error ($\sum D^2 = 1.45$), mostly contributed by moderate over-fractionation of CaO caused by the increased amount of apatite. This second model also more accurately produces the lack of Eu anomaly due to a greater difference in the K_d s of Sm, Eu and Gd. Model conditions are shown in Appendix D.2.3.

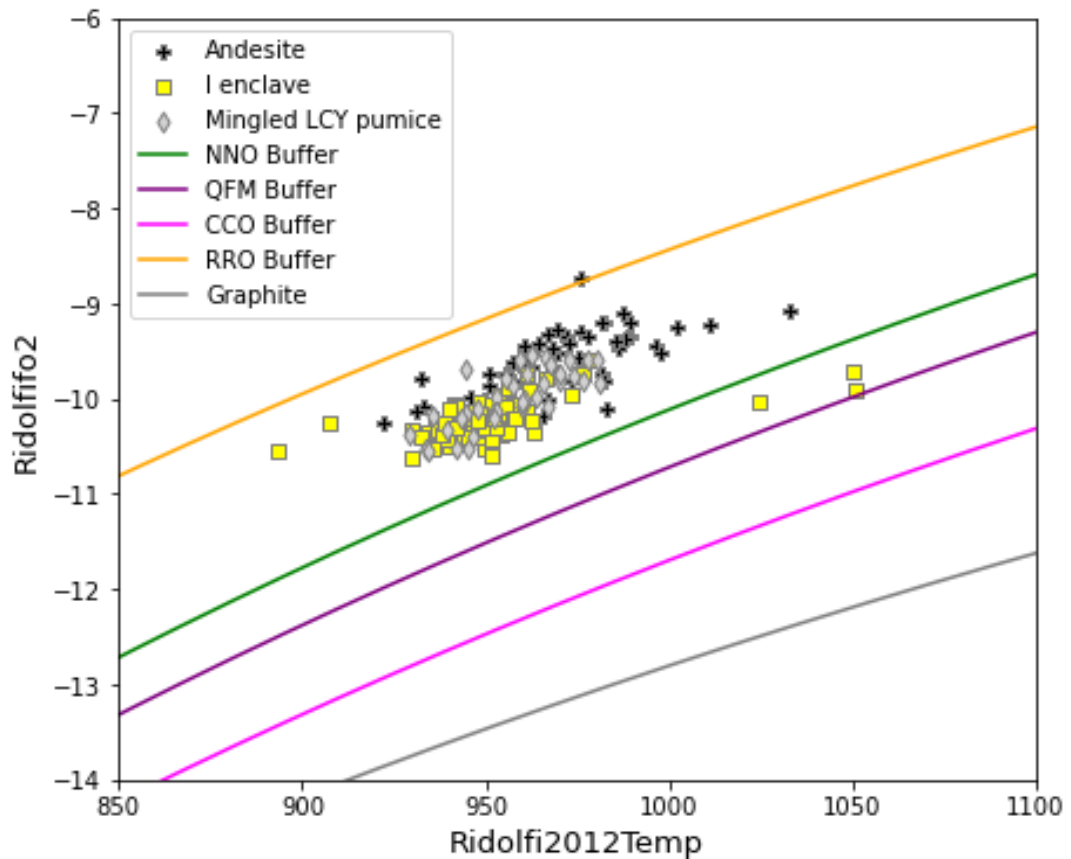


Figure 5.13. Log fO_2 vs. temperature using the Ridolfi & Renzulli (2012) amphibole oxythermometer, comparing the amphiboles present in the AVC stratovolcano andesite lavas, the I enclaves (samples Ati430_11a(e) and Ati505_06h(e), and the mingled LCY pumice (sample Ati502_06). For the latter, only amphiboles in equilibrium with the recharge magma (i.e. those with SiO_2 chemometry melt estimates <67 wt.%) are shown. All amphiboles display similar oxidation states, but the stratovolcanoes tend to be slightly higher (ΔNNO predominantly between 0.7-1.8 for the I enclave and the mingled LCY pumice and 1.4-2.9 for the stratovolcano). NNO – nickel-nickel oxide; QFM – quartz-fayalite-magnetite; CCO – carbon-carbon dioxide; RRO – rhenium-rhenium oxide.

This model shows that it is possible to create the enclave magma composition through a distinct petrogenetic mechanism using only fractional crystallisation. This magma was not exposed to the VHfMs (shown by the well-modelled LILE compositions, elements Cs-U in Fig. 5.12) and had a fractionating assemblage containing greater amounts of amphibole and lesser amounts of plagioclase (Appendices D).

5.2.4 Comparison of the recharge magma and the stratovolcano lavas and implications for the evolution of the magma system

There are several notable differences between the geochemistry and petrology of the AVC stratovolcano lavas and the recharge magmas which inform us about their separate petrogenetic mechanisms. As this shift in magma evolution styles also appears to be tied to the shift into explosive pumice eruptions, comparing these different magmas could be useful for developing our understanding of how the magmatic system underlying the AVC was evolving leading up to formation of the LCY magmas.

The enclave magma (sample Ati505_06h(e)) has high SiO_2 , and uniquely much higher P_2O_5 compared with all other AVC lavas (0.35 wt.% vs. 0.25-0.01 wt.%; Fig. 4.2). The dominant control on P_2O_5 concentration in arc magmas is apatite, and the temperature and aluminium saturation index ($\text{ASI} = \text{Al}_2\text{O}_3 / (\text{Na}_2\text{O} + \text{K}_2\text{O} + \text{CaO})$, on a molar basis) are the dominant factors that control apatite stability (Piccoli & Candela, 2002). Increasing temperatures and ASI values cause decreasing stability of apatite (London et al., 1999; Piccoli & Candela, 2002). Figure 5.14 shows that the enclave has a slightly lower ASI value than the stratovolcano andesite lavas with similar silica contents. The recharge magmas are also predicted to have similar temperatures to the stratovolcano lavas (Figs. 5.6-5.8). These factors suggest that, if both magmas were crystallising apatite, it would be more stable in the enclave and would have fractionated more. Subsequent accumulation of apatite could explain the enclave's enrichment in P_2O_5 , as well as the elevated values for several tracers such as Eu/Eu^* and Sr/Sr^* (Fig. 4.5). A nugget effect (elevated quantities of a specific element or elements in whole rock analyses due to incorporation of a higher amount of a mineral phase) for apatite would produce a similar outcome for P_2O_5 . Conspicuous amounts of apatite are present in these samples (Fig. 3.49) which could support the accumulation or nugget effect theories, however, there is no elevation in whole rock CaO contents to match P_2O_5 (Fig. 4.2), and the variations in the alkalis (Figs. 4.1 and 4.2) would require a different explanation. Additionally, the enclave has slightly lower values for the REEs compared to the stratovolcano series (Fig. 4.3); these elements are highly compatible in apatite, and if apatite were accumulating in the enclave or was present in greater amounts due to a nugget effect, then elevated values for these elements would be expected.

Instead, suppression of apatite may be the explanation. Reubi & Müntener (2022) showed that experimentally derived intermediate composition liquids typically have elevated P_2O_5

contents compared to most andesites in the rock record and produce ‘bell-shaped’ P_2O_5 curves against SiO_2 as it concentrates in the melt before apatite saturation. These curves peak between 60-65 wt.% SiO_2 at values between 0.3-0.4 wt.% P_2O_5 . This matches very well with the observed enclave composition (62.6 wt.% SiO_2 and 0.35 wt.% P_2O_5). They could therefore represent a melt formed through fractional crystallisation, while the stratovolcanoes obtained their flat P_2O_5 trends through mixing, a process proposed in section 5.1 and observed at numerous other stratovolcanoes worldwide (Reubi & Blundy, 2009; Tatsumi & Suzuki, 2009; Reubi & Müntener, 2022).

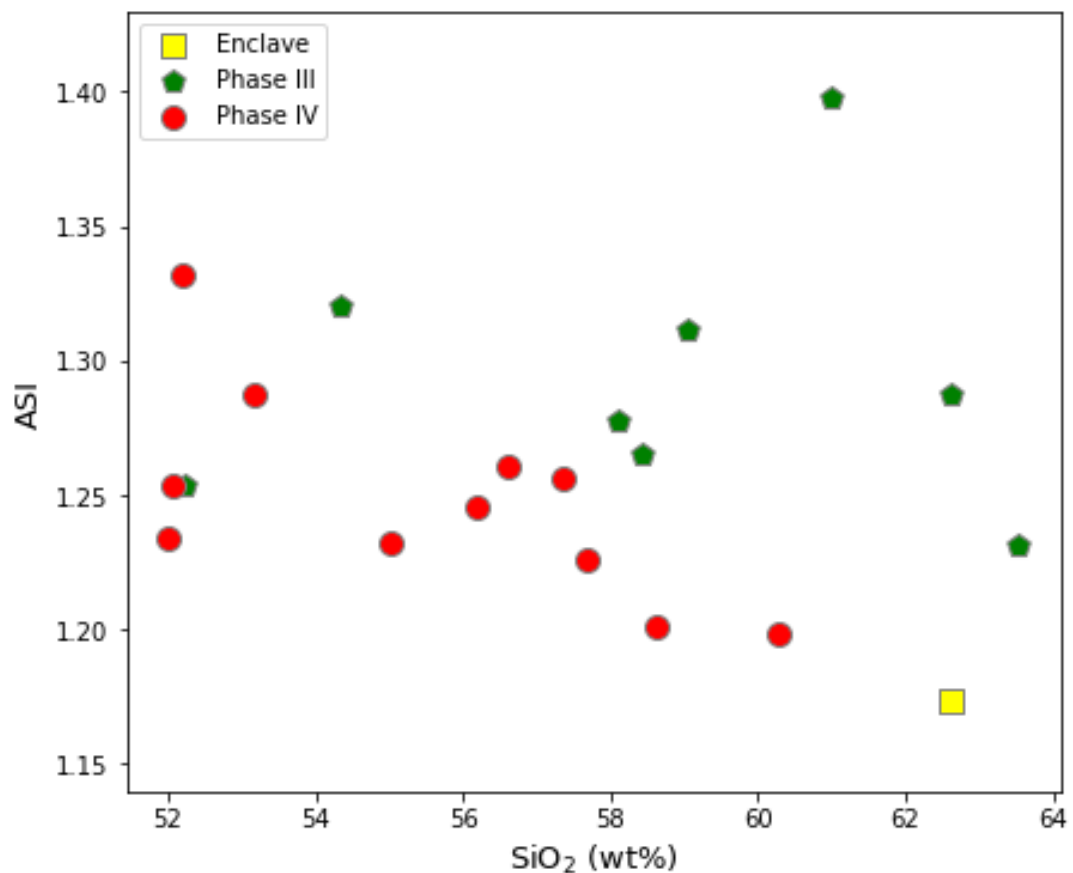


Figure 5.14. ASI vs. SiO_2 plot for the different phases of stratovolcano lavas and the enclave magma. Note the enclave magma has a lower value than all other mafic or intermediate lavas of the AVC.

The abundance of apatite can also be explained by previous suppression. The location of the crystals (in phenocryst rims or in the matrix) implies that it crystallised late, which would be expected if the apatite formation was initially suppressed and then occurred after the enclaves experienced undercooling during mingling. This also explains why there were no abnormalities in the CaO and REE concentrations. These elements were fractionated into other phases as would be expected during fractional crystallisation.

The geochemistry of the enclave also shows that mixing between magmas is unlikely the cause of its composition. If the enclave was generated through mixing of a mafic recharge with the host rhyolite, one would expect it to lie on a mixing line between the two. This is clearly not the case, as plots of several elements show the enclave lying far off any potential mixing lines (Figs 4.2, 4.3, and 4.6).

These differences are further shown in the trace element geochemistry of the enclave. Sr and Eu variations in bulk rock compositions suggest differences in the mineral phases present. Sr is primarily controlled by feldspars (e.g., Padilla & Gualda, 2016), while Eu is also heavily dependent on the oxidation state of the host magma, as Eu will be more compatible in plagioclase in more reduced magmas (Bachmann & Bergantz, 2008). Eu concentration can also be influenced by the presence of other phases such as amphiboles, apatites, Fe-Ti oxides, and/or assimilation of a melt with a Eu anomaly (Deering & Bachmann, 2010). The enclave's smaller Sr anomaly compared to those seen in the stratovolcano lavas of similar silica contents (Fig. 4.5) supports a smaller proportion of plagioclase in the fractionating assemblage, as suggested by the EME-AFC modelling (sections 5.1.2.2 and 5.2.3). This is further supported by the SrO concentrations in the plagioclase crystals; plagioclase in the enclaves have higher SrO contents than those of the andesitic stratovolcano lavas (Fig. 5.15), likely reflecting the enrichment in Sr in the host magmas.

The almost complete lack of an Eu anomaly in the enclave suggests a decoupling between the behaviours of Sr and Eu and therefore other phases have an influence. Fig. 5.13 compares the estimates for oxygen fugacity for the recharge magmas and the stratovolcano lavas obtained using the amphibole oxythermometer of Ridolfi & Renzulli (2012). The two magma-series have very similar oxidation states and therefore should have a similar Eu valence state and subsequent compatibility. These similar oxidation states but strongly differing Eu anomalies suggests that oxidation state was not the cause of the lack of Eu anomaly in the enclave.

Potential obscuring effects by other minerals could have an influence; REE-compatible phases such as apatite and amphibole have a positive effect on Eu anomalies (Rollinson, 1993; Deering & Bachmann, 2010), as Eu in its Eu^{3+} valence state does not fit as well into the minerals' lattices. Point-counting of mineral abundances shows that amphibole is more common in the recharge magmas than the stratovolcano magmas (32-40 vs. <30% by volume), and the results of EME-AFC modelling show that the recharge magma can be

modelled with a slightly greater proportion of amphibole (c.f. Figs. D.1 and D.2 in Appendix D). Using Eu-in-amphibole partition coefficients that reflect the relative incompatibility of Eu in the model runs can reproduce the observed lack of a negative Eu anomaly (section 5.2.3). Evidence for greater amphibole fractionation over plagioclase in the recharge magmas compared to the stratovolcano series is also shown by Sr/Y (Fig. 5.16). Greater proportions of amphibole and lesser proportions of plagioclase in the fractionating assemblage would result in depletion in Y, as well as having a weaker influence on Sr, resulting in a larger Sr/Y ratio.

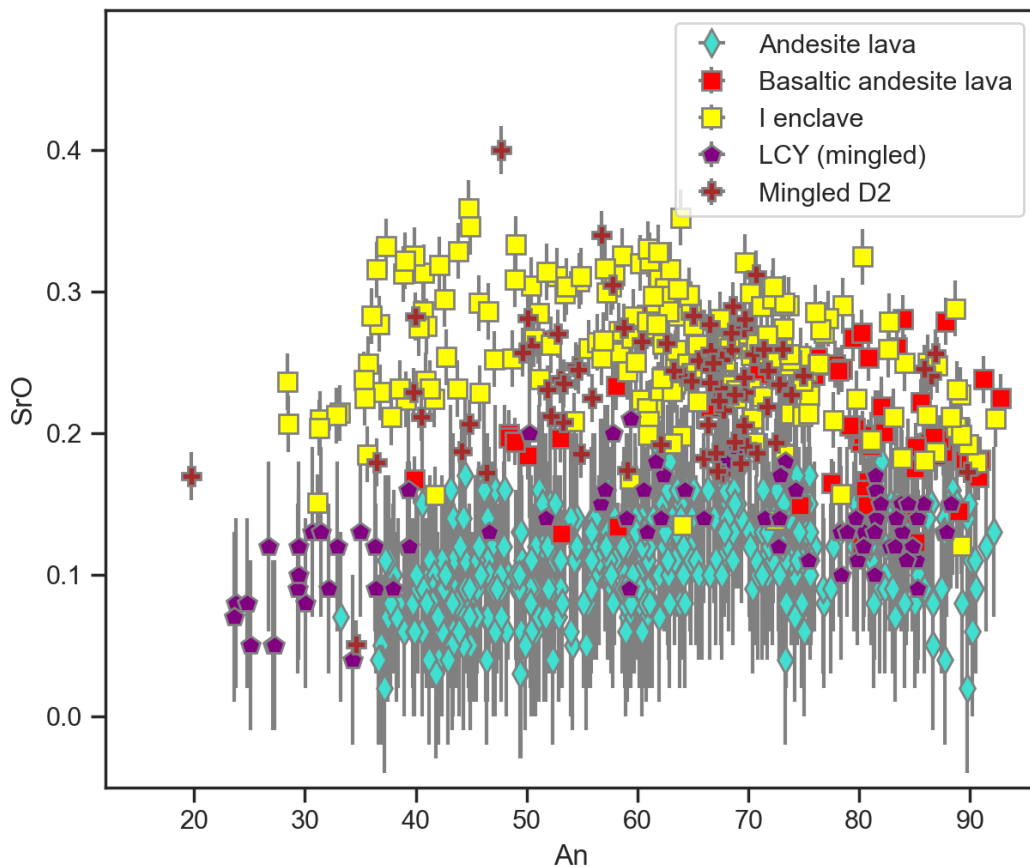


Figure 5.15. SrO content of plagioclase from the AVC stratovolcano lavas compared with those in the recharge magmas. At low An contents, plagioclase in the recharge magmas have higher SrO contents. Uncertainties are 1 s.d.

A plot of Zr/Hf vs. SiO_2 also shows a difference (Fig. 5.16). Values for the stratovolcano series drop off significantly and trend towards the VHKM field, while the enclave has the same Zr/Hf value as the more primitive stratovolcano lavas. Constant values for Zr/Hf imply that zircon was not saturated (Linnen & Keppler, 2002).

Further support for the dominance of fractional crystallisation on formation of the enclave magma is shown by the compatible elements. Low compatible element concentrations are

expected in rocks that have been formed predominantly by fractional crystallisation, and this is observed for the enclave (Fig. 4.6).

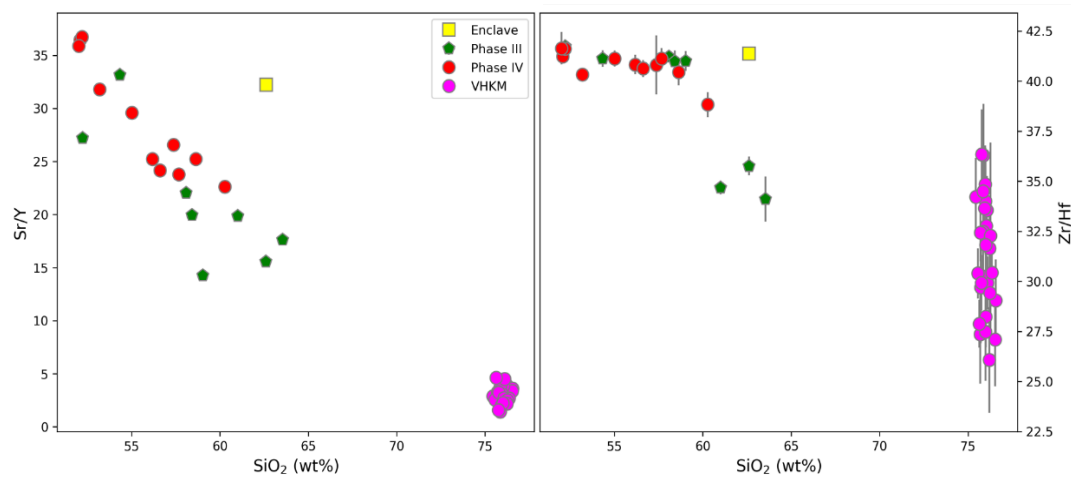


Figure 5.16. Left: Sr/Y ; and right: Zr/Hf vs. SiO_2 comparing the AVC stratovolcano lavas with the enclave (sample Ati505_06h(e)). Also included in this plot are the VHKMs from sample Ati427_08a. Analytical uncertainties are 2 s.e.

Decoupling of the enclave magma from the stratovolcano trends strongly suggests that there was a shift in intermediate magma generation mechanisms during the explosive phase of activity in the AVC. There is no enrichment in LILEs in the enclave magma, suggesting that it did not interact with VHKMs. This could be a result of the region of the crust that produced VHKMs had been destroyed during the formation and eruption of the LCY rhyolites, or because the enclave magmas were excluded from the regions of the upper crust in which the VHKMs were generated (section 5.1.3).

5.2.5 Amphibole chemometry

To test the compositional similarities of the LCY and I recharge magmas, as well as to test whether the amphiboles were in equilibrium with their host magma, chemometry estimates were obtained from amphibole compositions using the methods of Ridolfi & Renzulli (2012) and Zhang et al. (2017) and are shown in Fig. 5.17. Samples Ati502_06 (LCY mingled pumice) and Ati505_06h(e) (I enclave) were compared, and all amphiboles in these samples were tested. For the I enclave magma, these tests were performed with the assumption that all amphiboles were sourced from the hosting magma, while it is likely that, for the LCY mingled pumice, there would be amphiboles grown from a range of compositions. Most amphiboles in both samples predict equilibrium melt compositions of approximately 58-66 wt.% SiO_2 in the mingled LCY pumice compared to 64-68 wt.% SiO_2 for the I enclave. There are, however, several analyses that predict anomalously high SiO_2 equilibrium melt compositions.

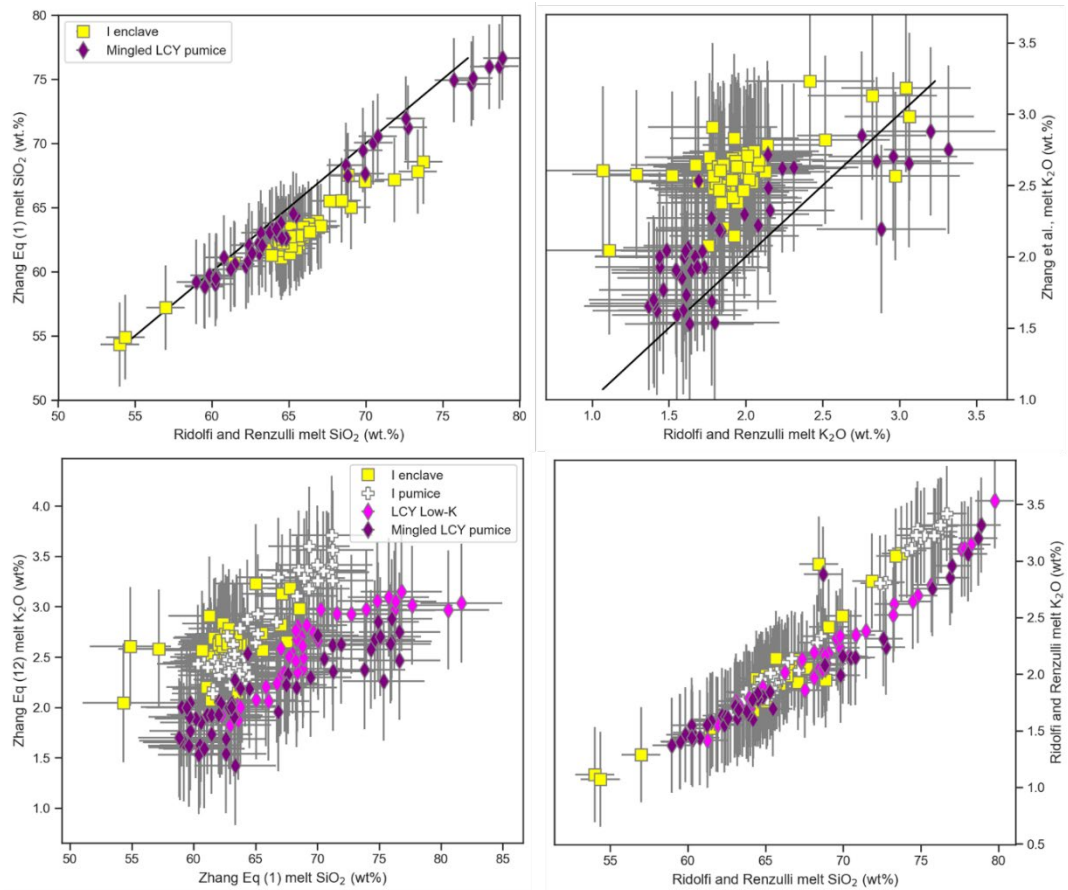


Figure 5.17. Amphibole chemometry of various magmas from the I and LCY pumice eruptions. Top: Plots of the results of the amphibole chemometry for the enclave from the I pumice (Ati505_06h(e)) and the LCY mingled pumice (Ati502_06), comparing the equations of Ridolfi and Renzulli (2012) and Zhang et al. (2017). Left: SiO_2 ; right: K_2O . Bottom: Plots of the results comparing SiO_2 vs. K_2O of both the samples plotted as well as unmingled pumices from the I and LCY eruptions. Left: Zhang et al. (2017); right: Ridolfi and Renzulli (2012). Both sets of equations show that the I chemical trends are more potassic than those of the LCY eruption. Shown model uncertainties are 1 s.e.

For the LCY mingled pumice, it is likely that these represent amphiboles that either were sourced from the rhyolite part of the mingled pumice and/or were grown during or after mingling and thus obtained intermediate disequilibrium compositions. Only one crystal from the I enclave yielded anomalously high melt SiO_2 contents. It is possible that this is a crystal from the rhyolite that had been transferred into the enclave, a process known to occur without coincident mingling of the melts (Singer et al., 2013).

The lower SiO_2 equilibrium melt compositions estimates from the mingled LCY pumice follows the known whole rock compositions. The published LCY recharge magma was a basaltic andesite (Rose et al., 1987, assuming that this analysis corresponds to the mingling mafic magma in sample Ati502_06), and the analysed I enclave was a high-silica andesite. Estimated melt K_2O contents were also different, being lower in the mingled LCY pumice (mostly 1.3-1.8 wt.% K_2O) compared to the I enclave (mostly 1.6-2.2 wt.% K_2O). While it might seem like the increased K_2O contents could simply be the result of the increased

degree of evolution suggested by the higher SiO_2 values, plots of estimated SiO_2 vs. K_2O using the equations of Zhang et al. (2017; Fig. 5.17) show that K_2O values are consistently higher in the I enclave than in the LCY mingled pumice. There is a caveat that the same is not clearly observed when using the equations of Ridolfi & Renzulli (2012), and it should also be noted that the model uncertainties for K_2O are proportionally much higher. Still, if this is accurate, it would imply that the recharge magmas from the I and LCY eruptions had subtly different K_2O compositions.

5.3 Origin of the LCY pumices

Previous studies have presented models for the petrogenesis of the LCY rhyolite suite (Rose et al., 1979, 1987). Here the origins of the rhyolites are revisited, relating the geochemical variations between them to the different andesite magmas discussed above. A previously unidentified LCY rhyolite pumice type is also discussed.

5.3.1 Identification of the LCY pumices

Previous studies of the LCY eruption identified two compositions of rhyolite pumices from the deposit, as well as a minor basaltic andesite component (Rose et al., 1979, 1987; Newhall, 1980). Fig. 5.18 compares the published LCY rhyolite bulk rock data with that from this study. In general, there is a good overlap between the compositions. The published data show a wider range of compositions, significantly for Al_2O_3 and Na_2O , as well as extending to lower silica contents.

This study has also identified a third kind of medium-K rhyolite pumice which is mineralogically (section 3.2.3.1) and geochemically (sections 4.1.3 and 4.2.3) distinct, containing biotite and cummingtonite as its ferromagnesian mineral phases. The low-K and medium-K LCY pumices are geochemically very similar, particularly in trace elements (Figs. 4.1-4.3 and 4.5-4.7), which suggests that they are petrogenetically related. Matrix glasses from examples of these pumices further support this, as the composition fields of the low-K and medium-K (samples Ati425_02 and Ati425_03, respectively) overlap (Figs. 4.14 and 5.19). Comparing bulk rock with the matrix glass analyses for the LCY rhyolites shows that there is very little difference between them (c.f. Figs 4.2 with 4.14, and 4.3 and 4.5 with 5.19). This is not unexpected due to the extremely crystal-poor nature of the pumices.

Published composition ranges for tephra shards identified as low-K rhyolites cover the medium-K range (Fig. 4a of Cisneros de León et al., 2021a; fields shown in Fig. 4.14). However their study did not compare the petrological aspects of the clasts, so they could

not identify this as a different rhyolite unit by its mineralogy. As they are close in composition and are potentially petrogenetically related, the medium-K LCY rhyolite could be considered a subgrouping of the low-K LCY rhyolite, and for simplicity they will be referred to as the 'lower-K' LCY rhyolites when discussing them and comparing them with the other pumices.

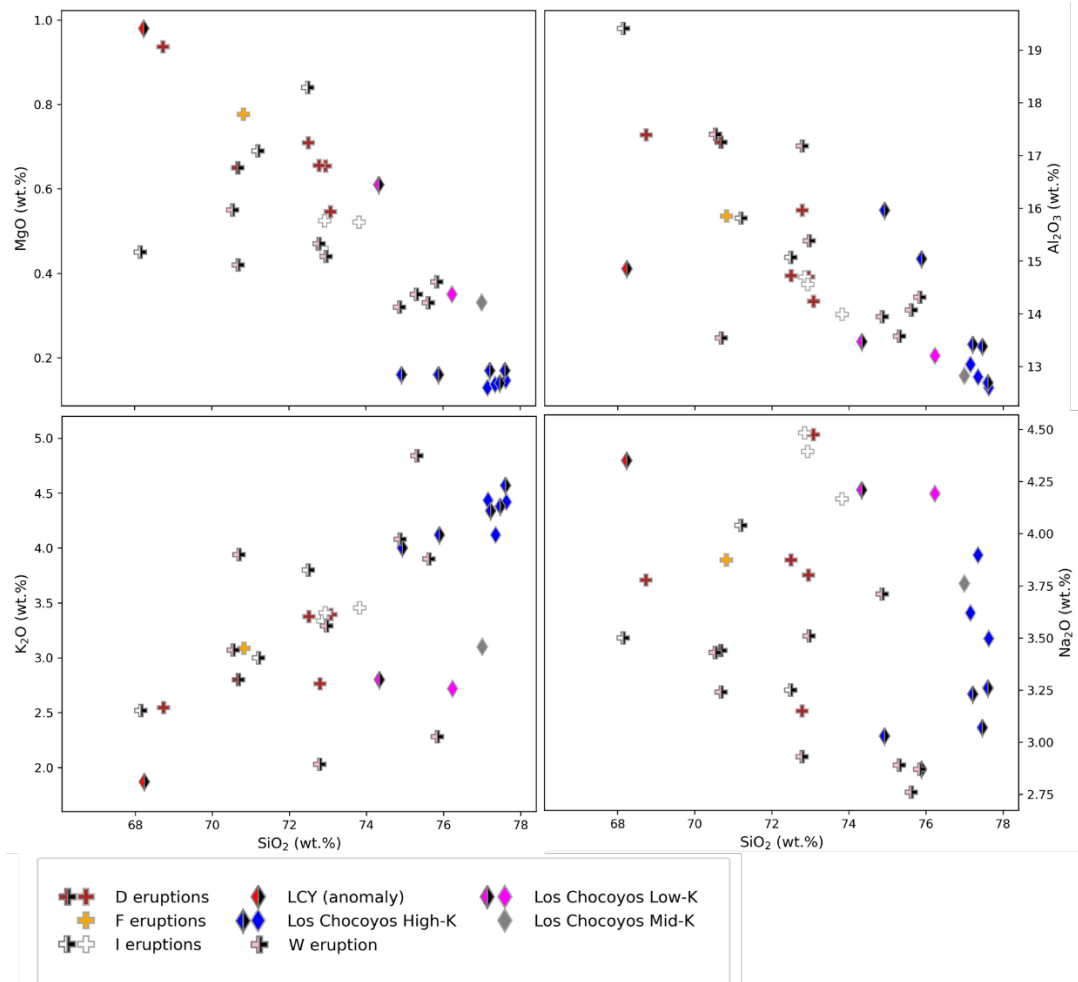


Fig. 5.18. Comparison of the bulk rock compositions of the AVC rhyolites. Filled symbols are from this study, while black halved symbols are published data from Rose et al. (1987) and the unpublished data from the W rhyolite from Steffan Kutterolf (GEOMAR). Also included is an anomalous LCY rhyodacite clast (red).

The absence of high-Ca amphiboles and presence of cummingtonite (a low temperature and pressure amphibole in silicic magmas (Geschwind and Rutherford, 1992; Nicholls et al., 1992; Nandedkar et al., 2016)) in the medium-K LCY rhyolite compared with a combination of high-Ca and cummingtonite amphiboles in the low-K rhyolite, and the similarity between the low- and medium-K rhyolite geochemistry, suggest that the medium-K rhyolite could be a low-temperature/pressure derivative of the low-K rhyolite. This is supported by a comparison of MgO and SiO₂ (Fig. 4.14). The medium-K rhyolite has higher SiO₂ and lower MgO, suggesting that it is slightly more evolved than the low-K rhyolite.

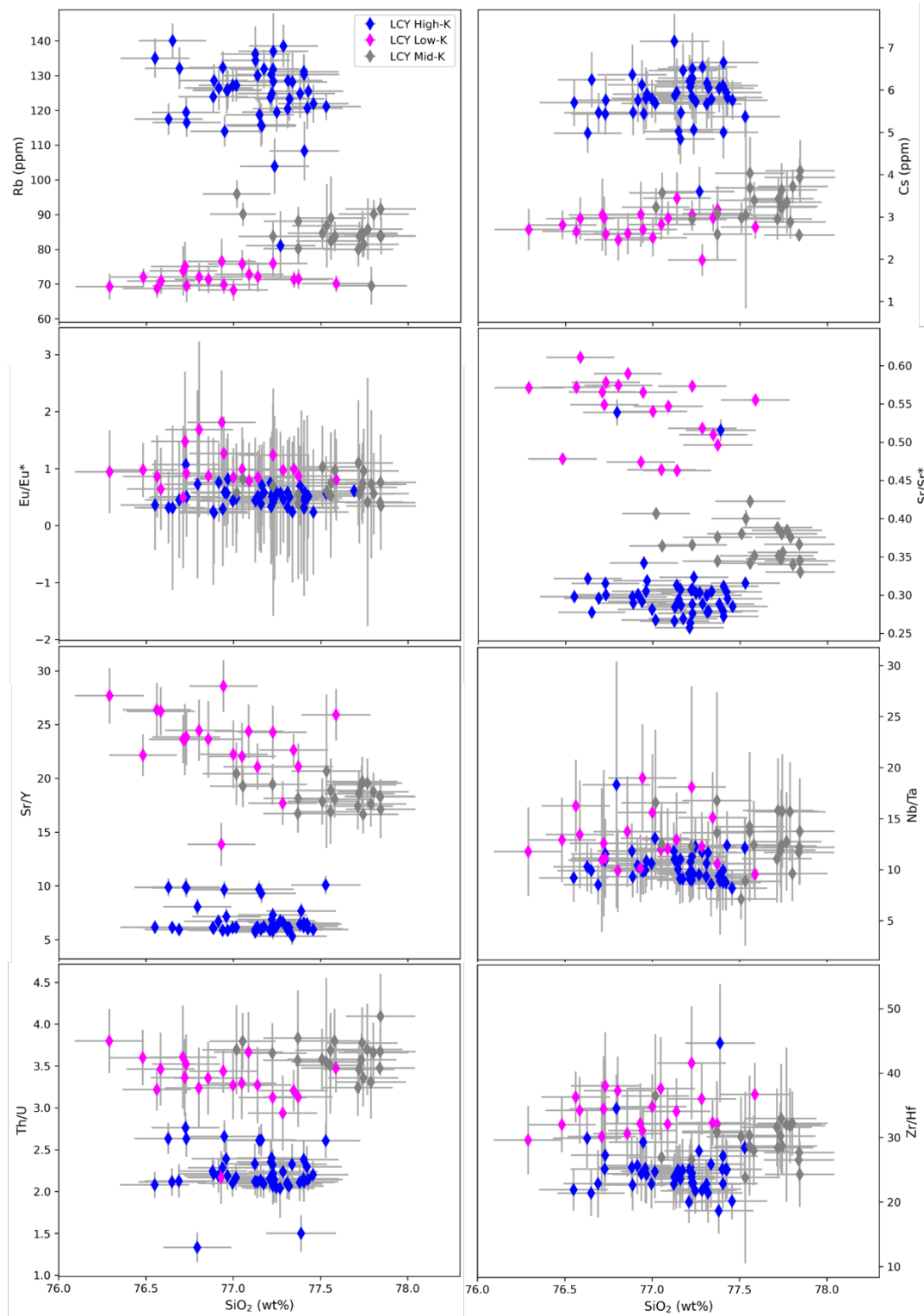


Figure 5.19. Bivariate plots for matrix glass trace elements and trace element ratios in the different LCY pumices (samples Ati425_02, Ati425_02(t) and Ati425_03). Analytical uncertainties are 2 s.e. on the vertical axes, and 1 s.d. on the horizontal.

5.3.2 Nature of the LCY rhyolites

Previous investigations of the LCY rhyolites have suggested that the high-K rhyolite was the product of further evolution of the low-K rhyolite (Rose et al., 1979). However, trace

element analyses in this study show that these two rhyolites have significantly different trace element compositions, particularly in the LILEs and the REEs (Figs. 4.3 and 4.7), that would be very difficult to relate petrogenetically. For the MREEs at least, in a system fractionating amphibole, the observed relative enrichment in these elements in the high-K LCY vs. low-K LCY rhyolites (Fig. 4.7) would be completely the opposite of what would be expected (Nandedkar et al., 2016). For further comparison, selected trace element concentrations and ratios in the glass are shown in Figure 5.19. To explain the compositional differences, different possible parental magmas and petrogenetic mechanisms for the different LCY rhyolites will be discussed.

Clues to their potential parent magmas come from their alkali and LILE contents. The high-K LCY rhyolite shows significant enrichments in K_2O and LILEs (in both pumice and glass), and these enrichments are matched by the most evolved stratovolcano lavas (Figs. 4.1 and 4.3). The K_2O contents of the high-silica stratovolcano lavas and the high-K LCY rhyolite both lie in the high-K calc-alkaline field in a K_2O vs SiO_2 discrimination diagram (Fig. 4.1). Similarly, the Na_2O contents are moderately depleted (Fig. 4.2). In comparison, the low-K LCY rhyolite and the enclave magma have the opposite relationship with LILEs and alkalis. These factors make a good initial case that the high-K LCY rhyolite could be related to the stratovolcano series magmas, while the low-K rhyolite was potentially related to a different suite of magmas. These magmas would not have received an enrichment in K_2O and the LILEs through mixing with VHKBs and could have compositions similar to the enclave magma. Further geochemical similarities between the LCY rhyolites and their potential parents are explored below.

The trace elements show the same trends as the LILEs and alkalis: the high-K LCY rhyolite again resembles the endmembers of the stratovolcano series, while the low-K rhyolite has compositions more similar to the enclave magma (Figs. 4.3 and 4.5). The mingled LCY-pumice sample (Ati502_06) which contains recharge magmas also contains lower-K rhyolites (section 3.2.5), yielding textural evidence that the low-K rhyolites could have been supplied by similar magmas. To test these relationships, modelling was performed to determine whether it was possible to produce these rhyolites from the hypothesised parental melts.

5.3.3 Modelling the formation of LCY rhyolites

Modelling was performed to attempt to reproduce the bulk-rock compositions of the low- and high-K LCY rhyolites using EME-AFC. Model run conditions are shown in Appendices

D.2.4 and D.2.5, while the full model spreadsheets are presented in Electronic Appendix III. Initial fractionating phase proportions were estimated from point counts of the respective starting materials (Fig. 3.30). However, as there is a compositional gap in analysed material between the starting materials and the final erupted pumices, phase abundances in the subsequent composition split in the model (> 62 and < 67 , and > 67 and < 72 wt.% SiO_2) were estimated both with experimental phase diagrams of appropriate composition magmas (e.g., Nandedkar et al., 2014; Marxer et al., 2022), and trial and error of these values to minimise model error. This also affected the choice of reference mineral compositions for the modelled minerals. For most minerals, only those analysed from the endmembers were used; however, for modelling the high-K LCY rhyolite, amphiboles from the compositionally similar F pumice were used, as no amphiboles were present in these pumices.

One significant drawback to the model for the final stages of evolution is the absence of quartz as a fractionating phase. As the model operates on a stepwise basis, based on incrementally increasing silica content, introducing quartz is not possible. Late-stage processes where silica content is buffered by the formation of quartz cannot be modelled. While quartz is present in the LCY rhyolites and the F pumice, it is absent in the D2 and I rhyolites. Quartz saturation is likely a late-stage process, and so its absence in the model likely does not have a significant effect for most of the modelling splits.

5.3.3.1 The low-K LCY rhyolite

It was assumed that the analysed enclave from the I pumice is an appropriate starting point for modelling the low-K LCY rhyolite due to their similar chemistries. Amphibole chemometry of the crystals in the enclaves and mingled pumices of these two eruptions shows that they grew from geochemically similar magmas (Fig. 5.17), so the assumption that they may be interchangeable has some merit. The biggest caveat is the P_2O_5 enrichment in the I enclave which was likely not present in the LCY recharge magmas. The cause of the large P_2O_5 enrichment in the I enclave is probably suppression of apatite crystallisation during the early phase of fractional crystallisation (section 5.2.4). As the crystals and groundmass of the mafic portions of the LCY recharge magma do not contain large amounts of apatite, the actual value for this element in these magmas may be much lower, and thus a much greater proportion of apatite is required to reach the observed P_2O_5 value of the lower-K rhyolite. This obviously has a significant impact on the trace element modelling as apatite is an important reservoir for several trace elements including

the REEs. Modelling was therefore focussed on re-creating the slope of the liquid line of descent for P_2O_5 rather than reaching the measured value.

Values for plagioclase, amphibole and orthopyroxene partition coefficients were adjusted to better fit the measured values (Electronic Appendix III). The final modelled phase proportions (Appendix D.2.4) have a model error $\sum D^2 = 2.11$, and the modelled liquid lines of descent are shown in Fig. 5.20. As with modelling of the recharge magma, several sets of trace element partition coefficients were tested. For apatite, zircon, amphibole and plagioclase, the values for the LILEs and REEs of Padilla & Gualda (2016) were used for the high-silica interval, while the values of Fujimaki et al. (1984) were used for the REEs in amphiboles in the lower-silica interval. Modelled trace elements are shown in Fig. 5.21.

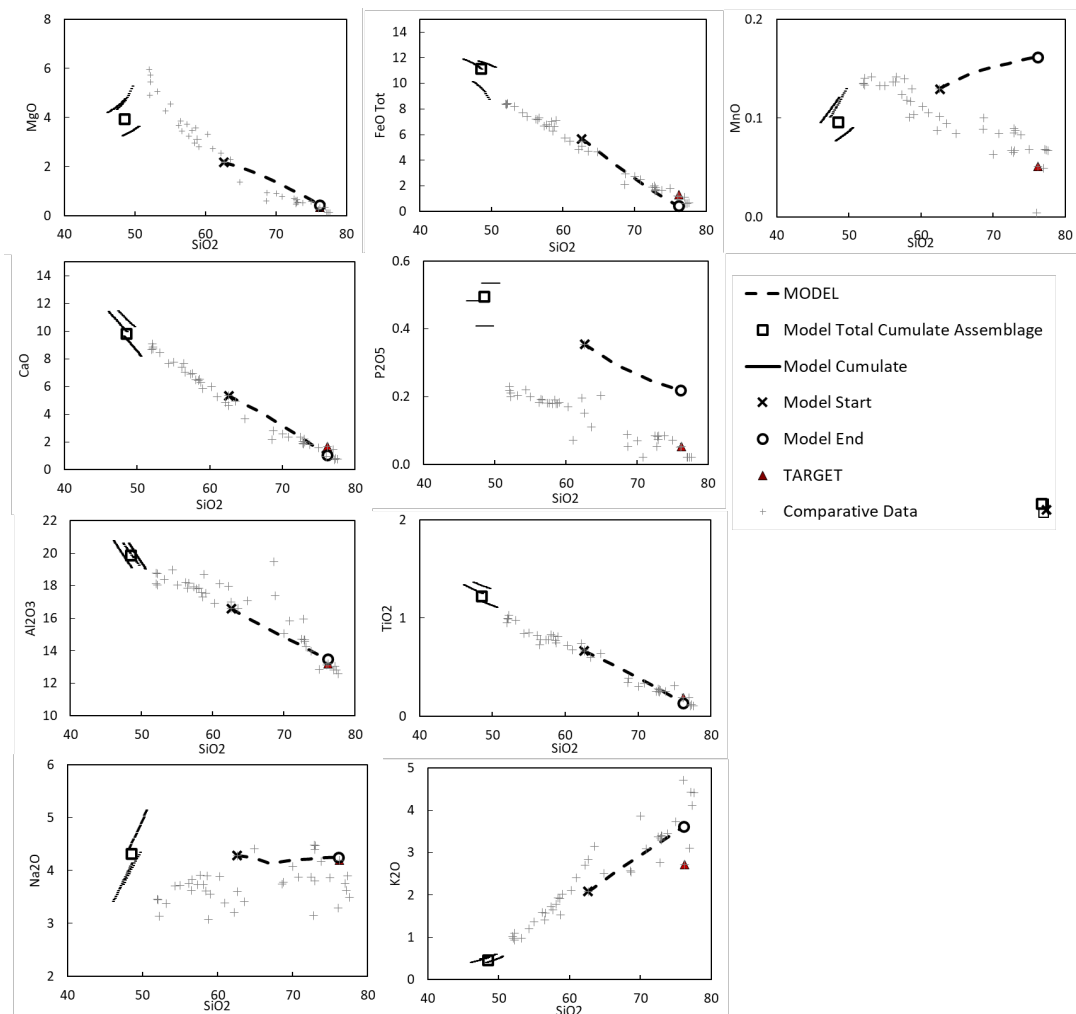


Figure 5.20. Major oxide results for EME-AFC modelling of the low-K LCY rhyolite. Most elements show a good fit, but MnO, P_2O_5 and K_2O show large errors which are discussed in the text

The largest differences between the modelled and measured major element trends are in K_2O and MnO (MnO again likely caused by the particular sensitivity of the model to this element). The model estimates much higher final K_2O concentrations than are observed.

Introduction of K-feldspar and/or biotite into the model can bring these down; however, as neither are found in either the parent or target magmas, it is an unlikely solution. The clue may again lie in the amphibole chemometry. Equations 13 and 14 of Zhang et al. (2017) produce lower estimates for melt K_2O content in the mingled LCY pumice-hosted amphiboles compared to those in the I enclaves (1.5-2.2 vs. 1.8-2.9 wt.% K_2O using eqn. 13 and 2.0-2.6 vs. 2.2-2.8 for eqn. 14; Fig. 5.17). Replacing the measured K_2O value of the starting material of the I enclave with the chemometry estimates from the LCY recharge magma produces a much better model fit but with the caveat that this assumption is based on chemometric results and not on analysed whole rock compositions. This difficulty in reproducing lower-K rhyolite compositions highlights the likely requirement for a compositional trend not enriched in K_2O .

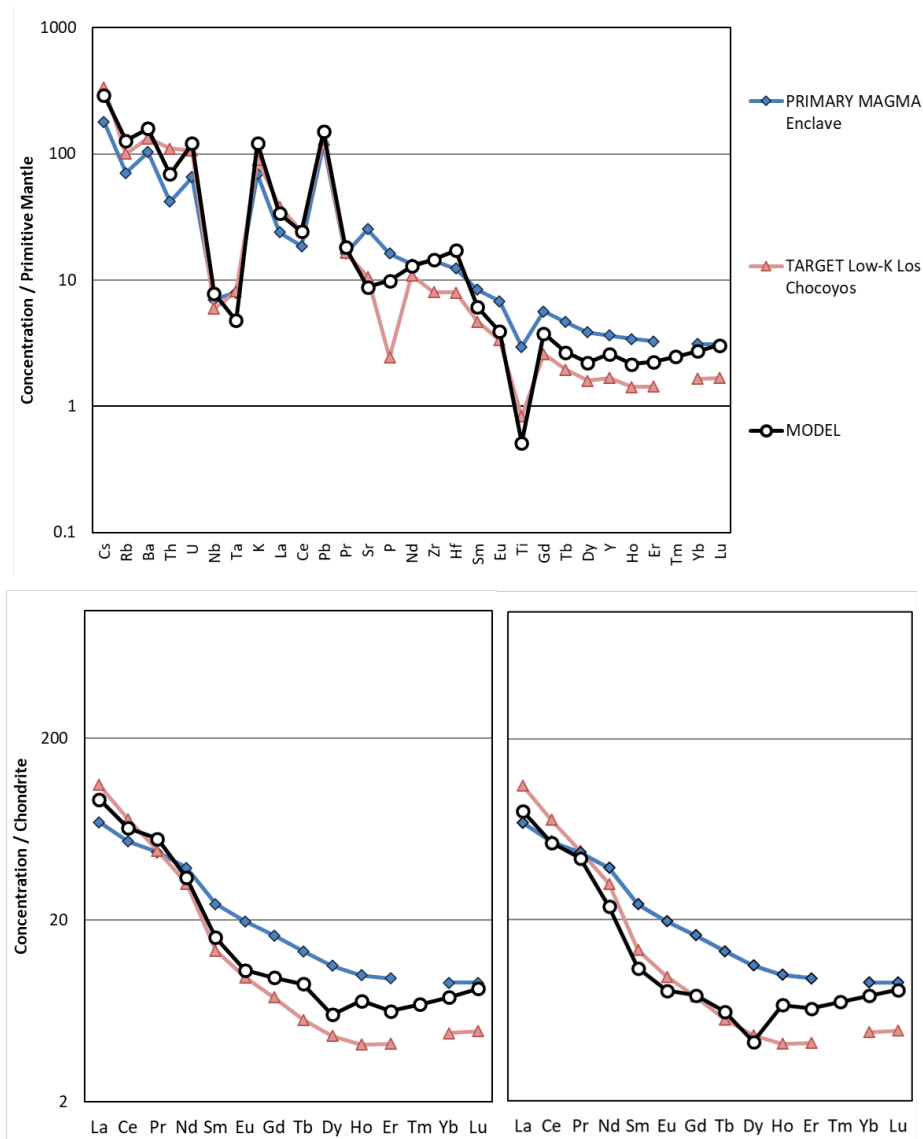


Figure 5.21. Trace element spider diagrams for the EME-AFC modelling of the low-K LCY rhyolite. Top: Incompatible elements; bottom left: original partition coefficients; bottom right: adjusted partition coefficients. Values for Primitive Mantle and Chondrite are from Sun & McDonough (1989).

The modelled trace element values accurately reproduce the observed composition. For the LILEs, the original model partition coefficients values work best, reproducing the observed saw-toothed pattern and concentrations in the elements Cs-U (Fig. 5.21). The exception is Th, whose enrichment in the low-K LCY rhyolite is not reproduced. Monazite (which was not included in the model) is a reservoir for Th, and so monazite dissolution could explain the Th-enrichment. There is strong textural evidence that re-heating of the low-K LCY rhyolite likely occurred (section 5.3.4), and the magma was then above the monazite saturation temperature, which would have caused monazite breakdown.

The LREE and MREEs are best modelled with both the amphibole REE K_d s for andesites of Fujimaki et al. (1984) and the apatite, zircon and amphibole REE K_d s for rhyolites of Padilla & Gualda (2016), which also reduce the Eu anomaly which was overpredicted with the default model K_d s. Again, if monazite dissolution has occurred, this would have also had a significant effect on the LREEs. Neither sets of K_d s accurately reproduce the HREE patterns, which are higher than the observed values. Fractionating greater amounts of zircon (in which the HREEs are more compatible than the other REEs) reduces the HREE values but at the expense of over-fractionating Zr. K_d s with higher values for the HREEs in zircon have been published (Yb = 490-564; Lu = 635-648; Mahood & Hildreth, 1983) and may lower the HREEs, but are not included in the model due to incompleteness.

5.3.3.2 *The high-K LCY rhyolite*

Due to the similarly enriched LILE concentrations, the high-K stratovolcano lavas were considered a good starting composition to model formation of the high-K LCY rhyolite. Major element results are very good, with a final model error $\sum D^2 = 0.04$ (Fig. 5.22). Model conditions are shown in Appendix D.2.5. The LILEs are modelled well, with the model reproducing the U-shaped Cs-U part of the spider diagram (Fig. 5.23), although Ba is over-depleted. The HFSEs are moderately well reproduced, as this model is the only one to accurately reproduce the Nd-Ta values. Zr and Hf are poorly modelled, despite efforts to reproduce the Zr/Hf ratio over the range of Zr concentrations; HREEs are similarly poorly modelled. The REEs are the least well modelled, as all values are overestimated, even using different partition coefficient values. For the LREEs, this might be because monazite was not included in the model. Overall, this model yielded a remarkably good fit of the observed major and minor elements of the rhyolite, but a lack of appropriate accessory phases and unknown appropriate trace element partition coefficients restricts the confidence in the reproduction of the trace element values.

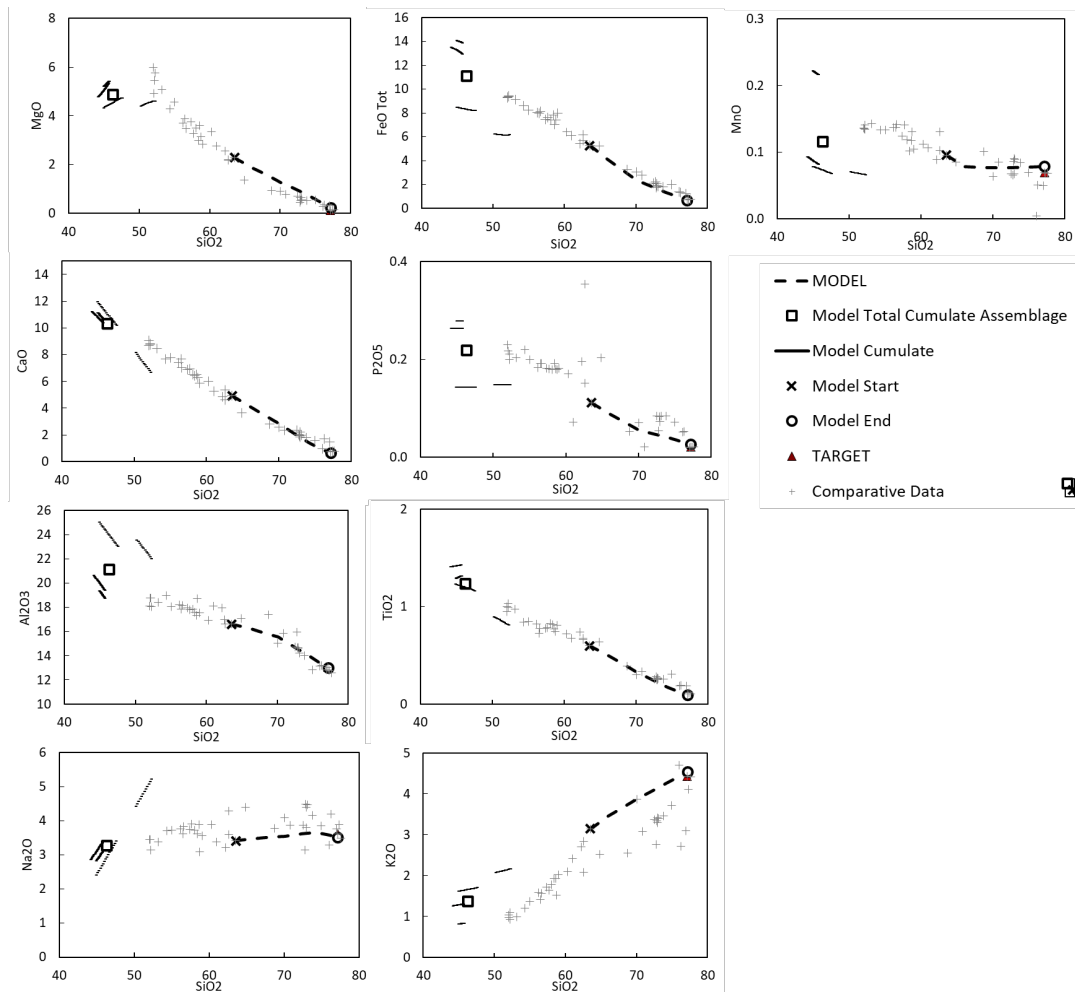


Figure 5.22. Major element results for the modelling of the high-K LCY rhyolite.

5.3.4 Storage conditions of the LCY rhyolites

The relatively few mineral phases in the LCY pumices makes estimation of their magmatic storage conditions difficult. Only the low-K LCY rhyolite contains a phase that can be used as a geobarometer (high-Ca amphibole), although with significant caveats (e.g., Ridolfi, 2021). Their very low crystallinities also make finding appropriate mineral pairs difficult (e.g., in the case of Fe-Ti oxide oxythermometry) and makes it more difficult to obtain an appropriate number of analyses to yield a representative mineral population. Nevertheless, using knowledge of the stability conditions of different minerals and the observed mineral assemblages can be useful for rough estimates of intensive variables.

Amphiboles are common in most rhyolites at moderate pressures and temperatures (e.g., Nandedkar et al., 2014). Below $\sim 800^{\circ}\text{C}$ and at 200-300 MPa, cummingtonite starts to dominate over high-Ca amphiboles and is the lowest temperature igneous amphibole species (Geschwind & Rutherford, 1992; Nicholls et al., 1992; Evans & Ghiorso, 1995) (Ridolfi et al., 2010). Cummingtonite is present in both the medium- and low-K LCY rhyolites,

while high-Ca amphiboles are only present in the low-K rhyolite. This implies that both magmas spent some time in the stability field of cummingtonite, but the dominance of cummingtonite in the medium-K rhyolite implies that it was stored at consistently lower temperatures and/or pressures. The overgrowth of high-Ca amphibole over cummingtonite observed in the low-K LCY rhyolite (Fig. 3.32A) could suggest that the low-K LCY was re-heated.

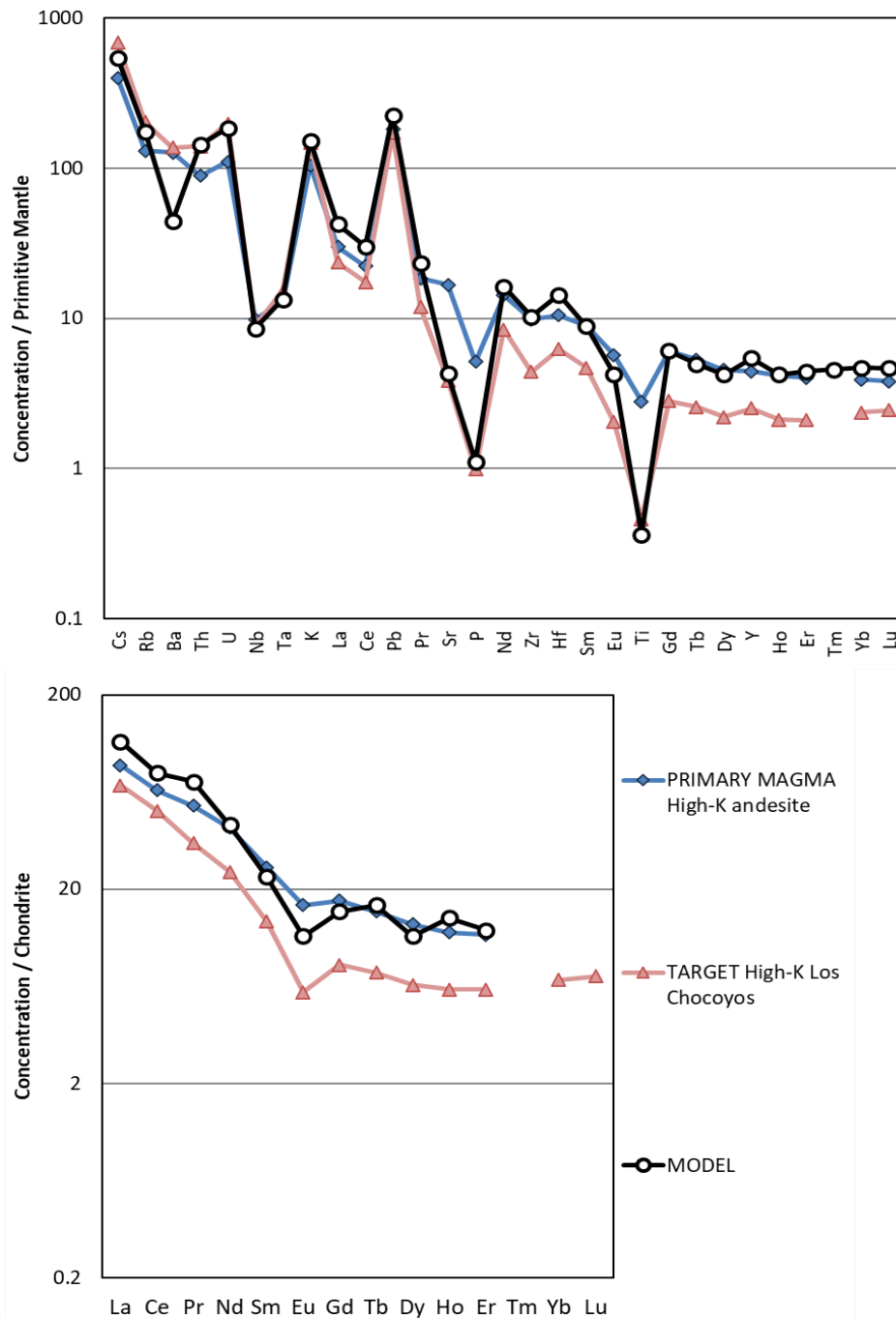


Figure 5.23. Trace element results for modelling the high-K LCY rhyolite. Almost all elements show little change from the starting point. Apart from Ba which is over fractionated, the LILEs (elements Cs-U on the top plot) show a very good fit

As well as storage conditions, biotite stability is strongly controlled by the host magma composition and so its presence is not a direct comparison of differing storage conditions between the LCY rhyolites. The fact that biotite is present in the medium- and high-K LCY rhyolites is likely simply a factor of the high K_2O contents in these magmas, rather than any control imposed by their storage conditions. Rhyolites from the CAVA can be used for comparison. Several pumices from Coatepeque (Kutterolf et al., 2020) and tephra from Amatitlán (Wunderman & Rose, 1984; Kutterolf et al., 2008a) have compositions that are similar to the high-K LCY rhyolite, and these both contain variable amounts of biotite and amphibole. In contrast, rhyolites from the Ilopango caldera show a different relationship. Some rhyolites are similar to the high- and low-K LCY rhyolites, but others do not contain any biotite or amphiboles (Suñe-Puchol, et al., 2019a), while the Tierra Blanca Joven rhyolites (Pedrazzi et al., 2019; Cisneros de León et al., 2021b) have compositions similar to the LCY low-K rhyolite and only contain amphiboles (Suñe-Puchol et al., 2019b). Thermobarometry of these amphiboles show that these magmas were hotter than the low-K LCY (Cisneros de León et al., 2021b). Some ignimbrites from Ilopango have compositions intermediate between the high- and low-K LCY rhyolites and only contain amphiboles. Unfortunately, thermobarometric studies have not been performed on most of these rhyolites, but it is clear that in this region, biotite tends to be more common in the more potassic rhyolites.

While amphiboles in AVC andesites to dacites are typically magnesio-hastingsites to tschermakitic pargasites, those in the most evolved rhyolites range further to magnesio-hornblendes (Fig. 3.36). Formula calculations for the thermobarometry models of Ridolfi et al. (2010), Ridolfi & Renzulli (2012) and Ridolfi (2021) are based on the 13-cation method, with the assumption that only Ca and Na fill the B-site (over Fe^{2+} , Mn or Mg). For the magnesio-hastingsites and tschermakitic pargasites this assumption works, but for the least aluminous (and therefore the more 'evolved') magnesio-hornblendes, the calculation fails as Fe^{2+} , Mn and Mg fill the C site and leave the B site with low totals. Many of the amphiboles in the AVC rhyolites therefore lie outside the above calibrations and using these methods to constrain the intensive variables of the rhyolite magma would result in unknown errors. These amphiboles are the endmember for the most evolved rhyolites (excluding cummingtonite) and therefore probably grew during the last storage phase before eruption. Thus, they cannot provide estimates for this final stage, and for constraints it can only be stated that they probably grew at conditions below the calibration limits (i.e. $<800^{\circ}C$ and/or <130 MPa).

In comparison, the thermometers of Putirka (2016) perform well at low temperatures and the magnesio-hornblende amphiboles fall within their calibration, and plagioclase-liquid hygrometers are still applicable. Figures 5.6-5.8 compare the results for the different LCY pumices.

5.3.4.1 The low-K LCY rhyolite

The low-K LCY rhyolite was the only magma in the LCY eruption that contained a phase that is commonly used for geobarometry (i.e., amphibole). To check the applicability of amphibole compositions for constraining the thermobarometry of the LCY rhyolite, amphibole equilibrium melts were estimated using the chemometric equations of Ridolfi & Renzulli (2012) and Zhang et al. (2017) (Fig. 5.17). These results were surprising, as they showed that the majority of these amphiboles were putatively in equilibrium with melts <75 wt.% SiO₂, with a full range of estimates from 62-78 wt.% SiO₂. This is almost identical to the pattern seen in the mingled LCY pumice, where amphiboles yielded a large spread of melt composition estimates (Fig. 5.17). For the mingled pumice, the likely cause of this spread is the mixing of two populations of amphiboles, one from the recharging magma and one from the rhyolite host, and then crystallisation of disequilibrium amphiboles that produce intermediate composition melt estimates. The almost identical spread in the texturally unmingled pumice was likely caused by the same process, but while the whole rock texture has been homogenised, the amphiboles have likely only partially re-equilibrated with the host rhyolite, something that has been commonly observed at other centres (Zhang et al., 2017; Keller et al., 2024). The re-heating caused by magma recharge also had a late effect on these rhyolites; in fact, higher T high-Ca amphibole rims are found around lower-T cummingtonite cores (Fig. 3.32A). This is clear evidence that the magma was re-heated before eruption.

As a consequence, few amphiboles in the low-K LCY rhyolite were actually in equilibrium with the host melt, and this therefore further reduced the number of amphiboles that could be used for thermobarometry. Thus, only amphiboles which had chemometric estimates that were > 75 wt.% SiO₂ were used. Using the recalibrated equations and algorithm of Ridolfi (2021), estimates for the storage conditions of 150-185 MPa ($\pm 12\%$; 18-22 MPa) and 842-870 ($\pm 22^\circ\text{C}$) were calculated from these amphiboles. Equation 5 of Putirka (2016) gave slightly lower values (786-847, $\pm 30^\circ\text{C}$). Iterative hygrometry of the low-An feldspar compositions (using equation 24a of Putirka (2008), the hygrometer of

Waters & Lange (2015), and the methodology of Wieser et al. (2022)) in this pressure range yields still lower estimates (770-814 $\pm 36^\circ\text{C}$), with 5.6-6.4 (± 0.35 wt.% H_2O).

Finally, based on the published appearance of monazite in the low-K LCY rhyolite (Cisneros de León et al., 2021a), monazite saturation temperature estimates can be performed using the equation of Montel (1993). For the glasses in the pumices, this produced a range of temperatures (739-770 $^\circ\text{C}$).

5.3.4.2 The medium-K LCY rhyolite

Like the high-K rhyolite, the medium-K rhyolite also has few mineral phases and low crystallinity that makes it difficult to constrain intensive variables. Monazite was not observed in thin section, however based on the observation of monazite in the high- and low-LCY rhyolites (Cisneros de León et al., 2021a), it may be assumed that it is present. Monazite saturation temperatures for the medium-K LCY rhyolite are the highest of the three LCY rhyolites, at 749-778 $^\circ\text{C}$ (note that these estimates do not actually constitute temperature estimates, rather maximum potential temperatures). Plagioclase-liquid hygrometers are presented for comparison; these calculations were performed in the same and lower pressure range (100-180 MPa) as for the low-K LCY rhyolite (assuming that the medium-K rhyolite was derived from the low-K rhyolite and is therefore unlikely to have formed at greater depths). These values gave temperature estimates of 755-780 ($\pm 36^\circ\text{C}$) with 6.1-6.7 (± 0.35 wt.% H_2O). These values are lower than those from the low-K LCY rhyolite, confirming that the medium-K LCY rhyolite was likely stored at a lower temperature than the low-K LCY rhyolite.

5.3.4.3 The high-K LCY rhyolite

The presence of monazite in the high-K rhyolite (Cisneros de León et al., 2021a) allows the maximum temperature estimates to be calculated using the monazite saturation equation of Montel (1993) for the analysed matrix glasses (700-734 $^\circ\text{C}$). Hygrometry gave temperature estimates within this range (710-738 $^\circ\text{C}$ and 720-748 $^\circ\text{C} \pm 36^\circ\text{C}$ for low pressure vs. high pressure limits) for a range of upper crustal pressures (50-200 MPa), with estimates of water content between 6.5-7.0 ± 0.35 wt.% (minima) and 6.7-7.3 wt.% (maxima). This shows that pressure has a minor control on these equations, and that these magmas were likely stored in the upper crust.

While it is not possible to constrain the depth of storage for the high-K LCY rhyolite, its stratigraphic position in the eruption deposit could be a clue to its previous location

relative to the lower-K rhyolites. Only the high-K LCY rhyolite is present in the basal fall unit, while all three rhyolites are found in the overlying ignimbrite (Rose et al., 1987). This likely suggests that the high-K LCY rhyolite magma body overlay the lower-K LCY rhyolite magmas and therefore erupted first.

5.3.5 Comparing the high- and lower-K LCY rhyolites

Several textural and geochemical features of these pumices provide details about the nature of the origin and evolution of these magmas. Some of the best details are obtained from their mineral populations, which can record sequential events.

One feature that is unique to these two pumices is the presence of small, rounded features in plagioclase, described in section 3.2.3.1 which have ‘shaded’ margins in BSE images (Fig. 5.24). These may be features produced during the polishing process such as partial collapse of the material into underlying vesicles, but it is unusual that they would only show up in two samples with very similar origins and no other pumices, as both these samples are found in the LCY ignimbrite phase (samples Ati425_02 and Ati425_03 low-K and medium-K LCY, respectively). If they are primary features, and since these are present in all sectors of the plagioclase crystals and sit across zone boundaries, they could be syn- or post-eruptive features caused by external factors. Processes such as decompression or post-emplacement reheating could be responsible, but the reason why the affected crystals are only found in the lower-K LCY rhyolites is unknown.

There is a notable difference between the plagioclase compositions in the two lower-K rhyolites. The patchy-zoned plagioclase regions in the medium-K magmas have much higher Or at low-An than those in the low-K rhyolite (Fig. 3.35), which for the later-formed (and likely lower-An) plagioclase would be expected due to the more potassic host melt. However, the value of the Or endmember for the patchy zones in the crystal is potentially higher than expected, and this region forms a “hockey-stick” shaped curve on this plot. These compositions pass equilibrium tests with the medium-K rhyolite melt. It is uncertain what would cause such elevated Or values in these specific regions.

Plagioclase crystals from the medium- and low-K rhyolites show similarities in their textures that imply similar histories. Both populations contain strongly patchy zoned high-An cores, with low-An regions where resorption and recrystallisation has occurred. They both also commonly have a moderate-An rim separated by a resorption surface (Fig. 3.31). These features suggest decompression-induced resorption and recrystallisation of the magmas

(Vance, 1965; Streck, 2008), followed by re-heating. This re-heating is shown by the mingled pumice (sample Ati502_06) which contains zones of both these rhyolites (section 3.2.5.1), as well as cummingtonite crystals rimmed by high-Ca amphibole (Fig. 3.32A), which crystallises at higher temperatures (Geschwind & Rutherford, 1992; Nicholls et al., 1992).

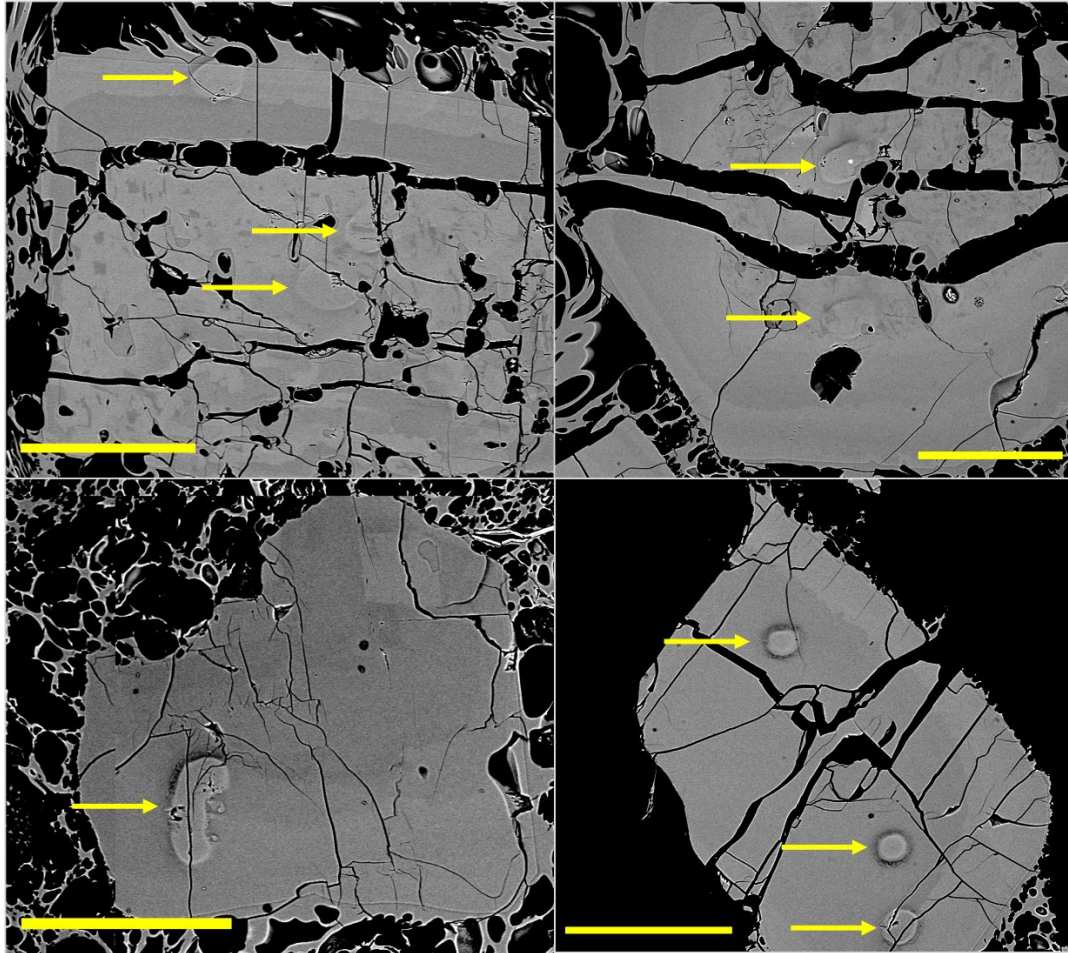


Figure 5.24. BSE photomicrographs of “bump” textures on plagioclase of the low-K (top row, sample Ati425_02) and medium-K (bottom row, sample Ati425_03) LCY rhyolites. Scale bars are all 0.25 mm, apart from lower left which is 0.2 mm. Note that the “bumps” are present in all sectors of the crystals and several sit across zone boundaries.

Another feature of the LCY rhyolites (that also feeds into the discussion about the origin of the post-LCY rhyolites; section 5.4) is their relatively homogeneous isotopic compositions. The rhyolites from the three pumices group tightly together on all bivariate isotope diagrams, and in general lie between the values of the pre- and post-LCY stratovolcano lavas (section 4.3.3; Figs. 4.9-4.13). As discussed in section 5.1.1, the main control on isotopic composition is distance from the trench, because the crust has a more radiogenic signature with increasing distance (Donnelly et al., 1990). The LCY magmas were formed in the intermediate region between the old and new lines of the arc front, and so it makes

sense that they would have intermediate isotopic values. There are two possibilities for the mechanism by which these values were obtained: 1) they were fuelled by magmas that are only sourced from this intermediate region (i.e. stratovolcanoes in the location where the caldera now lies that the high-K LCY pumices were derived from, and recharge magmas that the lower-K LCY pumices grew from), and so inherited their signature from these; and/or 2) extensive homogenisation of the magmas from the old, new and intermediate positions that occurred as the magmatic plumbing systems began to interconnect, resulting in an average value. Given the size of the magma bodies and the width of the centre, it seems much more likely that the second option was the dominant process that controlled their isotopic values. This is further discussed in Chapter 6.

More variations in the LCY rhyolites can be seen by studying the REEs. Due to the systematically variable compatibilities of the REEs in many common mineral phases, they can be excellent tools to investigate the evolution of magmas. The REEs are mainly controlled by amphibole, apatite, and ilmenite in more mafic magmas, whereas monazite, allanite and zircon become important in evolved magmas (Miller & Mittlefehldt, 1982; Padilla & Gualda, 2016). While most REE-compatible phases in more primitive lavas are more compatible with the MREE and HREEs (causing depletions in these elements in more evolved magmas), the minerals in more felsic magmas (monazite and allanite) tend to be more LREE-compatible, causing pronounced LREE-depletion in more felsic magmas (Miller & Mittlefehldt, 1982). The exception to this is zircon, which is more compatible with the HREEs.

The high-K LCY rhyolites are LREE-depleted compared to the lower-K LCY rhyolites and even with respect to the high-K stratovolcano andesites. Monazite occurs in the heavy mineral separates of the LCY fall and flow deposits (Cisneros de León et al., 2021a), and its presence shows that monazite was saturated in both the high- and low-K LCY rhyolites.

Crystallisation and fractionation of monazite would have a significant effect on REE concentrations, as shown by the variable values in the matrix glass and whole rock compositions. The analysed glass compositions of the high-K LCY rhyolite have lower LREE values than the whole rock compositions (shown by La in Fig. 5.25).

Calculated monazite saturation temperatures using the equation of Montel (1993) for the matrix glasses and whole rock compositions of the different LCY rhyolites (Table 5.1) show that the low-K LCY rhyolite was within the stability field of monazite (based on plagioclase and amphibole temperature estimates), which could partly explain the elevated LREE

values compared to those of the high-K rhyolite. Plagioclase hygrometry temperature estimates for the high-K LCY rhyolite show that it was also within the monazite stability field (Table 5.1), and the presence of monazite in the fall deposit of this eruption (exclusively composed of high-K rhyolite) shows that it was a stable phase. Monazite also strongly fractionates Th over U (Stepanov et al., 2012; Breiter, 2016). A plot of La vs. Th/U shows a strong positive correlation (Fig. 5.25), suggesting coupling between them, likely controlled by monazite.

| | Matrix glass monazite saturation temperature (°C) | Whole-rock monazite saturation temperature (°C) | Melt temperature estimate from plagioclase ($\pm 36^\circ\text{C}$) (/amphibole $\pm 22^\circ\text{C}$) |
|------------------------|---|--|---|
| High-K LCY rhyolite | 700-734 | 720-723 | 716-745 |
| Mid-K LCY rhyolite | 749-778 | 745 | 755-780 |
| Low-K LCY rhyolite | 739-770 | 733 | 770-813 (/796-830) |

Table 5.1. Temperature estimates of the different LCY pumices using monazite saturation temperatures, compared against plagioclase (and for the low-K LCY pumice additionally amphibole) thermometry estimates

Monazite occurs in the low-K LCY rhyolite (Cisneros de León et al., 2021a), even though these pumices show a weaker geochemical signature for monazite fractionation (i.e., similar relative enrichments in the LREEs and moderate relative enrichment in Th in both whole rock and matrix glass; Figs. 4.7, 5.19 and 5.25). Temperature estimates for the magma are marginally higher than the monazite stability field (Table 5.1), but as the lower-K LCY rhyolites likely underwent reheating, it is possible that these magmas spent some time within this field and crystallised monazite. The elevated LREE and Th/U trace element contents of the matrix glasses rule out monazite accumulation as the cause of this geochemical signature. It was shown above that reheating has likely affected the lower-K LCY rhyolites, which could have caused monazite dissolution, which is a better explanation for the higher LREE and Th/U ratios in the low-K LCY rhyolite.

Further evidence for monazite fractionation in the LCY rhyolites is given by a comparison of the Th/U ratios in the bulk rock and matrix glass. Fig. 5.25 compares the values for the matrix glasses with the whole rock compositions. The bulk rock values all overly their respective matrix glass fields, and monazite extracting Th over U could explain this difference.

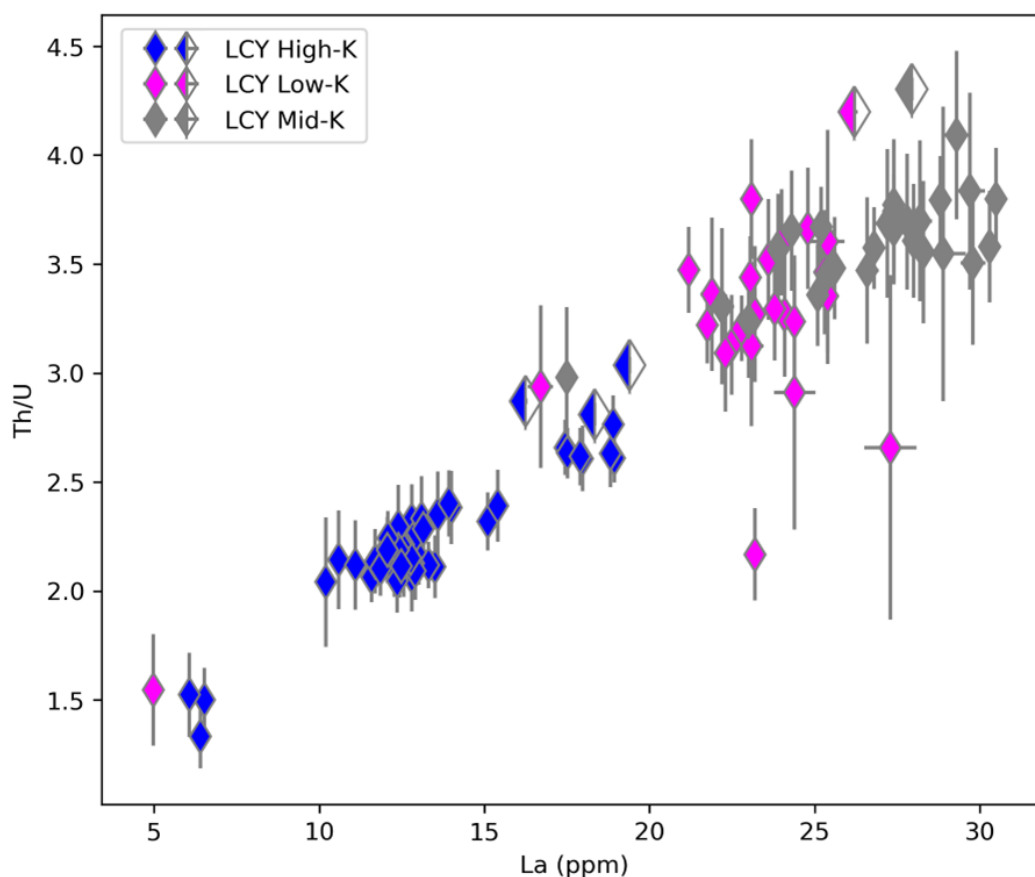


Figure 5.25. Matrix glass (full symbols) and whole rock (half-filled symbols) compositions from the different LCY pumices showing the correlation between La and Th/U. Analytical uncertainties are 2 s.e.

Tracers such as Zr/Hf, Sr/Y and Eu/Eu* ratios have elevated values in the matrix glasses of the lower-K rhyolites compared to the high-K rhyolites (Fig. 5.19), which mirrors the similarity between the recharge magma and the high-K lavas (section 5.2.4). In the stratovolcano andesite magmas and the enclave magma, these tracers are influenced by the relative inputs of plagioclase, amphibole and zircon, as well as the presence or absence of the VHKM. As these magmas likely were the parents of their respective rhyolite compositions, zircon and apatite would also have started to exert an influence. These accessory phases are both present and stable in the two different rhyolite groups, and therefore their effect on the trace element budget may be similar. Therefore, the initial elemental values may be more important to consider when comparing the final observed values in the erupted rhyolites.

This is not necessarily the case for all tracers. Eu/Eu* values in the lower-K rhyolites are still high. As the accessory phases that could act to obscure the negative effect of plagioclase on Eu/Eu* (i.e. amphibole, apatite, etc...) are present in similar proportions in both rhyolite groups, the relative effects of the major fractionating phases are again most responsible.

Greater amounts of amphibole fractionation in the lower-K rhyolites are therefore the most likely the cause of their small Eu/Eu* values.

5.3.6 The LCY crystal mush

Since the development of the crystal mush theories, studies examining crystal-poor rhyolite ignimbrites have invoked numerous related melt-extraction processes including crystal settling, compaction and filter pressing to explain their nature (section 1.2.1). The compositional diversity commonly shown by large caldera-forming events can also be explained by similarly complex mush systems containing many discrete melt-rich lenses (Cashman & Giordano 2014, and references therein). These parts of the mush paradigm appear to fit well with the observations made of the AVC, but then an explanation is required for the compositional variation observed in the high- and lower-K LCY rhyolites. For the high-K LCY rhyolite, it has been shown that it is most likely related to the high-K stratovolcano magmas (section 5.3.2). Assuming that a large enough mush system was developed underneath the pre-LCY stratovolcanoes (which is explored in Chapter 6), then this would be an excellent candidate for the source mush for this rhyolite.

The lower-K LCY rhyolites are slightly more difficult to explain. It has been shown the enclave magma from the post-LCY I eruption is a good candidate for a parent magma for this rhyolite, however this then requires a second portion of the LCY mush that is excluded from any potential contamination from LILE-enriched sources. It has been shown that the LILE enrichment and subsequent magma storage likely occurred in the upper crust (sections 5.1.2 and 5.1.3). The underlying regions of the crust therefore likely did not have any LILE enrichment and therefore could act as a good source mush for the low-K LCY rhyolite. The enclave magma therefore likely represents a deeper intermediate magma evolution, from which the low-K LCY rhyolite would eventually be an endmember. The deeper location of this mush is supported by the eruption stratigraphy. The fact that the lower-K LCY rhyolites were only erupted during the second phase of the LCY event could suggest that they were stored beneath the high-K LCY rhyolite and only erupted after sufficient volume of the overlying rhyolite had been removed (section 1.4.1).

5.4 The post-LCY pumices

Following the LCY eruption and formation of the Atitlán III caldera, the AVC entered a phase of recovery (defined as “the period during which magmas show clear signs of thermal rejuvenation of the system”; Bouvet de Maisonneuve et al., 2021) from the caldera-forming eruption, as newly arriving magmas began to interact with the remnants of

the LCY magma feeding system. These remnant magmas include unerupted portions of the different LCY rhyolites and/or portions of the underlying mush system from which the LCY magmas were erupted. Erupted magmas during this phase consist of either remobilised portions of the LCY system (either magmas and/or remobilised portions of the mush), the ascending mafic magmas, or a mixture of the two.

During this phase, a series of pumice eruptions occurred, along with the construction of Volcán San Pedro. These pumices exhibited a wide variety of compositions from basaltic andesites to rhyolites, and investigation of them reveals much about the AVC magma system during this time. In this section, several of the post-LCY pumices will be investigated to determine their origin and relationship to the remnants of the LCY magma system and any newly arriving magmas.

5.4.1 Origin of the intermediate tephra

5.4.1.1 The D1 andesite

The D1 andesite (sample Ati427_01a whole rock/sample Ati426_03a thin section) is geochemically quite similar to the stratovolcano magmas and lies within the observed trend (Figs. 4.1 and 4.2), the only major difference being its depletion in Na₂O. However, there are several petrological differences between the D1 and stratovolcano andesites. The most common ferromagnesian phase in the D1 pumice is amphibole. These crystals lack breakdown rims but instead have patchy zonation in the cores, and one or more reverse zones are common (Fig. 3.26). These textures indicate reheating or mafic recharge rather than decompression (Streck, 2008). Amphibole chemometry (Ridolfi & Renzulli, 2012; Zhang et al., 2017) gives clues about the nature of the magma or magmas from which they grew. Crystal cores show that they equilibrated with a rhyodacite with low K₂O content, similar to the lower-K rhyolites, while the lighter rims and patchy zones grew from a more mafic andesite (Fig. 5.26).

Amphibole thermobarometry was used on the crystals (Fig. 5.26) using the same methodology as detailed above. The darker cores in BSE images yielded cooler temperatures than the lighter rims, in line with their chemometry. Pressure estimates are confusing as the lighter, younger regions of the crystal gave higher pressure estimates than the material they overgrew. This could suggest that the magma body descended in the crust after mixing; however, a more likely explanation is that the composition of amphiboles is more strongly controlled by variables other than pressure (Putirka, 2016),

and that the apparent variations in pressure are more likely reflections of changes in magma temperature or chemistry that occurred during mixing. Therefore, the darker cores probably reflect more accurate estimates of storage pressures and suggest that the initial host magma body was stored at 174-344 MPa ($\pm 12\%$, 21-41 MPa) and 868-918 ($\pm 22^\circ\text{C}$).

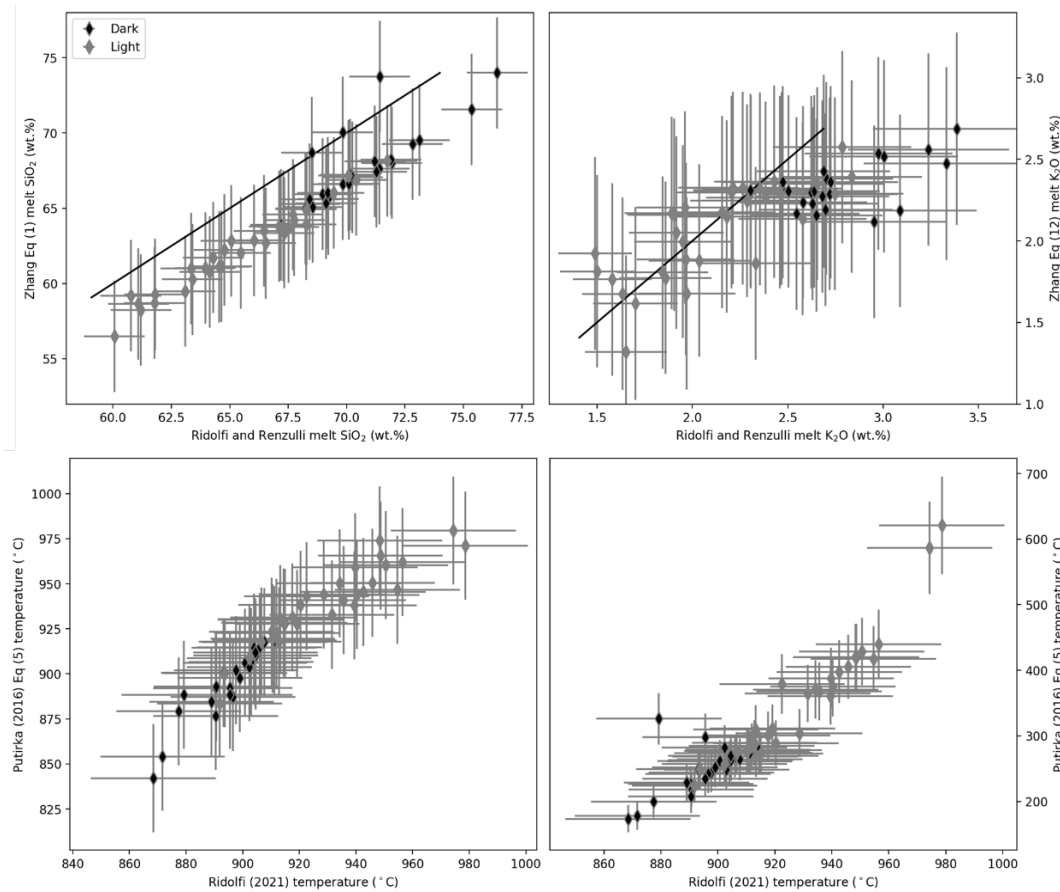


Figure 5.26. Amphibole chemometry and thermobarometry results for the darker cores (dark grey in BSE images, c.f. Fig. 3.26A) and lighter rims (light grey) in the D1 pumice (sample Ati426_03a). These show that the cores were likely in equilibrium with a dacitic-rhyolitic melt likely more silicic than the matrix glasses analysed (c.f. Fig. 4.15), while the rims grew out of more mafic magma. Note that the least silicic and potassic of the rim analyses estimates is well out of the range of matrix glasses measured (Fig. 4.15). Bottom left: Comparison of the Ridolfi (2021) and Putirka (2016) thermometers; bottom right: pressure vs. temperature estimates from the Ridolfi (2021) thermobarometer. Shown model uncertainties are 1 s.e.

Observations of the plagioclase crystal population also support the idea of reheating and mixing. These crystals are highly resorbed (Fig. 3.26) and have one of the narrowest compositional groupings found in AVC igneous materials at An_{58-90} . The minimum An value is also much higher than the highest minimum An values of any of the AVC lavas (Fig. 3.53). This is unusual, as it has a very similar population of plagioclase compositions as the basaltic andesites, despite having a much greater whole rock silica concentration (c.f. Figs. 4.1 and 3.53). This compositional bias could result from extensive resorption and recrystallisation of more An-poor crystals because of re-heating, and/or mixing of a crystal-

rich mafic magma with a plagioclase-poor evolved magma. The predominance of high-An cores suggests that most plagioclase crystals were sourced from the more mafic magma.

These more calcic plagioclase can potentially explain the disparity between the elevated matrix glass Na₂O contents (measured at 4.0-4.7 wt.%; Fig. 4.15) and the low whole rock Na₂O composition (3.1 wt.%; Fig. 4.2). The absence of more sodic plagioclase would act to drag down the whole rock Na₂O content. The elevated matrix glass Na₂O contents also rule out alkali remobilisation as a cause for the low value in the whole rock composition.

Several anomalies in the geochemistry of the D1 pumice sample could be explained by resorption of mineral phases in the more silicic endmember. Any remaining low-An plagioclase would also likely have been resorbed, contributing to elevated Na₂O contents in the observed melt (Fig. 4.15). Resorption of apatite could also explain the relatively elevated P₂O₅ in the matrix glasses (Fig. 4.15).

Mixing is further supported by the presence of a microphenocryst-rich region in sample Ati426_03a (Fig. 3.25), in which amphibole crystals are more primitive than the phenocryst cores elsewhere in the sample. The greater number of crystals and their smaller sizes suggests a greater degree of undercooling, which could mean that this portion of the sample represents the mafic endmember.

There is then an open question as to the endmembers of this mixing. The D1 pumice composition does not lie on any mixing lines between the most mafic compositions and any of the rhyolite pumices, primarily due to its extreme depletion in Na₂O. The resorption of low-An plagioclase is likely tied to this, and subsequent concentration of low-An plagioclase in the relatively sodic glass could result in a whole rock composition depleted in Na₂O.

Different methods were also attempted to further constrain the intensive variables of the D1 andesite. Orthopyroxene was present, but no crystals were in equilibrium with the matrix glass using the criteria of Putirka (2008). Plagioclase-liquid hygrometry was more successful, and yielded temperatures of 985-1023±36°C and 2.7-3.4 ±0.35 wt.% H₂O, although these must be considered with the caveat that lower-An crystals have probably been destroyed and thus only represent crystals from a mafic mixing endmember and/or those grown from the mixed melt.

5.4.1.2 The I1 basaltic andesite

The most common petrographic textures in the I1 sample (Ati505_06a) strongly imply the occurrence of mixing, including olivine with pyroxene and myrmekitic Fe-Ti overgrowths

(Fig. 3.27 B, C, and D; similar to the stratovolcano lavas discussed in section 5.1.2) and highly zoned plagioclase (Fig. 3.27A) . Clinopyroxene cores and mantles are sector-zoned (Fig. 3.27D and 5.27), indicative of moderate undercooling (Brophy et al., 1999; Armienti et al., 2013; Ubide et al., 2019) and have spongy rims which likely formed during disequilibrium crystallisation (Fig. 5.27; Hammer et al., 2016; Welsch et al., 2016).

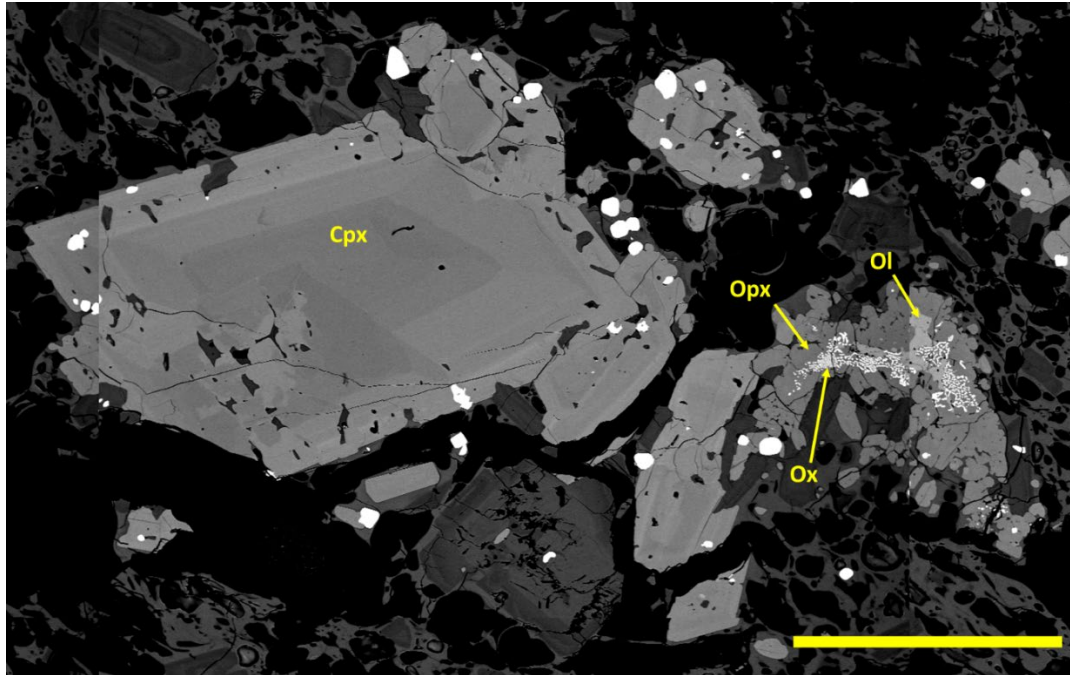


Figure 5.27. BSE photomicrograph close-up of Fig. 3.27B showing the common textures found within the ferromagnesian phases of the I1 scoria. Cpx-clinopyroxene, opx- orthopyroxene, ol-olivine, ox-Fe-Ti oxides. The clinopyroxenes are commonly heavily zoned in the cores and/or mantles, while their rims are typically spongy. The olivine and orthopyroxene are typically closely related, with the most common texture being overgrowths of orthopyroxene on the former. Myrmekitic Fe-Ti oxides are also commonly present. Scale bar = 0.5mm

The groundmass is heterogeneous, being mostly glass with very rare microlites, but numerous small (typically <0.4 mm wide) regions of microlite-rich groundmass of slightly different styles (Fig. 5.28) indicate greater degrees of undercooling, again implying mixing. These features suggest a lack of equilibrium, and so application of thermobarometers is difficult (Fig. 5.6-5.8). A solitary clinopyroxene-orthopyroxene pair satisfied the equilibrium tests and provided estimates of $930 \pm 60^{\circ}\text{C}$ and $175 \pm 320 \text{ MPa}$, although the model error is much greater than the estimated value and so is presented with caution. No clinopyroxenes are in equilibrium with the matrix glasses, while five analyses from the inner-most cores of clinopyroxene phenocrysts are in equilibrium with the whole rock composition. These provided estimates of $1016\text{-}1041 \pm 44.9^{\circ}\text{C}$ and $242\text{-}395 \pm 270 \text{ MPa}$, although again these pressure estimates have large uncertainties that significantly reduce their usefulness. Plagioclase-liquid hygrometry using the same methodology as

above and using crystals rims and glass compositions provided temperatures of 988-1039 $\pm 36^\circ\text{C}$ and $2.0\text{-}2.7 \pm 0.35 \text{ wt.}\% \text{H}_2\text{O}$.

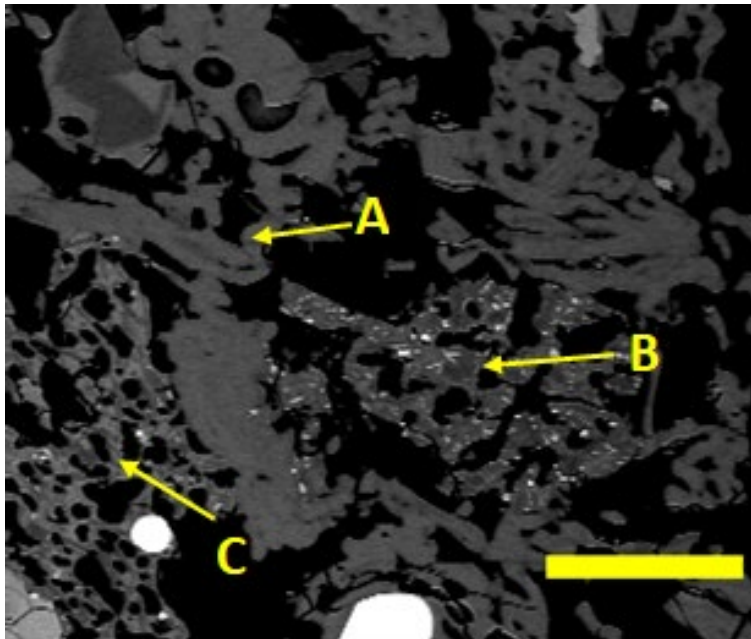


Figure 5.28. BSE photomicrograph of the groundmass of the I1 scoria (sample Ati505_06a). Note the three different types present: A) Microlite-free melt; B) Microlite-rich groundmass glass containing abundant Fe-Ti oxide grains; and C) Microlite- and vesicle-rich groundmass, with a greater proportion of plagioclase microlites compared to type B. Scale bar = 0.1mm

The geochemistry of the I1 basaltic andesite does not provide much further information about its formation. The composition lies well within the trend of the stratovolcano series, which itself was strongly influenced by mixing. It is unlikely that the more evolved magma involved was a VHKM (there are no VHKM present in this sample), instead the presence of the pumice at the base of the I series of rhyolite eruptions (Fig. 2.6) could suggest that it is the result of mixing of a basaltic andesite magma with a minor amount of one of these rhyolite magmas.

5.4.1.3 Origin of the intermediate tephras

The analysed intermediate clasts of the D and I eruptions show clear geochemical and petrological evidence that they have been formed through magma mixing. It is commonly observed that mafic and silicic magmas erupted together during this phase, either as mingled magmas or during the same eruptive phase (Figs. 2.5 and 2.6), meaning there was plenty of opportunity for mixing. Recharging magmas could mix with remnant rhyolite magmas and/or remobilised portions of the mush system (c.f., Deering et al., 2011a; Pamukcu et al., 2013; Wolff et al., 2015; 2020). The radiogenic isotope values of the D1 pumice are nearly identical to those of the rhyolite pumices (Figs. 4.9-4.13), suggesting that

it could be related to them. In contrast, the I1 scoria has lower $^{87}\text{Sr}/^{86}\text{Sr}$ and higher $^{143}\text{Nd}/^{144}\text{Nd}$ values than the range of the AVC pumices, as well as lower values for all Pb ratios (Figs. 4.9-4.13). Radiogenic isotope values are highly variable for the mafic magmas of the AVC (Fig. 4.9-4.13). It is more likely that the dominant parent of the I1 basaltic andesite was a more mafic magma like those erupted at the stratovolcanoes. This magma had different isotope composition to the LCY rhyolites, and that minor contamination did not significantly change this.

5.4.2 The post-LCY rhyolites

5.4.2.1 Characteristics of the post-LCY rhyolites

The post-LCY activity was highly complex and involved numerous eruptions that varied greatly in composition and style, both within and between these different eruption sequences. Providing a complete analysis examining all this complexity is beyond the scope of this study, and the analysed samples instead are a representative selection used to investigate the post-LCY recovery phase. Fig. 5.18 compares the bulk rock compositions from this study with published data. The post-LCY rhyolites show similar variability as seen in this study and there are no compositional groupings or trends in these pumices. Their range of compositions is similarly wide to those in this study. In the absence of a detailed study on the matrix glass compositions of these pumices, it is unknown whether this variation is the result of actual compositional variations in the melts, or simply the effect of the variable crystallinities shown by these deposits.

The post-LCY rhyolites share some similarities: they all contain both amphibole and biotite in variable amounts (but never cummingtonite). The analysed whole rock compositions are all less silicic rhyolites than the LCY rhyolites, and they have intermediate alkali contents between the high- and lower-K LCY compositions (Figs. 4.1 and 5.18). They also have very similar radiogenic isotopes (section 4.3.4), although with a greater spread of values. However, they have highly variable crystallinities (7-22 vol.%), which makes direct comparison of their whole rock compositions difficult due to the effect of crystal accumulation.

Comparison of their matrix glass compositions reveals further differences. Figure 4.14 compares the matrix glasses of the different AVC rhyolites. Clearly, the D2 and I rhyolite glasses are slightly less evolved than the LCY pumices (75-76.5 vs. 76.5-78 wt.% SiO_2). The F pumice has similar silica and K_2O values to the LCY pumices but shows sufficient

compositional differences to rule out it being remobilised unerupted magma (having slightly higher concentrations of MgO, FeO(t), CaO, and TiO₂; Fig. 4.14) .

Published zircon model ages (Cisneros de León et al., 2021a) suggest that a certain amount of cannibalisation of the LCY mush system occurred (at least for the I eruption). The maximum zircon ages for the I eruption (the last of the post-LCY eruptions) overlap with those from the LCY eruption, implying a continuum of melt presence in the centre during this phase (Fig. 1.15). Additional mafic recharge and renewed fractional crystallisation also likely played a part in their formation.

Derivation of the post-LCY rhyolites from the pre-existing magma system is supported by their radiogenic isotope signatures. All analysed post-LCY rhyolites fall within similar regions of the AVC isotope trends as the LCY pumices, but with small variations between eruptions (sections 4.3.3 and 4.3.4; Figs. 4.9-4.13), most significantly for the F rhyolite. This is further evidence that the evolved mush system was isotopically heterogeneous as small, localised eruptions from vents around the caldera (Rose et al., 1987) had different isotopic signatures.

In addition to remobilisation of the LCY mush, there is evidence for variable magma inputs in these eruption deposits, such as abundant and highly varied disequilibrium textures in the amphiboles compared to those in the low-K pumices, whose zonation is very weak and chemical variation between amphiboles is mostly between different crystals. The patchy and normal zonation, extensive resorption, and frequent inclusion of plagioclase and biotite (Fig. 5.29) are evidence of cumulate remobilisation and/or re-equilibration (Hammarstrom & Zen, 1992; Thornber et al., 2008).

The I pumice is slightly different, as two types of rhyolite pumice were petrographically analysed: a crystal-rich pumice with slightly less silicic matrix glass where the dominant amphibole textures are simple normal zones and rarer overgrowths of biotite (sample Ati505_06h; Fig. 5.29C), and a crystal-poor pumice (sample Ati428_01). These observations corroborate those made by Rose et al. (1987) who showed that several magma bodies were tapped during the I eruption (Fig. 5.18).

The various inputs to these magmas are also evidenced by a greater degree of complexity in the eruption deposits. All these deposits show significant compositional and mineralogical heterogeneity, with multiple phases and compositional gradation in their

chemistry (Rose et al., 1987). This heterogeneity is caused both by the presence of more mafic pumice phases, but also in variations in the rhyolite compositions.

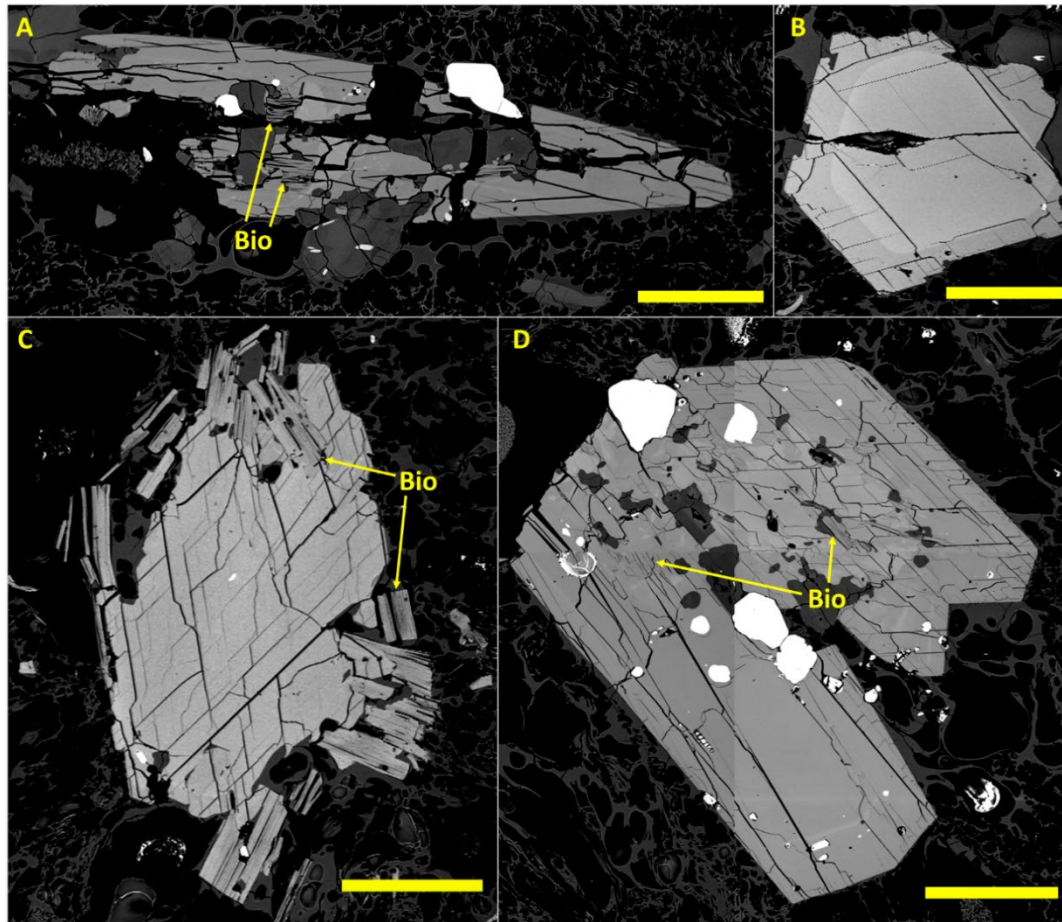


Figure 5.29. Comparison of amphiboles of the post-LCY pumices, including images from figures 3.38 and 3.40. A) D2-hosted amphibole with patchy zoning and inclusions of biotite, scale bar = 0.25 mm; B) I rhyolite-hosted amphibole showing strong zonation with a rounded core, scale bar = 0.2 mm; C) I rhyolite-hosted amphibole showing minor zonation but with biotite overgrowths, scale bar = 0.2 mm; D) F rhyolite-hosted amphibole with patchy zoning and inclusions of biotite and Fe-Ti oxides, scale bar = 0.4 mm

5.4.2.2 Storage conditions of the post-LCY magmas

The common presence of amphibole in the post-LCY rhyolites makes constraining the intensive variables for these pumices much simpler. High-Ca amphibole compositions (Fig. 3.36) show that the amphiboles are similar to those in the low-K LCY rhyolite. The absence of cummingtonite in these rhyolites also implies that their magmas equilibrated at higher temperatures and/or pressures than the LCY rhyolites. This further suggests that mafic recharge and remobilisation/reheating could be significant in forming these magmas, as the rhyolite magma system has been reheated above the temperatures obtained for the LCY rhyolites (section 5.3.4). Intensive variable estimates are shown in Figs. 5.6-5.8.

As with the low-K LCY magma, the most evolved amphiboles of the post-LCY pumices lie outside the calibration range of the geothermobarometers. The estimates are still provided

here but with the caveat that these should be taken as broad estimates. , The estimated storage conditions of the less evolved (more aluminous) amphiboles from these rocks are also presented, but with the caveat that amphiboles are unlikely to have been in equilibrium with the final melt. Silica estimates from both chemometers (Ridolfi & Renzulli, 2012; Zhang et al., 2017) for these more aluminous amphiboles are typically <75 wt.%. Thus, the estimates should be used with caution and mostly indicate that they crystallised at low pressures (<130 MPa).

Two thermometers were used that would be applicable for the low pressures and temperatures of these rocks. These are the plagioclase-liquid thermohygrometer using the method of Wieser et al. (2022) and equation 24a of Putirka (2008) and the hygrometer of Waters & Lange (2015), and the amphibole thermometers of Ridolfi (2021) and Putirka (2016). Results are shown in Figures 5.7 and 5.8. The plagioclase-liquid method yielded lower temperature estimates than the amphibole thermometers. While this may simply be a reflection of the variability of the models, it may also be the result of the magmas moving out of the amphibole stability field and recording the very last values before eruption.

The D2 rhyolites

All but one of the amphiboles in the D2 pumices do not satisfy the conditions of the Ridolfi (2021) method, due to the issues with low pressure, low-Al amphiboles. Their presence simply suggests that the melts were likely stored at low pressures. The one amphibole within the calibration had an estimate of 177 ± 21 MPa, while those out of the calibration range gave estimates of lower pressures (110-170 MPa). This amphibole's temperature estimate was $855 \pm 22^\circ\text{C}$, with those outside of the calibration range being again lower (825-855°C), using the Ridolfi & Renzulli (2012) equation. The calibration of Putirka (2016) covers the ranges of amphiboles in these magmas and use of their equation 5 gave estimates of $758\text{-}833 \pm 30^\circ\text{C}$. Plagioclase thermohygrometry using the above methods yielded similar values ($783\text{-}833 \pm 36^\circ\text{C}$), with $4.72\text{-}6.13 \pm 0.35$ wt.% H_2O .

The F rhyolites

Similar constraints to amphibole thermobarometry as described for the D2 rhyolite apply here. Estimates of incompatible amphiboles are $100\text{-}130 \pm 21$ MPa and $823\text{-}850 \pm 22^\circ\text{C}$, while those of more aluminous amphiboles span a wide range ($166\text{-}392 \pm 21$ MPa, $858\text{-}948 \pm 22^\circ\text{C}$). These estimates gave a wide range of chemometric silica estimates of 64-77 wt.% SiO_2 , showing that these amphiboles were not in equilibrium with the final rhyolite

composition. Temperature estimates using the model of Putirka (2016) were 740-804 $\pm 30^\circ\text{C}$.

Plagioclase hygrothermometry yielded a narrow range of temperatures (742-766 $\pm 36^\circ\text{C}$) with 5.89-6.45 ± 0.35 wt.% H_2O . These are slightly lower temperatures and higher average H_2O contents than those of the D2 rhyolite. While it is uncertain due to the unknown errors of the Ridolfi barometer at these compositions, the F pumice also yielded shallower average pressure estimates.

The I rhyolites

The two types of rhyolite pumice analysed from the I eruption show a similar range of mineral compositions to those found in the mingled pumice of the LCY eruption, and similarly the vast majority of these are not in equilibrium with their host rhyolite matrix glasses. For the crystal-rich pumice (sample Ati505_06h), the bimodal composition distributions formed by the strong normal zoning found in most amphibole crystals allows for simple estimations. The crystal cores have a very narrow range of chemistry-estimated model melt equilibrium compositions of 60-64 wt.% SiO_2 , very similar to those found in the I-hosted recharge magma (Fig. 5.30). Storage condition estimates for these amphiboles (assuming they have not experienced significant re-equilibration in the host rhyolites) are 276-409 MPa but with larger errors (± 44 MPa) and temperatures of 916-958 $\pm 22^\circ\text{C}$. This is again within the same range as those in the I enclaves (Fig. 5.8). The crystal rims yield a much narrower range of pressure and temperature estimates (184-199 ± 23 MPa; 898-919 $\pm 22^\circ\text{C}$). These rims appear to be in equilibrium with the lower-silica rhyolite matrix glass of the crystal-rich clast (Fig. 5.30) but still fall outside the calibration of Ridolfi (2021).

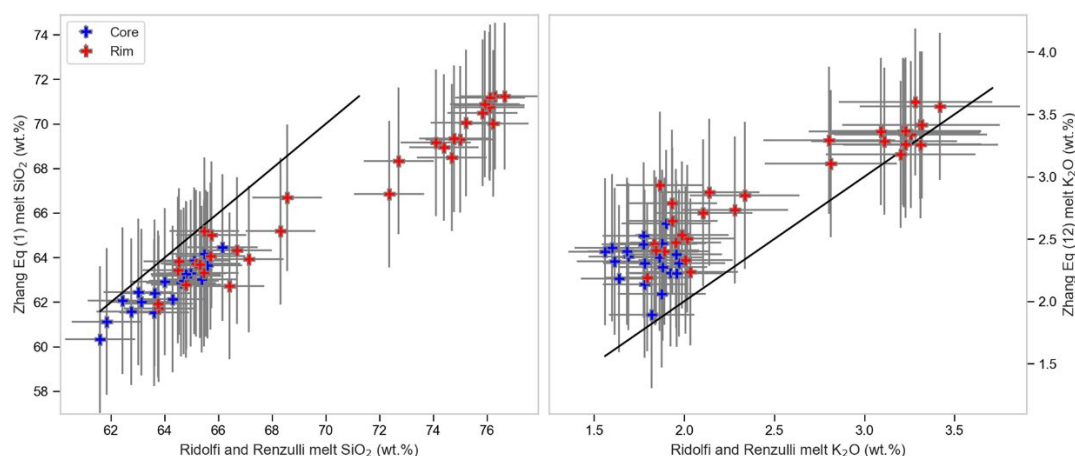


Figure 5.30. Comparisons of the amphibole chemometers of Zhang et al. (2017) and Ridolfi & Renzulli (2012) for the crystal rich I rhyolite (sample Ati505_06h) with 1:1 line. Shown uncertainties are 1 s.e.

A different story is given by the amphiboles of the crystal-poor pumice (Ati428_01). Very few crystals were in equilibrium with the rhyolite melts, with most having intermediate values similar to the range observed in the low-K LCY pumice. Only four analyses passed this test, and again these crystals are outside of the range calibrated for the Ridolfi (2021) model. This could suggest that they grew at pressures <130 MPa, however the calculated pressures were 160-174 MPa, much higher than those calculated for the other disequilibrium amphiboles of the post-LCY pumices. Plagioclase-liquid hygrometry for both showed fairly low temperatures ($760-806 \pm 36^\circ\text{C}$) with high H_2O contents ($5.75-6.62 \pm 0.35$ wt.% H_2O), similar to those from the F pumice.

5.4.2.3 Formation and history of the post-LCY rhyolites

As demonstrated above, the post-LCY rhyolites all share many similarities, including their major element and radiogenic isotope geochemistry, thermobarometry, and mineralogies. In general, these similarities tend to argue for a similar petrogenesis. Cumulate remobilisation and remelting appear to be the most likely petrogenetic mechanisms for them, although there is strong evidence that mafic recharge also had an effect.

There are several arguments for cumulate involvement. Texturally, these pumices commonly contain glomerocrysts showing cumulate assemblages (i.e., amphibole, plagioclase, biotite and Fe-Ti oxides; Fig. 3.39). Amphibole crystals frequently contain inclusions of biotite and plagioclase (Fig. 5.29A and D), which could again point to a possible cumulus source. Several geochemical lines of evidence support this idea. The radiogenic isotope values of the post-LCY pumices are all similar to the LCY rhyolites. Involvement of the LCY crystal mush would result in subsequent remobilised magmas inheriting a similar signature.

Several trace elements can also be used to track cumulate remelting. Elements like Sr, Zr, and the REEs, as well as ratios such as Sr/Sr^* and Zr/Hf can be elevated in remelted cumulates (Foley et al., 2020), and whole rock compositions of the post-LCY pumices show that they have elevated concentrations of these elements in comparison to the high-K LCY rhyolite (Figs. 4.3, 4.5, and 4.7). This unit was by far the most voluminous contributor to the LCY eruption volume. All $900 \pm 90 \text{ km}^3$ (Kutterolf et al., 2016) of the tephra fall-out was this composition, as well as an estimated 60% (Rose et al., 1979) of the 320 km^3 (Cisneros de León et al., 2021a) of the ignimbrite, meaning it made up ~90% of the total volume erupted. Proportionally, most of the cumulate mass in the LCY mush was related to the

high-K LCY rhyolites, and therefore this would be the most likely source for subsequent magmatism.

There is also strong evidence that renewed magma feeding was involved in the formation of the post-LCY rhyolites. Their eruption deposits contain evidence of direct recharge by more mafic magmas (shown by the mingled pumice in the D2 eruption deposit and the enclaves commonly present in the I eruption deposits; section 3.2.5). Amphiboles in the crystal-rich pumice from the I deposits (sample Ati505_06h) contain unique textures that further support this. They are normally zoned and commonly have rounded cores (with rare resorbed ‘voids’), and their rims are commonly overgrown by biotite (Fig. 5.29C). Amphibole chemometry of these cores showed that they originally grew from a high-silica andesite (Fig. 5.30). In fact, they overlap exactly with amphibole compositions from the enclaves (Fig. 5.31), meaning that the amphibole cores in the more crystal-rich rhyodacites almost certainly originated from the recharge magmas. The marginally varying isotopic signatures of the post-LCY rhyolites (section 4.3.4) could also be explained by mixing with recharge magmas – the recharging magmas affect the isotopic composition of the subsequent magmas.

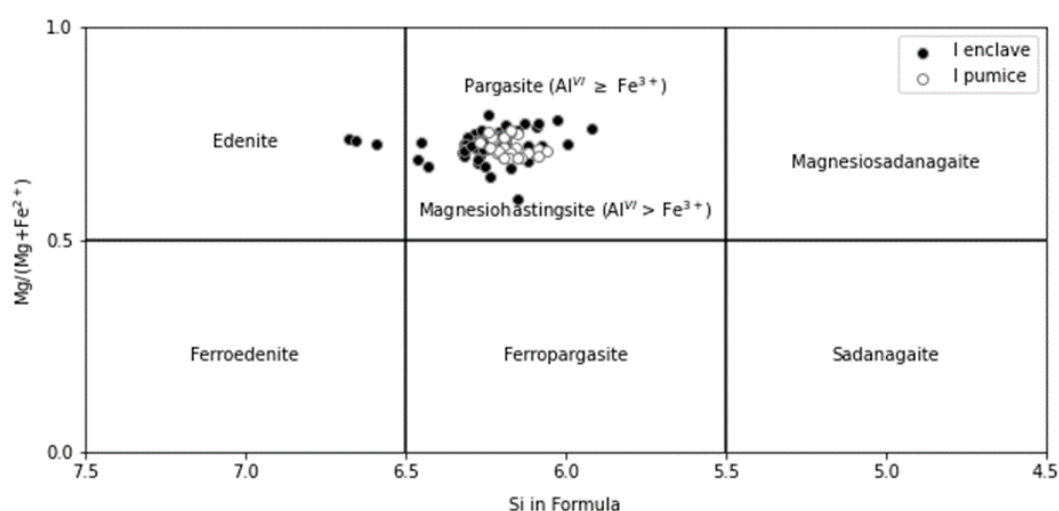


Figure 5.31. Amphibole discrimination diagram with the compositions of amphiboles in the I enclaves (samples Ati430_11a(e) and Ati505_06h(e) and the crystal cores of the crystal-rich I rhyolite (Ati505_06h), showing they overlap to a high degree

The petrography and petrology of these pumices implies mixing and homogenisation of the recharge magmas. Amphiboles are resorbed and rounded, followed by growth of lower-Al rims and final overgrowth by biotite. The plagioclase crystals also attest to relatively simple history of the magma, with few open-system events recorded throughout their growth as shown by their dominantly normally-zoned texture (Fig. 3.31). These crystals have also fairly high aspect ratios (maximum of 15), indicating relatively fast cooling. Overall, there is

a good amount of evidence that the post-LCY rhyolites were formed from the interaction of recharging magmas with remnants of the LCY mush system.

Chapter 6: Spatial and temporal evolution of the AVC

The AVC provides an unusual case study for large (>VEI 7) eruptions at convergent margins. Arc migration is common at convergent margins (e.g. Chapman et al., 2021), but in this segment of the CAVA arc it strongly controls the surface expression of the volcanism. The AVC stratovolcanoes either occur as pairs and/or in alignments, and their calderas tend to be situated immediately north of the arc front (Fig. 1.1). Arc migration is thought to be caused by slab rollback (Alonso-Henar et al., 2017).

In this chapter, the petrological and geochemical information gained from the different rock groups (Chapter 5) will be combined to create a model for the evolution of the AVC. This model will show how this information relates to the migration of the system and will present an explanation for how migration influenced the formation of the huge LCY magma bodies and why the AVC specifically produced such a large eruption. Crucial to the development of this model, the AVC has preserved the northernmost and southernmost pre-caldera stratovolcano edifices, thus providing the geochemical endmembers to constrain the inputs to the LCY magmas. Most regions that experience arc migration have relatively slow rates, typically <1.0 to 5.0 km Myr⁻¹ (Table 6.1). Estimates for the trenchward migration rate of the CAVA since approximately 1 Ma will be presented, showing that it has experienced an unusually fast rate compared to other arcs.

| Arc | Migration rate (km Myr ⁻¹) | Citation |
|--------------------------------------|--|----------|
| Aleutians | 0.6-5.0 | 1 |
| Sierra Nevada | 2.0-2.7 | 2,3 |
| Mexico | 18-75 | 4,5,6 |
| Costa Rica | 3.0-3.6 | 7,8 |
| Peru | 1.5-9.0 | 9 |
| Northern Chile | 1.2-1.9 | 8,10 |
| North Southern Volcanic Zone (Chile) | 9.0-10 | 11 |
| Andes between 33°S-38°S (Neogene) | 12.5 | 12 |
| Southern Patagonia | 8 | 13 |
| South Sandwich | 4.7 | 8 |
| Lesser Antilles | 1.1-1.4 | 14 |
| Tonga-Kermadec | 4-18 | 15 |

Table 6.1. Migration rates calculated for different global volcanic arcs. Citations are: 1 – Jicha & Kay (2018); 2 – Stern et al. (1981); 3 – Chen & Moore (1982); 4 – Morán-Zenteno et al. (1996); 5 – Morán-Zenteno et al. (2007); 6 – Keppie & Morán-Zenteno (2005); 7 – Vannucchi et al. (2001); 8 – Scholl & Huene (2007); 9 – Clift et al. (2003); 10 – Stern et al. (1991); 11 – Goss et al. (2013); 12 – Kay et al. (2005); 13 – De Arellano et al. (2012); 14 – Germa et al. (2011); 15 – Seebeck et al. (2014a).

6.1 Estimating the Quaternary arc migration rate

Figure 6.1 shows three centres from the central Guatemalan segment of the CAVA. These centres all have structures at least partially controlled by arc migration, for which age estimates are known (see below). These structures allow us to produce rough estimates for the rate of migration of activity at these centres, which were calculated based on estimates on where the oldest known vent of the lineament would be, what age the oldest material from it was, and its distance to the present arc front. There are significant uncertainties with these calculations, the most important being that while the more recent histories of these stratovolcanoes are well known, the age ranges of older parts of these systems are known to much lesser detail and these systems are often heavily eroded, making estimations of the locations and timings of the magmatism much more difficult.

In the case of Volcán Santa María (Fig. 6.1A), radiometric age dates for the pre-Santa María cinder cone Volcán del Valle are 163 ± 49 ka and the start of the formation of the Santa María cone occurred at 103 ± 19 ka (Escobar-Wolf et al., 2010). A further southward shift is represented by the 1902 eruption, which erupted through a lateral vent (Rose, 1972a). The subsequent formation of the Santiaguito dome system also through this vent (Rose, 1972b). The estimated distance from Volcán del Valle to Santiaguito is 4.0 km, providing a migration rate of approximately 25 km Myr^{-1} .

For the AVC, the two lineaments (San Marcos-Paquisis and Tecolote-Atitlán, Fig. 6B) were both used to provide migration rate estimates using ages and locations from Newhall (1980). Volcans San Pedro and Tolimán were not used to estimate age ranges as they were formed inside the caldera, and their magma ascent pathways may have been influenced by the structure of the caldera floor. A distance of 9.1 km separates the 1.4 ± 0.3 Ma Volcán San Marcos from the 0.44 ± 0.1 Ma Volcán Paquisis, providing a migration rate estimate of 9.5 km Myr^{-1} . For Volcán Tecolote, the age range for its activity is large (1.8-0.83 Ma), while activity is thought to have started on Volcán Atitlán at 0.01 Ma (Haapala et al., 2005). An estimated distance between these two edifices is 17 km and, using the maximum age, migration rates are estimated to be approximately 9 km Myr^{-1} .

Finally, the Acatenango-Fuego (Fig. 6C) massif provides a third estimate of migration rate. The Acatenango Antiguo edifice is built upon the LCY deposits (Basset, 1996; Vallance et al., 2001), providing a maximum age of between 75-98 ka (Cisneros de Leon et al., 2021a; Baudry et al., 2024), and estimates for the start of activity at Volcán de Fuego are

approximately 10 ka. There is approximately 3.5 km between the two edifices, giving a migration rate of between 35-55 km Ma⁻¹, depending on the age used.

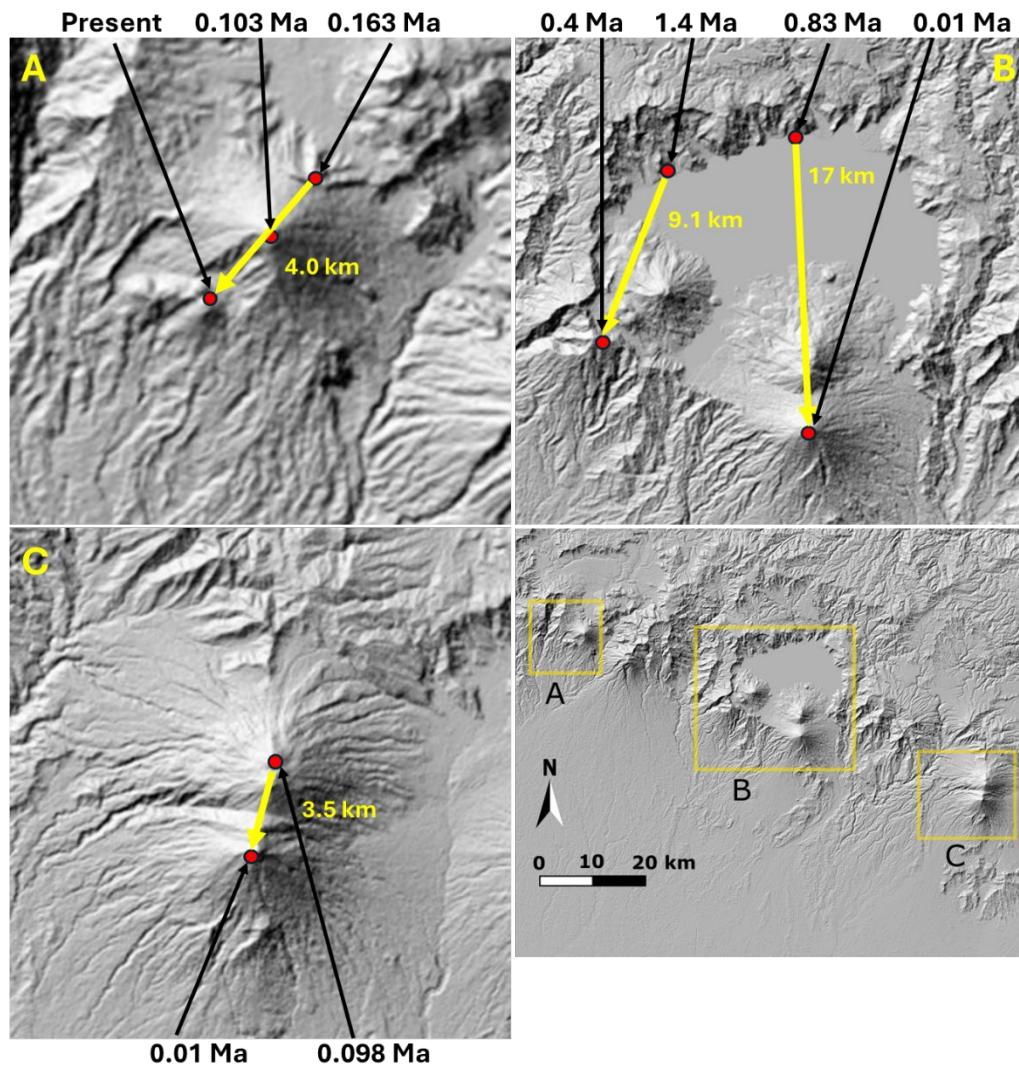


Figure 6.1. Maps of three different centres from the central Guatemalan segments of the CAVA: A) Santa María; B) AVC; C) Volcán de Fuego. Numbers in black are age dates for the indicated edifices (details and sources in text) while numbers in yellow are distances. For the AVC, the locations of the pre-LCY edifices have been destroyed by the formation of the Atitlán III caldera, and so the estimates for their positions from Newhall (1980, 1987) are used. Images are not to the same scale. A regional map is provided (lower right) to show the locations of these volcanoes and to provide scale.

These estimated migrations rates (9-55 km Myr⁻¹) are extremely variable and subject to large uncertainties due to the nature of the data used to calculate them. They should be approached with healthy caution until more accurate estimates can be made. Still, even the minimum estimate is well above the global average (typically 1-5 km Myr⁻¹; Cecil et al., 2012; Ducea et al., 2015; Gianni & Luján, 2021; Table 6.1). For the Santa María and Fuego centres, large uncertainties are caused by the very short distances between the different edifices. It may also be that migration occurs stepwise, and so large gaps between edifices may form quickly over short timescales but will not represent the regional average pace of

migration. In each centre, the formation of the arc front edifice occurred very recently (within the last 10 ka for each volcano, and even within the last 120 years for Santa María), possibly suggesting that a new migration step has occurred. Thus, the estimates from the AVC are more likely to be representative as they take a broad average over a longer timescale. However, even the calculated minimum values ($\sim 9 \text{ km Myr}^{-1}$) are higher than most other arcs (Table 6.1), suggesting that recent magmatism in the AVC has been migrating at an exceptional rate.

6.2 Evolution of the AVC

6.2.1 Phases of the AVC

Newhall (1980, 1987) identified cyclical phases of activity at the AVC, characterised by initial formation of stratovolcanoes followed by voluminous eruptions of silicic ignimbrites. The timing of these phases was constrained by a combination of K-Ar dating on biotites and amphiboles and subsequent palaeomagnetism studies (Newhall, 1980, 1987). The next phase reverts to stratovolcano activity dominated by more mafic magma but situated further south of the previous eruptions. Stratovolcano material from the early phases (phases I and II; Table 1.1) is not preserved except for xenoliths within the subsequently formed tuffs. Instead, we mostly rely on the materials erupted during the third and nascent fourth phases of activity to study the relationships between the pre- and post-caldera stratovolcanoes, and the silicic lavas associated with them.

The phases can be further broken down by changes in the style of activity. This section provides further details about the petrogenetic processes during the most recent phases (phases III and IV of Newhall (1980)). Combining the published knowledge of the history of the AVC (section 1.4) with the petrogenetic information presented in this study (Chapter 5) allows me to develop an evolutionary model for the AVC during this time. The different steps that have occurred in this evolution (Figures 6.2-6.5) are described below, and represent significant compositional and/or behavioural changes in volcanic activity here:

1. Initial formation of mafic (predominantly basaltic andesite) stratovolcano(es). These developed distinct isotopic signatures in the lower crust (Fig. 6.2; section 5.1.1).
2. Magmatic evolution in the stratovolcanoes to more LILE-enriched compositions due to mixing with VHKBs (section 5.1.2) and migration of magmatism like that at neighbouring volcanic centres (i.e., Santa María, Zunil, Fuego) to form volcanic

lineaments (section 6.1). An associated crystal mush formed beneath these lineaments and likely was present beneath the width of the system (section 5.1.2; Fig. 6.2). This step shows a marked change in the compositions of the stratovolcano lavas.

3. Extraction of LILE-enriched high-K rhyolite magmas from the stratovolcano crystal mush in the mid- to upper-crust, which accumulated in the upper crust (section 5.3). Based on their highly potassic compositions (Kutterolf et al., 2016; Schindlbeck et al., 2018), it is likely that the AOT and W rhyolites were initially sourced by this mechanism, followed by the high-K LCY rhyolite (section 5.3.2). This period may have been marked by a reduction or cessation of activity of the stratovolcanoes (Fig. 6.3).
4. Formation of the low- and medium-K LCY rhyolite magmas beneath the high-K LCY rhyolite body through fractionation of recharge magmas (section 5.3.3; Fig. 6.3). This may have been at the same time or after the extraction of the high-K LCY rhyolite. Due to their assumed storage position underlying the high-K rhyolite, it is unlikely that they were formed first.
5. The Los Chocoyos eruption occurs, with the initial eruption of high-K rhyolites, followed by a phase in which all rhyolite types were erupted, which resulted in the formation of the Atitlán III caldera (Rose et al., 1979).
6. Recovery period of activity that produced a wide range of eruption styles and chemistries, including eruption of the post-LCY pumices and formation of the San Pedro and Tolimán stratovolcanoes within the caldera (Newhall, 1980; Newhall et al., 1987; Fig. 6.4). The broad range of geochemistry and the petrology of the erupted products was likely caused by interaction of recharging magmas with the remnants of the crystal mush (section 5.4).
7. Finally, the mantle source of the magma shifted beyond the caldera margin and the Volcán Atitlán edifice was constructed south of the AVC (Fig. 6.5).

6.2.2 Timing of formation of the magma bodies

As described in section 1.4.1, the stratovolcano lavas preceding the LCY eruption formed >1.8-0.4 Ma ago (Newhall, 1980). The ubiquitous presence of high-K lavas in these stratovolcanoes (Newhall, 1980; section 5.1.2) suggests that similar magmatic systems fed all three, all involving the generation and subsequent mixing with VHKM (section 5.1.2). The likely prerequisites for VHKM formation are (a) the presence of large cumulate bodies and (b) a separate volatile phase within the magmatic system, both of which are more

likely in more mature systems (section 5.1.3). Previous magmatism likely means that significant thicknesses of cumulates underly the centre (both ignimbrite phases I and II and/or the older granitoid rocks found within the centre being possible contributors), however the volatile phase requires the presence of renewed magmatism (section 5.1.3). The most LILE-enriched lavas (i.e. those most exposed to VHKMs) are found in greater amounts at the top of the stratovolcano lava piles (Newhall, 1980), suggesting a high degree of maturity needs to be reached for their formation. This likely implies a well-developed mush system beneath these stratovolcanoes by this time (Fig. 6.2).

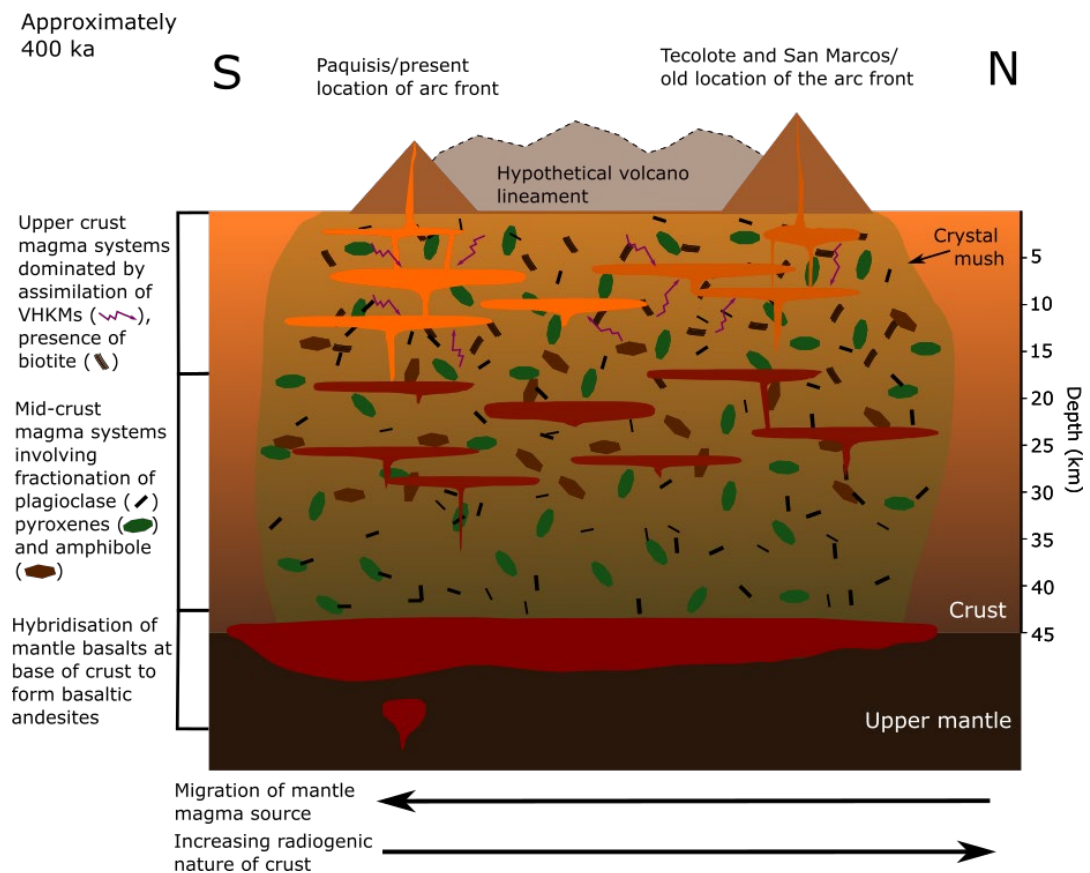


Figure 6.2: Cartoon of the likely physical layout of the AVC at approximately 400 ka, showing the evolution of magmatism beneath the stratovolcanoes. The arc front has migrated around 10 km from Volcán Tecolote/San Marcos to Volcán Paquisis, likely forming a pair of volcanic lineaments similar to the neighbouring Pecul-Zunil-Tzanjuyub lineament (Figs. 1.1 and 1.11). A crystal mush underlies this entire region. In the lower crust/crust-mantle boundary, hybridisation of mantle basalts with an assimilant derived from lower crustal pyroxenite cumulates produces basaltic andesites (section 5.1.1). These undergo fractionation in the mid-crust and, as the magma systems mature, mixing with VHKMs becomes a critical process, most likely occurring in the upper crust. Continental crust thickness from Carr (1984).

Published age dates of the pre-LCY rhyolite eruptions can be used to identify when the system began to accumulate eruptible volumes of rhyolite, and crucially this can be tied to the migration timings (on the assumption that the construction of Volcán Paquisis on the southern edge of the centre represents this migration). The two known rhyolite pumice eruptions that preceded the LCY event were the W pumice (155 ka; Cisneros de León et al.,

2021a) and the Atitlán Older Tephra (AOT; 306 ka; Kutterolf et al., 2016), although information about the AOT is sparse and its source location is not confidently confirmed. Zircon dates for the W-pumice show that zircon-saturated magmas were present at least 100 ka before eruption (Cisneros de León et al., 2021a; Fig. 1.15). Assuming that the AOT was also sourced from the AVC and that its magma body accumulated on a similar timescale to that of the W tephra, then evolved, zircon-saturated melts were present at the AVC around 400 ka ago, at the time when the arc front reached the southern margin of the Atitlán III caldera (Newhall, 1980). Both the W and AOT tephras also show similar enrichments in K₂O and Rb to the high-K LCY rhyolite (Kutterolf et al., 2016; Cisneros de León et al., 2021a), suggesting they have a similar origin (i.e., extraction from the LILE-enriched upper crust stratovolcano mush).

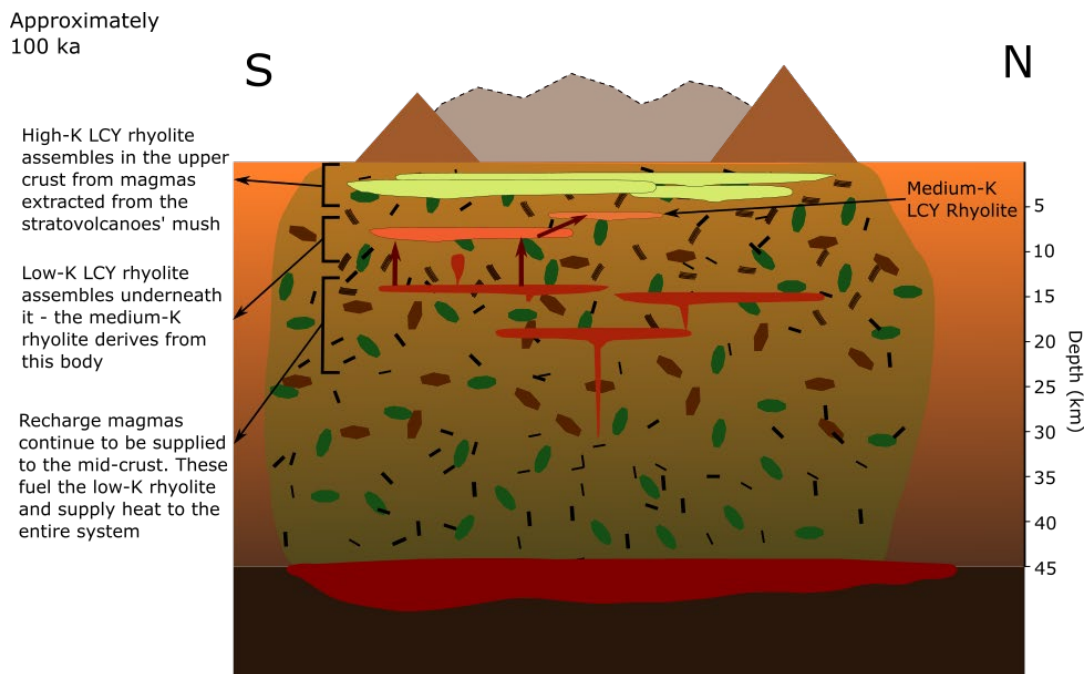


Figure 6.3: Cartoon showing the assembly of the different LCY magmas from the large crystal mush body underlying the AVC at this time. The high-K LCY magmas most likely began to assemble first and did so in the uppermost crust. They were extracted from the contaminated stratovolcano mush system, giving them their distinctive LILE-enriched signature. The low-K LCY magma formed underneath this body, derived predominantly from uncontaminated recharge magmas. Finally, the medium-K LCY rhyolite is derived from a portion of the low-K rhyolite. Their position in the crust is reflected in their place within the eruption deposit – only the high-K rhyolite is present in the initial pumice fall deposit, while all three are present in the ignimbrite phase.

After the initial extraction and eruption of the smaller pre-LCY pumice eruptions (the W and AOT), the LCY magma body began to accumulate (Fig. 6.3), shown by published zircon ages (Cisneros de Leon et al., 2021a). A likely prerequisite for the growth of large volume magma bodies is the presence of an exsolved volatile phase (e.g., Huppert & Woods, 2002; Bouvet de Maisonneuve et al., 2021). Evidence of this is observed in melt and fluid

inclusions hosted by the LCY rhyolites (Cisneros de León et al., 2021a; Hansteen et al., 2022).

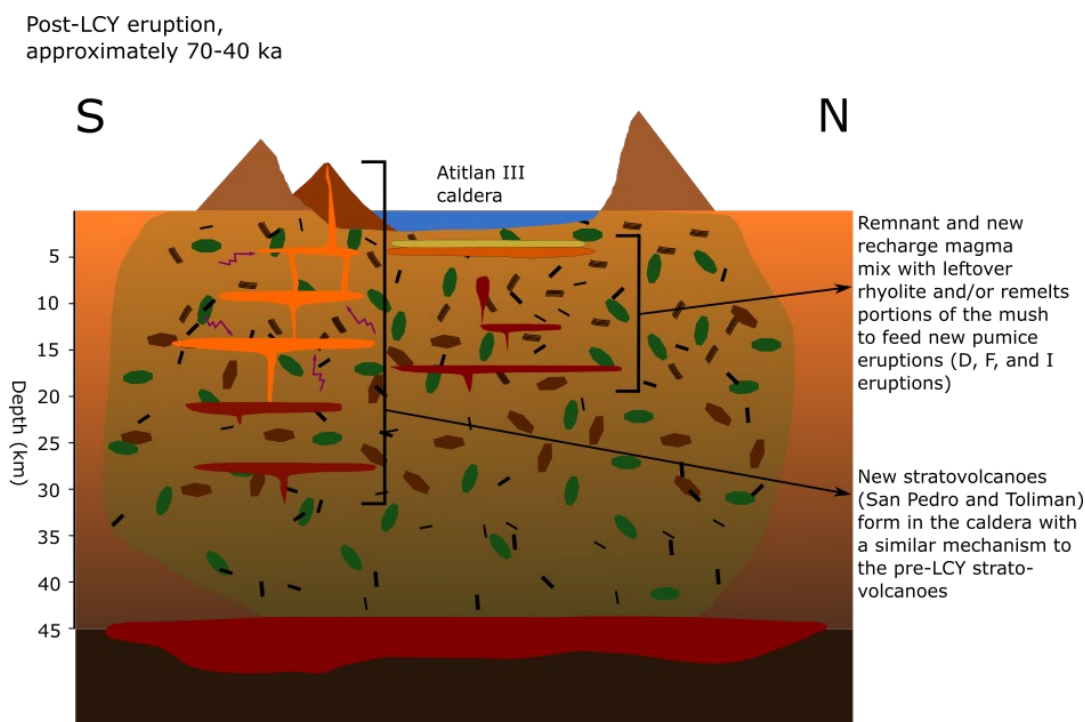


Figure 6.4: Cartoon showing the recovery of the Atitlán system following the LCY eruption. Several pumice eruptions with multiple phases occur during this time, and their textures and chemistries show they were likely derived from interaction of remobilised remnant recharge magmas, new recharge magmas, and remobilised and unerupted portions of the rhyolite and associated crystal mush. During this time the new San Pedro and Tolimán stratovolcanoes also formed within the caldera margins.

This study has shown that the lower-K LCY magmas were formed through a different mechanism, one decoupled from the upper crust stratovolcano mush system (section 5.3.3.1). Several lines of evidence (their restriction to the secondary ignimbrite phase of the eruption, the presence of amphibole and thermobarometric estimates of upper- to mid-crust depths from these amphiboles (section 5.3.4), their seclusion from the VHKM which are likely formed in the upper crust) suggest that these magmas were formed and stored beneath the high-K LCY magma body (section 5.3.5). This could be due to density contrasts: the upper crust magma system and the high-K LCY rhyolite body would have lower density compared to ascending primitive magmas. The upper crustal region could therefore act as a density barrier for ascending primitive magmas (e.g., Huber et al., 2012), cutting off supply to the stratovolcanoes. Instead these magmas would underplate this region and stall in a deeper region of the crust, and there undergo their unique evolution (section 5.3.3).

After the LCY eruption the system entered a state of recovery, as several different magmas interacted to form the post-LCY pumice materials (Fig. 6.4). As shown in Section 5.4, these included recharge magmas and remobilised parts of the magma system that fed the LCY

6.2.3 Variations in radiogenic isotope ratios within the AVC

Plots of SiO₂ vs. radiogenic isotope ratios for the volcanic rocks of the AVC (Fig. 4.9) show that there is no correlation between degree of evolution and the 'crustal' signal of each sample. Instead, there is an apparent correlation with distance from the trench, where in general the crustal signature is weaker in the samples situated closer to the trench (Fig. 4.10). This follows the observations of Walker et al. (1995), who showed that similar variations occur in the cinder cone fields of eastern Guatemala. If the isotopic variations developed in the lower crust during hybridisation (section 5.1.1), then they can be broadly used as a proxy for their position within the centre relative to the trench.

The range of stratovolcano lava isotopic compositions in the AVC suggests that the underlying crust is heterogeneous but with a simple overall trend with increasing 'crustal' signatures away from the trench (section 1.3.4). The magmatic systems of the overlying stratovolcanoes inherit these isotopic signatures, and the erupted lavas can therefore be used to trace the relative inputs from magmas sourced from different points in the mush system. It has been shown that the high-K LCY rhyolite was likely derived from these stratovolcano magmas (section 5.3.3), so a comparison of the isotopic signature of the rhyolites with those of the stratovolcano lavas should indicate the location from which these magmas were derived. The LCY magmas all lie in a similar intermediate position in isotope space (section 4.3), and the caldera lies in an intermediate area with respect to these stratovolcanoes (Fig. 6.6). The facts that the caldera (and likely the underlying feeding magma system) spans the width of the centre and has intermediate isotopic compositions compared to the stratovolcanoes suggest that this magma system was fed from the whole width and thus has a homogenised intermediate isotope composition. This width in turn is controlled by the arc migration, which will be further discussed in section 6.3.

An exception to the crustal isotope trend is seen in the lavas of Volcán Atitlán (Fig. 4.10). These show an elevated isotopic signature compared to nearby volcanoes at the present location of the arc front. Two possible explanations for the elevated crustal signatures of the Volcán Atitlán lavas can be invoked. One is that the crust here has a heterogeneous distribution of isotopic compositions (even over short distances like between Volcáns Tolimán and Atitlán, approximately 5 km), and these overprint the regional trend for increasing crustal signatures with distance from the trench (Walker et al., 1995). The isotopic signature of a magma is then retained over the lifetime of a portion of magma. The

other possibility is that the hotter and younger magmas are both more exposed to the country rock due to rising through less geochemically insulated magma conduits and are therefore more likely to effectively assimilate more material during ascent (e.g., González-Maurel et al., 2019).

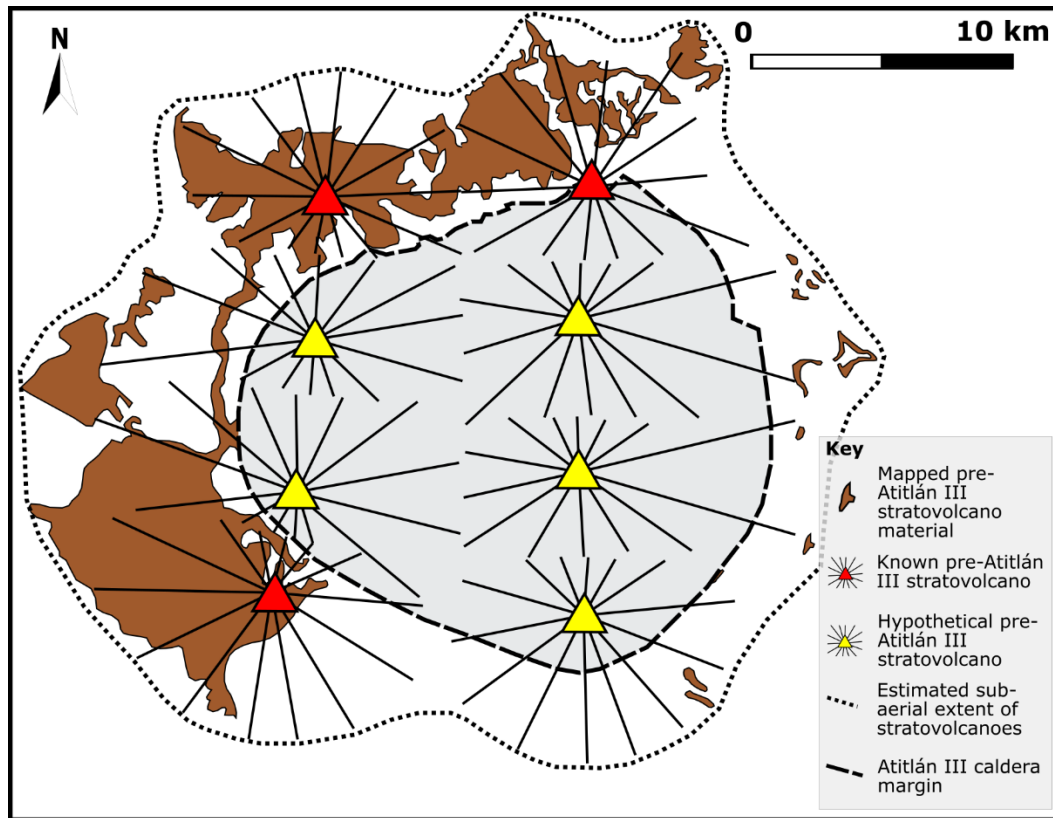


Figure 6.6: Map showing the hypothetical positioning of stratovolcanoes before the LCY eruption, superimposed over the position of the caldera. North-south volcano spacing is estimated based on that observed at Volcán de Fuego and Pecul-Zunil. Also shown are known outcrops of pre-LCY stratovolcano material from Newhall (1982, 1987). This shows that two closely spaced volcano lineaments can cover the area from which the LCY rhyolites were extracted. This is proposed with the assumption that the stratovolcano magmatism at the AVC formed lineaments similar to those observed in the region (c.f. the Zunil-Pecul lineament in Figs. 1.1 and 1.11).

While the second explanation is less likely for the lavas of Volcán Atitlán due to the probable presence of a protective mush system (shown by complexity of its petrology; section 5.1.1.2) and the relatively slower ascent rate (shown by the presence of fewer skeletal or acicular mineral forms; section 3.2.1.1), this may have played a factor in the composition of the Cerro las Minas lavas from Volcán Tecolote. While they likely have enriched isotopic signatures due to their position in the crust, their strong crustal signatures compared to other nearby lavas (section 4.3.1) could suggest further modification of their chemistry during their ascent by the second mechanism.

6.2.4 Rhyolite petrogenesis at the AVC

What the radiogenic isotope analyses crucially show is that all LCY tephras have very similar values that are intermediate between the values of the pre- and post-LCY stratovolcanoes. In the context of the petrogenesis of the LCY rhyolite suite, this could result from two processes: 1) mixing and homogenisation of magmas extracted from the entire width of the AVC mush system; 2) derivation from primitive melts that were generated in an intermediate position with intermediate isotope signals at the base of the crust. It is possible that both mechanisms were operating; the location of the caldera cuts through the positions of the old stratovolcanoes. Assuming that the mush system that fed the LCY eruption directly underlies its surface expression (i.e. the Atitlán III caldera), the mush system that fed the LCY magma bodies would have grown over and/or cannibalised the pre-LCY stratovolcanoes' own mush systems and could have had a greater input from the more central region. This study has shown that the high-K LCY rhyolites can easily be generated from the stratovolcano magmas (section 5.3.3.2), so it would seem likely that the stratovolcanoes' mush system strongly influenced the formation of these magma bodies.

It is also highly likely that intermediate composition stratovolcano magmatism occurred in the intermediate space where Lake Atitlán is now situated. While the evidence of this volcanism at the AVC would have been mostly destroyed during caldera formation, there is a continuum of exposed stratovolcano deposits on the western and eastern margins of the caldera (Newhall, 1982, 1987; Fig 6.6) that record this migration. The Ixtahuacan-Tzanjuyub-Zunil-Pecul volcano chain between the Xela and Atitlán centres is also a clear example of migrating magmatism being a gradual process with construction of new edifices on the southern margins of the old ones (Figs. 1.1 and 1.11). This appears to be the dominant form that stratovolcano volcanism takes in this region, so it is assumed that this was also the case at the AVC stratovolcanoes. This study has also shown that migration rates for the mantle-derived magmas were relatively rapid (section 6.1), driving this spread of magmatism.

In combination, the intermediate nature of both the isotopic values of the LCY pumices in comparison to the stratovolcanoes and their geography, as well as the likelihood that the largest magma body of the LCY eruption (the high-K rhyolites; Rose et al., 1987; Cisneros de León et al., 2021a) was derived from their mush systems, are good evidence that the preceding volcanic activity had a strong control on the formation of the LCY rhyolites.

The fact that all LCY rhyolites have very similar radiogenic isotope ratios, despite the wide differences in their major and trace element geochemistry, is more difficult to explain. Section 5.3 showed that the two main magma groups erupted during the LCY event (the lower-K and high-K magmas) were likely formed through very different processes, with the high-K rhyolites depending heavily on magmas extracted from the stratovolcanoes' mush systems, while the lower-K rhyolites predominantly forming through deeper fractionation of recharge magmas. Their concurrent formation is the result of several interacting processes.

A common occurrence within the lava flow sequences of the pre-LCY stratovolcanoes is the presence of the high-K andesites towards the top (Newhall, 1980; 1987). Their presence here suggests some degree of advanced maturity had been reached within the underlying magma system, as I have shown that the high-K andesites required a mature magmatic system to be produced (sections 5.1.2 and 5.1.3). Stating the assumption again that the space now occupied by the Atitlán III caldera previously contained stratovolcano systems with similar maturities, then the upper crust mush system beneath this region would contain large volumes of unerupted high-K andesites. Section 5.3.3 demonstrated that protracted crystallisation and extraction of these andesites can generate the AVC high-K rhyolites. Depth estimates for the processes that generated these melts (formation of VHkMs, storage of high-K andesites and eventual formation of high-K rhyolites) are all shallow (Section 5.3.4). The development of high-K, high-silica andesites is an indication that the maturity of the system had greatly increased, as their generation requires both an elevated geotherm and the presence of abundant hydrous phases (section 5.1.3). For the high-K magmas, this is tied to the generation of the VHkMs. The increased maturity of the system means that large volumes of biotite-bearing rocks had formed and/or the system was thermally mature enough that partial melting of biotite-bearing rocks could occur. Another potential source could have been the relatively common biotite-bearing intrusive rocks found locally (section 3.2.6). Once this shallow high-K magma system had reached a critical size, it could act as a barrier to further ascending magmas to feed the stratovolcanoes, preventing the ascent of new andesite magmas to the surface and switching the phase of volcanism at the centre. Alternatively, advanced crystallisation and lock-up of the crystal mushes could prevent eruption of more dacitic magmas and promote further fractionation towards high-K rhyolites (i.e., the Daly gap – Dufek & Bachmann, 2010). Either process can explain the composition gap that is observed between the stratovolcano series and the LCY rhyolites (section 4.1).

It is at this phase that rapid growth of the rhyolite system can occur (Huppert & Woods, 2002; Bouvet de Maisonneuve et al., 2021). This is tied to the overall increasing maturity of the system in which constant fluxing of magmas elevates the geotherm until a point is reached where eruption frequency is severely reduced as magmas stall and ascending magmas instead drive further growth of the evolved system, initiating a new phase which results in the formation and eruption of evolved magmas (Bouvet de Maisonneuve et al., 2021).

The analysed enclave material provided some clues as to the nature of the deeper magmatic plumbing systems during this new phase of activity (section 5.2). It has a unique geochemistry that is not present in the stratovolcano sequences (both pre- and post-caldera formation; section 5.2.4). As discussed in section 5.2.3, this intermediate composition material underwent a very different differentiation styles compared to the stratovolcano magmas. Thermobarometry suggests that the recharge magmas were restricted to pressures around 3-5.5 MPa, while the andesitic magmas differentiated over a much wider range of pressures <1-5 MPa, with most estimates being > 4 MPa (section 5.2.2). The cause of the exclusion of the recharge magmas from the uppermost crust could have been the presence of the low-density mush systems in the shallow crust, preventing further ascent of basaltic andesite or andesite magmas until a catastrophic eruption occurred. Until then, these magmas evolved in deeper portions of the crust, gaining their distinct geochemical signatures characterised by a lack of LILE-enrichment (thanks to insulation from the LILE-rich VHkMs), amphibole-related REE trends, and elevated Sr/Y, Eu/Eu* and Sr/Sr* values compared to the other andesites (section 5.2.4).

Over time, delivery of portions of these recharge magmas to the crust would result in development of the slightly deeper mush system from which the lower-K rhyolites could be formed and extracted to a shallower region of the crust (section 5.3.2). Once a potential caldera-forming system has matured and an exsolved volatile phase is persistently present within the system (which is likely the case at the AVC at this time: Cisneros de León et al., 2021a; Hansteen et al., 2022), this phase buffers pressurisation of the system and is one of the key variables that enable rapid growth of silicic magma bodies (Huppert & Woods, 2002; Bouvet de Maisonneuve et al., 2021), in addition to other variables such as thermal maturation of the system (section 1.2.1) The contemporaneous development of two compositionally distinct evolved magma systems is therefore not unlikely, as the buffering effect could apply to both systems. During this time, therefore, magmatism was defined by growth of the silicic systems, where one was fuelled by remnant magmas related to the

stratovolcano systems and the other developed beneath this, being fuelled instead by captured recharge magmas.

6.3 Arc migration and the formation of large-volume magma bodies

6.3.1 Formation of the silicic mush

The Atitlán III caldera lies within the region of stratovolcano activity for phase III, between the bisected edifices of Volcáns Tecolote and San Marcos in the north and Volcán Paquisis in the southwest (Figs. 1.1 and 6.6). Its location begs the question: why did it form in this area? Why did it not form at the arc front (i.e. similar to the position of Paquisis relative to the arc front)? Based on its position, it can be assumed that the magmas erupted during its formation were stored directly beneath it. Development of a large crystal mush in this region during formation of the stratovolcano magmas is the best explanation for the process that can form a sufficiently large source for the rhyolite magmas (section 6.2).

This study has shown that the intermediate isotopic signature of the LCY magmas can be caused by chemical homogenisation of the mush system underlying the centre and/or of the magmas extracted from it (section 5.3). The observations that the Atitlán III caldera is geographically central to the AVC as well as isotopically intermediate to the bounding stratovolcanoes compositions are good evidence that magmas were extracted from the whole width of the centre. Assuming that the expression of stratovolcano activity in the area now occupied by the caldera was likely a lineament stretching the width of this centre in a similar fashion to that of the neighbouring Zunil lineament (Fig. 6.6), then a well-developed crystal mush would have been located beneath most of the system (Fig. 6.2). Extraction and homogenisation of melts from this mush can account for the isotopically homogeneous nature of the high-K LCY rhyolite.

Evidence for isotopic heterogeneity within the silicic mush is also shown by some of the post-LCY rhyolites, which have a greater spread of radiogenic isotope ratios than the LCY rhyolites (sections 4.3.3 and 4.3.4). In particular, the F rhyolite has a markedly different isotopic signature to the LCY rhyolites (Figs. 4.9-4.13). This could be explained by the small volumes of these eruptions, as the magmas were generated from a small region of the mush and inherited its local signature and/or their isotopic compositions were more heavily influenced by recharge magmas (section 5.4.2.3).

6.3.2 Magmatic fluxing of a wide area by stratovolcano systems

The areal extent of the Atitlán III caldera is strongly correlated to the extent of the migration of the volcanic arc (controlling its diameter in the north-south direction), as well as the position of the two stratovolcano centres forming the lineaments (its east-west diameter; Fig. 6.6). Its margins therefore appear bounded by the extent of the stratovolcano activity. The geographical distribution of the pre-LCY stratovolcanoes implies a similar horizontal extent for their underlying magma systems, forming a large region that has been fluxed with both heat and magmas. Thus, migrating volcanic centres have the potential to provide heat and melts to a much wider area of the crust than systems which are fixed in place, creating a larger region in which magmas can be stored and evolve.

What is also important to note is that volcanic activity does not immediately cease at the landward volcano once activity has begun trenchward, and that the shift occurs gradually (Halsor & Rose, 1988). Cerro Quemado, in the centre of the proposed Xela caldera, experienced historical activity despite the new arc location having reached the arc front (Volcán Santa María) over 100 ka (Singer et al., 2011). Volcán Acatenango has also experienced historical activity despite Volcán de Fuego being active since 17 ka (Chesner & Rose, 1984). Volcán Tecolote also has an extended history between 1.8 and 0.83 Ma (Newhall, 1980). Despite magma being dominantly supplied to the new arc front, the old regions still experience significant magmatic activity, showing that magmas can still be present in previous positions of the volcanic arc after migration. During the assemblage of silicic magma volumes prior to eruption, magmas away from the arc front could therefore still be involved.

Recent advances in our understanding of the longevity of silicic magma systems have shown that crystal mushes can keep melts in an extractable state on timescales of 10^5 to 10^6 years (section 1.2.1; Costa, 2008; Gelman et al., 2013). For the AVC, this means that once magmatism reached the current location of the arc front (i.e., when Volcán Paquisis was formed), a region with a horizontal surface area of approximately 300 km² had experienced extensive magmatism within the previous several hundred thousand years, larger than would be typically expected at non-migrating systems. This migration scenario, and the relatively short distance between the two stratovolcano lineaments within the AVC (i.e., Volcán San Marcos-Volcán Paquisis-Volcán San Pedro and Volcán Tecolote-Volcán Tolimán-Volcán Atitlán), likely resulted in the formation of a large-volume mush system beneath what is now Lake Atitlán (Figs. 6.2, 6.6). The size of this body also probably helped

keep it in a thermally stable state, as migration had made the size of the region fluxed by magma much greater than in a non-migratory system. Migration resulted in a mush system with a much lower ratio of surface area to volume, reducing the amount of heat lost to the surrounding country rock (Annen, 2011). Repeated intrusions of magma over hundreds of thousands of years during the stratovolcano period would have also thermally ‘primed’ the surrounding crust, shifting it to a state where it can store magmas in an extractable state (Grunder et al., 2008; de Silva & Gregg, 2014; Bachmann & Huber, 2016). Finally, the relatively fast nature of the migration (section 6.1) likely means that the older areas of the AVC are still thermally mature while new magma systems further south are being developed, reducing the impact of cooling on the eruptibility of stored magmas.

This thermal maturation of the region has a further positive feedback that results in the region’s increased ability to store large amounts of melt in an eruptible state. The elevated temperatures in this large region would increase the ductility of the surrounding crust, reducing the possibility of brittle failure (and subsequent eruption) and instead promoting further magma accumulation (de Silva & Gregg, 2014).

As well as controlling the size of the region affected by magmatism, arc migration also has an impact on crustal melting. After migration, primitive magmas from the base of the crust ascend to previously un-fluxed regions of the centre. Abundant intrusive rocks containing hydrous phases are present in these regions (Williams & McBirney, 1969; Newhall, 1987; this study, section 2.1), and in at least one case it is known that mafic volcanism has interacted with them (Fig. 2.8). Dehydration melting of these phases after migration could be a key to providing melts and volatiles into the system (Hughes & Mahood, 2011). While a direct geochemical link between these intrusive rocks and the erupted rhyolites has not been established, the timing of the migration and the subsequent start of the explosive phase suggests that it may not be coincidental.

6.3.3 Timing of the storage and accumulation of the rhyolites

While arc migration may have had a role in controlling the size of the LCY magma bodies, it also may have had a control on the timing of their extraction. There is evidence from studies of other silicic centres and from thermochemical modelling that crystalline mushes would be likely kept at near-solidus or sub-solidus temperatures during the build-up phase of activity (Cooper & Kent, 2014; Andersen et al., 2017; Rubin et al., 2017; Szymanowski et al., 2017; Jackson et al., 2018). Once the system reaches thermal maturity, melt is

persistently present within the mush and percolates upwards, driven by gravity (Bachmann & Bergantz, 2004; Hildreth, 2004; Solano et al., 2012; Bachmann & Huber, 2016) and/or gas filter-pressing (Bachmann & Bergantz, 2006; Pistone et al., 2015).

Volcán Paquisis with an age of approximately 440 ka represents the final known stratovolcano activity preceding the start of the silicic eruption phase (evidence of any potentially younger edifices in the Tolimán-Atitlán lineament to the east would have been destroyed during caldera formation). Rhyolite melt extraction likely would have occurred after this time. At approximately 300-400 ka, this system was primed for the extraction of silicic magma. Local extraction of smaller bodies of magma occurred at least once (the W eruption, with possibly several other previous eruptions including the 306 ka AOT). Zircon dates from several of the AVC rhyolite eruptions could show that magmas typically began accumulating around 60-80 ka before eruption (assuming that the zircons were primary and not recycled), and there is a quasi-continuum of dated zircon crystallisation ages (and an inferred semi-continuous presence of zircon-saturated melt) from approximately 300 ka (Cisneros de León et al., 2021a). If we assume that the AOT was sourced from the AVC and followed a similar time period for melt accumulation, then extraction of melts from the mush system started shortly after the end of stratovolcano activity, and therefore melt was present in the system quasi-continuously from <400 to 67 ka. This is within the literature estimates for melt longevity in silicic systems (Gelman et al., 2013). Melt formation and storage would cease only once the recharge magmas ascending from the base of the crust have migrated outside this area.

6.3.4 A possible regional trend?

The observations outlined in section 6.2.2 suggest that arc migration is one of the main processes that controls when and where large volume silicic reservoirs formed in the AVC and subsequently controlled the possible timing and location of caldera-forming eruptions. This is especially evident when considering the position of the Atitlán III caldera to the north of the arc front. This is a common occurrence in the central Guatemalan segment of the CAVA: silicic calderas are located immediately north of the arc front at most volcanic centres (Fig. 1.1). The similar geographical relationships between the arc front stratovolcanoes and behind-the-front calderas in this region suggest that migration-controlled, large-volume silicic magmatism is common in this part of the arc. In particular, the proposed Xela caldera (Duffield et al., 1993) is the most similar to the AVC, and would

be an excellent site for further study of the influence of arc migration on silicic magma generation.

Schindlbeck et al. (2018) showed that there is a 'pulsed' regional temporal trend in the tephrostratigraphy, with increased tephra loads at intervals of 2-4 Ma. If the generation of silicic magmas at other centres in the CAVA is also controlled by arc migration, this could potentially explain the timing of these tephra pulses: they are periods where arc migration was marked by an increase in the volume of silicic tephra (Fig. 1.6). This hypothesis could explain the behaviour of the clearly migration-dominated centres between Xela in the west and Coatepeque in the east (Fig. 1.1). However, the centres along the rest of the arc to the southeast (El Salvador, Nicaragua and Costa Rica) do not have paired edifices nor do they have calderas/silicic centres located north of the arc front. Here, calderas are located at the arc front, and they therefore do not have a link between arc migration and magmatic processes. Schindlbeck et al. (2018) proposed instead that the pulsed nature of the activity was related to a combination of tectonic and climatic events (e.g., increased sedimentation affecting magma generation, changes in direction and velocity of subduction, etc...).

While arc migration does not appear to control the regional timing of silicic eruptions, it likely has a control on their volume. The individual tephra deposits of the CAVA increase in size towards the north-western segments (Kutterolf et al., 2008b), with the largest from the CAVA being the LCY event. The Tierra Blanca Joven (TBJ; 50-95 km³ DRE; Smith et al., 2020) and Olocuilta (>50 km³ DRE; Suñe-Puchol et al., 2019a) eruptions from the Ilopango caldera, and the L-tephra from Amatitlán caldera (42 km³ DRE; Kutterolf et al., 2016) are the next largest eruptions, all with rhyolite to dacite compositions. The size of the proposed Xela caldera is similar to that of the Atitlán III caldera (Duffield et al., 1993), possibly reflecting another large eruption. Tephra from the central and south-eastern portions of the arc tend to be smaller volume and more dacitic (Schindlbeck et al., 2016b; Fig. 1.2).

The silica content of the bulk rock rhyolite compositions also tends to increase towards the northwest. The high-K LCY rhyolites are the only pumices with >77 wt.% SiO₂. Most analysed pumices from the centres further east tend to have <75 wt.% SiO₂ (Wunderman & Rose, 1984; Suñe-Puchol et al., 2019a; Suñe-Puchol et al., 2019b; Pedrazzi et al., 2019). This correlates with variations in crustal thickness along the arc (Fig. 1.10), and increased crustal thickness has a well-established relationship with an increased occurrences of caldera-forming events as well as higher silica contents of the erupted magmas (Hughes & Mahood, 2008, 2011; section 1.2.3). As well the northern segment of the CAVA being the segment of

the arc where volcanic centres are most affected by arc migration, there are also several other factors that could cause magma bodies in this segment to have greater volumes than in other parts of the arc.

6.4 A perfect storm?

While arc migration appears to have a strong control on the evolution of the AVC (and possibly other neighbouring centres), if it were the only control then we would expect to see similarly sized silicic eruptions throughout the CAVA. However, the LCY eruption was the largest known eruption of the Quaternary here (Rose et al., 1987; Cisneros de León et al., 2021a). Preceding phases also produced colossal eruptions (the Maria Tecun tuffs; Newhall, 1980)). A significant question to answer is why this centre and those nearby have produced such enormous eruptions relative to the rest of the CAVA, suggesting that several other factors must have been in play. This study presented an explanation above as to how arc migration has allowed for magmas from the width of the centre to feed the LCY magma body. However, it is also important to consider the other influences that affect arc magmatism both along the CAVA and globally (section 1.2.3). With these in mind, I suggest that the formation of the LCY rhyolites was the result of a ‘perfect storm’ of circumstances.

There are several other factors that are correlated with the formation of large, evolved bodies of magma. One has to do with the specific nature of the CAVA relating to the segmentation of the arc. As outlined in section 1.3.1, the CAVA is segmented, likely due to rotation of crustal blocks (Burkart & Self, 1985). This has the effect of rotating the strike of the individual segments relative to the overall strike of the arc, and consequently the arc has a dextral offset every 100-200 km or so (Fig. 1.8). Gazel et al. (2021) suggested that this controls the volume of the centres within each segment, with the largest centres usually at the position of the arc segment that is approximately 90-110 km above the subducting slab (Fig. 1.9). Thus, they receive greater amounts of mantle-derived mafic melts than neighbouring centres, which are vital for maintaining and/or renewing silicic systems.

Another control is the subduction rate, which is commonly correlated to magma supply rate and has also been correlated with the frequency of caldera-forming eruptions (Hughes & Mahood, 2011; Sheldrake et al., 2020). The CAVA has one of the highest convergence rates of global volcanic arcs (Hughes & Mahood, 2011), and consequently it has one of the highest global eruption rates ($3.1 \times 10^{-3} \text{ km}^3$ per year per 100 km of arc length; Acocella & Funiello, 2010). A direct result of this is that the volcano spacing along strike in the CAVA is one of the shortest globally (De Bremond D’ars et al., 1995). This is especially important

in the AVC where two volcanoes/volcano lineaments are very closely spaced (Volcán San Pedro and Volcán Atitlán/Tolimán c.f. fig. 1.1). If it were not for the caldera, they would probably be considered separate systems. As it is, these two systems are inferred to have had a combined effect on the AVC magma supply; the location of the caldera between the two lineaments (Fig. 6.6) implies that it drew on magmas from both. This would increase the magma supply to the developing silicic system relative to centres with greater volcano spacings.

Structural factors are also important to consider. The northern segments of the CAVA also have two additional features that may influence magma storage: strike-slip faults underlying the arc front (Chaussard & Amelung, 2014; Wilson et al., 2021) and local crustal thickening, a factor widely correlated with evolved magma compositions (Hildreth & Moorbath, 1988; Hughes & Mahood, 2011). The strike-slip faults are caused by detachment of a fore-arc sliver, while local thickening is caused by the interactions of the Cocos, North American and Caribbean plate at their triple junction (section 1.3.1, Fig. 1.7). This has a combined effect of allowing large amounts of magma differentiation to occur and providing these magmas with pathways to ascend through the crust. In typically thickened arcs (e.g., the Andes), magma reservoirs are located at depth, while in the northern CAVA, despite being locally thickened, the magma reservoirs occur at shallow depths thanks to the strike slip faults underlying the arc.

The structural factors of the AVC show significant differences from those of the central and southern parts of the CAVA. The crust is much thinner, due to its transitional nature and to significant thinning (Gazel et al., 2021). Local spreading releases overpressure on the magma bodies, resulting in growth of the magma system and formation of plutonic bodies rather than magma eruption (Huber et al., 2019). Large silicic magma bodies therefore tend to freeze at depth in this region. Thinner crust is also globally related to less silicic (i.e., dacitic) tephras (Hughes & Mahood, 2011). The combined effect of these factors is smaller eruptions of less-silicic tephras than occurs to the northwest.

There are therefore many factors that combined to form the massive LCY magma body:

1. High magma supply rate, both because of high convergence rates creating high magma fluxes across the arc, as well as locally high flux related to the orientation of the arc segment above the slab (resulting in the close proximity of the stratovolcanoes).

2. Crustal thickness/thickening, a factor related to increasing silica composition of magmas (Hildreth & Moorbath, 1988; Hughes & Mahood, 2011) and/or higher magma reservoir sizes (Sheldrake et al., 2020).
3. Strike-slip faulting controlling the dynamics of magma ascent and storage (Wilson et al., 2021).
4. That arc migration has a strong control on the area (and therefore volume) that supplies magma to the final magma body, and likely also has an influence on the thermal history of the centre (section 6.3).

While it is undoubtedly true that numerous factors come into play when constraining the circumstances that lead to the formation of the large silicic magma bodies that fuel caldera-forming eruptions, this study has shown that arc migration can have a crucial role in specific systems. The CAVA is a key region where this is the case, and the effect of arc migration should be considered not just when examining the AVC, but in many other centres both in the CAVA and globally which have produced large silicic eruptions.

6.5 Global comparisons

6.5.1 Arc comparisons

The large number of factors that contribute to the prevalence of silicic calderas at convergent margins makes any identification of any single controlling factor very difficult. Comparing arcs with similar caldera densities to identify shared characteristic (including the presence or absence of an arc migration control) can be useful in determining the critical factors that influence elevated rates of caldera formation.

The northern segments of the CAVA have a caldera density of approximately 12 per 1000 km of arc length, and only the Kamchatka (18), northeast Japanese (12) and New Zealand (23) arcs have similar or greater values (Hughes & Mahood, 2011). These systems therefore represent the most explosive volcanic arcs on Earth and could be the best comparisons for the CAVA.

However, the case of the New Zealand arc is unique and should be discounted for this comparison. While there is certainly trenchwards migration of volcanic activity within the Taupo volcanic zone (TVZ; Villamor et al., 2017), and caldera-forming volcanism from this region is highly elevated, there are more direct factors that almost certainly control the scale of volcanism here. The most important of these factors is the action of the Taupo rift system, where significant extension occurs in the crust underlying the TVZ (Seebeck et al.,

2014b). This extension has likely allowed for elevated magmatism through promotion of mafic dyking to shallower regions of the crust (Deering et al., 2011b). In terms of structure, the Kamchatka arc most closely resembles the CAVA. They both overlie similar thicknesses of continental crust, have similar trench-normal convergence rates (76 vs. 71 mm/yr) and similar average slab dip (38 vs. 44°; Hughes & Mahood, 2011). The time that the arcs have been in their current positions is also similar, both being fairly young (approximately 5 Ma for Kamchatka (Ponomareva et al., 2007) vs. 2 Ma (section 1.3) for CAVA). With these broad similarities it might appear that these arcs would make great comparisons for the influence of migration on the generation of large volumes of silicic magmas. However, there are significant differences in their structures that make direct comparisons difficult. While the northern CAVA has a very simple structure with an evenly spaced, narrow, and linear arc front (Fig. 1.8), volcanism in the Kamchatka peninsula is more chaotic, with three zones of volcanism active since the Pliocene that are spread out over a width of over 200 km (Ponomareva et al., 2007).

The form of the volcanic structures is also different: whereas the volcanoes of the CAVA are clearly aligned and commonly have calderas directly behind the arc front, the volcanoes in the Kamchatka arc have no such linear features. There were therefore no effects related to short-term arc migration affecting the formation of the large-volume silicic magma bodies that fed the Kamchatka calderas as have been proposed for the AVC in section 6.3. Instead, the longer-term migration effects proposed by Hughes & Mahood (2011), such as exhaustion of fusible phases in unexploited lithosphere, may have been in operation.

In the northeast Japanese volcanic arc, voluminous caldera-forming volcanic activity is mostly constrained to a period of time prior to 1 Ma (Umeda et al., 2013). Around 1 Ma, the arc's stress regime changed from a mostly neutral arrangement to a dominantly compressive one, which had an effect on the style of volcanism with a shift to predominantly stratovolcano activity over caldera-forming events (Umeda et al., 2013). When observable, the structure of the volcanic systems around the calderas are again not influenced by arc migration, although the age of the calderas (typically >1 Ma) does mean that their structures have been significantly altered by subsequent volcanism and by erosion (Kondo et al., 2004). The elevated caldera frequency for this portion of the arc is instead suggested to be the result of high mantle-derived magma flux driving melting of the crust (Kimura et al., 2015; Yamamoto et al., 2018).

This, comparison of the northern CAVA with similarly explosive arcs shows some commonalities, but also crucial differences between them. All of these arcs are fairly young, a characteristic that has been highlighted as correlated with increased caldera density and potentially linked to arc migrations (Hughes & Mahood, 2011). However, these arcs also show distinct differences. None show the striking structural control that arc migration has had on the structure of volcanism at the CAVA, and instead there are individual characteristics of the arcs that have served to make them more explosive. In the case of the northern CAVA, it appears that short-term arc migration is one of them.

6.5.2 Comparison with other large caldera-forming eruptions

Based on comparisons with similar volcanic arcs, migration does not appear to have a strong control over the caldera density of an arc beyond the link to youthful arcs (Hughes & Mahood, 2011). Comparison with individual centres might reveal more information instead about why the AVC in particular has experienced abnormally large eruptions, and if other centres appear to have links to short-term migration. Eruptions on the order of magnitude of 100s of km³ that are not tied to flare-ups are rare for convergent margins (de Silva, 2008).

The arcs described above that have similar physical characteristics and caldera densities to the CAVA have produced only one large volume caldera-forming eruption of similar volume to the LCY event (the Karymshina event with 320 km³ DRE (Bindeman et al., 2019).

Comparison with the VOPRIPA database (Croweller et al., 2012; Brown et al., 2014) shows that very few similar eruptions have occurred at convergent margins. The exception are the eruptions of the Taupo volcanic zone, which cannot be directly compared due to its unique structural characteristics. Similarly, a structural control related to localised extension on the Great Sumatran Fault has been proposed as an explanation for the massive size of the Toba eruptions (Acocella, 2014), and so these are also not further examined. The other most similarly sized eruptions were from the Aira caldera and eruptions related to the Takidani pluton in Japan (although these are from the southwest and central portions of the Japanese arc respectively), and the Cerro Galán eruption in Chile (Croweller et al., 2012).

In Karymshina and Cerro Galán, the elevated eruption volumes appear to be related to delamination of the lower crust (Kay et al., 2011; Bindeman et al., 2019). The Japanese calderas are different; both systems (and indeed most felsic Japanese magmas) are heavily controlled by large scale crustal melting, which in turn is driven by voluminous production of mantle melts (Kimura et al., 2015; Nishihara et al., 2024). These centres overlie steeply

dipping portions of the Philippine Sea oceanic plate and it has been proposed that this focuses slab-derived fluids into a narrow region of the mantle, enhancing mantle melting in this region (Kimura et al., 2015). Slab melts have also been reported (Shibata et al., 2014).

These comparisons of the most voluminous caldera-forming eruptions at convergent margins show that each case is unique and confirms that there are several potential ways that large volumes of evolved melts can form. Short-term migration, while strongly related to the largest caldera-forming eruptions of the northern CAVA, is not a universal factor. These comparisons reinforce the idea that there is no single model for large caldera-forming eruptions (Wilson et al., 2021).

This conclusion should not be taken as a suggestion to ignore the potential effects short-term arc migration may have had on caldera systems. Not all investigations of calderas have investigated or will investigate the full volcanic history of the system. This may be because a study is focused on the evolved magmas or may simply be that the preexisting volcanic structures have been destroyed in the caldera-forming event and/or they have been eroded or buried. In the case of the AVC, we are fortunate that it is a relatively youthful system such that a large amount of its history is still preserved and accessible, allowing us to investigate the system in a holistic manner. I would encourage future studies of caldera systems (particularly those in regions where the magma source may be migrating rapidly) to consider the potential influence of arc migration on its evolution.

Chapter 7: Conclusions and future work

7.1 Introduction

In this thesis I have aimed to provide a petrogenetic model for the evolution of the AVC during the most recent phase of its volcanic activity. The culmination of this phase was the LCY event, a VEI 8 eruption that resulted in the formation of the Atitlán III caldera. A key aim of the thesis was to provide an explanation for the extremely large volume of magma involved in the LCY eruption. In Chapter 1, I outlined some potential avenues to investigate this. Key amongst these was the comparison of the location of the Atitlán III caldera with the changing positions of the preexisting stratovolcanoes. This comparison showed that it lies in an intermediate area between the oldest and youngest pre-LCY structures (Fig. 1.1). There is also a similar timing between the commencement of explosive eruptions of rhyolites and the migration. A subsequent hypothesis was developed that this correlation between the migration's timing and positioning had a direct control on the LCY event. In order to test this link, this project aimed to examine a potential petrogenetic relationship between the stratovolcanoes' magmas and those of the LCY event. Geochemical and petrological information of these rocks was obtained and used to form these models. Several potential mechanisms by which the migration of the stratovolcanoes controlled the positioning and timing of the subsequent episodes of explosive eruptions of evolved magmas were discussed. In this final chapter, I will summarise the main conclusions of my work and how they have addressed my stated research questions (how were the different magmas of the AVC formed, what effect did arc migration have on the centres evolution, and what are the broader implications for caldera-forming systems) and place them in the wider context of the global understanding of the evolution of centres hosting large-volumes of evolved magma. Finally, I will present several potential future avenues of research that will further add to our understanding of both the AVC and the CAVA.

7.2 Evolution of the AVC's magmatism

A key aim of this study was to explain the formation of the wide variety of different magmas that have been erupted in the AVC during the last 1.8 Myr. This involved tying together the obtained petrographical, mineralogical and geochemical information, as well as using published thermobarometric and compositional evolution models to analyse the data. Development of these petrogenetic models was key to my investigation of the evolution of the AVC in Chapter 6. I have found that there have been several main different

types of magma evolutionary trends acting here during this time: a stratovolcano trend that involves variable enrichment in LILEs through interaction with a rhyolite melt; a “high-K LCY” formation trend that appears related to the stratovolcano magmas; a “low-K LCY” trend that is instead removed from any interaction with the stratovolcanoes magma systems – this trend may also be related to the low-K andesite “enclave” found in the post-LCY sequence; and finally a post-LCY series that is controlled by the interaction of recharging magmas with the remnants of the LCY magma system.

The pre- and post-LCY stratovolcanoes in the AVC all show similar geochemical trends for major, minor and trace elements, although the analysed materials of the post-LCY stratovolcanoes are on average less silica rich than the pre-LCY stratovolcanoes (Figs. 4.1-4.3, 4.6). The major and trace element geochemical trends commonly showed an inflection point at ~57 wt.% SiO₂ (Fig. 5.3). Rocks with >57 wt.% SiO₂ typically fall on a mixing line between the composition of this inflection point and those of a series of rhyolite glasses that I had found in the stratovolcano samples (as both melt inclusions and residual glass in lava-hosted anteliths). Mixing between basaltic andesitic magmas and those glass melts probably controlled the compositional evolution of the stratovolcano magmas. This is further supported by textural evidence for magma mixing in the andesite lavas (section 5.1.2.1). Geochemical modelling of the stratovolcano magma series (section 5.1.2.2) confirmed that a combination of fractional crystallisation and addition of these melts can create the observed compositional variation. Petrological investigation of the stratovolcano samples showed that this magmatic evolution occurred in the middle to upper crust (section 5.1.2.3). This therefore controlled the location in the crust where any subsequent magma evolution may have occurred.

The origin of the rhyolite glasses found in the stratovolcano samples was further investigated because of their evident control on the evolution of the stratovolcano magmas. The glasses contained elevated concentrations of K₂O and LILEs, as well as low concentrations of Na₂O (section 4.4.1.3), which may indicate partial melting of biotite-rich rocks. I identified several potential source rocks, including two “anteliths” that I found in the AVC stratovolcano samples that contain large amounts of this glass. One of these samples (sample Ati427_08a) appears to have been erupted while undergoing a melt reaction and contains large volumes of glass as well as petrographic indications that the melt reaction involved pyroxene and biotite (Fig. 3.13; section 5.1.3.1). This further supports the hypothesis that partial melting of biotite-bearing rocks formed these rhyolite melts.

The nature of the source rocks for these rhyolitic melts is unclear. It would be unusual to find large volumes of biotite in cumulates formed from an andesitic magma series. Instead, hydration reactions involving cumulates could result in the formation of biotite. The conditions required for such reactions involve a thermally mature magma system with an exsolved aqueous phase. This has broader implications for the future activity of the AVC stratovolcanoes; the absence of the most highly evolved and potassic compositions (high-silica andesites and dacites) from the post-LCY stratovolcanoes, found in this and previous studies, could indicate that the influence of VHKM is not yet as dominant as it was in the later stages of the pre-LCY stratovolcanoes (although VHKM-like melt inclusions have been identified; Halsor, 1989). A future compositional shift towards more evolved and more potassic juvenile eruptive products would indicate a change in the nature of the magma systems. Petrological monitoring of future AVC eruptive activity will be required to confirm this change.

Finally, the isotopic compositions of the stratovolcano series revealed a crustal control (section 5.1.1.1). Mirroring observations from eastern Guatemala, the more landward stratovolcanoes have more “crustal” isotopic signatures (Figs. 4.9-4.13). AVC stratovolcano samples do not show any correlation between SiO_2 and any radiogenic isotope ratios, and so they most likely obtained their variable isotope signatures during magma hybridisation in the lower crust. Any further products of fractional crystallisation of these magmas would therefore inherit these signatures.

Two previously identified rhyolite pumice types have been described from the LCY eruption, these being the “high-K” biotite-bearing and “low-K” amphibole bearing types. I have described a new rhyolite pumice type from the LCY eruption which contains both biotite and cummingtonite (section 3.2.3.1), as well as having moderate K_2O concentrations in both whole rock and matrix glass (sections 4.1.3 and 4.4.1). Its similar trace element chemistry, slightly more evolved composition (higher SiO_2 and lower MgO) and lower temperature estimates compared to the low-K pumices were interpreted to mean that the “new pumice magma” was derived from the low-K pumice magma through fractional crystallisation. I subsequently defined it as a sub-group of the low-K LCY rhyolite pumice and have referred to it as the “medium-K LCY rhyolite” pumice (section 5.3.1).

Rose et al. (1979) suggested that the high-K LCY rhyolite magma was the daughter magma of the low-K rhyolite via fractional crystallisation. My interpretation of trace element data for these two magmas obtained in my study makes this scenario unlikely, as they have

highly differing trace element concentrations that would be difficult to reconcile with fractional crystallisation (primarily the contrasts between their LILE and REE contents; section 5.3.2). In fact, the high-K nature of the stratovolcano lavas precludes their magmas from being the parent. However, a low-K evolutionary path can be suggested. In this scenario, the high-K LCY rhyolite has most likely been extracted from the remnants of the mush systems beneath the pre-LCY stratovolcanoes, whose sparse remnant deposits span the width of the Atitlán III caldera. The pre-LCY stratovolcano lavas have distinct compositions with high K_2O and low Na_2O concentrations that are similar to those of the high-K LCY rhyolite. Therefore, the K_2O enrichment of the high-K rocks would derive from the mid- to upper-crust and would be tied to the mush systems left behind in the magma reservoirs beneath the stratovolcanoes. A magma system underlying this region could be a suitable environment in which low-K magmas could evolve. Because of the differences in the mineral assemblages of the LCY rhyolites, no direct geobarometric comparisons could be made between them. However, geothermometric estimates from minerals in the two different groups consistently show higher temperatures for the low-K rhyolite magma (section 5.3.4), as would be expected if it were derived from deeper in the crust.

While there is no evidence for the presence of more primitive low-K magmas in the LCY eruption deposits, low-K andesite material has been found in the post-LCY eruption sequence. This shows that low-K magmas can occur in the AVC, and it was hypothesised in this study that this material represents a low-K trend that formed at the AVC and resulted in the low-K LCY rhyolites eventual generation. This relationship was tested numerically to prove its possibility (section 5.3.3.1). The relatively minor proportion of low-K rhyolite pumice in the post-LCY deposits (~10%) suggests that this was a comparatively minor component, so this was not a dominant magmatic process.

The presence of two compositionally distinct rhyolites in the LCY eruption deposits has an interesting implication. Development of an evolved magma body (and likely an exsolved volatile phase) may promote the generation of further volumes of evolved magma. This process is promoted in two ways: 1) thermal maturation has brought the crust into a position where the growth of magma bodies can be more accommodated by elastic strain; 2) exsolution of a volatile phase (thought to commonly occur at such magma systems) also acts to buffer pressurisation of the crust and promote growth and further evolution of magmas (Huppert & Woods, 2002; Bouvet de Maisonneuve et al., 2021).

The post-LCY series of explosive eruptions was highly complex and involved a wide compositional range of magmas from basaltic andesites to rhyolites (sections 4.1.4 and 4.2.4). Providing detailed petrogenetic models for each individual unit of this sequence is beyond the scope of this project. Instead, through investigation of several selected pumices, I sought to develop a more generic model which addressed the main petrological processes that were in operation in the post-LCY phase of activity.

These rocks revealed that the AVC magma system was (not unexpectedly) in a somewhat chaotic state following the LCY eruption. All the investigated samples showed evidence of some degree of magma mixing (section 5.4). Glass compositions in the rhyolites showed that they were not direct remobilisations of unerupted portions of the LCY rhyolite magmas. Instead, it is more likely that they were remelted portions of the remnants of the LCY crystal mush system. The more primitive rocks analysed from this sequence (the D1 and I1 samples) also showed evidence of mixing between more and less evolved magmas (section 5.4.1). In these cases, there was a greater input from more primitive magmas.

If interaction between recharging mafic magmas and the remnants of the LCY magma system was the main petrogenetic process for the post-LCY sequence, the implication is that similar rhyolite pyroclastic eruptions are unlikely to occur in the future. There is no evidence for any continued magma supply to the region of the Atitlán III caldera, and instead it is currently focused around the Volcán Atitlán edifice. If juvenile magma is no longer being supplied to the Atitlán III caldera, then it is unlikely that further generation of magmas with compositions like those of the post-LCY sequence will occur. However, volcanism behind the arc front is clearly possible, as shown by the recent eruptions at Cerro Quemado at the neighbouring Xela centre (Conway et al., 1992). Monitoring of seismic activity at the AVC and the water level in Lake Atitlan would be important to assess this potential threat.

7.3 The effects of arc migration

Understanding the degree of control that regional arc migration had on the evolution of the AVC was one of the main driving factors that inspired this project (section 1.1). I have identified several effects that arc migration has had on different aspects of the AVC. The first is its control on the structure of the centre. The locations of the stratovolcanoes in comparison with the margins of the subsequent caldera shows a very tight overlap (Figs. 1.1 and 6.6). While the location of two closely spaced stratovolcanoes appears to control the width of the centre in the east-west direction, the relative ages of the north-south

stratovolcano materials show that arc migration has controlled the locations of stratovolcanoes in this direction. As the stratovolcano magma systems were also the source for most of the LCY rhyolites, their location also likely controlled the regions from which magmas would be extracted. Arc migration subsequently expanded the region experiencing magmatism, increasing both the potential volume of the crust in which magmas can accumulate and evolve (simply as magmatism occurs over a wider region) and also the volume of the crust that has been heated, making these crustal regions more suitable for magma storage.

Arc migration also appears to have been related to the timing of the start of the rhyolite eruptions. The youngest pre-LCY stratovolcano material is 440 ka old (Newhall, 1980), close to the age of the AOT eruption (306 ka; Kutterolf et al., 2016). However, the timing of the pre-LCY activity is not well constrained, there being only one dated sample from Volcán Paquisis. There are no age estimates for the large amount of stratovolcano material on the margins of the Atitlán III caldera. Constraining the timing of arc migration is key to understanding the shift in the volcanic activity from stratovolcano construction into voluminous eruptions of rhyolite pumice.

This gap in our understanding of the AVC also highlights the need for a holistic approach to investigating caldera systems worldwide. It is vital to understand both the timing, positioning and chemistry of the magmatism that preceded a caldera-forming event to fully understand why that event occurred, and what conditions might give rise to a similar event in the future. Considering the potentially devastating impact that a future VEI 8 eruption may have both regionally and worldwide, it is crucial to understand these conditions as comprehensively as possible. This is also important for identifying other regions of the Earth where such volcanism may occur.

7.4 Broader implications of this study

This thesis has addressed several gaps in the current understanding of both the local (AVC) and regional (CAVA) volcanic activity, as well as highlighting a potential additional aspect of caldera-forming volcanism that has previously been unaddressed. In this section I discuss the broader implications of this project.

7.4.1 Regional activity

This study has investigated several different aspects of the AVC magmatism and has highlighted important links between older stratovolcano magmatism and the evolution

towards large-volume highly explosive rhyolitic eruptions. These links are primarily the control of arc migration on the location and timing of magma evolution, as well as the control that the earlier episodes of magmatism had on the eventual composition of the magmas that erupted in the AVC. It is clear from this study that a holistic approach, in which all aspects of the centre's past activity (its location, timing and composition) are investigated, is necessary to develop as complete an understanding of the AVC as possible. Without the detailed investigation of the pre-LCY stratovolcano activity, I would not be able to provide an explanation for the composition of the LCY rhyolites, nor would I understand why the Atitlán III caldera is situated where it is. Studying pre-caldera activity is therefore vital for any study of caldera-forming eruptions.

The presence of the other major calderas behind the current arc-front in Guatemala, in a similar relative position to the Atitlán III caldera (Fig. 1.1), suggests that their locations were also similarly controlled by arc migration. These calderas have not been well studied and there have been no petrogenetic investigations of their products. With the preliminary estimates of arc migration rates for the northern CAVA, I have shown that arc migration rates in this region (at least in the last 1.8 Ma) have likely been very high (section 6.1). For any future studies that investigate these calderas, I would strongly recommend including the study of the earlier activity at the centre. I also highlight the likelihood that a good proportion of this activity occurred north of the current arc front and may even be further north of any caldera structures.

Identification of this rapid migration rate also has implications for future medium- and long-term hazard assessments at Guatemalan volcanic centres. It is unlikely that another event rivalling the size of the LCY eruptions will occur soon in the CAVA, however the future positions of stratovolcanoes are likely to be constrained by further migration. The most impactful case would certainly be that of Volcán Santa María/Santiago, where the vent for the 1902 eruption and subsequent dome construction was situated well to the southwest of the summit (Rose et al., 1972a, 1972b). Future hazard assessments of Guatemalan volcanoes should consider the potential for eruptions to start to occur in regions south of the current arc front. Installation of seismic arrays and/or GPS stations would enable detection of any shifts in the location of the magma supply.

7.4.2 Global considerations

The conclusions of this study are directly relevant to volcanism in the northern portion of the CAVA, where arc migration has a readily apparent influence of the structure of

volcanism. While it is not clear that other similarly-sized calderas at other convergent margins are controlled by arc migration (section 6.5), the more general conclusions of this study can still be applied. Consideration of a centre's entire magmatic history is important, as is addressing any other potential structural or geochemical controls on magmatism. Purely petrological studies of the explosive sequences of caldera systems may lack this crucial context, and the application of radiometric dating techniques to an entire eruptive sequence is therefore very important. Focusing on the common zircon dating methods for evolved magmatic products may miss significant information that could be revealed by using other methods on less evolved magmas (e.g. $^{40}\text{Ar}/^{39}\text{Ar}$ methods; Schaen et al., 2020). This study benefitted greatly from previously published dates, and higher resolution dating of the AVC stratovolcanoes is important for future study of the AVC.

The conclusions from this study have been directed primarily at other convergent margins, and more specifically to convergent margins that have elevated occurrences of calderas (section 6.5). There are however potential applications to any volcanic centres that have undergone migration. Hotspot-related volcanism could clearly be implicated based on the strong control that plate movement over the hotspot has on the position of volcanism.

7.5 Future work

In this project I have outlined a possible explanation for magmatic evolution at the AVC and the role that arc migration and other factors had in supersizing it relative to other caldera-forming eruptions. While this is a good explanation for the individual centre, to test this conceptual model fully, further studies on neighbouring systems (and other centres globally) would be beneficial. Future studies that would further develop our understanding of this model would be:

7.5.1 Petrogenetic studies and/or tephra identification of nearby centres

The Xela and Amatitlán centres (Fig. 1.1) are prime candidates for further investigation of the impact of arc migration, as they share many similar characteristics that would allow for direct comparisons with the AVC. Similar research questions would be applicable, namely “What are the origins of the different eruptive products of these centres?” and “What effect did arc migration have on the formation of the magma bodies that fed their caldera-forming eruptions?”. However, the lack of detailed knowledge of the pre-caldera stratigraphy (and in the case of Xela, lack of knowledge of even the potential caldera-

related units) leads to the need to address a more basic question “What was the timing, volume and sequence of volcanic activity at these centres?”.

Subsequently, in addition to applying the methods that have been used for this study, more fieldwork would be required for both examples. My research in the AVC had the advantage of extensive previous studies (section 2.1) that meant that most sampling sites were identified prior to the fieldwork. In the case of Amatitlán, pre-existing stratovolcano structures have not been described, while for Xela several stratovolcano structures bordering the proposed caldera (Rose, 1987; Foley et al., 1990) have been identified but there are no radiometric age dates nor any formal correlation of tephra deposits thought to be sourced from the centre. Mapping and sampling of these regions would be vital for any further study. However, the geological complexity and the relative lack of knowledge of this region means this work would require several PhD projects.

For Xela, it would be crucial to perform tephra correlation studies to identify any tephra deposits that were sourced from this system, and then to formally determine whether this depression is a volcanic caldera. In the positive case, radiometric age dates should be obtained for the volcanic materials, including zircon U-series dating of tephra deposits and $^{40}\text{Ar}/^{39}\text{Ar}$ dating of stratovolcano lavas. Once this work has been undertaken, petrological and geochemical studies similar to those performed in this work should be completed to determine the nature of the relationship between any identified tephra deposits and older stratovolcanoes.

The explosive history of the Amatitlán system to the east of the AVC is already partly understood (Kutterolf et al., 2016; Cisneros de León et al., 2023). Less work would be required to investigate this system, involving investigation of the regions north of the caldera to identify any pre-existing stratovolcanoes, and radiometric dating of these to constrain temporal relationships. Similar petrological and geochemical study of these deposits could then investigate the relationship between identified pre-existing stratovolcanoes (if any) and the tephra deposits.

The aim of these proposed studies would be to further investigate the influence of arc migration on the timing, volume and chemistry of the erupted magmas. These investigations would also have major implications for volcanology at the CAVA. The nature of the Xela “caldera” is one of the biggest unanswered questions for this region. Formally classifying it as a volcanic structure would be a major step towards confirming that caldera-forming events are an important part of volcanic activity in this section of the CAVA.

Gaining a more complete understanding of the Xela system is also of major importance, as of the current associated stratovolcanoes, only the history of Santa María/Santiaguito is well known (e.g., Singer et al., 2011, 2013). The Xela depression is host to Quetzaltenango, the second largest city in Guatemala, highlighting the importance of comprehensive hazard assessments for this area and its associated stratovolcanoes.

7.5.2 Constraining the arc migration rate of the northern CAVA

A significant aspect of this work is related to the nature of arc migration at this AVC. There has not yet been a comprehensive study to constrain arc migration rates across the entire CAVA. Such a study would be useful in comparing the rates of arc migration to global values. This study would aim to investigate “What is the arc migration rate of the northern CAVA and is it consistent along strike?”. If migration rates are consistent along the arc, as could be suggested by the relative positions of the nearby calderas, then they may have had a similar effect on the nearby calderas as seen at the AVC. However, if arc migration rates were found to vary, this could suggest that each volcanic centre would have a unique relationship with its deep magma supply.

The estimates in section 6.1 show that it is likely that arc migration rates in the central Guatemalan section of the CAVA are higher than the global average. As caldera-forming volcanism appears to be common at most of the northern volcanic centres, candidate centres for a migration rate study are rarer as most evidence has been destroyed. Two possible options are: the Pecul-Zunil-Tzanjuyub lineament immediately west of the AVC (Figs. 1.1 and 1.11) which provides a continuous record of volcanism over a 10 km long north-south aligned segment, while the continuous western edge of the San Marcos-Paquisis lineament in the AVC also preserves a similarly long stretch of stratovolcano deposits that have not been destroyed by the Atitlán III caldera. Other candidate regions could be identified following more precise mapping of the area around the arc front.

This study would require an extensive field campaign to obtain enough samples to precisely show the migration trend. Ages would best be estimated by $^{40}\text{Ar}/^{39}\text{Ar}$ methods, because of: 1) lack of other commonly used phases (e.g. zircon for U-Pb dating); 2) most volcanic material is expected to be <2 Ma; 3) the abundance of K-rich phases (plagioclase, amphibole, biotite and groundmass) that would be appropriate for analysis (Schaen et al., 2020).

Such a study would have further implications beyond the impact of arc migration on silicic magma formation. In this section of the CAVA, arc migration has a dominant control on the structure of the present stratovolcanoes (section 1.3.1). Constraining the migration rate of the arc would be crucial for medium-term hazard assessments at the currently active stratovolcanoes, as if the migration rate is high then future activity might occur further south than may be expected. This work has the potential to provide further constraints on the timing of stratovolcano activity around the AVC prior to the LCY event, as this is currently poorly known.

7.5.3 Further work into the AVC

This study has revealed a great deal of information about the nature of the Quaternary AVC magmatism. As is always the case, it has also brought up several more questions that should be investigated. In this section, I will outline several interesting avenues for future work in the AVC.

7.5.3.1 Further geochemical and petrological investigations

Recharge magmas

This study has revealed several units in the AVC that would be good candidates for further investigation. Some may be related to the recharge magmas that have been commonly observed (section 2.1). Samples representing these magmas have proved difficult to isolate but have great potential for investigating this system as they provide a record of the inputs of heat and material needed to grow and/or mobilise large volumes of silicic magmas (Ruprecht et al., 2020). They also have the potential to describe alternate magma histories that should be investigated. Answering the question of the extent to which these recharge magmas are related to their hosts would be the major aim of such a project.

The enclave which I extracted from the I eruption deposits appears to lie on a separate geochemical trend to the AVC stratovolcanoes (sections 4.1.2 and 4.2.1). It would be valuable to obtain several more samples to confirm or refute this interpretation. Adding further enclaves from the W, LCY, and D2 eruptions (as well as attempting to identify recharge magmas in other eruption deposits in which they have not yet been found) would also be significant additions to this dataset. Thus, fieldwork targeting extraction of discrete enclaves from the silicic eruptions of the AVC would be very useful. As well as whole rock major and trace element data which may reveal potential alternate petrogenetic pathways which recharge magmas may follow, isotopic studies on them could help reveal where in

the centre magmatism was occurring (due to the geographic control on radiogenic isotope values observed here; section 4.3).

This project would therefore aim to test the hypothesis outlined in this study that the enclave magma potentially represents a diverged trend for andesite lavas that experienced a different magmatic evolution to that of the stratovolcano andesites. This would also be important in testing whether the enclave's elevated P_2O_5 concentration is related to a nugget effect, or if it does indeed highlight apatite suppression, suggesting a fractional crystallisation origin over the mixing-dominated stratovolcano trends. Finally, these recharge magmas are probably highly instrumental in feeding both material and heat to growing evolved magma bodies. Constraining the full suite of recharge magma compositions from the AVC would contribute extensively towards our understanding of the formation of large eruptions of evolved magmas, as well as the evolution of the whole AVC.

Pre-LCY eruptions

Expanding our knowledge of the explosive phase of AVC activity is also critical to understanding the evolution of the magma system. Probably due to their widespread exposure around and inside the Atitlán III caldera, the post-LCY phase of activity has more been readily studied. Outcrops of the pre-LCY eruptions (the W tephra and the AOT) are not as easily sampled due to their probable destruction or concealment by the voluminous LCY deposits, yet they contain highly important information regarding the nature of the shift from effusive stratovolcano construction into large volume explosive eruptions of silicic magmas. This project would aim to the question "What was the petrogenesis as well as the eruption size of the pre-LCY pumice eruptions?" This project would further contribute to our understanding of the conditions that can lead towards the formation of one of the largest Quaternary volcanic eruptions of the region.

The pre-LCY phase III volcanoes

A deeper investigation of the pre-LCY phase III stratovolcanoes would be similarly important for understanding the formation of the high-K LCY rhyolite (as well as potentially the preceding AOT and W eruptions). This study has identified the stratovolcano magma system as its most likely source and, while Volcán Tecolote has been investigated here in some depth, Volcáns Paquisis and San Marcos should be examined further. The remnants of other stratovolcano deposits on the caldera margins (Fig. 6.6) also warrant further investigation. This study has suggested that the dominant driver of the evolution of the

stratovolcano magma was generation and mixing of VHKM with these magma systems, however gaps in the dataset need to be filled to confirm that this was the case. Tied to this study is the requirement for deeper investigations into the anteliths. The two anteliths described in this study (section 3.2.1.1) have yielded excellent evidence about the nature of the magmatic systems beneath these volcanoes, and addition of more samples would further our understanding of the magma system from which the LCY rhyolite later developed.

This future study would therefore aim to address the gaps in our knowledge of the compositional range of the pre-LCY stratovolcanoes in the AVC, and would aim to answer the research question “Were the evolutions of the stratovolcanoes at the AVC comparable to that of Volcán Tecolote?”. Samples from Volcáns San Marcos and Paquisis fall on a similar trend to those from Volcán Tecolote but lack the resolution to confirm that they show identical compositional trends. If it can be shown that both contain similar anteliths to those observed in this study, as well as showing similar evolved compositions to the Volcán Tecolote lavas, then it would add further support to the hypothesis that the AVC rhyolite volcanism was tied to the stratovolcanoes that preceded it. This would also be useful in consolidating our understanding of the evolution of AVC stratovolcanoes, aiding in the petrological monitoring of future volcanism here.

7.5.3.2 *In situ* isotope studies

Tied to the theory that arc migration influenced the formation of the LCY rhyolite magmas is the hypothesis that the sources for the different LCY magmas came from the width of the centre (section 6.3.1). Good evidence for this is found in the relatively isotopically disparate post-LCY pumices, which seem to sample isotopically diverse regions of the recovering mush system (section 6.3.1). Further evidence could be provided by microscale analyses of the crystal populations of the different AVC pumices. Numerous studies have shown that crystal populations preserve the isotopic composition of their original magmas (e.g. Weber et al., 2023), showing that it is common for large volume eruptions to sample multiple magma bodies and/or to have variable source regions. Use of these *in situ* techniques on the Atitlán rhyolite samples would be extremely useful to test the validity of this theory. Drawing from the conclusion of this work that the parent magmas had a range of radiogenic isotope values, I would expect that some of the crystal population would reflect the range observed in the rock record. This assumes that some of the crystal populations/crystal cores were not grown from the homogenised rhyolite magma but were

instead relict crystals drawn up from the crystal mush. The large range in textures of the plagioclase seen in all analysed LCY rhyolite samples (section 3.2.3.1) could point towards this. This project would therefore aim to answer the following research question: “Do the crystal populations of the AVC pumices (and the LCY pumices more specifically) have varied isotopic compositions that reflect the variations observed in the rock record here?”

In situ isotope analyses would also be useful to test the origin of the pre- and post-LCY pumices. They show slightly more variable radiogenic isotope values, which is thought to be caused by remobilisation of discrete parts of the LCY crystal mush which are not completely homogenised (section 5.4.2.3). If this is reflected in the crystal populations, then it would help to show that the underlying mush system of the AVC was isotopically heterogeneous.

Major mineral phases to target would include clinopyroxene, apatite and plagioclase. These are useful for investigating the Sr-isotope system because of the similarity between Ca^{2+} and Sr^{2+} ions (e.g., Kimura et al., 2013; Yang et al., 2014; Tong et al., 2016). The method used in such studies is usually laser ablation multi-collector inductively couple plasma mass spectrometry (LA-MC-ICP-MS). Oxygen isotopes in quartz have also been used extensively (e.g., Bindeman, 2008), using both micro-drilling and ion microprobe methods.

Quartz, apatite and plagioclase are relatively abundant in the AVC rhyolite samples, although the crystal-poor nature of the pumices means that large volumes of pumice would be required to extract a robust crystal dataset. This project would require a field campaign to collect the required pumice samples and would aim to sample all the pumice units that have been described to form a detailed population.

7.5.3.3 Thermal modelling

A final piece of further work could be achieved through thermal modelling. Our understanding of the thermal evolution and subsequent longevity of magma bodies, how magmatic intrusions influence the thermal structure of the crust, and our ability to model these processes is well advanced thanks to the works of Annen and collaborators (e.g., Annen & Sparks, 2002; Annen, 2009, 2011, 2017; Annen et al., 2015; Blundy & Annen, 2016). Developing a “top-down” 2D version of the model or even a 3D version that includes a migrating magma source using published magma fluxes for the CAVA (Kutterolf et al., 2008) and the estimated migration rates from this study (or from future work as outlined in section 7.2.2) could provide a useful test to constrain the conditions under which the LCY magma body (and even the preceding AOT and W magmas) could have formed. This

project would therefore aim to test whether a migrating magma source can supply enough heat into the crust to grow and sustain a magma body large enough to feed the LCY eruption. It could also test whether this migration increases the volume of the crust which can maintain a magma body in an extractible state in comparison to a volume where the magma supply is fixed. The results of this could be instrumental in identifying what regions of volcanism globally could be susceptible to large-scale silicic magmatism.

The structure of the model would be based on the models presented in Blundy & Annen (2016) and Annen (2017). Further adaptation of the model would be important to allow for variation in the emplacement of the sills that provide the modelled heat. There are then several variables that would be controlled: the magma emplacement rate, the arc migration rate, and the thermal diffusivity of the country rock. Field work targeting an understanding of the underlying crust of the AVC would be of great importance for this final variable, because crystalline xenoliths as well as outcrops of plutonic rocks have been identified in this study (section 2.1). Use of these rocks could provide estimates for thermal diffusivity values, at least of the upper crust. Variation of the key variables in the ranges that could be expected for the CAVA would be very useful for testing whether growth of magma bodies in migrating systems is feasible. This model would also have significant potential applications for any other system in which arc migration is a potential factor.

References

- Abers, G. A., Plank, T., & Hacker, B. R. (2003). The wet Nicaraguan slab. *Geophysical Research Letters*, 30(2), 1–4. <https://doi.org/10.1029/2002GL015649>
- Acocella, V. (2014). Structural control on magmatism along divergent and convergent plate boundaries: Overview, model, problems. *Earth-Science Reviews*, 136, 226–288. <https://doi.org/10.1016/j.earscirev.2014.05.006>
- Acocella, V., & Funiciello, F. (2010). Kinematic setting and structural control of arc volcanism. *Earth and Planetary Science Letters*, 289(1–2), 43–53. <https://doi.org/10.1016/j.epsl.2009.10.027>
- Allan, A. S. R., Wilson, C. J. N., Millet, M. A., & Wysoczanski, R. J. (2012). The invisible hand: Tectonic triggering and modulation of a rhyolitic supereruption. *Geology*, 40(6), 563–566. <https://doi.org/10.1130/G32969.1>
- Allan, A. S. R., Barker, S. J., Millet, M. A., Morgan, D. J., Rooyackers, S. M., Schipper, C. I., & Wilson, C. J. N. (2017). A cascade of magmatic events during the assembly and eruption of a super-sized magma body. *Contributions to Mineralogy and Petrology*, 172(7), 1–34. <https://doi.org/10.1007/s00410-017-1367-8>
- Alonso-Henar, J., Alvarez-Gomez, J. A., & Martinez-Diaz, J. J. (2017). Neogene-quaternary evolution from transpressional to transtensional tectonics in Northern Central America controlled by Cocos Caribbean subduction coupling change. *Journal of Iberian Geology*, 43, 519–538. <https://doi.org/10.1007/s41513-017-0034-2>
- Alvarado, G. E., Dengo, C., Martens, U., Bundschuh, J., Aguilar, T., & Bonis, S. (2007). Stratigraphy and geologic history. In J. Bundschuh & G. E. Alvarado (Eds.), *Central America: geology, resources and hazards* (pp. 345–394). Taylor & Francis, London. <https://doi.org/10.1201/9780203947043>
- Álvarez-Gómez, J. A., Meijer, P. T., Martínez-Díaz, J. J., & Capote, R. (2008). Constraints from finite element modeling on the active tectonics of northern Central America and the Middle America Trench. *Tectonics*, 27, TC1008. <https://doi.org/10.1029/2007TC002162>
- Álvarez-Gómez, J. A., Staller Vázquez, A., Martínez-Díaz, J. J., Canora, C., Alonso-Henar, J., Insua-Arévalo, J. M., & Béjar-Pizarro, M. (2019). Push-pull driving of the Central America Forearc in the context of the Cocos-Caribbean-North America triple junction. *Scientific Reports*, 9(1), 11164. <https://doi.org/10.1038/s41598-019-47617-3>
- Andersen, N. L., Singer, B. S., Jicha, B. R., Beard, B. L., Johnson, C. M., & Licciardi, J. M. (2017). Pleistocene to Holocene growth of a large upper crustal rhyolitic magma reservoir beneath the active Laguna del Maule Volcanic Field, Central Chile. *Journal of Petrology*, 58(1), 85–114. <https://doi.org/10.1093/petrology/egx006>
- Andersen, N. L., Singer, B. S., & Coble, M. A. (2019). Repeated Rhyolite Eruption From Heterogeneous Hot Zones Embedded Within a Cool, Shallow Magma Reservoir. *Journal of Geophysical Research: Solid Earth*, 124(3), 2582–2600. <https://doi.org/10.1029/2018JB016418>
- Andrews, G. D. M., Busby, C. J., Brown, S. R., Fisher, C. M., Davila-harris, P., Strickland, A., Vervoort, J. D., Pettus, H. D., Mcdowell, F. W., Murray, B. P., & Brown, S. (2022). Petrogenesis of voluminous silicic magmas in the Sierra Madre Occidental large igneous province, Mexican Cordillera: Insights from zircon and Hf-O isotopes. *Geosphere* 18(3), 946–984. <https://doi.org/10.1130/GES02430.1>
- Annen, C. (2009). From plutons to magma chambers: Thermal constraints on the accumulation of eruptible silicic magma in the upper crust. *Earth and Planetary Science Letters*, 284(3–4), 409–416. <https://doi.org/10.1016/j.epsl.2009.05.006>
- Annen, C. (2011). Implications of incremental emplacement of magma bodies for magma differentiation, thermal aureole dimensions and plutonism-volcanism relationships. *Tectonophysics*, 500(1–4), 3–10. <https://doi.org/10.1016/j.tecto.2009.04.010>

- Annen, C. (2017). Factors affecting the thickness of thermal aureoles. *Frontiers in Earth Science*, 5(October), 1–13. <https://doi.org/10.3389/feart.2017.00082>
- Annen, C., & Sparks, R. S. J. (2002). Effects of repetitive emplacement of basaltic intrusions on thermal evolution and melt generation in the crust. *Earth and Planetary Science Letters*, 203(3–4), 937–955. [https://doi.org/10.1016/S0012-821X\(02\)00929-9](https://doi.org/10.1016/S0012-821X(02)00929-9)
- Annen, C., Blundy, J. D., & Sparks, R. S. J. (2006). The genesis of intermediate and silicic magmas in deep crustal hot zones. *Journal of Petrology*, 47(3), 505–539. <https://doi.org/10.1093/petrology/egi084>
- Annen, C., Blundy, J. D., Leuthold, J., & Sparks, R. S. J. (2015). Construction and evolution of igneous bodies: Towards an integrated perspective of crustal magmatism. *Lithos*, 230, 206–221. <https://doi.org/10.1016/j.lithos.2015.05.008>
- Annen, C., Pinel, V., & Burgisser, A. (2023). Re-evaluation of the role of volatiles in the rupture of magma chambers and the triggering of crystal-rich eruptions. *Journal of Volcanology and Geothermal Research*, 435, 107755. <https://doi.org/10.1016/j.jvolgeores.2023.107755>
- Armienti, P., Pareschi, M. T., Innocenti, F., & Pompilio, M. (1994). Effects of magma storage and ascent on the kinetics of crystal growth - The case of the 1991-93 Mt. Etna eruption. *Contributions to Mineralogy and Petrology*, 115(4), 402–414. <https://doi.org/10.1007/BF00320974>
- Armienti, P., Perinelli, C., & Putirka, K. D. (2013). A new model to estimate deep-level magma ascent rates, with applications to Mt. Etna (Sicily, Italy). *Journal of Petrology*, 54(4), 795–813. <https://doi.org/10.1093/petrology/egs085>
- Arzilli, F., Morgavi, D., Petrelli, M., Polacci, M., Burton, M., Di Genova, D., Spina, L., La Spina, G., Hartley, M. E., Romero, J. E., Fellowes, J., Diaz-Alvarado, J., & Perugini, D. (2019). The unexpected explosive sub-Plinian eruption of Calbuco volcano (22–23 April 2015; southern Chile): Triggering mechanism implications. *Journal of Volcanology and Geothermal Research*, 378, 35–50. <https://doi.org/10.1016/j.jvolgeores.2019.04.006>
- Atherton, M. P., & Petford, N. (1993). Generation of sodium-rich magmas from newly underplated basaltic crust. *Nature*, 362(6416), 1991–1993. <https://doi.org/10.1038/362144a0>
- Bach, P., Smith, I. E. M., & Malpas, J. G. (2012). The origin of garnets in andesitic rocks from the Northland arc, New Zealand, and their implication for sub-arc processes. *Journal of Petrology*, 53(6), 1169–1195. <https://doi.org/10.1093/petrology/egs012>
- Bachmann, O., & Bergantz, G. W. (2004). On the origin of crystal-poor rhyolites: Extracted from batholithic crystal mushes. *Journal of Petrology*, 45(8), 1565–1582. <https://doi.org/10.1093/petrology/egh019>
- Bachmann, O., & Bergantz, G. W. (2006). Gas percolation in upper-crustal silicic crystal mushes as a mechanism for upward heat advection and rejuvenation of near-solidus magma bodies. *Journal of Volcanology and Geothermal Research*, 149(1–2), 85–102. <https://doi.org/10.1016/j.jvolgeores.2005.06.002>
- Bachmann, O., & Bergantz, G. W. (2008). Rhyolites and their source mushes across tectonic settings. *Journal of Petrology*, 49(12), 2277–2285. <https://doi.org/10.1093/petrology/egn068>
- Bachmann, O., & Huber, C. (2016). Silicic magma reservoirs in the Earth's crust. *American Mineralogist*, 101, 2377–2404. <https://doi.org/10.2138/am-2016-5675>
- Bachmann, O., Miller, C. F., & de Silva, S. L. (2007). The volcanic-plutonic connection as a stage for understanding crustal magmatism. *Journal of Volcanology and Geothermal Research*, 167(1–4), 1–23. <https://doi.org/10.1016/j.jvolgeores.2007.08.002>
- Bacon, C. R. (1986). Magmatic inclusions in silicic and intermediate volcanic rocks. *Journal of Geophysical Research*, 91(B6), 6091–6112. <https://doi.org/10.1029/jb091ib06p06091>
- Bacon, C. R., & Druitt, T. H. (1988). Compositional evolution of the zoned calc-alkaline magma chamber of Mount Mazama, Crater Lake, Oregon. *Contributions to Mineralogy and Petrology*, 98(2), 224–256. <https://doi.org/10.1007/BF00402114>

- Bacon, C. R., & Lanphere, M. A. (2006). Eruptive history and geochronology of Mount Mazama and the Crater Lake region, Oregon. *Bulletin of the Geological Society of America*, 118(11–12), 1331–1359. <https://doi.org/10.1130/B25906.1>
- Basset, T. S. (1996). Histoire éruptive et évaluation des aléas du volcan Acateño (Guatemala). PhD thesis, University of Geneva. <https://doi.org/10.13097/archive-ouverte/unige>
- Baudry, A., Singer, B. S., Jicha, B., Jilly-Rehak, C. E., Vazquez, J. A., & Keller, C. B. (2024). A Bayesian age from dispersed plagioclase and zircon dates in the Los Chocoyos ash, Central America. *Earth and Planetary Science Letters*, 643(July), 118826. <https://doi.org/10.1016/j.epsl.2024.118826>
- Beard, J. S., Ragland, P. C., & Rushmer, T. (2004). Hydration crystallization reactions between anhydrous minerals and hydrous melt to yield amphibole and biotite in igneous rocks: Description and implications. *Journal of Geology*, 112(5), 617–621. <https://doi.org/10.1086/422670>
- Beard, J. S., Ragland, P. C., & Crawford, M. L. (2005a). Reactive bulk assimilation: A model for crust-mantle mixing in silicic magmas. *Geology*, 33(8), 681–684. <https://doi.org/10.1130/G21470.1>
- Beard, J. S., Ragland, P. C., & Crawford, M. L. (2005b). Using incongruent equilibrium hydration reactions to model latter-stage crystallization in plutons: Examples from the Bell Island Tonalite, Alaska. *Journal of Geology*, 113(5), 589–599. <https://doi.org/10.1086/431911>
- Bégué, F., Deering, C. D., Gravley, D. M., Kennedy, B. M., Chambefort, I., Gualda, G. A. R., & Bachmann, O. (2014). Extraction, storage and eruption of multiple isolated magma batches in the paired Mamaku and Ohakuri eruption, Taupo volcanic zone, New Zealand. *Journal of Petrology*, 55(8), 1653–1684. <https://doi.org/10.1093/petrology/egu038>
- Berlo, K., Stix, J., Roggensack, K., & Ghaleb, B. (2012). A tale of two magmas, Fuego, Guatemala. *Bulletin of Volcanology*, 74(2), 377–390. <https://doi.org/10.1007/s00445-011-0530-8>
- Best, M. G., Christiansen, E. H., de Silva, S., & Lipman, P. W. (2016). Slab-rollback ignimbrite flareups in the southern Great Basin and other Cenozoic American arcs: A distinct style of arc volcanism. *Geosphere*, 12(4), 1097–1135. <https://doi.org/10.1130/GES01285.1>
- Bindeman, I. (2008). Oxygen isotopes in mantle and crustal magmas as revealed by single crystal analysis. *Reviews in Mineralogy and Geochemistry*, 69(1), 445–478. <https://doi.org/10.2138/rmg.2008.69.12>
- Bindeman, I. N., & Simakin, A. G. (2014). Rhyolites — Hard to produce , but easy to recycle and sequester: Integrating microgeochemical observations and numerical models. *Geosphere*, 10(5), 930–957. <https://doi.org/10.1130/GES00969.1>
- Bindeman, I. N., Leonov, V. L., Colón, D. P., Rogozin, A. N., Shipley, N., Jicha, B., Loewen, M. W., & Gerya, T. V. (2019). Isotopic and petrologic investigation, and a thermomechanical model of genesis of large-volume rhyolites in arc environments: Karymshina volcanic complex, Kamchatka, Russia. *Frontiers in Earth Science*, 6(238). <https://doi.org/10.3389/feart.2018.00238>
- Blake, S. (1984). Volatile oversteaturation during the evolution of silicic magma chambers as an eruption trigger. *Journal of Geophysical Research*, 89(B10), 8237–8244. <https://doi.org/10.1029/JB089iB10p08237>
- Blundy, J. D., & Wood, B. J. (1991). Crystal-chemical controls on the partitioning of Sr and Ba between plagioclase feldspar, silicate melts, and hydrothermal solutions. *Geochimica et Cosmochimica Acta*, 55(1), 193–209. [https://doi.org/10.1016/0016-7037\(91\)90411-W](https://doi.org/10.1016/0016-7037(91)90411-W)
- Blundy, J. D., & Annen, C. (2016). Crustal Magmatic Systems from the Perspective of Heat Transfer. *Elements*, 12(2), 115–120. <https://doi.org/10.2113/gselements.12.2.115>
- Blundy, J., Cashman, K. V., & Berlo, K. (2008). Evolving magma storage conditions beneath Mount St. Helens inferred from chemical variations in melt inclusions from the 1980-1986 and current (2004-2006) eruptions. *US Geological Survey Professional Paper*, 1750, 755–790. <https://doi.org/10.3133/pp175033>

- Bornhorst, T. J., W. I. Rose, & C. A. Chesner. (1982). Quaternary Barahona caldera complex. *Eos Transactions, AGU* 63, 1155.
- Boro, J. R., Wolff, J. A., & Neill, O. K. (2020). Anatomy of a Recharge Magma: Dacite Pumice Blocks in the Tshirege Member of the Bandelier Tuff, Valles Caldera, New Mexico. *Contributions to Mineralogy and Petrology*, 175, 96. <https://doi.org/10.1130/abs/2016am-287073>
- Bouvet de Maisonneuve, C., Forni, F., & Bachmann, O. (2021). Magma reservoir evolution during the build up to and recovery from caldera-forming eruptions – A generalizable model? *Earth-Science Reviews*, 218, 103684. <https://doi.org/10.1016/j.earscirev.2021.103684>
- Bowen, N. L. (1928). The evolution of igneous rocks. Princeton University Press, Princetown, New Jersey. <https://doi.org/10.1038/124474a0>
- Brandmeier, M. (2014). A remote sensing and geospatial statistical approach to understanding distribution and evolution of ignimbrites in the Central Andes with a focus on Southern Peru. PhD thesis, Georg-August-Universität, Göttingen. <http://dx.doi.org/10.53846/goediss-4426>
- Breiter, K. (2016). Monazite and zircon as major carriers of Th, U, and Y in peraluminous granites: examples from the Bohemian Massif. *Mineralogy and Petrology*, 110(6), 767–785. <https://doi.org/10.1007/s00710-016-0448-0>
- Brocard, G., & Moran-Ical, S. D. (2014). Phreatic clastic dikes and other degassing structures in Los Chocoyos pumice. *Revista Guatemalteca de Ciencias de La Tierra*, 1, 55–65.
- Brophy, J. G. (1991). Composition gaps, critical crystallinity, and fractional crystallization in orogenic (calc-alkaline) magmatic systems. *Contributions to Mineralogy and Petrology*, 109(2), 173–182. <https://doi.org/10.1007/BF00306477>
- Brophy, J. G., Whittington, C. S., & Park, Y. (1999). Sector-zoned augite megacrysts in Aleutian high alumina basalts: Implications for the conditions of basalt crystallization and the generation of calc-alkaline series magmas. *Contributions to Mineralogy and Petrology*, 135, 277–290. <https://doi.org/10.1007/s004100050512>
- Brown, S. J. A., & Fletcher, I. R. (1999). SHRIMP U-Pb dating of the preeruption growth history of zircons from the 340 ka Whakamaru Ignimbrite, New Zealand: Evidence for >250 k.y. magma residence times. *Geology*, 27(11), 1035–1038. [https://doi.org/10.1130/0091-7613\(1999\)027<1035:SUPDOT>2.3.CO;2](https://doi.org/10.1130/0091-7613(1999)027<1035:SUPDOT>2.3.CO;2)
- Brown, S. K., Crosweller, H. S., Sparks, R. S. J., Cottrell, E., Deligne, N. I., Guerrero, N. O., Hobbs, L., Kiyosugi, K., Loughlin, S. C., Siebert, L., & Takarada, S. (2014). Characterisation of the Quaternary eruption record: Analysis of the Large Magnitude Explosive Volcanic Eruptions (LaMEVE) database. *Journal of Applied Volcanology*, 3(1), 1–22. <https://doi.org/10.1186/2191-5040-3-5>
- Browne, B. L., & Gardner, J. E. (2006). The influence of magma ascent path on the texture, mineralogy, and formation of hornblende reaction rims. *Earth and Planetary Science Letters*, 246(3–4), 161–176. <https://doi.org/10.1016/j.epsl.2006.05.006>
- Brueckner, H. K., Avé Lallemant, H. G., Sisson, V. B., Harlow, G. E., Hemming, S. R., Martens, U., Tsujimori, T., & Sorensen, S. S. (2009). Metamorphic reworking of a high pressure-low temperature mélange along the Motagua fault, Guatemala: A record of Neocomian and Maastrichtian transpressional tectonics. *Earth and Planetary Science Letters*, 284(1–2), 228–235. <https://doi.org/10.1016/j.epsl.2009.04.032>
- Bryan, S. E. (2007). Silicic large igneous provinces. *Episodes*, 30(1), 20–31. <https://doi.org/10.18814/epiiugs/2007/v30i1/004>
- Bryan, S. E., & Ferrari, L. (2013). Large igneous provinces and silicic large igneous provinces: Progress in our understanding over the last 25 years. *Bulletin of the Geological Society of America*, 125(7–8), 1053–1078. <https://doi.org/10.1130/B30820.1>
- Bryan, S. E., Ferrari, L., Reiners, P. W., Allen, C. M., Petrone, C. M., Ramos-rosique, A., & Campbell, I. H. (2008). New insights into crustal contributions to large-volume rhyolite generation in the mid-Tertiary Sierra Madre Occidental province, Mexico, revealed by U-Pb

- geochronology. *Journal of Petrology*, 49(1), 47–77.
<https://doi.org/10.1093/petrology/egm070>
- Buchs, D. M., Arculus, R. J., Baumgartner, P. O., Baumgartner-Mora, C., & Ulianov, A. (2010). Late Cretaceous arc development on the SW margin of the Caribbean Plate: Insights from the Gofito, Costa Rica, and Azuero, Panama, complexes. *Geochemistry, Geophysics, Geosystems*, 11(7), Q07S24. <https://doi.org/10.1029/2009GC002901>
- Buckley, V. J. E., Sparks, R. S. J., & Wood, B. J. (2006). Hornblende dehydration reactions during magma ascent at Soufrière Hills Volcano, Montserrat. *Contributions to Mineralogy and Petrology*, 151(2), 121–140. <https://doi.org/10.1007/s00410-005-0060-5>
- Burkart, B., & Self, S. (1985). Extension and rotation of crustal blocks in northern Central America and effect on the volcanic arc. *Geology*, 13(1), 22–26. [https://doi.org/10.1130/0091-7613\(1985\)13<22:EAROCB>2.0.CO;2](https://doi.org/10.1130/0091-7613(1985)13<22:EAROCB>2.0.CO;2)
- Burton-Johnson, A., Macpherson, C. G., Ottley, C. J., Nowell, G. M., & Boyce, A. J. (2019). Generation of the Mt Kinabalu granite by crustal contamination of intraplate magma modelled by Equilibrated Major Element Assimilation with Fractional Crystallization (EME-AFC). *Journal of Petrology*, 60(7), 1461–1487. <https://doi.org/10.1093/petrology/egz036>
- Cabaniss, H. E., Gregg, P. M., & Grosfils, E. B. (2018). The role of tectonic stress in triggering large silicic caldera eruptions. *Geophysical Research Letters*, 45(9), 3889–3895.
<https://doi.org/10.1029/2018GL077393>
- Caricchi, L., Townsend, M., Rivalta, E., & Namiki, A. (2021). The build-up and triggers of volcanic eruptions. *Nature Reviews Earth and Environment*, 2(7), 458–476.
<https://doi.org/10.1038/s43017-021-00174-8>
- Carr, M. J. (1974). Tectonics of the Pacific margin of Northern Central America. PhD thesis, Dartmouth College, Hanover, New Hampshire.
- Carr, M. J. (1984). Symmetrical and Segmented variation of physical and geochemical characteristics of the Central American volcanic front. *Journal of Volcanology and Geothermal Research*, 20(3-4), 231–252. [https://doi.org/10.1016/0377-0273\(84\)90041-6](https://doi.org/10.1016/0377-0273(84)90041-6)
- Carr, M. J., Feigenson, M. D., & Bennett, E. A. (1990). Incompatible element and isotopic evidence for tectonic control of source mixing and melt extraction along the Central American arc. *Contributions to Mineralogy and Petrology*, 105(4), 369–380.
<https://doi.org/10.1007/BF00286825>
- Carr, M. J., Feigenson, M. D., Patino, L. C., & Walker, J. A. (2003). Volcanism and geochemistry in Central America: Progress and Problems. *Geophysical Monograph-American Geophysical Union*, 138, 153–174. <https://doi.org/10.1029/138GM09>
- Carr, M., Patiño, L., & Feigenson, M. (2007). Petrology and geochemistry of lavas. In J. Bundschuh & G. E. Alvarado (Eds.), *Central America: geology, resources and hazards* (pp. 345–394). Taylor & Francis, London. <https://doi.org/10.1201/9780203947043>
- Carr, M. J., Feigenson, M. D., Bolge, L. L., Walker, J. A., & Gazel, E. (2014). RU _ CAGeochem , a database and sample repository for Central American volcanic rocks at Rutgers University RU _ CAGeochem , a database and sample repository for Central American volcanic rocks at Rutgers University. *Geoscience Data Journal*, 1(1). <https://doi.org/10.1002/gdj3.10>
- Case, J., Holcombe, T. L., & Martin, R. G. (1984). Map of geologic provinces in the Caribbean region. *Geological Society of America Memoir*, 162. <https://doi.org/10.1130/MEM162-p1>
- Cashman, K. V., & Giordano, G. (2014). Calderas and magma reservoirs. *Journal of Volcanology and Geothermal Research*, 288, 28–45. <https://doi.org/10.1016/j.jvolgeores.2014.09.007>
- Cashman, K. V., Sparks, R. S. J., & Blundy, J. D. (2017). Vertically extensive and unstable magmatic systems: A unified view of igneous processes. *Science*, 355(6331), eaag3055.
<https://doi.org/10.1126/science.aag3055>
- Cassidy, M., & Mani, L. (2022). Huge volcanic eruptions: time to prepare. *Nature*, 608(7923), 469–471. <https://doi.org/10.1038/d41586-022-02177-x>

- Cassidy, M., Ebmeier, S. K., Helo, C., Watt, S. F. L., Caudron, C., Odell, A., Spaans, K., Kristianto, P., Triastuty, H., Gunawan, H., & Castro, J. M. (2019). Explosive eruptions with little warning: experimental petrology and volcano monitoring observations from the 2014 eruption of Kelud, Indonesia. *Geochemistry, Geophysics, Geosystems*, 20(8), 4218–4247. <https://doi.org/10.1029/2018GC008161>
- Cawthorn, R. G., & O'Hara, M. J. (1976). Amphibole fractionation in calc-alkaline magma genesis. *American Journal of Science*, 276(3), 309–329. <https://doi.org/10.2475/ajs.276.3.309>
- Cecil, M. R., Rotberg, G. L., Ducea, M. N., Saleeby, J. B., & Gehrels, G. E. (2012). Magmatic growth and batholithic root development in the northern Sierra Nevada, California. *Geosphere*, 8(3), 592–606. <https://doi.org/10.1130/GES00729.1>
- Chan, L. H., Leeman, W. P., & You, C. F. (1999). Lithium isotopic composition of Central American volcanic arc lavas: Implications for modification of subarc mantle by slab-derived fluids. *Chemical Geology*, 160, 255–280. [https://doi.org/10.1016/S0009-2541\(01\)00298-4](https://doi.org/10.1016/S0009-2541(01)00298-4)
- Chapman, J. B., Shields, J. E., Ducea, M. N., Paterson, S. R., Attia, S., & Ardill, K. E. (2021). The causes of continental arc flare ups and drivers of episodic magmatic activity in Cordilleran orogenic systems. *Lithos*, 398, 106307. <https://doi.org/10.1016/j.lithos.2021.106307>
- Charlier, B. L. A., Wilson, C. J. N., Lowenstern, J. B., Blake, S., van Calsteren, P. W., & Davidson, J. P. (2005). Magma generation at a large, hyperactive silicic volcano (Taupo, New Zealand) revealed by U-Th and U-Pb systematics in zircons. *Journal of Petrology*, 46(1), 3–32. <https://doi.org/10.1093/petrology/egh060>
- Chaussard, E., & Amelung, F. (2014). Regional controls on magma ascent and storage in volcanic arcs. *Geochemistry, Geophysics, Geosystems*, 15(4), 1407–1418. <https://doi.org/10.1002/2013GC005216.Received>
- Chen, J. H., & Moore, J. G. (1982). Uranium-Lead isotopic ages from the Sierra Nevada batholith, California. *Journal of Geophysical Research*, 87(B6), 4761–4784. <https://doi.org/10.1029/JB087iB06p04761>
- Chesner, C. A., & Rose, W. I. (1984). Geochemistry and evolution of the Fuego volcanic complex, Guatemala. *Journal of Volcanology and Geothermal Research*, 21, 25–44. [https://doi.org/10.1016/0377-0273\(84\)90014-3](https://doi.org/10.1016/0377-0273(84)90014-3)
- Chiari, M., Dumitrica, P., Marroni, M., Pandolfi, L., & Principi, G. (2006). Radiolarian biostratigraphic evidence for a late Jurassic age of the El Tambor group ophiolites (Guatemala). *Ofioliti*, 31(2), 141–150. <https://doi.org/10.4454/ofioliti.v31i2.336>
- Cisneros de León, A., Schindlbeck-Belo, J. C., Kutterolf, S., Danišik, M., Schmitt, A. K., Freundt, A., Pérez, W., Harvey, J. C., Wang, K. L., & Lee, H. Y. (2021a). A history of violence: magma incubation, timing and tephra distribution of the Los Chocoyos supereruption (Atitlán Caldera, Guatemala). *Journal of Quaternary Science*, 36(2), 169–179. <https://doi.org/10.1002/jqs.3265>
- Cisneros de León, A., Schmitt, A. K., Kutterolf, S., Schindlbeck-Belo, J. C., Hernández, W., Sims, K. W. W., Garrison, J., Kant, L. B., Weber, B., Wang, K. L., Lee, H. Y., & Trumbull, R. B. (2021b). Zircon and Melt Extraction From a Long-Lived and Vertically Extensive Magma System Underneath Ilopango Caldera (El Salvador). *Geochemistry, Geophysics, Geosystems*, 22(5), 1–22. <https://doi.org/10.1029/2020GC009507>
- Cisneros de León, A., Mittal, T., Silva, S. L. de, Self, S., Schmitt, A. K., & Kutterolf, S. (2022). On synchronous supereruptions. *Frontier in Earth Science*, 10. <https://doi.org/10.3389/feart.2022.827252>
- Cisneros de León, A., M. Danišik, Julie C. Schindlbeck-Belo, Steffen Kutterolf, A. K. Schmitt, Armin Freundt, José Kling, K-L. Wang, and H-Y. Lee. (2023). Timing and recurrence intervals for voluminous silicic eruptions from Amatitlán caldera (Guatemala). *Quaternary Science Reviews* 301. <https://doi.org/10.1016/j.quascirev.2022.107935>

- Clift, P. D., Pecher, I., Kukowski, N., & Hampel, A. (2003). Tectonic erosion of the Peruvian forearc, Lima Basin, by subduction and Nazca Ridge collision. *Tectonics*, 22(3). <https://doi.org/10.1029/2002TC001386>
- Coney, P. J., Smith, R. B., & Eaton, G. P. (1978). Mesozoic-Cenozoic cordilleran plate tectonics. *Cenozoic tectonics and regional geophysics of the western Cordillera: Geological Society of America Memoir*, 152, 33-50. <https://doi.org/10.1130/MEM152-p33>
- Conte, A. M. (1993). High temperature amphibole breakdown in calcalkaline subvolcanic rocks from Sarroch District (Sardinia, Italy): implication for mixing processes. *Neues Jahrbuch Für Mineralogie Monatshefte* 1993, 3. [WOS:A1993KV45400004](https://doi.org/10.1130/MEM152-p33)
- Conway, F. M., Vallance, J. W., Rose, W. I., Johns, G. W., & Paniagua, S. (1992). Cerro Quemado, Guatemala: the volcanic history and hazards of an exogenous volcanic dome complex. *Journal of Volcanology and Geothermal Research*, 52(4). [https://doi.org/10.1016/0377-0273\(92\)90051-E](https://doi.org/10.1016/0377-0273(92)90051-E)
- Coombs, M. L., & Gardner, J. E. (2004). Reaction rim growth on olivine in silicic melts: Implications for magma mixing. *American Mineralogist*, 89(5-6), 748-758. <https://doi.org/10.2138/am-2004-5-608>
- Cooper, G. F., Davidson, J. P., & Blundy, J. D. (2016). Plutonic xenoliths from Martinique, Lesser Antilles: evidence for open system processes and reactive melt flow in island arc crust. *Contributions to Mineralogy and Petrology*, 171(10), 1-21. <https://doi.org/10.1007/s00410-016-1299-8>
- Cooper, G. F., Blundy, J. D., Macpherson, C. G., Humphreys, M. C. S., & Davidson, J. P. (2019). Evidence from plutonic xenoliths for magma differentiation, mixing and storage in a volatile-rich crystal mush beneath St. Eustatius, Lesser Antilles. *Contributions to Mineralogy and Petrology*, 174(5), 1-24. <https://doi.org/10.1007/s00410-019-1576-4>
- Cooper, K. M., & Reid, M. R. (2003). Re-examination of crystal ages in recent Mount St. Helens lavas: Implications for magma reservoir processes. *Earth and Planetary Science Letters*, 213(1-2), 149-167. [https://doi.org/10.1016/S0012-821X\(03\)00262-0](https://doi.org/10.1016/S0012-821X(03)00262-0)
- Cooper, K. M., & Kent, A. J. R. (2014). Rapid remobilization of magmatic crystals kept in cold storage. *Nature*, 506(7489), 480-483. <https://doi.org/10.1038/nature12991>
- Costa, F. (2008). Residence times of silicic magmas associated with calderas. *Developments in Volcanology*, 10, 1-55. [https://doi.org/10.1016/S1871-644X\(07\)00001-0](https://doi.org/10.1016/S1871-644X(07)00001-0)
- Costa, F., Shea, T., & Ubide, T. (2020). Diffusion chronometry and the timescales of magmatic processes. *Nature Reviews Earth and Environment*, 1(4), 201-214. <https://doi.org/10.1038/s43017-020-0038-x>
- Crosweller, H. S., Arora, B., Brown, S. K., Cottrell, E., Deligne, N. I., Guerrero, N. O., Hobbs, L., Kiyosugi, K., Loughlin, S. C., Lowndes, J., Nayembil, M., Siebert, L., Sparks, R. S. J., Takarada, S., & Venzke, E. (2012). Global database on large magnitude explosive volcanic eruptions (LaMEVE). *Journal of Applied Volcanology*, 1(1), 1-13. <https://doi.org/10.1186/2191-5040-1-4>
- Danišík, M., Schmitt, A. K., Stockli, D. F., Lovera, O. M., Dunkl, I., & Evans, N. J. (2017). Application of combined U-Th-disequilibrium/U-Pb and (U-Th)/He zircon dating to tephrochronology. *Quaternary Geochronology*, 40, 23-32. <https://doi.org/10.1016/j.quageo.2016.07.005>
- Davidson, J., Turner, S., Handley, H., Macpherson, C., & Dosseto, A. (2007). Amphibole "sponge" in arc crust? *Geology*, 35(9), 787-790. <https://doi.org/10.1130/G23637A.1>
- de Arellano, C. R., Putlitz, B., Müntener, O., & Ovtcharova, M. (2012). High precision U/Pb zircon dating of the Chaltén Plutonic Complex (Cerro Fitz Roy, Patagonia) and its relationship to arc migration in the southernmost Andes. *Tectonics*, 31(4). <https://doi.org/10.1029/2011TC003048>
- de Bremond d'Ars, J., Jaupart, C., & Sparks, R. S. J. (1995). Distribution of volcanoes in active margins. *Journal of Geophysical Research*, 100(B10), 20421-20432. <https://doi.org/10.1029/95jb02153>

- de Silva, S. (2008). Arc magmatism, calderas, and supervolcanoes. *Geology*, 36(8), 671–672. <https://doi.org/10.1130/focus082008.1>
- de Silva, S. L., & Gosnold, W. D. (2007). Episodic construction of batholiths: Insights from the spatiotemporal development of an ignimbrite flare-up. *Journal of Volcanology and Geothermal Research*, 167(1–4), 320–335. <https://doi.org/10.1016/j.jvolgeores.2007.07.015>
- de Silva, S. L., & Gregg, P. M. (2014). Thermomechanical feedbacks in magmatic systems: Implications for growth, longevity, and evolution of large caldera-forming magma reservoirs and their supereruptions. *Journal of Volcanology and Geothermal Research*, 282, 77–91. <https://doi.org/10.1016/j.jvolgeores.2014.06.001>
- de Silva, S., Zandt, G., Trumbull, R., Viramonte, J. G., Salas, G., & Jiménez, N. (2006). Large ignimbrite eruptions and volcano-tectonic depressions in the Central Andes: A thermomechanical perspective. *Geological Society of London Special Publication*, 269, 47–63. <https://doi.org/10.1144/GSL.SP.2006.269.01.04#>
- de Silva, S. L., Riggs, N. R., & Barth, A. P. (2015). Quickening the pulse: Fractal tempos in continental arc magmatism. *Elements*, 11(2), 113–118. <https://doi.org/10.2113/gselements.11.2.113>
- Deer, W. A., Howie, R. A., & Zussman, J. (1992). *An introduction to the Rock-forming minerals* (3rd edition). Mineralogical Society of Great Britain and Northern Ireland. 978-0-90305-627-4
- Deering, C. D., & Bachmann, O. (2010). Trace element indicators of crystal accumulation in silicic igneous rocks. *Earth and Planetary Science Letters*, 297(1–2), 324–331. <https://doi.org/10.1016/j.epsl.2010.06.034>
- Deering, C. D., Cole, J. W., & Vogel, T. A. (2008). A rhyolite compositional continuum governed by lower crustal source conditions in the Taupo Volcanic Zone, New Zealand. *Journal of Petrology*, 49(12), 2245–2276. <https://doi.org/10.1093/petrology/egn067>
- Deering, C. D., Bachmann, O., & Vogel, T. A. (2011a). The Ammonia Tanks Tuff: Erupting a melt-rich rhyolite cap and its remobilized crystal cumulate. *Earth and Planetary Science Letters*, 310(3–4), 518–525. <https://doi.org/10.1016/j.epsl.2011.08.032>
- Deering, C. D., Bachmann, O., Dufek, J., & Gravley, D. M. (2011b). Rift-related transition from andesite to rhyolite volcanism in the Taupo volcanic zone (New Zealand) controlled by crystal-melt dynamics in mush zones with variable mineral assemblages. *Journal of Petrology*, 52(11), 2243–2263. <https://doi.org/10.1093/petrology/egr046>
- Deering, C. D., Keller, B., Schoene, B., Bachmann, O., Beane, R., & Ovtcharova, M. (2016). Zircon record of the plutonic-volcanic connection and protracted rhyolite melt evolution. *Geology*, 44(4), 267–270. <https://doi.org/10.1130/G37539.1>
- DeMets, C. (2001). A new estimate for present-day Cocos-Caribbean plate motion: Implications for slip along the Central American volcanic arc. *Geophysical Research Letters*, 28(21), 4043–4046. <https://doi.org/10.1029/2001GL013518>
- Dengo, G., Bohnenberger, O., & Bonis, S. (1970). Tectonics and volcanism along the Pacific Marginal Zone of Central America. *Geologische Rundschau*, 59(3), 1215–1232. <https://doi.org/10.1007/BF02042290>
- Denton, C. A., Johnson, B. C., Wakita, S., Freed, A. M., Melosh, H. J., & Stern, S. A. (2021). Pluto's antipodal terrains imply a thick subsurface ocean and hydrated core. *Geophysical Research Letters*, 48(2), e2020GL091596. <https://doi.org/10.1029/2020GL091596>
- DePaolo, D. J. (1981). Trace element and isotopic effects of combined wallrock assimilation and fractional crystallization. *Earth and Planetary Science Letters*, 53(2), 189–202. [https://doi.org/10.1016/0012-821X\(81\)90153-9](https://doi.org/10.1016/0012-821X(81)90153-9)
- DePaolo, D. J., & Wasserburg, G. J. (1979). Petrogenetic mixing models and Nd-Sr isotopic patterns. *Geochimica et Cosmochimica Acta*, 43(4), 615–627. [https://doi.org/10.1016/0016-7037\(79\)90169-8](https://doi.org/10.1016/0016-7037(79)90169-8)

- Di Martino, C., Forni, F., Frezzotti, M. L., Palmeri, R., Webster, J. D., Ayuso, R. A., Lucchi, F., & Tranne, C. A. (2011). Formation of cordierite-bearing lavas during anatexis in the lower crust beneath Lipari Island (Aeolian arc, Italy). *Contributions to Mineralogy and Petrology*, 162(5), 1011–1030. <https://doi.org/10.1007/s00410-011-0637-0>
- Dickinson, W. R. (1975). Potash-Depth (K-h) relations in continental margin and intra-oceanic magmatic arcs. *Geology*, 3(2), 53–56. [https://doi.org/10.1130/0091-7613\(1975\)3<53:PKRICM>2.0.CO;2](https://doi.org/10.1130/0091-7613(1975)3<53:PKRICM>2.0.CO;2)
- DIGIS Team. (2021). GEOROC Compilation: Basaltic andesites, andesites, dacites, rhyolites. GEOROC. Goettingen Research Online / Data, V1. <https://doi.org/https://doi.org/10.25625/2JETOA>
- Dollfus, A., & Montserrat, E. (1868). Geological voyage in the Republics of Guatemala and El Salvador. *Scientific mission to Mexico and in Central America*.
- Donnelly, Thomas, W., Horne, G. S., Finch, R. C., & Lopez-Ramos, E. (1990). Northern Central America: the Maya and Chortis blocks. In G. Dengo & J. E. Case (Eds.), *The Geology of North America, H*, 37–76. Geological Society of America, Boulder, Colorado. <https://doi.org/10.1130/DNAG-GNA-H.37>
- Ducea, M. N., Saleeby, J. B., & Bergantz, G. (2015). The architecture, chemistry, and evolution of continental magmatic arcs. *Annual Review of Earth and Planetary Sciences*, 43, 299–331. <https://doi.org/10.1146/annurev-earth-060614-105049>
- Dufek, J., & Bachmann, O. (2010). Quantum magmatism: Magmatic compositional gaps generated by melt-crystal dynamics. *Geology*, 38(8), 687–690. <https://doi.org/10.1130/G30831.1>
- Duffield, W., Heiken, G., Foley, D., & McEwen, A. (1993). Oblique synoptic images, produced from digital data, display strong evidence of a “new” caldera in southwestern Guatemala. *Journal of Volcanology and Geothermal Research*, 55(3–4), 217–224. [https://doi.org/10.1016/0377-0273\(93\)90038-S](https://doi.org/10.1016/0377-0273(93)90038-S)
- Edmonds, M., & Woods, A. W. (2018). Exsolved volatiles in magma reservoirs. *Journal of Volcanology and Geothermal Research*, 368, 13–30. <https://doi.org/10.1016/j.jvolgeores.2018.10.018>
- Eichelberger, J. C. (1980). Vesiculation of mafic magma during replenishment of silicic magma reservoirs. *Nature*, 288, 446–450. <https://doi.org/10.1038/288446a0>
- Eiler, J. M., Carr, M. J., Reagan, M., & Stolper, E. (2005). Oxygen isotope constraints on the sources of Central American arc lavas. *Geochemistry, Geophysics, Geosystems*, 6(7), Q07007. <https://doi.org/10.1029/2004GC000804>
- Ellis, A., DeMets, C., McCaffrey, R., Briole, P., Cosenza Muralles, B., Flores, O., Guzmán-Speziale, M., Hernández, D., Kostoglodov, V., LaFemina, P., Lord, N., Lasserre, C., Lyon-Caen, H., Rodriguez Maradiaga, M., Molina, E., Rivera, J., Rogers, R., Staller, A., & Tikoff, B. (2019). GPS constraints on deformation in northern Central America from 1999 to 2017, Part 2: Block rotations and fault slip rates, fault locking and distributed deformation. *Geophysical Journal International*, 218(2), 729–754. <https://doi.org/10.1093/gji/ggz173>
- Ellis, B. S., Bachmann, O., & Wolff, J. A. (2014). Cumulate fragments in silicic ignimbrites: The case of the Snake River Plain. *Geology*, 42(5), 431–434. <https://doi.org/10.1130/G35399.1>
- Escobar-Wolf, R. P., Diehl, J. F., Singer, B. S., & Rose, W. I. (2010). $^{40}\text{Ar}/^{39}\text{Ar}$ and paleomagnetic constraints on the evolution of Volcán de Santa María, Guatemala. *Bulletin of the Geological Society of America*, 122(5–6), 757–771. <https://doi.org/10.1130/B26569.1>
- Etheridge, M. A., Daczko, N. R., Chapman, T., & Stuart, C. A. (2021). Mechanisms of melt extraction during lower crustal partial melting. *Journal of Metamorphic Geology*, 39(1), 57–75. <https://doi.org/10.1111/jmg.12561>
- Evans, B. W., & Ghiorso, M. S. (1995). Thermodynamics and petrology of cummingtonite. *American Mineralogist*, 80(7–8), 649–663. <https://doi.org/10.2138/am-1995-7-801>

- Farmer, G. L., Bailey, T., & Elkins-Tanton, L. T. (2008). Mantle source volumes and the origin of the mid-Tertiary ignimbrite flare-up in the southern Rocky Mountains, western U.S. *Lithos*, 102(1–2), 279–294. <https://doi.org/10.1016/j.lithos.2007.08.014>
- Farrell, J., Smith, B. R., Husen, S., & Diehl, T. (2014). Tomography from 26 years of seismicity revealing that the spatial extent of the Yellowstone crustal magma reservoir extends well beyond the Yellowstone caldera. *AGU Publications, Geophysical Research Letters*, 41, 3068–3073. <https://doi.org/10.1002/2014GL059588>
- Feigenson, M. D., & Carr, M. J. (1986). Positively correlated Nd and Sr isotope ratios of lavas from the Central American volcanic front. *Geology*, 14(1), 79–82. [https://doi.org/10.1130/0091-7613\(1986\)14<79:PCNASI>2.0.CO;2](https://doi.org/10.1130/0091-7613(1986)14<79:PCNASI>2.0.CO;2)
- Feigenson, M. D., & Carr, M. J. (1993). The source of Central American lavas: inferences from geochemical inverse modelling. *Contributions to Mineralogy and Petrology*, 113(2), 226–235. <https://doi.org/10.1007/BF00283230>
- Feigenson, M. D., Carr, M. J., Maharaj, S. V., Juliano, S., & Bolge, L. L. (2004). Lead isotope composition of Central American volcanoes: Influence of the Galapagos plume. *Geochemistry, Geophysics, Geosystems*, 5(6), Q06001. <https://doi.org/10.1029/2003GC000621>
- Ferrari, L., Lopéz-Martínez, M., & Rosas-Elguera, J. (2002). Ignimbrite flare-up and deformation in the southern Sierra Madre Occidental, western Mexico: Implications for the late subduction history of the Farallon plate. *Tectonics*, 21(4), 17-1–17-24. <https://doi.org/10.1029/2001TC001302>
- Ferrari, L., Valencia-Moreno, M., & Bryan, S. E. (2007). Magmatism and tectonics of the Sierra Madre Occidental and its relation with the evolution of the western margin of North America. In S. A. Alaniz-Álvarez & Á. F. Nieto-Samaniego (Eds.) *Geology of Mexico: Celebrating the Centenary of the Geological Society of Mexico: Geological Society of America Special Paper*, 422. [https://doi.org/10.1130/2007.2422\(01\)](https://doi.org/10.1130/2007.2422(01))
- Fialko, Y., & Simons, M. (2001). Evidence for on-going inflation of the Socorro magma body, New Mexico, from interferometric synthetic aperture radar imaging. *Geophysical Research Letters*, 28(18), 3549–3552. <https://doi.org/10.1029/2001GL013318>
- Flores, K. E., Martens, U. C., Harlow, G. E., Brueckner, H. K., & Pearson, N. J. (2013). Jadeite formed during subduction: In situ zircon geochronology constraints from two different tectonic events within the Guatemala Suture Zone. *Earth and Planetary Science Letters*, 371, 67–81. <https://doi.org/10.1016/j.epsl.2013.04.015>
- Foden, J. D., & Green, D. H. (1992). Possible role of amphibole in the origin of andesite: some experimental and natural evidence. *Contributions to Mineralogy and Petrology*, 109(4), 479–493. <https://doi.org/10.1007/BF00306551>
- Foley, D., Moore, J. N., Lutz, S. J., Palma, J. C., Ross, H. P., Tobias, E., & Tripp, A. C. (1990). Geology and Geophysics of the Zunil Geothermal System, Guatemala. *Geothermal Resources Council Transactions*, 14(II). <https://www.geothermal-library.org/index.php?mode=pubs&action=view&record=1002055>
- Foley, M. L., Miller, C. F., & Gualda, G. A. R. (2020). Architecture of a super-sized magma chamber and remobilization of its basal cumulate (Peach Spring Tuff, USA). *Journal of Petrology*, 61(1). <https://doi.org/10.1093/petrology/egaa020>
- Fowler, S. J., & Spera, F. J. (2010). A metamodel for crustal magmatism: Phase equilibria of giant ignimbrites. *Journal of Petrology*, 51(9), 1783–1830. <https://doi.org/10.1093/petrology/egq039>
- Franco, A., Lasserre, C., Lyon-Caen, H., Kostoglodov, V., Molina, E., Guzman-Speziale, M., Monterosso, D., Robles, V., Figueroa, C., Amaya, W., Barrier, E., Chiquin, L., Moran, S., Flores, O., Romero, J., Santiago, J. A., Manea, M., & Manea, V. C. (2012). Fault kinematics in northern Central America and coupling along the subduction interface of the Cocos

- Plate, from GPS data in Chiapas (Mexico), Guatemala and El Salvador. *Geophysical Journal International*, 189(3), 1223–1236. <https://doi.org/10.1111/j.1365-246X.2012.05390.x>
- Freyduth, H., Brandmeier, M., & Wörner, G. (2015). The origin and crust/mantle mass balance of Central Andean ignimbrite magmatism constrained by oxygen and strontium isotopes and erupted volumes. *Contributions to Mineralogy and Petrology*, 169, 58. <https://doi.org/10.1007/s00410-015-1152-5>
- Fujimaki, H., Tatsumoto, M., & Aoki, K. (1984). Partition coefficients of Hf, Zr, and REE between phenocrysts and groundmasses. *Journal of Geophysical Research*, 89(S02), 662–672. <https://doi.org/10.1029/JB089iS02p0B662>
- Funk, J., Mann, P., McIntosh, K., & Stephens, J. (2009). Cenozoic tectonics of the Nicaraguan depression, Nicaragua, and Median Trough, El Salvador, based on seismic-reflection profiling and remote-sensing data. *Bulletin of the Geological Society of America*, 121(11–12), 1491–1521. <https://doi.org/10.1130/B26428.1>
- Garcia, M. O., & Jacobson, S. S. (1979). Crystal clots, amphibole fractionation and the evolution of calc-alkaline magmas. *Contributions to Mineralogy and Petrology*, 69, 319–327. <https://doi.org/10.1007/BF00372257>
- Garnier, B., Tikoff, B., Flores, O., Jicha, B., DeMets, C., Cosenza-Murales, B., Hernandez, W., & Greene, D. (2022). Deformation in Western Guatemala Associated With the NAFA (North America-Central American Forearc-Caribbean) Triple Junction: Neotectonic Strain Localization Into the Guatemala City Graben. *Tectonics*, 41(2). <https://doi.org/10.1029/2021TC006739>
- Gazel, E., Carr, M. J., Hoernle, K., Feigenson, M. D., Szymanski, D., Hauff, F., & Van Den Bogaard, P. (2009). Galapagos-OIB signature in southern Central America: Mantle refertilization by arc-hot spot interaction. *Geochemistry, Geophysics, Geosystems*, 10(2), Q02S11. <https://doi.org/10.1029/2008GC002246>
- Gazel, E., Hoernle, K., Carr, M. J., Herzberg, C., Saginor, I., den Bogaard, P. van, Hauff, F., Feigenson, M., & Swisher, C. (2011). Plume-subduction interaction in southern Central America: Mantle upwelling and slab melting. *Lithos*, 121(1–4), 117–134. <https://doi.org/10.1016/j.lithos.2010.10.008>
- Gazel, E., Hayes, J. L., Hoernle, K., Kelemen, P., Everson, E., Holbrook, W. S., Hauff, F., Van Den Bogaard, P., Vance, E. A., Chu, S., Calvert, A. J., Carr, M. J., & Yogodzinski, G. M. (2015). Continental crust generated in oceanic arcs. *Nature Geoscience*, 8(4), 321–327. <https://doi.org/10.1038/ngeo2392>
- Gazel, E., Flores, K. E., & Carr, M. J. (2021). Architectural and tectonic control on the segmentation of the Central American volcanic arc. *Annual Review of Earth and Planetary Sciences*, 49, 495–521. <https://doi.org/10.1146/annurev-earth-082420-055108>
- Geldmacher, J., Hoernle, K., van den Bogaard, P., Hauff, F., & Klügel, A. (2008). Age and geochemistry of the central American forearc basement (DSDP Leg 67 and 84): Insights into Mesozoic arc volcanism and seamount accretion on the fringe of the Caribbean LIP. *Journal of Petrology*, 49(10). <https://doi.org/10.1093/petrology/egn046>
- Gelman, S. E., Gutiérrez, F. J., & Bachmann, O. (2013). On the longevity of large upper crustal silicic magma reservoirs. *Geology*, 41(7), 759–762. <https://doi.org/10.1130/G34241.1>
- Germa, A., Quidelleur, X., Labanieh, S., Chauvel, C., & Lahitte, P. (2011). The volcanic evolution of Martinique Island: Insights from K-Ar dating into the Lesser Antilles arc migration since the Oligocene. *Journal of Volcanology and Geothermal Research*, 208(3–4), 122–135. <https://doi.org/10.1016/j.jvolgeores.2011.09.007>
- Geschwind, C. H., & Rutherford, M. J. (1992). Cumingtonite and the evolution of the Mount St. Helens (Washington) magma system: an experimental study. *Geology*, 20(11), 1011–1014. [https://doi.org/10.1130/0091-7613\(1992\)020<1011:CATEOT>2.3.CO;2](https://doi.org/10.1130/0091-7613(1992)020<1011:CATEOT>2.3.CO;2)
- Ghiorso, M. S., & Sack, R. O. (1995). Chemical mass transfer in magmatic processes IV. A revised and internally consistent thermodynamic model for the interpolation and extrapolation of

- liquid-solid equilibria in magmatic systems at elevated temperatures and pressures. *Contributions to Mineralogy and Petrology*, 119(2–3), 197–212. <https://doi.org/10.1007/BF00307281>
- Gianni, G. M., & Luján, S. P. (2021). Geodynamic controls on magmatic arc migration and quiescence. *Earth-Science Reviews*, 218. <https://doi.org/10.1016/j.earscirev.2021.103676>
- Gill, J. (1981). Orogenic andesites and plate tectonics. Springer, Heidelberg. <https://doi.org/10.1007/978-3-642-68012-0>
- González-Maurel, O., Godoy, B., le Roux, P., Rodríguez, I., Marín, C., Menzies, A., Bertin, D., Morata, D., & Vargas, M. (2019). Magmatic differentiation at La Poruña scoria cone, Central Andes, northern Chile: Evidence for assimilation during turbulent ascent processes, and genetic links with mafic eruptions at adjacent San Pedro volcano. *Lithos*, 338, 128–140. <https://doi.org/10.1016/j.lithos.2019.03.033>
- Goss, A. R., Kay, S. M., & Mpodozis, C. (2013). Andean Adakite-like high-Mg Andesites on the Northern Margin of the Chilean-Pampean Flat-slab (27–28.58°S) Associated with Frontal Arc Migration and Fore-arc Subduction Erosion. *Journal of Petrology*, 54(11), 2193–2234. <https://doi.org/10.1093/petrology/egt044>
- Gregg, P. M., De Silva, S. L., Grosfils, E. B., & Parmigiani, J. P. (2012). Catastrophic caldera-forming eruptions: Thermomechanics and implications for eruption triggering and maximum caldera dimensions on Earth. *Journal of Volcanology and Geothermal Research*, 241, 1–12. <https://doi.org/10.1016/j.jvolgeores.2012.06.009>
- Grevemeyer, I., Ranero, C. R., Flueh, E. R., Kläschen, D., & Bialas, J. (2007). Passive and active seismological study of bending-related faulting and mantle serpentinization at the Middle America trench. *Earth and Planetary Science Letters*, 258(3–4), 528–542. <https://doi.org/10.1016/j.epsl.2007.04.013>
- Grove, T. L., & Kinzler, R. J. (1986). Petrogenesis of andesites. *Annual Review of Earth & Planetary Sciences*, 14, 417–454. <https://doi.org/10.1146/annurev.ea.14.050186.002221>
- Grove, T., Parman, S., Bowring, S., Price, R., & Baker, M. (2002). The role of an H₂O-rich fluid component in the generation of primitive basaltic andesites and andesites from the Mt. Shasta region, N California. *Contributions to Mineralogy and Petrology*, 142(4), 375–396. <https://doi.org/10.1007/s004100100299>
- Grove, T. L., Elkins-Tanton, L. T., Parman, S. W., Chatterjee, N., Müntener, O., & Gaetani, G. A. (2003). Fractional crystallization and mantle-melting controls on calc-alkaline differentiation trends. *Contributions to Mineralogy and Petrology*, 145(5), 515–533. <https://doi.org/10.1007/s00410-003-0448-z>
- Grunder, A. L., Klemetti, E. W., Feeley, T. C., & McKee, C. M. (2008). Eleven million years of arc volcanism at the Aucanquilcha Volcanic Cluster, northern Chilean Andes: implications for the life span and emplacement of plutons. *Earth and Environmental Science Transactions of The Royal Society of Edinburgh*, 97(4), 415–436. <https://doi.org/10.1017/S0263593300001541>
- Gualda, G. A. R., Ghiorso, M. S., Lemons, R. V., & Carley, T. L. (2012). Rhyolite-MELTS: A modified calibration of MELTS optimized for silica-rich, fluid-bearing magmatic systems. *Journal of Petrology*, 53(5), 875–890. <https://doi.org/10.1093/petrology/egr080>
- Guzman-Speziale, M. (2001). Active seismic deformation in the grabens of northern Central America and its relationship to the relative motion of the North America-Caribbean plate boundary. *Tectonophysics*, 337, 39–51. [https://doi.org/10.1016/S0040-1951\(01\)00110-X](https://doi.org/10.1016/S0040-1951(01)00110-X)
- Guzmán-Speziale, M. (2010). Beyond the Motagua and Polochic faults: Active strike-slip faulting along the Western North America-Caribbean plate boundary zone. *Tectonophysics*, 496(1–4), 17–27. <https://doi.org/10.1016/j.tecto.2010.10.002>
- Halsor, S. P. (1989). Large glass inclusions in plagioclase phenocrysts and their bearing on the origin of mixed andesitic lavas at Tolimán volcano, Guatemala. *Bulletin of Volcanology*, 51(4), 271–280. <https://doi.org/10.1007/BF01073516>

- Halsor, S. P., & Rose, W. I. (1988). Common characteristics of paired volcanoes in northern Central America. *Journal of Geophysical Research*, 93(85), 4467–4476. <https://doi.org/10.1029/JB093iB05p04467>
- Halsor, S. P., & Rose, W. I. (1991). Mineralogical relations and magma mixing in calc-alkaline andesites from Lake Atitlan, Guatemala. *Mineralogy and Petrology*, 45, 47–67. <https://doi.org/10.1007/BF01164502>
- Hammarstrom, J. M., & Zen, E. A. (1992). Discussion of Blundy and Holland's (1990) "Calcic amphibole equilibria and a new amphibole-plagioclase geothermometer." *Contributions to Mineralogy and Petrology*, 111(2), 264–266. <https://doi.org/10.1007/BF00348957>
- Hammer, J., Jacob, S., Welsch, B., Hellebrand, E., & Sinton, J. (2016). Clinopyroxene in postshield Haleakala ankaramite: 1. Efficacy of thermobarometry. *Contributions to Mineralogy and Petrology*, 171, 6. <https://doi.org/10.1007/s00410-015-1212-x>
- Hansteen, T. H., Burkert, C., Freundt, A., & Kutterolf, S. (2022). The role of a pre-eruptive fluid phase for the volatile budget and atmospheric influence of large explosive eruptions in Central America. *Cities on Volcanoes 11, Heraklion, Crete*.
- Harford, C. L., & Sparks, R. S. J. (2001). Recent remobilisation of shallow-level intrusions on Montserrat revealed by hydrogen isotope composition of amphiboles. *Earth and Planetary Science Letters*, 185(3–4), 285–297. [https://doi.org/10.1016/S0012-821X\(00\)00373-3](https://doi.org/10.1016/S0012-821X(00)00373-3)
- Harlow, G. E., & Davies, R. (2004). Status report on stability of K-rich phases at mantle conditions. *Lithos*, 77(1–4), 647–653. <https://doi.org/10.1016/j.lithos.2004.04.010>
- Harper, M., Weinstein, B., Woodcock, T., Simon, C., Chebee7i, Swanson-Hysell, N., Gitter Badger, T., Maximiliano, G., & Zuidhof, G. (2015). python-ternary: Ternary Plots in Python. *Zenodo*, <https://doi.org/10.5281/zenodo.594435>
- Hauff, F., Hoernle, K., van den Bogaard, P., Alvarado, G., & Garbe-Schönberg, D. (2000). Age and geochemistry of basaltic complexes in western Costa Rica: Contributions to the geotectonic evolution of Central America. *Geochemistry, Geophysics, Geosystems*, 1(5). <https://doi.org/10.1029/1999gc000020>
- Hawthorne, F. C., Oberti, R., Harlow, G. E., Maresch, W. V., Martin, R. F., Schumacher, J. C., & Welch, M. D. (2012). Nomenclature of the amphibole supergroup. *American Mineralogist*, 97(11–12), 2031–2048. <https://doi.org/10.2138/am.2012.4276>
- Heliker, C. (1995). Inclusions in Mount St. Helens dacite erupted from 1980 through 1983. *Journal of Volcanology and Geothermal Research*, 66(1–4), 115–135. [https://doi.org/10.1016/0377-0273\(94\)00074-Q](https://doi.org/10.1016/0377-0273(94)00074-Q)
- Hermes, O. D., & Cornell, W. C. (1981). Quenched crystal mush and associated magma compositions as indicated by intercumulus glasses from Mt. Vesuvius, Italy. *Journal of Volcanology and Geothermal Research*, 9(2–3), 133–149. [https://doi.org/10.1016/0377-0273\(81\)90002-0](https://doi.org/10.1016/0377-0273(81)90002-0)
- Heydolph, K., Hoernle, K., Hauff, F., van den Bogaard, P., Portnyagin, M., Bindeman, I., & Garbe-Schönberg, D. (2012). Along and across arc geochemical variations in NW Central America: Evidence for involvement of lithospheric pyroxenite. *Geochimica et Cosmochimica Acta*, 84, 459–491. <https://doi.org/10.1016/j.gca.2012.01.035>
- Hildreth, W. (1981). Gradients in Silicic Magma Chambers: Implications for Lithospheric Magmatism. *Journal of Geophysical Research: Solid Earth*, 86(B11), 10153–10192. <https://doi.org/10.1029/JB086iB11p10153>
- Hildreth, W. (2004). Volcanological perspectives on Long Valley, Mammoth Mountain, and Mono Craters: Several contiguous but discrete systems. *Journal of Volcanology and Geothermal Research*, 136(3–4), 169–198. <https://doi.org/10.1016/j.jvolgeores.2004.05.019>
- Hildreth, W., & Moorbath, S. (1988). Crustal contributions to arc magmatism in the Andes of Central Chile. *Contributions to Mineralogy and Petrology*, 98(4), 455–489. <https://doi.org/10.1007/BF00372365>

- Hildreth, W., & Fierstein, J. (2000). Katmai volcanic cluster and the great eruption of 1912. *Bulletin of the Geological Society of America*, 112(10), 1594–1620. [https://doi.org/10.1130/0016-7606\(2000\)112<1594:KVCATG>2.0.CO;2](https://doi.org/10.1130/0016-7606(2000)112<1594:KVCATG>2.0.CO;2)
- Hildreth, W., & Wilson, C. J. N. (2007). Compositional Zoning of the Bishop Tuff. *Journal of Petrology*, 48(5), 951–999. <https://doi.org/10.1093/petrology/egm007>
- Hoernle, K., Abt, D. L., Fischer, K. M., Nichols, H., Hauff, F., Abers, G. A., van den Bogaard, P., Heydolph, K., Alvarado, G., Protti, M., & Strauch, W. (2008). Arc-parallel flow in the mantle wedge beneath Costa Rica and Nicaragua. *Nature*, 451(7182), 1094–1097. <https://doi.org/10.1038/nature06550>
- Holtzman, B. K., Groebner, N. J., Zimmerman, M. E., Ginsberg, S. B., & Kohlstedt, D. L. (2003). Stress-driven melt segregation in partially molten rocks. *Geochemistry, Geophysics, Geosystems*, 4(5). <https://doi.org/10.1029/2001GC000258>
- Huber, C., Bachmann, O., & Manga, M. (2009). Homogenization processes in silicic magma chambers by stirring and mushification (latent heat buffering). *Earth and Planetary Science Letters*, 283(1–4), 38–47. <https://doi.org/10.1016/j.epsl.2009.03.029>
- Huber, C., Bachmann, O., & Dufek, J. (2012). Crystal-poor versus crystal-rich ignimbrites: A competition between stirring and reactivation. *Geology*, 40(2), 115–118. <https://doi.org/10.1130/G32425.1>
- Huber, C., Townsend, M., Degruyter, W., & Bachmann, O. (2019). Optimal depth of subvolcanic magma chamber growth controlled by volatiles and crust rheology. *Nature Geoscience*, 12(9), 762–768. <https://doi.org/10.1038/s41561-019-0415-6>
- Hughes, G. R., & Mahood, G. A. (2008). Tectonic controls on the nature of large silicic calderas in volcanic arcs. *Geology*, 36(8), 627–630. <https://doi.org/10.1130/G24796A.1>
- Hughes, G. R., & Mahood, G. A. (2011). Silicic calderas in arc settings: Characteristics, distribution, and tectonic controls. *Bulletin of the Geological Society of America*, 123(7–8), 1577–1595. <https://doi.org/10.1130/B30232.1>
- Humphreys, M. C. S., Edmonds, M., Christopher, T., & Hards, V. (2010). Magma hybridisation and diffusive exchange recorded in heterogeneous glasses from Soufrière Hills Volcano, Montserrat. *Geophysical Research Letters*, 37(4). <https://doi.org/10.1029/2009GL041926>
- Huppert, H. E., & Sparks, R. S. J. (1988). The generation of granitic magmas by intrusion of basalt into continental crust. *Journal of Petrology*, 29(3), 599–624. <https://doi.org/10.1093/petrology/29.3.599>
- Huppert, H. E., & Woods, A. W. (2002). The role of volatiles in magma chamber dynamics. *Nature*, 420(6915), 493–495. <https://doi.org/10.1038/nature01211>
- Innes, H. M., Hutchison, W., Sigl, M., Crick, L., Abbott, P. M., Bigler, M., Chellman, N. J., Davies, S. M., Kutterolf, S., McConnell, J. R., Severi, M., Sparks, R. S. J., Svensson, A., Wolff, E. W., Rae, J. W. B., & Burke, A. (2025). Ice core evidence for the Los Chocoyos supereruption disputes millennial-scale climate impact. *Communications Earth and Environment*, 6, 137. <https://doi.org/10.1038/s43247-025-02095-6>
- Ivancic, M., Grevemeyer, I., Berhorst, A., Flueh, E. R., & McIntosh, K. (2008). Impact of bending related faulting on the seismic properties of the incoming oceanic plate offshore of Nicaragua. *Journal of Geophysical Research: Solid Earth*, 113(B5), B05410. <https://doi.org/10.1029/2007JB005291>
- Jackson, M. D., Blundy, J., & Sparks, R. S. J. (2018). Chemical differentiation, cold storage and remobilization of magma in the Earth's crust. *Nature*, 564(7736), 405–409. <https://doi.org/10.1038/s41586-018-0746-2>
- Jicha, B. R., & Kay, S. M. (2018). Quantifying arc migration and the role of forearc subduction erosion in the central Aleutians. *Journal of Volcanology and Geothermal Research*, 360, 84–99. <https://doi.org/10.1016/j.jvolgeores.2018.06.016>

- Jicha, B. R., Smith, K. E., Singer, B. S., Beard, B. L., Johnson, C. M., & Rogers, N. W. (2010). Crustal assimilation no match for slab fluids beneath Volcán de Santa María, Guatemala. *Geology*, 38(9), 859–862. <https://doi.org/10.1130/G31062.1>
- Jorgenson, C., Higgins, O., Petrelli, M., Bégué, F., & Caricchi, L. (2022). A machine learning-based approach to clinopyroxene thermobarometry: model optimization and distribution for use in Earth sciences. *Journal of Geophysical Research: Solid Earth*, 127(4), 1–21. <https://doi.org/10.1029/2021JB022904>
- Karakas, O., Degruyter, W., Bachmann, O., & Dufek, J. (2017). Lifetime and size of shallow magma bodies controlled by crustal-scale magmatism. *Nature Geoscience*, 10(6), 446–450. <https://doi.org/10.1038/ngeo2959>
- Kay, S. M., & Coira, B. L. (2009). Shallowing and steepening subduction zones, continental lithospheric loss, magmatism, and crustal flow under the Central Andean Altiplano-Puna Plateau. In S. M. Kay, V. A. Ramos, & W. R. Dickinson (Eds.), *Backbone of the Americas: Shallow Subduction, Plateau Uplift, and Ridge and Terrane Collision: Geological Society of America Memoir*, 204, pp.229–259. [https://doi.org/10.1130/2009.1204\(11\)](https://doi.org/10.1130/2009.1204(11))
- Kay, S. M., Coira, B., Wörner, G., Kay, R. W., & Singer, B. S. (2011). Geochemical, isotopic and single crystal $^{40}\text{Ar}/^{39}\text{Ar}$ age constraints on the evolution of the Cerro Galán ignimbrites. *Bulletin of Volcanology*, 73(10), 1487–1511. <https://doi.org/10.1007/s00445-010-0410-7>
- Kay, S. M., Godoy, E., & Kurtz, A. (2005). Episodic arc migration, crustal thickening, subduction erosion, and magmatism in the south-central Andes. *Bulletin of the Geological Society of America*, 117(1–2), 67–88. <https://doi.org/10.1130/B25431.1>
- Kay, S. M., Coira, B. L., Caffee, P. J., & Chen, C. H. (2010). Regional chemical diversity, crustal and mantle sources and evolution of central Andean Puna plateau ignimbrites. *Journal of Volcanology and Geothermal Research*, 198(1–2), 81–111. <https://doi.org/10.1016/j.jvolgeores.2010.08.013>
- Keller, F., Wanke, M., Kueter, N., Guillong, M., & Bachmann, O. (2024). An Amphibole Perspective on the Recent Magmatic Evolution of Mount St. Helens. *Journal of Petrology*, 65(1), 1–18. <https://doi.org/10.1093/petrology/egad093>
- Kent, A. J. R. (2008). Met inclusions in basaltic and related volcanic rocks. *Reviews in Mineralogy and Geochemistry*, 69, 273–331. <https://doi.org/10.2138/rmg.2008.69.8>
- Keppie, J. D., & Morán-Zenteno, D. J. (2005). Tectonic Implications of Alternative Cenozoic Reconstructions for Southern Mexico and the Chortis Block. *International Geology Review*, 47(5), 473–491. <https://doi.org/10.2747/0020-6814.47.5.473>
- Kimura, J. I., Takahashi, T., & Chang, Q. (2013). A new analytical bias correction for in situ Sr isotope analysis of plagioclase crystals using laser-ablation multiple-collector inductively coupled plasma mass spectrometry. *Journal of Analytical Atomic Spectrometry*, 28(6), 945–957. <https://doi.org/10.1039/c3ja30329b>
- Kimura, J. I., Nagahashi, Y., Satoguchi, Y., & Chang, Q. (2015). Origins of felsic magmas in Japanese subduction zone: Geochemical characterizations of tephra from caldera-forming eruptions <5Ma. *Geochemistry Geophysics Geosystems*, 16, 2147–2174. <https://doi.org/10.1002/2015GC005854>
- Koch, A. J., & McLean, H. (1975). Pleistocene tephra and ash-flow deposits in the volcanic highlands of Guatemala. *Bulletin of the Geological Society of America*, 86(4), 529–541. [https://doi.org/10.1130/0016-7606\(1975\)86<529:PTAADl>2.0.CO;2](https://doi.org/10.1130/0016-7606(1975)86<529:PTAADl>2.0.CO;2)
- Kondo, H., Tanaka, K., Mizuochi, Y., & Ninomiya, A. (2004). Long-term changes in distribution and chemistry of middle Miocene to Quaternary volcanism in the Chokai-Kurikoma area across the Northeast Japan Arc. *Island Arc*, 13(1), 18–46. <https://doi.org/10.1111/j.1440-1738.2003.00417.x>
- Kovalenko, D. V., Naumov, V. B., Prokofiev, V. Y., Ageeva, O. A., Andreeva, O. A., Kovaltchuk, E. V., Erofeeva, K. G., & Ugryumova, N. Y. (2017). Chemical composition of melts of the Early Eocene volcanic center at Cape Khairuzova, western Kamchatka: Evidence from

- inclusions in minerals. *Petrology*, 25(1), 66–86.
<https://doi.org/10.1134/S0869591117010052>
- Krawczynski, M. J., Grove, T. L., & Behrens, H. (2012). Amphibole stability in primitive arc magmas: Effects of temperature, H₂O content, and oxygen fugacity. *Contributions to Mineralogy and Petrology*, 164(2), 317–339. <https://doi.org/10.1007/s00410-012-0740-x>
- Kutterolf, S., Freundt, A., Pérez, W., Mörz, T., Schacht, U., Wehrmann, H., & Schmincke, H.-U. (2008a). Pacific offshore record of plinian arc volcanism in Central America: 1. Along-arc correlations. *Geochemistry, Geophysics, Geosystems*, 9(2), Q02S01.
<https://doi.org/10.1029/2007gc001631>
- Kutterolf, S., Freundt, A., & Pérez, W. (2008b). Pacific offshore record of plinian arc volcanism in Central America: 2. Tephra volumes and erupted masses. *Geochemistry, Geophysics, Geosystems*, 9(2), Q02S02. <https://doi.org/10.1029/2007gc001791>
- Kutterolf, S., Schindlbeck, J. C., Anselmetti, F. S., Ariztegui, D., Brenner, M., Curtis, J., P. W., & Wang, K. (2016). A 400-ka tephrochronological framework for Central America from Lake Peten Itza (Guatemala) sediments. *Quaternary Science Reviews*, 150, 200–220.
<https://doi.org/10.1016/j.quascirev.2016.08.023>
- Kutterolf, S., Schindlbeck- Belo, J. C., Rohr, I., Rademacher, M., de León, A. C., Eisele, S., Freundt, A., Hernandez, W., & Wang, K. L. (2020). The Arce Tephra: Two subsequent paroxysmal Plinian eruptions from Coatepeque Caldera (El Salvador). *Journal of Volcanology and Geothermal Research*, 390. <https://doi.org/10.1016/j.jvolgeores.2019.106673>
- Le Breton, N., & Thompson, A. B. (1988). Fluid-absent (dehydration) melting of biotite in metapelites in the early stages of crustal anatexis. *Contributions to Mineralogy and Petrology*, 99, 226–237. <https://doi.org/10.1007/BF00371463>
- Le Maitre, R. W., Streckeisen, A., Zanettin, B., Le Bas, M. J., Bonin, B., & Bateman, P. (2002). *Igneous rocks: a classification and glossary of terms: recommendations of the International Union of Geological Sciences Subcommittee on the Systematics of Igneous Rocks*. Cambridge University Press.
<https://doi.org/https://doi.org/10.1017/CBO9780511535581>
- Leeman, W. P., Carr, M. J., & Morris, J. D. (1994). Boron geochemistry of the Central American Volcanic Arc: Constraints on the genesis of subduction-related magmas. *Geochimica et Cosmochimica Acta*, 58(1), 149–168. [https://doi.org/10.1016/0016-7037\(94\)90453-7](https://doi.org/10.1016/0016-7037(94)90453-7)
- Li, X., Zhang, C., Behrens, H., & Holtz, F. (2020). Calculating biotite formula from electron microprobe analysis data using a machine learning method based on principal components regression. *Lithos*, 356, 105371.
<https://doi.org/10.1016/j.lithos.2020.105371>
- Lin, J., Svensson, A., Hvidberg, C. S., Lohmann, J., Kristiansen, S., Dahl-Jensen, D., Steffensen, J. P., Rasmussen, S. O., Cook, E., Kjær, H. A., Vinther, B. M., Fischer, H., Stocker, T., Sigl, M., Bigler, M., Severi, M., Traversi, R., & Mulvaney, R. (2022). Magnitude, frequency, and climate forcing of global volcanism during the last glacial period as seen in Greenland and Antarctic ice cores (60–9ka). *Climate of the Past*, 18(3), 485–506.
<https://doi.org/10.5194/cp-18-485-2022>
- Linde, A. T., & Sacks, I. S. (1998). Triggering of volcanic eruptions. *Nature*, 395(6705), 888–890.
<https://doi.org/10.1038/27650>
- Linnen, R. L., & Keppler, H. (2002). Melt composition control of Zr/Hf fractionation in magmatic processes. *Geochimica et Cosmochimica Acta*, 66(18), 3293–3301.
[https://doi.org/10.1016/S0016-7037\(02\)00924-9](https://doi.org/10.1016/S0016-7037(02)00924-9)
- Lipman, P. W. (1967). Mineral and chemical variations within an ash-flow sheet from Aso caldera, Southwestern Japan. *Contributions to Mineralogy and Petrology*, 16(4), 300–327.
<https://doi.org/10.1007/BF00371528>
- Lipman, P. W., Doe, B. R., Hedge, C. E., & Steven, T. A. (1978). Petrologic evolution of the San Juan volcanic field, southwestern Colorado: Pb and Sr isotope evidence. *Bulletin of the*

- Geological Society of America*, 89(1), 59–82. [https://doi.org/10.1130/0016-7606\(1978\)89<59:PEOTSJ>2.0.CO;2](https://doi.org/10.1130/0016-7606(1978)89<59:PEOTSJ>2.0.CO;2)
- Liu, B., & Lee, C. T. (2020). Large silicic eruptions, episodic recharge, and the transcrustal magmatic system. *Geochemistry, Geophysics, Geosystems*, 21(9), e2020GC009220. <https://doi.org/10.1029/2020GC009220>
- Liu, E. J., Cashman, K. V., Miller, E., Moore, H., Edmonds, M., Kunz, B. E., Jenner, F., & Chigna, G. (2020). Petrologic monitoring at Volcán de Fuego, Guatemala. *Journal of Volcanology and Geothermal Research*, 405, 107044. <https://doi.org/10.1016/j.jvolgeores.2020.107044>
- Lofgren, G. E. (1974). Temperature induced zoning in synthetic plagioclase feldspar. In W. S. MacKenzie & J. Zussman (Eds.), *The feldspars*, pp. 362–375, Manchester University Press, Manchester.
- London, D., Wolf, M. B., Morgan VI, G. B., & Garrido, M. G. (1999). Experimental silicate-phosphate equilibria in peraluminous granitic magmas, with a case study of the Albuquerque batholith at Tres Arroyos, Badajoz, Spain. *Journal of Petrology*, 40(1), 215–240. <https://doi.org/10.1093/petroj/40.1.215>
- Lubbers, J., Deering, C., & Bachmann, O. (2020). Genesis of rhyolitic melts in the upper crust: Fractionation and remobilization of an intermediate cumulate at Lake City caldera, Colorado, USA. *Journal of Volcanology and Geothermal Research*, 392, 106750. <https://doi.org/10.1016/j.jvolgeores.2019.106750>
- Lücke, O. H. (2014). Moho structure of Central America based on three-dimensional lithospheric density modelling of satellite-derived gravity data. *International Journal of Earth Sciences*, 103(7), 1733–1745. <https://doi.org/10.1007/s00531-012-0787-y>
- Lyon-Caen, H., Barrier, E., Lasserre, C., Franco, A., Arzu, I., Chiquin, L., Chiquin, M., Duquesnoy, T., Flores, O., Galicia, O., Luna, J., Molina, E., Porras, O., Requena, J., Robles, V., Romero, J., & Wolf, R. (2006). Kinematics of the North American-Caribbean-Cocos plates in Central America from new GPS measurements across the Polochic-Motagua fault system. *Geophysical Research Letters*, 33(19), L19309. <https://doi.org/10.1029/2006GL027694>
- MacKenzie, L., Abers, G. A., Fischer, K. M., Syracuse, E. M., Protti, J. M., Gonzalez, V., & Strauch, W. (2008). Crustal structure along the southern Central American volcanic front. *Geochemistry, Geophysics, Geosystems*, 9(8), Q08S09. <https://doi.org/10.1029/2008GC001991>
- Macpherson, C. G., Dreher, S. T., & Thirlwall, M. F. (2006). Adakites without slab melting: High pressure differentiation of island arc magma, Mindanao, the Philippines. *Earth and Planetary Science Letters*, 243(3–4), 581–593. <https://doi.org/10.1016/j.epsl.2005.12.034>
- Mahood, G., & Hildreth, W. (1983). Large partition coefficients for trace elements in high-silica rhyolites. *Geochimica et Cosmochimica Acta*, 47(1), 11–30. [https://doi.org/10.1016/0016-7037\(83\)90087-X](https://doi.org/10.1016/0016-7037(83)90087-X)
- Malfait, B. T., & Dinkelman, M. G. (1972). Circum-Caribbean tectonic and igneous activity and the evolution of the Caribbean Plate. *GSA Bulletin*, 83(2). [https://doi.org/10.1130/0016-7606\(1972\)83\[251:CTAIAA\]2.0.CO;2](https://doi.org/10.1130/0016-7606(1972)83[251:CTAIAA]2.0.CO;2)
- Malfait, W. J., Seifert, R., Petitgirard, S., Perrillat, J. P., Mezouar, M., Ota, T., Nakamura, E., Lerch, P., & Sanchez-Valle, C. (2014). Supervolcano eruptions driven by melt buoyancy in large silicic magma chambers. *Nature Geoscience*, 7(2), 122–125. <https://doi.org/10.1038/ngeo2042>
- Manton, W. I. (1996). The Grenville of Honduras. *Geological Society of America, Annual Meeting, Program with Abstracts*, A-493.
- Mark, D. F., Petraglia, M., Smith, V. C., Morgan, L. E., Barfod, D. N., Ellis, B. S., Pearce, N. J., Pal, J. N., & Korisettar, R. (2014). A high-precision $^{40}\text{Ar}/^{39}\text{Ar}$ age for the Young Toba Tuff and dating of ultra-distal tephra: Forcing of Quaternary climate and implications for hominin occupation of India. *Quaternary Geochronology*, 21(1), 90–103. <https://doi.org/10.1016/j.quageo.2012.12.004>

- Mark, D. F., Renne, P. R., Dymock, R., Smith, V. C., Simon, J. I., Morgan, L. E., Staff, R. A., & Ellis, B. S. (2017). High-precision $^{40}\text{Ar}/^{39}\text{Ar}$ dating of Pleistocene tuffs and temporal anchoring of the Matuyama-Brunhes boundary. *Quaternary Geochronology*, 39, 1–23. <https://doi.org/10.1016/j.quageo.2017.01.002>
- Martin, V. M., Morgan, D. J., Jerram, D. A., Caddick, M. J., Prior, D. J., & Davidson, J. P. (2008). Bang! Month-scale eruption triggering at Santorini volcano. *Science*, 321(5893), 1178. <https://doi.org/10.1126/science.1159584>
- Marxer, F., Ulmer, P., & Müntener, O. (2022). Polybaric fractional crystallisation of arc magmas: an experimental study simulating trans-crustal magmatic systems. *Contributions to Mineralogy and Petrology*, 177, 3. <https://doi.org/10.1007/s00410-021-01856-8>
- McBirney, A. R. (1969). Andesitic and rhyolitic volcanism of orogenic belts. In P. J. Hart (Ed.), *The Earth's Crust and Upper Mantle*, pp. 501–507. American Geophysical Union, Washington D. C. <https://doi.org/10.1029/GM013p0501>
- McKenzie, D. (1985). The extraction of magma from the crust and mantle. *Earth and Planetary Science Letters*, 74(1), 81–91. [https://doi.org/10.1016/0012-821X\(85\)90168-2](https://doi.org/10.1016/0012-821X(85)90168-2)
- Michell, J. (1759). Conjectures concerning the cause, and observations upon the phaenomena of earthquakes; particularly of that great earthquake of the first November, 1755, which proved so fatal to the city of Lisbon, and whose effects were felt as far as Africa and more or less throughout almost all Europe. *Philosophical Transactions of the Royal Society of London*, 51, 566–634. <https://doi.org/10.1080/14786441808652061>
- Miller, C. F., & Mittlefehldt, D. W. (1982). Depletion of light rare-earth elements in felsic magmas. *Geology*, 10(3), 129–133. [https://doi.org/10.1130/0091-7613\(1982\)10<129:DOLREI>2.0.CO;2](https://doi.org/10.1130/0091-7613(1982)10<129:DOLREI>2.0.CO;2)
- Miller, C. F., & Wark, D. A. (2008). Supervolcanoes and their explosive supereruptions. *Elements*, 4, 11–16. <https://doi.org/10.2113/GSELEMENTS.4.1.11>
- Montel, J. M. (1993). A model for monazite/melt equilibrium and application to the generation of granitic magmas. *Chemical Geology*, 110(1–3), 127–146. [https://doi.org/10.1016/0009-2541\(93\)90250-M](https://doi.org/10.1016/0009-2541(93)90250-M)
- Moore, G., & Carmichael, I. S. E. (1998). The hydrous phase equilibria (to 3 kbar) of an andesite and basaltic andesite from western Mexico: Constraints on water content and conditions of phenocryst growth. *Contributions to Mineralogy and Petrology*, 130(3–4), 304–319. <https://doi.org/10.1007/s004100050367>
- Morán-Zenteno, D. J., Corona-Chavez, P., & Tolson, G. (1996). Uplift and subduction erosion in southwestern Mexico since the Oligocene: pluton geobarometry constraints. *Earth and Planetary Science Letters*, 141(1–4), 51–65. [https://doi.org/10.1016/0012-821X\(96\)00067-2#](https://doi.org/10.1016/0012-821X(96)00067-2#)
- Morán-Zenteno, D. J., Cerca, M., & Keppie, J. D. (2007). The Cenozoic tectonic and magmatic evolution of southwestern México: Advances and problems of interpretation. *Special Paper of the Geological Society of America*, 422(03), 71–91. [https://doi.org/10.1130/2007.2422\(03\)](https://doi.org/10.1130/2007.2422(03))
- Morimoto, N., Fabries, J., Ferguson, A. K., Ginzburg, I. V., Ross, M., Seifert, F. A., Zussman, J., Aoki, K., & Gottardi, G. (1988). Nomenclature of pyroxenes. *American Mineralogist*, 73, 1123–1133. <https://doi.org/10.1007/BF01226262>
- Münker, C., Weyer, S., Scherer, E., & Mezger, K. (2001). Separation of high field strength elements (Nb, Ta, Zr, Hf) and Lu from rock samples for MC-ICPMS measurements. *Geochemistry, Geophysics, Geosystems*, 2, 1064. <https://doi.org/10.1029/2001GC000183>
- Müntener, O., Kelemen, P. B., & Grove, T. L. (2001). The role of H₂O during crystallization of primitive arc magmas under uppermost mantle conditions and genesis of igneous pyroxenites: An experimental study. *Contributions to Mineralogy and Petrology*, 141(6), 643–658. <https://doi.org/10.1007/s004100100266>

- Nakada, S., Bacon, C. R., & Gartner, A. E. (1994). Origin of phenocrysts and compositional diversity in pre-Mazama rhyodacite lavas, Crater Lake, Oregon. *Journal of Petrology*, 35(1), 127–162. <https://doi.org/10.1093/petrology/35.1.127>
- Nakamura, K. (1975). Volcano structure and possible mechanical correlation between volcanic eruptions and earthquakes. *Bulletin of the Volcanological Society of Japan*, 20, 229–240. http://dx.doi.org/10.18940/kazanc.20.TOKUBE_229
- Nandedkar, R. H., Ulmer, P., & Müntener, O. (2014). Fractional crystallization of primitive, hydrous arc magmas: An experimental study at 0.7 GPa. *Contributions to Mineralogy and Petrology*, 167(6), 1–27. <https://doi.org/10.1007/s00410-014-1015-5>
- Nandedkar, R. H., Hürlimann, N., Ulmer, P., & Müntener, O. (2016). Amphibole–melt trace element partitioning of fractionating calc-alkaline magmas in the lower crust: an experimental study. *Contributions to Mineralogy and Petrology*, 171, 71. <https://doi.org/10.1007/s00410-016-1278-0>
- Newhall, C. G. (1980). Geology of the Lake Atitlán area, Guatemala: A study of subduction zone volcanism and caldera formation. PhD thesis, Dartmouth College, Hanover, New Hampshire. <https://doi.org/10.1349/ddlp.3296>
- Newhall, C. G. (1982). Geological map of Solola, Hoja 1960 II, 1:50000, Instituto Geográfico Nacional.
- Newhall, C. G. (1987). Geology of the Lake Atitlán Region, Western Guatemala. *Journal of Volcanology and Geothermal Research*, 33(1–3), 23–55. [https://doi.org/10.1016/0377-0273\(87\)90053-9](https://doi.org/10.1016/0377-0273(87)90053-9)
- Newhall, C. G., & Self, S. (1982). The volcanic explosivity index (VEI): an estimate of explosive magnitude for historical volcanism. *Journal of Geophysical Research*, 87(C2), 1231–1238. <https://doi.org/10.1029/jc087ic02p01231>
- Newhall, C. G., Paull, C. K., Bradbury, J. P., Higuera-Gundy, A., Poppe, L. J., Self, S., Bonar Sharpless, N., & Ziagos, J. (1987). Recent geologic history of lake Atitlán, a caldera lake in western Guatemala. *Journal of Volcanology and Geothermal Research*, 33(1–3), 81–107. [https://doi.org/10.1016/0377-0273\(87\)90055-2](https://doi.org/10.1016/0377-0273(87)90055-2)
- Newhall, C., Self, S., & Robock, A. (2018). Anticipating future Volcanic Explosivity Index (VEI) 7 eruptions and their chilling impacts. *Geosphere*, 14(2), 572–603. <https://doi.org/10.1130/GES01513.1>
- Nicholls, I. A., Oba, T., & Conrad, W. K. (1992). The nature of primary rhyolitic magmas involved in crustal evolution: Evidence from an experimental study of cumingtonite-bearing rhyolites, Taupo Volcanic Zone, New Zealand. *Geochimica et Cosmochimica Acta*, 56(3), 955–962. [https://doi.org/10.1016/0016-7037\(92\)90039-L](https://doi.org/10.1016/0016-7037(92)90039-L)
- Nishihara, A., Tatsumi, Y., Kaneko, K., Kimura, J. I., Chang, Q., Geshi, N., Miyazaki, T., Vaglarov, B. S., Hinata, H., & Suzuki-Kamata, K. (2023). Voluminous magma formation for the 30-ka Aira caldera-forming eruption in SW Japan: contributions of crust-derived felsic and mafic magmas. *Frontiers in Earth Science*, 11, 1–19. <https://doi.org/10.3389/feart.2023.1283844>
- Norrish, K., & Hutton, J. T. (1969). An accurate X-ray spectrographic method for the analysis of a wide range of geological samples. *Geochimica et Cosmochimica Acta*, 33(4), 431–453. [https://doi.org/10.1016/0016-7037\(69\)90126-4](https://doi.org/10.1016/0016-7037(69)90126-4)
- Nowell, G. M., & Parrish, R. R. (2001). Simultaneous acquisition of isotope compositions and parent/daughter ratios by non-isotope dilution solution-mode plasma ionisation multi-collector mass spectrometry (PIMMS). In G. Holland & S. D. Tanner (Eds.) *Plasma Source Mass Spectrometry: The New Millenium* pp. 298–310. Royal Society of Chemistry, Cambridge. <http://dx.doi.org/10.1039/9781847551696-00298>
- O'Hara, M. J., & Fry, N. (1996). The highly compatible trace element paradox - Fractional crystallization revisited. *Journal of Petrology*, 37(4), 859–890. <https://doi.org/10.1093/petrology/37.4.859>

- Padilla, A. J., & Gualda, G. A. R. (2016). Crystal-melt elemental partitioning in silicic magmatic systems: An example from the Peach Spring Tuff high-silica rhyolite, Southwest USA. *Chemical Geology*, 440, 326–344. <https://doi.org/10.1016/j.chemgeo.2016.07.004>
- Pamukcu, A. S., Carley, T. L., Gualda, G. A. R., Miller, C. F., & Ferguson, C. A. (2013). The evolution of the Peach Spring giant magma body: Evidence from accessory mineral textures and compositions, bulk pumice and glass geochemistry, and rhyolite-MELTS modeling. *Journal of Petrology*, 54(6), 1109–1148. <https://doi.org/10.1093/petrology/egt007>
- Paterson, S. R., & Ducea, M. N. (2015). Arc magmatic tempos: Gathering the evidence. *Elements*, 11(2), 91–98. <https://doi.org/10.2113/gselements.11.2.91>
- Patiño Douce, A. E., & Beard, J. S. (1995). Dehydration-melting of biotite gneiss and quartz amphibolite from 3 to 15 kbar. *Journal of Petrology*, 36(3), 707–738. <https://doi.org/10.1093/petrology/36.3.707>
- Patiño Douce, A. E., & Beard, J. S. (1996). Effects of P, $f(\text{O}_2)$ and Mg/Fe ratio on dehydration melting of model metagreywackes. *Journal of Petrology*, 37(5), 999–1024. <https://doi.org/10.1093/petrology/37.5.999>
- Patino, L. C., Carr, M. J., & Feigenson, M. D. (1997). Cross-arc geochemical variations in volcanic fields in Honduras C.A.: progressive changes in source with distance from the volcanic front. *Contributions to Mineralogy and Petrology*, 129(4), 341–351. <https://doi.org/10.1007/s004100050341>
- Patino, L. C., Carr, M. J., & Feigenson, M. D. (2000). Local and regional variations in Central American arc lavas controlled by variations in subducted sediment input. *Contributions to Mineralogy and Petrology*, 138(3), 265–283. <https://doi.org/10.1007/s004100050562>
- Patino, L. C., Velbel, M. A., Price, J. R., & Wade, J. A. (2003). Trace element mobility during spheroidal weathering of basalts and andesites in Hawaii and Guatemala. *Chemical Geology*, 202(3–4), 343–364. <https://doi.org/10.1016/j.chemgeo.2003.01.002>
- Peccerillo, A., & Taylor, S. R. (1976). Geochemistry of Eocene calc-alkaline volcanic rocks from the Kastamonu area, Northern Turkey. *Contributions to Mineralogy and Petrology*, 58(1), 63–81. <https://doi.org/10.1007/BF00384745>
- Pedrazzi, D., Sunye-Puchol, I., Aguirre-Díaz, G., Costa, A., Smith, V. C., Poret, M., Dávila-Harris, P., Miggins, D. P., Hernández, W., & Gutiérrez, E. (2019). The Ilopango Tierra Blanca Joven (TBJ) eruption, El Salvador: Volcano-stratigraphy and physical characterization of the major Holocene event of Central America. *Journal of Volcanology and Geothermal Research*, 377, 81–102. <https://doi.org/10.1016/j.jvolgeores.2019.03.006>
- Peters, S. T. M., Troll, V. R., Weis, F. A., Dallai, L., Chadwick, J. P., & Schulz, B. (2017). Amphibole megacrysts as a probe into the deep plumbing system of Merapi volcano, Central Java, Indonesia. *Contributions to Mineralogy and Petrology*, 172, 16. <https://doi.org/10.1007/s00410-017-1338-0>
- Petrelli, M., & Zellmer, G. F. (2020). Rates and Timescales of Magma Transfer, Storage, Emplacement, and Eruption. In F. Vetere (Ed.), *Dynamic Magma Evolution* (pp. 1–41). Geophysical Monograph Series. <https://doi.org/https://doi.org/10.1002/9781119521143.ch1>
- Petrelli, M., El Omari, K., Spina, L., Le Guer, Y., La Spina, G., & Perugini, D. (2018). Timescales of water accumulation in magmas and implications for short warning times of explosive eruptions. *Nature Communications*, 9(1). <https://doi.org/10.1038/s41467-018-02987-6>
- Pflaker, G. (1976). Tectonic aspects of the Guatemala earthquake of 4 February 1976. *Science*, 193(4259), 1201–1208. <https://doi:10.1126/science.193.4259.1201>
- Phipps Morgan, J., Ranero, C. R., & Vannucchi, P. (2008). Intra-arc extension in Central America: Links between plate motions, tectonics, volcanism, and geochemistry. *Earth and Planetary Science Letters*, 272(1–2), 365–371. <https://doi.org/10.1016/j.epsl.2008.05.004>
- Piccoli, P. M., & Candela, P. A. (2002). Apatite in igneous systems. *Reviews in Mineralogy and Geochemistry*, 48(1), 255–292. <https://doi.org/10.2138/rmg.2002.48.6>

- Pierce, K. L., & Morgan, L. A. (2009). Is the track of the Yellowstone hotspot driven by a deep mantle plume? - Review of volcanism, faulting, and uplift in light of new data. *Journal of Volcanology and Geothermal Research*, 188(1–3), 1–25.
<https://doi.org/10.1016/j.jvolgeores.2009.07.009>
- Pistone, M., Arzilli, F., Dobson, K. J., Cordonnier, B., Reusser, E., Ulmer, P., Marone, F., Whittington, A. G., Mancini, L., Fife, J. L., & Blundy, J. D. (2015). Gas-driven filter pressing in magmas: Insights into in-situ melt segregation from crystal mushes. *Geology*, 43(8), 699–702. <https://doi.org/10.1130/G36766.1>
- Ponomareva, V., Melekestsev, I., Braitseva, O., Churikova, T., Pevzner, M., & Sulerzhitsky, L. (2007). Late Pleistocene-Holocene volcanism on the Kamchatka Peninsula, northwest Pacific region. *Geophysical Monograph Series*, 172, 165–198.
<https://doi.org/10.1029/172GM15>
- Pouchou, J. L., & Pichoir, F. (1984). PAP correction procedure for improved quantitative analysis. In J. T. Armstrong (Ed.), *Microbeam Analysis*, pp. 104–106. San Francisco Press, San Francisco.
- Putirka, K. (2008). Thermometers and barometers for volcanic systems. *Reviews in Mineralogy and Geochemistry*, 69(1), 61–120. <https://doi.org/10.2138/rmg.2008.69.3>
- Putirka, K. (2016). Amphibole thermometers and barometers for igneous systems and some implications for eruption mechanisms of felsic magmas at arc volcanoes. *American Mineralogist*, 101(4), 841–858. <https://doi.org/10.2138/am-2016-5506>
- Ranero, C. R., Morgan, J. P., McIntosh, K. D., & Reichert, C. (2003). Flexural faulting and mantle serpentinization at the Middle American trench. *Nature*, 425(6956), 367–373.
<https://doi.org/10.1038/nature01961>
- Rapp, R. P., & Watson, E. B. (1995). Dehydration melting of metabasalt at 8–32 kbar: Implications for continental growth and crust-mantle recycling. *Journal of Petrology*, 36(4), 891–931.
<https://doi.org/10.1093/petrology/36.4.891>
- Ratschbacher, L., Franz, L., Min, M., Bachmann, R., Martens, U., Stanek, K., Stubner, K., Nelson, B. K., Herrmann, U., Weber, B., Lopez-Martinez, M., Jonckheere, R., Sperner, B., Tichomirowa, M., McWilliams, M. O., Gordon, M., Meschede, M., Bock, P., Gordon, M., ... Bock, P. (2009). The North American – Caribbean Plate boundary in Mexico – Guatemala – Honduras. In J. K. H. Lorente & J. L. Pindell (Eds.), *The Origin and Evolution of the Caribbean Plate* pp. 219–293, Geological Society, London.
<https://doi.org/10.1144/SP328.11>
- Reubi, O., & Blundy, J. (2008). Assimilation of plutonic roots, formation of high-K “exotic” melt inclusions and genesis of andesitic magmas at Volcán de Colima, Mexico. *Journal of Petrology*, 49(12), 2221–2243. <https://doi.org/10.1093/petrology/egn066>
- Reubi, O., & Blundy, J. (2009). A dearth of intermediate melts at subduction zone volcanoes and the petrogenesis of arc andesites. *Nature*, 461, 1269–1273.
<https://doi.org/10.1038/nature08510>
- Reubi, O., & Müntener, O. (2022). Making andesites and the continental crust: Mind the step when wet. *Journal of Petrology*, 63(6), egac044.
<https://doi.org/10.1093/petrology/egac044>
- Richards, M. A., Alvarez, W., Self, S., Karlstrom, L., Renne, P. R., Manga, M., Sprain, C. J., Smit, J., Vanderkluisen, L., & Gibson, S. A. (2015). Triggering of the largest Deccan eruptions by the Chicxulub impact. *Bulletin of the Geological Society of America*, 127(11–12), 1507–1520.
<https://doi.org/10.1130/B31167.1>
- Ridolfi, F. (2021). Amp-tb2: An updated model for calcic amphibole thermobarometry. *Minerals*, 11(3), 324. <https://doi.org/10.3390/min11030324>
- Ridolfi, F., & Renzulli, A. (2012). Calcic amphiboles in calc-alkaline and alkaline magmas: Thermobarometric and chemometric empirical equations valid up to 1,130°C and 2.2 GPa.

- Contributions to Mineralogy and Petrology*, 163(5), 877–895.
<https://doi.org/10.1007/s00410-011-0704-6>
- Ridolfi, F., Puerini, M., Renzulli, A., Menna, M., & Toulkeridis, T. (2008). The magmatic feeding system of El Reventador volcano (Sub-Andean zone, Ecuador) constrained by texture, mineralogy and thermobarometry of the 2002 erupted products. *Journal of Volcanology and Geothermal Research*, 176(1), 94–106.
<https://doi.org/10.1016/j.jvolgeores.2008.03.003>
- Ridolfi, F., Renzulli, A., & Puerini, M. (2010). Stability and chemical equilibrium of amphibole in calc-alkaline magmas: An overview, new thermobarometric formulations and application to subduction-related volcanoes. *Contributions to Mineralogy and Petrology*, 160(1), 45–66. <https://doi.org/10.1007/s00410-009-0465-7>
- Roberts, M. P., & Clemens, J. D. (1993). Origin of high-potassium, calc-alkaline, I-type granitoids. *Geology*, 21(9), 825–828. [https://doi.org/10.1130/0091-7613\(1993\)021%3C0825:OOHPTA%3E2.3.CO;2](https://doi.org/10.1130/0091-7613(1993)021%3C0825:OOHPTA%3E2.3.CO;2)
- Rogers, G., & Hawkesworth, C. J. (1989). A geochemical traverse across the North Chilean Andes: evidence for crust generation from the mantle wedge. *Earth and Planetary Science Letters*, 91(3–4), 271–285. [https://doi.org/10.1016/0012-821X\(89\)90003-4](https://doi.org/10.1016/0012-821X(89)90003-4)
- Rogers, R. D., & Mann, P. (2007). Transtensional deformation of the western Caribbean-North America plate boundary zone. *Geological Society of America Special Paper*, 428(3), 37–64. [https://doi.org/10.1130/2007.2428\(03\)](https://doi.org/10.1130/2007.2428(03))
- Rollinson, H. R. (1993). *Using geochemical data: evaluation, presentation, interpretation*. Taylor & Francis, London. <https://doi.org/10.4324/9781315845548>
- Romick, J. D., Kay, S. M., & Kay, R. W. (1992). The influence of amphibole fractionation on the evolution of calc-alkaline andesite and dacite tephra from the central Aleutians, Alaska. *Contributions to Mineralogy and Petrology*, 112(1), 101–118.
<https://doi.org/10.1007/BF00310958>
- Rose, W. I. (1972a). Notes on the 1902 Eruption of Santa Maria Volcano, Guatemala. *Bulletin Volcanologique*, 36, 29–45. <https://doi.org/10.1007/BF02596981>
- Rose, W. I. (1972b). Santiaguito Volcanic Dome, Guatemala. *Geological Society of America Bulletin*, 83(5), 1413–1434. [https://doi.org/10.1130/0016-7606\(1972\)83\[1413:SVDG\]2.0.CO;2](https://doi.org/10.1130/0016-7606(1972)83[1413:SVDG]2.0.CO;2)
- Rose, W. I. (1987). Santa María, Guatemala: Bimodal soda-rich calc-alkalic stratovolcano. *Journal of Volcanology and Geothermal Research*, 33(1–3), 109–129.
[https://doi.org/10.1016/0377-0273\(87\)90056-4](https://doi.org/10.1016/0377-0273(87)90056-4)
- Rose, W. I., Grant, N. K., & Easter, J. (1979). Geochemistry of the Los Chocoyos ash, Quezaltenango Valley, Guatemala. *Geological Society of America Special Paper*, 180, 87–99.
<https://doi.org/10.1130/SPE180-p87>
- Rose, W. I., Penfield, G. T., Drexler, J. W., & Larson, P. B. (1980). Geochemistry of the andesite flank lavas of three composite cones within the Atitlán Cauldron, Guatemala. *Bulletin of Volcanology*, 43(1), 131–153. <https://doi.org/10.1007/BF02597617>
- Rose, W. I., Newhall, C. G., Bornhorst, T. J., & Self, S. (1987). Quaternary silicic pyroclastic deposits of Atitlán Caldera, Guatemala. *Journal of Volcanology and Geothermal Research*, 33(1–3), 57–80. [https://doi.org/10.1016/0377-0273\(87\)90054-0](https://doi.org/10.1016/0377-0273(87)90054-0)
- Rose, W. I., Conway, F. M., Pullinger, C. R., Deino, A., & McIntosh, W. C. (1999). An improved age framework for late Quaternary silicic eruptions in northern Central America. *Bulletin of Volcanology*, 61, 106–120. <https://doi.org/10.1007/s004450050266>
- Rottier, B., Audétat, A., Koděra, P., & Lexa, J. (2020). Magmatic evolution of the mineralized Štiavnica volcano (Central Slovakia): Evidence from thermobarometry, melt inclusions, and sulfide inclusions. *Journal of Volcanology and Geothermal Research*, 401, 106967.
<https://doi.org/10.1016/j.jvolgeores.2020.106967>

- Rougier, J., Sparks, R. S. J., Cashman, K. V., & Brown, S. K. (2018). The global magnitude–frequency relationship for large explosive volcanic eruptions. *Earth and Planetary Science Letters*, 482, 621–629. <https://doi.org/10.1016/j.epsl.2017.11.015>
- Rubin, A. E., Cooper, K. M., Till, C. B., Kent, A. J. R., Costa, F., Bose, M., Gravley, D., Deering, C., & Cole, J. (2017). Rapid cooling and cold storage in a silicic magma reservoir recorded in individual crystals. *Science*, 356(6343), 1154–1157. <https://doi.org/10.1126/science.aam8720>
- Rüpke, L. H., Morgan, J. P., Hort, M., & Connolly, J. A. D. (2002). Are the regional variations in Central American arc lavas due to differing basaltic versus peridotitic slab sources of fluids? *Geology*, 30(11), 1035–1038. [https://doi.org/10.1130/0091-7613\(2002\)030<1035:ATRVIC>2.0.CO;2](https://doi.org/10.1130/0091-7613(2002)030<1035:ATRVIC>2.0.CO;2)
- Ruprecht, P., Simon, A. C., & Fiege, A. (2020). The survival of mafic magmatic enclaves and the timing of magma recharge. *Geophysical Research Letters*, 47, e2020GL087186. <https://doi.org/10.1029/2020GL087186>
- Rutherford, M. J., & Hill, P. M. (1993). Magma ascent rates from amphibole breakdown: An experimental study applied to the 1980–1986 Mount St. Helens eruptions. *Journal of Geophysical Research*, 98(B11), 19667–19685. <https://doi.org/10.1029/93JB01613>
- Rutherford, M. J., & Devine, J. D. (2008). Magmatic conditions and processes in the storage zone of the 2004–2006 Mount St. Helens dacite. *US Geological Survey Professional Paper*, 1750, 703–726. <https://doi.org/10.3133/pp175031>
- Sadofsky, S. J., Portnyagin, M., Hoernle, K., & van den Bogaard, P. (2008). Subduction cycling of volatiles and trace elements through the Central American volcanic arc: Evidence from melt inclusions. *Contributions to Mineralogy and Petrology*, 155(4), 433–456. <https://doi.org/10.1007/s00410-007-0251-3>
- Saginer, I., Gazel, E., Carr, M. J., Swisher, C. C., & Turrin, B. (2011). New Pliocene–Pleistocene $^{40}\text{Ar}/^{39}\text{Ar}$ ages fill in temporal gaps in the Nicaraguan volcanic record. *Journal of Volcanology and Geothermal Research*, 202(1–2), 143–152. <https://doi.org/10.1016/j.jvolgeores.2011.02.002>
- Saginer, I., Gazel, E., Condie, C., & Carr, M. J. (2013). Evolution of geochemical variations along the Central American volcanic front. *Geochemistry, Geophysics, Geosystems*, 14(10), 4504–4522. <https://doi.org/10.1002/ggge.20259>
- Salisbury, M. J., Jicha, B. R., de Silva, S. L., Singer, B. S., Jiménez, N. C., & Ort, M. H. (2011). $^{40}\text{Ar}/^{39}\text{Ar}$ chronostratigraphy of Altiplano–Puna volcanic complex ignimbrites reveals the development of a major magmatic province. *Bulletin of the Geological Society of America*, 123(5), 821–840. <https://doi.org/10.1130/B30280.1>
- Sapper, K. (1897). Northern Central America with a trip to the highland of Anahuac: Travels and studies of the years 1888–1895. Friedrich Viewig, Braunschweig.
- Sapper, K. (1925). The Volcanoes of Central America. Max Niemeyer, Halle.
- Schaen, A. J., Jicha, B. R., Hodges, K. V., Vermeesch, P., Stelten, M. E., Mercer, C. M., Phillips, D., Rivera, T. A., Jourdan, F., Matchan, E. L., Hemming, S. R., Morgan, L. E., Kelley, S. P., Cassata, W. S., Heizler, M. T., Vasconcelos, P. M., Benowitz, J. A., Koppers, A. P., Mark, D. F., Niespolo, E. M., Sprain, C. J., Hames, W. E., Kuiper, K. F., Turrin, B. D., Renne, P. R., Ross, J., Nomade, S., Guillou, H., Webb, L. E., Cohen, B. A., Calvert, A. T., Joyce, N., Ganerød, M., Wijbrans, J., Ishizuka, O., He, H., Ramirez, A., Pfänder, J. A., Lopez-Martínez, M., Qiu, H., Singer, B. S. (2020). Interpreting and reporting $^{40}\text{Ar}/^{39}\text{Ar}$ geochronologic data. *GSA Bulletin*, 133(3–4), 461–487. <https://doi.org/10.1130/B35560.1/5084442/b35560.pdf>
- Schindlbeck, J. C., Kutterolf, S., Freundt, A., Alvarado, G. E., Wang, K.-L., Straub, S. M., Hemming, S. R., Frische, M., & Woodhead, J. D. (2016a). Late Cenozoic tephrostratigraphy offshore the southern Central American Volcanic Arc: 1. Tephra ages and provenance. *Geochemistry Geophysics Geosystems*, 17, 4641–4668. <https://doi.org/10.1002/2015GC006205.Received>

- Schindlbeck, J. C., Kutterolf, S., Freundt, A., Straub, S. M., Vannucchi, P., & Alvarado, G. E. (2016b). Late Cenozoic tephrostratigraphy offshore the southern Central American Volcanic Arc: 2. Implications for magma production rates and subduction erosion. *Geochemistry, Geophysics, Geosystems*, 17(11), 4641–4668. <https://doi.org/10.1002/2016GC006503>
- Schindlbeck, J. C., Kutterolf, S., Freundt, A., Eisele, S., Wang, K. L., & Frische, M. (2018). Miocene to Holocene marine tephrostratigraphy offshore northern Central America and southern Mexico: Pulsed activity of known volcanic complexes. *Geochemistry, Geophysics, Geosystems*, 19(11), 4143–4173. <https://doi.org/10.1029/2018GC007832>
- Schmidt, M. W., & Sigmarsson, O. (1998). Peritectic decomposition of amphibole in shallow magma chambers causing explosive volcanism at Pico de Orizaba, Mexico. *Terra Abstracts*, 10(56).
- Schmitt, A. K. (2011). Uranium series accessory crystal dating of magmatic processes. *Annual Review of Earth and Planetary Sciences*, 39, 321–349. <https://doi.org/10.1146/annurev-earth-040610-133330>
- Schmitt, A. K., de Silva, S. L., Trumbull, R. B., & Emmermann, R. (2001). Magma evolution in the Purico ignimbrite complex, northern Chile: Evidence for zoning of a dacitic magma by injection of rhyolitic melts following mafic recharge. *Contributions to Mineralogy and Petrology*, 140(6), 680–700. <https://doi.org/10.1007/s004100000214>
- Scholl, D. W., & von Huene, R. (2007). Crustal recycling at modern subduction zones applied to the past—Issues of growth and preservation of continental basement crust, mantle geochemistry, and supercontinent reconstruction. In R. D. Jr. Hatchler, M. P. Carlson, J. H. McBride, & J. R. Martínez Catalán (Eds.), *4-D Framework of Continental Crust*. GSA Memoirs. [https://doi.org/https://doi.org/10.1130/2007.1200\(02\)](https://doi.org/https://doi.org/10.1130/2007.1200(02))
- Schultz, P. H., & Gault, D. E. (1975). Seismic effects from major basin formations on the Moon and Mercury. *The Moon*, 12(2), 159–177. <https://doi.org/10.1007/BF00577875>
- Seebeck, H., Nicol, A., Giba, M., Pettinga, J., & Walsh, J. (2014a). Geometry of the subducting Pacific plate since 20 Ma, Hikurangi margin, New Zealand. *Journal of the Geological Society*, 171(1), 131–143. <https://doi.org/10.1144/jgs2012-145>
- Seebeck, H., Nicol, A., Villamor, P., Ristau, J., & Pettinga, J. (2014b). Structure and kinematics of the Taupo Rift, New Zealand. *Tectonics*, 33(6), 1178–1199. <https://doi.org/10.1002/2014TC003569>
- Seropian, G., Kennedy, B. M., Walter, T. R., Ichihara, M., & Jolly, A. D. (2021). A review framework of how earthquakes trigger volcanic eruptions. *Nature Communications*, 12, 1004. <https://doi.org/10.1038/s41467-021-21166-8>
- Sheldrake, T. E., Scutari, M., & Caricchi, L. (2020). Tectonic controls on global variations in the record of large-magnitude explosive eruptions in volcanic arcs. *Frontiers in Earth Science*, 8, 127. <https://doi.org/10.3389/feart.2020.00127>
- Shibata, T., Yoshikawa, M., Itoh, J., Ujiie, O., Miyoshi, M., & Takemura, K. (2014). Along-arc geochemical variations in quaternary magmas of northern Kyushu Island, Japan. *Geological Society of London Special Publication*, 385(1), 15–29. <https://doi.org/10.1144/SP385.13>
- Singer, B. S., Smith, K. E., Jicha, B. R., Beard, B. L., Johnson, C. M., & Rogers, N. W. (2011). Tracking open-system differentiation during growth of Santa María Volcano, Guatemala. *Journal of Petrology*, 52(12), 2335–2363. <https://doi.org/10.1093/petrology/egr047>
- Singer, B. S., Spicuzza, M. J., Jicha, B. R., Rogers, N. W., Fournelle, J. H., Smith, K. E., Kita, N. T., Johnson, C. M., Valley, J. W., Greene, S. E., & Beard, B. L. (2013). Lying in wait: deep and shallow evolution of dacite beneath Volcán de Santa María, Guatemala. In A. Gómez-Tuena, S. M. Straub & G. F. Zellmer (Eds.), *Orogenic andesites and crustal growth* (pp. 209–234). Geological Society of London Special Publications, London <https://doi.org/10.1144/sp385.2>

- Sisson, T. W., & Bacon, C. R. (1999). Gas-driven filter pressing in magmas. *Geology*, 27(7), 613–616. [https://doi.org/10.1130/0091-7613\(1999\)027<0613:GDFPIM>2.3.CO;2](https://doi.org/10.1130/0091-7613(1999)027<0613:GDFPIM>2.3.CO;2)
- Sisson, T. W., Ratajeski, K., Hankins, W. B., & Glazner, A. F. (2005). Voluminous granitic magmas from common basaltic sources. *Contributions to Mineralogy and Petrology*, 148(6), 635–661. <https://doi.org/10.1007/s00410-004-0632-9>
- Smith, D. R., & Leeman, W. P. (1987). Petrogenesis of Mount St. Helens dacitic magmas (USA). *Journal of Geophysical Research*, 92(B10), 10313–10334. <https://doi.org/10.1029/jb092ib10p10313>
- Smith, R. L. (1979). Ash-flow magmatism. *Geological Society of America Special Paper*, 180. <https://doi.org/10.1130/SPE180-p5>
- Smith, V. C., Costa, A., Aguirre-Díaz, G., Pedrazzi, D., Scifo, A., Plunkett, G., Poret, M., Tournigand, P. Y., Miles, D., Dee, M. W., McConnell, J. R., Sunyé-Puchol, I., Harris, P. D., Sigl, M., Pilcher, J. R., Chellman, N., & Gutiérrez, E. (2020). The magnitude and impact of the 431 CE Tierra Blanca Joven eruption of Ilopango, El Salvador. *Proceedings of the National Academy of Sciences of the United States of America*, 117(42), 26061–26068. <https://doi.org/10.1073/pnas.2003008117>
- Snyder, D. (2000). Thermal effects of the intrusion of basaltic magma into a more silicic magma chamber and implications for eruption triggering. *Earth and Planetary Science Letters*, 175(3–4), 257–273. [https://doi.org/10.1016/S0012-821X\(99\)00301-5](https://doi.org/10.1016/S0012-821X(99)00301-5)
- Sparks, R. S. J., & Marshall, L. A. (1986). Thermal and mechanical constraints on mixing between mafic and silicic magmas. *Journal of Volcanology and Geothermal Research*, 29(1–4), 99–124. [https://doi.org/10.1016/0377-0273\(86\)90041-7](https://doi.org/10.1016/0377-0273(86)90041-7)
- Sparks, R. S. J., Blundy, J. D., Cashman, K. V., Jackson, M., Rust, A., & Wilson, C. J. N. (2022). Large silicic magma bodies and very large magnitude explosive eruptions. *Bulletin of Volcanology*, 84(1), 4–9. <https://doi.org/10.1007/s00445-021-01510-y>
- Spear, F. S. (1993). Metamorphic phase equilibria and pressure-temperature-time paths. *Mineralogical Society of America Monograph*.
- Spera, F. J., & Bohrsen, W. A. (2001). Energy-constrained open-system magmatic processes I: General model and energy-constrained assimilation and fractional crystallization (EC-AFC) formulation. *Journal of Petrology*, 42(5), 999–1018. <https://doi.org/10.1093/petrology/42.5.999>
- Spinks, K. D., Acocella, V., Cole, J. W., & Bassett, K. N. (2005). Structural control of volcanism and caldera development in the transtensional Taupo Volcanic Zone, New Zealand. *Journal of Volcanology and Geothermal Research*, 144(1–4), 7–22. <https://doi.org/10.1016/j.jvolgeores.2004.11.014>
- Staller, A., Martínez-Díaz, J. J., Benito, B., Alonso-Henar, J., Hernández, D., Hernández-Rey, R., & Díaz, M. (2016). Present-day crustal deformation along the El Salvador Fault Zone from ZFESNet GPS network. *Tectonophysics*, 670, 66–81. <https://doi.org/10.1016/j.tecto.2015.12.017>
- Stechern, A., Just, T., Holtz, F., Blume-Oeste, M., & Namur, O. (2017). Decoding magma plumbing and geochemical evolution beneath the Lastarria volcanic complex (Northern Chile)—Evidence for multiple magma storage regions. *Journal of Volcanology and Geothermal Research*, 338, 25–45. <https://doi.org/10.1016/j.jvolgeores.2017.03.018>
- Stepanov, A. S., Hermann, J., Rubatto, D., & Rapp, R. P. (2012). Experimental study of monazite/melt partitioning with implications for the REE, Th and U geochemistry of crustal rocks. *Chemical Geology*, 300, 200–220. <https://doi.org/10.1016/j.chemgeo.2012.01.007>
- Stern, C. R., Mohseni, P. P., & Fuenzalida, P. R. (1991). Petrochemistry and tectonic significance of lower Cretaceous Barros Arana Formation basalts, southernmost Chilean Andes. *Journal of South American Earth Sciences*, 4(4), 331–342. [https://doi.org/10.1016/0895-9811\(91\)90005-6](https://doi.org/10.1016/0895-9811(91)90005-6)

- Stern, T. W., Bateman, P. C., Morgan, B. A., Newell, M. F., & Peck, D. L. (1981). Isotopic U-Pb ages of zircon from the granitoids of the central Sierra Nevada, California. *U.S. Geological Survey Professional Papers*, 1185. <https://doi.org/10.3133/pp1185>
- Stock, M. J., Humphreys, M. C. S., Smith, V. C., Isaia, R., & Pyle, D. M. (2016). Late-stage volatile saturation as a potential trigger for explosive volcanic eruptions. *Nature Geoscience*, 9(3), 249–254. <https://doi.org/10.1038/ngeo2639>
- Stoiber, R. E., & Carr, M. J. (1973). Quaternary volcanic and tectonic segmentation of Central America. *Bulletin Volcanologique*, 37(3), 304–325. <https://doi.org/10.1007/BF02597631>
- Stoppa, L., Kutterolf, S., Rausch, J., Grobety, B., Pettke, T., Wang, K., & Hemming, S. (2018). The Malpaisillo Formation: A sequence of explosive eruptions in the mid to late Pleistocene (Nicaragua, Central America). *Journal of Volcanology and Geothermal Research*, 359, 47–67. <https://doi.org/10.1016/j.jvolgeores.2018.06.015>
- Storey, M., Roberts, R. G., & Saidin, M. (2012). Astronomically calibrated $^{40}\text{Ar}/^{39}\text{Ar}$ age for the Toba supereruption and global synchronization of late Quaternary records. *Proceedings of the National Academy of Sciences of the United States of America*, 109(46), 18684–18688. <https://doi.org/10.1073/pnas.1208178109>
- Streck, M. J. (2008). Mineral textures and zoning as evidence for open system processes. *Reviews in Mineralogy and Geochemistry*, 69(1983), 595–622. <https://doi.org/10.2138/rmg.2008.69.15>
- Sun, S. S., & McDonough, W. F. (1989). Chemical and isotopic systematics of oceanic basalts: Implications for mantle composition and processes. *Geological Society Special Publication*, 42(1), 313–345. <https://doi.org/10.1144/GSL.SP.1989.042.01.19>
- Suñe-Puchol, I., Aguirre-Díaz, G. J., Dávila-Harris, P., Miggins, D. P., Pedrazzi, D., Costa, A., Ortega-Obregón, C., Lacan, P., Hernández, W., & Gutiérrez, E. (2019a). The Ilopango caldera complex, El Salvador: Origin and early ignimbrite-forming eruptions of a graben/pull-apart caldera structure. *Journal of Volcanology and Geothermal Research*, 371, 1–19. <https://doi.org/10.1016/j.jvolgeores.2018.12.004>
- Suñe-Puchol, I., Aguirre-Díaz, G. J., Pedrazzi, D., Dávila-Harris, P., Miggins, D. P., Costa, A., Ortega-Obregón, C., Lacan, P., Gutiérrez, E., & Hernández, W. (2019b). The Ilopango caldera complex, El Salvador: Stratigraphic revision of the complete eruptive sequence and recurrence of large explosive eruptions. *Journal of Volcanology and Geothermal Research*, 374, 100–119. <https://doi.org/10.1016/j.jvolgeores.2019.02.011>
- Sun, S. S., & McDonough, W. F. (1989). Chemical and isotopic systematics of oceanic basalts: Implications for mantle composition and processes. *Geological Society Special Publication*, 42(1), 313–345. <https://doi.org/10.1144/GSL.SP.1989.042.01.19>
- Syracuse, E. M., & Abers, G. A. (2006). Global compilation of variations in slab depth beneath arc volcanoes and implications. *Geochemistry, Geophysics, Geosystems*, 7, Q05017. <https://doi.org/10.1029/2005GC001045>
- Szymanowski, D., Wotzlaw, J. F., Ellis, B. S., Bachmann, O., Guillong, M., & Von Quadt, A. (2017). Protracted near-solidus storage and pre-eruptive rejuvenation of large magma reservoirs. *Nature Geoscience*, 10(10), 777–782. <https://doi.org/10.1038/ngeo3020>
- Tait, S., Jaupart, C., & Vergnolle, S. (1989). Pressure, gas content and eruption periodicity of a shallow, crystallising magma chamber. *Earth and Planetary Science Letters*, 92(1), 107–123. [https://doi.org/10.1016/0012-821X\(89\)90025-3](https://doi.org/10.1016/0012-821X(89)90025-3)
- Tatsumi, Y., & Suzuki, T. (2009). Tholeiitic vs calc-alkalic differentiation and evolution of arc crust: Constraints from melting experiments on a basalt from the Izu-Bonin-Mariana arc. *Journal of Petrology*, 50(8), 1575–1603. <https://doi.org/10.1093/petrology/egp044>
- Tepper, J. H., Nelson, B. K., Bergantz, G. W., & Irving, A. J. (1993). Petrology of the Chilliwack batholith, North Cascades, Washington: Generation of calc-alkaline granitoids by melting of mafic lower crust with variable water fugacity. *Contributions to Mineralogy and Petrology*, 113(3), 333–351. <https://doi.org/10.1007/BF00286926>

- Thompson, A. B. (1982). Dehydration melting of pelitic rocks and the generation of H₂O-undersaturated granitic liquids. *American Journal of Science*, 282(10), 1567-1595. <https://doi.org/10.2475/ajs.282.10.1567>
- Thompson, G., Smith, I., & Malpas, J. (2001). Origin of oceanic phonolites by crystal fractionation and the problem of the Daly gap: An example from Rarotonga. *Contributions to Mineralogy and Petrology*, 142(3), 336–346. <https://doi.org/10.1007/s004100100294>
- Thornber, C. R., Pallister, J. S., Lowers, H. A., Rowe, M. C., Mandeville, C. W., & Meeker, G. P. (2008). Chemistry, mineralogy, and petrology of amphibole in Mount St. Helens 2004-2006 dacite. *US Geological Survey Professional Paper*, 1750, 727–754. <https://doi.org/10.3133/pp175032>
- Tollan, P. M. E., Bindeman, I., & Blundy, J. D. (2012). Cumulate xenoliths from St. Vincent, Lesser Antilles Island Arc: A window into upper crustal differentiation of mantle-derived basalts. *Contributions to Mineralogy and Petrology*, 163(2), 189–208. <https://doi.org/10.1007/s00410-011-0665-9>
- Tolstykh, M. L., Naumov, V. B., & Babansky, A. D. (2007). Composition, volatile components, and trace elements in andesitic melts of the Kurile-Kamchatka region. *Acta Petrologica Sinica*, 23(1), 93-104.
- Tommasini, S., Bindi, L., Savia, L., Mangler, M. F., Orlando, A., & Petrone, C. M. (2022). Critical assessment of pressure estimates in volcanic plumbing systems: The case study of Popocatepetl volcano, Mexico. *Lithos*, 408, 106540. <https://doi.org/10.1016/j.lithos.2021.106540>
- Tong, X., Liu, Y., Hu, Z., Chen, H., Zhou, L., Hu, Q., Xu, R., Deng, L., Chen, C., Yang, L., & Gao, S. (2016). Accurate Determination of Sr Isotopic Compositions in Clinopyroxene and Silicate Glasses by LA-MC-ICP-MS. *Geostandards and Geoanalytical Research*, 40(1), 85–99. <https://doi.org/10.1111/j.1751-908X.2015.00315.x>
- Torres-de Leon, R., Solari, L. A., Ortega-Gutierrez, F., & Martens, U. (2012). The Chortís Block—southwestern México connections: U-Pb zircon geochronology constraints. *American Journal of Science*, 312(3), 288–313. <https://doi.org/10.2475/03.2012.02>
- Townsend, M., Huber, C., Degruyter, W., & Bachmann, O. (2019). Magma chamber growth during intercaldera periods: Insights from thermo-mechanical modelling with applications to Laguna del Maule, Campi Flegrei, Santorini, and Aso. *Geochemistry, Geophysics, Geosystems*, 20(3), 1574–1591. <https://doi.org/10.1029/2018GC008103>
- Trail, D., Watson, E. B., & Tailby, N. D. (2012). Ce and Eu anomalies in zircon as proxies for the oxidation state of magmas. *Geochimica et Cosmochimica Acta*, 97, 70–87. <https://doi.org/10.1016/j.gca.2012.08.032>
- Tsujimori, T., Sisson, V. B., Liou, J. G., Harlow, G. E., & Sorensen, S. S. (2006). Petrologic characterization of Guatemalan lawsonite eclogite: Eclogitization of subducted oceanic crust in a cold subduction zone. In B. R. Hacker, W. C. McClelland, & J. G. Liou (Eds.), *Ultra high-pressure metamorphism: Deep continental subduction*. Geological Society of America, Boulder, Colorado. [https://doi.org/10.1130/2006.2403\(09\)](https://doi.org/10.1130/2006.2403(09))
- Turner, S. J., & Langmuir, C. H. (2015). What processes control the chemical compositions of arc front stratovolcanoes? *Geochemistry Geophysics Geosystems*, 16(1), 267–300. <https://doi.org/10.1002/2014GC005684.Key>
- Turner, S. P., Foden, J. D., & Morrison, R. S. (1992). Derivation of some A-type magmas by fractionation of basaltic magma: An example from the Padthaway Ridge, South Australia. *Lithos*, 28(2), 151–179. [https://doi.org/10.1016/0024-4937\(92\)90029-X](https://doi.org/10.1016/0024-4937(92)90029-X)
- Ubide, T., Mollo, S., Zhao, J., Nazzari, M., & Scarlato, P. (2019). Sector-zoned clinopyroxene as a recorder of magma history, eruption triggers, and ascent rates. *Geochimica et Cosmochimica Acta*, 251, 265–283. <https://doi.org/10.1016/j.gca.2019.02.021>

- Umeda, K., Ban, M., Hayashi, S., & Kusano, T. (2013). Tectonic shortening and coeval volcanism during the Quaternary, Northeast Japan arc. *Journal of Earth System Science*, 122(1), 137–147. <https://doi.org/10.1007/s12040-012-0245-z>
- Vallance, J. W., Schilling, S. P., Matias, O., Rose, W. I., & Howell, M. M. (2001). Volcano Hazards at Fuego and Acatenango, Guatemala. *US Geological Survey Open-File Report 01-431*. <https://doi.org/10.3133/ofr01431>
- Van Avendonk, H. J. A., Holbrook, W. S., Lizarralde, D., & Denyer, P. (2011). Structure and serpentinization of the subducting Cocos plate offshore Nicaragua and Costa Rica. *Geochemistry, Geophysics, Geosystems*, 12, Q06009. <https://doi.org/10.1029/2011GC003592>
- Vance, J. A. (1965). Zoning in igneous plagioclase: Patchy zoning. *The Journal of Geology*, 73(4), 636–651. <https://doi.org/10.1086/627099>
- Vannucchi, P., Scholl, D. W., Meschede, M., & McDougall-Reid, K. (2001). Tectonic erosion and consequent collapse of the Pacific margin of Costa Rica: Combined implications from ODP Leg 170, seismic offshore data, and regional geology of the Nicoya Peninsula. *Tectonics*, 20(5), 649–668. <https://doi.org/10.1029/2000TC001223>
- Vazquez, J. A., & Reid, M. R. (2002). Constraining the timing of magmatic evolution in the Youngest Toba Tuff rhyolite through dating of zoning in allanite. Twelfth Annual VM Goldschmidt Conference.
- Vielzeuf, D., & Holloway, J. R. (1988). Experimental determination of the fluid-absent melting relations in the pelitic system - Consequences for crustal differentiation. *Contributions to Mineralogy and Petrology*, 98(3), 257–276. <https://doi.org/10.1007/BF00375178>
- Vielzeuf, D., & Montel, J. M. (1994). Partial melting of metagreywackes. Part I. Fluid-absent experiments and phase relationships. *Contributions to Mineralogy and Petrology*, 117(4), 375–393. <https://doi.org/10.1007/BF00307272>
- Villamor, P., Berryman, K. R., Ellis, S. M., Schreurs, G., Wallace, L. M., Leonard, G. S., Langridge, R. M., & Ries, W. F. (2017). Rapid Evolution of Subduction-Related Continental Intraarc Rifts: The Taupo Rift, New Zealand. *Tectonics*, 36(10), 2250–2272. <https://doi.org/10.1002/2017TC004715>
- Vogel, T. A., Patino, L. C., Alvarado, G. E., & Gans, P. B. (2004). Silicic ignimbrites within the Costa Rican volcanic front: Evidence for the formation of continental crust. *Earth and Planetary Science Letters*, 226(1–2), 149–159. <https://doi.org/10.1016/j.epsl.2004.07.013>
- Vogel, T. A., Patino, L. C., Eaton, J. K., Valley, J. W., Rose, W. I., Alvarado, G. E., & Viray, E. L. (2006). Origin of silicic magmas along the Central American volcanic front: Genetic relationship to mafic melts. *Journal of Volcanology and Geothermal Research*, 156, 217–228. <https://doi.org/10.1016/j.jvolgeores.2006.03.002>
- Vukadinovic, D. (1993). Are Sr enrichments in arc basalts due to plagioclase accumulation? *Geology*, 21(7), 611–614. [https://doi.org/10.1130/0091-7613\(1993\)021<0611:ASEIAB>2.3.CO;2](https://doi.org/10.1130/0091-7613(1993)021<0611:ASEIAB>2.3.CO;2)
- Walker, J. A., Carr, M. J., Patino, L. C., Johnson, C. M., Feigenson, M. D., & Ward, R. L. (1995). Abrupt change in magma generation processes across the Central American arc in southeastern Guatemala: flux-dominated melting near the base of the wedge to decompression melting near the top of the wedge. *Contributions to Mineralogy and Petrology*, 120(3–4), 378–390. <https://doi.org/10.1007/BF00306515>
- Walker, J. A., Patino, L. C., Cameron, B. I., & Carr, M. J. (2000). Petrogenetic insights provided by compositional transects across the Central American arc: Southeastern Guatemala and Honduras. *Journal of Geophysical Research*, 105(B8), 18949–18963. <https://doi.org/10.1029/2000JB900173>
- Walker, J. A., Mickelson, J. E., Thomas, R. B., Patino, L. C., Cameron, B., Carr, M. J., Feigenson, M. D., & Edwards, R. L. (2007). U-series disequilibria in Guatemalan lavas, crustal contamination, and implications for magma genesis along the Central American

- subduction zone. *Journal of Geophysical Research: Solid Earth*, 112, B06205.
<https://doi.org/10.1029/2006JB004589>
- Walker, J. A., Singer, B. S., Jicha, B. R., Cameron, B. I., Carr, M. J., & Olney, J. L. (2011). Monogenetic, behind-the-front volcanism in southeastern Guatemala and western El Salvador: $^{40}\text{Ar}/^{39}\text{Ar}$ ages and tectonic implications. *Lithos*, 123(1–4), 243–253.
<https://doi.org/10.1016/j.lithos.2010.09.016>
- Waters, L. E., & Lange, R. A. (2015). An updated calibration of the plagioclase-liquid hygrometer-thermometer applicable to basalts through rhyolites. *American Mineralogist*, 100(10), 2172–2184. <https://doi.org/10.2138/am-2015-5232>
- Watts, A. W., Greeley, R., & Melosh, H. J. (1991). The formation of terrains antipodal to major impacts. *Icarus*, 93(1), 159–168. [https://doi.org/10.1016/0019-1035\(91\)90170-X](https://doi.org/10.1016/0019-1035(91)90170-X)
- Weber, G., Blundy, J., & Bevan, D. (2023). Mush amalgamation, short residence, and sparse detectability of eruptible magma before Andean super-eruptions. *Geochemistry, Geophysics, Geosystems*, 24, e2022GC010732. <https://doi.org/10.1029/2022gc010732>
- Wehrmann, H., Hoernle, K., Garbe-Schönberg, D., Jacques, G., Mahlke, J., & Schumann, K. (2014). Insights from trace element geochemistry as to the roles of subduction zone geometry and subduction input on the chemistry of arc magmas. *International Journal of Earth Sciences*, 103(7), 1929–1944. <https://doi.org/10.1007/s00531-013-0917-1>
- Weinberg, R. F., & Hasalová, P. (2015). Water-fluxed melting of the continental crust: A review. *Lithos*, 212, 158–188. <https://doi.org/10.1016/j.lithos.2014.08.021>
- Welsch, B., Hammer, J., Baronnet, A., Jacob, S., Hellebrand, E., & Sinton, J. (2016). Clinopyroxene in postshield Haleakala ankaramite: 2. Texture, compositional zoning and supersaturation in the magma. *Contributions to Mineralogy and Petrology*, 171, 6.
<https://doi.org/10.1007/s00410-015-1213-9>
- Whattam, S. A., & Stern, R. J. (2015). Late Cretaceous plume-induced subduction initiation along the southern margin of the Caribbean and NW South America: The first documented example with implications for the onset of plate tectonics. *Gondwana Research*, 27(1), 38–63. <https://doi.org/10.1016/j.gr.2014.07.011>
- Whattam, S. A., & Stern, R. J. (2016). Arc magmatic evolution and the construction of continental crust at the Central American Volcanic Arc system. *International Geology Review*, 58(6), 653–686. <https://doi.org/10.1080/00206814.2015.1103668>
- Wickham, S. M. (1987). The segregation and emplacement of granitic magmas. *Journal of Geological Society*, 144(2), 281–297. <https://doi.org/10.1144/gsjgs.144.2.0281>
- Wieser, P. E., Petrelli, M., Lubbers, J., Wieser, E., Özyayın, S., Kent, A. J. R., & Till, C. B. (2022). Thermobar: An open-source Python3 tool for thermobarometry and hygrometry. *Volcanica*, 5(2), 349–384. <https://doi.org/10.30909/vol.05.02.349384>
- Wieser, P. E., Kent, A. J. R., Till, C. B., Donovan, J., Neave, D. A., Blatter, D. L., & Krawczynski, M. J. (2023a). Barometers Behaving Badly I: Assessing the Influence of Analytical and Experimental Uncertainty on Clinopyroxene Thermobarometry Calculations at Crustal Conditions. *Journal of Petrology*, 64(2), egac126.
<https://doi.org/10.1093/petrology/egac126>
- Wieser, P. E., Kent, A. J. R., & Till, C. B. (2023b). Barometers behaving badly II: A critical evaluation of Cpx-only and Cpx-Liq thermobarometry in variably-hydrous arc magmas. *Journal of Petrology* 64, egad050. <https://doi.org/10.1093/petrology/egad050>
- Williams, D. A., & Greeley, R. (1994). Assessment of Antipodal-Impact Terrains on Mars. *Icarus*, 110(2), 196–202. <https://doi.org/10.1006/icar.1994.1116>
- Williams, H., & McBirney, A. R. (1969). Volcanic history of Honduras. *University of California Publications in Geological Sciences*, 85, 1–101.
- Wilson, C. J. N., Cooper, G. F., Chamberlain, K. J., Barker, S. J., Myers, M. L., Kemp, F. I., & Farrell, J. (2021). No single model for supersized eruptions and their magma bodies. *Nature*

- Reviews Earth & Environment*, 2(9), 610–627. <https://doi.org/10.1038/s43017-021-00191-7>
- Wolff, J. A., Ellis, B. S., Ramos, F. C., Starkel, W. A., Boroughs, S., Olin, P. H., & Bachmann, O. (2015). Remelting of cumulates as a process for producing chemical zoning in silicic tuffs: A comparison of cool, wet and hot, dry rhyolitic magma systems. *Lithos*, 236, 275–286. <https://doi.org/10.1016/j.lithos.2015.09.002>
- Wolff, J. A., Forni, F., Ellis, B. S., & Szymanowski, D. (2020). Europium and barium enrichments in compositionally zoned felsic tuffs: A smoking gun for the origin of chemical and physical gradients by cumulate melting. *Earth and Planetary Science Letters*, 540, 116251. <https://doi.org/10.1016/j.epsl.2020.116251>
- Wunderman, R. L., & Rose, W. I. (1984). Amatitlán, an actively resurging cauldron 10 km south of Guatemala City. *Journal of Geophysical Research: Solid Earth*, 89(B10), 8525–8539. <https://doi.org/10.1029/JB089iB10p08525>
- Yamamoto, T., Kudo, T., & Isizuka, O. (2018). Temporal variations in volumetric magma eruption rates of Quaternary volcanoes in Japan. *Earth, Planets and Space*, 70(1). <https://doi.org/10.1186/s40623-018-0849-x>
- Yang, Y. H., Wu, F. Y., Yang, J. H., Chew, D. M., Xie, L. W., Chu, Z. Y., Zhang, Y. Bin, & Huang, C. (2014). Sr and Nd isotopic compositions of apatite reference materials used in U-Th-Pb geochronology. *Chemical Geology*, 385, 35–55. <https://doi.org/10.1016/j.chemgeo.2014.07.012>
- Yokoyama, I. (1971). Volcanic eruptions triggered by tectonic earthquakes. *Bulletin of the Geophysical Institute of Hokkaido University*, 25, 129–139. <https://doi.org/10.14943/gbhu.25.129>
- Zellmer, G. F., Pistone, M., Izuka, Y., Andrews, B. J., Gómez-Tuena, A., Straub, S. M., & Cottrell, E. (2016). Petrogenesis of antecryst-bearing arc basalts from the Trans-Mexican Volcanic Belt: Insights into along-arc variations in magma-mush ponding depths, H₂O contents, and surface heat flux. *American Mineralogist*, 101(11), 2405–2422. <https://doi.org/10.2138/am-2016-5701>
- Zhang, J., Humphreys, M. C. S., Cooper, G. F., Davidson, J. P., & Macpherson, C. G. (2017). Magma mush chemistry at subduction zones, revealed by new melt major element inversion from calcic amphiboles. *American Mineralogist*, 102(6), 1353–1367. <https://doi.org/10.2138/am-2017-5928>

Appendix A: Whole Rock Data

This appendix consists of three sections: section A.1 in which the major and minor elements are presented along with the data for the secondary standards; section A.2 in which the trace elements are presented along with the data for the secondary standards; and finally section A.3 in which the radiometric isotopes are presented along with the data for the secondary standards.

A.1 Major and minor elements

Table A.1: Non-normalised whole rock major element concentrations in wt.% oxide. Fe2O3(T) is all Fe analysed as Fe³⁺, all values in weight percent.

| Sample | Unit | SiO2 | TiO2 | Al2O3 | Fe2O3(T) | MnO | MgO | CaO | Na2O | K2O | P2O5 | LOI | Total |
|----------------|--------------------|------|------|-------|----------|------|------|------|------|------|------|-------|-------|
| Ati425.02t | High-K LCY | 71.8 | 0.10 | 12.1 | 0.64 | 0.06 | 0.12 | 0.67 | 3.37 | 4.13 | 0.02 | 5.84 | 98.95 |
| Ati425.03 | Medium-K LCY | 74.5 | 0.18 | 12.4 | 1.21 | 0.05 | 0.32 | 1.41 | 3.64 | 3.00 | 0.02 | 3.27 | 100.1 |
| Ati425.03(b) | High-K LCY | 74.2 | 0.10 | 12.0 | 0.72 | 0.07 | 0.14 | 0.73 | 3.34 | 4.22 | 0.02 | 3.63 | 99.15 |
| Ati426.01 | Granodiorite | 69.5 | 0.30 | 15.0 | 3.00 | 0.06 | 0.91 | 2.55 | 4.05 | 3.84 | 0.07 | 0.49 | 99.77 |
| Ati426.02 | Granodiorite | 72.5 | 0.30 | 12.4 | 1.93 | 0.07 | 0.54 | 1.51 | 3.73 | 3.60 | 0.07 | 3.05 | 99.72 |
| Ati426.03h | D2 | 68.5 | 0.24 | 13.9 | 1.97 | 0.06 | 0.67 | 2.21 | 3.66 | 3.19 | 0.08 | 4.45 | 98.94 |
| Ati427.01a | D1 | 55.9 | 0.71 | 17.8 | 7.05 | 0.12 | 2.98 | 5.98 | 2.93 | 1.45 | 0.17 | 4.91 | 99.97 |
| Ati427.01j | D2 | 70.3 | 0.24 | 14.2 | 1.99 | 0.07 | 0.63 | 2.13 | 3.66 | 3.17 | 0.07 | 4.51 | 100.8 |
| Ati427.02a | D2 | 65.3 | 0.37 | 16.5 | 3.08 | 0.01 | 0.89 | 2.68 | 3.59 | 2.42 | 0.05 | 5.66 | 100.7 |
| Ati427.04f | F | 67.5 | 0.32 | 15.1 | 2.65 | 0.08 | 0.74 | 2.24 | 3.69 | 2.94 | 0.02 | 5.16 | 100.4 |
| Ati427.08a | Tecolote | 62.7 | 0.59 | 16.4 | 5.20 | 0.09 | 2.25 | 4.86 | 3.36 | 3.10 | 0.11 | 1.83 | 100.4 |
| Ati427.08b | Tecolote | 59.7 | 0.66 | 17.7 | 6.00 | 0.10 | 2.70 | 5.16 | 3.31 | 2.36 | 0.07 | 2.23 | 100.1 |
| Ati427.11 | Cerro Las Minas | 52.2 | 1.03 | 18.0 | 9.44 | 0.14 | 5.75 | 8.84 | 3.14 | 1.10 | 0.20 | 0.24 | 100.2 |
| Ati429.04 | Low-K Los Chocoyos | 71.8 | 0.18 | 12.4 | 1.23 | 0.05 | 0.33 | 1.59 | 3.95 | 2.56 | 0.05 | 5.33 | 99.55 |
| Ati430.11a | I | 69.9 | 0.24 | 14.1 | 1.69 | 0.08 | 0.44 | 1.84 | 4.30 | 3.20 | 0.08 | 4.29 | 100.2 |
| Ati430.11b | I | 69.6 | 0.26 | 13.9 | 1.79 | 0.09 | 0.50 | 1.78 | 4.19 | 3.25 | 0.07 | 4.16 | 99.52 |
| Ati501.02 | Paquisis | 61.9 | 0.67 | 16.8 | 6.09 | 0.10 | 2.17 | 4.55 | 3.56 | 2.81 | 0.15 | 1.49 | 100.3 |
| Ati501.03 | Paquisis | 54.3 | 0.84 | 19.0 | 8.60 | 0.13 | 4.29 | 7.67 | 3.71 | 1.20 | 0.22 | 0.49 | 100.4 |
| Ati501.05a | Atitlán | 52.7 | 1.01 | 19.0 | 9.41 | 0.14 | 4.99 | 9.19 | 3.49 | 0.99 | 0.22 | -0.34 | 100.8 |
| Ati501.05b | Atitlán | 52.1 | 0.99 | 18.7 | 9.36 | 0.13 | 5.45 | 8.70 | 3.13 | 0.93 | 0.21 | 0.90 | 100.7 |
| Ati501.05c | Atitlán | 52.0 | 0.95 | 18.1 | 9.35 | 0.14 | 5.98 | 8.67 | 3.45 | 1.03 | 0.23 | -0.30 | 99.64 |
| Ati501.06a | D2 | 69.6 | 0.25 | 13.6 | 1.76 | 0.08 | 0.52 | 1.89 | 4.26 | 3.23 | 0.08 | 3.89 | 99.09 |
| Ati501.06c | Andesite Scoria | 52.4 | 0.96 | 18.1 | 9.00 | 0.14 | 5.00 | 8.32 | 3.32 | 0.97 | 0.20 | 1.07 | 99.5 |
| Ati502.06 | High-K LCY | 73.4 | 0.11 | 12.2 | 0.65 | 0.07 | 0.13 | 0.76 | 3.70 | 3.91 | 0.02 | 5.00 | 99.93 |
| Ati503.02 | Leucogranite | 73.4 | 0.18 | 12.7 | 1.31 | 0.00 | 0.26 | 0.92 | 3.18 | 4.54 | 0.05 | 2.98 | 99.48 |
| Ati503.05 | Tolimán | 56.8 | 0.77 | 17.8 | 7.38 | 0.12 | 3.71 | 6.84 | 3.70 | 1.70 | 0.18 | 0.73 | 99.77 |
| Ati503.07 | Tolimán | 60.2 | 0.72 | 16.9 | 6.39 | 0.11 | 3.33 | 5.99 | 3.88 | 2.10 | 0.17 | 0.55 | 100.4 |
| Ati503.08 | Tolimán | 58.6 | 0.77 | 17.3 | 7.01 | 0.12 | 3.59 | 6.52 | 3.89 | 1.92 | 0.18 | 0.53 | 100.4 |
| Ati504.03 | San Marcos | 58.2 | 0.83 | 17.9 | 7.44 | 0.12 | 3.50 | 6.52 | 3.74 | 1.79 | 0.18 | 0.46 | 100.7 |
| Ati504.06a | Tecolote | 58.3 | 0.80 | 17.3 | 7.87 | 0.10 | 2.80 | 5.79 | 3.51 | 2.00 | 0.18 | 2.01 | 100.7 |
| Ati504.06b | Tecolote | 58.0 | 0.81 | 17.5 | 7.78 | 0.10 | 2.96 | 6.40 | 3.59 | 1.92 | 0.19 | 1.33 | 100.6 |
| Ati505.01 | San Pedro | 57.6 | 0.78 | 17.8 | 7.58 | 0.14 | 3.26 | 6.94 | 3.90 | 1.64 | 0.18 | 0.61 | 100.4 |
| Ati505.03 | San Pedro | 55.3 | 0.81 | 17.9 | 7.93 | 0.14 | 3.64 | 7.27 | 3.70 | 1.56 | 0.18 | 0.96 | 99.45 |
| Ati505.04 | San Pedro | 55.0 | 0.85 | 18.0 | 8.26 | 0.13 | 4.57 | 7.75 | 3.72 | 1.37 | 0.20 | 0.25 | 100.2 |
| Ati505.05 | San Pedro | 56.2 | 0.77 | 18.0 | 8.1 | 0.14 | 3.44 | 6.99 | 3.80 | 1.56 | 0.19 | 0.82 | 100.1 |
| Ati505.06a | I1 | 56.0 | 0.72 | 17.7 | 7.93 | 0.14 | 3.86 | 7.61 | 3.59 | 1.40 | 0.19 | 1.04 | 100.2 |
| Ati505.06h | I | 69.5 | 0.24 | 13.2 | 1.71 | 0.08 | 0.49 | 1.70 | 3.92 | 3.25 | 0.08 | 5.28 | 99.35 |
| Ati505.06h (e) | I (enclave) | 60.1 | 0.64 | 16.0 | 5.47 | 0.13 | 2.08 | 5.14 | 4.11 | 2.00 | 0.34 | 2.98 | 99.02 |

*Samples Ati425.03, Ati425.03(b), Ati426.01, Ati426.02, Ati427.04a, Ati427.04f, Ati427.08a, Ati429.04, Ati501.06a, Ati503.02, Ati505.06h, Ati505.06h (e) were analysed in a second run.

Table A.2 Normalised whole rock major element concentrations (wt.%). Samples as in Table A.1

| Sample | Unit | SiO ₂ | Al ₂ O ₃ | Fe ₂ O _{3t} | MnO | MgO | CaO | Na ₂ O | K ₂ O | TiO ₂ | P ₂ O ₅ | Total |
|----------------|-------------|------------------|--------------------------------|---------------------------------|------|------|------|-------------------|------------------|------------------|-------------------------------|-------|
| Ati425.02t | LCY High-K | 77.2 | 13.0 | 0.69 | 0.07 | 0.13 | 0.72 | 3.62 | 4.44 | 0.11 | 0.02 | 100 |
| Ati425.03 | LCY Mid-K | 77.0 | 12.8 | 1.25 | 0.05 | 0.33 | 1.46 | 3.76 | 3.10 | 0.19 | 0.02 | 100 |
| Ati425.03(b) | LCY High-K | 77.6 | 12.6 | 0.75 | 0.07 | 0.15 | 0.76 | 3.50 | 4.42 | 0.10 | 0.02 | 100 |
| Ati426.01 | Intrusives | 70.0 | 15.1 | 3.02 | 0.06 | 0.92 | 2.57 | 4.08 | 3.87 | 0.30 | 0.07 | 100 |
| Ati426.02 | Intrusives | 75.0 | 12.9 | 2.00 | 0.07 | 0.56 | 1.56 | 3.86 | 3.72 | 0.31 | 0.07 | 100 |
| Ati426.03h | D2 | 72.5 | 14.7 | 2.08 | 0.07 | 0.71 | 2.34 | 3.87 | 3.38 | 0.25 | 0.08 | 100 |
| Ati427.01a | D1 | 58.8 | 18.7 | 7.42 | 0.13 | 3.13 | 6.29 | 3.08 | 1.53 | 0.75 | 0.18 | 100 |
| Ati427.01j | D2 | 73.0 | 14.7 | 2.07 | 0.07 | 0.65 | 2.21 | 3.80 | 3.29 | 0.25 | 0.07 | 100 |
| Ati427.02a | D2 | 68.7 | 17.4 | 3.24 | 0.10 | 0.94 | 2.82 | 3.78 | 2.55 | 0.39 | 0.05 | 100 |
| Ati427.04f/g | F | 70.8 | 15.9 | 2.78 | 0.09 | 0.78 | 2.35 | 3.87 | 3.09 | 0.34 | 0.02 | 100 |
| Ati427.08a | Phase III | 63.5 | 16.6 | 5.27 | 0.10 | 2.28 | 4.93 | 3.41 | 3.14 | 0.60 | 0.11 | 100 |
| Ati427.08b | Phase III | 61.0 | 18.1 | 6.13 | 0.11 | 2.76 | 5.27 | 3.38 | 2.41 | 0.67 | 0.07 | 100 |
| Ati427.11 | Phase III | 52.2 | 18.0 | 9.44 | 0.14 | 5.75 | 8.84 | 3.14 | 1.10 | 1.03 | 0.20 | 100 |
| Ati429.04 | LCY Low-K | 76.2 | 13.2 | 1.31 | 0.05 | 0.35 | 1.69 | 4.19 | 2.72 | 0.19 | 0.05 | 100 |
| Ati430.11a | I | 72.9 | 14.7 | 1.76 | 0.09 | 0.46 | 1.92 | 4.48 | 3.34 | 0.25 | 0.08 | 100 |
| Ati430.11b | I | 72.9 | 14.6 | 1.88 | 0.09 | 0.52 | 1.87 | 4.39 | 3.41 | 0.27 | 0.07 | 100 |
| Ati501.02 | Phase III | 62.6 | 17.0 | 6.16 | 0.10 | 2.20 | 4.60 | 3.60 | 2.84 | 0.68 | 0.15 | 100 |
| Ati501.03 | Phase III | 54.3 | 19.0 | 8.61 | 0.13 | 4.29 | 7.68 | 3.71 | 1.20 | 0.84 | 0.22 | 100 |
| Ati501.05a | Phase IV | 52.1 | 18.8 | 9.30 | 0.14 | 4.93 | 9.09 | 3.45 | 0.98 | 1.00 | 0.22 | 100 |
| Ati501.05b | Phase IV | 52.2 | 18.8 | 9.38 | 0.13 | 5.46 | 8.72 | 3.14 | 0.93 | 0.99 | 0.21 | 100 |
| Ati501.05c | Phase IV | 52.0 | 18.1 | 9.36 | 0.14 | 5.98 | 8.68 | 3.45 | 1.03 | 0.95 | 0.23 | 100 |
| Ati501.06a | D2 | 73.1 | 14.2 | 1.85 | 0.09 | 0.55 | 1.99 | 4.47 | 3.39 | 0.26 | 0.08 | 100 |
| Ati501.06c | Phase IV | 53.2 | 18.4 | 9.14 | 0.14 | 5.08 | 8.45 | 3.37 | 0.99 | 0.98 | 0.20 | 100 |
| Ati502.06 | LCY High-K | 77.4 | 12.8 | 0.68 | 0.07 | 0.14 | 0.80 | 3.90 | 4.12 | 0.12 | 0.02 | 100 |
| Ati503.02 | Intrusives | 76.0 | 13.1 | 1.36 | 0.00 | 0.27 | 0.95 | 3.30 | 4.70 | 0.19 | 0.05 | 100 |
| Ati503.05 | Phase IV | 57.4 | 17.9 | 7.45 | 0.12 | 3.75 | 6.91 | 3.74 | 1.72 | 0.78 | 0.18 | 100 |
| Ati503.07 | Phase IV | 60.3 | 16.9 | 6.40 | 0.11 | 3.34 | 6.00 | 3.89 | 2.10 | 0.72 | 0.17 | 100 |
| Ati503.08 | Phase IV | 58.6 | 17.3 | 7.02 | 0.12 | 3.59 | 6.53 | 3.90 | 1.92 | 0.77 | 0.18 | 100 |
| Ati504.03 | Phase III | 58.1 | 17.9 | 7.42 | 0.12 | 3.49 | 6.50 | 3.73 | 1.79 | 0.83 | 0.18 | 100 |
| Ati504.06a | Phase III | 59.0 | 17.5 | 7.97 | 0.10 | 2.84 | 5.87 | 3.56 | 2.03 | 0.81 | 0.18 | 100 |
| Ati504.06b | Phase III | 58.4 | 17.6 | 7.84 | 0.10 | 2.98 | 6.45 | 3.62 | 1.93 | 0.82 | 0.19 | 100 |
| Ati505.01 | Phase IV | 57.7 | 17.8 | 7.60 | 0.14 | 3.27 | 6.95 | 3.91 | 1.64 | 0.78 | 0.18 | 100 |
| Ati505.03 | Phase IV | 56.2 | 18.2 | 8.05 | 0.14 | 3.70 | 7.38 | 3.76 | 1.58 | 0.82 | 0.18 | 100 |
| Ati505.04 | Phase IV | 55.0 | 18.0 | 8.26 | 0.13 | 4.57 | 7.75 | 3.72 | 1.37 | 0.85 | 0.20 | 100 |
| Ati505.05 | Phase IV | 56.6 | 18.2 | 8.16 | 0.14 | 3.46 | 7.04 | 3.83 | 1.57 | 0.78 | 0.19 | 100 |
| Ati505.06a | I1 | 56.5 | 17.8 | 8.00 | 0.14 | 3.89 | 7.67 | 3.62 | 1.41 | 0.73 | 0.19 | 100 |
| Ati505.06h | I | 73.8 | 14.0 | 1.82 | 0.08 | 0.52 | 1.81 | 4.17 | 3.45 | 0.26 | 0.09 | 100 |
| Ati505.06h (e) | I (enclave) | 62.6 | 16.6 | 5.70 | 0.13 | 2.17 | 5.35 | 4.28 | 2.08 | 0.67 | 0.35 | 100 |

Table A.3: Detection limits and relative error for the secondary standards, random duplicate and method blank for the first run batch of samples. All values apart from relative error in wt.%.

| | SiO ₂ | Al ₂ O ₃ | Fe ₂ O ₃ (T) | MnO | MgO | CaO | Na ₂ O | K ₂ O | TiO ₂ | P ₂ O ₅ | LOI | Total |
|------------------------------|------------------|--------------------------------|------------------------------------|---------|--------|--------|-------------------|------------------|------------------|-------------------------------|------|--------|
| Detection Limit | 0.01 | 0.01 | 0.01 | 0.001 | 0.01 | 0.01 | 0.01 | 0.01 | 0.01 | 0.01 | | |
| FK-N Meas | 65.08 | 18.82 | 0.08 | - | - | 0.10 | 2.51 | 12.98 | 0.01 | 0.01 | | |
| FK-N Cert | 65.00 | 18.60 | 0.09 | - | - | 0.11 | 2.58 | 12.80 | 0.02 | 0.02 | | |
| Relative error (%) | 0.12 | 1.18 | 11.11 | - | - | 9.09 | 2.71 | 1.41 | 50.00 | 58.33 | | |
| IF-G Meas | 40.08 | 0.12 | 55.77 | 0.04 | 1.80 | 1.49 | 0.02 | - | 0.01 | 0.06 | | |
| IF-G Cert | 41.20 | 0.15 | 55.80 | 0.04 | 1.89 | 1.55 | 0.03 | - | 0.01 | 0.06 | | |
| Relative error (%) | 2.72 | 21.33 | 0.06 | 9.52 | 4.87 | 4.13 | 37.50 | - | 28.57 | 1.59 | | |
| BE-N Meas | 38.54 | 10.19 | 13.11 | 0.20 | 13.19 | 14.19 | 3.23 | 1.36 | 2.70 | 1.08 | | |
| BE-N Cert | 38.20 | 10.10 | 12.80 | 0.20 | 13.10 | 13.90 | 3.18 | 1.39 | 2.61 | 1.05 | | |
| Relative error (%) | 0.89 | 0.89 | 2.42 | 2.00 | 0.69 | 2.09 | 1.57 | 2.16 | 3.45 | 2.86 | | |
| DR-N Meas | 53.27 | 17.64 | 9.76 | 0.22 | 4.35 | 7.09 | 3.02 | 1.72 | 1.07 | 0.24 | | |
| DR-N Cert | 52.85 | 17.52 | 9.70 | 0.22 | 4.40 | 7.05 | 2.99 | 1.70 | 1.09 | 0.25 | | |
| Relative error (%) | 0.79 | 0.68 | 0.62 | 0.45 | 1.14 | 0.57 | 1.00 | 1.18 | 1.83 | 4.00 | | |
| NIST 696 Meas | 3.68 | 54.07 | 8.63 | 0.00 | 0.02 | 0.02 | - | 0.02 | 2.58 | 0.06 | | |
| NIST 696 Cert | 3.79 | 54.50 | 8.70 | 0.00 | 0.01 | 0.02 | - | 0.01 | 2.64 | 0.05 | | |
| Relative error (%) | 2.90 | 0.79 | 0.80 | 50.00 | 66.67 | 11.11 | - | 122.22 | 2.27 | 20.00 | | |
| BIR-1a Meas | 47.89 | 15.68 | 11.69 | 0.18 | 9.78 | 13.48 | 1.83 | 0.02 | 0.97 | 0.03 | | |
| BIR-1a Cert | 47.96 | 15.50 | 11.30 | 0.18 | 9.70 | 13.30 | 1.82 | 0.03 | 0.96 | 0.02 | | |
| Relative error (%) | 0.15 | 1.16 | 3.45 | 0.57 | 0.82 | 1.35 | 0.55 | 33.33 | 1.04 | 42.86 | | |
| BIR-1a Meas | 48.09 | 15.65 | 11.70 | 0.18 | 9.80 | 13.49 | 1.82 | 0.02 | 0.98 | 0.02 | | |
| BIR-1a Cert | 47.96 | 15.50 | 11.30 | 0.18 | 9.70 | 13.30 | 1.82 | 0.03 | 0.96 | 0.02 | | |
| Relative error (%) | 0.26 | 0.95 | 3.50 | 1.14 | 1.02 | 1.39 | 0.11 | 26.67 | 1.56 | 9.52 | | |
| SCH-1 Meas | 8.22 | 0.93 | 88.27 | 1.01 | 0.03 | - | 0.03 | 0.03 | 0.05 | 0.13 | | |
| SCH-1 Cert | 8.09 | 0.96 | 86.84 | 1.00 | 0.03 | - | 0.03 | 0.03 | 0.05 | 0.12 | | |
| Relative error (%) | 1.55 | 3.53 | 1.65 | 0.90 | 0.00 | - | 19.23 | 6.45 | 3.85 | 4.84 | | |
| KH3 Meas | 8.76 | 2.32 | - | 0.09 | 0.68 | 47.81 | 0.12 | - | 0.13 | 0.13 | | |
| KH3 Cert | 8.59 | 2.40 | - | 0.08 | 0.65 | 47.60 | 0.10 | - | 0.13 | 0.12 | | |
| Relative error (%) | 2.00 | 3.25 | - | 11.25 | 4.46 | 0.43 | 19.00 | - | 3.08 | 8.55 | | |
| NCS DC73304 (GBW 07106) Meas | 89.72 | 3.66 | 3.18 | - | 0.05 | 0.27 | 0.07 | 0.63 | - | 0.23 | | |
| NCS DC73304 (GBW 07106) Cert | 90.36 | 3.52 | 3.22 | - | 0.08 | 0.30 | 0.06 | 0.65 | - | 0.22 | | |
| Relative error (%) | 0.71 | 3.98 | 1.24 | - | 39.02 | 10.00 | 14.75 | 3.08 | - | 3.60 | | |
| NCS DC19003a Meas | 3.97 | 4.31 | 75.32 | 0.36 | 3.34 | 1.09 | - | - | 12.91 | - | | |
| NCS DC19003a Cert | 3.96 | 4.40 | 75.45 | 0.36 | 3.17 | 1.05 | - | - | 12.96 | - | | |
| Relative error (%) | 0.18 | 1.95 | 0.17 | 0.00 | 5.36 | 3.52 | - | - | 0.36 | - | | |
| NCS DC11016 Meas | 4.43 | 0.85 | 95.78 | 0.08 | 0.47 | 0.35 | - | 0.06 | 0.27 | - | | |
| NCS DC11016 Cert | 4.47 | 0.94 | 95.85 | 0.08 | 0.45 | 0.31 | - | 0.06 | 0.27 | - | | |
| Relative error (%) | 0.83 | 9.57 | 0.07 | 2.47 | 3.33 | 12.58 | - | 6.35 | 0.75 | - | | |
| NIST 88b (XRF) Meas | 1.12 | 0.33 | 0.28 | 0.02 | 21.11 | 30.36 | 0.05 | - | 0.03 | 0.01 | | |
| NIST 88b (XRF) Cert | 1.13 | 0.36 | 0.28 | 0.02 | 21.00 | 30.10 | 0.03 | - | 0.02 | 0.00 | | |
| Relative error (%) | 0.88 | 8.06 | 0.00 | 0.00 | 0.53 | 0.87 | 73.33 | - | 40.00 | 200.00 | | |
| Ati502.06 Orig | 73.82 | 12.18 | 0.65 | 0.07 | 0.12 | 0.77 | 3.71 | 3.94 | 0.11 | 0.02 | 4.97 | 100.30 |
| Ati502.06 Dup | 73.04 | 12.11 | 0.65 | 0.06 | 0.13 | 0.76 | 3.70 | 3.89 | 0.10 | 0.03 | 5.03 | 99.50 |
| Relative error (%) | 1.07 | 0.58 | 0.00 | 4.76 | 7.69 | 1.32 | 0.27 | 1.29 | 10.00 | 33.33 | | |
| Method Blank | < 0.01 | < 0.01 | < 0.01 | < 0.001 | < 0.01 | < 0.01 | < 0.01 | < 0.01 | < 0.01 | < 0.01 | | |

Table A.4: Detection limits and relative error for the secondary standards for the second run batch of samples. All values apart from relative error in wt.%.

| | SiO2 | Al2O3 | Fe2O3(T) | MnO | MgO | CaO | Na2O | K2O | TiO2 | P2O5 |
|------------------------------|-------|-------|----------|-------|-------|-------|-------|-------|-------|--------|
| Detection Limit | 0.01 | 0.01 | 0.01 | 0.00 | 0.01 | 0.01 | 0.01 | 0.01 | 0.01 | 0.01 |
| BE-N Meas | 38.03 | 9.95 | 12.94 | 0.20 | 13.14 | 13.93 | 3.09 | 1.36 | 2.73 | 1.11 |
| BE-N Cert | 38.20 | 10.10 | 12.80 | 0.20 | 13.10 | 13.90 | 3.18 | 1.39 | 2.61 | 1.05 |
| Relative error (%) | 0.45 | 1.49 | 1.09 | 1.50 | 0.31 | 0.22 | 2.83 | 2.16 | 4.60 | 5.71 |
| BE-N Meas | 38.29 | 10.11 | 13.01 | 0.20 | 13.29 | 14.00 | 3.15 | 1.38 | 2.67 | 1.09 |
| BE-N Cert | 38.20 | 10.10 | 12.80 | 0.20 | 13.10 | 13.90 | 3.18 | 1.39 | 2.61 | 1.05 |
| Relative error (%) | 0.24 | 0.10 | 1.64 | 1.50 | 1.45 | 0.72 | 0.94 | 0.72 | 2.30 | 3.81 |
| DR-N Meas | 52.49 | 17.35 | 9.73 | 0.22 | 4.42 | 7.01 | 2.96 | 1.71 | 1.06 | 0.24 |
| DR-N Cert | 52.85 | 17.52 | 9.70 | 0.22 | 4.40 | 7.05 | 2.99 | 1.70 | 1.09 | 0.25 |
| Relative error (%) | 0.68 | 0.97 | 0.31 | 1.36 | 0.45 | 0.57 | 1.00 | 0.59 | 2.75 | 4.00 |
| GS-N Meas | 65.66 | 14.59 | 3.64 | 0.05 | 2.32 | 2.48 | 3.78 | 4.68 | 0.65 | 0.29 |
| GS-N Cert | 65.80 | 14.67 | 3.75 | 0.06 | 2.30 | 2.50 | 3.77 | 4.63 | 0.68 | 0.28 |
| Relative error (%) | 0.21 | 0.55 | 2.93 | 8.93 | 0.87 | 0.80 | 0.27 | 1.08 | 4.41 | 3.57 |
| GS-N Meas | 65.49 | 14.58 | 3.70 | 0.05 | 2.38 | 2.52 | 3.80 | 4.69 | 0.66 | 0.29 |
| GS-N Cert | 65.80 | 14.67 | 3.75 | 0.06 | 2.30 | 2.50 | 3.77 | 4.63 | 0.68 | 0.28 |
| Relative error (%) | 0.47 | 0.61 | 1.33 | 7.14 | 3.48 | 0.80 | 0.80 | 1.30 | 2.94 | 3.57 |
| PM-S Meas | 46.64 | 16.95 | 10.18 | 0.16 | 9.48 | 12.50 | 2.08 | 0.14 | 1.11 | 0.03 |
| PM-S Cert | 47.00 | 17.15 | 10.10 | 0.16 | 9.34 | 12.48 | 2.08 | 0.14 | 1.10 | 0.03 |
| Relative error (%) | 0.77 | 1.17 | 0.79 | 0.63 | 1.50 | 0.16 | 0.00 | 0.00 | 0.91 | 0.00 |
| WS-E Meas | 51.21 | 13.72 | 13.43 | 0.18 | 5.76 | 9.12 | 2.52 | 1.02 | 2.47 | 0.31 |
| WS-E Cert | 50.70 | 13.78 | 13.15 | 0.17 | 5.55 | 8.95 | 2.47 | 1.00 | 2.40 | 0.30 |
| Relative error (%) | 1.01 | 0.44 | 2.13 | 3.53 | 3.78 | 1.90 | 2.02 | 2.00 | 2.92 | 3.33 |
| NCS DC86316 Meas | 70.80 | 13.83 | 0.33 | 0.02 | 0.08 | 0.65 | 4.33 | 3.97 | 0.69 | 0.06 |
| NCS DC86316 Cert | 70.73 | 14.57 | 0.38 | 0.02 | 0.08 | 0.63 | 4.20 | 3.90 | 0.64 | 0.04 |
| Relative error (%) | 0.10 | 5.08 | 13.16 | 19.05 | 1.27 | 3.17 | 3.10 | 1.79 | 7.81 | 50.00 |
| NCS DC73304 (GBW 07106) Meas | 90.94 | 3.56 | 3.23 | - | 0.05 | 0.28 | 0.07 | 0.65 | - | 0.24 |
| NCS DC73304 (GBW 07106) Cert | 90.36 | 3.52 | 3.22 | - | 0.08 | 0.30 | 0.06 | 0.65 | - | 0.22 |
| Relative error (%) | 0.64 | 1.14 | 0.31 | - | 39.02 | 6.67 | 14.75 | 0.00 | - | 8.11 |
| AMIS 0129 Meas | 9.62 | 2.74 | 62.77 | 0.36 | 2.19 | 0.81 | - | - | 23.46 | - |
| AMIS 0129 Cert | 9.57 | 2.75 | 62.31 | 0.36 | 2.07 | 0.80 | - | - | 22.94 | - |
| Relative error (%) | 0.52 | 0.36 | 0.74 | 1.39 | 5.80 | 1.25 | - | - | 2.27 | - |
| SARM 3 Meas | 51.46 | 13.78 | 10.04 | 0.73 | 0.29 | 3.17 | 8.44 | 5.38 | 0.48 | - |
| SARM 3 Cert | 52.40 | 13.64 | 9.91 | 0.77 | 0.28 | 3.22 | 8.37 | 5.51 | 0.48 | - |
| Relative error (%) | 1.79 | 1.03 | 1.31 | 5.45 | 3.57 | 1.55 | 0.84 | 2.36 | 0.00 | - |
| OREAS 22f (Fusion XRF) Meas | 97.32 | 0.27 | 0.72 | 0.01 | 0.05 | 0.02 | 0.03 | - | 0.06 | 0.01 |
| OREAS 22f (Fusion XRF) Cert | 98.69 | 0.26 | 0.80 | 0.01 | 0.03 | 0.04 | 0.02 | - | 0.05 | 0.00 |
| Relative error (%) | 1.39 | 3.85 | 10.00 | 30.00 | 66.67 | 50.00 | 50.00 | - | 20.00 | 150.00 |
| AMIS 0454 (XRF) Meas | 2.12 | 0.72 | 53.66 | 1.21 | 0.77 | 0.20 | - | 0.04 | 45.40 | 0.03 |
| AMIS 0454 (XRF) Cert | 2.23 | 0.73 | 52.53 | 1.19 | 0.74 | 0.22 | - | 0.05 | 44.45 | 0.03 |
| Relative error (%) | 4.93 | 1.37 | 2.15 | 1.93 | 4.05 | 9.09 | - | 20.00 | 2.14 | 0.00 |

A.2 Trace elements

Table A.5: Trace element concentrations for the whole rock samples. All concentrations in parts per million. Sample runs were the same as described in Table B.1.

| Sample | Unit | Li | Sc | V | Cr | Mn | Co | Ni | Cu | Zn | Ga | Rb | Sr | Y | Zr | Nb | Sn | Sb | Cs | Ba |
|----------------|-----------------|------|------|------|------|------|------|------|------|------|------|------|-----|------|-----|------|-----|-----|-----|------|
| Ati425.02t | High-K LCY | 23.8 | 2.1 | 1.7 | 0.8 | 492 | 0.2 | 0.6 | 8.2 | 21.1 | 11.9 | 129 | 81 | 11.4 | 49 | 6.4 | 2.7 | 1.0 | 5.4 | 960 |
| Ati425.03 | Medium-K LCY | 23.8 | 2.0 | 7.2 | 2.0 | 364 | 1.0 | 0.4 | 2.5 | 30.5 | 12.5 | 73.4 | 203 | 8.0 | 74 | 4.4 | 1.1 | 0.5 | 2.9 | 961 |
| Ati425.03(b) | High-K LCY | 29.7 | 2.3 | 2.0 | 2.0 | 497 | 0.3 | 0.5 | 1.3 | 22.5 | 12.3 | 123 | 89 | 11.1 | 51 | 6.3 | 1.1 | 0.9 | 5.8 | 1029 |
| Ati426.01 | Granodiorite | 13.4 | 6.0 | 44.9 | 3.0 | 479 | 5.4 | 1.9 | 7.9 | 44.0 | 16.7 | 155 | 215 | 15.8 | 8 | 6.6 | 2.1 | 0.2 | 6.3 | 667 |
| Ati426.02 | Granodiorite | 32.5 | 4.5 | 24.5 | 3.0 | 519 | 2.2 | 1.0 | 4.2 | 38.6 | 14.7 | 128 | 156 | 23.2 | 45 | 9.4 | 2.2 | 0.5 | 4.3 | 765 |
| Ati426.03h | D2 | 23.2 | 3.1 | 24.5 | 1.6 | 511 | 3.0 | 0.9 | 4.8 | 36.2 | 13.7 | 95.2 | 267 | 10.1 | 102 | 5.2 | 0.9 | 0.6 | 3.7 | 905 |
| Ati427.01a | D1 | 15.0 | 15.0 | 154 | 4.8 | 1007 | 18.2 | 5.1 | 21.4 | 88.3 | 20.0 | 42.1 | 479 | 18.7 | 149 | 4.3 | 1.2 | 0.2 | 1.6 | 682 |
| Ati427.01j | D2 | 26.1 | 3.2 | 22.9 | 1.5 | 506 | 2.7 | 1.3 | 4.9 | 36.3 | 13.9 | 95.2 | 256 | 9.5 | 106 | 5.2 | 0.9 | 0.6 | 3.8 | 912 |
| Ati427.02a | D2 | 26.5 | 3.2 | 15.9 | 0.9 | 668 | 1.5 | 0.7 | 4.7 | 404 | 18.2 | 69.7 | 303 | 14.8 | 102 | 7.3 | 1.4 | 0.5 | 3.0 | 941 |
| Ati427.04f | F | 26.8 | 4.5 | 31.7 | 1.7 | 622 | 4.1 | 1.2 | 10.6 | 48.9 | 15.3 | 91.7 | 228 | 15.5 | 90 | 6.2 | 1.5 | 0.6 | 4.0 | 887 |
| Ati427.08a | Tecolote | 16.1 | 14.1 | 107 | 14.9 | 715 | 12.3 | 4.6 | 8.4 | 64.8 | 17.9 | 82.8 | 354 | 20.1 | 110 | 7.0 | 1.8 | 0.5 | 3.2 | 892 |
| Ati427.08b | Tecolote | 16.2 | 15.5 | 111 | 21.3 | 845 | 15.7 | 5.4 | 40.1 | 84.2 | 20.2 | 61.8 | 406 | 20.5 | 116 | 7.5 | 1.1 | 0.6 | 2.2 | 927 |
| Ati427.11 | Cerro Las Minas | 11.4 | 26.3 | 229 | 88.9 | 1124 | 27.0 | 33.8 | 36.6 | 90.0 | 19.4 | 21.1 | 540 | 19.8 | 129 | 4.3 | 1.2 | 0.2 | 0.6 | 493 |
| Ati429.04 | Low-K LCY | 25.1 | 2.0 | 7.5 | 1.8 | 370 | 0.9 | 0.5 | 1.9 | 30.7 | 12.6 | 63.9 | 224 | 7.6 | 90 | 4.2 | 0.9 | 0.4 | 2.7 | 926 |
| Ati430.11a | I | 23.2 | 2.5 | 14.2 | 1.2 | 676 | 1.5 | 0.7 | 2.2 | 50.1 | 14.6 | 97.9 | 250 | 13.1 | 87 | 6.2 | 1.4 | 0.5 | 3.1 | 854 |
| Ati430.11b | I | 21.6 | 2.2 | 12.4 | 0.4 | 642 | 1.1 | 0.5 | 3.9 | 47.4 | 14.0 | 86.9 | 246 | 13.5 | 83 | 5.8 | 1.1 | 0.5 | 3.0 | 823 |
| Ati501.02 | Paquisis | 17.3 | 13.5 | 138 | 11.6 | 813 | 14.8 | 6.8 | 24.5 | 76.9 | 19.3 | 92.0 | 392 | 25.2 | 128 | 5.9 | 1.5 | 0.6 | 2.1 | 788 |
| Ati501.03 | Paquisis | 12.7 | 18.7 | 204 | 6.0 | 1127 | 26.3 | 14.6 | 54.1 | 106 | 22.4 | 26.8 | 651 | 19.6 | 130 | 4.1 | 1.1 | 0.2 | 0.8 | 583 |
| Ati501.05a | Atitlán | 11.8 | 26.2 | 274 | 55.7 | 1148 | 30.1 | 24.0 | 79.4 | 103 | 22.2 | 19.7 | 668 | 18.3 | 113 | 3.7 | 1.2 | 0.2 | 0.8 | 483 |
| Ati501.05b | Atitlán | 11.0 | 24.6 | 229 | 103 | 1080 | 31.3 | 38.0 | 82.9 | 100 | 21.2 | 19.1 | 631 | 17.2 | 114 | 3.8 | 1.1 | 0.1 | 0.7 | 477 |
| Ati501.05c | Atitlán | 11.5 | 24.5 | 242 | 119 | 1124 | 33.1 | 45.2 | 67.1 | 101 | 20.9 | 20.0 | 619 | 17.2 | 117 | 3.9 | 1.2 | 0.2 | 0.8 | 483 |
| Ati501.06a | D2 | 24.3 | 2.9 | 12.9 | 1.6 | 657 | 1.4 | 0.7 | 7.3 | 47.2 | 14.4 | 91.5 | 236 | 13.1 | 106 | 6.1 | 1.3 | 0.5 | 3.2 | 903 |
| Ati501.06c | Andesite Scoria | 9.9 | 23.4 | 228 | 68.7 | 1174 | 30.1 | 36.0 | 57.6 | 96.6 | 20.4 | 23.1 | 618 | 19.4 | 116 | 3.1 | 1.0 | 0.2 | 0.9 | 457 |
| Ati502.06 | High-K LCY | 33.1 | 2.3 | 2.2 | 0.8 | 542 | 0.3 | 0.6 | 9.2 | 17.6 | 13.0 | 133 | 103 | 12.2 | 52 | 6.9 | 2.4 | 1.0 | 5.7 | 1032 |
| Ati503.02 | Leucogranite | 13.4 | 3.2 | 12.4 | 8.5 | 49 | 1.2 | 0.9 | 29.7 | 4.2 | 15.4 | 194 | 125 | 17.4 | 38 | 14.9 | 9.2 | 0.1 | 2.7 | 642 |
| Ati503.05 | Tolimán | 15.3 | 17.9 | 178 | 17.7 | 1032 | 21.8 | 13.7 | 53.3 | 87.3 | 19.8 | 40.6 | 536 | 20.2 | 145 | 4.2 | 1.3 | 0.3 | 1.5 | 615 |
| Ati503.07 | Tolimán | 20.0 | 16.7 | 150 | 73.5 | 927 | 18.5 | 21.9 | 20.2 | 85.4 | 19.2 | 57.7 | 473 | 20.9 | 153 | 5.3 | 1.5 | 0.4 | 2.3 | 770 |
| Ati503.08 | Tolimán | 16.7 | 16.8 | 159 | 39.3 | 905 | 19.3 | 17.1 | 23.8 | 82.3 | 17.9 | 47.7 | 485 | 19.2 | 153 | 5.5 | 1.3 | 0.3 | 1.8 | 663 |
| Ati504.03 | San Marcos | 13.1 | 17.9 | 170 | 10.2 | 916 | 18.7 | 7.1 | 23.0 | 83.3 | 18.7 | 48.5 | 456 | 20.7 | 150 | 5.3 | 1.2 | 0.2 | 1.1 | 645 |
| Ati504.06a | Tecolote | 9.2 | 16.8 | 169 | 1.9 | 810 | 17.2 | 2.9 | 26.9 | 99.1 | 19.7 | 62.7 | 450 | 31.5 | 181 | 5.9 | 1.6 | 0.6 | 3.7 | 719 |
| Ati504.06b | Tecolote | 14.7 | 17.1 | 175 | 1.8 | 857 | 18.0 | 3.1 | 14.2 | 98.9 | 19.4 | 58.8 | 497 | 24.9 | 188 | 6.0 | 1.6 | 0.4 | 1.7 | 694 |
| Ati505.01 | San Pedro | 15.0 | 16.6 | 173 | 6.2 | 1053 | 19.2 | 6.7 | 33.6 | 157 | 18.1 | 38.2 | 507 | 21.3 | 139 | 3.9 | 1.3 | 0.3 | 1.7 | 641 |
| Ati505.03 | San Pedro | 13.7 | 18.4 | 197 | 8.1 | 1101 | 22.4 | 8.8 | 32.0 | 162 | 18.7 | 36.8 | 547 | 21.7 | 137 | 3.9 | 1.3 | 0.2 | 1.6 | 622 |
| Ati505.04 | San Pedro | 11.4 | 18.7 | 190 | 53.2 | 1051 | 24.8 | 25.9 | 42.1 | 98.1 | 18.2 | 29.5 | 574 | 19.4 | 129 | 3.8 | 1.3 | 0.2 | 1.2 | 563 |
| Ati505.05 | San Pedro | 14.0 | 15.4 | 168 | 4.5 | 1082 | 20.8 | 6.9 | 38.0 | 88.9 | 17.8 | 35.1 | 513 | 21.2 | 132 | 3.6 | 1.2 | 0.2 | 1.5 | 593 |
| Ati505.06a | I1 | 13.3 | 17.8 | 173 | 28.2 | 1022 | 21.5 | 10.1 | 58.0 | 160 | 17.5 | 29.7 | 566 | 17.9 | 125 | 3.3 | 1.1 | 0.2 | 1.1 | 534 |
| Ati505.06h | I | 23.8 | 2.8 | 13.0 | 1.1 | 629 | 1.2 | 0.4 | 3.7 | 45.3 | 13.8 | 93.0 | 224 | 12.5 | 116 | 5.8 | 1.1 | 0.5 | 3.1 | 854 |
| Ati505.06h (e) | I (enclave) | 15.1 | 10.4 | 84.0 | 1.7 | 941 | 6.9 | 0.5 | 5.0 | 80.9 | 17.8 | 45.0 | 536 | 16.6 | 158 | 5.0 | 1.1 | 0.3 | 1.4 | 724 |

Table A.5 (cont.)

| Sample | Unit | La | Ce | Pr | Nd | Sm | Eu | Gd | Tb | Dy | Ho | Er | Yb | Lu | Hf | Ta | Tl | Pb | Th | U |
|----------------|-----------------|------|------|-----|------|-----|-----|-----|-----|-----|-----|-----|-----|-----|-----|-----|-----|------|------|------|
| Ati425.02t | High-K LCY | 16.2 | 31.1 | 3.3 | 11.4 | 2.1 | 0.3 | 1.7 | 0.3 | 1.6 | 0.3 | 1.0 | 1.2 | 0.2 | 1.9 | 0.6 | 0.7 | 12.2 | 12.0 | 4.2 |
| Ati425.03 | Medium-K LCY | 27.9 | 47.2 | 4.9 | 15.8 | 2.3 | 0.6 | 1.6 | 0.2 | 1.3 | 0.3 | 0.7 | 0.8 | 0.1 | 2.2 | 0.3 | 0.4 | 9.7 | 10.2 | 2.4 |
| Ati425.03(b) | High-K LCY | 18.3 | 33.7 | 3.7 | 12.2 | 2.1 | 0.4 | 1.7 | 0.3 | 1.6 | 0.3 | 1.0 | 1.1 | 0.2 | 2.0 | 0.6 | 0.7 | 12.3 | 12.0 | 4.3 |
| Ati426.01 | Granodiorite | 28.9 | 50.1 | 5.3 | 17.6 | 3.1 | 0.6 | 2.6 | 0.4 | 2.4 | 0.5 | 1.5 | 1.6 | 0.2 | 0.3 | 0.7 | 1.1 | 12.9 | 13.7 | 3.1 |
| Ati426.02 | Granodiorite | 20.4 | 46.1 | 5.9 | 22.1 | 4.6 | 0.8 | 4.0 | 0.6 | 3.8 | 0.8 | 2.2 | 2.0 | 0.3 | 1.3 | 1.1 | 0.9 | 14.2 | 8.6 | 2.2 |
| Ati426.03h | D2 | 17.0 | 31.5 | 3.3 | 11.6 | 2.0 | 0.5 | 1.6 | 0.2 | 1.4 | 0.3 | 0.9 | 1.1 | 0.2 | 2.8 | 0.5 | 0.5 | 10.7 | 9.4 | 3.1 |
| Ati427.01a | D1 | 16.4 | 31.2 | 4.2 | 17.7 | 3.8 | 1.0 | 3.4 | 0.5 | 3.0 | 0.6 | 1.7 | 1.7 | 0.3 | 3.6 | 0.3 | 0.3 | 8.6 | 3.9 | 1.2 |
| Ati427.01j | D2 | 17.4 | 31.8 | 3.3 | 11.5 | 2.0 | 0.5 | 1.6 | 0.2 | 1.4 | 0.3 | 0.9 | 1.0 | 0.2 | 2.8 | 0.5 | 0.5 | 10.7 | 9.6 | 3.2 |
| Ati427.02a | D2 | 20.2 | 34.7 | 4.3 | 15.9 | 3.0 | 0.7 | 2.5 | 0.4 | 2.3 | 0.5 | 1.3 | 1.5 | 0.2 | 3.2 | 0.6 | 0.7 | 14.7 | 10.1 | 2.7 |
| Ati427.04f | F | 18.7 | 37.2 | 4.3 | 15.7 | 3.0 | 0.7 | 2.6 | 0.4 | 2.4 | 0.5 | 1.5 | 1.7 | 0.3 | 2.8 | 0.5 | 0.6 | 12.1 | 7.4 | 2.7 |
| Ati427.08a | Tecolote | 20.6 | 39.5 | 5.1 | 19.3 | 4.0 | 1.0 | 3.6 | 0.6 | 3.3 | 0.7 | 1.9 | 1.9 | 0.3 | 3.2 | 0.5 | 0.5 | 12.9 | 7.6 | 2.3 |
| Ati427.08b | Tecolote | 17.6 | 37.4 | 4.4 | 17.8 | 3.9 | 1.0 | 3.5 | 0.6 | 3.3 | 0.7 | 1.9 | 2.0 | 0.3 | 3.3 | 0.7 | 0.6 | 23.0 | 7.7 | 1.6 |
| Ati427.11 | Cerro Las Minas | 11.9 | 26.3 | 3.5 | 16.0 | 3.8 | 1.2 | 3.7 | 0.6 | 3.3 | 0.7 | 1.8 | 1.8 | 0.3 | 3.1 | 0.2 | 0.1 | 6.3 | 1.1 | 0.4 |
| Ati429.04 | Low-K LCY | 26.2 | 43.7 | 4.6 | 14.8 | 2.1 | 0.6 | 1.5 | 0.2 | 1.2 | 0.2 | 0.7 | 0.8 | 0.1 | 2.5 | 0.3 | 0.4 | 9.3 | 9.4 | 2.2 |
| Ati430.11a | I | 17.8 | 35.7 | 3.8 | 14.1 | 2.6 | 0.6 | 2.1 | 0.3 | 1.9 | 0.4 | 1.2 | 1.4 | 0.2 | 2.7 | 0.5 | 0.6 | 13.6 | 7.9 | 2.8 |
| Ati430.11b | I | 17.8 | 33.8 | 3.9 | 14.8 | 2.7 | 0.7 | 2.2 | 0.3 | 2.0 | 0.4 | 1.2 | 1.4 | 0.2 | 2.6 | 0.5 | 0.6 | 12.9 | 7.6 | 2.7 |
| Ati501.02 | Paquisis | 19.9 | 38.8 | 5.3 | 22.0 | 4.7 | 1.1 | 4.3 | 0.7 | 3.8 | 0.8 | 2.3 | 2.4 | 0.3 | 3.6 | 0.5 | 0.8 | 8.9 | 8.0 | 2.8 |
| Ati501.03 | Paquisis | 13.3 | 27.7 | 3.8 | 17.1 | 3.9 | 1.2 | 3.6 | 0.6 | 3.1 | 0.7 | 1.8 | 1.7 | 0.2 | 3.2 | 0.3 | 0.1 | 6.0 | 1.8 | 0.6 |
| Ati501.05a | Atitlán | 10.8 | 25.4 | 3.4 | 15.3 | 3.6 | 1.1 | 3.5 | 0.5 | 3.1 | 0.6 | 1.7 | 1.6 | 0.2 | 2.7 | 0.2 | 0.1 | 5.5 | 1.4 | 0.6 |
| Ati501.05b | Atitlán | 11.2 | 26.1 | 3.5 | 15.5 | 3.6 | 1.1 | 3.4 | 0.5 | 2.9 | 0.6 | 1.6 | 1.4 | 0.2 | 2.7 | 0.2 | 0.1 | 5.3 | 1.3 | 0.5 |
| Ati501.05c | Atitlán | 11.1 | 26.2 | 3.4 | 15.3 | 3.6 | 1.1 | 3.4 | 0.5 | 2.9 | 0.6 | 1.6 | 1.5 | 0.2 | 2.8 | 0.2 | 0.1 | 5.4 | 1.4 | 0.5 |
| Ati501.06a | D2 | 17.6 | 35.3 | 3.9 | 14.1 | 2.6 | 0.7 | 2.2 | 0.3 | 2.0 | 0.4 | 1.2 | 1.4 | 0.2 | 2.9 | 0.5 | 0.7 | 13.6 | 8.1 | 2.9 |
| Ati501.06c | Andesite Scoria | 9.8 | 23.2 | 3.2 | 14.8 | 3.6 | 1.2 | 3.6 | 0.6 | 3.2 | 0.7 | 1.7 | 1.7 | 0.2 | 2.9 | 0.2 | 0.2 | 5.5 | 1.9 | 0.7 |
| Ati502.06 | High-K LCY | 19.4 | 36.2 | 3.8 | 12.9 | 2.3 | 0.4 | 1.8 | 0.3 | 1.7 | 0.4 | 1.0 | 1.3 | 0.2 | 2.0 | 0.8 | 0.5 | 8.6 | 13.3 | 4.4 |
| Ati503.02 | Leucogranite | 27.3 | 55.9 | 6.5 | 22.5 | 4.5 | 0.5 | 3.5 | 0.5 | 3.1 | 0.6 | 1.6 | 1.8 | 0.2 | 1.3 | 1.3 | 1.3 | 21.7 | 22.9 | 14.2 |
| Ati503.05 | Tolimán | 12.6 | 28.0 | 3.6 | 15.7 | 3.7 | 1.0 | 3.5 | 0.6 | 3.2 | 0.7 | 1.8 | 1.9 | 0.3 | 3.5 | 0.3 | 0.2 | 7.0 | 3.3 | 1.2 |
| Ati503.07 | Tolimán | 16.1 | 34.0 | 4.2 | 17.7 | 3.9 | 1.1 | 3.6 | 0.6 | 3.3 | 0.7 | 1.9 | 2.0 | 0.3 | 4.0 | 0.4 | 0.3 | 9.5 | 5.0 | 1.8 |
| Ati503.08 | Tolimán | 14.0 | 30.1 | 3.7 | 16.1 | 3.6 | 1.0 | 3.4 | 0.5 | 3.0 | 0.6 | 1.7 | 1.8 | 0.3 | 3.8 | 0.3 | 0.2 | 7.9 | 4.0 | 1.4 |
| Ati504.03 | San Marcos | 15.6 | 32.2 | 4.0 | 17.1 | 3.8 | 1.1 | 3.6 | 0.6 | 3.3 | 0.7 | 1.9 | 2.0 | 0.3 | 3.6 | 0.3 | 0.3 | 7.5 | 3.6 | 1.2 |
| Ati504.06a | Tecolote | 17.4 | 38.1 | 5.1 | 22.8 | 5.3 | 1.4 | 5.2 | 0.8 | 4.8 | 1.0 | 2.8 | 2.9 | 0.4 | 4.4 | 0.4 | 0.3 | 7.6 | 4.8 | 1.8 |
| Ati504.06b | Tecolote | 15.7 | 34.9 | 4.4 | 19.5 | 4.6 | 1.2 | 4.3 | 0.7 | 4.0 | 0.8 | 2.3 | 2.4 | 0.3 | 4.6 | 0.8 | 0.3 | 6.9 | 4.8 | 1.8 |
| Ati505.01 | San Pedro | 12.1 | 27.4 | 3.5 | 15.4 | 3.6 | 1.1 | 3.5 | 0.6 | 3.3 | 0.7 | 2.0 | 2.1 | 0.3 | 3.4 | 0.2 | 0.1 | 7.0 | 3.1 | 1.1 |
| Ati505.03 | San Pedro | 12.2 | 27.5 | 3.6 | 15.8 | 3.8 | 1.1 | 3.6 | 0.6 | 3.4 | 0.7 | 2.0 | 2.1 | 0.3 | 3.3 | 0.3 | 0.1 | 6.7 | 3.0 | 1.1 |
| Ati505.04 | San Pedro | 11.5 | 26.6 | 3.4 | 15.3 | 3.6 | 1.1 | 3.4 | 0.5 | 3.1 | 0.6 | 1.8 | 1.9 | 0.3 | 3.1 | 0.2 | 0.1 | 6.5 | 2.2 | 0.8 |
| Ati505.05 | San Pedro | 11.0 | 25.3 | 3.3 | 14.8 | 3.5 | 1.0 | 3.5 | 0.6 | 3.3 | 0.7 | 2.0 | 2.1 | 0.3 | 3.2 | 0.4 | 0.1 | 6.4 | 2.6 | 1.0 |
| Ati505.06a | I1 | 10.8 | 25.4 | 3.2 | 14.1 | 3.3 | 1.0 | 3.1 | 0.5 | 2.8 | 0.6 | 1.6 | 1.7 | 0.2 | 3.1 | 0.2 | 0.2 | 6.1 | 2.4 | 0.8 |
| Ati505.06h | I | 16.8 | 32.4 | 3.7 | 13.3 | 2.4 | 0.6 | 2.0 | 0.3 | 1.9 | 0.4 | 1.2 | 1.3 | 0.2 | 3.2 | 0.6 | 0.6 | 13.1 | 7.3 | 2.8 |
| Ati505.06h (e) | I (enclave) | 16.4 | 33.1 | 4.5 | 18.0 | 3.7 | 1.1 | 3.4 | 0.5 | 2.8 | 0.6 | 1.6 | 1.5 | 0.2 | 3.8 | 0.3 | 0.3 | 8.4 | 3.5 | 1.4 |

Table A.6: Whole rock trace element accuracy and precision quantification for the reference materials of the first batch of samples. Meas. – Measured value; Cert. – Certified value. Both in parts per million

| | DL | BIR-1 | | | | W-2 | | | | DNC-1 | | | | BHVO-2 | | | | AGV-1 | | | | BCR-2 | | | | RGM-1 | | | |
|----|---------|---------|---------|-------|-------|---------|---------|-------|------|---------|---------|-------|------|----------|----------|-------|------|---------|---------|-------|------|----------|----------|-------|------|---------|---------|-------|------|
| | | Meas. | Cert. | Err % | RSD | Meas. | Cert. | Err % | RSD | Meas. | Cert. | Err % | RSD | Meas. | Cert. | Err % | RSD | Meas. | Cert. | Err % | RSD | Meas. | Cert. | Err % | RSD | Meas. | Cert. | Err % | RSD |
| Li | 0.0032 | 3.45 | 3.20 | 7.57 | 1.55 | 9.97 | 9.21 | 8.26 | 0.95 | 5.22 | 5.24 | 0.42 | 1.23 | 4.55 | 4.50 | 1.08 | 1.02 | 10.96 | 10.72 | 2.24 | 1.12 | 10.00 | 9.13 | 9.58 | 0.29 | 65.56 | 60.70 | 8.00 | 0.28 |
| Sc | 0.0066 | 43.94 | 43.21 | 1.70 | 0.93 | 35.97 | 35.86 | 0.30 | 1.41 | 31.69 | 31.40 | 0.94 | 1.52 | 29.85 | 31.83 | 6.23 | 0.94 | 12.24 | 12.43 | 1.57 | 1.12 | 33.88 | 33.53 | 1.05 | 0.59 | 4.87 | 4.74 | 2.83 | 0.80 |
| Ti | 0.0249 | 5906.34 | 5755.19 | 2.63 | 1.22 | 6851.00 | 6366.68 | 7.61 | 0.80 | 3103.08 | 2901.58 | 6.94 | 1.41 | 16231.76 | 16372.33 | 0.86 | 0.91 | 6551.02 | 6294.74 | 4.07 | 0.87 | 14494.27 | 13578.66 | 6.74 | 0.74 | 1691.80 | 1591.07 | 6.33 | 1.12 |
| V | 0.0052 | 329.19 | 320.60 | 2.68 | 0.78 | 268.91 | 265.80 | 1.17 | 0.65 | 151.32 | 147.50 | 2.59 | 0.79 | 298.61 | 318.20 | 6.16 | 1.50 | 119.51 | 119.40 | 0.09 | 0.91 | 417.33 | 417.60 | 0.06 | 0.88 | 11.08 | 11.76 | 5.75 | 0.82 |
| Cr | 0.0136 | 400.34 | 392.90 | 1.89 | 0.96 | 90.92 | 92.00 | 1.17 | 1.24 | 280.09 | 270.10 | 3.70 | 1.01 | 270.34 | 287.20 | 5.87 | 1.40 | 8.07 | 9.47 | 14.86 | 0.71 | 15.20 | 15.85 | 4.10 | 0.52 | 1.70 | 4.45 | 61.77 | 2.17 |
| Mn | 0.0116 | 1364.78 | 1355.53 | 0.68 | 0.81 | 1324.39 | 1293.56 | 2.38 | 0.85 | 1152.45 | 1146.39 | 0.53 | 0.73 | 1243.40 | 1309.05 | 5.02 | 1.69 | 732.81 | 748.25 | 2.06 | 1.14 | 1540.34 | 1522.84 | 1.15 | 0.55 | 281.08 | 299.77 | 6.23 | 0.70 |
| Co | 0.0007 | 52.97 | 52.22 | 1.43 | 1.35 | 44.16 | 44.37 | 0.47 | 1.17 | 56.67 | 56.75 | 0.14 | 1.90 | 40.83 | 44.89 | 9.04 | 1.22 | 14.54 | 15.14 | 3.97 | 0.72 | 36.13 | 37.33 | 3.23 | 0.70 | 1.90 | 2.04 | 7.06 | 1.41 |
| Ni | 0.0170 | 165.75 | 168.90 | 1.86 | 0.59 | 70.44 | 72.00 | 2.17 | 1.61 | 253.26 | 247.00 | 2.53 | 0.96 | 107.52 | 119.80 | 10.25 | 0.35 | 13.68 | 15.41 | 11.23 | 0.42 | 11.34 | 12.57 | 9.75 | 0.87 | 1.29 | 3.41 | 62.07 | 1.50 |
| Cu | 0.0424 | 128.09 | 120.70 | 6.12 | 1.02 | 111.93 | 105.90 | 5.69 | 0.93 | 102.88 | 99.70 | 3.19 | 0.67 | 123.83 | 129.30 | 4.23 | 1.42 | 56.86 | 58.42 | 2.68 | 0.86 | 17.12 | 19.66 | 12.91 | 0.31 | 11.42 | 11.09 | 3.01 | 1.34 |
| Zn | 1.0786 | 73.45 | 70.40 | 4.33 | 1.24 | 79.76 | 77.70 | 2.65 | 0.83 | 67.40 | 70.10 | 3.86 | 0.66 | 98.27 | 103.90 | 5.42 | 1.56 | 90.60 | 86.80 | 4.37 | 0.66 | 136.37 | 129.50 | 5.31 | 0.64 | 33.49 | 33.20 | 0.89 | 0.70 |
| Ga | 0.0011 | 15.87 | 15.46 | 2.63 | 1.27 | 18.57 | 17.88 | 3.88 | 0.46 | 14.03 | 14.70 | 4.57 | 1.01 | 20.62 | 21.37 | 3.49 | 1.24 | 20.69 | 20.36 | 1.62 | 1.09 | 22.59 | 22.07 | 2.34 | 1.22 | 16.56 | 16.06 | 3.10 | 1.15 |
| Rb | 0.0029 | 0.21 | 0.21 | 0.64 | 3.79 | 20.65 | 20.23 | 2.10 | 0.80 | 3.70 | 4.70 | 21.18 | 0.93 | 8.81 | 9.26 | 4.86 | 0.72 | 67.96 | 67.80 | 0.23 | 0.73 | 48.37 | 46.02 | 5.12 | 0.61 | 160.88 | 149.50 | 7.61 | 0.68 |
| Sr | 0.0063 | 112.55 | 108.60 | 3.64 | 0.75 | 202.52 | 195.40 | 3.64 | 1.60 | 148.07 | 144.00 | 2.83 | 1.03 | 377.39 | 394.10 | 4.24 | 0.60 | 664.13 | 661.00 | 0.47 | 0.88 | 346.15 | 337.40 | 2.59 | 1.11 | 109.44 | 104.80 | 4.43 | 0.55 |
| Y | 0.0004 | 17.30 | 15.60 | 10.90 | 0.79 | 23.67 | 21.82 | 8.48 | 1.01 | 19.10 | 18.50 | 3.22 | 0.42 | 26.58 | 25.91 | 2.58 | 0.50 | 20.59 | 19.69 | 4.58 | 0.60 | 38.93 | 36.07 | 7.93 | 0.84 | 25.02 | 23.48 | 6.55 | 0.45 |
| Zr | 0.0057 | 15.47 | 14.80 | 4.50 | 0.32 | 94.89 | 93.30 | 1.71 | 0.67 | 38.02 | 38.50 | 1.25 | 1.10 | 167.00 | 171.20 | 2.45 | 0.62 | 235.92 | 231.50 | 1.91 | 0.80 | 192.77 | 186.50 | 3.36 | 0.60 | 234.40 | 227.90 | 2.85 | 1.08 |
| Nb | 0.0003 | 0.58 | 0.55 | 5.64 | 1.46 | 8.12 | 7.51 | 8.18 | 0.69 | 1.67 | 3.19 | 47.60 | 1.28 | 18.78 | 18.10 | 3.77 | 1.09 | 15.34 | 14.53 | 5.55 | 0.66 | 13.55 | 12.44 | 8.95 | 0.67 | 9.86 | 9.13 | 8.01 | 0.94 |
| Sn | 0.0167 | 0.54 | 0.70 | 22.42 | 1.92 | 1.98 | 1.92 | 2.91 | 1.23 | - | - | - | 2.43 | 1.79 | 1.78 | 0.71 | 1.08 | 4.82 | 4.88 | 1.31 | 1.25 | 2.36 | 2.28 | 3.70 | 1.52 | 4.41 | 4.34 | 1.72 | 0.97 |
| Sb | 0.0007 | 0.55 | 0.46 | 18.67 | 1.02 | 0.82 | 0.81 | 1.82 | 0.65 | 0.99 | 0.96 | 2.69 | 0.98 | 0.09 | 0.10 | 13.64 | 5.36 | 4.30 | 4.24 | 1.31 | 0.55 | 0.30 | 0.30 | 0.15 | 1.52 | 1.21 | 1.23 | 1.42 | 0.88 |
| Cs | 0.0011 | 0.00 | 0.01 | 23.54 | 23.63 | 0.90 | 0.92 | 1.39 | 1.62 | 0.21 | 0.44 | 53.37 | 4.60 | 0.09 | 0.10 | 7.67 | 4.34 | 1.25 | 1.25 | 0.13 | 1.01 | 1.16 | 1.16 | 0.10 | 1.59 | 10.16 | 10.10 | 0.59 | 1.06 |
| Ba | 0.0008 | 6.31 | 6.75 | 6.58 | 0.87 | 169.83 | 172.80 | 1.72 | 1.34 | 102.81 | 117.60 | 12.58 | 0.86 | 122.17 | 130.90 | 6.67 | 0.44 | 1203.15 | 1218.00 | 1.22 | 0.33 | 679.73 | 683.90 | 0.61 | 0.86 | 824.10 | 826.80 | 0.33 | 0.87 |
| La | 0.0003 | 0.61 | 0.63 | 3.01 | 0.91 | 11.28 | 10.63 | 6.11 | 0.95 | 3.68 | 3.58 | 2.91 | 0.55 | 14.76 | 15.20 | 2.91 | 0.78 | 38.95 | 38.19 | 2.00 | 0.41 | 25.85 | 25.08 | 3.09 | 0.51 | 23.77 | 22.94 | 3.61 | 0.96 |
| Ce | 0.0005 | 1.99 | 1.92 | 3.89 | 1.06 | 24.55 | 23.21 | 5.75 | 0.65 | 8.54 | 9.14 | 6.52 | 0.39 | 36.03 | 37.53 | 3.99 | 0.83 | 70.67 | 68.61 | 3.00 | 0.71 | 54.74 | 53.12 | 3.05 | 0.60 | 47.48 | 46.01 | 3.19 | 0.51 |
| Pr | 0.00003 | 0.37 | 0.37 | 0.15 | 1.21 | 3.09 | 3.02 | 2.35 | 0.57 | - | - | - | 0.76 | 4.98 | 5.34 | 6.72 | 0.64 | 8.37 | 8.31 | 0.68 | 0.39 | 6.87 | 6.83 | 0.59 | 0.60 | 5.28 | 5.29 | 0.05 | 0.63 |
| Nd | 0.0003 | 2.48 | 2.40 | 3.49 | 0.70 | 13.90 | 13.09 | 6.20 | 0.46 | 5.09 | 5.20 | 2.05 | 1.03 | 23.73 | 24.27 | 2.23 | 0.87 | 32.75 | 32.07 | 2.11 | 0.86 | 29.93 | 28.26 | 5.90 | 0.65 | 19.95 | 19.19 | 3.96 | 1.19 |
| Sm | 0.0015 | 1.17 | 1.11 | 4.69 | 2.49 | 3.54 | 3.30 | 7.36 | 1.08 | 1.50 | 1.41 | 6.25 | 0.69 | 5.97 | 6.02 | 0.86 | 0.52 | 5.99 | 5.76 | 3.92 | 0.75 | 6.94 | 6.55 | 6.03 | 0.52 | 4.14 | 3.97 | 4.31 | 1.17 |
| Eu | 0.0003 | 0.54 | 0.52 | 4.43 | 1.44 | 1.16 | 1.09 | 6.34 | 1.64 | 0.60 | 0.59 | 2.41 | 2.49 | 1.95 | 2.04 | 4.47 | 1.90 | 1.68 | 1.66 | 1.14 | 0.84 | 2.06 | 1.99 | 3.34 | 0.82 | 0.64 | 0.62 | 3.66 | 2.06 |
| Gd | 0.0005 | 1.93 | 1.81 | 6.43 | 0.95 | 3.92 | 3.71 | 5.63 | 1.44 | 2.08 | 2.20 | 5.51 | 0.20 | 5.95 | 6.21 | 4.13 | 0.63 | 4.79 | 4.86 | 1.38 | 0.22 | 6.90 | 6.81 | 1.25 | 0.54 | 3.67 | 3.68 | 0.25 | 0.87 |
| Tb | 0.0002 | 0.39 | 0.36 | 7.02 | 0.89 | 0.66 | 0.63 | 5.19 | 0.79 | 0.41 | 0.42 | 3.03 | 0.97 | 0.92 | 0.94 | 2.49 | 0.72 | 0.67 | 0.67 | 0.40 | 0.46 | 1.11 | 1.08 | 2.70 | 0.65 | 0.62 | 0.60 | 3.73 | 1.00 |
| Dy | 0.00 | 2.65 | 2.54 | 4.04 | 0.72 | 3.97 | 3.81 | 4.43 | 0.69 | 2.79 | 3.00 | 6.84 | 1.02 | 5.02 | 5.28 | 4.89 | 1.03 | 3.56 | 3.58 | 0.63 | 0.55 | 6.48 | 6.42 | 0.79 | 0.81 | 3.69 | 3.67 | 0.62 | 1.33 |
| Hf | 0.0023 | 0.61 | 0.58 | 5.16 | 2.19 | 2.50 | 2.44 | 2.44 | 0.51 | 1.01 | 1.01 | 0.38 | 1.40 | 4.16 | 4.47 | 6.93 | 0.34 | 5.07 | 5.09 | 0.27 | 0.99 | 4.91 | 4.97 | 1.31 | 1.40 | 5.95 | 6.03 | 1.35 | 1.08 |
| Ta | 0.0005 | 0.07 | 0.04 | 63.73 | 3.17 | 0.57 | 0.49 | 16.72 | 0.91 | 0.10 | 0.10 | 4.87 | 1.86 | 1.18 | 1.15 | 1.93 | 1.84 | 0.89 | 0.87 | 2.90 | 0.88 | 0.83 | 0.79 | 6.19 | 0.86 | 0.97 | 0.95 | 2.57 | 1.08 |
| Ho | 0.00003 | 0.62 | 0.57 | 7.63 | 0.62 | 0.85 | 0.79 | 7.96 | 1.07 | 0.66 | 0.44 | 49.77 | 1.29 | 0.96 | 0.99 | 2.57 | 0.74 | 0.70 | 0.68 | 3.27 | 1.02 | 1.37 | 1.31 | 4.05 | 0.75 | 0.80 | 0.76 | 4.21 | 1.20 |
| Er | 0.0005 | 1.79 | 1.68 | 6.32 | 1.53 | 2.34 | 2.21 | 6.03 | 0.34 | 1.98 | 31.70 | 93.75 | 0.84 | 2.40 | 2.51 | 4.45 | 0.72 | 1.86 | 1.83 | 1.93 | 0.63 | 3.74 | 3.67 | 2.03 | 0.55 | 2.35 | 2.29 | 2.33 | 0.87 |
| Yb | 0.0089 | 1.68 | 1.63 | 2.70 | 3.05 | 2.13 | 2.05 | 3.70 | 5.61 | 1.89 | 1.98 | 4.34 | 0.61 | 1.87 | 1.99 | 6.45 | 3.80 | 1.72 | 1.66 | 3.44 | 3.90 | 3.48 | 3.39 | 2.70 | 2.09 | 2.65 | 2.47 | 7.23 | 2.78 |
| Lu | 0.0007 | 0.26 | 0.25 | 5.47 | 2.33 | 0.32 | 0.31 | 4.53 | 0.38 | 0.31 | 0.32 | 3.40 | 1.02 | 0.26 | 0.28 | 4.70 | 1.29 | 0.25 | 0.25 | 0.98 | 0.84 | 0.52 | 0.50 | 2.13 | 0.85 | 0.39 | 0.40 | 0.54 | 1.10 |
| Tl | 0.0006 | 0.00 | 0.00 | 7.07 | 21.38 | 0.10 | 0.10 | 0.81 | 1.89 | 0.02 | 0.10 | 76.44 | 9.15 | 0.02 | 0.02 | 4.81 | 5.42 | 0.35 | 0.34 | 3.50 | 1.34 | 0.29 | 0.27 | 9.36 | 2.10 | 0.99 | 0.99 | 0.17 | 0.59 |
| Pb | 0.0215 | 3.39 | 3.04 | 11.68 | 0.63 | 7.92 | 7.83 | 1.20 | 0.82 | - | - | - | 0.76 | 1.42 | 1.65 | 14.02 | 1.14 | 36.78 | 36.35 | 1.18 | 0.19 | 10.27 | 10.59 | 3.06 | 0.55 | 23.64 | 23.37 | 1.16 | 0.34 |
| Th | 0.0003 | 0.03 | 0.03 | 2.58 | 3.07 | 2.27 | 2.18 | 4.29 | 0.88 | 0.25 | 0.22 | 13.48 | 1.76 | 1.17 | 1.22 | 4.50 | 0.62 | 6.49 | 6.35 | 2.22 | 0.31 | 6.17 | 5.83 | 5.93 | 1.51 | 15.87 | 14.56 | 8.97 | 0.73 |
| U | 0.0002 | 0.01 | 0.01 | 0.35 | 5.31 | 0.51 | 0.50 | 1.18 | 1.70 | 0.05 | 0.10 | 45.77 | 2.68 | 0.38 | 0.41 | 6.66 | 1.02 | 1.90 | 1.90 | 0.16 | 0.81 | 1.67 | 1.68 | 0.59 | 1.18 | 5.68 | 5.58 | 1.73 | 0.66 |

Table A.7: Whole rock trace element accuracy and precision quantification for the reference materials of the second batch of samples. Units as in table A.6

| | DL | BIR-1 | | | | W-2 | | | | DNC-1 | | | | BHVO-2 | | | | AGV-1 | | | | RGM-1 | | | | BE-N | | | |
|----|--------|---------|---------|-------|-------|---------|---------|-------|------|---------|---------|-------|-------|----------|----------|-------|------|---------|---------|-------|------|---------|---------|-------|------|----------|----------|-------|------|
| | | Meas. | Cert. | Err % | RSD | Meas. | Cert. | Err % | RSD | Meas. | Cert. | Err % | RSD | Meas. | Cert. | Err % | RSD | Meas. | Cert. | Err % | RSD | Meas. | Cert. | Err % | RSD | Meas. | Cert. | Err % | RSD |
| Li | 0.0032 | 3.22 | 3.20 | 0.56 | 1.20 | 9.60 | 9.21 | 4.26 | 1.40 | 4.92 | 5.24 | 6.05 | 0.90 | 4.68 | 4.50 | 3.89 | 1.00 | 10.85 | 10.72 | 1.23 | 1.60 | 63.07 | 60.70 | 3.90 | 1.10 | 13.40 | 13.00 | 3.05 | 1.40 |
| Sc | 0.0023 | 43.37 | 43.21 | 0.36 | 0.40 | 36.14 | 35.86 | 0.77 | 0.80 | 31.23 | 31.40 | 0.54 | 1.60 | 31.73 | 31.83 | 0.31 | 1.40 | 12.50 | 12.43 | 0.52 | 1.50 | 4.96 | 4.74 | 4.68 | 0.70 | 23.69 | 22.00 | 7.66 | 1.00 |
| Ti | 0.0651 | 5637.15 | 5755.19 | 2.05 | 1.10 | 6326.24 | 6366.68 | 0.64 | 0.60 | 2913.45 | 2901.58 | 0.41 | 1.10 | 16244.35 | 16372.33 | 0.78 | 0.60 | 6222.89 | 6294.74 | 1.14 | 0.70 | 1558.15 | 1591.07 | 2.07 | 0.60 | 16324.45 | 15658.92 | 4.25 | 0.90 |
| V | 0.0024 | 317.37 | 320.60 | 1.01 | 1.00 | 268.64 | 265.80 | 1.07 | 1.40 | 153.16 | 147.50 | 3.84 | 1.30 | 321.80 | 318.20 | 1.13 | 0.20 | 121.20 | 119.40 | 1.51 | 0.30 | 11.26 | 11.76 | 4.29 | 0.80 | 238.15 | 235.00 | 1.34 | 0.30 |
| Cr | 0.0200 | 382.99 | 392.90 | 2.52 | 0.80 | 89.46 | 92.00 | 2.76 | 1.30 | 279.01 | 270.10 | 3.30 | 1.60 | 286.53 | 287.20 | 0.23 | 1.10 | 8.14 | 9.47 | 14.08 | 0.80 | 1.85 | 4.45 | 58.38 | 0.90 | 359.58 | 360.00 | 0.12 | 0.60 |
| Mn | 0.0037 | 1326.68 | 1355.53 | 2.13 | 1.20 | 1286.15 | 1293.56 | 0.57 | 1.90 | 1151.52 | 1146.39 | 0.45 | 2.00 | 1306.08 | 1309.05 | 0.23 | 1.20 | 735.85 | 748.25 | 1.66 | 1.00 | 283.86 | 299.77 | 5.31 | 0.70 | 1552.90 | 1550.73 | 0.14 | 0.70 |
| Co | 0.0050 | 52.12 | 52.22 | 0.19 | 1.50 | 44.18 | 44.37 | 0.43 | 1.50 | 57.90 | 56.75 | 2.03 | 1.80 | 44.82 | 44.89 | 0.17 | 1.10 | 15.39 | 15.14 | 1.64 | 1.60 | 1.97 | 2.04 | 3.82 | 0.70 | 58.91 | 60.00 | 1.81 | 1.10 |
| Ni | 0.0088 | 168.84 | 168.90 | 0.04 | 0.70 | 70.07 | 72.00 | 2.68 | 0.60 | 265.92 | 247.00 | 7.66 | 1.10 | 118.23 | 119.80 | 1.31 | 0.40 | 14.60 | 15.41 | 5.23 | 1.60 | 1.58 | 3.41 | 53.67 | 3.50 | 273.78 | 267.00 | 2.54 | 0.90 |
| Cu | 0.0083 | 124.32 | 120.70 | 3.00 | 1.60 | 108.90 | 105.90 | 2.84 | 0.70 | 98.62 | 99.70 | 1.09 | 0.70 | 130.95 | 129.30 | 1.28 | 0.40 | 57.82 | 58.42 | 1.02 | 1.40 | 10.83 | 11.09 | 2.39 | 1.20 | 70.99 | 72.00 | 1.41 | 0.50 |
| Zn | 0.0064 | 70.79 | 70.40 | 0.56 | 1.70 | 77.26 | 77.70 | 0.56 | 1.60 | 65.98 | 70.10 | 5.88 | 1.50 | 105.37 | 103.90 | 1.41 | 1.00 | 90.04 | 86.80 | 3.73 | 1.10 | 31.89 | 33.20 | 3.93 | 1.20 | 121.45 | 120.00 | 1.21 | 0.70 |
| Ga | 0.0012 | 15.27 | 15.46 | 1.20 | 0.80 | 17.56 | 17.88 | 1.81 | 2.10 | 13.64 | 14.70 | 7.22 | 4.20 | 21.16 | 21.37 | 0.98 | 0.80 | 20.08 | 20.36 | 1.39 | 1.10 | 15.95 | 16.06 | 0.72 | 1.00 | 18.37 | 17.00 | 8.04 | 1.10 |
| Rb | 0.0019 | 0.19 | 0.21 | 9.52 | 1.00 | 19.50 | 20.23 | 3.63 | 1.00 | 3.54 | 4.70 | 24.77 | 1.40 | 9.12 | 9.26 | 1.55 | 1.00 | 64.53 | 67.80 | 4.82 | 0.80 | 151.10 | 149.50 | 1.07 | 1.30 | 48.32 | 47.00 | 2.81 | 1.50 |
| Sr | 0.0004 | 105.55 | 108.60 | 2.81 | 0.50 | 195.84 | 195.40 | 0.22 | 0.80 | 142.37 | 144.00 | 1.13 | 1.00 | 394.82 | 394.10 | 0.18 | 0.90 | 651.06 | 661.00 | 1.50 | 1.00 | 103.88 | 104.80 | 0.88 | 1.20 | 1391.99 | 1370.00 | 1.60 | 1.10 |
| Y | 0.0004 | 15.61 | 15.60 | 0.08 | 0.80 | 22.75 | 21.82 | 4.28 | 1.30 | 18.25 | 18.50 | 1.36 | 1.90 | 27.41 | 25.91 | 5.79 | 0.60 | 19.75 | 19.69 | 0.31 | 0.60 | 24.06 | 23.48 | 2.46 | 1.50 | 30.64 | 30.00 | 2.12 | 1.00 |
| Zr | 0.0035 | 15.24 | 14.80 | 3.00 | 1.40 | 92.40 | 93.30 | 0.96 | 1.10 | 37.86 | 38.50 | 1.67 | 1.00 | 174.26 | 171.20 | 1.79 | 0.90 | 232.87 | 231.50 | 0.59 | 1.80 | 229.01 | 227.90 | 0.49 | 0.50 | 282.33 | 260.00 | 8.59 | 1.50 |
| Nb | 0.0004 | 0.56 | 0.55 | 0.90 | 1.70 | 7.72 | 7.51 | 2.81 | 1.50 | 1.58 | 3.19 | 50.41 | 0.90 | 19.17 | 18.10 | 5.91 | 1.30 | 15.00 | 14.53 | 3.23 | 0.90 | 9.72 | 9.13 | 6.44 | 0.80 | 124.12 | 105.00 | 18.21 | 0.80 |
| Sn | 0.0027 | 0.81 | 0.70 | 14.84 | 0.60 | 2.07 | 1.92 | 7.71 | 1.40 | - | - | - | 2.30 | 1.99 | 1.78 | 12.11 | 1.30 | 4.29 | 4.88 | 12.19 | 1.20 | 4.39 | 4.34 | 1.04 | 1.10 | 2.08 | 2.00 | 3.80 | 0.90 |
| Sb | 0.0011 | 0.47 | 0.46 | 1.30 | 1.90 | 0.91 | 0.81 | 12.24 | 2.40 | 0.81 | 0.96 | 15.52 | 0.60 | 0.10 | 0.10 | 7.16 | 6.00 | 4.53 | 4.24 | 6.84 | 0.60 | 1.23 | 1.23 | 0.24 | 1.30 | 0.17 | 0.26 | 33.85 | 3.30 |
| Cs | 0.0002 | 0.01 | 0.01 | 22.60 | 4.70 | 0.88 | 0.92 | 3.61 | 1.10 | 0.21 | 0.44 | 53.18 | 1.50 | 0.10 | 0.10 | 2.61 | 1.90 | 1.24 | 1.25 | 0.64 | 0.60 | 10.11 | 10.10 | 0.11 | 0.70 | 0.73 | 0.80 | 9.00 | 1.40 |
| Ba | 0.0022 | 6.20 | 6.75 | 8.10 | 0.90 | 166.89 | 172.80 | 3.42 | 1.30 | 102.19 | 117.60 | 13.10 | 1.40 | 130.11 | 130.90 | 0.61 | 1.30 | 1214.81 | 1218.00 | 0.26 | 0.40 | 830.00 | 826.80 | 0.39 | 0.50 | 1047.38 | 1025.00 | 2.18 | 1.10 |
| La | 0.0003 | 0.60 | 0.63 | 4.78 | 0.90 | 10.70 | 10.63 | 0.64 | 0.90 | 3.59 | 3.58 | 0.25 | 0.70 | 15.40 | 15.20 | 1.34 | 0.70 | 38.38 | 38.19 | 0.50 | 5.00 | 23.25 | 22.94 | 1.36 | 0.80 | 82.52 | 82.00 | 0.63 | 0.50 |
| Ce | 0.0003 | 1.92 | 1.92 | 0.21 | 0.40 | 23.18 | 23.21 | 0.13 | 1.20 | 8.27 | 9.14 | 9.56 | 1.10 | 37.27 | 37.53 | 0.68 | 0.50 | 69.38 | 68.61 | 1.12 | 5.40 | 45.44 | 46.01 | 1.24 | 1.10 | 152.94 | 152.00 | 0.62 | 0.20 |
| Pr | 0.0001 | 0.37 | 0.37 | 0.46 | 1.10 | 3.02 | 3.02 | 0.07 | 0.80 | - | - | - | 1.10 | 5.37 | 5.34 | 0.58 | 0.50 | 8.51 | 8.31 | 2.42 | 5.50 | 5.28 | 5.29 | 0.15 | 0.70 | 17.56 | 17.50 | 0.33 | 0.60 |
| Nd | 0.0008 | 2.38 | 2.40 | 0.58 | 1.40 | 13.00 | 13.09 | 0.73 | 0.80 | 4.94 | 5.20 | 5.04 | 0.90 | 24.54 | 24.27 | 1.09 | 0.50 | 31.77 | 32.07 | 0.94 | 4.90 | 19.07 | 19.19 | 0.61 | 0.50 | 69.29 | 67.00 | 3.42 | 1.40 |
| Sm | 0.0003 | 1.10 | 1.11 | 0.90 | 1.00 | 3.33 | 3.30 | 0.79 | 1.20 | 1.44 | 1.41 | 2.27 | 1.20 | 6.17 | 6.02 | 2.51 | 0.70 | 5.82 | 5.76 | 0.88 | 4.70 | 3.96 | 3.97 | 0.23 | 1.00 | 12.07 | 12.20 | 1.03 | 0.50 |
| Eu | 0.0006 | 0.51 | 0.52 | 2.71 | 1.70 | 1.08 | 1.09 | 0.64 | 0.60 | 0.58 | 0.59 | 1.86 | 2.00 | 2.01 | 2.04 | 1.57 | 0.90 | 1.64 | 1.66 | 0.84 | 5.50 | 0.63 | 0.62 | 0.80 | 2.00 | 3.63 | 3.60 | 0.89 | 1.00 |
| Gd | 0.0002 | 1.86 | 1.81 | 2.76 | 1.90 | 3.70 | 3.71 | 0.24 | 0.80 | 2.05 | 2.20 | 6.73 | 0.50 | 6.25 | 6.21 | 0.66 | 0.60 | 4.73 | 4.86 | 2.71 | 3.90 | 3.59 | 3.68 | 2.55 | 1.40 | 9.94 | 9.70 | 2.44 | 1.00 |
| Tb | 0.0001 | 0.37 | 0.36 | 3.23 | 1.10 | 0.63 | 0.63 | 0.16 | 1.00 | 0.40 | 0.42 | 4.76 | 0.60 | 0.95 | 0.94 | 1.58 | 1.00 | 0.66 | 0.67 | 1.34 | 5.00 | 0.60 | 0.60 | 0.00 | 0.40 | 1.30 | 1.30 | 0.31 | 0.80 |
| Dy | 0.0000 | 2.57 | 2.54 | 1.14 | 0.70 | 3.85 | 3.81 | 1.02 | 0.50 | 2.76 | 3.00 | 8.13 | 0.30 | 5.31 | 5.28 | 0.59 | 0.50 | 3.58 | 3.58 | 0.20 | 5.60 | 3.63 | 3.67 | 1.01 | 1.10 | 6.36 | 6.40 | 0.58 | 0.90 |
| Hf | 0.0004 | 0.59 | 0.58 | 1.51 | 1.20 | 2.41 | 2.44 | 1.43 | 1.10 | 1.02 | 1.01 | 0.50 | 0.70 | 4.40 | 4.47 | 1.50 | 1.10 | 5.02 | 5.09 | 1.28 | 0.80 | 5.83 | 6.03 | 3.32 | 1.30 | 5.78 | 5.60 | 3.20 | 1.60 |
| Ta | 0.0003 | 0.05 | 0.04 | 11.11 | 2.00 | 0.49 | 0.49 | 0.61 | 2.10 | 0.10 | 0.10 | 3.00 | 5.80 | 1.22 | 1.15 | 5.37 | 0.70 | 0.87 | 0.87 | 0.58 | 1.20 | 0.94 | 0.95 | 1.26 | 2.10 | 5.96 | 5.70 | 4.63 | 0.50 |
| Ho | 0.0001 | 0.59 | 0.57 | 2.31 | 1.00 | 0.80 | 0.79 | 1.67 | 1.00 | 0.64 | 0.44 | 46.36 | 0.60 | 1.00 | 0.99 | 0.84 | 0.60 | 0.69 | 0.68 | 0.88 | 5.10 | 0.77 | 0.76 | 0.79 | 1.40 | 1.09 | 1.10 | 1.27 | 0.90 |
| Er | 0.0010 | 1.73 | 1.68 | 2.86 | 0.80 | 2.28 | 2.21 | 3.03 | 0.90 | 1.95 | 31.70 | 93.84 | 0.60 | 2.56 | 2.51 | 1.75 | 1.00 | 1.86 | 1.83 | 1.64 | 5.20 | 2.32 | 2.29 | 1.09 | 0.70 | 2.57 | 2.50 | 2.96 | 1.20 |
| Yb | 0.0061 | 1.61 | 1.63 | 1.59 | 3.30 | 2.05 | 2.05 | 0.10 | 2.20 | 1.96 | 1.98 | 0.91 | 2.00 | 1.96 | 1.99 | 1.55 | 1.90 | 1.63 | 1.66 | 1.75 | 3.80 | 2.48 | 2.47 | 0.36 | 2.10 | 1.80 | 1.80 | 0.06 | 2.60 |
| Lu | 0.0007 | 0.25 | 0.25 | 1.05 | 0.90 | 0.31 | 0.31 | 0.97 | 0.20 | 0.31 | 0.32 | 4.69 | 0.60 | 0.28 | 0.28 | 0.58 | 0.80 | 0.24 | 0.25 | 3.10 | 5.70 | 0.39 | 0.40 | 3.02 | 1.00 | 0.24 | 0.24 | 1.67 | 1.10 |
| Tl | 0.0013 | 0.00 | 0.00 | 52.38 | 44.50 | 0.11 | 0.10 | 2.88 | 2.40 | 0.02 | 0.10 | 76.00 | 10.30 | 0.02 | 0.02 | 1.79 | 4.60 | 0.36 | 0.34 | 5.34 | 1.40 | 0.99 | 0.99 | 0.10 | 1.70 | 0.03 | 0.04 | 17.50 | 8.80 |
| Pb | 0.0027 | 2.95 | 3.04 | 3.03 | 1.00 | 8.22 | 7.83 | 4.94 | 0.50 | 5.97 | - | - | 0.70 | 1.52 | 1.65 | 7.86 | 1.20 | 37.47 | 36.35 | 3.09 | 0.60 | 23.02 | 23.37 | 1.51 | 0.40 | 3.91 | 4.00 | 2.20 | 0.80 |
| Th | 0.0003 | 0.03 | 0.03 | 2.44 | 4.60 | 2.10 | 2.18 | 3.67 | 1.50 | 0.25 | 0.22 | 11.36 | 1.90 | 1.16 | 1.22 | 4.98 | 0.90 | 6.01 | 6.35 | 5.40 | 1.20 | 14.67 | 14.56 | 0.76 | 1.30 | 10.81 | 10.40 | 3.90 | 1.50 |
| U | 0.0002 | 0.01 | 0.01 | 14.37 | 9.80 | 0.49 | 0.50 | 2.34 | 0.60 | 0.06 | 0.10 | 42.00 | 3.80 | 0.41 | 0.41 | 0.00 | 3.20 | 1.88 | 1.90 | 1.26 | 1.70 | 5.61 | 5.58 | 0.45 | 1.10 | 2.42 | 2.40 | 0.92 | 0.80 |

A.3 Radiogenic isotopes

Table A.8. Radiogenic isotope ratios and analytical errors

| Sample | Unit | $^{87}\text{Sr}/^{86}\text{Sr}$ | ± 2SE | $^{143}\text{Nd}/^{144}\text{Nd}$ | ± 2SE | $^{176}\text{Hf}/^{177}\text{Hf}$ | ± 2SE | $^{206}\text{Pb}/^{204}\text{Pb}$ | ± 2SE | $^{207}\text{Pb}/^{204}\text{Pb}$ | ± 2SE | $^{208}\text{Pb}/^{204}\text{Pb}$ | ± 2SE |
|----------------|-----------------|---------------------------------|----------|-----------------------------------|----------|-----------------------------------|----------|-----------------------------------|--------|-----------------------------------|--------|-----------------------------------|--------|
| Ati425.02t | High-K LCY | 0.704016 | 0.000011 | 0.512862 | 0.000006 | 0.282986 | 0.000007 | 18.6886 | 0.0009 | 15.5982 | 0.0008 | 38.4582 | 0.0023 |
| Ati425.03 | Medium-K LCY | 0.703998 | 0.000015 | 0.512856 | 0.000005 | 0.283152 | 0.000004 | 18.6961 | 0.0007 | 15.5988 | 0.0007 | 38.4636 | 0.0021 |
| Ati425.03(b) | High-K LCY | 0.704017 | 0.000011 | 0.512856 | 0.000005 | 0.282973 | 0.000005 | 18.6947 | 0.0039 | 15.5950 | 0.0025 | 38.4566 | 0.0083 |
| Ati426.01 | Granodiorite | 0.704391 | 0.000006 | 0.512802 | 0.000005 | - | - | 18.7403 | 0.0007 | 15.6158 | 0.0007 | 38.5643 | 0.0019 |
| Ati426.02 | Granodiorite | 0.705008 | 0.000007 | 0.512630 | 0.000008 | 0.283030 | 0.000005 | 18.7655 | 0.0007 | 15.6341 | 0.0007 | 38.6282 | 0.0020 |
| Ati426.03h | D2 | 0.704032 | 0.00001 | 0.512857 | 0.000005 | 0.282998 | 0.000006 | 18.6892 | 0.0006 | 15.5971 | 0.0006 | 38.4553 | 0.0016 |
| Ati427.01a | D1 | 0.704072 | 0.000009 | 0.512852 | 0.000006 | 0.282993 | 0.000004 | 18.6915 | 0.0006 | 15.5967 | 0.0006 | 38.4554 | 0.0017 |
| Ati427.01j | D2 | 0.704037 | 0.000026 | 0.512866 | 0.000006 | 0.282999 | 0.000006 | 18.6939 | 0.0005 | 15.5981 | 0.0006 | 38.4618 | 0.0018 |
| Ati427.02a | D2 | 0.704032 | 0.000009 | 0.512850 | 0.000005 | 0.282995 | 0.000005 | 18.6780 | 0.0006 | 15.5976 | 0.0006 | 38.4495 | 0.0016 |
| Ati427.04f | F | 0.703991 | 0.000007 | 0.512867 | 0.000008 | 0.283033 | 0.000005 | 18.7199 | 0.0007 | 15.5987 | 0.0007 | 38.4814 | 0.0020 |
| Ati427.08a | Tecolote | 0.704380 | 0.000006 | 0.512747 | 0.000007 | 0.282876 | 0.000005 | 18.7453 | 0.0006 | 15.6207 | 0.0006 | 38.5721 | 0.0018 |
| Ati427.08b | Tecolote | 0.704341 | 0.000009 | 0.512742 | 0.000007 | 0.282892 | 0.000005 | 18.7487 | 0.0006 | 15.6280 | 0.0005 | 38.5961 | 0.0015 |
| Ati427.11 | Cerro Las Minas | 0.704464 | 0.000009 | 0.512738 | 0.000009 | 0.282890 | 0.000006 | 18.6975 | 0.0007 | 15.6179 | 0.0007 | 38.5320 | 0.0019 |
| Ati429.04 | Low-K LCY | 0.704007 | 0.000007 | 0.512855 | 0.000005 | 0.282985 | 0.000004 | 18.6917 | 0.0009 | 15.5982 | 0.0010 | 38.4580 | 0.0028 |
| Ati430.11a | I | 0.703996 | 0.000012 | 0.512844 | 0.000011 | 0.282996 | 0.000006 | 18.7027 | 0.0006 | 15.5999 | 0.0006 | 38.4749 | 0.0017 |
| Ati430.11b | I | 0.704012 | 0.000012 | 0.512866 | 0.00001 | 0.282996 | 0.000005 | 18.6983 | 0.0006 | 15.5999 | 0.0006 | 38.4707 | 0.0016 |
| Ati501.02 | Paquisis | 0.704066 | 0.000009 | 0.512833 | 0.000007 | 0.282966 | 0.000005 | 18.7113 | 0.0006 | 15.6051 | 0.0005 | 38.4969 | 0.0015 |
| Ati501.03 | Paquisis | 0.704096 | 0.000009 | 0.512848 | 0.000007 | 0.282987 | 0.000005 | 18.6571 | 0.0006 | 15.5958 | 0.0007 | 38.4252 | 0.0018 |
| Ati501.05a | Atitlán | 0.704075 | 0.000006 | 0.512839 | 0.000009 | 0.282986 | 0.000005 | 18.6907 | 0.0006 | 15.6021 | 0.0005 | 38.4712 | 0.0017 |
| Ati501.05b | Atitlán | 0.704025 | 0.000018 | 0.512831 | 0.000004 | 0.282969 | 0.000007 | 18.7057 | 0.0006 | 15.6047 | 0.0006 | 38.4904 | 0.0015 |
| Ati501.05c | Atitlán | 0.704081 | 0.000009 | 0.512834 | 0.000008 | 0.282980 | 0.000004 | 18.7012 | 0.0004 | 15.6035 | 0.0004 | 38.4843 | 0.0012 |
| Ati501.06a | D2 | 0.703998 | 0.000009 | 0.512851 | 0.000004 | 0.282977 | 0.000004 | 18.7051 | 0.0006 | 15.6014 | 0.0006 | 38.4775 | 0.0017 |
| Ati501.06c | Andesite Scoria | 0.704000 | 0.000011 | 0.512876 | 0.000003 | 0.283026 | 0.000005 | 18.6838 | 0.0007 | 15.5955 | 0.0006 | 38.4431 | 0.0019 |
| Ati502.06 | High-K LCY | 0.704021 | 0.00001 | 0.512852 | 0.000004 | 0.282990 | 0.000006 | 18.6928 | 0.0006 | 15.6014 | 0.0007 | 38.4710 | 0.0018 |
| Ati503.02 | Leucogranite | 0.705009 | 0.000014 | 0.512741 | 0.000005 | 0.282960 | 0.000007 | 18.7412 | 0.0006 | 15.6105 | 0.0006 | 38.5233 | 0.0019 |
| Ati503.05 | Tolimán | 0.703920 | 0.000011 | 0.512897 | 0.000005 | 0.283024 | 0.000004 | 18.6801 | 0.0004 | 15.5942 | 0.0004 | 38.4387 | 0.0014 |
| Ati503.07 | Tolimán | 0.704005 | 0.000009 | 0.512864 | 0.000005 | 0.283011 | 0.000004 | 18.6909 | 0.0005 | 15.5974 | 0.0005 | 38.4573 | 0.0015 |
| Ati503.08 | Tolimán | 0.703966 | 0.000007 | 0.512873 | 0.000004 | 0.283010 | 0.000004 | 18.6934 | 0.0005 | 15.5961 | 0.0005 | 38.4544 | 0.0016 |
| Ati504.03 | San Marcos | 0.704292 | 0.000008 | 0.512771 | 0.000005 | 0.282901 | 0.000006 | 18.7300 | 0.0005 | 15.6162 | 0.0005 | 38.5480 | 0.0015 |
| Ati504.06a | Tecolote | 0.704211 | 0.000008 | 0.512781 | 0.000007 | 0.282920 | 0.000004 | 18.6995 | 0.0006 | 15.6091 | 0.0006 | 38.5043 | 0.0016 |
| Ati504.06b | Tecolote | 0.704220 | 0.000005 | 0.512797 | 0.000008 | 0.282910 | 0.000004 | 18.7100 | 0.0005 | 15.6089 | 0.0004 | 38.5093 | 0.0014 |
| Ati505.01 | San Pedro | 0.703959 | 0.000005 | 0.512889 | 0.000004 | 0.283005 | 0.000004 | 18.6783 | 0.0005 | 15.5917 | 0.0004 | 38.4303 | 0.0012 |
| Ati505.03 | San Pedro | 0.703992 | 0.000006 | 0.512887 | 0.000009 | 0.282993 | 0.000005 | 18.6762 | 0.0005 | 15.5923 | 0.0005 | 38.4309 | 0.0015 |
| Ati505.04 | San Pedro | 0.704005 | 0.000006 | 0.512883 | 0.00001 | 0.282987 | 0.000004 | 18.6612 | 0.0006 | 15.5931 | 0.0006 | 38.4225 | 0.0016 |
| Ati505.05 | San Pedro | 0.703905 | 0.000007 | 0.512895 | 0.000009 | 0.283017 | 0.000005 | 18.6645 | 0.0004 | 15.5925 | 0.0004 | 38.4225 | 0.0011 |
| Ati505.06a | I1 | 0.703835 | 0.000005 | 0.512910 | 0.000008 | 0.283016 | 0.000004 | 18.6698 | 0.0006 | 15.5896 | 0.0006 | 38.4185 | 0.0019 |
| Ati505.06h | I | 0.703991 | 0.000007 | 0.512853 | 0.000005 | 0.282972 | 0.000005 | 18.7024 | 0.0009 | 15.6013 | 0.0008 | 38.4763 | 0.0023 |
| Ati505.06h (e) | I (enclave) | 0.703954 | 0.00001 | 0.512835 | 0.000007 | 0.282965 | 0.000004 | 18.6893 | 0.0006 | 15.5985 | 0.0006 | 38.4569 | 0.0018 |

Table A.9. $^{87}\text{Sr}/^{86}\text{Sr}$ measured secondary standard accuracy and precision

| Name | $^{87}\text{Sr}/^{86}\text{Sr}$ | $\pm 2\text{SE}$ |
|-------------|---------------------------------|------------------|
| BCR-2 Meas. | 0.704998 | 0.000011 |
| BCR-2 Meas. | 0.705019 | 0.000010 |
| BCR-2 Ref. | 0.70492 | |
| BCR-2 Acc. | 0.013 | |
| BCR-2 RSD | 0.0021 | |

Table A.10. $^{143}\text{Nd}/^{144}\text{Nd}$ measured secondary standard accuracy and precision

| Name | $^{143}\text{Nd}/^{144}\text{Nd}$ | $\pm 2\text{SE}$ |
|-------------|-----------------------------------|------------------|
| BCR-2 Meas. | 0.512647 | 0.000019 |
| BCR-2 Meas. | 0.512647 | 0.000007 |
| BCR-2 Meas. | 0.512637 | 0.000008 |
| BCR-2 Meas. | 0.512642 | 0.000005 |
| BCR-2 Meas. | 0.512642 | 0.000006 |
| BCR-2 Meas. | 0.512641 | 0.000005 |
| BCR-2 Meas. | 0.512643 | 0.000006 |
| BCR-2 Meas. | 0.512642 | 0.000004 |
| BCR-2 Ref. | 0.512635 | |
| BCR-2 Acc. | 0.0015 | |
| BCR-2 RSD | 0.00063 | |

Table A.11. $^{176}\text{Hf}/^{177}\text{Hf}$ measured secondary standard accuracy and precision

| Name | $^{176}\text{Hf}/^{177}\text{Hf}$ | $\pm 2\text{SE}$ |
|-------------|-----------------------------------|------------------|
| BCR-2 Meas. | 0.282951 | 0.000004 |
| BCR-2 Meas. | 0.283043 | 0.000005 |
| BCR-2 Ref. | 0.282865 | |
| BCR-2 Acc. | 0.047 | |
| BCR-2 RSD | 0.023 | |

Table A.12 Pb isotope measured secondary standard accuracy and precision.

| Sample | Pb206/Pb204 | ± 2SE | Pb207/Pb204 | ± 2SE | Pb208/Pb204 | ± 2SE |
|------------|-------------|--------|-------------|--------|-------------|--------|
| BCR-2 | 18.7608 | 0.0006 | 15.6282 | 0.0005 | 38.7412 | 0.0015 |
| BCR-2 | 18.7621 | 0.0006 | 15.6277 | 0.0007 | 38.7483 | 0.0019 |
| BCR-2 Av. | 18.7614 | | 15.6279 | | 38.7448 | |
| BCR-2 Ref. | 18.7540 | | 15.6220 | | 38.7260 | |
| BCR-2 Acc. | 0.040 | | 0.038 | | 0.048 | |
| BCR-2 RSD | 0.0049 | | 0.0025 | | 0.013 | |

Appendix B: Microanalysis data

This Appendix consists of two sections, section B.1 showing the secondary standard data analysed on the two EPMA's (JEOL 8530F and Cameca SX100) used in this study (Tables B.1 and B.2), the standard deviations of the data (Tables B.3 and B.4), representative analytical uncertainties for selected phases (Table B.5), and data for the EPMA calibration standards. Section B.2 shows the secondary standard data analysed for the two runs of the LA-ICP-MS trace elements (Tables B.7 and B.8), the accuracy and precisions of the secondary standards (Tables B.9 and B.10), and the metadata for the two runs (Tables B.11 and B.12).

B.1 EPMA data

Table B.1. EPMA secondary standard data for the JEOL 8530F, showing the measured and reference values, calculated accuracy and precision, and detection limits. These show the repeated analyses of international standards of the period of analysis. All values in wt.% unless stated otherwise, all Fe analysed as FeO.

| SAMPLE | SiO ₂ | TiO ₂ | Al ₂ O ₃ | FeO | MnO | MgO | CaO | Na ₂ O | K ₂ O | P ₂ O ₅ | F | Cl | TOTAL |
|--------------------------------------|------------------|------------------|--------------------------------|-------|-------|-------|-------|-------------------|------------------|-------------------------------|-------|-------|-------|
| BCR-2G Det.Lim. | 0.012 | 0.011 | 0.009 | 0.021 | 0.021 | 0.008 | 0.007 | 0.010 | 0.008 | 0.017 | 0.004 | 0.014 | |
| BCR-2G Reference | 54.1 | 2.27 | 13.4 | 12.4 | 0.19 | 3.56 | 7.06 | 3.16 | 2 | 0.37 | 0.02 | 0.01 | 98.4 |
| BCR-2G Measured | 54.4 | 2.21 | 13.1 | 12.0 | 0.17 | 3.51 | 6.94 | 2.89 | 2.09 | 0.31 | 0.10 | 0.008 | 97.8 |
| BCR-2G Measured | 54.5 | 2.21 | 13.1 | 12.2 | 0.18 | 3.56 | 7.02 | 2.97 | 2.07 | 0.36 | 0.11 | 0.007 | 98.3 |
| BCR-2G Measured | 54.5 | 2.18 | 13.0 | 12.2 | 0.18 | 3.50 | 6.96 | 2.95 | 2.05 | 0.36 | 0.12 | 0.007 | 98.1 |
| BCR-2G Mean acc. (%) | 0.76 | 2.94 | 2.53 | 2.19 | 5.70 | 0.99 | 1.18 | 7.08 | 3.52 | 7.41 | 445 | 25.5 | |
| BCR-2G RSD (%) | 0.10 | 0.85 | 0.29 | 0.78 | 2.55 | 0.9 | 0.62 | 1.55 | 0.89 | 7.41 | 10.7 | 7.00 | |
| Olivine_EagleStation Det.Lim. | 0.013 | | | 0.021 | 0.021 | 0.008 | 0.007 | | | | | | |
| Olivine_EagleStation Ref. | 39.2 | | | 18.5 | 0.22 | 41.7 | 0.050 | | | | | | 99.7 |
| Olivine_EagleStation Mea. | 39.3 | | | 18.6 | 0.18 | 41.5 | 0.06 | | | | | | 99.6 |
| Olivine_EagleStation Mea. | 39.4 | | | 18.8 | 0.16 | 41.9 | 0.06 | | | | | | 100.3 |
| Olivine_EagleStation Mea. | 39.4 | | | 18.6 | 0.15 | 41.7 | 0.06 | | | | | | 100.0 |
| Olivine_EagleStation Mean acc. (%) | 0.37 | | | 0.87 | 25.1 | 0.33 | 17.8 | | | | | | |
| Olivine_EagleStation RSD (%) | 0.11 | | | 0.61 | 8.82 | 0.49 | 1.81 | | | | | | |
| IsleOfRhum_Plagioclase Det.Lim. | 0.012 | 0.011 | 0.008 | 0.020 | | | 0.007 | 0.009 | 0.008 | | | | |
| IsleOfRhum_Plagioclase Ref. | 46.2 | 0.05 | 33.8 | 0.45 | | | 17.3 | 1.42 | 0.03 | | | | 99.3 |
| IsleOfRhum_Plagioclase Mea. | 46.8 | 0.04 | 33.3 | 0.38 | | | 17.6 | 1.41 | 0.04 | | | | 99.7 |
| IsleOfRhum_Plagioclase Mea. | 46.6 | 0.04 | 33.3 | 0.46 | | | 17.6 | 1.35 | 0.03 | | | | 99.6 |
| IsleOfRhum_Plagioclase Mea. | 46.3 | 0.03 | 33.2 | 0.47 | | | 17.7 | 1.35 | 0.03 | | | | 99.2 |
| IsleOfRhum_Plagioclase Mean acc. (%) | 0.82 | 34.9 | 1.52 | 6.96 | | | 1.92 | 3.53 | 20.3 | | | | |
| IsleOfRhum_Plagioclase RSD (%) | 0.48 | 14.9 | 0.24 | 10.6 | | | 0.30 | 2.56 | 16.5 | | | | |

Table B.2 EPMA secondary standard data for the Cameca SX100, showing the measured and reference values, calculated accuracy and precision, and detection limits. These show the repeated analyses of international standards of the period of analysis. All values in wt.% unless stated otherwise, all Fe analysed as FeO. Below detection limit - bdl

| SAMPLE | SiO ₂ | TiO ₂ | Al ₂ O ₃ | FeO | MnO | MgO | CaO | Na ₂ O | K ₂ O | P ₂ O ₅ | F | Cl | TOTAL |
|--------------------------------------|------------------|------------------|--------------------------------|-------|-------|-------|-------|-------------------|------------------|-------------------------------|-------|-------|-------|
| BCR-2G Det.Lim. | 0.054 | 0.002 | 0.079 | 0.045 | 0.028 | 0.055 | 0.086 | 0.048 | 0.063 | 0.023 | 0.211 | 0.147 | |
| BCR-2G Ref. | 54.1 | 2.27 | 13.4 | 12.4 | 0.19 | 3.56 | 7.06 | 3.16 | 2.00 | 0.37 | 0.02 | 0.01 | 98.4 |
| BCR-2G Meas. | 55.2 | 2.31 | 13.5 | 12.3 | 0.16 | 3.68 | 7.28 | 3.02 | 2.15 | 0.35 | 0.05 | bdl | 100.0 |
| BCR-2G Meas. | 54.9 | 2.33 | 13.5 | 12.3 | 0.17 | 3.64 | 7.37 | 3.12 | 2.05 | 0.36 | bdl | bdl | 99.7 |
| BCR-2G Meas. | 55.0 | 2.37 | 13.4 | 12.2 | 0.26 | 3.66 | 7.26 | 3.06 | 2.13 | 0.43 | 0.02 | bdl | 99.8 |
| BCR-2G Meas. | 55.0 | 2.30 | 13.4 | 12.6 | 0.18 | 3.62 | 7.29 | 2.99 | 2.06 | 0.34 | 0.01 | 0.01 | 99.8 |
| BCR-2G Meas. | 54.7 | 2.30 | 13.5 | 12.3 | 0.20 | 3.59 | 7.30 | 3.07 | 2.12 | 0.29 | bdl | bdl | 99.4 |
| BCR-2G Mean Acc. (%) | 1.57 | 2.29 | 0.52 | 1.03 | 14.7 | 2.19 | 3.40 | 3.42 | 5.10 | 10.8 | 80.0 | 80.0 | |
| BCR-2G RSD (%) | 0.33 | 1.27 | 0.34 | 1.11 | 20.5 | 0.96 | 0.57 | 1.63 | 2.11 | 14.2 | 130 | 224 | |
| Olivine_EagleStation Det.Lim. | 0.035 | | | 0.031 | 0.027 | 0.036 | 0.056 | | | | | | |
| Olivine_EagleStation Ref. | 39.2 | | | 18.5 | 0.22 | 41.7 | 0.05 | | | | | | |
| Olivine_EagleStation Meas. | 39.7 | | | 19.3 | 0.16 | 42.4 | 0.05 | | | | | | 101.7 |
| Olivine_EagleStation Meas. | 39.9 | | | 19.2 | 0.20 | 42.3 | 0.08 | | | | | | 101.8 |
| Olivine_EagleStation Meas. | 39.8 | | | 19.4 | 0.20 | 42.5 | 0.07 | | | | | | 102.0 |
| Olivine_EagleStation Meas. | 39.8 | | | 18.9 | 0.25 | 42.3 | 0.06 | | | | | | 101.4 |
| Olivine_EagleStation Mean Acc. (%) | 1.49 | | | 3.64 | 14.8 | 1.58 | 30.00 | | | | | | |
| Olivine_EagleStation RSD (%) | 0.25 | | | 0.94 | 18.2 | 0.20 | 19.9 | | | | | | |
| IsleOfRhum_Plagioclase Det.Lim. | 0.035 | 0.001 | 0.053 | 0.034 | | | 0.057 | 0.038 | 0.044 | | | | |
| IsleOfRhum_Plagioclase Ref. | 46.2 | 0.05 | 33.8 | 0.45 | | | 17.3 | 1.42 | 0.03 | | | | |
| IsleOfRhum_Plagioclase Meas. | 46.0 | 0.05 | 33.1 | 0.45 | | | 18.1 | 1.43 | 0.03 | | | | 99.3 |
| IsleOfRhum_Plagioclase Meas. | 46.3 | 0.05 | 33.3 | 0.53 | | | 18.0 | 1.42 | 0.03 | | | | 99.8 |
| IsleOfRhum_Plagioclase Meas. | 46.1 | 0.04 | 33.3 | 0.50 | | | 18.1 | 1.45 | 0.02 | | | | 99.8 |
| IsleOfRhum_Plagioclase Meas. | 46.3 | 0.03 | 33.3 | 0.33 | | | 18.2 | 1.46 | 0.04 | | | | 99.8 |
| IsleOfRhum_Plagioclase Meas. | 46.3 | 0.03 | 33.4 | 0.43 | | | 18.2 | 1.44 | 0.06 | | | | 100.0 |
| IsleOfRhum_Plagioclase Meas. | 46.0 | 0.02 | 32.8 | 0.33 | | | 17.8 | 1.45 | 0.11 | | | | 98.7 |
| IsleOfRhum_Plagioclase Meas. | 46.1 | 0.05 | 33.2 | 0.38 | | | 18.1 | 1.49 | 0.03 | | | | 99.5 |
| IsleOfRhum_Plagioclase Mean Acc. (%) | 0.24 | 22.9 | 1.75 | 14.6 | | | 4.47 | 2.01 | 61.9 | | | | |
| IsleOfRhum_Plagioclase RSD (%) | 0.29 | 31.5 | 0.58 | 18.7 | | | 0.73 | 1.57 | 67.8 | | | | |

Table B.3 Secondary standard measured standard deviations for the JEOL 8530F. Values in wt.%

| SAMPLE | Si SD | Ti SD | Al SD | Fe SD | Mn SD | Mg SD | Ca SD | Na SD | K SD | P SD | F SD | Cl SD |
|------------------------|-------|-------|-------|-------|-------|-------|-------|-------|------|------|------|-------|
| BCR-2G | 0.18 | 0.04 | 0.15 | 0.11 | 0.02 | 0.04 | 0.05 | 0.08 | 0.05 | 0.09 | 0.67 | 0.03 |
| BCR-2G | 0.18 | 0.04 | 0.15 | 0.11 | 0.02 | 0.04 | 0.05 | 0.08 | 0.05 | 0.10 | 0.84 | 0.02 |
| BCR-2G | 0.18 | 0.04 | 0.15 | 0.11 | 0.02 | 0.04 | 0.05 | 0.08 | 0.05 | 0.10 | 0.94 | 0.02 |
| Olivine_EagleStation | 0.16 | | | 0.14 | 0.02 | 0.14 | 0.01 | | | | | |
| Olivine_EagleStation | 0.16 | | | 0.14 | 0.02 | 0.14 | 0.01 | | | | | |
| Olivine_EagleStation | 0.16 | | | 0.14 | 0.02 | 0.14 | 0.01 | | | | | |
| IsleOfRhum_Plagioclase | 0.17 | 0.01 | 0.24 | 0.03 | | | 0.07 | 0.05 | 0.01 | | | |
| IsleOfRhum_Plagioclase | 0.17 | 0.01 | 0.24 | 0.03 | | | 0.07 | 0.05 | 0.01 | | | |
| IsleOfRhum_Plagioclase | 0.17 | 0.01 | 0.24 | 0.03 | | | 0.07 | 0.05 | 0.01 | | | |

Table B.4 Secondary standard measured standard deviation for the Cameca SX100. Values in wt.%

| SAMPLE | Si SD | Ti SD | Al SD | Fe SD | Mn SD | Mg SD | Ca SD | Na SD | K SD | P SD | F SD | Cl SD |
|------------------------|-------|-------|-------|-------|-------|-------|-------|-------|------|------|------|-------|
| BCR-2G | 0.32 | 0.07 | 0.1 | 0.67 | 0.12 | 0.06 | 0.13 | 0.08 | 0.11 | 0.05 | 0.05 | 0.02 |
| BCR-2G | 0.32 | 0.07 | 0.1 | 0.66 | 0.11 | 0.06 | 0.13 | 0.08 | 0.11 | 0.05 | 0.05 | 0.02 |
| BCR-2G | 0.32 | 0.07 | 0.1 | 0.65 | 0.09 | 0.06 | 0.13 | 0.08 | 0.11 | 0.05 | 0.05 | 0.02 |
| BCR-2G | 0.32 | 0.06 | 0.1 | 0.67 | 0.12 | 0.06 | 0.13 | 0.08 | 0.11 | 0.05 | 0.04 | 0.02 |
| BCR-2G | 0.32 | 0.07 | 0.1 | 0.66 | 0.11 | 0.06 | 0.13 | 0.08 | 0.11 | 0.05 | 0.04 | 0.02 |
| IsleOfRhum_Plagioclase | 0.25 | 0.02 | 0.14 | 0.13 | | | 0.17 | 0.04 | 0.02 | | | |
| IsleOfRhum_Plagioclase | 0.25 | 0.02 | 0.14 | 0.13 | | | 0.17 | 0.04 | 0.02 | | | |
| IsleOfRhum_Plagioclase | 0.25 | 0.02 | 0.14 | 0.13 | | | 0.17 | 0.04 | 0.02 | | | |
| IsleOfRhum_Plagioclase | 0.25 | 0.02 | 0.14 | 0.13 | | | 0.17 | 0.04 | 0.02 | | | |
| IsleOfRhum_Plagioclase | 0.25 | 0.02 | 0.14 | 0.12 | | | 0.17 | 0.04 | 0.02 | | | |
| IsleOfRhum_Plagioclase | 0.25 | 0.02 | 0.14 | 0.13 | | | 0.17 | 0.04 | 0.03 | | | |
| IsleOfRhum_Plagioclase | 0.25 | 0.02 | 0.14 | 0.12 | | | 0.17 | 0.04 | 0.02 | | | |
| Olivine_EagleStation | 0.22 | | | 0.60 | 0.08 | 0.16 | 0.02 | | | | | |
| Olivine_EagleStation | 0.22 | | | 0.59 | 0.07 | 0.16 | 0.02 | | | | | |
| Olivine_EagleStation | 0.22 | | | 0.60 | 0.07 | 0.16 | 0.02 | | | | | |
| Olivine_EagleStation | 0.22 | | | 0.59 | 0.07 | 0.16 | 0.02 | | | | | |

Table B.5: Representative analytical uncertainties ($\pm 1\sigma\%$) for EPMA analysed phases

| Element | Amphibole | Biotite | Olivine | Plagioclase | Clinopyroxene | Orthopyroxene | Glass |
|---------|-----------|---------|---------|-------------|---------------|---------------|-------|
| Al | 0.10 | 0.1 | 0.02 | 0.2 | 0.06 | 0.09 | 0.2 |
| Ba | | | | 0.06 | | | |
| Ca | 0.12 | 0.02 | 0.02 | 0.2 | 0.2 | 0.14 | 0.3 |
| Cl | 0.03 | 0.03 | | | | | 4.6 |
| Cr | | | 0.01 | | 0.02 | 0.01 | |
| F | 0.06 | 0.08 | | | | | |
| Fe | 0.11 | 0.1 | 0.13 | 0.03 | 0.09 | 0.1 | 0.6 |
| K | 0.03 | 0.3 | 0.02 | 0.02 | 0.02 | 0.03 | 0.7 |
| Mg | 0.16 | 0.2 | 0.5 | 0.01 | 0.2 | 0.1 | 0.9 |
| Mn | 0.03 | 0.02 | 0.02 | 0.02 | 0.02 | 0.02 | 6.1 |
| Na | 0.11 | 0.08 | 0.03 | 0.1 | 0.06 | 0.1 | 1.1 |
| P | | | | | | | 8.6 |
| Si | 1.7 | 0.2 | 0.2 | 0.1 | 0.2 | 0.2 | 0.3 |
| Sr | | | | 0.05 | | | |
| Ti | 0.02 | 0.07 | 0.02 | 0.02 | 0.04 | 0.04 | 0.9 |

Table B.6: Standard deviations and detection limits for the EPMA calibration standards

| Element | Standard | Standard Deviation (%) | Detection limit (ppm) |
|-----------|-------------|---------------------------|--------------------------|
| <i>Al</i> | <i>COR2</i> | 0.03 | 13 |
| <i>Ba</i> | <i>BAR2</i> | 0.2 | 133 |
| <i>Ca</i> | <i>WOL3</i> | 0.06 | 22 |
| <i>Cl</i> | <i>HAL2</i> | 0.05 | 24 |
| <i>Cr</i> | <i>CRO2</i> | 0.06 | 32 |
| <i>F</i> | <i>TOP2</i> | 0.1 | 78 |
| <i>Fe</i> | <i>FEO</i> | 0.06 | 36 |
| <i>K</i> | <i>ORT2</i> | 0.09 | 13 |
| <i>Mg</i> | <i>FOR</i> | 0.04 | 16 |
| <i>Mn</i> | <i>MNT</i> | 0.09 | 28 |
| <i>Na</i> | <i>JAD3</i> | 0.2 | 45 |
| <i>Si</i> | <i>WOL3</i> | 0.2 | 29 |
| <i>Sr</i> | <i>STO</i> | 0.2 | 148 |
| <i>Ti</i> | <i>RUT</i> | 0.03 | 16 |

B.2 LA-ICP-MS data

Table B.7. Glass LA-ICP-MS standard data (first run). All values in ppm.

| Standard | Al | Ca | Sc | V | Cr | Cr | Co | Ni | Zn | Rb | Sr | Y | Zr | Nb | Cs | Ba | La |
|------------|-------|-------|------|------|------|------|------|------|------|------|------|------|------|------|------|------|------|
| BCR2g-1 | 64900 | 46100 | 31.6 | 394 | 14.0 | 11.8 | 38.4 | 12.4 | 182 | 47.8 | 304 | 29.5 | 157 | 10.9 | 1.2 | 598 | 21.4 |
| BCR2g-2 | 64600 | 45400 | 29.9 | 388 | 14.8 | 15.8 | 37.1 | 12.2 | 182 | 47.0 | 301 | 28.6 | 156 | 10.7 | 1.0 | 589 | 21.3 |
| BCR2g-3 | 65900 | 45200 | 32.3 | 396 | 13.8 | 14.3 | 36.3 | 11.9 | 180 | 48.4 | 309 | 29.1 | 162 | 10.6 | 1.1 | 609 | 22.4 |
| BCR2g-4 | 64800 | 45500 | 30.5 | 397 | 13.7 | 11.7 | 37.2 | 11.1 | 182 | 45.9 | 300 | 29.9 | 160 | 10.9 | 1.2 | 598 | 22.3 |
| BCR2g-5 | 66140 | 46700 | 30.4 | 399 | 12.3 | 13.7 | 36.5 | 11.6 | 173 | 48.4 | 312 | 30 | 160 | 10.7 | 1.2 | 613 | 21.9 |
| BCR2g-6 | 66300 | 46300 | 31.2 | 403 | 12.2 | 13.7 | 38.2 | 12.0 | 174 | 46.8 | 308 | 29.6 | 161 | 10.8 | 1.1 | 623 | 22.9 |
| BCR2g-7 | 67100 | 45300 | 31.3 | 414 | 28.2 | 15.2 | 38.1 | 11.8 | 182 | 48.5 | 312 | 30.8 | 163 | 10.9 | 1.1 | 618 | 22.9 |
| BCR2g-8 | 66500 | 47600 | 32.1 | 414 | 30.8 | 14.9 | 37.9 | 11.5 | 189 | 47.1 | 308 | 30.2 | 163 | 10.9 | 1.1 | 635 | 22.9 |
| BCR2g-9 | 65000 | 46200 | 30.7 | 404 | 12.5 | 13.7 | 37.4 | 11.4 | 177 | 47.2 | 311 | 29.5 | 160 | 10.4 | 1.1 | 611 | 23.0 |
| BCR2g-10 | 65800 | 46100 | 30.8 | 409 | 12.3 | 16.9 | 37.4 | 13.8 | 173 | 48.5 | 314 | 30.3 | 164 | 11.1 | 1.3 | 624 | 22.5 |
| BCR2g-11 | 66100 | 46300 | 30.6 | 403 | 13.1 | 16.4 | 36 | 11.5 | 174 | 47.4 | 303 | 29.6 | 156 | 11.0 | 1.1 | 612 | 21.5 |
| BCR2g-12 | 66100 | 46400 | 31.0 | 406 | 12.1 | 13.2 | 38.3 | 12.3 | 179 | 47.0 | 313 | 29.1 | 160 | 10.9 | 1.2 | 618 | 22.3 |
| BCR2g-13 | 67700 | 46400 | 30.5 | 412 | 15.8 | 15.6 | 38.5 | 11.7 | 177 | 47.5 | 308 | 29.4 | 162 | 11.6 | 1.1 | 629 | 22.2 |
| BCR2g-14 | 67400 | 46500 | 31.3 | 419 | 17.0 | 15.7 | 36.9 | 12.7 | 174 | 47.2 | 318 | 30.1 | 163 | 11.6 | 1.1 | 627 | 23.3 |
| BCR2g-15 | 66900 | 47000 | 31.6 | 415 | 15.7 | 13.7 | 36.6 | 11.8 | 174 | 47.2 | 308 | 29.5 | 159 | 11.4 | 1.3 | 610 | 21.7 |
| BCR2g-16 | 66700 | 46200 | 30.8 | 409 | 16.8 | 14.9 | 37.5 | 10.8 | 171 | 45.7 | 306 | 29.6 | 158 | 10.8 | 1.1 | 610 | 21.9 |
| GSD-1g-1 | 65680 | 46700 | 45.3 | 38.5 | 39.3 | 43.4 | 38.8 | 57.5 | 65.7 | 38.8 | 61.1 | 35.5 | 35.7 | 36.5 | 30.4 | 61.4 | 33.4 |
| GSD-1g-2 | 66300 | 47000 | 45.2 | 38.5 | 38.2 | 42.6 | 38.6 | 55.7 | 63.4 | 37.2 | 61.9 | 34.9 | 35.2 | 38.1 | 30.1 | 61.1 | 33.4 |
| GSD-1g-3 | 66100 | 46800 | 46.0 | 38.8 | 38.4 | 41.2 | 39.2 | 54.0 | 61.8 | 37.0 | 63.0 | 36.1 | 36.5 | 39.4 | 31.8 | 64.3 | 34.9 |
| GSD-1g-4 | 66900 | 46100 | 46.6 | 38.1 | 38.5 | 39.2 | 38.5 | 59.6 | 65.1 | 38.1 | 64.3 | 36.4 | 36.9 | 38.9 | 32.0 | 64.9 | 36.2 |
| GSD-1g-5 | 68000 | 46200 | 46.2 | 40.6 | 37.9 | 41.3 | 40.0 | 59.4 | 66.0 | 40.0 | 63.0 | 37.2 | 38.7 | 39.3 | 31.8 | 64.7 | 36.4 |
| GSD-1g-6 | 68100 | 47700 | 46.1 | 40.5 | 37.4 | 42.7 | 40.0 | 59.5 | 61.5 | 37.4 | 63.6 | 36.6 | 38.1 | 39.4 | 32.3 | 63.3 | 35.7 |
| GSD-1g-7 | 66900 | 46500 | 48.0 | 40.4 | 49.7 | 43.0 | 40.1 | 58.1 | 63.6 | 39.4 | 64.0 | 36.4 | 38.0 | 39.7 | 31.9 | 64.0 | 35.4 |
| GSD-1g-8 | 67000 | 46500 | 45.7 | 42.1 | 52.1 | 43.0 | 40.0 | 58.5 | 65.0 | 37.5 | 64.4 | 37.1 | 36.8 | 39.0 | 31.9 | 62.2 | 35.3 |
| GSD-1g-9 | 67100 | 46500 | 47.0 | 39.1 | 38.7 | 38.1 | 38.6 | 59.3 | 68.3 | 38.3 | 64.0 | 37.3 | 38.3 | 39.3 | 31.4 | 61.3 | 35.7 |
| GSD-1g-10 | 67500 | 47300 | 47.9 | 40 | 39.7 | 43.5 | 40.4 | 57.4 | 59.9 | 36.1 | 65.1 | 36.9 | 37.1 | 40.1 | 31.0 | 61.0 | 35.5 |
| GSD-1g-11 | 67600 | 47000 | 48.5 | 41.4 | 42.0 | 41.0 | 40.5 | 58.6 | 64.3 | 36.7 | 64.3 | 37.6 | 39.0 | 40.1 | 32.0 | 64.3 | 35.6 |
| GSD-1g-12 | 67100 | 47000 | 45.5 | 41.9 | 41.6 | 42.7 | 40.8 | 59.0 | 66.2 | 38.0 | 64.2 | 36.3 | 37.0 | 38.5 | 31.6 | 61.7 | 35.6 |
| GSD-1g-13 | 67400 | 47700 | 47.6 | 40.5 | 40.1 | 41.3 | 40.5 | 57.7 | 59.5 | 37.6 | 64.4 | 36.8 | 36.7 | 40.2 | 32.5 | 63.0 | 35.1 |
| GSD-1g-14 | 68000 | 46400 | 47.3 | 40.6 | 38.7 | 41.1 | 39.9 | 58.1 | 61.0 | 37.2 | 63.8 | 38.4 | 37.2 | 40.1 | 31.2 | 61.6 | 35.7 |
| GSD-1g-15 | 68400 | 47800 | 48.2 | 42.1 | 41.8 | 41.3 | 41.0 | 57.1 | 63.4 | 38.0 | 65.6 | 36.8 | 37.2 | 40.8 | 31.9 | 63.5 | 35.7 |
| GSD-1g-16 | 68500 | 48200 | 47.2 | 40.8 | 43.2 | 40.8 | 39.1 | 59.1 | 60.8 | 37.8 | 65.0 | 38.3 | 38.2 | 40.8 | 31.8 | 64.6 | 35.5 |
| NIST610-1 | 10420 | 81800 | 452 | 438 | 417 | 424 | 422 | 457 | 515 | 430 | 517 | 458 | 447 | 469 | 379 | 462 | 446 |
| NIST610-2 | 10380 | 83100 | 450 | 440 | 409 | 434 | 419 | 452 | 506 | 429 | 519 | 461 | 452 | 471 | 376 | 460 | 447 |
| NIST610-3 | 10230 | 80700 | 448 | 440 | 404 | 425 | 415 | 451 | 490 | 430 | 510 | 454 | 439 | 456 | 370 | 444 | 444 |
| NIST610-4 | 10380 | 83700 | 451 | 453 | 369 | 409 | 425 | 463 | 505 | 433 | 528 | 464 | 453 | 475 | 365 | 453 | 452 |
| NIST610-5 | 10380 | 79400 | 454 | 459 | 363 | 415 | 423 | 461 | 509 | 423 | 524 | 461 | 452 | 471 | 369 | 455 | 451 |
| NIST610-6 | 10230 | 80100 | 443 | 453 | 332 | 380 | 415 | 455 | 507 | 423 | 515 | 459 | 446 | 466 | 360 | 447 | 446 |
| NIST610-8 | 10360 | 81200 | 454 | 455 | 641 | 428 | 419 | 455 | 492 | 429 | 519 | 451 | 443 | 467 | 380 | 452 | 457 |
| NIST610-7 | 10410 | 83100 | 454 | 456 | 372 | 423 | 427 | 467 | 505 | 422 | 515 | 455 | 441 | 463 | 379 | 440 | 440 |
| NIST610-9 | 10260 | 81200 | 455 | 446 | 351 | 421 | 417 | 460 | 493 | 425 | 516 | 452 | 441 | 468 | 363 | 438 | 440 |
| NIST610-10 | 10300 | 81500 | 451 | 456 | 476 | 429 | 413 | 458 | 505 | 420 | 511 | 453 | 439 | 471 | 373 | 445 | 441 |
| NIST610-11 | 10380 | 83900 | 459 | 462 | 487 | 445 | 426 | 468 | 505 | 420 | 518 | 459 | 450 | 475 | 373 | 453 | 446 |
| NIST610-12 | 10090 | 79800 | 454 | 453 | 364 | 411 | 405 | 446 | 478 | 412 | 506 | 450 | 435 | 463 | 364 | 436 | 431 |
| NIST610-13 | 10290 | 79100 | 450 | 455 | 345 | 392 | 411 | 460 | 488 | 416 | 508 | 449 | 436 | 458 | 358 | 434 | 433 |
| NIST610-14 | 10020 | 79800 | 440 | 452 | 444 | 431 | 418 | 450 | 478 | 409 | 503 | 442 | 430 | 461 | 362 | 427 | 421 |
| NIST610-15 | 10120 | 81100 | 453 | 452 | 453 | 434 | 406 | 450 | 476 | 406 | 508 | 438 | 429 | 462 | 366 | 433 | 416 |
| NIST610-16 | 10290 | 82900 | 463 | 466 | 466 | 430 | 422 | 463 | 486 | 419 | 516 | 444 | 440 | 462 | 373 | 452 | 444 |
| NIST612-1 | 10630 | 86100 | 40.7 | 37.6 | 36.0 | 35.6 | 33.8 | 37.6 | 37.4 | 30.7 | 75.6 | 37.1 | 37.0 | 36.7 | 42.4 | 39.3 | 35.0 |
| NIST612-2 | 10710 | 83800 | 38.7 | 39.2 | 36.8 | 37.0 | 35.9 | 38.5 | 38.5 | 31.5 | 77.4 | 38.5 | 37.5 | 39.8 | 42.0 | 37.6 | 36.0 |
| NIST612-3 | 10730 | 85500 | 39.5 | 39.4 | 35.4 | 33.8 | 36.6 | 39.7 | 37.1 | 30.7 | 77.8 | 37.8 | 38.0 | 39.4 | 42.5 | 39.6 | 35.9 |
| NIST612-4 | 10810 | 85300 | 40.0 | 39.2 | 37.4 | 38.2 | 35.0 | 39.9 | 40.7 | 32.0 | 80.0 | 39.2 | 38.6 | 39.0 | 43.7 | 41.7 | 36.8 |
| NIST612-5 | 10840 | 86300 | 40.7 | 38.6 | 36.2 | 38.2 | 35.6 | 39.0 | 40.6 | 31.2 | 79.0 | 37.5 | 38.9 | 39.4 | 42.6 | 40.0 | 36.4 |
| NIST612-6 | 10680 | 82900 | 40.6 | 39.2 | 36.6 | 37.5 | 34.9 | 39.8 | 39.9 | 31.4 | 79.1 | 39.3 | 37.6 | 39.3 | 43.1 | 39.3 | 36.3 |
| NIST612-7 | 10980 | 88300 | 40.8 | 39.4 | 39.8 | 38.7 | 36.4 | 39.6 | 39.3 | 33.2 | 80.1 | 39.9 | 40.3 | 39.3 | 43.9 | 40.3 | 37.6 |
| NIST612-8 | 10850 | 84500 | 41.4 | 38.8 | 34.2 | 33.2 | 36.0 | 38.3 | 39.8 | 32.2 | 80.2 | 38.3 | 38.0 | 39.0 | 42.7 | 37.4 | 35.9 |
| NIST612-9 | 10620 | 83300 | 39.5 | 38.2 | 35.9 | 34 | 36.3 | 38.9 | 38.6 | 31.4 | 77.5 | 38.3 | 38.1 | 38.4 | 42.4 | 37.3 | 34.7 |
| NIST612-10 | 10810 | 84800 | 39.9 | 38.6 | 36.9 | 41.2 | 35.4 | 38.4 | 39.2 | 31.1 | 77.3 | 38.0 | 37.2 | 37.9 | 42.3 | 38.9 | 35.9 |
| NIST612-11 | 10720 | 86100 | 39.7 | 37.5 | 36.6 | 36.1 | 37.0 | 36.1 | 39.8 | 31.2 | 79.4 | 39.0 | 37.2 | 39.7 | 42.9 | 39.8 | 36.7 |
| NIST612-12 | 10780 | 84500 | 38.9 | 39.1 | 36.1 | 32.8 | 35.1 | 39.3 | 37.5 | 32.0 | 78.5 | 38.9 | 37.4 | 39.7 | 42.9 | 39.4 | 36.2 |
| NIST612-13 | 10760 | 84200 | 40.1 | 39.2 | 36.1 | 35.1 | 35.1 | 39.3 | 39.1 | 31.5 | 79.5 | 38.7 | 37.3 | 39.5 | 42.9 | 38.5 | 36.3 |
| NIST612-14 | 10680 | 87000 | 40.2 | 39.1 | 36.9 | 38.2 | 35.4 | 38.4 | 44.5 | 31.5 | 78.1 | 37.6 | 37.7 | 38.2 | 43.0 | 41.1 | 36.3 |
| NIST612-15 | 10760 | 84800 | 40.2 | 39.2 | 36.5 | 38.3 | 34.3 | 40.0 | 37.9 | 31.4 | 77.2 | 38.0 | 37.7 | 38.1 | 42.2 | 38.5 | 35.7 |
| NIST612-16 | 10700 | 85100 | 39.4 | 39.1 | 36.3 | 35.4 | 35.0 | 38.3 | 37.0 | 30.2 | 77.6 | 37.7 | 38.9 | 38.9 | 42.5 | 40.2 | 35.3 |

Table B.7. Glass LA-ICP-MS secondary standard data (first run, cont.)

| Standard | Ce | Pr | Nd | Sm | Eu | Gd | Tb | Dy | Ho | Er | Tm | Yb | Lu | Hf | Ta | Pb | Th | U |
|------------|------|------|------|------|------|------|------|------|------|------|------|------|------|------|------|------|------|-------|
| BCR2g-1 | 45.3 | 5.8 | 24.8 | 5.6 | 1.8 | 6.0 | 1.0 | 5.7 | 1.2 | 3.1 | 0.4 | 3.2 | 0.5 | 4.4 | 0.7 | 10.7 | 5.1 | 1.6 |
| BCR2g-2 | 44.9 | 5.7 | 26.9 | 5.6 | 1.6 | 5.9 | 0.8 | 6.1 | 1.1 | 3.7 | 0.4 | 3.3 | 0.4 | 4.2 | 0.6 | 10.8 | 5.2 | 1.6 |
| BCR2g-3 | 47.3 | 6.0 | 24.8 | 6.4 | 1.9 | 5.5 | 0.8 | 6.1 | 1.2 | 3.0 | 0.5 | 3.2 | 0.4 | 4.4 | 0.5 | 10.7 | 5.2 | 1.6 |
| BCR2g-4 | 46.4 | 5.8 | 25.1 | 6.1 | 1.7 | 5.3 | 0.9 | 5.7 | 1.2 | 3.3 | 0.5 | 3.2 | 0.5 | 4.4 | 0.7 | 10.7 | 5.3 | 1.6 |
| BCR2g-5 | 47.8 | 6.2 | 26.8 | 5.4 | 1.9 | 5.3 | 0.9 | 5.6 | 1.1 | 3.5 | 0.4 | 3.0 | 0.4 | 4.3 | 0.6 | 10.8 | 5.3 | 1.5 |
| BCR2g-6 | 47.1 | 5.9 | 23.0 | 5.2 | 1.8 | 5.7 | 0.9 | 5.7 | 1.1 | 3.6 | 0.5 | 3.4 | 0.4 | 4.3 | 0.7 | 10.7 | 5.3 | 1.5 |
| BCR2g-7 | 47.7 | 6.2 | 24.9 | 5.8 | 1.7 | 5.9 | 1.0 | 5.8 | 1.2 | 3.9 | 0.4 | 2.8 | 0.5 | 4.3 | 0.6 | 11.1 | 5.4 | 1.5 |
| BCR2g-8 | 47.8 | 6.1 | 25.9 | 6.2 | 1.8 | 5.8 | 0.92 | 5.9 | 1.1 | 3.8 | 0.5 | 3.1 | 0.5 | 4.3 | 0.7 | 11.3 | 5.5 | 1.6 |
| BCR2g-9 | 47.5 | 5.9 | 24.5 | 6.1 | 1.8 | 5.9 | 0.9 | 5.7 | 1.2 | 3.4 | 0.5 | 3.2 | 0.4 | 4.4 | 0.6 | 10.8 | 5.5 | 1.5 |
| BCR2g-10 | 47.7 | 6.2 | 25.9 | 6.3 | 1.8 | 6.0 | 1.0 | 6.4 | 1.1 | 3.1 | 0.5 | 3.3 | 0.4 | 4.6 | 0.6 | 11.2 | 5.4 | 1.7 |
| BCR2g-11 | 47.5 | 6.0 | 26.3 | 6.2 | 1.7 | 6.1 | 0.9 | 5.5 | 1.0 | 3.1 | 0.5 | 3.6 | 0.5 | 4.4 | 0.7 | 10.3 | 5.4 | 1.5 |
| BCR2g-12 | 47.2 | 6.0 | 25.0 | 5.6 | 1.8 | 6.3 | 1.1 | 5.5 | 1.1 | 3.5 | 0.4 | 2.5 | 0.4 | 4.4 | 0.6 | 10.8 | 5.3 | 1.5 |
| BCR2g-13 | 48.5 | 5.7 | 26.8 | 6.6 | 1.7 | 5.1 | 0.8 | 5.5 | 1.1 | 3.2 | 0.5 | 3.2 | 0.4 | 4.5 | 0.6 | 10.7 | 5.5 | 1.6 |
| BCR2g-14 | 48.0 | 6.1 | 24.4 | 5.9 | 1.9 | 6.5 | 0.9 | 5.5 | 1.2 | 3.3 | 0.4 | 3.5 | 0.4 | 4.7 | 0.6 | 10.7 | 5.5 | 1.6 |
| BCR2g-15 | 48.8 | 5.9 | 25.3 | 6.1 | 1.7 | 5.6 | 0.9 | 6.1 | 1.2 | 3.3 | 0.5 | 3.5 | 0.5 | 4.5 | 0.6 | 10.2 | 5.2 | 1.6 |
| BCR2g-16 | 46.6 | 5.9 | 25.9 | 5.3 | 1.6 | 5.6 | 0.9 | 6.4 | 1.1 | 3.17 | 0.5 | 2.9 | 0.4 | 4.5 | 0.6 | 11.0 | 5.3 | 1.6 |
| GSD-1g-1 | 35.8 | 39.0 | 36.6 | 39.7 | 35.9 | 43.2 | 43.1 | 46.7 | 44.2 | 35.9 | 43.6 | 44.4 | 45.4 | 35.2 | 37.0 | 49.3 | 36.3 | 37.0 |
| GSD-1g-2 | 34.7 | 40.1 | 41.3 | 39.9 | 36.8 | 43.3 | 42.8 | 45.1 | 44.0 | 35.9 | 43.9 | 47.9 | 46.1 | 35.0 | 36.4 | 49.4 | 37.6 | 38.3 |
| GSD-1g-3 | 37.2 | 40.0 | 41.1 | 40.6 | 36.0 | 44.4 | 42.9 | 44.9 | 45.7 | 35.6 | 44.2 | 48.2 | 47.0 | 36.4 | 38.0 | 48.5 | 36.9 | 37.4 |
| GSD-1g-4 | 37.4 | 40.7 | 40.0 | 41.8 | 37.9 | 43.7 | 42.7 | 45.0 | 45.0 | 35.9 | 44.7 | 48.6 | 48.0 | 37.0 | 37.3 | 49.9 | 37.7 | 37.8 |
| GSD-1g-5 | 38.3 | 41.8 | 40.7 | 42.4 | 38.9 | 43.1 | 44.0 | 45.9 | 46.0 | 36.7 | 46.4 | 47.1 | 47.8 | 37.7 | 38.3 | 50.1 | 38.7 | 38.2 |
| GSD-1g-6 | 37.1 | 41.0 | 41.1 | 40.9 | 36.6 | 45.4 | 43.5 | 45.4 | 45.2 | 38.8 | 45.5 | 47.3 | 48.1 | 37.4 | 38.5 | 49.0 | 38.8 | 38.5 |
| GSD-1g-7 | 37.7 | 41.3 | 40.4 | 42.9 | 38.3 | 44.6 | 43.1 | 46.7 | 44.7 | 35.8 | 45.5 | 47.5 | 48.1 | 37.1 | 37.8 | 49.9 | 38.6 | 38.3 |
| GSD-1g-8 | 38.4 | 41.6 | 38.9 | 43.9 | 37.0 | 45.1 | 44.0 | 46.2 | 45.7 | 37.0 | 44.6 | 47.5 | 47.3 | 36.6 | 38.1 | 49.0 | 38.2 | 38.3 |
| GSD-1g-9 | 37.4 | 40.8 | 41.9 | 44.3 | 36.6 | 43.6 | 43.9 | 45.5 | 45.3 | 35.5 | 44.8 | 47.1 | 47.3 | 36.9 | 37.8 | 48.7 | 37.5 | 38.6 |
| GSD-1g-10 | 37.4 | 41.1 | 39.5 | 44 | 37.5 | 43.7 | 42.9 | 44.3 | 45.5 | 35.4 | 45.1 | 46.1 | 48.0 | 35.8 | 37.5 | 49.6 | 37.6 | 38.4 |
| GSD-1g-11 | 37.9 | 42.6 | 41.2 | 44.5 | 38.4 | 44 | 43.6 | 46.1 | 46.5 | 36.8 | 44.0 | 48.2 | 47.2 | 36.9 | 37.7 | 50.0 | 38.4 | 38.6 |
| GSD-1g-12 | 38.3 | 41.7 | 42.9 | 43.9 | 37.5 | 44.5 | 44.0 | 46.3 | 45.1 | 35.9 | 45.8 | 47.0 | 47.2 | 36.9 | 38.1 | 47.8 | 37.7 | 37.6 |
| GSD-1g-13 | 37.5 | 41.1 | 42.4 | 44 | 37.7 | 44.7 | 42.7 | 45.5 | 45.5 | 34.7 | 45.0 | 48.4 | 47.6 | 37.0 | 37.1 | 47.2 | 38.1 | 38.6 |
| GSD-1g-14 | 37.6 | 41.4 | 42.6 | 44.9 | 36.5 | 44.3 | 44.1 | 46.3 | 46.4 | 36.3 | 45.5 | 47.8 | 48.5 | 36.7 | 38.3 | 48.7 | 38.2 | 38.5 |
| GSD-1g-15 | 37.7 | 40.8 | 40.5 | 44.2 | 36.9 | 41.7 | 44.9 | 47.5 | 44.6 | 34.3 | 44.5 | 44.7 | 48.5 | 36.0 | 38.3 | 48.7 | 38.6 | 39.1 |
| GSD-1g-16 | 38.7 | 41.6 | 41.0 | 45.1 | 37.3 | 42.3 | 44.5 | 47.9 | 44.7 | 36.0 | 45.6 | 46.6 | 49.0 | 36.8 | 37.5 | 48.4 | 38.9 | 39.1 |
| NIST610-1 | 452 | 456 | 438 | 449 | 457 | 446 | 456 | 439 | 455 | 448 | 435 | 470 | 456 | 430 | 464 | 459 | 459 | 480 |
| NIST610-2 | 454 | 449 | 426 | 442 | 455 | 447 | 453 | 440 | 459 | 457 | 435 | 468 | 456 | 434 | 465 | 460 | 459 | 471 |
| NIST610-3 | 457 | 456 | 438 | 447 | 454 | 445 | 445 | 428 | 456 | 455 | 434 | 464 | 458 | 428 | 453 | 438 | 455 | 459 |
| NIST610-4 | 464 | 465 | 452 | 458 | 462 | 448 | 456 | 446 | 468 | 467 | 446 | 481 | 460 | 443 | 464 | 422 | 465 | 465 |
| NIST610-5 | 462 | 463 | 449 | 466 | 462 | 444 | 449 | 436 | 462 | 456 | 442 | 471 | 447 | 441 | 463 | 423 | 465 | 464 |
| NIST610-6 | 462 | 452 | 438 | 451 | 459 | 442 | 444 | 434 | 458 | 459 | 433 | 472 | 441 | 427 | 458 | 414 | 459 | 462 |
| NIST610-8 | 465 | 456 | 442 | 463 | 458 | 436 | 446 | 427 | 464 | 456 | 436 | 463 | 442 | 438 | 461 | 452 | 466 | 468 |
| NIST610-7 | 454 | 451 | 441 | 457 | 452 | 431 | 438 | 426 | 455 | 450 | 431 | 461 | 440 | 425 | 455 | 452 | 458 | 468 |
| NIST610-9 | 456 | 452 | 432 | 464 | 452 | 433 | 441 | 422 | 455 | 454 | 432 | 462 | 442 | 427 | 456 | 432 | 451 | 457 |
| NIST610-10 | 454 | 445 | 434 | 465 | 453 | 425 | 435 | 431 | 452 | 449 | 432 | 454 | 447 | 431 | 452 | 438 | 459 | 467 |
| NIST610-11 | 457 | 451 | 437 | 469 | 451 | 438 | 443 | 433 | 456 | 453 | 432 | 469 | 450 | 435 | 455 | 441 | 464 | 470 |
| NIST610-12 | 449 | 435 | 430 | 455 | 443 | 423 | 431 | 422 | 444 | 437 | 422 | 445 | 441 | 423 | 450 | 408 | 460 | 454 |
| NIST610-13 | 454 | 441 | 433 | 456 | 446 | 422 | 432 | 423 | 448 | 440 | 430 | 453 | 438 | 426 | 445 | 403 | 459 | 463 |
| NIST610-14 | 446 | 435 | 428 | 459 | 444 | 420 | 433 | 424 | 438 | 433 | 420 | 445 | 434 | 413 | 437 | 426 | 452 | 463 |
| NIST610-15 | 448 | 429 | 422 | 457 | 437 | 418 | 432 | 425 | 441 | 434 | 422 | 456 | 442 | 419 | 435 | 425 | 455 | 466 |
| NIST610-16 | 461 | 450 | 438 | 467 | 443 | 419 | 442 | 428 | 446 | 444 | 431 | 450 | 454 | 428 | 461 | 446 | 460 | 475.7 |
| NIST612-1 | 37.6 | 37.5 | 35.8 | 38.2 | 35.3 | 36.6 | 37.4 | 34.6 | 37.5 | 37.4 | 36.8 | 39.6 | 36.0 | 35.4 | 36.5 | 38.5 | 37.1 | 36.8 |
| NIST612-2 | 37.8 | 37.4 | 35.3 | 36.8 | 35.0 | 36.7 | 37.3 | 34.8 | 37.3 | 37.0 | 36.2 | 38.9 | 37.1 | 36.2 | 37.6 | 38.6 | 37.1 | 37.9 |
| NIST612-3 | 39.9 | 37.4 | 32.7 | 37.8 | 36.0 | 37.2 | 37.1 | 36.8 | 38.9 | 39.1 | 36.7 | 39.4 | 38.4 | 37.3 | 37.9 | 38.2 | 38.1 | 36.9 |
| NIST612-4 | 38.0 | 38.6 | 38.0 | 38.6 | 36.0 | 38.0 | 38.8 | 36.1 | 38.6 | 39.1 | 37.6 | 39.4 | 37.7 | 37.3 | 38.1 | 39.0 | 38.1 | 37.9 |
| NIST612-5 | 39.1 | 38.5 | 36.0 | 37.7 | 36.4 | 38.0 | 37.9 | 36.5 | 39.7 | 38.2 | 36.8 | 39.7 | 36.7 | 37.2 | 37.2 | 39.2 | 38.0 | 38.0 |
| NIST612-6 | 38.8 | 38.2 | 37.0 | 37.9 | 34.5 | 37.7 | 37.2 | 34.6 | 37.6 | 37.8 | 36.4 | 39.2 | 37.1 | 36.8 | 37.7 | 38.2 | 38.0 | 37.0 |
| NIST612-7 | 39.4 | 38.8 | 35.0 | 37.4 | 36.4 | 37.4 | 38.4 | 34.7 | 38.7 | 39.0 | 38.0 | 41.4 | 38.1 | 37.7 | 39.3 | 40.5 | 39.0 | 38.0 |
| NIST612-8 | 38.5 | 38.5 | 35.2 | 38.7 | 36.9 | 36.4 | 37.7 | 36.9 | 39.0 | 39.2 | 36.8 | 37.2 | 37.2 | 37.7 | 38.5 | 37.5 | 38.5 | 37.6 |
| NIST612-9 | 37.9 | 37.7 | 34.4 | 36.3 | 35.2 | 38.7 | 36.7 | 34.9 | 38.0 | 36.7 | 36.2 | 38.1 | 36.3 | 36.3 | 37.8 | 37.5 | 37.4 | 36.7 |
| NIST612-10 | 37.9 | 37.1 | 35.8 | 36.7 | 34.9 | 36.9 | 37.1 | 35.1 | 38.3 | 37.9 | 35.8 | 37.7 | 36.4 | 36.4 | 36.9 | 38.5 | 37.2 | 37.3 |
| NIST612-11 | 38.7 | 38.2 | 35.9 | 38.7 | 35.7 | 36.7 | 38.6 | 35.9 | 39.0 | 38.0 | 37.5 | 41.4 | 36.6 | 36.7 | 37.3 | 39.6 | 37.8 | 37.8 |
| NIST612-12 | 39.0 | 38.8 | 36.9 | 37.0 | 35.7 | 38.2 | 37.6 | 35.5 | 37.7 | 37.4 | 36.8 | 39.6 | 37.3 | 37.2 | 37.9 | 38.8 | 37.8 | 37.2 |
| NIST612-13 | 38.2 | 37.2 | 36.7 | 38.2 | 35.9 | 38.4 | 38.1 | 36.8 | 38.8 | 37.4 | 37.5 | 38.7 | 37.7 | 35.9 | 38.0 | 38.8 | 38.0 | 37.8 |
| NIST612-14 | 38.5 | 38.7 | 34.6 | 38.3 | 36.0 | 37.1 | 38 | 34.1 | 37.7 | 38.0 | 37.6 | 39.6 | 36.9 | 37.4 | 37.6 | 38.3 | 37.9 | 37.7 |
| NIST612-15 | 38.2 | 37.6 | 34.7 | 39.0 | 35.3 | 35.9 | 37.7 | 36.7 | 38.0 | 39.1 | 36.4 | 39.3 | 36.9 | 36.0 | 37.4 | 39.1 | 37.6 | 37.8 |
| NIST612-16 | 38.1 | 37.5 | 35.5 | 36.6 | 35.0 | 37.3 | 37.0 | 34.2 | 38.1 | 37.6 | 35.9 | 39.1 | 36.7 | 36.2 | 36.9 | 38.3 | 37.5 | 36.8 |

Table B.8. Glass LA-ICP-MS secondary standard data (second run). All values in ppm.

| Sample | Mg | Si | Mn | Rb | Sr | Cs | Ba | La | Ce | Pr | Nd | Sm | Eu | Gd | Tb | Dy | Ho | Er | Tm | Yb | Lu | Pb | Th | U |
|-----------|-------|--------|------|------|------|------|------|------|------|------|------|------|------|------|------|------|------|------|------|------|------|------|------|------|
| BCR-2g-1 | 21870 | 254290 | 1421 | 46.2 | 312 | 1.2 | 618 | 22.6 | 48.4 | 6.2 | 26.4 | 6.1 | 1.7 | 6.2 | 1.0 | 6.0 | 1.2 | 3.3 | 0.4 | 3.0 | 0.5 | 11.4 | 5.5 | 1.6 |
| BCR-2g-2 | 22460 | 254290 | 1440 | 47.3 | 315 | 1.4 | 593 | 22.6 | 48.0 | 5.7 | 27.6 | 6.2 | 1.8 | 6.1 | 0.9 | 6.1 | 1.2 | 3.3 | 0.4 | 3.3 | 0.5 | 9.4 | 5.6 | 1.6 |
| BCR-2g-3 | 21470 | 254290 | 1386 | 45.5 | 306 | 1.2 | 595 | 22.3 | 46.9 | 5.8 | 24.1 | 6.4 | 1.8 | 5.6 | 0.8 | 5.2 | 1.1 | 3.2 | 0.5 | 2.7 | 0.5 | 10.7 | 5.2 | 1.5 |
| BCR-2g-4 | 21310 | 254290 | 1394 | 45.8 | 300 | 1.2 | 603 | 21.9 | 46.7 | 5.7 | 25.5 | 6.1 | 1.8 | 6.2 | 0.9 | 5.3 | 1.1 | 3.4 | 0.5 | 2.9 | 0.4 | 11.7 | 5.1 | 1.5 |
| BCR-2g-5 | 20580 | 254290 | 1391 | 46.2 | 299 | 1.1 | 597 | 21.9 | 45.8 | 5.6 | 25.4 | 5.5 | 1.7 | 6.0 | 0.9 | 5.6 | 1.2 | 3.1 | 0.5 | 2.8 | 0.5 | 10.5 | 5.4 | 1.5 |
| BCR-2g-6 | 21240 | 254290 | 1412 | 45.4 | 308 | 1.1 | 610 | 22.5 | 45.9 | 6.0 | 26.3 | 5.6 | 1.7 | 5.1 | 0.9 | 5.6 | 1.2 | 3.0 | 0.4 | 2.9 | 0.5 | 10.8 | 5.5 | 1.5 |
| BCR-2g-7 | 20080 | 254290 | 1421 | 45.7 | 306 | 1.2 | 613 | 21.4 | 46.7 | 5.5 | 24.4 | 6.1 | 1.7 | 7.0 | 1.0 | 5.7 | 1.2 | 3.5 | 0.5 | 3.1 | 0.5 | 10.6 | 5.5 | 1.8 |
| BCR-2g-8 | 20160 | 254290 | 1413 | 46.5 | 309 | 1.0 | 600 | 22.3 | 46.1 | 5.7 | 27.0 | 5.4 | 1.7 | 5.7 | 1.0 | 5.6 | 1.1 | 3.09 | 0.4 | 2.9 | 0.5 | 10.9 | 5.0 | 1.7 |
| GSD-1g-1 | 22410 | 248680 | 200 | 39.9 | 63.5 | 31.4 | 59.5 | 35.3 | 37.0 | 41.5 | 41.7 | 45.3 | 37.2 | 44.0 | 42.7 | 46.6 | 45.1 | 35.2 | 45.6 | 47.5 | 48.0 | 48.9 | 39.6 | 37.8 |
| GSD-1g-2 | 21830 | 248680 | 200 | 38.1 | 63.7 | 31.1 | 60.7 | 34.3 | 36.8 | 40.5 | 39.9 | 41.0 | 36.7 | 41.4 | 43.1 | 45.3 | 45.2 | 35.5 | 44.2 | 47.1 | 47.0 | 48.5 | 39.5 | 39.3 |
| GSD-1g-3 | 21880 | 248680 | 195 | 36.6 | 63.8 | 30.3 | 58.8 | 35.5 | 37.4 | 41.0 | 40.6 | 45.3 | 36.8 | 43.9 | 42.9 | 47.5 | 44.8 | 36.4 | 45.6 | 46.8 | 47.1 | 47.6 | 40.9 | 38.4 |
| GSD-1g-4 | 21340 | 248680 | 199 | 35.3 | 62.4 | 31.3 | 65.1 | 35.6 | 37.4 | 41.2 | 40.3 | 41.9 | 36.3 | 44.2 | 43.4 | 45.9 | 45.3 | 36.7 | 45.5 | 45.3 | 47.5 | 48.5 | 41.1 | 39.0 |
| GSD-1g-5 | 21170 | 248680 | 195 | 35.7 | 61.0 | 30.8 | 61.6 | 34.3 | 37.3 | 40.0 | 40.0 | 43.4 | 35.6 | 43.1 | 43.2 | 45.8 | 44.7 | 36.5 | 44.3 | 45.6 | 46.4 | 47.5 | 37.9 | 38.1 |
| GSD-1g-6 | 20810 | 248680 | 192 | 36.0 | 62.5 | 30.6 | 63.0 | 34.7 | 36.1 | 39.8 | 39.7 | 41.9 | 36.2 | 40.7 | 43.0 | 44.8 | 43.8 | 37.0 | 44.9 | 45.1 | 46.7 | 48.7 | 40.7 | 37.6 |
| GSD-1g-7 | 20320 | 248680 | 196 | 37.2 | 61.1 | 31.4 | 64.7 | 33.6 | 37.2 | 40.0 | 40.9 | 42.1 | 34.9 | 40.0 | 42.4 | 46.1 | 43.6 | 35.6 | 44.4 | 45.0 | 45.7 | 47.8 | 37.5 | 37.8 |
| NIST610-1 | 543 | 325800 | 445 | 439 | 520 | 376 | 434 | 436 | 456 | 448 | 441 | 445 | 452 | 443 | 440 | 433 | 451 | 444 | 436 | 464 | 443 | 441 | 450 | 469 |
| NIST610-2 | 541 | 325800 | 448 | 429 | 520 | 385 | 450 | 433 | 446 | 441 | 443 | 440 | 452 | 430 | 436 | 430 | 448 | 441 | 429 | 452 | 442 | 449 | 458 | 469 |
| NIST610-3 | 518 | 325800 | 434 | 412 | 507 | 379 | 433 | 428 | 443 | 434 | 439 | 438 | 444 | 428 | 426 | 417 | 441 | 432 | 416 | 442 | 433 | 433 | 445 | 451 |
| NIST610-4 | 534 | 325800 | 447 | 435 | 516 | 384 | 441 | 434 | 458 | 450 | 441 | 457 | 456 | 455 | 446 | 438 | 452 | 452 | 433 | 462 | 444 | 445 | 457 | 465 |
| NIST610-5 | 515 | 325800 | 432 | 416 | 508 | 369 | 431 | 426 | 442 | 435 | 438 | 453 | 436 | 431 | 435 | 430 | 440 | 449 | 433 | 447 | 430 | 438 | 457 | 459 |
| NIST610-6 | 514 | 325800 | 439 | 415 | 507 | 377 | 439 | 429 | 448 | 442 | 438 | 458 | 442 | 433 | 436 | 422 | 444 | 447 | 429 | 447 | 434 | 440 | 456 | 462 |
| NIST610-7 | 490 | 325800 | 440 | 411 | 518 | 378 | 446 | 431 | 447 | 451 | 436 | 449 | 436 | 418 | 440 | 432 | 449 | 458 | 431 | 442 | 433 | 444 | 460 | 464 |
| NIST610-8 | 482 | 325800 | 438 | 418 | 505 | 376 | 463 | 425 | 450 | 437 | 429 | 449 | 437 | 425 | 432 | 420 | 442 | 452 | 425 | 447 | 430 | 439 | 455 | 458 |
| NIST612-1 | 68.4 | 337020 | 40.4 | 31.4 | 78.8 | 43.2 | 40.7 | 35.8 | 37.9 | 38.0 | 35.8 | 36.6 | 35.4 | 38.3 | 37.6 | 35.3 | 38.1 | 38.2 | 37.3 | 39.5 | 36.9 | 39.2 | 38.0 | 37.8 |
| NIST612-2 | 69.0 | 337020 | 37.5 | 31.5 | 77.4 | 41.6 | 37.0 | 36.1 | 39.7 | 37.8 | 35.8 | 39.4 | 36.5 | 37.2 | 37.5 | 35.8 | 38.7 | 37.4 | 36.5 | 38.6 | 37.1 | 37.8 | 37.6 | 37.2 |
| NIST612-3 | 67.0 | 337020 | 38.1 | 31.7 | 79.4 | 44.2 | 41.2 | 37.1 | 38.9 | 38.1 | 36.0 | 38.4 | 35.9 | 37.6 | 38.4 | 36.9 | 38.6 | 38.9 | 37.2 | 40.1 | 37.5 | 39.1 | 39.1 | 37.4 |
| NIST612-4 | 64.8 | 337020 | 38.3 | 31.4 | 79.7 | 42.7 | 41.9 | 35.8 | 38.0 | 38.2 | 33.7 | 36.1 | 34.5 | 36.9 | 37.0 | 34.2 | 38.3 | 38.2 | 36.4 | 39.0 | 36.8 | 38.5 | 36.8 | 37.8 |
| NIST612-5 | 70.2 | 337020 | 40.2 | 30.6 | 77.6 | 42.2 | 36.6 | 34.7 | 36.6 | 36.8 | 36.2 | 38.5 | 35.4 | 35.2 | 37.3 | 35.1 | 37.3 | 37.3 | 36.5 | 38.5 | 36.9 | 39.0 | 37.0 | 36.9 |
| NIST612-6 | 70.2 | 337020 | 37.9 | 31.5 | 76.3 | 41.9 | 37.0 | 35.9 | 38.0 | 38.1 | 35.9 | 37.1 | 35.2 | 37.0 | 37.5 | 35.5 | 38.4 | 37.8 | 36.5 | 39.5 | 36.4 | 38.0 | 38.1 | 36.6 |
| NIST612-7 | 67.0 | 337020 | 40.0 | 32.1 | 79.8 | 43.2 | 41.1 | 36.9 | 39.4 | 38.8 | 35.7 | 36.9 | 36.4 | 38.6 | 38.1 | 35.9 | 39.5 | 37.9 | 37.5 | 39.8 | 37.7 | 39.2 | 38.7 | 38.0 |
| NIST612-8 | 67.6 | 337020 | 37.5 | 31.2 | 78.4 | 42.7 | 39.9 | 35.8 | 38.9 | 37.5 | 35.2 | 38.8 | 35.6 | 37.8 | 37.3 | 35.5 | 37.7 | 38.4 | 36.6 | 38.7 | 36.8 | 38.1 | 37.2 | 37.5 |

Table B.9. Glass LA-ICP-MS secondary standard accuracy and precision (first run). Values in ppm unless otherwise stated

| Standard | Al | Ca | Sc | V | Cr | Cr | Co | Ni | Zn | Rb | Sr | Y | Zr | Nb | Cs | Ba |
|------------------------|-------|----------|------|------|------|------|------|-------|------|-------|-------|------|------|------|------|------|
| BCR2g average | 66121 | 46200 | 31 | 405 | 15.9 | 14.5 | 37.4 | 11.9 | 178 | 47.4 | 308 | 29.7 | 160 | 11 | 1.1 | 614 |
| BCR2g Reference | 70700 | 50400 | 33 | 425 | 17 | 17 | 38 | 13 | 125 | 47 | 342 | 35 | 184 | 12.5 | 1.16 | 683 |
| BCR2g rel. error (%) | 6.5 | 8.3 | 5.9 | 4.7 | 6.2 | 15 | 1.6 | 8.4 | 42.2 | 0.7 | 9.8 | 15.2 | 12.9 | 12.4 | 1.4 | 10.1 |
| BCR2g RSD (%) | 1.4 | 1.4 | 2.1 | 2.2 | 34.8 | 10.4 | 2.1 | 5.9 | 2.7 | 1.8 | 1.6 | 1.8 | 1.6 | 3.1 | 7.1 | 2.0 |
| GSD-1g average | 67286 | 46963 | 46.8 | 40.2 | 41.1 | 41.6 | 39.8 | 58 | 63.5 | 37.8 | 63.9 | 36.8 | 37.3 | 39.4 | 31.6 | 62.9 |
| GSD-1g Reference | 70700 | 53550 | 52 | 44 | 42 | 42 | 40 | 58 | 54 | 37.3 | 69.4 | 42 | 42 | 42 | 32 | 67 |
| GSD-1g rel. error (%) | 4.8 | 12.3 | 10.1 | 8.5 | 2.2 | 0.9 | 0.6 | 0.1 | 17.5 | 1.4 | 8 | 12.4 | 11.2 | 6.2 | 1.3 | 6.1 |
| GSD-1g RSD (%) | 1.2 | 1.3 | 2.3 | 3.3 | 10.2 | 3.6 | 2.1 | 2.6 | 4.0 | 2.6 | 1.8 | 2.5 | 2.8 | 2.7 | 2.0 | 2.3 |
| NIST610 average | 10284 | 81400 | 452 | 452 | 418 | 421 | 418 | 457 | 496 | 422 | 515 | 453 | 442 | 466 | 369 | 446 |
| NIST610 reference | 10296 | 81396 | 455 | 450 | 408 | 408 | 410 | 458.7 | 460 | 425.7 | 515.5 | 462 | 448 | 465 | 366 | 452 |
| NIST610 rel.error (%) | 0.1 | 0.005 | 0.7 | 0.5 | 2.5 | 3.1 | 1.9 | 0.3 | 7.9 | 1 | 0.2 | 1.9 | 1.3 | 0.2 | 0.9 | 1.4 |
| NIST610 RSD (%) | 1.2 | 1.9 | 1.2 | 1.7 | 18.5 | 3.9 | 1.6 | 1.4 | 2.5 | 1.9 | 1.3 | 1.6 | 1.7 | 1.2 | 1.9 | 2.3 |
| NIST612 average | 10754 | 85156.25 | 40 | 38.8 | 36.5 | 36.5 | 35.5 | 38.8 | 39.2 | 31.5 | 78.4 | 38.4 | 38 | 38.9 | 42.8 | 39.3 |
| NIST612 reference | 10718 | 84966 | 39.9 | 38.8 | 36.4 | 36.4 | 35.5 | 38.8 | 39.1 | 31.4 | 78.4 | 38.3 | 37.9 | 38.9 | 42.7 | 39.3 |
| NIST612 rel. error (%) | 0.3 | 0.2 | 0.3 | 0.1 | 0.2 | 0.2 | 0.04 | 0.05 | 0.2 | 0.2 | 0.01 | 0.2 | 0.2 | 0 | 0.1 | 0 |
| NIST612 RSD (%) | 0.9 | 1.6 | 1.8 | 1.5 | 3.1 | 6.4 | 2.4 | 2.6 | 4.7 | 2.2 | 1.7 | 2.0 | 2.3 | 2.2 | 1.2 | 3.2 |

Table B.9. (continued)

| Standard | La | Ce | Pr | Nd | Sm | Eu | Gd | Tb | Dy | Ho | Er | Tm | Yb | Lu | Hf | Ta | Pb | Th | U |
|------------------------|------|------|------|------|------|------|------|------|------|------|------|------|------|------|------|------|------|------|------|
| BCR2g average | 22.3 | 47.3 | 6 | 25.4 | 5.9 | 1.8 | 5.8 | 0.9 | 5.8 | 1.1 | 3.4 | 0.5 | 3.2 | 0.4 | 4.4 | 0.6 | 10.8 | 5.3 | 1.6 |
| BCR2g Reference | 24.7 | 53.3 | 6.7 | 28.9 | 6.59 | 1.97 | 6.71 | 1.02 | 6.44 | 1.27 | 3.7 | 0.51 | 3.39 | 0.5 | 4.84 | 0.78 | 11 | 5.9 | 1.69 |
| BCR2g rel. error (%) | 9.8 | 11.3 | 11 | 12.1 | 10.5 | 10.5 | 13.8 | 10.4 | 9.5 | 10.4 | 8.8 | 9.3 | 6.2 | 13 | 8.8 | 19.9 | 2 | 9.5 | 7.2 |
| BCR2g RSD (%) | 2.8 | 2.2 | 2.8 | 4.1 | 7.0 | 5.4 | 6.5 | 8.8 | 5.3 | 5.4 | 8.0 | 10.8 | 8.8 | 11.4 | 2.9 | 9.2 | 2.6 | 2.4 | 3.8 |
| GSD-1g average | 35.3 | 37.4 | 41 | 40.8 | 42.9 | 37.2 | 43.9 | 43.5 | 46 | 45.3 | 36 | 44.9 | 47.2 | 47.6 | 36.6 | 37.7 | 49 | 38 | 38.3 |
| GSD-1g Reference | 39.1 | 41.4 | 45 | 44.7 | 47.8 | 41 | 50.7 | 47 | 51.2 | 49 | 40.1 | 49 | 50.9 | 51.5 | 39 | 40 | 50 | 41 | 41 |
| GSD-1g rel. error (%) | 9.7 | 9.6 | 8.8 | 8.8 | 10.2 | 9.2 | 13.5 | 7.4 | 10.2 | 7.6 | 10.1 | 8.3 | 7.4 | 7.6 | 6.2 | 5.7 | 2 | 7.3 | 6.7 |
| GSD-1g RSD (%) | 2.4 | 2.6 | 2.1 | 3.8 | 4.2 | 2.3 | 2.3 | 1.6 | 2.1 | 1.6 | 2.8 | 1.7 | 2.6 | 1.9 | 2.0 | 1.5 | 1.7 | 1.9 | 1.5 |
| NIST610 average | 441 | 456 | 449 | 436 | 458 | 452 | 434 | 442 | 430 | 454 | 450 | 432 | 462 | 447 | 429 | 455 | 434 | 459 | 466 |
| NIST610 reference | 440 | 453 | 448 | 430 | 453 | 447 | 449 | 437 | 437 | 449 | 455 | 435 | 450 | 439 | 435 | 446 | 426 | 457 | 462 |
| NIST610 rel.error (%) | 0.2 | 0.6 | 0.3 | 1.4 | 1.1 | 1.1 | 3.4 | 1.2 | 1.5 | 1 | 1.2 | 0.7 | 2.6 | 1.8 | 1.3 | 1.9 | 1.8 | 0.4 | 0.9 |
| NIST610 RSD (%) | 2.5 | 1.3 | 2.2 | 1.8 | 1.7 | 1.6 | 2.6 | 1.9 | 1.7 | 1.8 | 2.1 | 1.6 | 2.2 | 1.8 | 1.8 | 2.0 | 4.0 | 1.0 | 1.4 |
| NIST612 average | 36.1 | 38.5 | 38 | 35.6 | 37.7 | 35.6 | 37.3 | 37.7 | 35.5 | 38.3 | 38.1 | 36.8 | 39.3 | 37.1 | 36.7 | 37.7 | 38.7 | 37.8 | 37.5 |
| NIST612 reference | 36 | 38.4 | 37.9 | 35.5 | 37.7 | 35.6 | 37.3 | 37.6 | 35.5 | 38.3 | 38 | 36.8 | 39.2 | 37 | 36.7 | 37.6 | 38.6 | 37.8 | 37.4 |
| NIST612 rel. error (%) | 0.2 | 0.2 | 0.2 | 0.3 | 0.1 | 0.1 | 0.1 | 0.2 | 0.04 | 0 | 0.1 | 0 | 0.2 | 0.2 | 0.1 | 0.2 | 0.2 | 0.05 | 0.2 |
| NIST612 RSD (%) | 1.9 | 1.7 | 1.6 | 3.5 | 2.3 | 1.8 | 2.1 | 1.6 | 2.8 | 1.8 | 2.1 | 1.8 | 2.8 | 1.8 | 1.9 | 1.8 | 1.9 | 1.3 | 1.3 |

Table B.10. Glass LA-ICP-MS secondary standard accuracy and precision (second run). Values in ppm unless otherwise stated.

| Sample | Mg | Si | Mn | Rb | Sr | Cs | Ba | La | Ce | Pr | Nd | Sm | Eu | Gd | Tb | Dy | Ho | Er | Tm | Yb | Lu | Pb | Th | U |
|------------------------|-------|--------|------|-------|-------|------|------|------|------|------|------|------|------|------|------|------|------|------|------|------|------|------|-------|-------|
| BCR-2g average | 21146 | 254290 | 1410 | 46.1 | 307 | 1.2 | 604 | 22.2 | 46.8 | 5.8 | 25.8 | 5.9 | 1.7 | 6 | 0.9 | 5.6 | 1.2 | 3.2 | 0.5 | 3 | 0.5 | 10.8 | 5.4 | 1.6 |
| BCR-2g reference | 21467 | 254048 | 1550 | 47 | 342 | 1.2 | 683 | 24.7 | 53.3 | 6.7 | 28.9 | 6.6 | 2 | 6.7 | 1 | 6.4 | 1.3 | 3.7 | 0.5 | 3.4 | 0.5 | 11 | 5.9 | 1.7 |
| BCR-2g rel. error (%) | 1.5 | 0.1 | 9 | 2 | 10.3 | 1.3 | 11.6 | 10.2 | 12.2 | 13.8 | 10.6 | 10.1 | 11.8 | 10.8 | 9.3 | 12.5 | 8.5 | 12.5 | 11.8 | 13 | 3.1 | 2.3 | 9.3 | 6.1 |
| BCR-2g RSD (%) | 3.9 | 0.0 | 1.3 | 1.4 | 1.8 | 9.9 | 1.5 | 1.9 | 2.0 | 3.9 | 4.7 | 6.2 | 3.0 | 9.3 | 7.6 | 5.4 | 4.5 | 5.2 | 11.9 | 6.3 | 7.3 | 6.3 | 4.1 | 7.1 |
| GSD-1g average | 21394 | 248680 | 197 | 37 | 62.6 | 31 | 61.9 | 34.8 | 37 | 40.6 | 40.4 | 43 | 36.2 | 42.5 | 43 | 46 | 44.6 | 36.1 | 44.9 | 46.1 | 46.9 | 48.2 | 39.6 | 38.3 |
| GSD-1g reference | 21708 | 248444 | 220 | 37.3 | 69.4 | 32 | 67 | 39.1 | 41.4 | 45 | 44.7 | 47.8 | 41 | 50.7 | 47 | 51.2 | 49 | 40.1 | 49 | 50.9 | 51.5 | 50 | 41 | 41 |
| GSD-1g rel. error (%) | 1.4 | 0.1 | 10.6 | 0.9 | 9.8 | 3.2 | 7.6 | 11.1 | 10.6 | 9.8 | 9.5 | 10.1 | 11.6 | 16.2 | 8.6 | 10.2 | 8.9 | 9.9 | 8.3 | 9.5 | 8.9 | 3.6 | 3.4 | 6.6 |
| GSD-1g RSD (%) | 3.3 | 0.0 | 1.5 | 4.3 | 1.9 | 1.4 | 4.0 | 2.1 | 1.3 | 1.7 | 1.7 | 4.0 | 2.2 | 4.1 | 0.8 | 1.9 | 1.5 | 1.9 | 1.4 | 2.3 | 1.6 | 1.2 | 3.6 | 1.7 |
| NIST610 average | 517 | 325800 | 440 | 422 | 513 | 378 | 442 | 430 | 449 | 442 | 438 | 449 | 444 | 433 | 436 | 428 | 446 | 447 | 429 | 450 | 436 | 441 | 455 | 462 |
| NIST610 reference | 432 | 325499 | 444 | 425.7 | 515.5 | 366 | 452 | 440 | 453 | 448 | 430 | 453 | 447 | 449 | 437 | 437 | 449 | 455 | 435 | 450 | 439 | 426 | 457.2 | 461.5 |
| NIST610 rel. error (%) | 19.7 | 0.1 | 0.8 | 0.9 | 0.6 | 3.3 | 2.2 | 2.2 | 0.9 | 1.3 | 1.9 | 1 | 0.6 | 3.6 | 0.1 | 2.1 | 0.7 | 1.8 | 1.4 | 0.1 | 0.7 | 3.6 | 0.5 | 0.1 |
| NIST610 RSD (%) | 4.3 | 0.0 | 1.3 | 2.6 | 1.3 | 1.3 | 2.4 | 0.9 | 1.3 | 1.5 | 1.0 | 1.6 | 1.8 | 2.6 | 1.4 | 1.7 | 1.1 | 1.8 | 1.4 | 1.9 | 1.4 | 1.1 | 1.1 | 1.3 |
| NIST612 average | 68 | 337020 | 38.7 | 31.4 | 78.4 | 42.7 | 39.4 | 36 | 38.4 | 37.9 | 35.5 | 37.7 | 35.6 | 37.3 | 37.6 | 35.5 | 38.3 | 38 | 36.8 | 39.2 | 37 | 38.6 | 37.8 | 37.4 |
| NIST612 reference | 68 | 337000 | 38.7 | 31.4 | 78.4 | 42.7 | 39.3 | 36 | 38.4 | 37.9 | 35.5 | 37.7 | 35.6 | 37.3 | 37.6 | 35.5 | 38.3 | 38 | 36.8 | 39.2 | 37 | 38.6 | 37.8 | 37.4 |
| NIST612 rel. error (%) | 0.04 | 0.01 | 0.1 | 0.1 | 0.03 | 0.03 | 0.3 | 0.03 | 0.1 | 0.03 | 0.1 | 0.1 | 0.04 | 0.1 | 0.03 | 0.1 | 0.1 | 0.03 | 0.03 | 0.03 | 0.03 | 0.03 | 0.03 | 0 |
| NIST612 RSD (%) | 2.7 | 0.0 | 3.2 | 1.4 | 1.6 | 1.9 | 5.6 | 2.1 | 2.6 | 1.5 | 2.2 | 3.2 | 1.8 | 2.8 | 1.2 | 2.2 | 1.7 | 1.4 | 1.2 | 1.5 | 1.1 | 1.5 | 2.2 | 1.3 |

Table B.11. LA-ICP-MS metadata for the first run (matrix glass)

| Laboratory & Sample Preparation | |
|--|--|
| Laboratory name | Imaging and Analysis Centre, Natural History Museum, London |
| Sample type/mineral | Rhyolite glass (matrix glass) |
| Sample preparation | Conventional thin section preparation, resin impregnation and mounting, polishing down to 30 nm thickness |
| Imaging | BSE imaging on FEI Quanta 650 FEG SEM, voltage 20 kV, working distance 10 mm |
| Laser ablation system | |
| Make, Model & type | ESI New Wave Research NWR193 |
| Ablation cell & volume | Two-volume (TwoVol2) |
| Laser wavelength (nm) | 193 |
| Pulse width (ns) | <4 ns |
| Fluence (J.cm ⁻²) | 3.5 J.cm ⁻² |
| Repetition rate (Hz) | 7 Hz |
| Ablation duration (secs) | 45 s |
| Ablation pit depth / ablation rate | 16mm pit depth, 0.08mm/pulse |
| Spot diameter (mm) nominal/actual | 25 mm |
| Sampling mode / pattern | Static spot ablation |
| Carrier gas | 100% He in the cell, Ar make-up gas combined using a glass signal smoother |
| Cell carrier gas flow | 0.7 - 0.8 l/min He |
| ICP-MS Instrument | |
| Make, Model & type | Agilent 7700x quadrupole ICP-MS |
| Sample introduction | Ablation aerosol |
| RF power | 1350 W |
| Make-up gas flow (Ar) | 0.8 l/min |
| Detection system | Dual (pulse counting, analogue – calibrated daily) |
| Masses measured | ²⁷ Al, ²⁹ Si, ⁴³ Ca, ⁵¹ V, ⁵³ Cr, ⁵⁹ Co, ⁶⁰ Ni, ⁶⁶ Zr, ⁸⁵ Rb, ⁸⁸ Sr, ⁸⁹ Y, ⁹³ Nb, ¹³³ Cs, ¹³⁷ Ba, ¹³⁹ La, ¹⁴⁰ Ce, ¹⁴¹ Pr, ¹⁴⁵ Nd, ¹⁴⁷ Sm, ¹⁵¹ Eu, ¹⁵⁷ Gd, ¹⁵⁹ Tb, ¹⁶³ Dy, ¹⁶⁵ Ho, ¹⁶⁷ Er, ¹⁶⁹ Tm, ¹⁷³ Yb, ¹⁷⁵ Lu, ¹⁷⁷ Hf, ¹⁸¹ Ta, ²⁰⁴ Pb, ²⁰⁶ Pb, ²⁰⁷ Pb, ²⁰⁸ Pb, ²³² Th and ²³⁸ U |
| Integration time per peak/dwell times (ms) | 5-30 ms: 10 ms was used with the exception of ²⁷ Al, ⁴³ Ca and ⁶⁶ Zr (5 ms); ¹³⁹ La and ¹⁴¹ Pr (20 ms); and ²⁰⁶ Pb, ²⁰⁷ Pb, and ²³⁸ U (30 ms). |
| Total sweep time | ~0.5 secs |
| Typical oxide rate (ThO/Th) | 0.18% |
| Data Processing | |
| Gas blank | 30 second on-peak zero subtracted |
| Calibration strategy | NIST-612 the primary reference material for and BCR2g, GSD-1g and NIST610 as secondaries. |
| Data processing package used / Correction for LIEF | lilite 3.61 |
| Mass discrimination | Normalised to reference material |
| Quality control / Validation | Analyses of secondaries, standard deviation and biases are reported |

Table B.12. LA-ICP-MS metadata for the second run (melt inclusions)






| Laboratory & Sample Preparation | |
|--|--|
| Laboratory name | Imaging and Analysis Centre, Natural History Museum, London |
| Sample type/mineral | Rhyolite glass (melt inclusions) |
| Sample preparation | Conventional thin section preparation, resin impregnation and mounting, polishing down to 30 nm thickness |
| Imaging | BSE imaging on FEI Quanta 650 FEG SEM, voltage 20 kV, working distance 10 mm |
| Laser ablation system | |
| Make, Model & type | ESI New Wave Research NWR193 |
| Ablation cell & volume | Two-volume (TwoVol2) |
| Laser wavelength (nm) | 193 |
| Pulse width (ns) | <4 ns |
| Fluence (J.cm ⁻²) | 2.8 J.cm ⁻² |
| Repetition rate (Hz) | 6 Hz |
| Ablation duration (secs) | 45 s |
| Ablation pit depth / ablation rate | 16mm pit depth, 0.08mm/pulse |
| Spot diameter (mm) nominal/actual | 10-15 mm |
| Sampling mode / pattern | Static spot ablation |
| Carrier gas | 100% He in the cell, Ar make-up gas combined using a glass signal smoother |
| Cell carrier gas flow | 0.7 - 0.8 l/min He |
| ICP-MS Instrument | |
| Make, Model & type | Agilent 7700x quadrupole ICP-MS |
| Sample introduction | Ablation aerosol |
| RF power | 1350 W |
| Make-up gas flow (Ar) | 0.8 l/min |
| Detection system | Dual (pulse counting, analogue – calibrated daily) |
| Masses measured | ²⁸ Si, ⁸⁵ Rb, ⁸⁸ Sr, ¹³³ Cs, ¹³⁷ Ba, ¹³⁹ La, ¹⁴⁰ Ce, ¹⁴¹ Pr, ¹⁴⁵ Nd, ¹⁴⁷ Sm, ¹⁵¹ Eu, ¹⁵⁷ Gd, ¹⁵⁹ Tb, ¹⁶³ Dy, ¹⁶⁵ Ho, ¹⁶⁷ Er, ¹⁶⁹ Tm, ¹⁷³ Yb, ¹⁷⁵ Lu, ²⁰⁴ Pb, ²⁰⁶ Pb, ²⁰⁷ Pb, ²⁰⁸ Pb, ²³² Th and ²³⁸ U |
| Integration time per peak/dwell times (ms) | 5-30 ms: 10 ms was used with the exception of ¹³⁹ La and ¹⁴¹ Pr (20 ms); and ²⁰⁶ Pb, ²⁰⁷ Pb, and ²³⁸ U (30 ms). |
| Total sweep time | ~0.5 secs |
| Typical oxide rate (ThO/Th) | 0.18% |
| Data Processing | |
| Gas blank | 30 second on-peak zero subtracted |
| Calibration strategy | NIST-612 the primary reference material for and BCR2g, GSD-1g and NIST610 as secondaries. |
| Data processing package used / Correction for LIEF | lolite 3.61 |
| Mass discrimination | Normalised to reference material |
| Quality control / Validation | Analyses of secondaries, standard deviation and biases are reported |

Appendix C – GEOROC K₂O discrimination plots

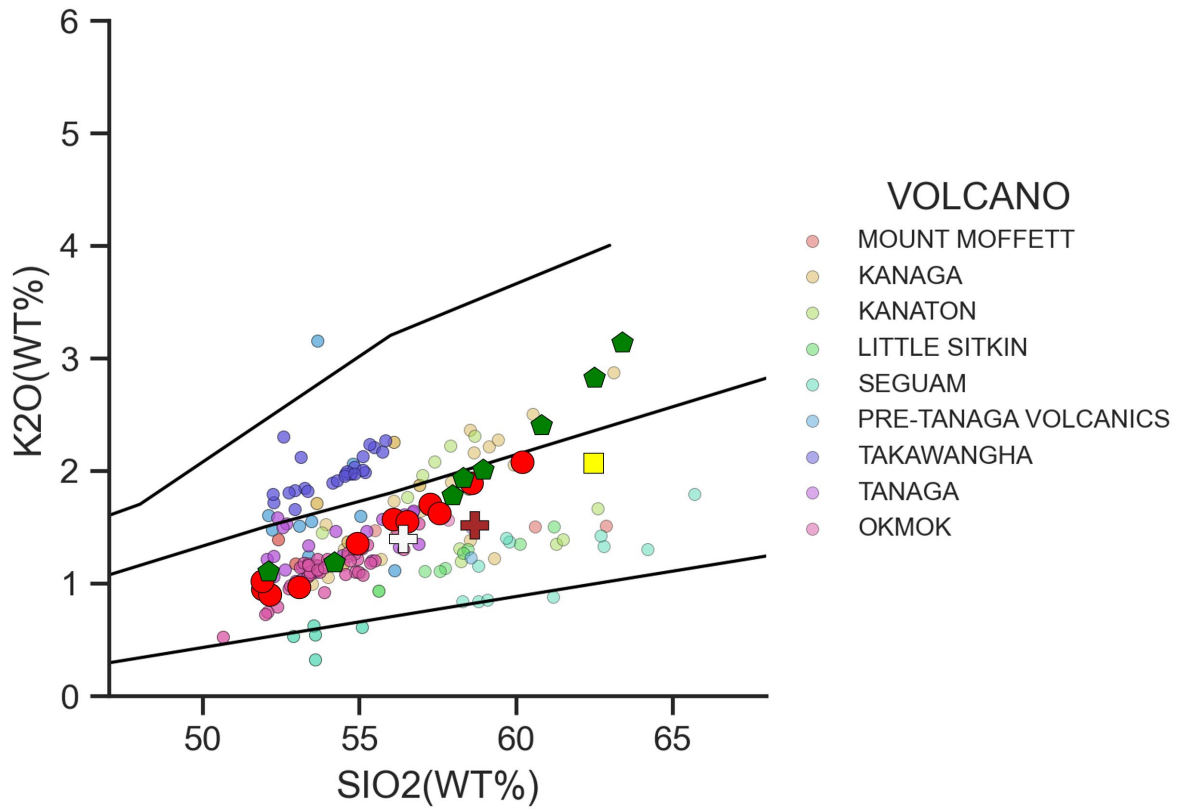
This appendix shows K₂O discrimination diagrams (fields after Peccerillo & Taylor, 1976) comparing the AVC basaltic andesite and andesite composition materials with different subduction arcs from around the globe (data obtained from the GEOROC database). The intention of these comparisons is to show that the K₂O trend that is observed at the AVC is not commonly observed elsewhere. Where similar trends are seen at other subduction zones, they are typically reserved for regions where the crust is thicker (e.g., regions of the Andean arc or the Trans-Mexican volcanic belt). Subductions zones involving thinner continental crust or oceanic crust (e.g., the Aleutian or Antilles arcs) rarely have compositions that extend into the high-K calc alkaline region of the plots.

The data points from GEOROC are divided by individual volcano or volcanic centre. In regions where there is a very high density of named volcanoes, the plots are divided alphabetically so that a reasonable number of volcanoes are shown in individual plots.

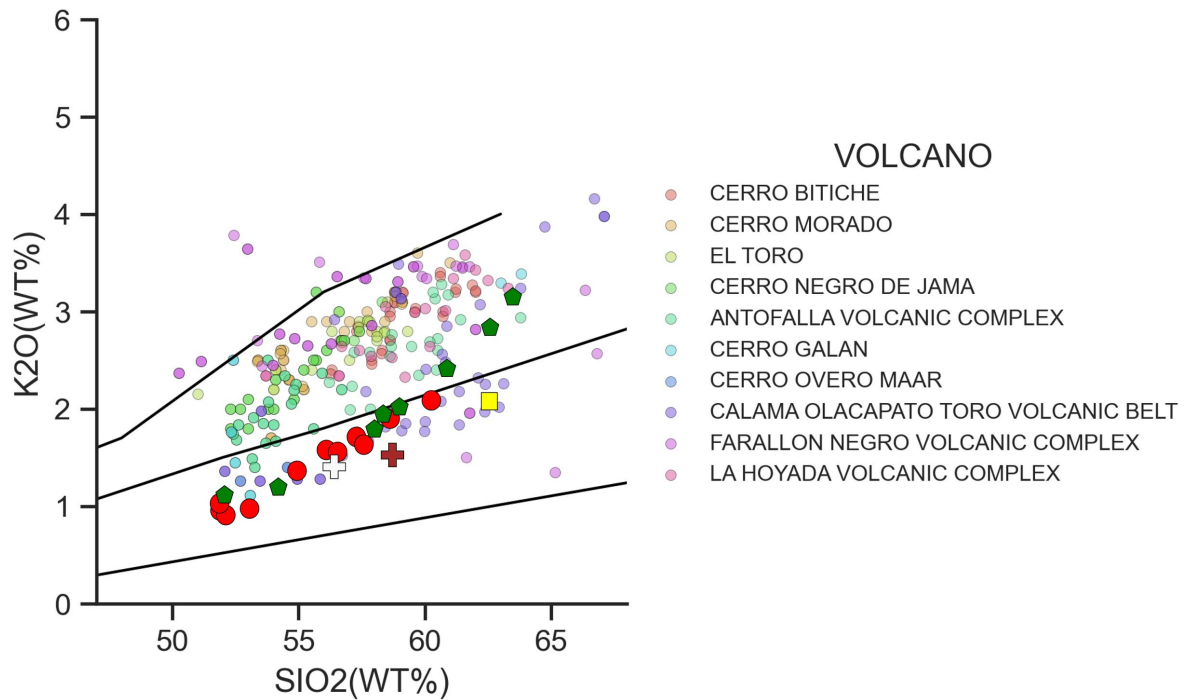
The large solid symbols are the same as for the plots of AVC geochemistry in the body of the thesis, and their values are shown again below:

| | |
|---|-------------|
|  | Phase III |
|  | Phase IV |
|  | D eruptions |
|  | I eruptions |
|  | Enclave |

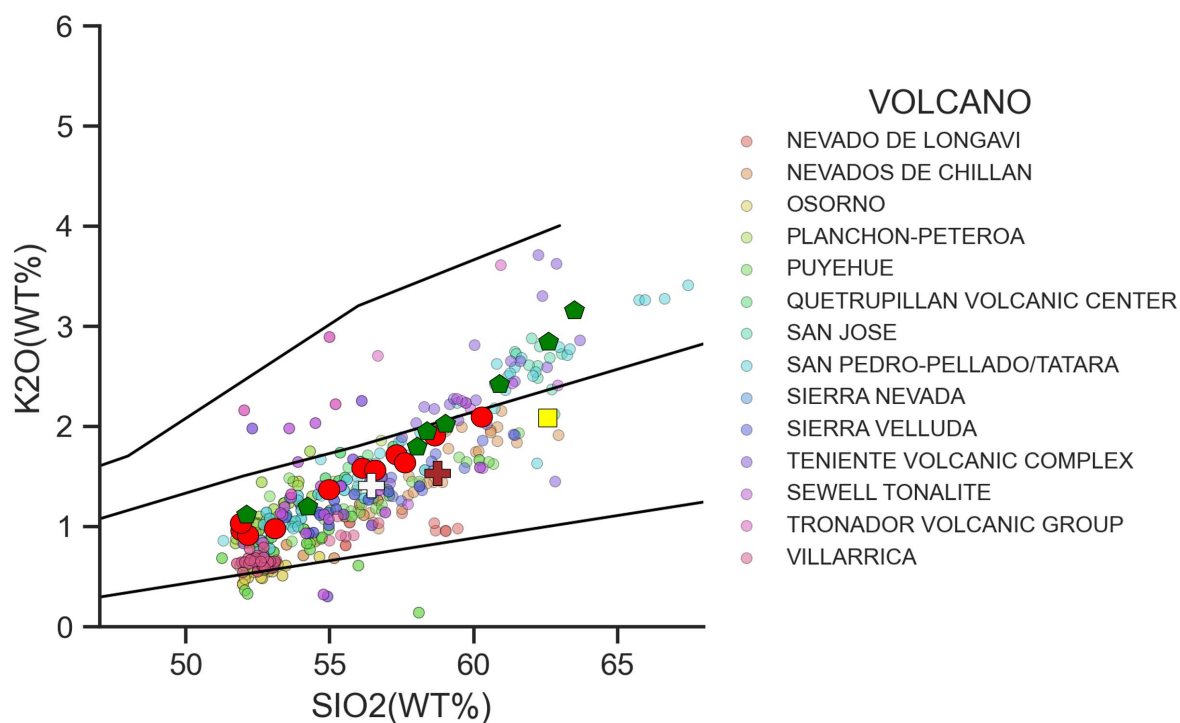
ALEUTIAN ARC / CENTRAL ALEUTIAN ARC



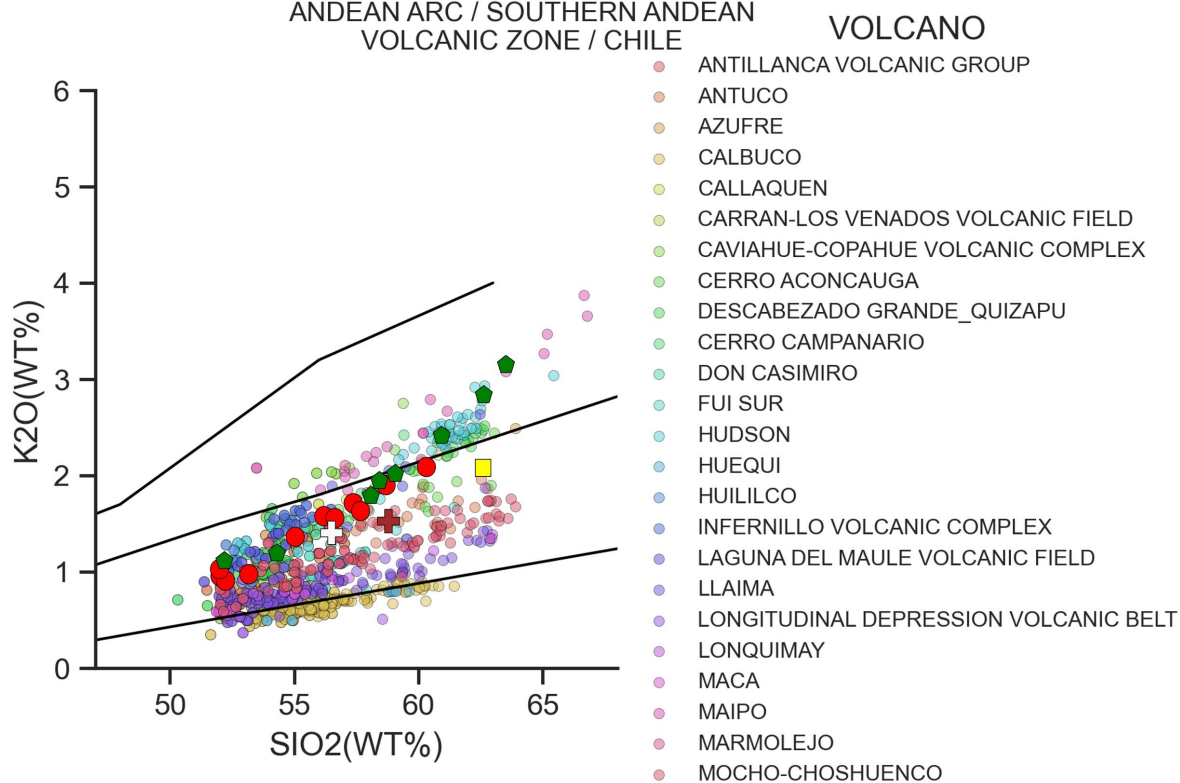
ANDEAN ARC / CENTRAL ANDEAN VOLCANIC ZONE / ARGENTINA



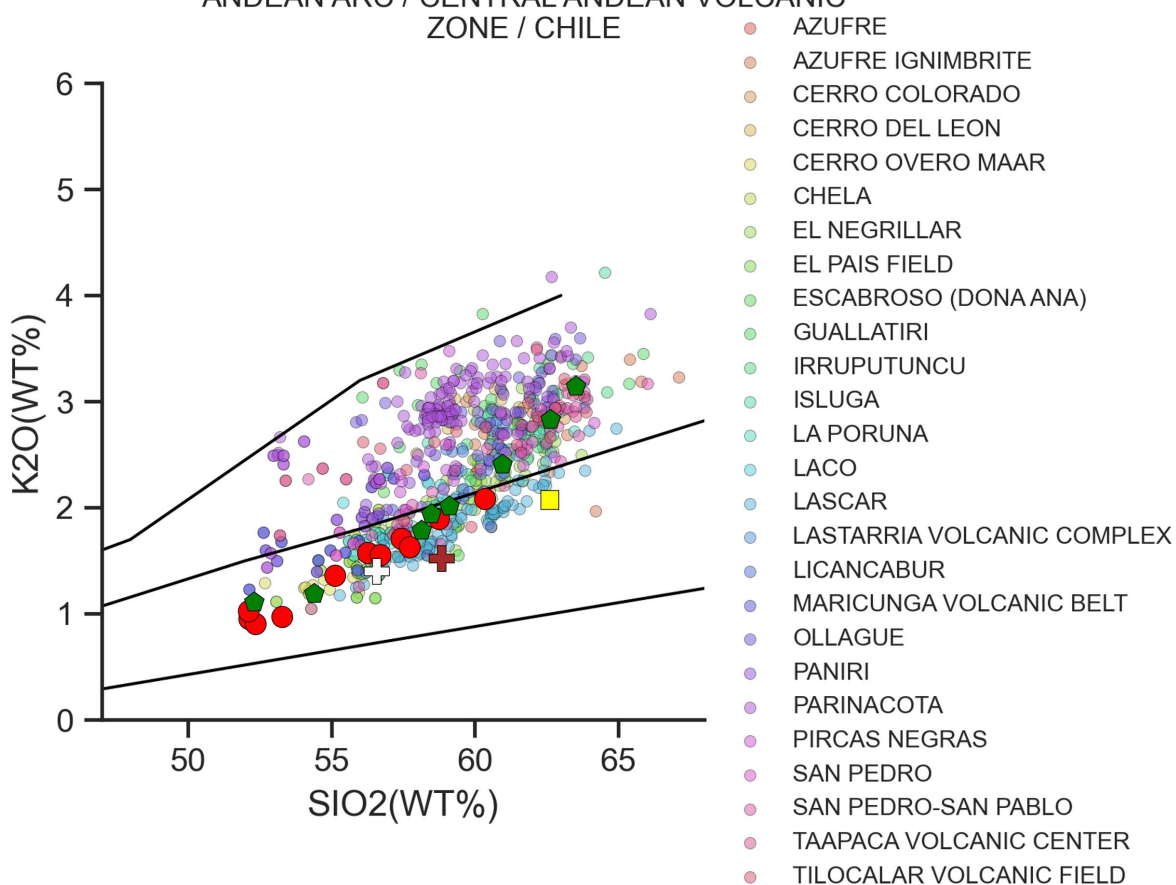
ANDEAN ARC / SOUTHERN ANDEAN
VOLCANIC ZONE / CHILE



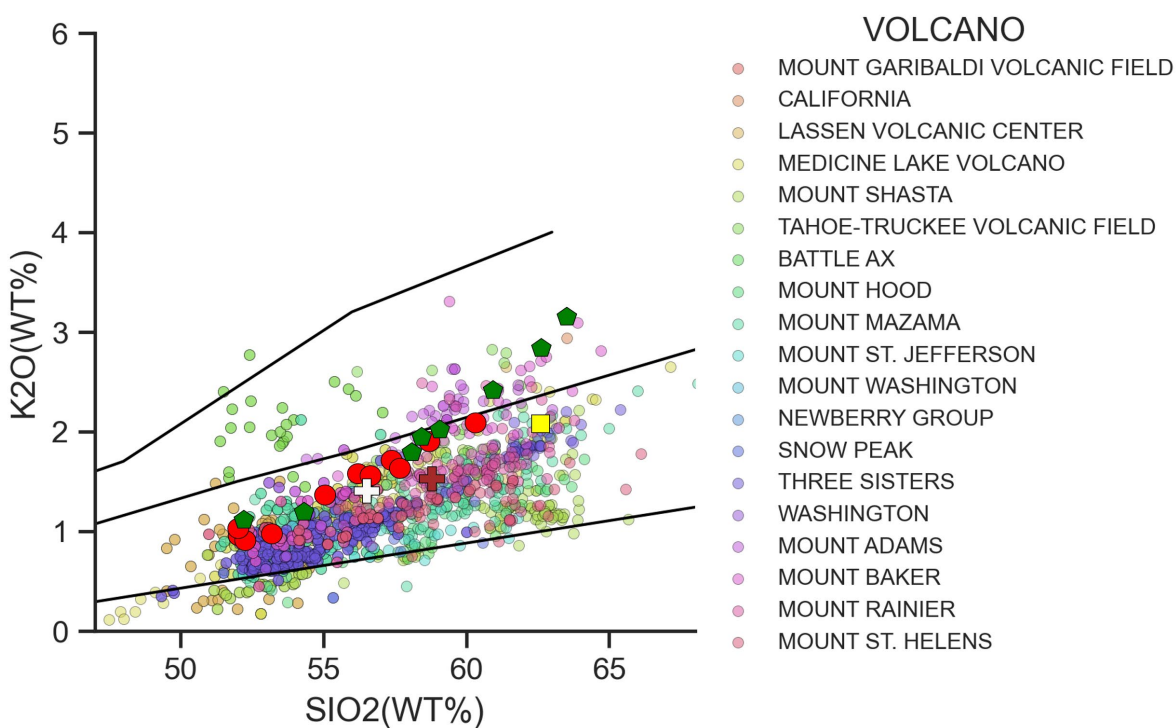
ANDEAN ARC / SOUTHERN ANDEAN
VOLCANIC ZONE / CHILE



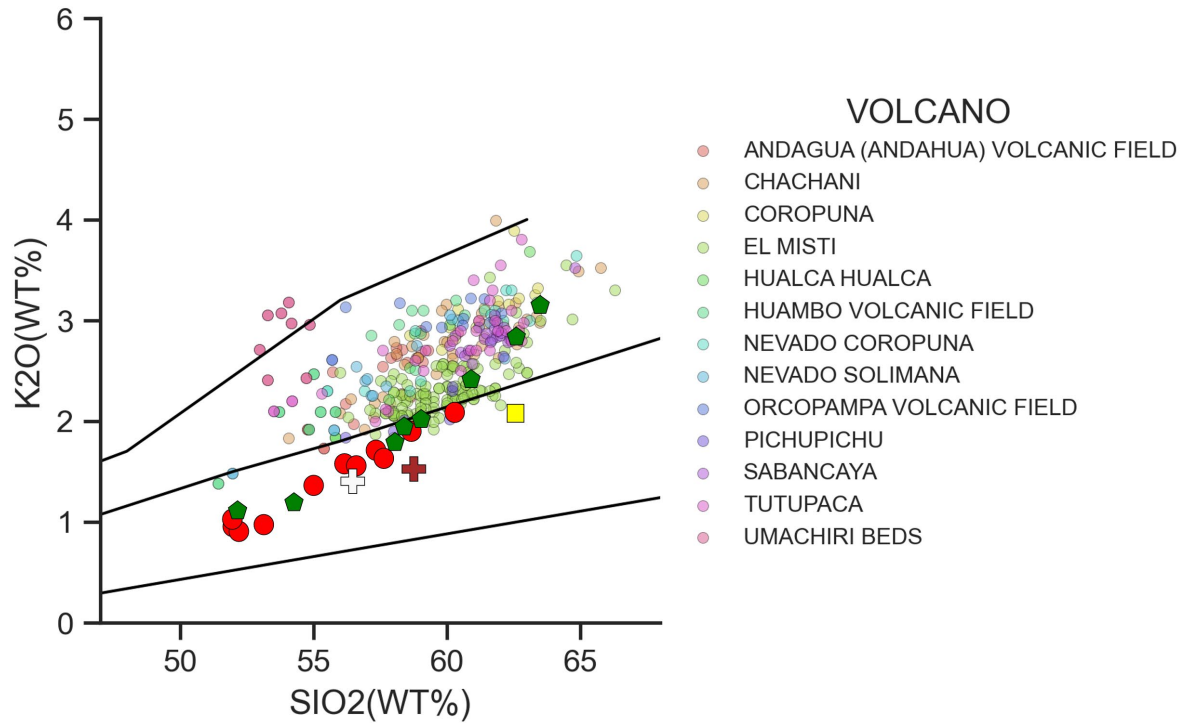
ANDEAN ARC / CENTRAL ANDEAN VOLCANIC ZONE / CHILE



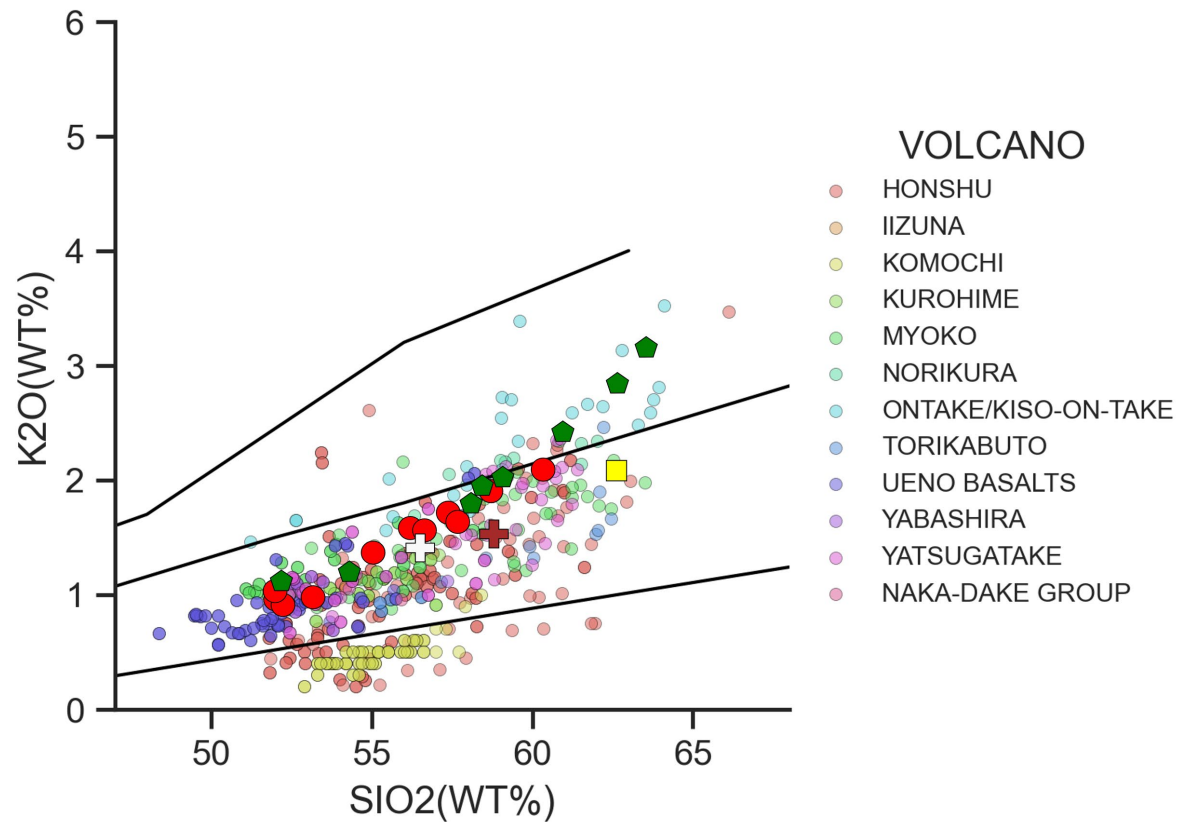
CASCADES / HIGH CASCADES



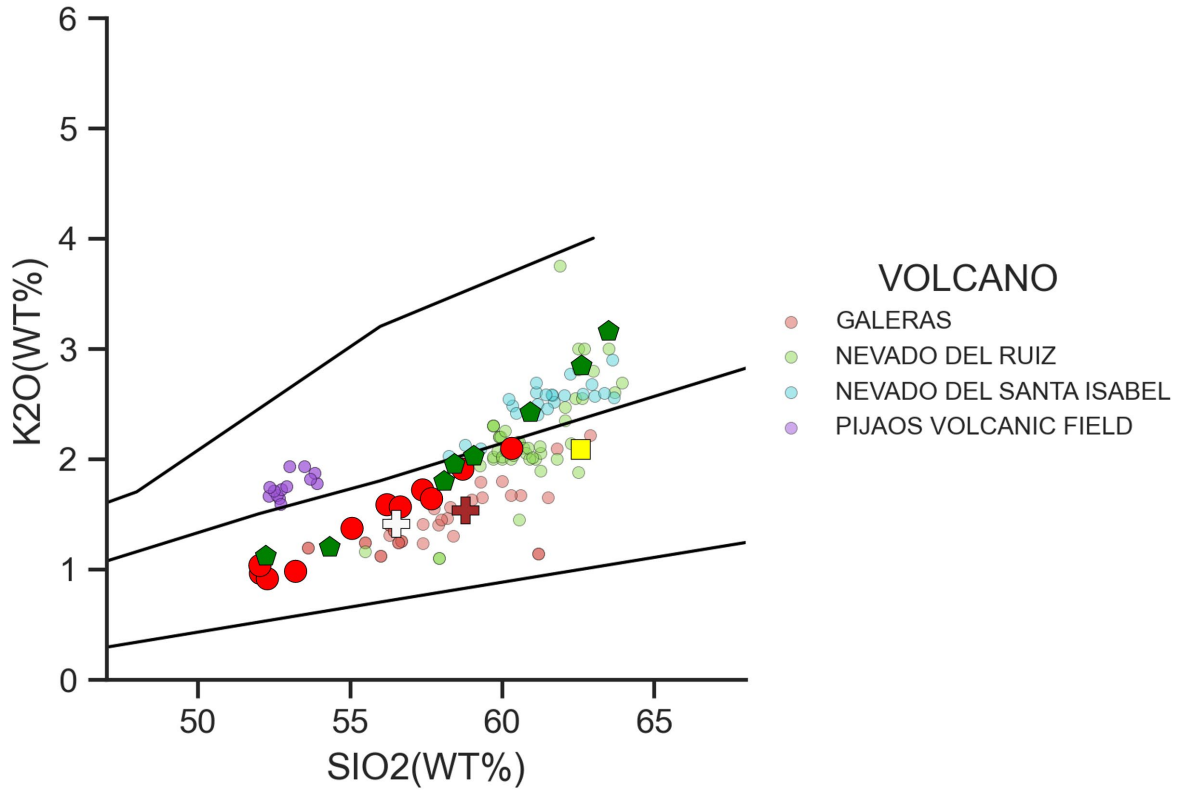
ANDEAN ARC / CENTRAL ANDEAN VOLCANIC
ZONE / PERU



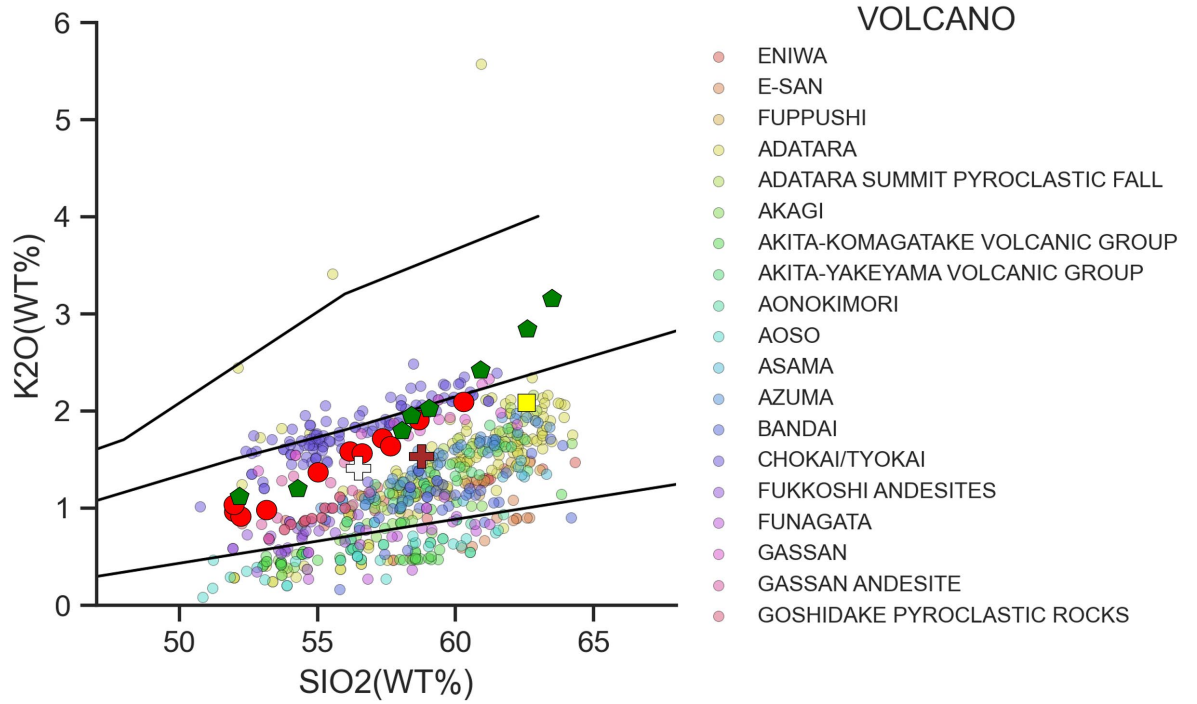
HONSHU ARC / CENTRAL HONSHU
ARC



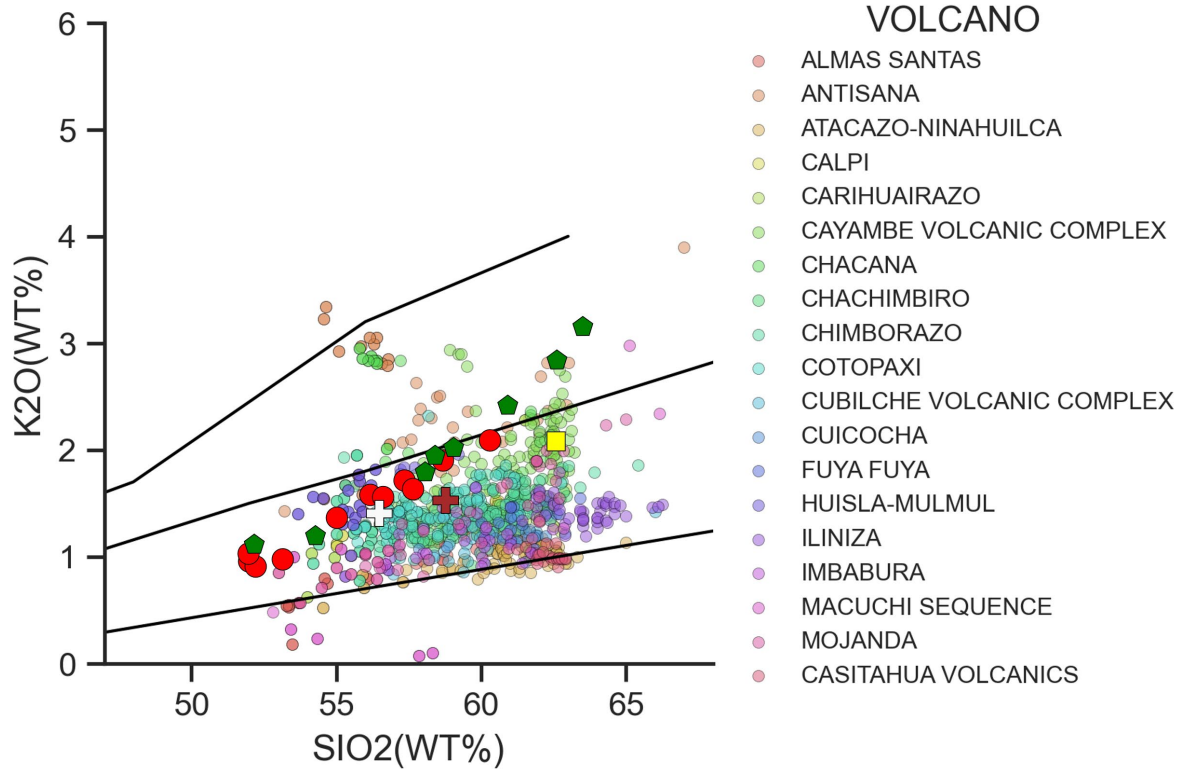
ANDEAN ARC / NORTHERN ANDEAN VOLCANIC
ZONE / COLOMBIA



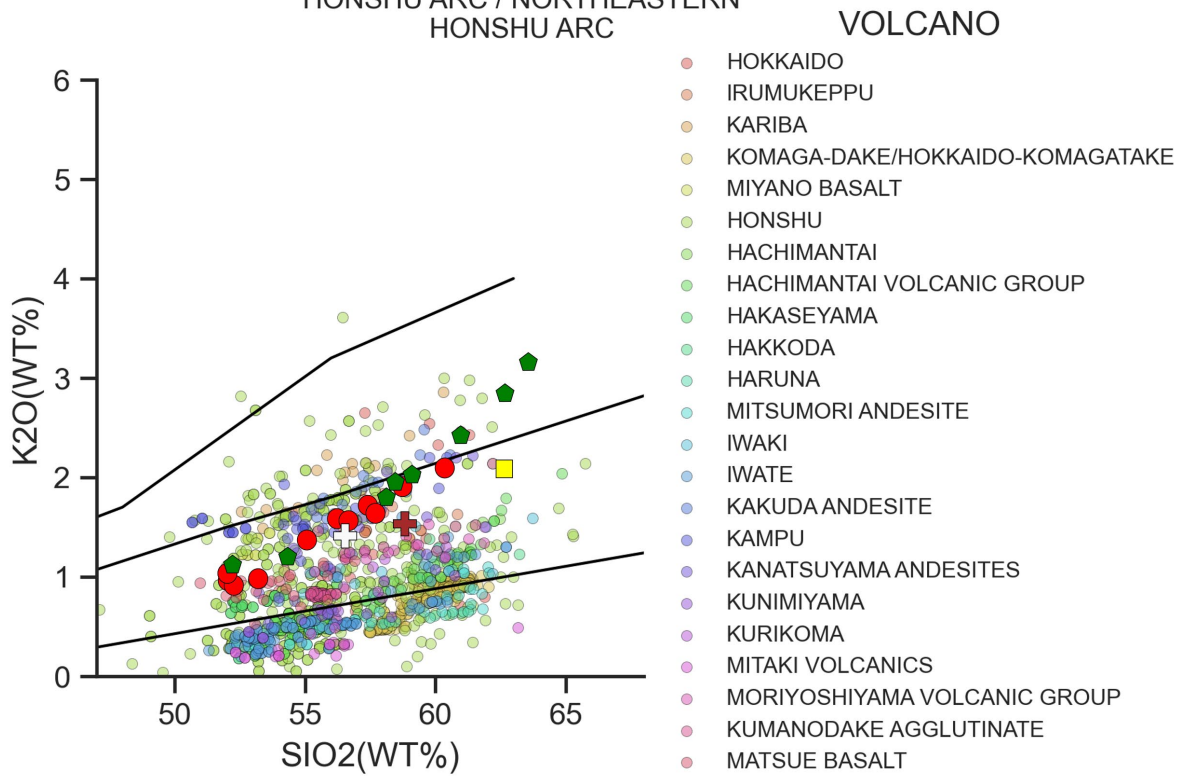
HONSHU ARC / NORTHEASTERN
HONSHU ARC



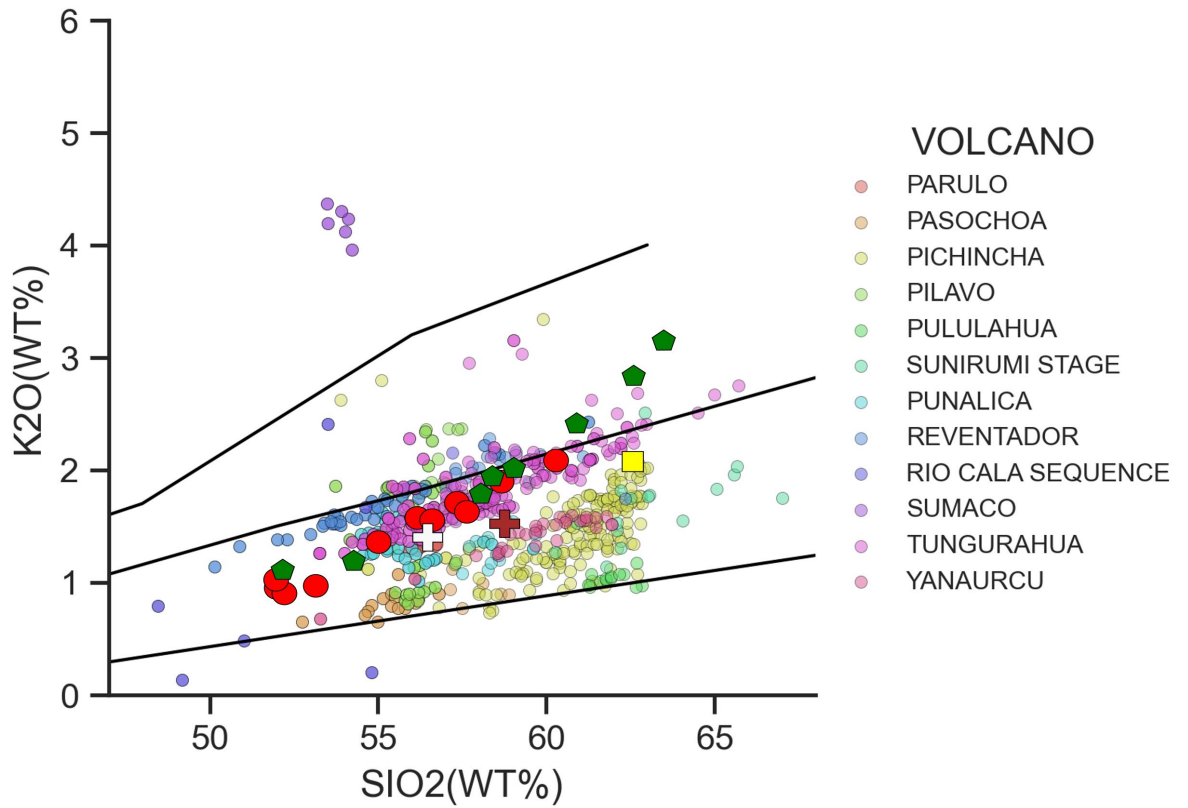
ANDEAN ARC / NORTHERN ANDEAN
VOLCANIC ZONE / ECUADOR



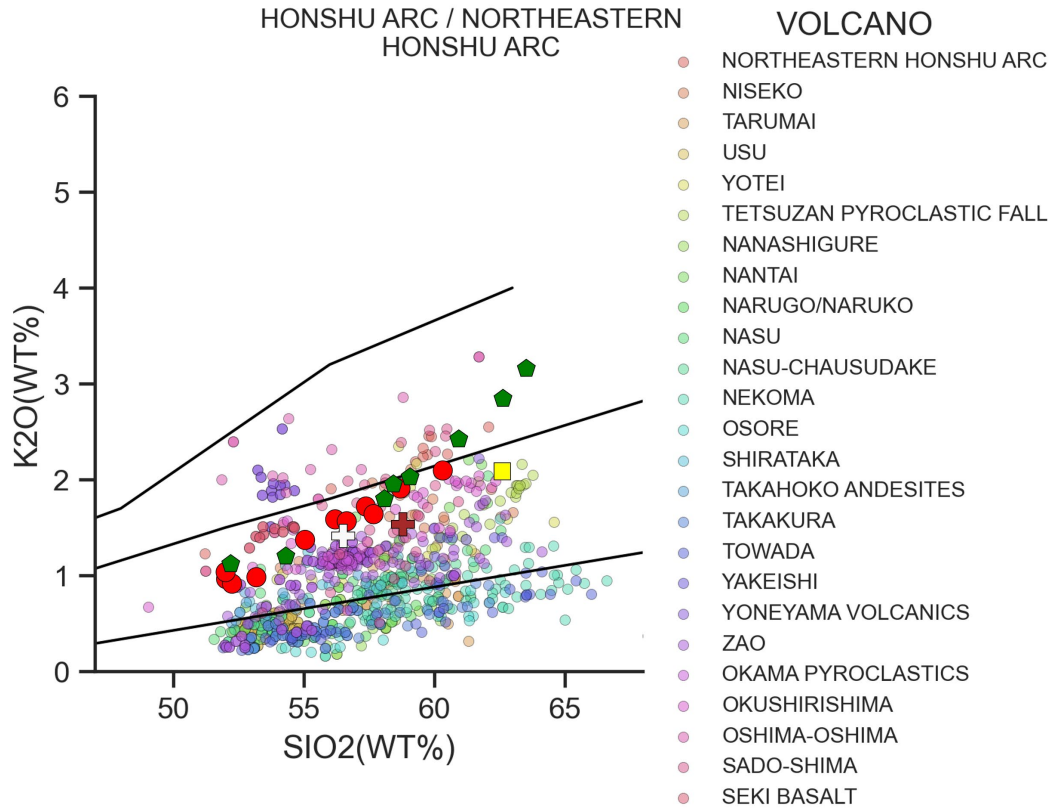
HONSHU ARC / NORTHEASTERN
HONSHU ARC



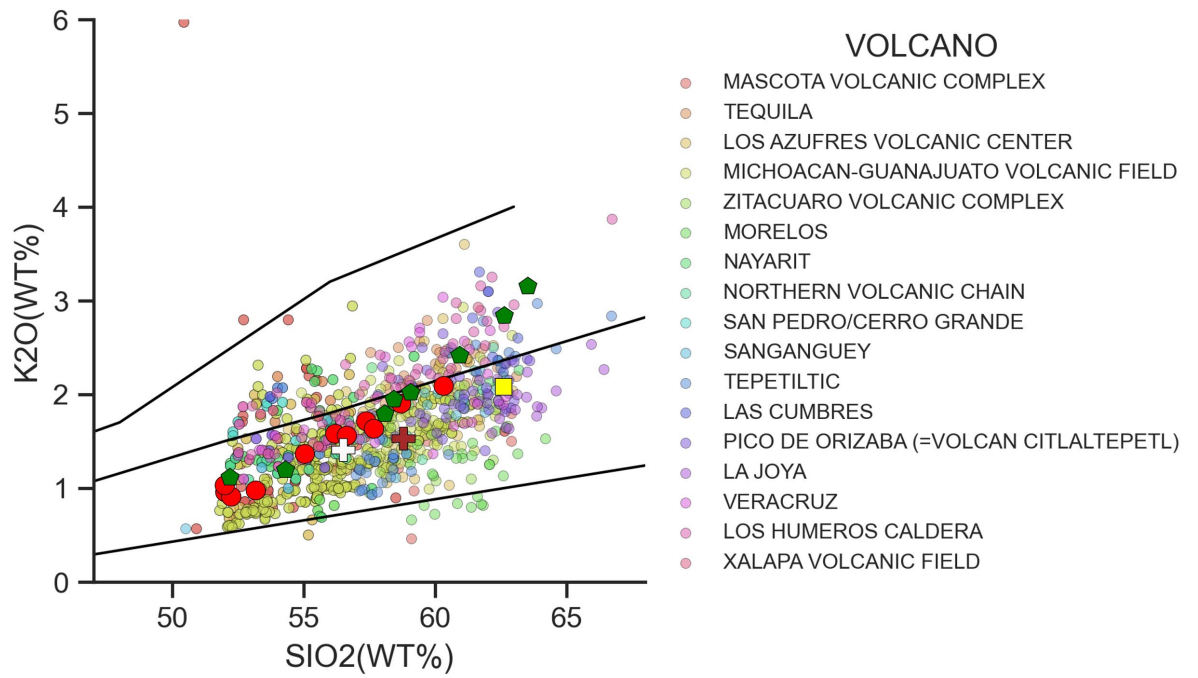
ANDEAN ARC / NORTHERN ANDEAN
VOLCANIC ZONE / ECUADOR



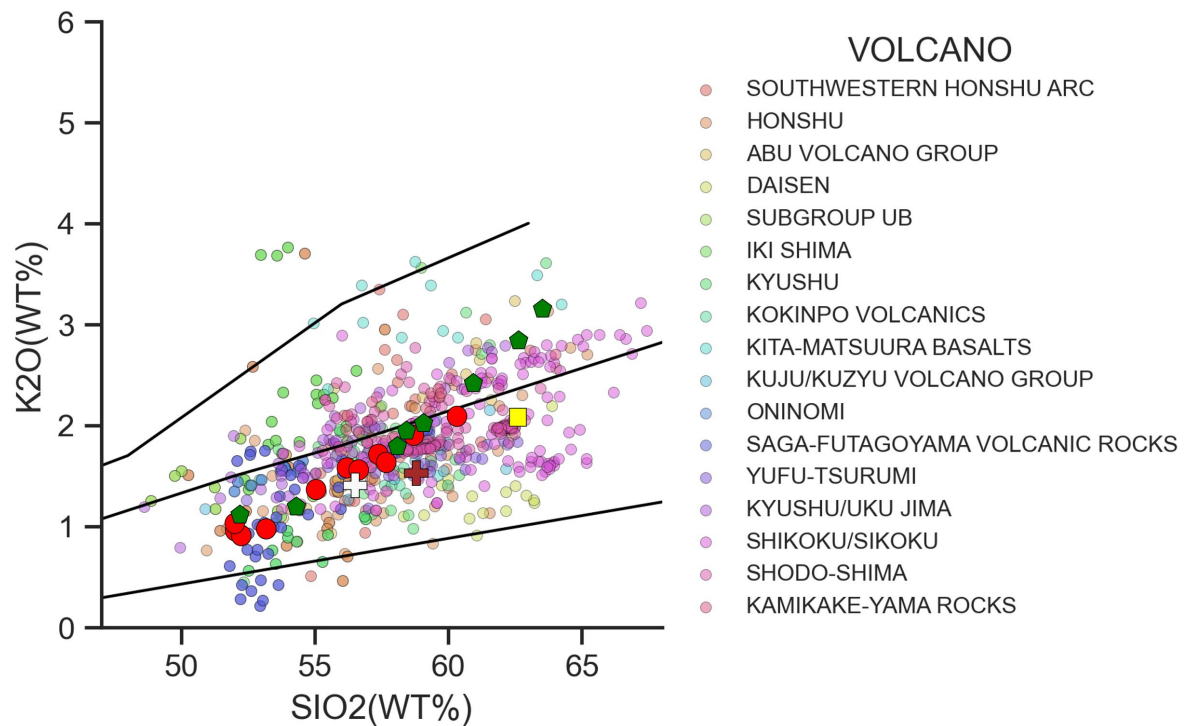
HONSHU ARC / NORTHEASTERN
HONSHU ARC

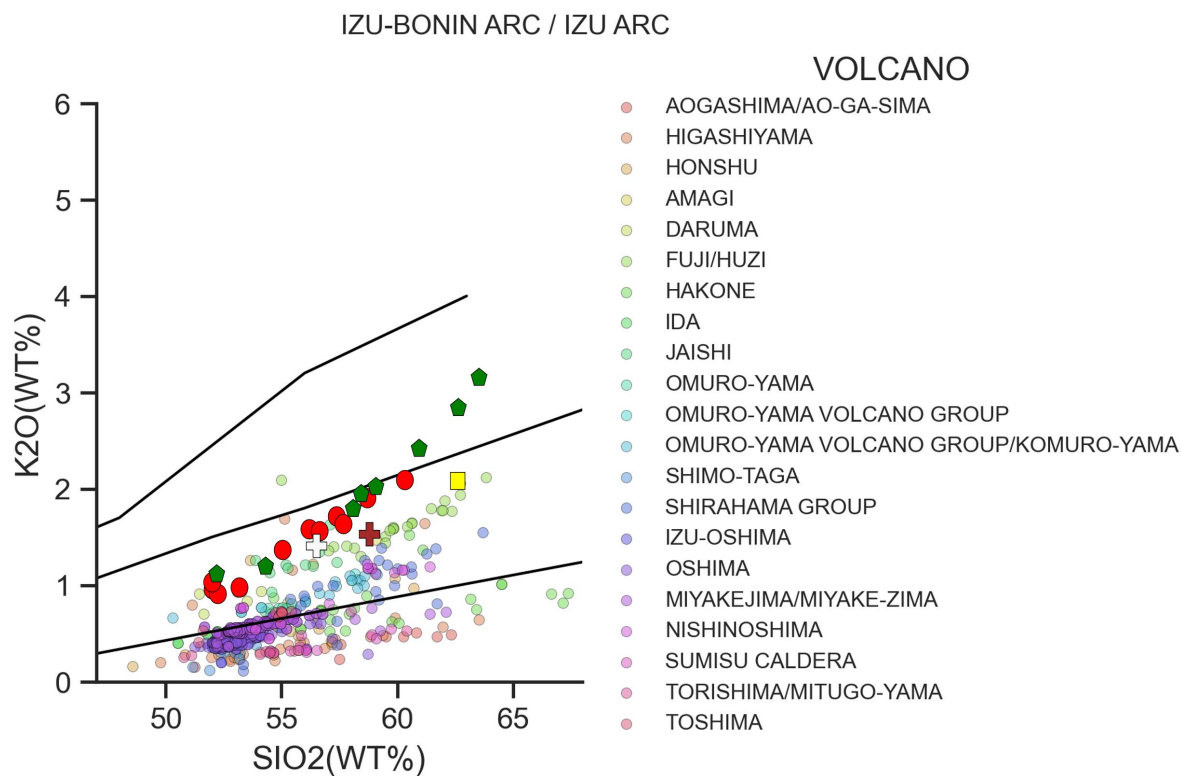
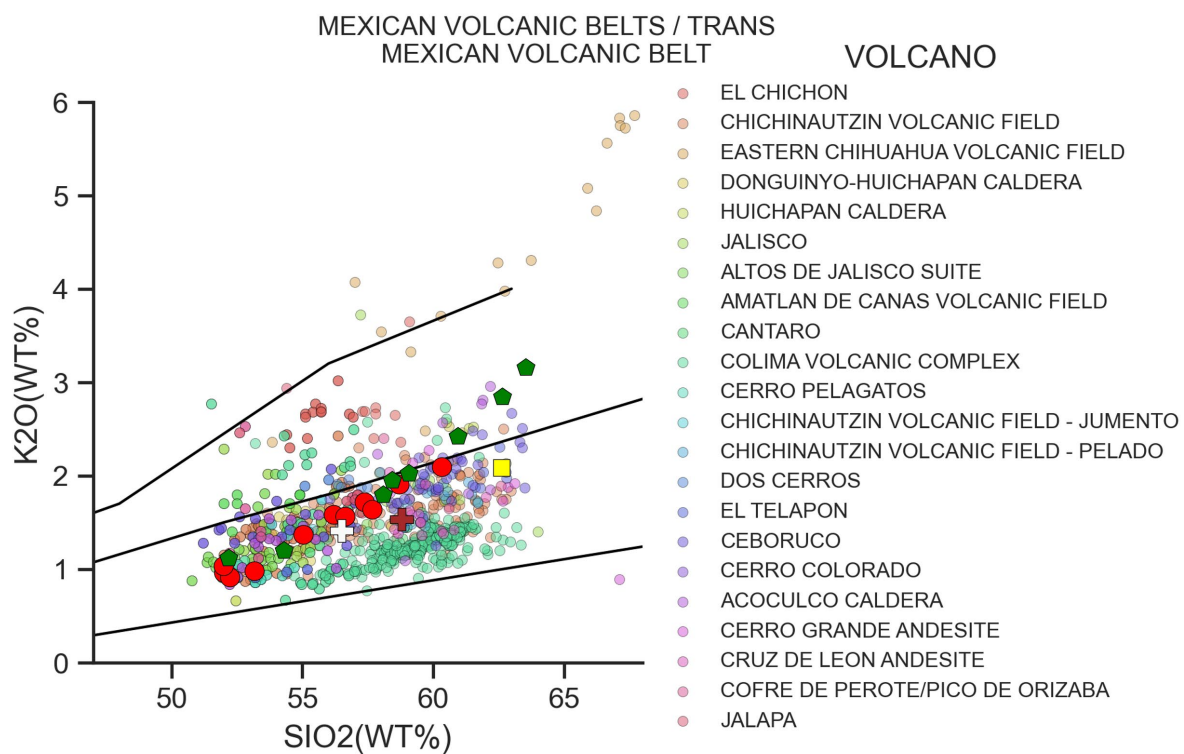


MEXICAN VOLCANIC BELTS / TRANS
MEXICAN VOLCANIC BELT

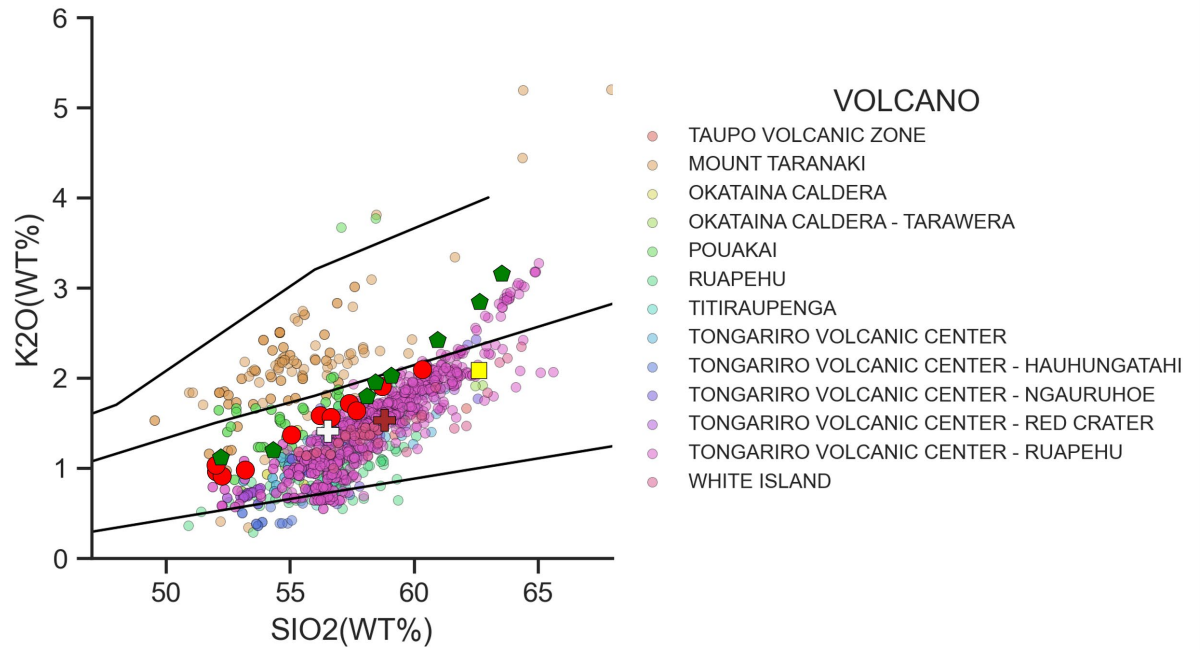


HONSHU ARC / SOUTHWESTERN
HONSHU ARC

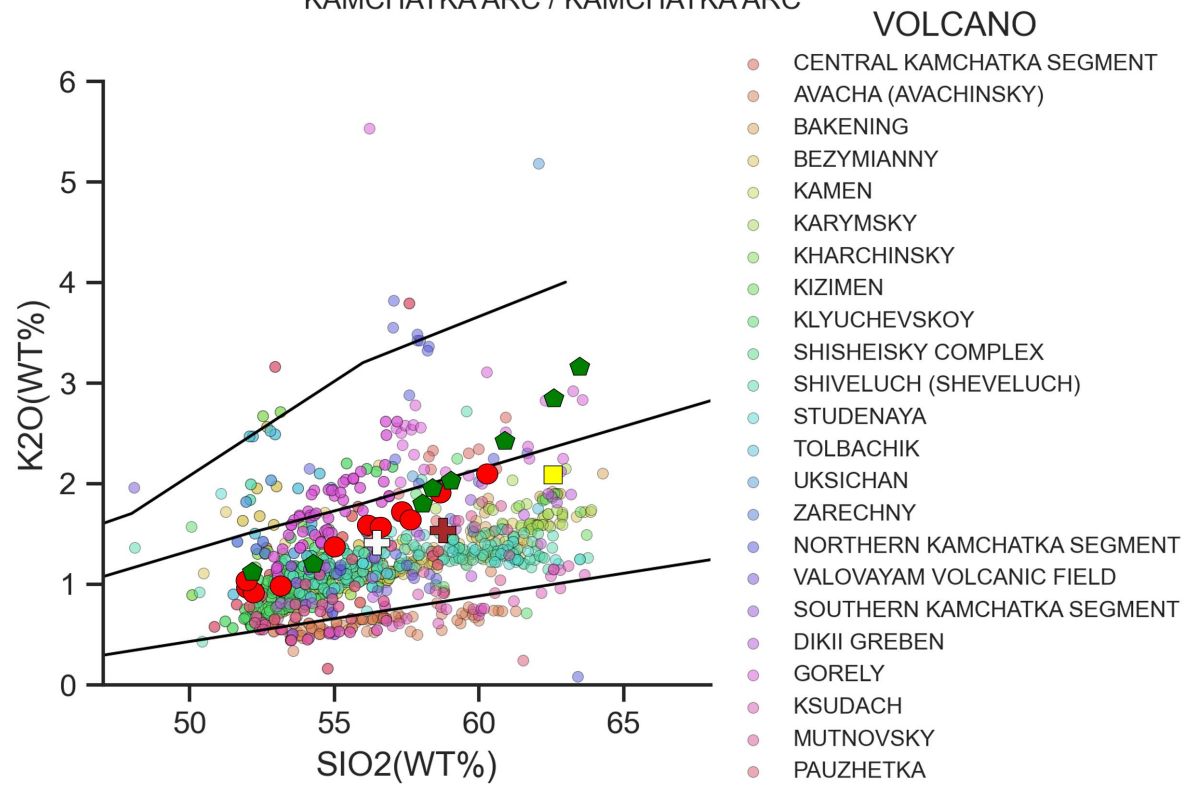




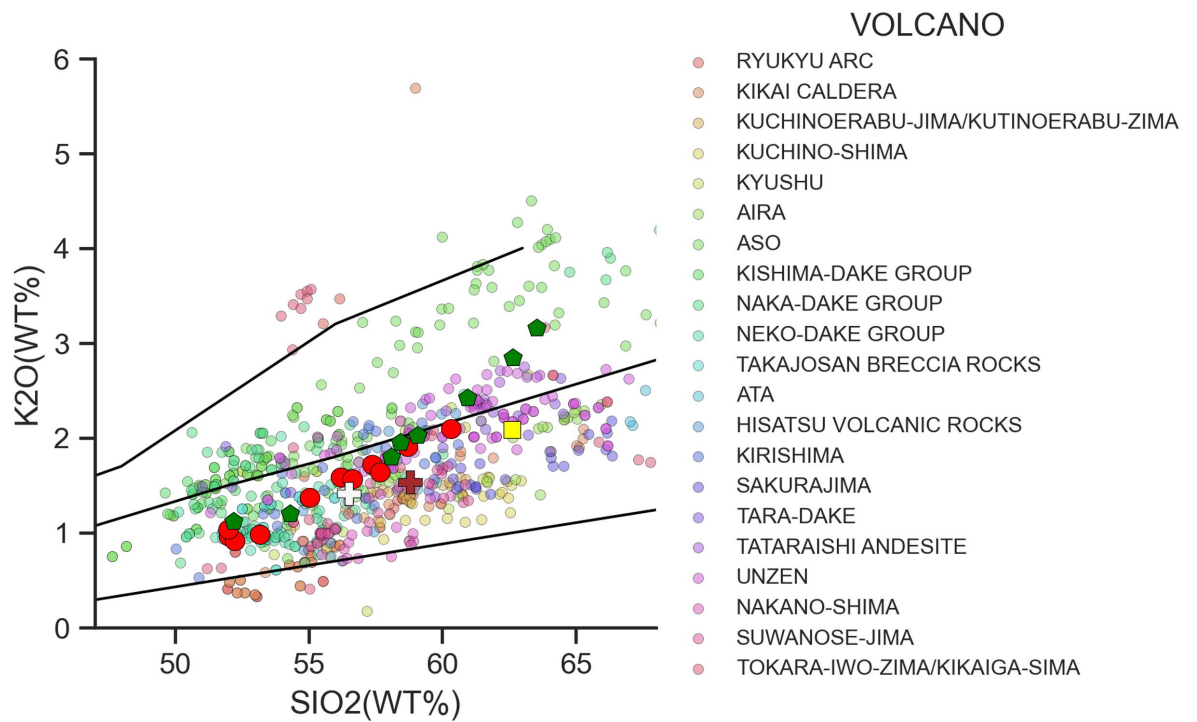
NEW ZEALAND / COROMANDEL-TAUPO



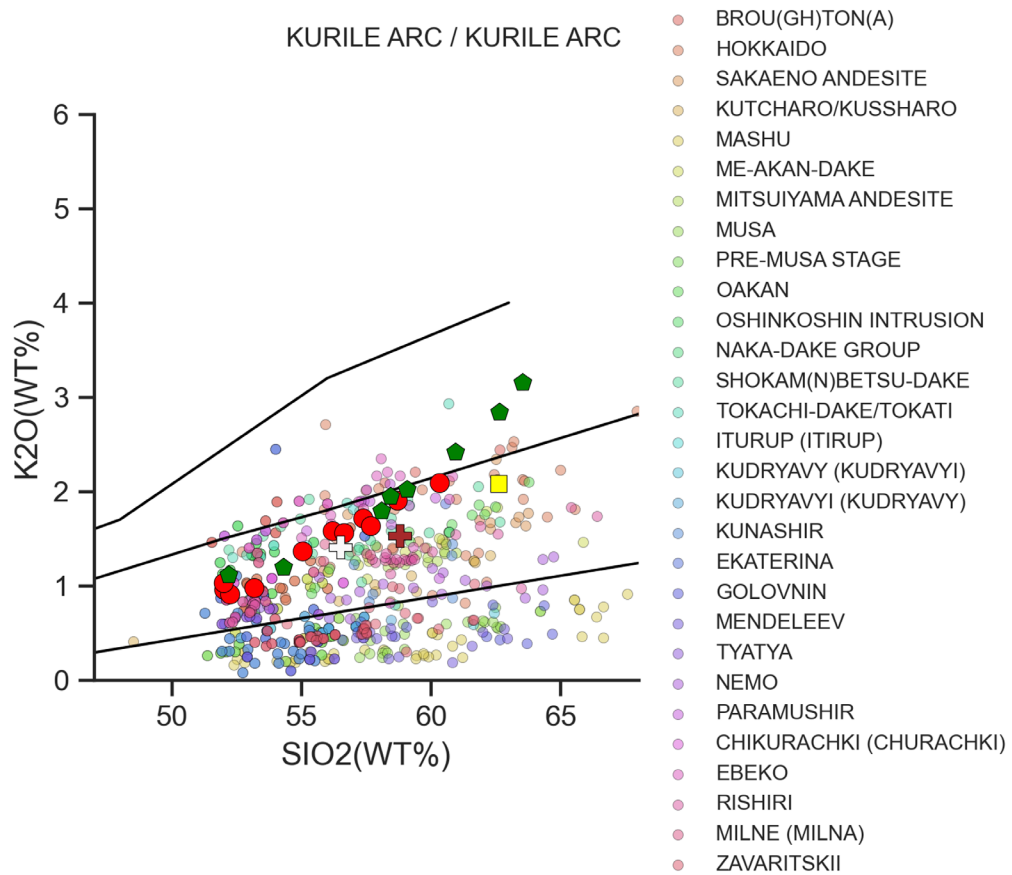
KAMCHATKA ARC / KAMCHATKA ARC

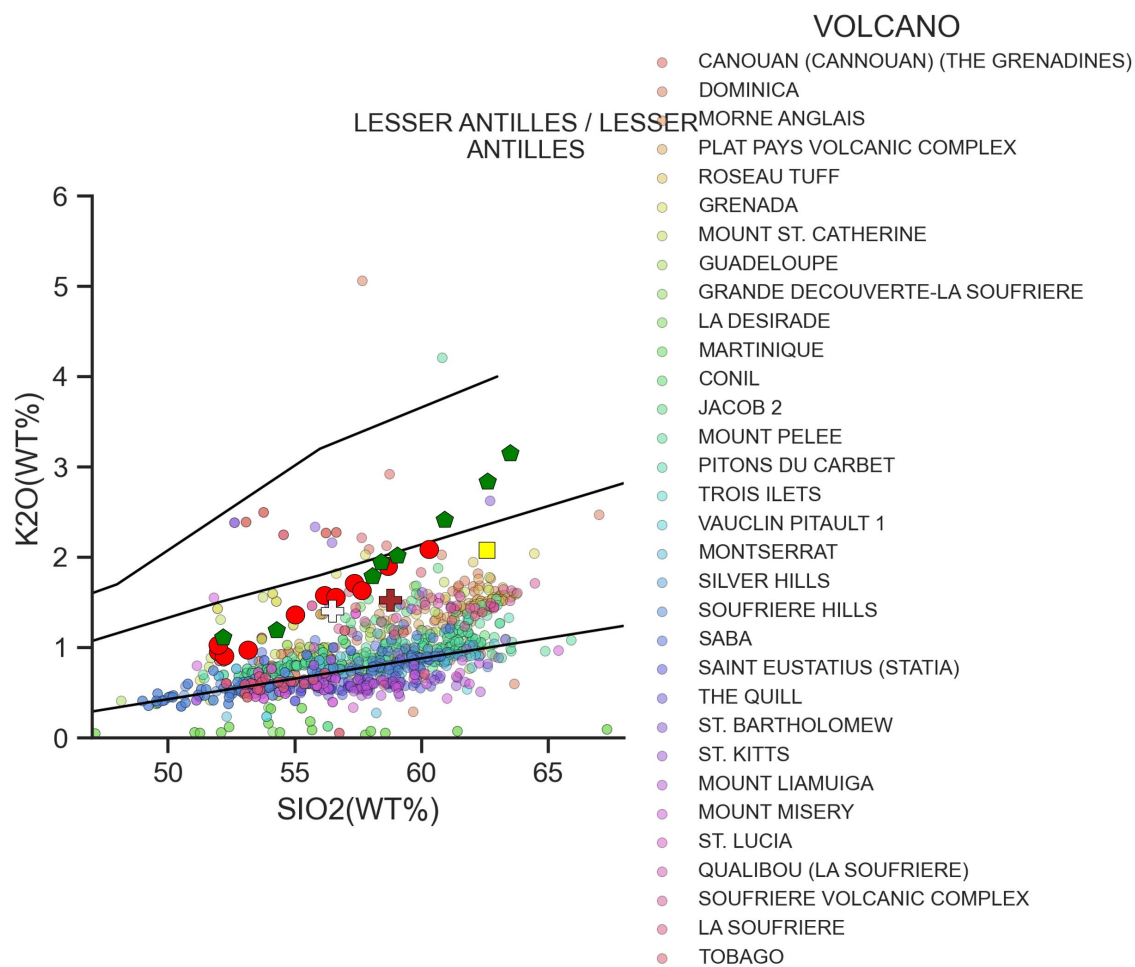
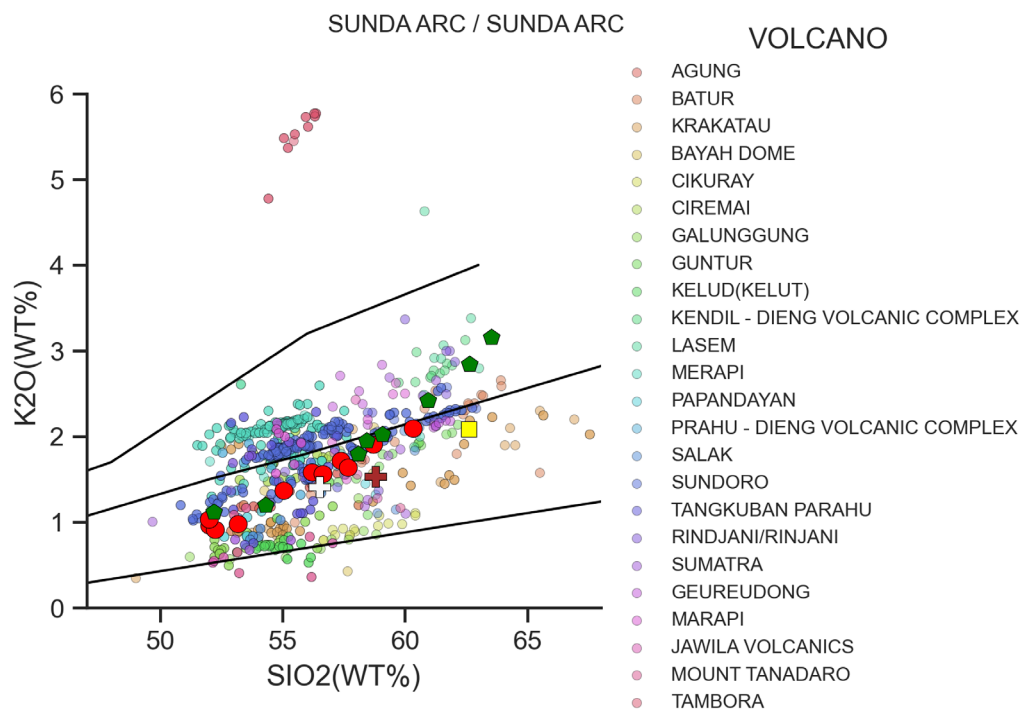


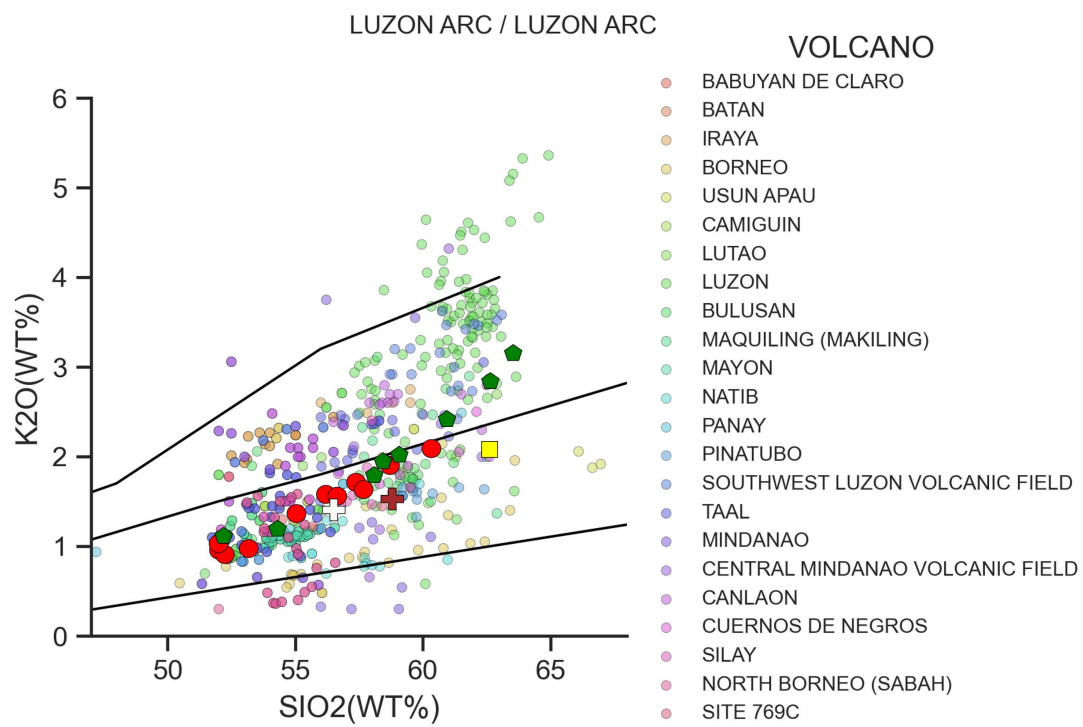
RYUKYU ARC / RYUKYU ARC



KURILE ARC / KURILE ARC







Appendix D – EME-AFC

D.1 Introduction to EME-AFC

Equilibrated Major Element Assimilation and Fractional Crystallisation (EME-AFC; Burton-Johnson et al., 2019) is a computational model designed to calculate liquid lines of descent for magmas, tracking major and trace elements as well as several isotope species. It was initially designed as a response to the thermodynamic modelling approach that is popular and is used by the MELTS family of models (Ghiorso and Sack, 1995), which while successful, does not have the ability to model systems which have fractionating assemblages with abundant hydrous minerals.

To get around the complexity of the thermodynamic approach with respect to hydrous phases, EME-AFC instead uses partition coefficients to iteratively model the changes of a fractionating and assimilating melt body. It uses two-component partition coefficients (e.g., plagioclase-melt: $K_D = (Al^{Plag} \times Si^{Liq}) / (Si^{Plag} \times Al^{Liq})$) to model mineral compositions and their fractionation, while using published partition coefficients from the GERM database to model the evolution of trace elements.

The model works as such (see the READ ME tab of the model spreadsheets in Electronic Appendix X for full instructions and background):

1. Edit the desired trace element partition coefficients for your particular minerals
2. Enter the analysed compositions for fractionating minerals, the primary magma, target composition, assimilant, and comparative whole rock data
3. Model the system (by trying to achieve as small a value for $\sum D^2$ – the sum of differences between the model and target compositions) using the different variables that are available:
 - The relative abundances of the fractionating assemblage at the different SiO₂ splits
 - The SiO₂ content at which the model splits
 - The values of the two-component major element partition coefficients
 - The rate of assimilation vs. fractionation
 - The degree of partial melting of the assimilant

The following figures show the final variables that were chosen for each of the modelling runs that were performed. The boxes (in order from top to bottom) show the fractionating assemblage, the ratio of assimilation to fractionation (ratio = M_a/M_c), the model splits, the melting proportion of the assimilant, the estimated two-component partition coefficients for the major elements, the final model errors and final modelled melt major element composition, and the modelled mineral compositions. For the modelled mineral compositions, the red symbols are the model's composition estimates, while the grey symbols are analysed mineral compositions from the rocks that are used for comparison.

D.2 Model variables and partition coefficients

D.2.1 Modelled stratovolcano series

| Fractionating Assemblage | | | | | | | | | | | | | INPUT |
|---|---------------|---------------|------------|----------|----------|---------|---------|-----------|----------|--------|--------|--------|--------|
| Ol | Cpx | Opx | Hbl | Pl | Kfs | Bt | Ap | Mag | Ilm | Zrn | Rt | Grt | OUTPUT |
| Basalt SiO ₂ wt.% < 53 | | | | | | | | | | | | | TOTAL |
| 15.0 | 15.0 | | | 60.0 | | | 0.50 | 4.00 | 2.00 | | | | 96.5 |
| 15.5 | 15.5 | | | 62.2 | | | 0.52 | 4.15 | 2.07 | | | | 100 % |
| Basaltic Andesite SiO ₂ wt.% > 53 & < 57 | | | | | | | | | | | | | |
| 4.0 | 20.0 | 10.0 | 1.0 | 60.0 | | | 0.50 | 4.00 | 2.00 | | | | 101.5 |
| 3.9 | 19.7 | 9.9 | 1.0 | 59.1 | | | 0.49 | 3.94 | 1.97 | | | | 100 % |
| Andesite SiO ₂ wt.% > 57 & < 63 | | | | | | | | | | | | | |
| 2.0 | 16.0 | 26.0 | 65.0 | | | | 1.00 | 4.00 | 1.00 | 0.05 | | | 115.1 |
| 1.7 | 13.9 | 22.6 | 56.5 | | | | 0.87 | 3.48 | 0.87 | 0.04 | | | 100 % |
| Dacite / Rhyolite SiO ₂ wt.% > 63 | | | | | | | | | | | | | |
| 2.0 | 18.0 | 28.0 | 65.0 | | | | 1.00 | 4.00 | 1.00 | 0.10 | | | 119.1 |
| 1.7 | 15.1 | 23.5 | 54.6 | | | | 0.84 | 3.36 | 0.84 | 0.08 | | | 100 % |
| Olivine | Clinopyroxene | Orthopyroxene | Hornblende | Plagiocl | K-Feldsp | Biotite | Apatite | Magnetite | ilmenite | Zircon | Rutile | Garnet | |

| | | |
|---------------------------------|----------|---|
| Assimilation ($r = M_d/M_c$) | | Split model when SiO ₂ wt.% > 53 |
| Liquid SiO ₂ wt% | $r (<1)$ | Split model when SiO ₂ wt.% > 57 |
| < 53 | 0 | Split model when SiO ₂ wt.% > 63 |
| > 53 & < 57 | 0.15 | Target SiO ₂ |
| > 57 & < 63 | 0.33 | 63.54 |
| > 63 | 0.33 | |
| Batch Modal Melting (Trace El.) | | |
| $F_{\text{Assimilation}}$ | | 1 |

Only phases fractionated in the model displayed

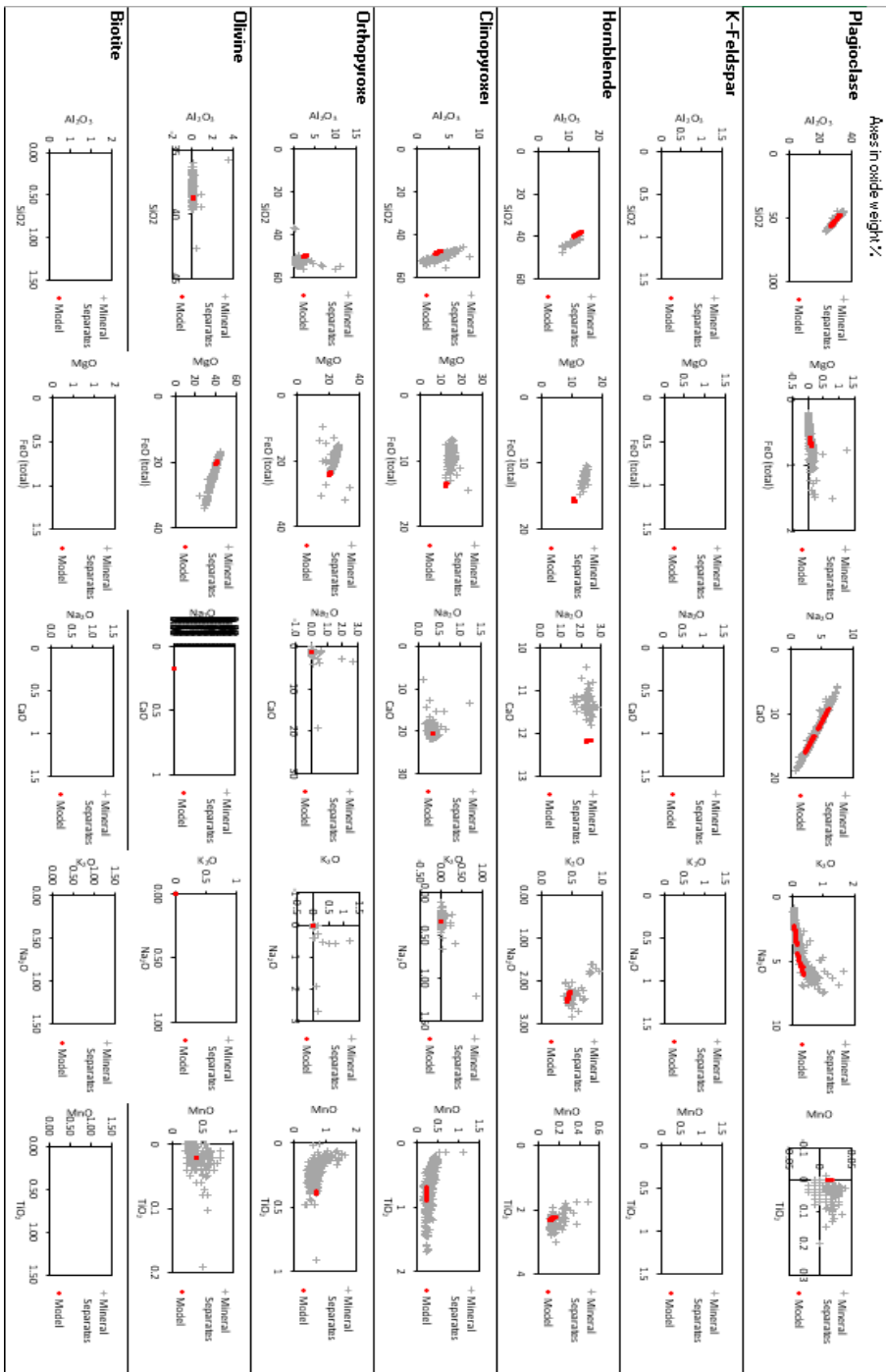
Experimental Values

| Two-Component Partition Coefficients | | | | | | Min | Max | Mean |
|---|------|---------------------------|------------------|--|--|------|------|------|
| Plagioclase $K_D = (Al^{Plag} \times Si^{Liq}) / (Si^{Plag} \times Al^{Liq})$ | 2.46 | All SiO | <Not used in mod | | | 1.79 | 4.20 | 2.46 |
| Plagioclase $K_D = (Al^{Plag} \times Si^{Liq}) / (Si^{Plag} \times Al^{Liq})$ | 2.00 | SiO ₂ wt% < 53 | | | | | | |
| Plagioclase $K_D = (Al^{Plag} \times Si^{Liq}) / (Si^{Plag} \times Al^{Liq})$ | 2.00 | SiO ₂ wt% > 53 | | | | 1.79 | 2.22 | 2.01 |
| Plagioclase $K_D = (Al^{Plag} \times Si^{Liq}) / (Si^{Plag} \times Al^{Liq})$ | 1.90 | SiO ₂ wt% > 57 | | | | 1.90 | 2.85 | 2.31 |
| Plagioclase $K_D = (Al^{Plag} \times Si^{Liq}) / (Si^{Plag} \times Al^{Liq})$ | 2.05 | SiO ₂ wt% > 63 | | | | 2.05 | 4.20 | 2.80 |
| Plagioclase $K_D = (K^{Plag} \times Na^{Liq}) / (Na^{Plag} \times K^{Liq})$ | 0.05 | | | | | 0.03 | 0.19 | 0.09 |
| K-Feldspar $K_D = (K^{Kfs} \times Na^{Liq}) / (Na^{Kfs} \times K^{Liq})$ | 7.00 | (estimate from graphs) | | | | | | |
| Hornblende $K_D = (Fe^{Hb} \times Mg^{Liq}) / (Mg^{Hb} \times Fe^{Liq})$ | 0.36 | | | | | 0.23 | 0.53 | 0.36 |
| Hornblende $K_D = (Al^{Hb} \times Si^{Liq}) / (Si^{Hb} \times Al^{Liq})$ | 1.13 | | | | | 0.26 | 1.60 | 1.13 |
| Clinopyroxene $K_D = (Fe^{Cpx} \times Mg^{Liq}) / (Mg^{Cpx} \times Fe^{Liq})$ | 0.28 | | | | | 0.20 | 0.51 | 0.28 |
| Clinopyroxene $K_D = (Al^{Cpx} \times Si^{Liq}) / (Si^{Cpx} \times Al^{Liq})$ | 0.27 | | | | | 0.12 | 0.68 | 0.27 |
| Orthopyroxene $K_D = (Fe^{Opx} \times Mg^{Liq}) / (Mg^{Opx} \times Fe^{Liq})$ | 0.28 | | | | | 0.20 | 0.53 | 0.28 |
| Orthopyroxene $K_D = (Al^{Opx} \times Si^{Liq}) / (Si^{Opx} \times Al^{Liq})$ | 0.19 | | | | | 0.07 | 0.52 | 0.19 |
| Olivine $K_D = (Fe^{Ol} \times Mg^{Liq}) / (Mg^{Ol} \times Fe^{Liq})$ | 0.28 | | | | | 0.24 | 0.33 | 0.28 |
| Biotite $K_D = (Al^{Bt} \times Si^{Liq}) / (Si^{Bt} \times Al^{Liq})$ | 2.52 | | | | | 2.52 | 2.52 | 2.52 |
| Garnet $K_D = (Fe^{Grt} \times Mg^{Liq}) / (Mg^{Grt} \times Fe^{Liq})$ | 0.97 | | | | | 0.60 | 1.59 | 0.97 |

| D ² (Model Error) | | | | | | | | | | | ΣD ² | ΣD ² exc. SiO ₂ |
|------------------------------|------------------|--------------------------------|--------|------|------|------|-------------------|------------------|-------------------------------|--|-----------------|---------------------------------------|
| SiO ₂ | TiO ₂ | Al ₂ O ₃ | FeOtot | MnO | MgO | CaO | Na ₂ O | K ₂ O | P ₂ O ₅ | | 1.69 | 1.67 |
| 0.02 | 0.00 | 0.00 | 0.35 | 0.00 | 0.03 | 0.50 | 0.79 | 0.00 | 0.00 | | | |

(based on 100% normalized values)

| Modelled Melt Major Elements (wt %) | | | | | | | | | | | Isotopes | | | | | | | |
|-------------------------------------|------------------|--------------------------------|--------|------|------|------|-------------------|------------------|-------------------------------|-------|----------|---------|---------|---------|-----------|-----------|----------------------|----------------------|
| SiO ₂ | TiO ₂ | Al ₂ O ₃ | FeOtot | MnO | MgO | CaO | Na ₂ O | K ₂ O | P ₂ O ₅ | TOTAL | 206/204 | 207/204 | 208/204 | 87/86Sr | 143/144Nd | 176/177Hf | ε ¹⁸ O WR | ε ⁷⁰ O Zn |
| 63.40 | 0.65 | 16.53 | 4.16 | 0.12 | 2.45 | 4.22 | 4.29 | 3.11 | 0.12 | 39.04 | 0.00 | 0.00 | 0.00 | 0.00 | 0.00 | 0.00 | *DIV/OI | *DIV/OI |



D.2.2 Modelling of the enclave magma

| Fractionating Assemblage | | | | | | | | | | | | | INPUT |
|--------------------------|------------|-----------------------|-------------|----------|----------|---------|---------|-----------|----------|--------|--------|--------|--------|
| Ol | Cpx | Opx | Hbl | Pl | Kfs | Bt | Ap | Mag | Ilm | Zrn | Rt | Grt | OUTPUT |
| Basalt | | SiO ₂ wt.% | < 52 | | | | | | | | | | TOTAL |
| | | | | | | | | | | | | | 0.0 |
| #DIV/O! | ##### | #DIV/O! | #DIV/O! | ##### | #DIV/O! | ##### | ##### | ##### | ##### | ##### | ##### | ##### | ##### |
| Basaltic Andesite | | SiO2 wt.% | > 52 & < 57 | | | | | | | | | | |
| 5.7 | 9.5 | 1.9 | 19.0 | 57.0 | 0.0 | 0.0 | 0.19 | 5.70 | 0.95 | | | | 100.0 |
| 5.7 | 9.5 | 1.9 | 19.0 | 57.0 | | | 0.19 | 5.70 | 0.95 | | | | 100 % |
| Andesite | | SiO2 wt.% | > 57 & < 63 | | | | | | | | | | |
| 1.2 | 6.2 | 1.2 | 37.2 | 49.6 | 0.0 | 0.0 | 0.12 | 3.72 | 0.62 | 0.01 | | | 100.0 |
| 1.2 | 6.2 | 1.2 | 37.2 | 49.6 | | | 0.12 | 3.72 | 0.62 | 0.01 | | | 100 % |
| Dacite / Rhyolite | | SiO2 wt.% | > 63 | | | | | | | | | | |
| | | | | | | | | | | | | | 0.0 |
| #DIV/O! | ##### | #DIV/O! | #DIV/O! | ##### | #DIV/O! | ##### | ##### | ##### | ##### | ##### | ##### | ##### | ##### |
| Olivine | Clinopyrox | Orthopyrox | Hornblende | Plagiocl | K-Feldsp | Biotite | Apatite | Magnetite | ilmenite | Zircon | Rutile | Garnet | |

| Assimilation ($r = M_d/M_c$) | | Split model when SiO ₂ wt.% > | 52 |
|--------------------------------|----------|--|-------|
| Liquid SiO ₂ wt% | $r (<1)$ | Split model when SiO ₂ wt.% > | 57 |
| < 52 | 0 | Split model when SiO ₂ wt.% > | 63 |
| > 52 & < 57 | 0 | Target SiO ₂ | 62.61 |
| > 57 & < 63 | 0 | | |
| > 63 | 0 | | |

| Batch Modal Melting (Trace El.) | |
|---------------------------------|-----|
| $F_{\text{Assimilant}}$ | 0.1 |

Only phases fractionated in the model displayed

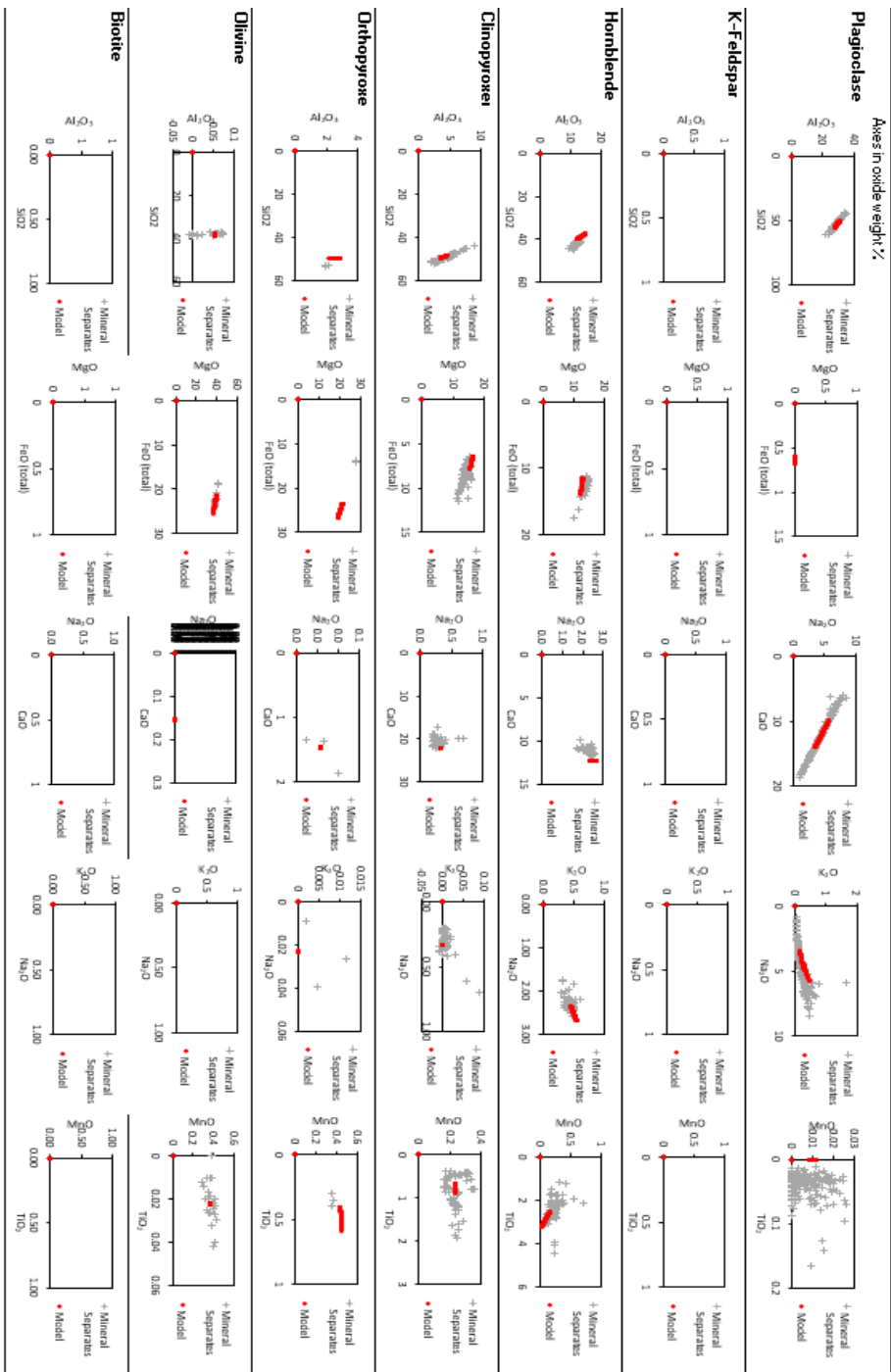
Experimental Values

| Two-Component Partition Coefficients | | | | | Min | Max | Mean |
|---|------|------------------------|------------------|--|------|------|------|
| Plagioclase $K_D = (Al^{Plag} \times Si^{Liq}) / (Si^{Plag} \times Al^{Liq})$ | 2.46 | All SiO | <Not used in mod | | 1.79 | 4.20 | 2.46 |
| Plagioclase $K_D = (Al^{Plag} \times Si^{Liq}) / (Si^{Plag} \times Al^{Liq})$ | 2.01 | SiO ₂ wt% < | 52 | | | | |
| Plagioclase $K_D = (Al^{Plag} \times Si^{Liq}) / (Si^{Plag} \times Al^{Liq})$ | 1.79 | SiO ₂ wt% > | 52 | | 1.79 | 2.22 | 2.01 |
| Plagioclase $K_D = (Al^{Plag} \times Si^{Liq}) / (Si^{Plag} \times Al^{Liq})$ | 1.90 | SiO ₂ wt% > | 57 | | 1.90 | 2.85 | 2.31 |
| Plagioclase $K_D = (Al^{Plag} \times Si^{Liq}) / (Si^{Plag} \times Al^{Liq})$ | 2.80 | SiO ₂ wt% > | 63 | | 2.05 | 4.20 | 2.80 |
| Plagioclase $K_D = (K^{Plag} \times Na^{Liq}) / (Na^{Plag} \times K^{Liq})$ | 0.09 | | | | 0.03 | 0.19 | 0.09 |
| K-Feldspar $K_D = (K^{Kfs} \times Na^{Liq}) / (Na^{Kfs} \times K^{Liq})$ | 7.00 | (estimate from graphs) | | | | | |
| Hornblende $K_D = (Fe^{Hb} \times Mg^{Liq}) / (Mg^{Hb} \times Fe^{Liq})$ | 0.23 | | | | 0.23 | 0.53 | 0.36 |
| Hornblende $K_D = (Al^{Hb} \times Si^{Liq}) / (Si^{Hb} \times Al^{Liq})$ | 1.13 | | | | 0.26 | 1.60 | 1.13 |
| Clinopyroxene $K_D = (Fe^{Cpx} \times Mg^{Liq}) / (Mg^{Cpx} \times Fe^{Liq})$ | 0.10 | | | | 0.20 | 0.51 | 0.28 |
| Clinopyroxene $K_D = (Al^{Cpx} \times Si^{Liq}) / (Si^{Cpx} \times Al^{Liq})$ | 0.30 | | | | 0.12 | 0.68 | 0.27 |
| Orthopyroxene $K_D = (Fe^{Opx} \times Mg^{Liq}) / (Mg^{Opx} \times Fe^{Liq})$ | 0.28 | | | | 0.20 | 0.53 | 0.28 |
| Orthopyroxene $K_D = (Al^{Opx} \times Si^{Liq}) / (Si^{Opx} \times Al^{Liq})$ | 0.19 | | | | 0.07 | 0.52 | 0.19 |
| Olivine $K_D = (Fe^{Ol} \times Mg^{Liq}) / (Mg^{Ol} \times Fe^{Liq})$ | 0.32 | | | | 0.24 | 0.33 | 0.28 |
| Biotite $K_D = (Al^{Bt} \times Si^{Liq}) / (Si^{Bt} \times Al^{Liq})$ | 2.52 | | | | 2.52 | 2.52 | 2.52 |
| Garnet $K_D = (Fe^{Grt} \times Mg^{Liq}) / (Mg^{Grt} \times Fe^{Liq})$ | 0.97 | | | | 0.60 | 1.59 | 0.97 |

| D ² (Model Error) | | | | | | | | | | | | |
|------------------------------|------------------|--------------------------------|--------------------|------|------|------|-------------------|------------------|-------------------------------|--|--------------|---------------------------------|
| SiO ₂ | TiO ₂ | Al ₂ O ₃ | FeO _{tot} | MnO | MgO | CaO | Na ₂ O | K ₂ O | P ₂ O ₅ | | ΣD^2 | $\Sigma D^2 \text{ exc. SiO}_2$ |
| 0.02 | 0.00 | 0.11 | 0.26 | 0.01 | 0.04 | 0.50 | 0.05 | 0.00 | 0.01 | | 1.00 | 0.98 |

(based on 100% normalised values)

| Modelled Melt Major Elements (wt %) | | | | | | | | | | | Isotopes | | | | | | | | | |
|-------------------------------------|------------------|--------------------------------|--------------------|------|------|------|-------------------|------------------|-------------------------------|-------|----------|---------|---------|---------|-----------|-----------|------------------|------------------|------------------|----|
| SiO ₂ | TiO ₂ | Al ₂ O ₃ | FeO _{tot} | MnO | MgO | CaO | Na ₂ O | K ₂ O | P ₂ O ₅ | TOTAL | 206/204 | 207/204 | 208/204 | 87/86Sr | 143/144Nd | 176/177Hf | $\delta^{18}O$ ‰ | $\delta^{19}O$ ‰ | $\delta^{42}O$ ‰ | Zn |
| 62.47 | 0.61 | 16.94 | 5.19 | 0.23 | 2.35 | 4.64 | 4.05 | 2.11 | 0.45 | 99.04 | 0.00 | 0.00 | 0.00 | 0.00 | 0.00 | 0.00 | #DIV/O! | #DIV/O! | #DIV/O! | |



D.2.3 Modelling the enclave with apatite

| Fractionating Assemblage | | | | | | | | | | | | | INPUT | |
|--------------------------|------------|------------|-----------------------|----------|-------------|---------|---------|----------|----------|--------|--------|--------|--------|-------|
| Ol | Cpx | Opx | Hbl | Pl | Kfs | Bt | Ap | Mag | Ilm | Zrn | Rt | Grt | OUTPUT | |
| Basalt | | | SiO ₂ wt.% | | < 52 | | | | | | | | | TOTAL |
| | | | | | | | | | | | | | 0.0 | |
| #DIV/O! | ##### | #DIV/O! | #DIV/O! | ##### | #DIV/O! | ##### | ##### | ##### | ##### | ##### | ##### | ##### | ##### | |
| Basaltic Andesite | | | SiO ₂ wt.% | | > 52 & < 57 | | | | | | | | | |
| 5.7 | 9.5 | | 22.0 | 53.0 | 0.0 | 0.0 | 0.57 | 5.68 | 0.95 | | | | 97.3 | |
| 5.8 | 9.7 | | 22.6 | 54.4 | | | 0.58 | 5.84 | 0.97 | | | | 100 % | |
| Andesite | | | SiO ₂ wt.% | | > 57 & < 63 | | | | | | | | | |
| 1.2 | 6.2 | 1.2 | 37.1 | 55.0 | 0.0 | 0.0 | 0.60 | 3.71 | 0.62 | 0.01 | | | 105.7 | |
| 1.2 | 5.8 | 1.2 | 35.1 | 52.0 | | | 0.57 | 3.51 | 0.58 | 0.01 | | | 100 % | |
| Dacite / Rhyolite | | | SiO ₂ wt.% | | > 63 | | | | | | | | | |
| | | | | | | | | | | | | | 0.0 | |
| #DIV/O! | ##### | #DIV/O! | #DIV/O! | ##### | #DIV/O! | ##### | ##### | ##### | ##### | ##### | ##### | ##### | ##### | |
| Olivine | Clinopyrox | Orthopyrox | Hornblende | Plagiocl | K-Feldsp | Biotite | Apatite | Magnetit | ilmenite | Zircon | Rutile | Garnet | | |

| | | | | |
|--------------------------------|----------|--|---|--|
| Assimilation ($r = M_d/M_c$) | | | Split model when SiO ₂ wt.% > 52 | |
| Liquid SiO ₂ wt% | $r (<1)$ | | Split model when SiO ₂ wt.% > 57 | |
| < 52 | 0 | | Split model when SiO ₂ wt.% > 63 | |
| > 52 & < 57 | 0 | | Target SiO ₂ | |
| > 57 & < 63 | 0 | | 62.61 | |
| > 63 | 0 | | | |
| | | | Batch Modal Melting (Trace El.) | |
| | | | $F_{\text{Assimilan}}$ 0.1 | |

Only phases fractionated in the model displayed

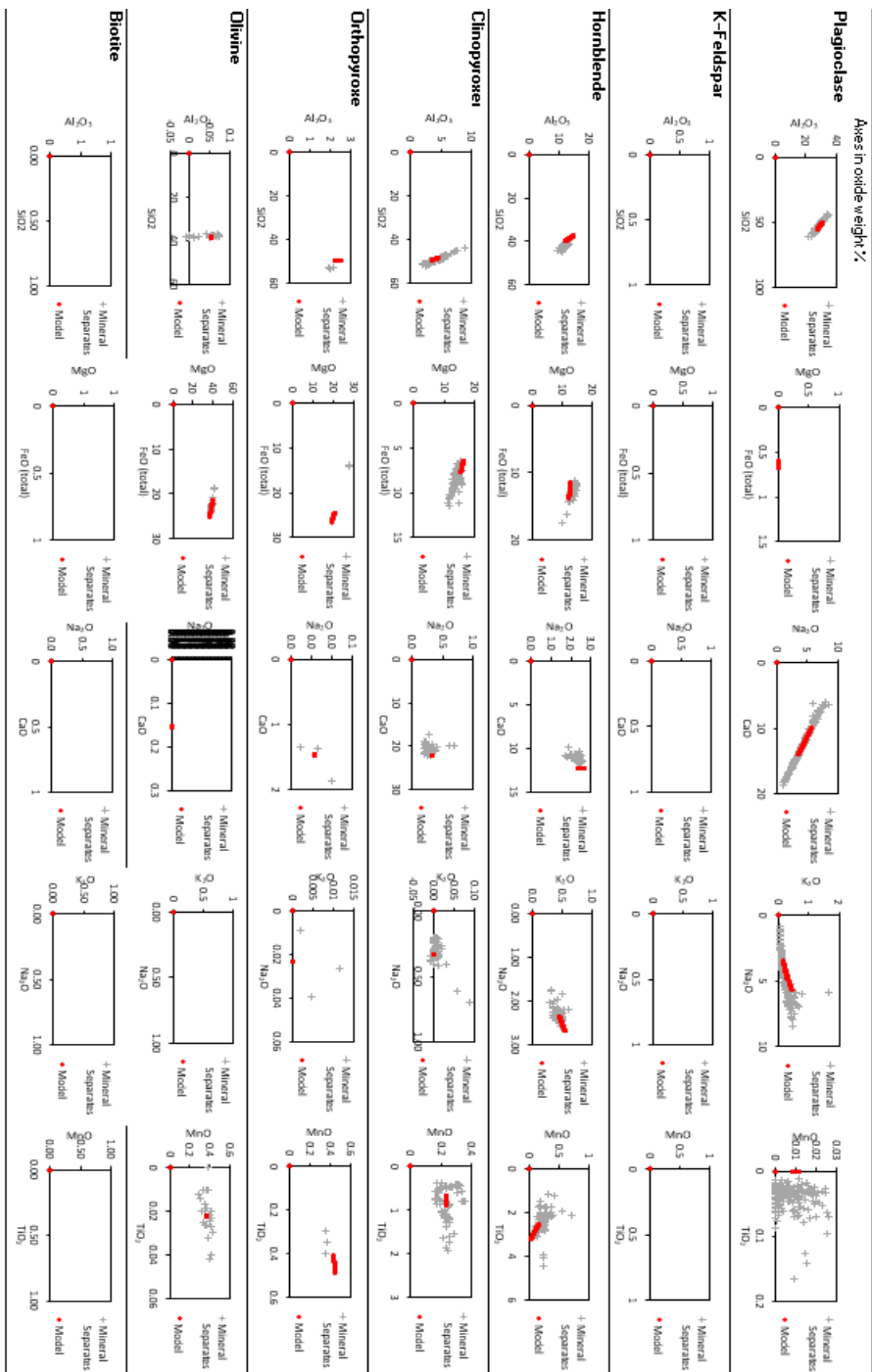
Experimental Values

| Two-Component Partition Coefficients | | | | Min | Max | Mean |
|---|------|---------------------------|-------------------|------|------|------|
| Plagioclase $K_D = (Al^{Plag} \times Si^{Liq}) / (Si^{Plag} \times Al^{Liq})$ | 2.46 | All SiO | <-Not used in mod | 1.79 | 4.20 | 2.46 |
| Plagioclase $K_D = (Al^{Plag} \times Si^{Liq}) / (Si^{Plag} \times Al^{Liq})$ | 2.01 | SiO ₂ wt% < 52 | | | | |
| Plagioclase $K_D = (Al^{Plag} \times Si^{Liq}) / (Si^{Plag} \times Al^{Liq})$ | 1.79 | SiO ₂ wt% > 52 | | 1.79 | 2.22 | 2.01 |
| Plagioclase $K_D = (Al^{Plag} \times Si^{Liq}) / (Si^{Plag} \times Al^{Liq})$ | 1.90 | SiO ₂ wt% > 57 | | 1.90 | 2.85 | 2.31 |
| Plagioclase $K_D = (Al^{Plag} \times Si^{Liq}) / (Si^{Plag} \times Al^{Liq})$ | 2.80 | SiO ₂ wt% > 63 | | 2.05 | 4.20 | 2.80 |
| Plagioclase $K_D = (K^{Plag} \times Na^{Liq}) / (Na^{Plag} \times K^{Liq})$ | 0.09 | | | 0.03 | 0.19 | 0.09 |
| K-Feldspar $K_D = (K^{Kfs} \times Na^{Liq}) / (Na^{Kfs} \times K^{Liq})$ | 7.00 | (estimate from graphs) | | | | |
| Hornblende $K_D = (Fe^{Hb} \times Mg^{Liq}) / (Mg^{Hb} \times Fe^{Liq})$ | 0.23 | | | 0.23 | 0.53 | 0.36 |
| Hornblende $K_D = (Al^{Hb} \times Si^{Liq}) / (Si^{Hb} \times Al^{Liq})$ | 1.13 | | | 0.26 | 1.60 | 1.13 |
| Clinopyroxel $K_D = (Fe^{Cpx} \times Mg^{Liq}) / (Mg^{Cpx} \times Fe^{Liq})$ | 0.10 | | | 0.20 | 0.51 | 0.28 |
| Clinopyroxel $K_D = (Al^{Cpx} \times Si^{Liq}) / (Si^{Cpx} \times Al^{Liq})$ | 0.30 | | | 0.12 | 0.68 | 0.27 |
| Orthopyroxel $K_D = (Fe^{Opx} \times Mg^{Liq}) / (Mg^{Opx} \times Fe^{Liq})$ | 0.28 | | | 0.20 | 0.53 | 0.28 |
| Orthopyroxel $K_D = (Al^{Opx} \times Si^{Liq}) / (Si^{Opx} \times Al^{Liq})$ | 0.19 | | | 0.07 | 0.52 | 0.19 |
| Olivine $K_D = (Fe^{Ol} \times Mg^{Liq}) / (Mg^{Ol} \times Fe^{Liq})$ | 0.32 | | | 0.24 | 0.33 | 0.28 |
| Biotite $K_D = (Al^{Bt} \times Si^{Liq}) / (Si^{Bt} \times Al^{Liq})$ | 2.52 | | | 2.52 | 2.52 | 2.52 |
| Garnet $K_D = (Fe^{Grt} \times Mg^{Liq}) / (Mg^{Grt} \times Fe^{Liq})$ | 0.97 | | | 0.60 | 1.59 | 0.97 |

| D ² (Model Error) | | | | | | | | | | | | |
|------------------------------|------------------|--------------------------------|--------|------|------|------|-------------------|------------------|-------------------------------|--|--------------|---------------------------------|
| SiO ₂ | TiO ₂ | Al ₂ O ₃ | FeOtot | MnO | MgO | CaO | Na ₂ O | K ₂ O | P ₂ O ₅ | | ΣD^2 | $\Sigma D^2 \text{ exc. SiO}_2$ |
| 0.01 | 0.01 | 0.19 | 0.02 | 0.01 | 0.16 | 0.93 | 0.07 | 0.00 | 0.03 | | 1.45 | 1.43 |

(based on 100% normalised values)

| Modelled Melt Major Elements (wt %) | | | | | | | | | | | Isotopes | | | | | | | | | |
|-------------------------------------|------------------|--------------------------------|--------|------|------|------|-------------------|------------------|-------------------------------|-------|----------|---------|---------|---------|-----------|-----------|--------------------------|--------------------------|---------|--|
| SiO ₂ | TiO ₂ | Al ₂ O ₃ | FeOtot | MnO | MgO | CaO | Na ₂ O | K ₂ O | P ₂ O ₅ | TOTAL | 206/204 | 207/204 | 208/204 | 87/86Sr | 143/144Nd | 176/177Hf | $\delta^{18}O \text{ ‰}$ | $\delta^{15}O \text{ ‰}$ | Zn | |
| 62.49 | 0.54 | 17.05 | 5.55 | 0.24 | 2.56 | 4.39 | 4.02 | 2.03 | 0.17 | 99.04 | 0.00 | 0.00 | 0.00 | 0.00 | 0.00 | 0.00 | 0.00 | #DIV/O! | #DIV/O! | |



D.2.4 Modelling of the low-K LCY rhyolite

| Fractionating Assemblage | | | | | | | | | | | | | INPUT | |
|--------------------------|------------|-----------------------|-------------|----------|----------|---------|---------|--------|----------|--------|--------|--------|--------|-------|
| Ol | Cpx | Opx | Hbl | Pl | Kfs | Bt | Ap | Mag | Ilm | Zrn | Rt | Grt | OUTPUT | |
| Basalt | | SiO ₂ wt.% | < 62 | | | | | | | | | | | TOTAL |
| 1.2 | 1.2 | 6.1 | 24.3 | 60.8 | 0.0 | 0.0 | 0.61 | 4.87 | 0.85 | 0.00 | | | 100.0 | |
| 1.2 | 1.2 | 6.1 | 24.3 | 60.8 | | | 0.61 | 4.87 | 0.85 | | | | 100 % | |
| Basaltic Andesite | | SiO ₂ wt.% | > 62 & < 67 | | | | | | | | | | | |
| | | 6.2 | 24.8 | 61.9 | 0.0 | 0.0 | 1.24 | 4.96 | 0.87 | 0.02 | | | 100.0 | |
| | | 6.2 | 24.8 | 61.9 | | | 1.24 | 4.96 | 0.87 | 0.02 | | | 100 % | |
| Andesite | | SiO ₂ wt.% | > 67 & < 72 | | | | | | | | | | | |
| | | 4.5 | 33.4 | 55.7 | 0.0 | 0.0 | 1.11 | 4.45 | 0.89 | 0.02 | | | 100.0 | |
| | | 4.5 | 33.4 | 55.7 | | | 1.11 | 4.45 | 0.89 | 0.02 | | | 100 % | |
| Dacite / Rhyolite | | SiO ₂ wt.% | > 72 | | | | | | | | | | | |
| | | 37.7 | 56.6 | 0.0 | 0.0 | 0.94 | 3.77 | 0.94 | 0.02 | | | 100.0 | | |
| | | 37.7 | 56.6 | | | 0.94 | 3.77 | 0.94 | 0.02 | | | | 100 % | |
| Olivine | Clinopyrox | Orthopyrox | Hornblende | Plagiocl | K-Feldsp | Biotite | Apatite | Magnet | ilmenite | Zircon | Rutile | Garnet | | |

| | | | |
|--------------------------------|----------|--|-------|
| Assimilation ($r = M_a/M_c$) | | Split model when SiO ₂ wt.% > | 62 |
| Liquid SiO ₂ wt% | $r (<1)$ | Split model when SiO ₂ wt.% > | 67 |
| < 62 | 0 | Split model when SiO ₂ wt.% > | 72 |
| > 62 & < 67 | 0 | Target SiO ₂ | 76.24 |
| > 67 & < 63 | 0 | | |
| > 72 | 0 | | |

| | |
|---------------------------------|-----|
| Batch Modal Melting (Trace El.) | |
| $F_{\text{Assimilant}}$ | 0.1 |

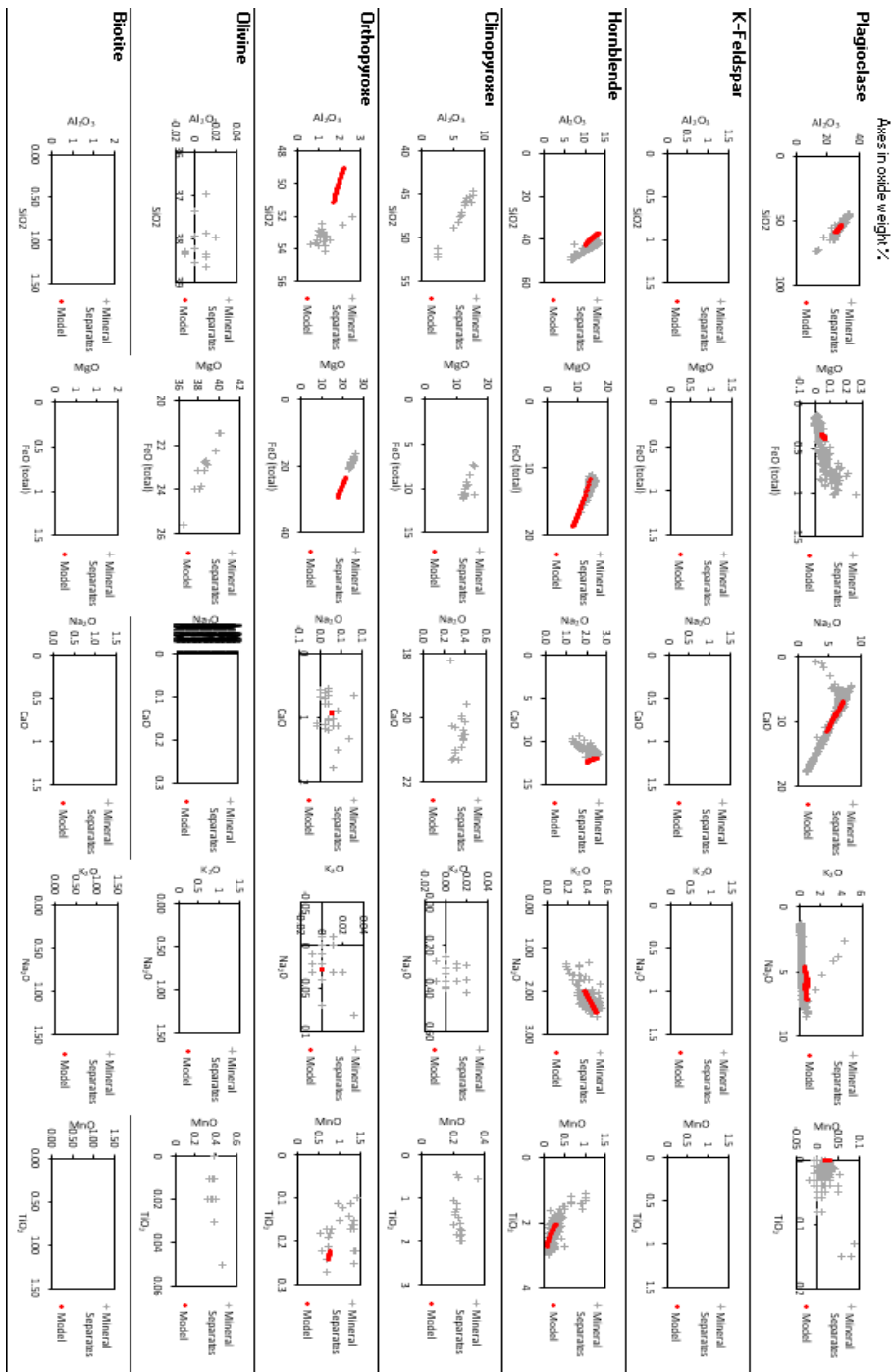
Only phases fractionated in the model displayed

Experimental Values

| Two-Component Partition Coefficients | | | | | | Min | Max | Mean |
|---|------|------------------------|------------------|--|--|------|------|------|
| Plagioclase $K_D = (Al^{Plag} \times Si^{Liq}) / (Si^{Plag} \times Al^{Liq})$ | 2.46 | All SiO | <Not used in mod | | | 1.79 | 4.20 | 2.46 |
| Plagioclase $K_D = (Al^{Plag} \times Si^{Liq}) / (Si^{Plag} \times Al^{Liq})$ | 2.38 | SiO ₂ wt% | < 62 | | | | | |
| Plagioclase $K_D = (Al^{Plag} \times Si^{Liq}) / (Si^{Plag} \times Al^{Liq})$ | 1.90 | SiO ₂ wt% | > 62 | | | 1.90 | 3.24 | 2.38 |
| Plagioclase $K_D = (Al^{Plag} \times Si^{Liq}) / (Si^{Plag} \times Al^{Liq})$ | 2.46 | SiO ₂ wt% | > 67 | | | 2.46 | 4.20 | 3.25 |
| Plagioclase $K_D = (Al^{Plag} \times Si^{Liq}) / (Si^{Plag} \times Al^{Liq})$ | 2.72 | SiO ₂ wt% | > 72 | | | 2.72 | 3.06 | 2.90 |
| Plagioclase $K_D = (K^{Plag} \times Na^{Liq}) / (Na^{Plag} \times K^{Liq})$ | 0.09 | | | | | 0.03 | 0.19 | 0.09 |
| K-Feldspar $K_D = (K^{Kfs} \times Na^{Liq}) / (Na^{Kfs} \times K^{Liq})$ | 7.00 | (estimate from graphs) | | | | | | |
| Hornblende $K_D = (Fe^{Hb} \times Mg^{Liq}) / (Mg^{Hb} \times Fe^{Liq})$ | 0.36 | | | | | 0.23 | 0.53 | 0.36 |
| Hornblende $K_D = (Al^{Hb} \times Si^{Liq}) / (Si^{Hb} \times Al^{Liq})$ | 1.40 | | | | | 0.26 | 1.60 | 1.13 |
| Clinopyroxene $K_D = (Fe^{Cpx} \times Mg^{Liq}) / (Mg^{Cpx} \times Fe^{Liq})$ | 0.28 | | | | | 0.20 | 0.51 | 0.28 |
| Clinopyroxene $K_D = (Al^{Cpx} \times Si^{Liq}) / (Si^{Cpx} \times Al^{Liq})$ | 0.27 | | | | | 0.12 | 0.68 | 0.27 |
| Orthopyroxene $K_D = (Fe^{Opx} \times Mg^{Liq}) / (Mg^{Opx} \times Fe^{Liq})$ | 0.28 | | | | | 0.20 | 0.53 | 0.28 |
| Orthopyroxene $K_D = (Al^{Opx} \times Si^{Liq}) / (Si^{Opx} \times Al^{Liq})$ | 0.19 | | | | | 0.07 | 0.52 | 0.19 |
| Olivine $K_D = (Fe^{Ol} \times Mg^{Liq}) / (Mg^{Ol} \times Fe^{Liq})$ | 0.28 | | | | | 0.24 | 0.33 | 0.28 |
| Biotite $K_D = (Al^{Bt} \times Si^{Liq}) / (Si^{Bt} \times Al^{Liq})$ | 2.52 | | | | | 2.52 | 2.52 | 2.52 |
| Garnet $K_D = (Fe^{Grt} \times Mg^{Liq}) / (Mg^{Grt} \times Fe^{Liq})$ | 0.97 | | | | | 0.60 | 1.59 | 0.97 |

| | | | | | | | | | | | | | |
|------------------------------|------------------|--------------------------------|--------------------|------|------|------|-------------------|------------------|-------------------------------|------|------|-----------------------------------|---------------------------------|
| D ² (Model Error) | | | | | | | | | | | | | |
| SiO ₂ | TiO ₂ | Al ₂ O ₃ | FeO _{tot} | MnO | MgO | CaO | Na ₂ O | K ₂ O | P ₂ O ₅ | | | ΣD^2 | $\Sigma D^2 \text{ exc. SiO}_2$ |
| 0.01 | 0.00 | 0.08 | 0.78 | 0.01 | 0.01 | 0.37 | 0.00 | 0.82 | 0.03 | 2.11 | 2.10 | (based on 100% normalised values) | |

| Modelled Melt Major Elements (wt %) | | | | | | | | | | | Isotopes | | | | | | | | |
|-------------------------------------|------------------|--------------------------------|--------------------|------|------|------|-------------------|------------------|-------------------------------|-------|----------|---------|---------|---------|-----------|-----------|---------------------|---------------------|--|
| SiO ₂ | TiO ₂ | Al ₂ O ₃ | FeO _{tot} | MnO | MgO | CaO | Na ₂ O | K ₂ O | P ₂ O ₅ | TOTAL | 206/204 | 207/204 | 208/204 | 87/86Sr | 143/144Nd | 176/177Hf | δ ¹⁸ O ‰ | δ ¹³ C ‰ | |
| 76.15 | 0.13 | 13.48 | 0.42 | 0.16 | 0.43 | 1.08 | 4.25 | 3.62 | 0.22 | 99.94 | 0.00 | 0.00 | 0.00 | 0.00 | 0.00 | 0.00 | #DIV/0! | #DIV/0! | |



D.2.5 Modelling of the high-K LCY rhyolite

| Fractionating Assemblage | | | | | | | | | | | | | INPUT |
|--------------------------|---------------|-----------------------|----------------|------|------------|---------|---------|-----------|----------|--------|--------|--------|--------|
| Ol | Cpx | Opx | Hbl | Pl | Kfs | Bt | Ap | Mag | Ilm | Zrn | Rt | Grt | OUTPUT |
| Basalt | | SiO ₂ wt.% | < 66 | | | | | | | | | | TOTAL |
| 0.0 | | 5.1 | 38.8 | 41.0 | 0.0 | 5.0 | 0.60 | 3.00 | 0.00 | 0.02 | | | 93.5 |
| | | 5.5 | 41.5 | 43.8 | | 5.3 | 0.64 | 3.21 | | 0.02 | | | 100 % |
| Basaltic Andesite | | SiO ₂ wt.% | > 66 & < 70 | | | | | | | | | | |
| | | 0.0 | 38.8 | 46.0 | 0.0 | 9.7 | 0.60 | 4.00 | 0.00 | 0.02 | | | 99.1 |
| | | | 39.1 | 46.4 | | 9.8 | 0.61 | 4.04 | | 0.02 | | | 100 % |
| Andesite | | SiO ₂ wt.% | > 70 & < 74 | | | | | | | | | | |
| 0.0 | 0.0 | 0.0 | 19.5 | 65.5 | 0.0 | 14.7 | 0.34 | 3.00 | 0.50 | 0.01 | | | 103.5 |
| | | | 18.9 | 63.2 | | 14.2 | 0.33 | 2.90 | 0.48 | 0.01 | | | 100 % |
| Dacite / Rhyolite | | SiO ₂ wt.% | > 74 | | | | | | | | | | |
| | | 0.0 | 7.0 | 68.7 | 0.0 | 17.0 | 0.33 | 3.00 | 0.50 | 0.01 | 0.00 | 0.00 | 96.6 |
| | | | 7.2 | 71.2 | | 17.6 | 0.35 | 3.11 | 0.52 | 0.01 | | | 100 % |
| Olivine | Clinopyroxene | Orthopyroxene | 13 Plagioclase | | K-Feldspar | Biotite | Apatite | Magnetite | Ilmenite | Zircon | Rutile | Garnet | |

| | | |
|--------------------------------|----------|--|
| Assimilation ($r = M_a/M_c$) | | |
| Liquid SiO ₂ wt% | r (<1) | |
| < 66 | 0 | |
| > 66 & < 70 | 0 | |
| > 70 & < 69 | 0 | |
| > 74 | 0 | |

| | |
|--|-------|
| Split model when SiO ₂ wt.% > | 66 |
| Split model when SiO ₂ wt.% > | 70 |
| Split model when SiO ₂ wt.% > | 74 |
| Target SiO ₂ | 77.16 |

| | |
|---------------------------------|---|
| Batch Modal Melting (Trace El.) | |
| $F_{\text{Assimilant}}$ | 0 |

Only phases fractionated in the model displayed

Experimental Values

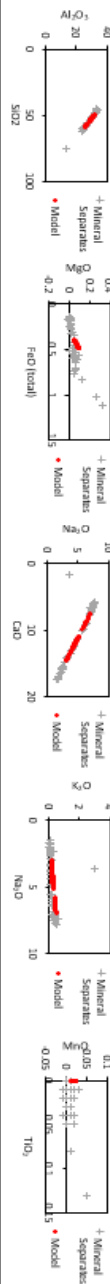
| Two-Component Partition Coefficients | | | | | Min | Max | Mean |
|---|------|---------------------------|--|--|------|------|------|
| Plagioclase $K_D = (Al^{Plag} \times Si^{Liq}) / (Si^{Plag} \times Al^{Liq})$ | 2.46 | All SiO <-Not used in mod | | | 1.79 | 4.20 | 2.46 |
| Plagioclase $K_D = (Al^{Plag} \times Si^{Liq}) / (Si^{Plag} \times Al^{Liq})$ | 2.30 | SiO ₂ wt% < 66 | | | | | |
| Plagioclase $K_D = (Al^{Plag} \times Si^{Liq}) / (Si^{Plag} \times Al^{Liq})$ | 2.46 | SiO ₂ wt% > 66 | | | 2.46 | 4.20 | 3.25 |
| Plagioclase $K_D = (Al^{Plag} \times Si^{Liq}) / (Si^{Plag} \times Al^{Liq})$ | 3.02 | SiO ₂ wt% > 70 | | | 3.02 | 3.02 | 3.02 |
| Plagioclase $K_D = (Al^{Plag} \times Si^{Liq}) / (Si^{Plag} \times Al^{Liq})$ | 2.72 | SiO ₂ wt% > 74 | | | 2.72 | 3.06 | 2.86 |
| Plagioclase $K_D = (K^{Plag} \times Na^{Liq}) / (Na^{Plag} \times K^{Liq})$ | 0.03 | | | | 0.03 | 0.19 | 0.09 |
| K-Feldspar $K_D = (K^{Kfs} \times Na^{Liq}) / (Na^{Kfs} \times K^{Liq})$ | 2.00 | (estimate from graphs) | | | | | |
| Hornblende $K_D = (Fe^{Hbl} \times Mg^{Liq}) / (Mg^{Hbl} \times Fe^{Liq})$ | 0.53 | | | | 0.23 | 0.53 | 0.36 |
| Hornblende $K_D = (Al^{Hbl} \times Si^{Liq}) / (Si^{Hbl} \times Al^{Liq})$ | 1.13 | | | | 0.26 | 1.60 | 1.13 |
| Clinopyroxene $K_D = (Fe^{Cpx} \times Mg^{Liq}) / (Mg^{Cpx} \times Fe^{Liq})$ | 0.20 | | | | 0.20 | 0.51 | 0.28 |
| Clinopyroxene $K_D = (Al^{Cpx} \times Si^{Liq}) / (Si^{Cpx} \times Al^{Liq})$ | 0.27 | | | | 0.12 | 0.68 | 0.27 |
| Orthopyroxene $K_D = (Fe^{Opx} \times Mg^{Liq}) / (Mg^{Opx} \times Fe^{Liq})$ | 0.20 | | | | 0.20 | 0.53 | 0.28 |
| Orthopyroxene $K_D = (Al^{Opx} \times Si^{Liq}) / (Si^{Opx} \times Al^{Liq})$ | 0.07 | | | | 0.07 | 0.52 | 0.19 |
| Olivine $K_D = (Fe^{Ol} \times Mg^{Liq}) / (Mg^{Ol} \times Fe^{Liq})$ | 0.29 | | | | 0.24 | 0.33 | 0.28 |
| Biotite $K_D = (Al^{Bt} \times Si^{Liq}) / (Si^{Bt} \times Al^{Liq})$ | 2.52 | | | | 2.52 | 2.52 | 2.52 |
| Garnet $K_D = (Fe^{Grt} \times Mg^{Liq}) / (Mg^{Grt} \times Fe^{Liq})$ | 0.97 | | | | 0.60 | 1.59 | 0.97 |

| D ² (Model Error) | | | | | | | | | | | ΣD ² | ΣD ² exc. SiO ₂ | (based on 100% normalised values) |
|------------------------------|------------------|--------------------------------|--------|------|------|------|-------------------|------------------|-------------------------------|------|-----------------|---------------------------------------|-----------------------------------|
| SiO ₂ | TiO ₂ | Al ₂ O ₃ | FeOtot | MnO | MgO | CaO | Na ₂ O | K ₂ O | P ₂ O ₅ | | 0.04 | 0.04 | |
| 0.00 | 0.00 | 0.00 | 0.00 | 0.00 | 0.00 | 0.01 | 0.00 | 0.01 | 0.01 | 0.00 | | | |

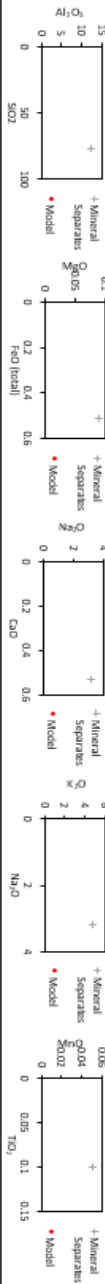
| Modelled Melt Major Elements (wt %) | | | | | | | | | | | Isotopes | | | | | | | | |
|-------------------------------------|------------------|--------------------------------|--------|------|------|------|-------------------|------------------|-------------------------------|-------|----------|----------|----------|---------|-----------|-----------|----------------------|-----------------------|--|
| SiO ₂ | TiO ₂ | Al ₂ O ₃ | FeOtot | MnO | MgO | CaO | Na ₂ O | K ₂ O | P ₂ O ₅ | TOTAL | 206/204I | 207/204I | 208/204I | 87/86Sr | 143/144Nd | 176/177Hf | δ ¹⁸ O WR | δ ¹⁸ O Zrn | |
| 77.15 | 0.09 | 13.01 | 0.69 | 0.08 | 0.22 | 0.66 | 3.51 | 4.54 | 0.03 | 99.98 | 0.00 | 0.00 | 0.00 | 0.00 | 0.00 | 0.00 | #DIV/0! | #DIV/0! | |

Axes in oxide weight %

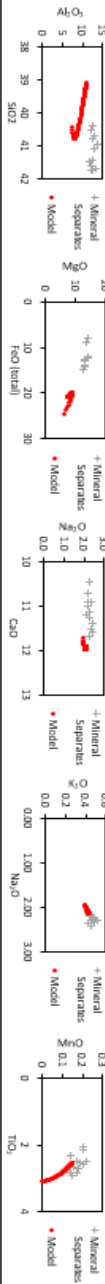
Plagioclase



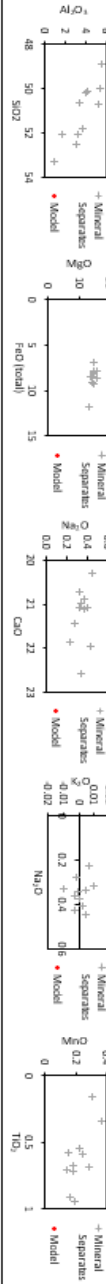
K-Feldspar



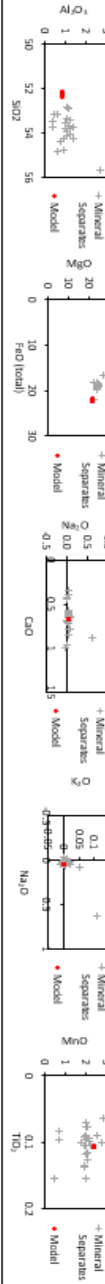
Hornblende



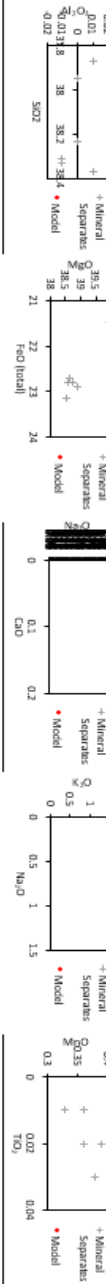
Chinopyroxene



Orthopyroxene



Olivine



Biotite



Electronic Appendices

The links to the Electronic Appendices are provided here:

Electronic Appendix I: Digital sample map

<https://www.google.com/maps/d/edit?mid=1fYzgMetl6zLkyvrJVnynZy5NzjZj9Pc&usp=sharing>

Electronic Appendix II: Microanalysis compositions

https://1drv.ms/f/c/7d917b0c08c04e4a/EhTDG54rBbBCv-MJZVdsJu4B550q3b-U4Ko_xyqVJzfDnw?e=ri1k33

Electronic Appendix III: EME-AFC spreadsheets

<https://1drv.ms/f/c/7d917b0c08c04e4a/EiHSG-QcielAolj-iUQ07vABEvu2bENG0zFrLQQC8aBuOQ?e=NjQNVY>